Mechanistic enzymology of short-form ATP phosphoribosyltransferase and bifunctional phosphoribosyl-ATP pyrophosphohydrolase/ phosphoribosyl-AMP cyclohydrolase

Gemma Fisher

A thesis submitted for the degree of PhD
at the
University of St Andrews

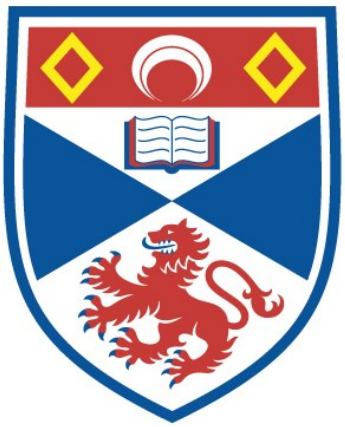

2022

Candidate's declaration

I, Gemma Fisher, do hereby certify that this thesis, submitted for the degree of PhD, which is approximately 48,000 words in length, has been written by me, and that it is the record of work carried out by me, or principally by myself in collaboration with others as acknowledged, and that it has not been submitted in any previous application for any degree. I confirm that any appendices included in my thesis contain only material permitted by the 'Assessment of Postgraduate Research Students' policy.

I was admitted as a research student at the University of St Andrews in September 2017.

I received funding from an organisation or institution and have acknowledged the funder(s) in the full text of my thesis.

Date: 19/09/2022 Signature of candidate

Supervisor's declaration

I hereby certify that the candidate has fulfilled the conditions of the Resolution and Regulations appropriate for the degree of PhD in the University of St Andrews and that the candidate is qualified to submit this thesis in application for that degree. I confirm that any appendices included in the thesis contain only material permitted by the 'Assessment of Postgraduate Research Students' policy.

Date: 19/09/2022 Signature of supervisor

Date: 21/09/2022 Signature of supervisor

Permission for publication

In submitting this thesis to the University of St Andrews we understand that we are giving permission for it to be made available for use in accordance with the regulations of the University Library for the time being in force, subject to any copyright vested in the work not being affected thereby. We also understand, unless exempt by an award of an embargo as requested below, that the title and the abstract will be published, and that a copy of the work may be made and supplied to any bona fide library or research worker, that this thesis will be electronically accessible for personal or research use and that the library has the right to migrate this thesis into new electronic forms as required to ensure continued access to the thesis.

I, Gemma Fisher, confirm that my thesis does not contain any third-party material that requires copyright clearance.

The following is an agreed request by candidate and supervisor regarding the publication of this thesis:

Printed copy

Embargo on all of print copy for a period of 2 years on the following ground(s):

- Publication would preclude future publication

Supporting statement for printed embargo request

The data from my thesis will be included manuscripts currently being drafted for publication.

Electronic copy

Embargo on all of electronic copy for a period of 2 years on the following ground(s):

- Publication would preclude future publication

Supporting statement for electronic embargo request

The data from my thesis will be included manuscripts currently being drafted for publication.

Title and Abstract

- I require an embargo on the abstract only.

Date: 19/09/2022 Signature of candidate

Date: 19/09/2022 Signature of supervisor

Date: 21/09/2022 Signature of supervisor

Underpinning Research Data or Digital Outputs

Candidate's declaration

I, Gemma Fisher, understand that by declaring that I have original research data or digital outputs, I should make every effort in meeting the University's and research funders' requirements on the deposit and sharing of research data or research digital outputs.

Date: 19/09/2022 Signature of candidate

Permission for publication of underpinning research data or digital outputs

We understand that for any original research data or digital outputs which are deposited, we are giving permission for them to be made available for use in accordance with the requirements of the University and research funders, for the time being in force.

We also understand that the title and the description will be published, and that the underpinning research data or digital outputs will be electronically accessible for use in accordance with the license specified at the point of deposit, unless exempt by award of an embargo as requested below.

The following is an agreed request by candidate and supervisor regarding the publication of underpinning research data or digital outputs:

No embargo on underpinning research data or digital outputs.

Date: 19/09/2022 Signature of candidate

Date: 19/09/2022 Signature of supervisor

Date: 21/09/2022 Signature of supervisor

Abstract

Adenosine 5′-triphosphate phosphoribosyltransferase (ATPPRT) catalyses the first reaction of the histidine biosynthetic pathway. Short-form ATPPRT, denoted $HisG_S$, is allosterically activated by HisZ, which also mediates histidine feedback inhibition. A $HisG_S$ variant that exhibits a high rate of reaction in the absence of HisZ is desirable for industrial histidine biosynthesis. First, this work sought to define the mechanism underpinning allosteric activation of *Psychrobacter arcticus* $HisG_S$ by HisZ. Knowledge of this mechanism could drive mutagenic strategies to improve turnover by mimicking allosteric activation. The second and third steps of the histidine biosynthetic pathway are catalysed by HisE and HisI, respectively. These enzymes may be encoded by a single polypeptide chain, termed HisIE. HisIE is a possible target for novel antimicrobial development in several multi-drug resistant organisms, including carbapenem-resistant *Acinetobacter baumannii* Secondly, this work sought to initiate biochemical characterisation of HisIE from *A. baumannii* .

This work established binding of HisZ shifts the rate-limiting step of reactions catalysed by $HisG_S$ from interconversion between ternary complexes to product release. Characterisation of $HisG_S$ variants indicated two conserved arginine residues, R32 and R56, are required for stabilisation of the transition state. A model of allosteric activation of $HisG_s$ by HisZ is proposed in which binding of HisZ modifies the conformational sampling of these arginine residues such that conformations with these residues in position to stabilise the transition state are sampled more frequently. This work also documents the first reported characterisations of the steady-state kinetic parameters and the rate-limiting steps of a bifunctional HisIE.

Ultimately, this work suggests efforts to engineer a constitutively activated short-form $HisG_S$ for industrial histidine biosynthesis should seek to introduce mutations which narrow the conformational sampling of R32 and R56. Furthermore, this work has paved the way for future characterisation of the catalytic mechanism of HisIE with a view towards novel antimicrobial development.

Acknowledgements

First and foremost, I would like to thank Dr Rafael G. da Silva for his unwavering support, guidance and encouragement throughout my PhD. I'm especially grateful to him for instilling in me a drive to keep challenging myself (and the science), which has shaped my development as a scientist and a person. I'd also like to thank Prof Rebecca J. M Goss for all of her support and advice over these past years.

I'm especially grateful to those who have taken the time to provide me with training in a variety of techniques. In particular, I'd like to thank Dr Magnus S. Alphey for training in X-ray crystallography, his endless patience was much appreciated. Additionally, Dr Alphey's expertise on the crystal structures of *Pa*HisG$_S$ and *Pa*ATPPRT was invaluable to this work. I'd also like to thank Dr Clarissa. M. Czekster for training in ITC and for all of her scientific advice these past 5 years. Furthermore, I'd like to thank Dr Huanting Liu for sharing his protocol for site-directed mutagenesis.

I must also extend my thanks to Dr Alison Dickson and Greice Zickuhr who performed LC-MS analysis of samples for the HisIE projects. An additional thank you must go to Drs Sally Shirran and Silvia Synowsky from the BSRC Mass Spectrometry Facility who analysed the proteins studied in this work via mass spectrometry.

The data presented in Chapters 3 and 4 was supported by the work of our collaborators, Dr Marina Corbella (Uppsala University), Prof Lynn Kamerlin (Uppsala University), and Dr Jennifer S. Hirschi (Binghampton University). I thank our collaborators for their exceptionally hard work and for sharing their results with us – I've learned a lot from these collaborations!

A special thank you must go to members past and present of the da Silva group. I'm particularly grateful to Teresa, whom I feel lucky to count as a close friend, for welcoming me to the da Silva group on Day 1, for her insightful scientific and not-so scientific advice these past 5 years and for always making time for an afterwork Nandos! To Ben, thank you for being my ATPPRT buddy, the unofficial RGdS IT manager and for also being onboard with the afterwork Nandos! Thank you to John for providing us with an enviable supply of protein for characterisation. To Catherine, Pamela, and Suneeta, thank you for making the da Silva group a wonderful place to work and study!

I'd like to extend another special thank you to everyone in Level 2 of the BSRC annex, particularly to Stephen, Verena, Flora, Aga, Catriona, Chris, Emmajay, Martha, and Hannes who helped us to reassemble our lab after the BMS fire and have made us feel at home ever since. To Flora, I'm so grateful to have shared this whole experience with you, thank you for being the best thesis writing buddy! My colleagues in the BSRC have been a constant source of advice and support over the past years.

I'm especially grateful for the support of my family and friends over the past 5 years, which enabled me to take up this challenge. To my friend, Januka for always being ready for an academic or not-so academic debate (especially during lockdown!). To my sister Sarah, whose constant stream of TikToks never failed to make me laugh, even on the longest days in the lab. To my Dad and Josephine, thank you for always reminding me how proud you are of me. To my mum, who continues to be constantly available to provide support, encouragement and motivation. Finally, I'd like to express my huge gratitude to my grandparents, Catherine and Sam Lowther, who have always been my biggest supporters!

Costas, there are no words to convey my gratitude to you. Thank you for your constant support, encouragement to pursue my interests and for never being tired of teaching me Python, Inkscape and all of the mathematics that I have forgotten since high-school!

A very special final thank you to Cosmo, our walks on the beach were the highlight of my final weeks writing up this work.

The research underpinning this thesis has received funding from the Biotechnology and Biological Sciences Research Council (BBSRC) [Grant BB/M010996/1] via an EASTBIO Doctoral Training Partnership studentship.

Abbreviations

A. baumannii	*Acinetobacter baumannii*
*Ab*HisIE	*Acinetobacter baumannii* HisIE
ADP	adenosine 5′-diphosphate
AMP	adenosine 5′-monophosphate
ATP	adenosine 5′-triphosphate
ATPPRT	adenosine 5′-triphosphate phosphoribosyltransferase
B. cereus	*Bacillus cereus*
C. jejuni	*Campylobacter jejuni*
C. violaceum	*Chromobacterium violaceum*
C.glutamicium	*Corneybacterium glutamicium*
CV	Column volume
DLS	Dynamic light scattering
DNA	Deoxyribonucleic acid
DSF	Differential scanning fluorimetry
DTT	Dithiothreitol
dUTPase	2′-deoxyuridine 5′-triphosphate hydrolase
E. coli	*Escherichia coli*
EDTA	Ethylenediaminetetraacetic acid
ESI-MS	Electrospray ionisation-mass spectrometry
FPLC	Fast protein liquid chromatography
HEPES	4-(2-hydroxyethyl)-1-piperazineethanesulfonic acid
ICP-ES	inductively coupled plasma emission spectra
IPTG	Isopropyl β-D-1-thiogalctopyranoside
ITC	Isothermal titration calorimetry
KIE	Kinetic isotope effect
L. lactis	*Lactococcus lactis*
L. major	*Leishmania major*

LB	Lysogeny broth
LC-MS	Liquid chromatography-mass spectrometry
M. thermoautotrophicum	*Methaobacterium thermoautotrophicum*
M. tuberculosis	*Mycobacterium tuberculosis*
M. vannielii	*Methanococcus vannielii*
MWCO	Molecular weight cut-off
NMR	Nuclear magnetic resonance
OD	Optical density
P. arcticus	*Psychrobacter arcticus*
PaATPPRT	*Psychrobacter arcticus* adenosine 5′-triphosphate phosphoribosyltransferase
$PaHisG_S$	*P. arcticus HisG*
PCR	Polymerase chain reaction
PPase	Pyrophosphatase
PPi	Pyrophosphate
PRAMP	Phosphoribosyl adenosine 5′-monophosphate
PRAMP-CH	Phosphoribosyl adenosine 5′-monophosphate cyclohydrolase
PRATP	Phosphoribosyl adenosine 5′-triphosphate
PRATP-PH	Phosphoribosyl adenosine 5′-triphosphate pyrophosphohydrolase
PRPP	Phosphoribosyl pyrophosphate
RLS	Rate-limiting step
S. coelicolor	*Streptomyces coelicolor*
S. Typhimurium	*Salmonella* Typhimurium
SDS-PAGE	Sodium dodecyl sulfate polyacrylamide gel electrophoresis
SKIE	Solvent kinetic isotope effect
SKVE	Solvent kinetic viscosity effect
SSM	Site-saturation mutagenesis

T. brucei	*Trypanosoma brucei*
T. cruzi	*Trypanosoma cruzi*
TEVP	Tobacco etch virus protease
T_M	Melting temperature
WT	Wild-type
η_{rel}	Relative viscosity

Throughout this work, amino acids are expressed as their triple or single letter code.

Amino acid	1-letter code
L-alanine	A
L-Arginine	R
L-Asparagine	N
L-Aspartic Acid	D
L-Cysteine	C
L-Glutamic acid	E
L-Glutamine	Q
L-glycine	G
L-Histidine	H
L-Isoleucine	I
L-Leucine	L
L-Lysine	K
L-Methionine	M
L-phenylalanine	F
L-Proline	P
L-Serine	S
L-Threonine	T
L-Tryptophan	W
L-Tyrosine	Y
L-Valine	V

Table of Contents

Table of Figures

Table of Tables

Chapter 1 Introduction

Histidine is an amino acid biosynthesised by prokaryotes, lower eukaryotes and plants[1]. The histidine biosynthetic pathway encompasses ten biochemical steps and is conserved amongst histidine biosynthesising organisms[1]. The pathway has been harnessed for industrial production of histidine in bacteria[2]. Approximately, 400 tonnes of histidine are produced per annum by industrial fermentation[3]. Histidine is added to a wide-range of commercial products, including those with medicinal[4,5], nutritional[6–8] and cosmetic applications[9]. More recently, the histidine biosynthetic pathway has been highlighted as a source of potential targets for novel antimicrobial development in a range of pathogenic micoorganisms[10–15]. The histidine biosynthetic pathway is an alluring target for drug development as mammals do not biosynthesise histidine which bodes well for development of highly selective inhibitors with minimal off-target effects. However, it should be noted the histidine biosynthetic pathway is only a viable drug-target in pathogens which cannot scavenge histidine from the host. Elucidating the catalytic and regulatory mechanisms of enzymes on the histidine biosynthetic pathway has the potential to both drive development of improved biocatalysts for industrial histidine production and/or guide inhibitor development with a view towards generating novel antimicrobial agents.

The aims of this work are to elucidate the catalytic and regulatory mechanisms of ATPPRT from *Psychrobacter arcticus* and to initiate biochemical characterisation of bifunctional HisIE from *Acinetobacter baumannii.* ATPPRT from *P. arcticus* has previously been investigated by the da Silva laboratory and was primed for thorough mechanistic characterisation with a view toward generation of histidine-insensitive variants for industrial histidine biosynthesis. HisIE from *A. baumannii* was selected for biochemical characterisation as recent work[10] indicated this enzyme may be a suitable target for novel antimicrobial development against multi-drug resistant *A. baumannii*.

1.1 The histidine biosynthetic pathway

The histidine biosynthetic pathway encompasses ten biochemical steps[1], Figure 1.1. ATPPRT (EC: 2.4.2.17) catalyses the first committed and flux-controlling reaction of the histidine biosynthetic pathway, a condensation reaction between 5-phospho-α-D-ribosyl-1-pyrophosphate (PRPP) **1** and adenosine 5′-triphosphate (ATP) **2** producing N^1-(5-phospho-β-D-ribosyl)-ATP (PRATP) **3** and pyrophosphate (PP_i) **4**[16]. The chemical equilibrium of the reaction catalysed by ATPPRT strongly favours reactants[17]. HisE (PRATP pyrophosphohydrolase) (EC: 3.6.1.31) catalyses the second reaction of the pathway, hydrolysis of the α-β phosphate linkage of PRATP **3** producing N^1-(5-phospho-β-D-ribosyl)-adenosine-5′-monophosphate (PRAMP) **5** and PPi[18] **4**. PRAMP **6** is then converted to pro-phosphoribosylforimino-5-aminoimidazole-4-carboxamide ribonucleotide (ProFAR) **7** by HisI (PRAMP cyclohydroalse) (EC: 3.5.4.19)[18]. A single polypeptide chain may encode for a bifunctional enzyme with both HisE and HisI or these activities may be encoded by distinct polypeptide chains[19]. The remaining seven steps of the histidine biosynthetic pathway are catalysed by HisA (ProFAR isomerase) (EC: 5.3.1.16), HisH/HisF (imidazole-glycerol phosphate synthase) (EC: 4.3.2.10), HisB (imidazoleglycerol-phosphate dehydratase) (EC: 4.2.1.19), HisC (histidinol-phosphate aminotransferase) (EC: 2.6.1.9), HisB (histidinol-phosphate phosphatase) (EC:3.1.3.15) and HisD (histidinol dehydrogenase) (EC: 1.1.1.23)[1].

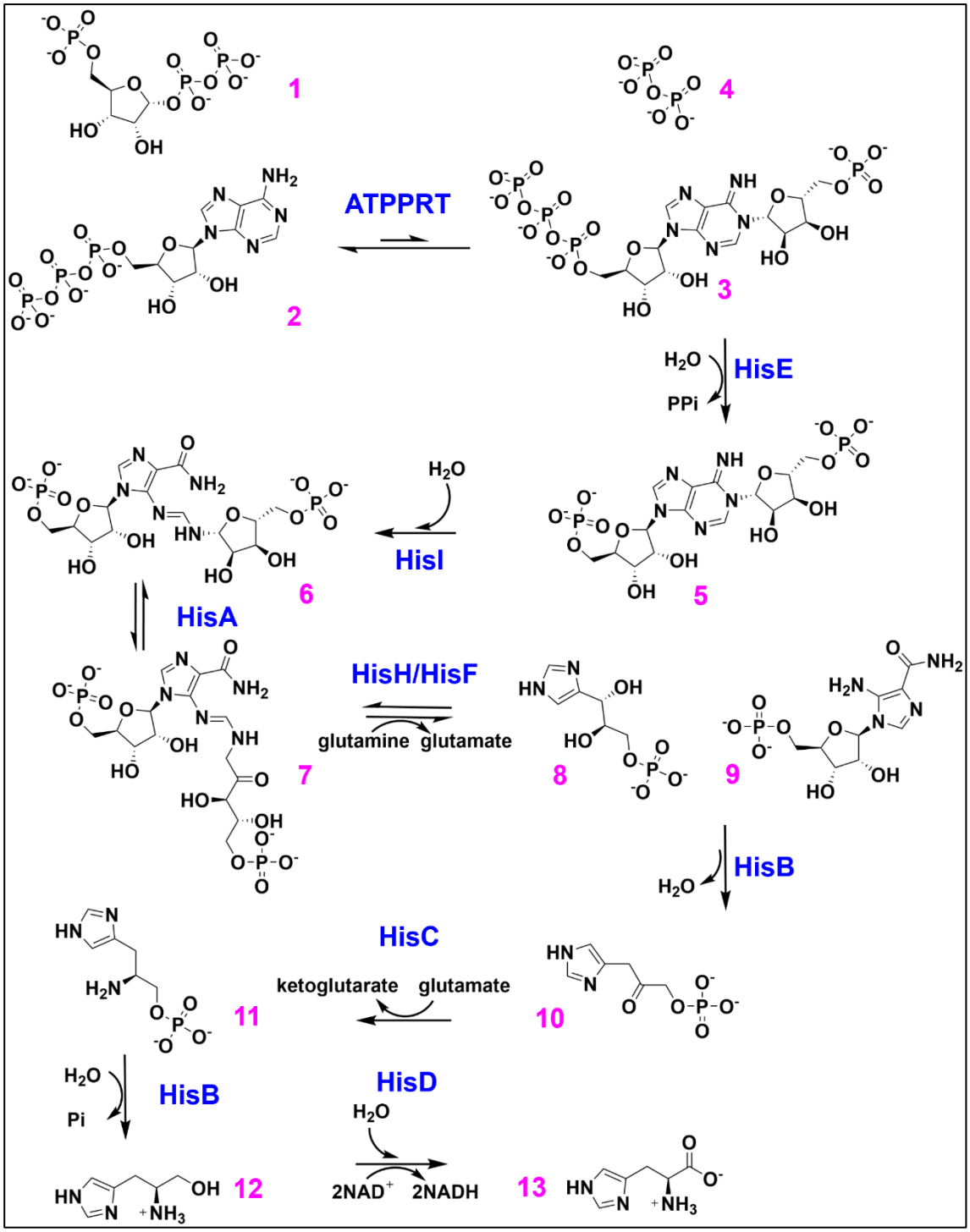

Figure 1.1 The histidine biosynthetic pathway. PRPP **1**, ATP **2**, PRATP **3**, PPi **4** PRAMP **5**, ProFAR **6**, phosphoribulosyl-formimino-aminoimidazole-4-carboxamide ribonucleotide-phosphate **7**, imidazole-glycerol-phosphate **8**, 5-aminoimidazole-4-carboxamide ribonucleotide (AICAR) **9**, imidazole-acetol-phosphate **10**, L-histidinol-phosphate **11**, L-histidinol **12**, L-histidine **13.** HisD catalyses two successive oxidation reactions.

Histidine biosynthesis is both tightly and extensively regulated. Transcription of the histidine operon(s) is regulated by guanosine tetraphosphate (ppGpp), a transcriptional activator, and via a classical attenuation mechanism which links transcription to the availability of His-tRNA^{His}, the intracellular histidine concentration, histidyl tRNA synthetase activity, and chromosomal DNA supercoiling levels[1]. Additionally, ATPPRT is allosterically inhibited by the end product of the pathway, histidine[21] and orthosterically by AMP[21,22]. Inhibition of ATPPRT by AMP and histidine is synergistic[22–24].

As previously highlighted, this work is concerned with ATPPRT from *P. arcticus* and bifunctional HisIE from *A. baumannii*, literature on these enzymes specifically is reviewed below.

1.2 ATPPRT

1.2.1 Overview of ATPPRT

ATPPRT catalyses the first step of histidine biosynthesis, a condensation reaction between PRPP **1** and ATP **2** producing PRATP **3** and pyrophosphate **4**, Figure 1.1. ATPPRT is the product of the *hisg* gene, of which there are two forms, a short-form denoted HisG$_S$ and long-form denoted HisG$_L$. HisG$_L$ has an 80-100 amino acid extension at the C-terminus relative to HisG$_S$[25]. Most organisms that biosynthesize histidine possess only one form of HisG, aside from bacteria from the *Geobacter* clade which encode both functional HisG$_S$ and HisG$_L$[26,27]. HisG$_L$ is a homohexamer in which each individual polypeptide chain contains catalytic and regulatory domains[24,28,29]. The C-terminal extension in HisG$_L$-type ATPPRTs relative to HisG$_S$-type ATPPRT corresponds to a regulatory domain which mediates histidine feedback inhibition[24,30]. HisGs possesses analogous catalytic domains to that of HisG$_L$ but lacks a histidine-binding domain[25,31,32]. Instead, HisG$_S$ forms a hetero-octamer with a histidyl-tRNA-synthetase paralogue, HisZ. The hetero-octamer is composed of four HisG$_S$ polypeptide chains and four HisZ polypeptide chains[25,33]. HisZ mediates histidine feedback inhibition of HisG$_S$-type ATPPRTs[32,34,35]. Initially, it was incorrectly hypothesised that HisZ was required for HisG$_S$ activity, however, subsequent work has demonstrated HisG$_S$ is catalytically active in the absence of HisZ, although, catalytic activity is enhanced by addition of HisZ[32,35].

The catalytic activity of $HisG_S$ is insensitive to histidine inhibition in the absence of HisZ[32,35].

1.2.2 ATPPRT Structure

Both $HisG_L$ and $HisG_S$ type ATPPRTs have been extensively structurally characterised. $HisG_L$ monomers assemble in a trimer of dimers arrangement to form a functional hexamer[24,28,30], Figure 1.2A. The crystal structures of $HisG_L$ from *Mycobacterium tuberculosis*[30,36,37], *Escherichia coil*[28] and *Campylobacter jejuni*[24,38] with and without substrates and products have been published. $HisG_S$ and HisZ form a hetero-octamer in which four HisZ molecules assemble into an X-shaped core that is flanked by two $HisG_S$ dimers[31,32], Figure 1.2B. Prior to the undertaking of this work structures of $HisG_S$-type ATPPRTs, with both $HisG_S$ and HisZ subunits present, from *Lactococcus lactis*[34], *Thermotoga maritima*[39] *and P. arcticus*[32] had been published. Additional ligand-bound crystal structures of *P. arcticus* ATPPRT, with both $HisG_S$ and HisZ subunits, and of the catalytic $HisG_S$ domain in the absence of HisZ, solved by Dr Magnus S. Alphey, were published as this work was undertaken[40]. These structures are discussed throughout Chapters 3 and 4.

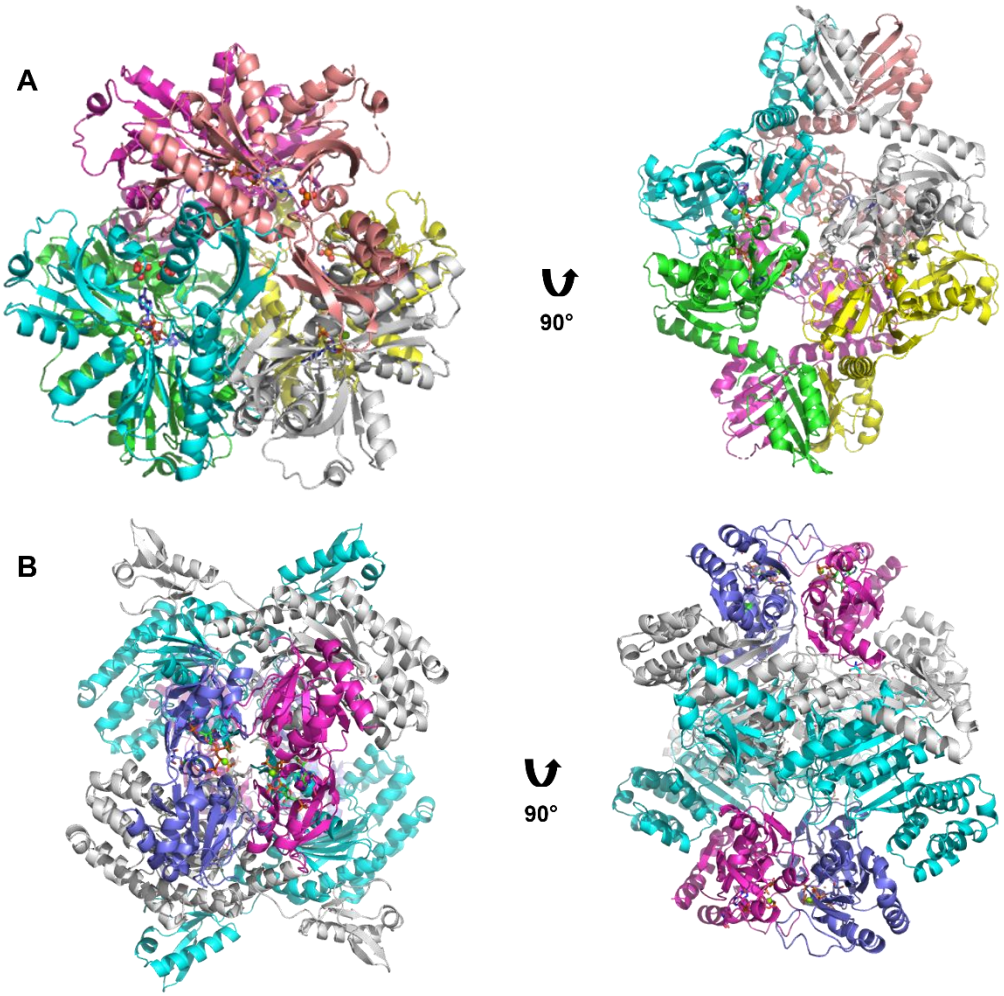

Figure 1.2 Crystal structures of ATPPRT from $HisG_L$ and $HisG_S$-type ATPPRTs. Crystal structures of ATPPRT from (A) *C. jejuni* ($HisG_L$) (PDB ID: 4YB7) and (B) *P. arcticus* (HisGs/HisZ) (PDB ID: 6FU2) Proteins are shown with ribbon diagrams. (A) $HisG_L$ subunits are shown in coral, cyan, green, grey, magenta and yellow. (B) $HisG_S$ subunits are shown in magenta and purple. (B) HisZ subunits are shown in cyan and grey. ATP (A and B) and PRPP (B) are depicted with stick models with carbon in either (A) purple or 9B) green nitrogen in blue, phosphorus in orange and oxygen in red. Mg^{2+} is depicted by green spheres. Images were generated in Pymol.

1.2.3 ATPPRT active site

PRPP binding residues are conserved amongst ATPPRTs[28,34]. The 5-phosphate moiety of PRPP is anchored in the active site by interactions to a conserved phosphate binding loop which includes a [T/S]GX[T/S] motif (T180-T183 in *P. arcticus* ATPPRT) and the 2-OH and 3-OH groups of PRPP are recognised by two conserved acidic residues (E163 and D176 in *P. arcticus* ATPPRT)[28,34,40], Figure 1.3A. Mutagenetic studies carried out in *L. lactis* ATPPRT, a $HisG_S$-type ATPPRT, revealed only a 2-3 fold decrease in k_{cat} upon mutation of either of the conserved threonine residues but approximately 300- and 50-fold increases in K_M^{PRPP} [31]. Mutagenesis of the conserved aspartate which binds the 3-OH of PRPP to alanine also induced only a negligible effect on k_{cat} and an approximately 4-fold increase in K_M^{PRPP} [31]. Residues that bind ATP are less well defined than those that bind PRPP. A highly conserved arginine residue (R32 in *P. arcticus* ATPPRT) stacks against the adenine base of ATP and a conserved acidic residue (D94 in *P. arcticus* ATPPRT) recognises the 2′-OH and 3′-OH of the ribose moiety[24,28,40], Figure 1.3A. Interactions with the triphosphate moiety vary by species and the arginine residue is not conserved in ATPPRT from *M. tuberculosis*. A critical feature of the ATPPRT active site is the Mg^{2+} ion which is sandwiched by the diphosphate and triphosphate moieties of PRPP and ATP in crystal structures of *P. arcticus* ATPPRT[40], Figure 1.3A. Mg^{2+} is likely required to attenuate the negative charge in the active site. Transition state modelling of the reaction catalysed by $HisG_S$ from *P. arcticus*, carried out by the da Silva Laboratory in collaboration with Dr Jennifer S. Hirschi (Binghampton University), indicated that a second additional Mg^{2+} ion, not captured in crystal structures, is required to facilitate departure of the pyrophosphate leaving group at the transition state[40]. The transition state-modelling was published alongside data from Chapter 3 of this work.

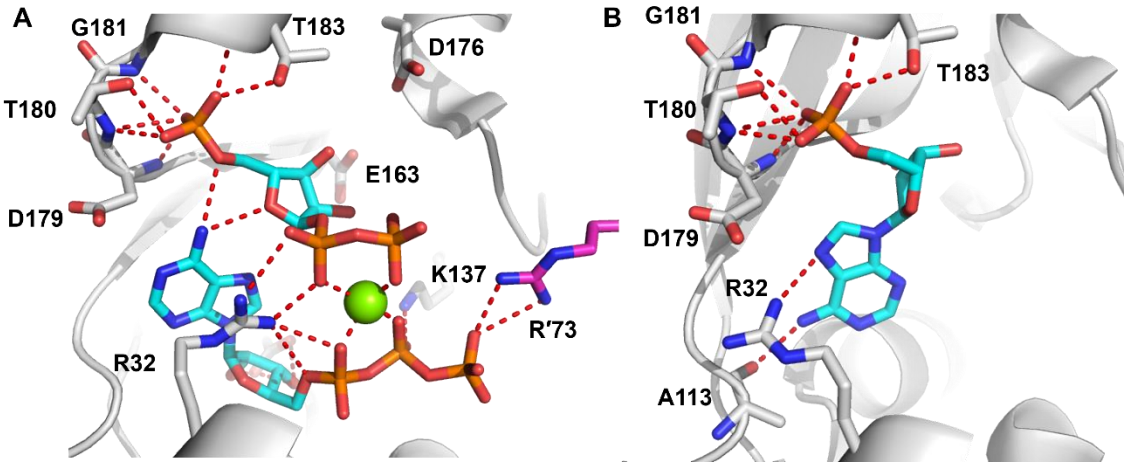

Figure 1.3 Active site of $HisG_S$. Crystal structures of *P. arcticus* $HisG_S$ with either (A) PRPP and ATP (PDB ID: 6FCT) or (B) AMP bound (PDB ID: 6FD9). Ligands are presented as stick models with carbon in cyan, nitrogen in blue, oxygen in red and phosphorus in orange. *Pa*HisGs subunit backbones are shown as ribbon diagrams in either grey (ligand-bound subunit) or magenta (adjacent subunit) selected residues are depicted as stick models with carbon in either grey or magenta, nitrogen in blue and oxygen in red. Mg^{2+} is depicted by green spheres. Polar interactions are represented by dashed lines. Images were generated in Pymol.

1.2.4 Catalytic mechanism of ATPPRT

ATPPRTs represent a novel class of phosphoribosyltransferase[28]. *In vitro* data demonstrated ATPPRT enzyme is Mg^{2+} dependent and displays optimal activity under mild-basic conditions (pH 8.0 – 10.0)[17,21,41]. A Bi-Bi kinetic mechanism in which ATP is the first substrate to bind and pyrophosphate is the first product to leave was proposed for $HisG_L$-type ATPPRTs[42]. Prior to this work, the kinetic mechanism of HisGs-type ATPPRTs had not been characterised. The kinetic mechanism of both types of ATPPRT is explored in greater detail in Chapter 3.

Despite the plethora of crystal structures, prior to this work, no catalytic residues had been identified that were essential for catalysis by either $HisG_S$- or $HisG_L$-type ATPPRTs. Champagne and colleagues studied the active site of *L. lactis* ATPPRT and postulated that interactions with S140, and cross-dimer contacts with K8 and K50 may activate the pyrophosphate leaving group[31,34], Figure 1.4. K8A and K50A variants of *L. lactis* ATPPRT were constructed in order to test this hypothesis. The k_{cat} of the K8A variant was only 2.3-fold less than that of WT *L. lactis* ATPPRT, not indicative of an essential role in catalysis[31,34]. Furthermore the k_{cat} of the K50A variant was 2.5-fold greater than that of WT *L. lactis* ATPPRT, also not indicative of a key role in catalysis[31]. Champagne

and colleagues further hypothesised that flexible loop which protrudes into the active site of the adjacent monomer is a key feature of ATPPRT catalysis which serves to exclude solvent from the active site[34], Figure 1.4.

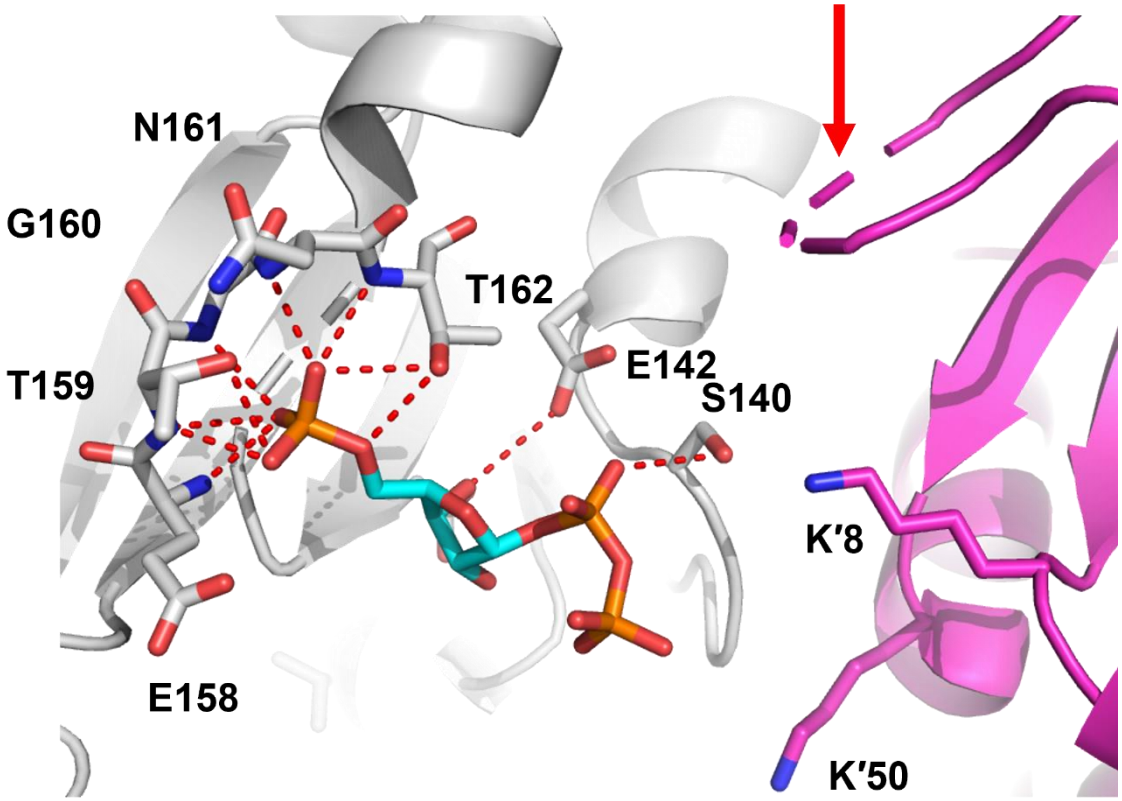

Figure 1.4 Active site of *L. lactis* ATPPRT. *L. lactis* active site with PRPP bound (PDB ID: 1Z7N). PRPP is depicted as a stick model with carbon in cyan, nitrogen in blue, oxygen in red and phosphorus in orange. HisGs subunit backbones are shown as ribbon diagrams in either grey (PRPP-bound subunit) or magenta (adjacent subunit) selected residues are labelled and depicted as stick models with carbon in either grey or magenta, nitrogen in blue and oxygen in red. Mg^{2+} is depicted by green spheres. Red arrow indicates flexible loop proposed to exclude solvent from the active site encompassing residues 21-43. Polar interactions are represented by dashed lines. Images were generated in Pymol.

An extensive transition state analysis examining ATPPRT from *C. jejuni*, *M. tuberculosis* and *L. lactis*, carried out by Moggré and colleagues, studied the reaction catalysed by ATPPRT in reverse with phosphonoacetic-acid as a substitute for pyrophosphate[37]. It was concluded that experimentally determined large 1-^{3}H, low to moderate 1-^{14}C and large 1′-^{15}N KIEs primary kinetic isotope effects (KIEs) most closely matched theoretical KIEs generated from computational transition state models with low bond order to the incoming phosphonoacetic-acid and no significant bond order to the adenine leaving-group[37]. Thus, an S_N2-like transition state was ruled out in favour of an S_N1-like/ D_N*A_N transition state for all three enzymes[37], Figure 1.5A. Champagne and colleagues highlighted that the primary roles of the enzyme in such a mechanism would be orientating the substrates for catalysis and excluding water from the active site[31]. It was noted that the transition state modelling carried out by Moggré and colleagues, employed a molecule of PRATP truncated at the N9-C1′′ bond, thus excluding a ribose sugar and the triphosphate group from the analysis. Later transition state modelling carried out by the da Silva group in collaboration with Dr Jennifer S. Hirschi (Binghampton University) suggested an S_N2-like, transition state structure is possible for reactions catalysed by $HisG_S$ from *P. arcticus* [40], Figure 1.5B.

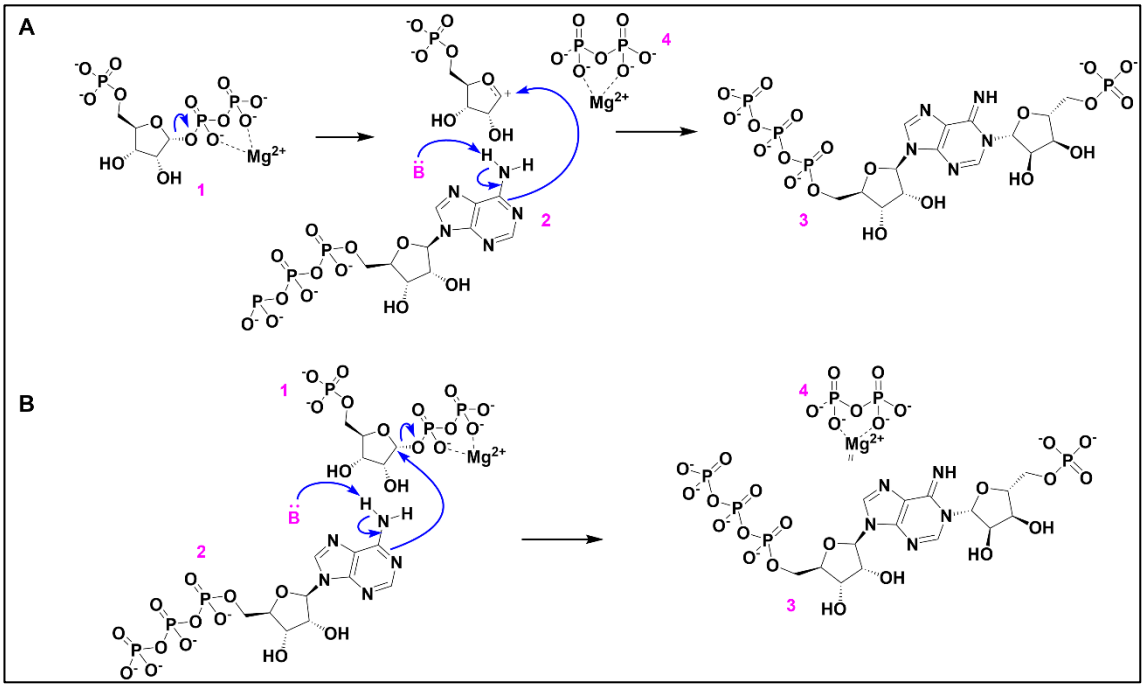

Figure 1.5 Possible chemical mechanisms underpinning catalysis by ATPPRT. (A) An S_N-1-like mechanism in which the PPi leaving group leaves before the nucleophilic attack generating a riboxocarbenium ion intermediate. (B) An S_N-2-like mechanism in which nucleophilic attack and loss of the PPi leaving group occur concurrently. PRPP **1**, ATP **2**, PRATP **3** and PPi **4.** B denotes a, as yet unidentified, catalytic base**.**

1.2.5 Regulation of ATPPRT

As previously stated, ATPPRTs are allosterically inhibited by histidine[21] and orthosterically inhibited by AMP[21,22]. Inhibition by AMP and histidine is synergistic[22–24]. AMP inhibition is competitive with respect to both substrates in reactions catalysed by ATPPRT from *S.* Typhimurium[22], *C. jejuni*[24] and *P. arcticus*[43]. The data for *P. arcticus* inhibition by AMP was collected by Dr Catherine M. Thomson, a former PhD student in the da Silva laboratory, and was published alongside data from Chapter 3 of this work. Competitive inhibition by AMP with respect to both substrates has been rationalised by crystal structures of AMP bound ATPPRT from *C. jejuni*[24], *E. coli*[28], *M. tuberculosis*[30] and *P. arcticus*[40] all of which depict a single molecule of AMP bound across both the PRPP and ATP binding sites, Figure 1.3B. The 5′-phosphate of AMP resides in the highly conserved motif which binds the 5-phosphate of PRPP, whereas the adenine base resides in the ATP binding-site. Inhibition of ATPPRT from *S.* Typhimurium and *C. glutamcium* by adenosine 5′-diphosphate (ADP) has also been reported and is explored within the context of a $HisG_S$-type ATPPRT in Chapter 3.

Histidine inhibition was demonstrated to be non-competitive with respect to both substrates in reactions catalysed by ATPPRT from *C. jejuni*[24], *S.* Typhimurium[21], *P. arcticus*[44] and *A. baumannii*[45]. Histidine inhibition is non-competitive with respect to PRPP and uncompetitive with respect to ATP in reactions catalysed by ATPPRT from *M. tuberculosis*[29]. Histidine inhibition was also shown to be non-competitive with respect to PRPP in reactions catalysed by *L. lactis* ATPPRT[31]. Pre-steady state data collected with ATPPRT from *P. arcticus* and *M. tuberculosis* demonstrated that histidine binding traps the enzyme in an inactive form[29,44].

Histidine binds at Domain III of $HisG_L$-type ATPPRTs, specifically, at the subunit interface. Approximately six molecules of histidine bind each $HisG_L$ hexamer[24,30,46]. It was initially incorrectly hypothesised that histidine binding induced dissociation of $HisG_L$-type ATPPRT hexamers, multiple reports have since confirmed that $HisG_L$-type ATPPRTs form hexamers in the presence and absence of histidine[24,29,46]. Subsequent work identified that histidine binding to $HisG_L$-type ATPPRTs induces twisting/rotation of the C-terminal regulatory domain resulting in an overall more compact structure compared with apo $HisG_L$[24]. However, a simplistic model of allosteric inhibition

encompassing a shift in the protein conformational equilibrium from an active relaxed 'R' state to an inhibited tense 'T' state upon histidine binding was rejected upon discovery of an allosteric activator 3-(2-Thienyl-L-alanine) (TIH) which leads to the same overall conformational tightening of the $HisG_L$ hexamer as histidine and an observation that the tense state predominates in solution at alkaline pH even in the absence of histidine[36,46].

Histidine exerts an inhibitory effect by binding to the HisZ subunit of $HisG_S$-type ATPPRTs. The histidine-binding residues of histidyl tRNA-synthetase (HisRS) are conserved in HisZ[25]. Unexpectedly, a crystal structure of *T. maritima* ATPPRT, a $HisG_S$-type ATPPRT, depicted histidine binding at the subunit interface of $HisG_S$ and HisZ, an area with no sequence similarity to HisRS[39]. However, mutations of *L. lactis* ATPPRT which confer insensitivity to histidine (E130A and Y268F/Y269F) can be mapped to the histidine-binding residues common to HisZ and HisRS[34]. A subsequent *P. arcticus* ATPPRT:PRPP:histidine structure, solved by Dr Catherine M. Thomson, depicted histidine binding to the conserved histidine binding site[44], Figure 1.6. These data suggest the mode of histidine binding in the *T. martiima* ATPPRT:histidine structure may be a crystallographic artefact. The *P. arcticus* ATPPRT:PRPP:histidine structure also facilitated the identification of amino acid network connecting the histidine binding-site to the active site. Y263, which residues on the histidine binding loop of *P. arcticus* HisZ, is rotated approximately 180° in histidine bound structures compared with non-histidine bound structures[44], Figure 1.6. This rotation facilitates an interaction between Y263 and H104 which resides on a loop that makes contact with the *Pa*HisZ:*Pa*$HisG_S$ interface[44], Figure 1.6. Site-directed mutagenesis of Y263 suggested that although the network identified may play a role in histidine-feedback inhibition, other, as yet unidentified, elements must also contribute to signal transmission[44]. Future experiments which explore $HisG_S$- and $HisG_L$-type ATPPRT dynamics in the context of histidine binding may add to the current understanding of histidine feedback inhibition.

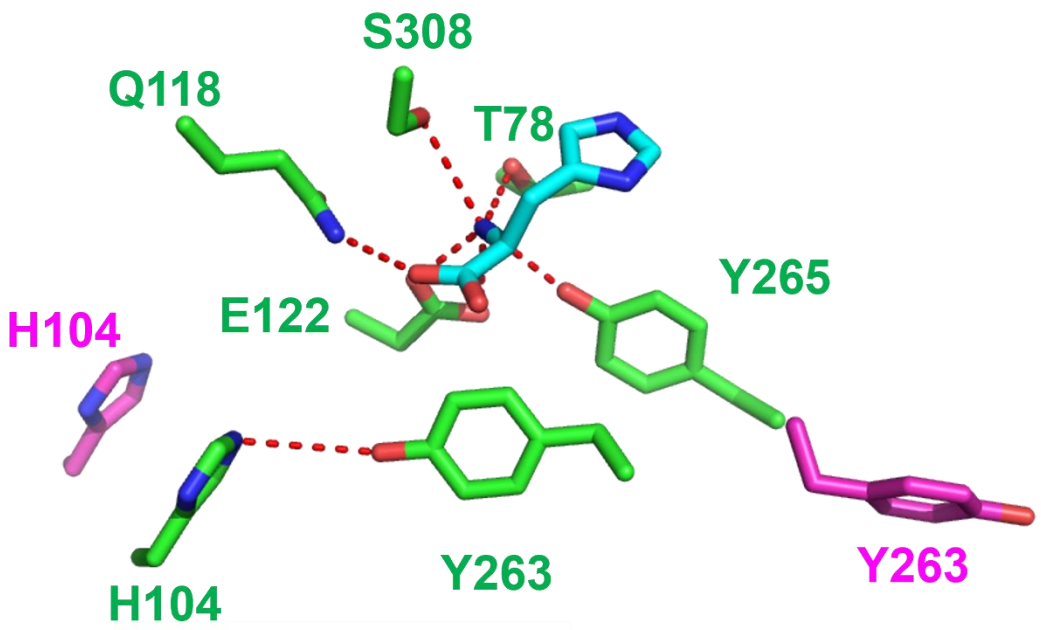

Figure 1.6 Histidine-binding site of *P. arcticus* HisZ. Close-up view of the histidine-binding site of the *P. arcticus* ATPPRT:PRPP:histidine structure (PDB ID: 6R02) depicting histidine bound to residues common to *P. arcticus* HisZ and HisRS. Histidine depicted as a stick model with carbon in cyan, nitrogen in blue, and oxygen in red. Selected residues from the *P. arcticus* histidine-binding site are shown in stick models with carbon in green, nitrogen in blue and oxygen in red. Y263 and H104 from the activated *P. arcticus* ATPPRT:PRPP:ATP structure (PDB ID: 6FU2) were overlaid with the histidine-bound structure and are shown as stick models with carbon in magenta, nitrogen in blue and oxygen in red. Red dashed lines depict polar interactions. A polar interaction is observed between Y263 and H104 of *P. arcticus* HisZ in the histidine-bound structure but not in the activated structure. Image generated in Pymol.

Allosteric activation of $HisG_S$ by HisZ has not been studied as extensively as histidine feedback inhibition, prior to this work no structural and scarce kinetic data from $HisG_S$ in the absence of HisZ were available. The first crystal structures of $HisG_S$ in the absence of HisZ, solved by Dr Magnus S. Alphey, were published during the time this work was undertaken[40] and are discussed throughout Chapters 3 and 4. Elucidating the mechanism of allosteric activation of $HisG_S$ by HisZ may provide a blueprint for rationale engineering of a $HisG_S$ for biosynthetic production of histidine free from histidine feedback inhibition and would likely increase understanding at the molecular level of the complex regulation governing histidine biosynthesis.

1.3 HisIE

1.3.1 Overview of HisE, HisI and HisIE

After PRATP **3** is produced by ATPPRT, the α-β phosphate linkage is hydrolysed by HisE producing PRAMP **5** which undergoes further hydrolysis, catalysed by HisI, resulting in ProFAR **6,** Figure 1,1. HisIE fusions are found in all histidine-biosynthesising eukaryotes and several unrelated bacterial lineages, likely the result of multiple independent fusion events[19]. HisE and HisI activities are encoded by a bi-functional protein termed HISN2 in plants which is analogous to bacterial HisIE[47]. Most archaea encode distinct monofunctional HisI and HisE. The presence of HisIE fusions in Thermococci and Thermoplasmata has been attributed to horizontal gene transfer[19]. HisE, HisI and bifunctional HisIE have not been as extensively studied as ATPPRT and prior to 2019, structural and mechanistic data was only available from monofunctional HisE and HisI.

1.3.2 HisE

HisE is a member of the α-helical NTP pyrophosphohydrolase superfamily[48]. Members of the α-helical NTP pyrophosphohydrolase superfamily exhibit an entirely α-helical structure and possess a conserved Mg^{2+}-binding site, composed of four acidic residues spread across two core-alpha helices[48]. Other members of the superfamily include MazG, a nucleoside triphosphate pyrophosphohydrolase[49,50] and a class of 2′-deoxyuridine 5′-triphosphate hydrolase (dUTPases) found in trypanosomatides, Gram-positive bacteria

and entero-bacterial T4-like phages[48]. The aforementioned dUTPases form dimers, adopt an all α-helix fold[51–54] and hydrolyse dUTP and dUDP[54], whereas the β-dUTPases, found in most other organisms, are trimeric, adopt an all β-fold and are inhibited by dUDP[55,56]. More recently characterised members of the superfamily include the nucleoside triphosphosphate pyrophosphohydrolases DR2231[57,58], from *Deinococcus radiodurans*, and RS21-C6, found in all vertebrate genomes and green plants[59,60].

In a 1965 study of S. Typhimurium extracts Smith and Ames defined the second step of histidine biosynthesis as the Mg^{2+}-dependent hydrolysis of PRATP **5** to PRAMP **6** by HisE[18], Figure 1.1. Since this study, several apo crystal structures of HisE from *M. tuberculosis* (PDB ID: 1Y6X and 3C90)[61], *Bacillus cereus* (PDB ID: 1YVW), *Chromobacterium violaceum* (PDB ID: 2A7W) and *Streptomyces coelicolor* (PDB ID: 1YXB) have been reported, however, no further functional characterisation of these enzymes has been reported.

HisE from *M. tuberculosis*, *B. cereus*, *S. coelicolor*, and *C. violaceum* crystallised as tetramers. MazG, another member of the α-helical NTP pyrophosphohydrolase superfamily, from *Bacillus* also crystallised as tetramers and form tetramers in solution[49,50]. HisE crystal structures depict a core-region composed of two long, anti-parallel α-helices, which pack against the same two α-helices from the adjacent monomer to form a four α-helix bundle, Figure 1.7A. The four α-helix bundle is flanked by additional smaller α-helices that make up the N- and C-terminus of each monomer. The HisE tetramer is formed by a dimer of dimers[61], Figure 1.7A. The putative Mg^{2+}-binding site residues of HisE from *B. cereus* are highlighted in Figure 1.7B and 1.7C. So far, a substrate binding pocket of HisE has not been identified.

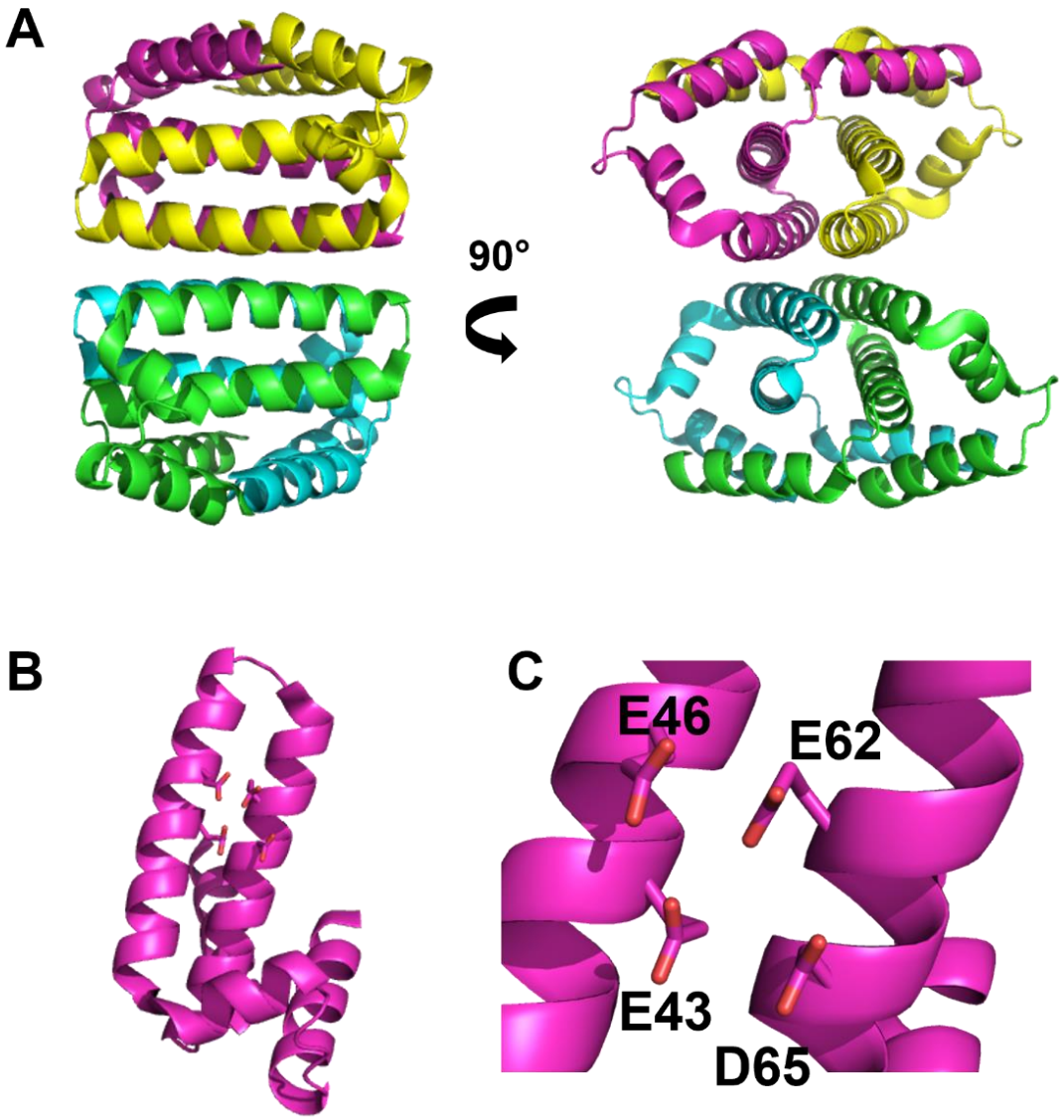

Figure 1.7 Crystal structure of HisE from *B. cereus* (PDB ID: 1YWV). (A) *B. cereus* HisE tetramer. (B) Isolated *B. cereus* HisE monomer. (C) Close-up view of the putative Mg^{2+}-binding site of HisE. HisE subunits are shown as ribbon diagrams and coloured by chain. Residues of the putative Mg^{2+}-binding site labelled and shown as stick models with carbon in magenta and oxygen in red. Images were generated in Pymol.

Although functional studies of HisE have not been carried out, a catalytic mechanism for the related dUTPases has been proposed[51,52,62]. The proposed mechanism entails a Mg^{2+}-activated water which attacks the β-phosphate of dUTP[51,52], Figure 1.8. An additional Mg^{2+} ion is posited to stabilise the transition state and to facilitate departure of the pyrophosphate leaving group[51,52]. The proposed mechanism was derived from crystal structures of *C. jejuni* and *Leishmania major* α-dUTPases in complex with non-hydrolysable substrate analogues and is similar to the two-metal ion mechanism proposed for DNA polymerase I[51,52,62]. Further support for the proposed mechanism came from in solution studies of the α-dUTPase from *Trypanosoma brucei* in ^{18}O-enriched water which demonstrated that ^{18}O is incorporated into the pyrophosphate product, consistent with nucleophilic attack occurring on the β-phosphate[62]. A similar catalytic mechanism was proposed for DR2231[57]. HisE may also employ a similar catalytic mechanism to the dimeric α-dUTPases as HisE adopts a similar core structure to the dimeric α-dUTPases and requires Mg^{2+} for activity[18,48,61]. However, further structural and mechanistic data are required to uncover the catalytic mechanism of HisE.

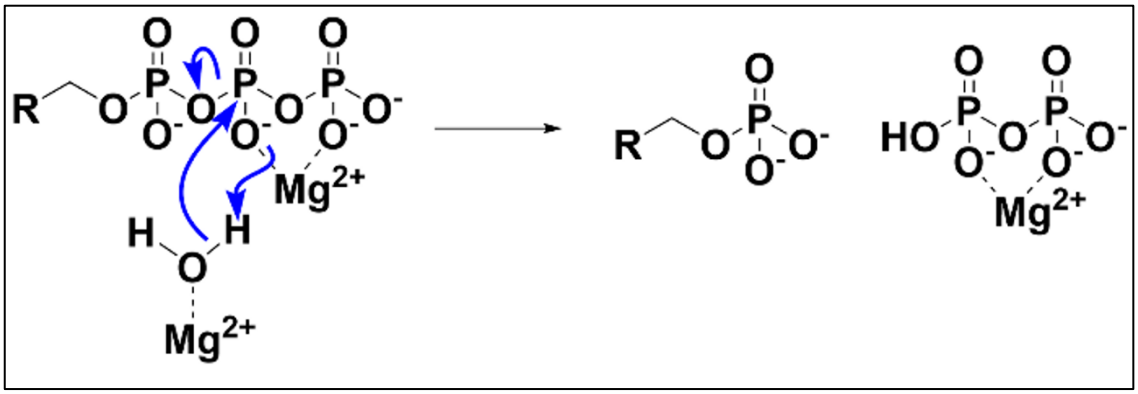

Figure 1.8 Proposed catalytic mechanism for the dimeric α-dUTPases. A catalytic water is activated by Mg^{2+} for a nucleophilic attack on the β-phosphate of dUTP. Scheme modified from Hemsworth, González-Pacanowska and Wilson, 2013[62].

1.3.3 HisI

HisI catalyses cyclohydrolysis of PRAMP **5** to produce ProFAR **6,** Figure 1.1[18,63]. The catalytic mechanism of HisI has been investigated via structural and functional studies. Functional studies of HisI from *Methanococcus vannielii* and *Methanobacterium thermoautotrophicum* identified a high affinity Zn^{2+}-binding site (K_D < 5 nM) and a lower affinity Mg^{2+}-binding site (K_s = 4.6 ± 0.7 μM)[63,64]. Both Zn^{2+} and Mg^{2+} ions are required for cyclohydrolase activity[63,64]. *M. thermoautotrophicum* and *M. vannielii* HisI co-purify with Zn^{2+} [63,64].

A crystal structure of HisI from *M. thermoautotrophicum* (PDB ID: 1ZPS) is the only reported structure of a monofunctional HisI[64], Figure 1.9. HisI from *M. thermoautotrophicum* crystalised as a dimer and HisI from both *M. thermoautotrophicum* and *M. vannielii* form dimers in solution[63,64]. Each HisI monomer consists of core mixed β-sheet which packs against the mixed β-sheet of the adjacent monomer on one face whilst an additional β-hairpin and α-helix pack against the opposite face of the mixed β-sheet, Figure 1.9A.

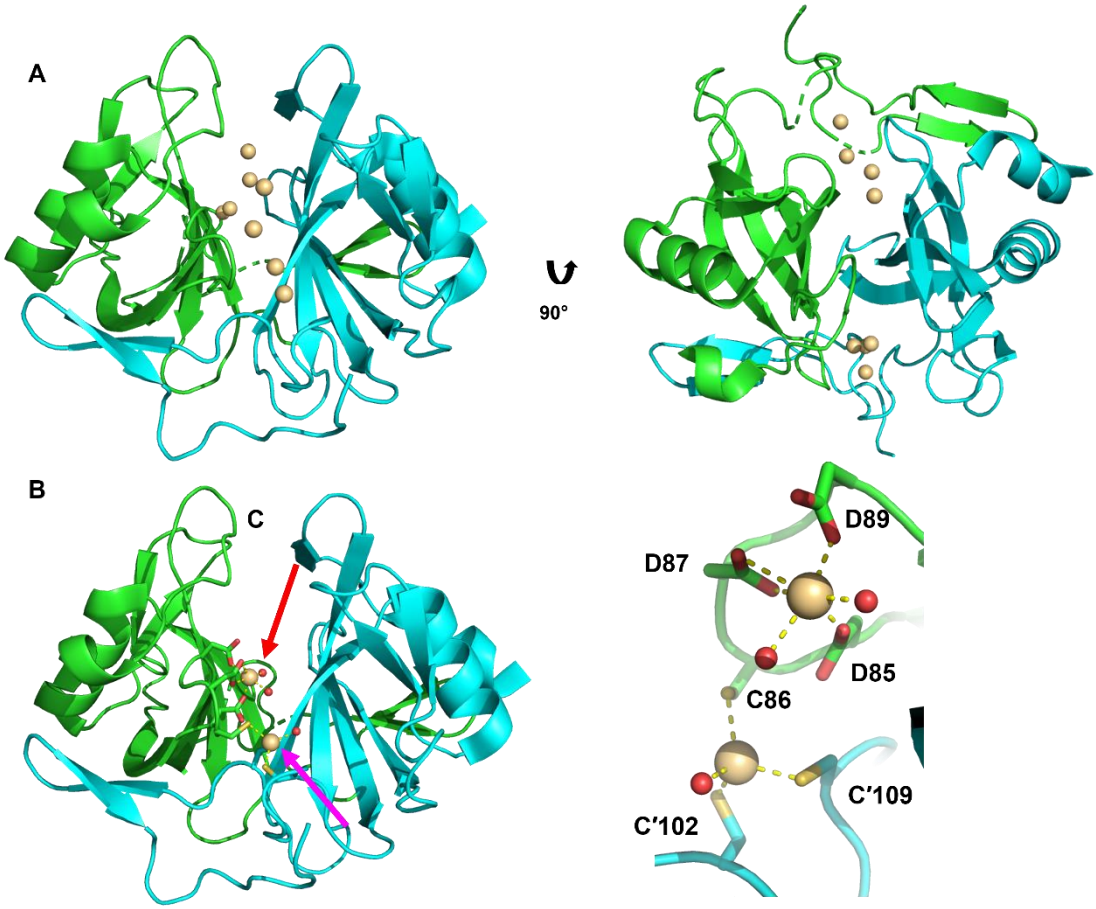

Figure 1.9 Crystal structure of HisI from *M. thermoautotrophicum* (PDB ID: 1ZPS). (A and B) *M. thermoautotrophicum* HisI dimer with Cd^{2+} ions bound at the subunit interface. Magenta and red arrows in (B) indicate the proposed Zn^{2+} and Mg^{2+} binding-sites, respectively. (C) Close-up view of the Zn^{2+}- and Mg^{2+}-binding sites. HisI subunits are shown with ribbon diagrams and coloured cyan and green, residues of the putative Zn^{2+} and Mg^{2+} binding-sites are labelled and shown as stick models with nitrogen in blue, oxygen, in red, and carbon in either green or cyan. Cd^{2+} ions are depicted by a beige sphere. Water molecules are presented as red spheres. Two Cd^{2+} ions are omitted for clarity in (C). Images were generated in Pymol.

From the crystal structure of *M. thermoautotrophicum* HisI, a metal-binding site formed by a water molecule and three cysteine residues, C86 from one monomer and C′102 and C′109 from the adjacent monomer, was proposed to represent the high-affinity Zn^{2+}-binding site, Figures 1.9B and 1.9C. In the crystal structure this site was occupied by a Cd^{2+} ion[64]. The proposal was supported by site-directed mutagenesis of equivalent cysteine residues in *M. vannielii* HisI (C92A, C109A, C116A, C109A/C116A), which resulted in inactive enzymes and it was shown via inductively coupled plasma emission spectra (ICP-ES) that the C92A, C109A/C116A mutants cannot bind Zn^{2+}[65]. Furthermore, treatment of HisI from *M. vannielii* with methyl methane thiosulfonate or 5,5′-dithiobis(2-nitrobenzoic acid) which specifically bind to thiol groups, inactivated the enzyme and impaired Zn^{2+} binding[65].

The crystal structure of *M. thermoautotrophicum* HisI depicted an additional Cd^{2+} ion coordinated by three conserved aspartate residues which was proposed to be the Mg^{2+}-binding site, Figures 1.9B and 1.9C. Mutation of an equivalent aspartate residue, D94, in *M. vannielii* HisI to alanine resulted in an inactive enzyme that cannot rescue a $hisI^{-}$ mutant strain of *E. coli* UTH903[65]. These data and the close proximity of this metal binding-site to the putative Zn^{2+}-binding site are in support of a model in which the conserved aspartates bind Mg^{2+}. Interestingly, the putative Zn^{2+}-binding site is formed primarily by residues of the opposite dimer to that of the putative Mg^{2+}-binding site, thus, dimerisation is likely essential for activity[64].

A PRAMP analogue, 6-OH PRAMP, was docked into the *M. thermoautotrophicum* HisI crystal structure and several contacts were predicted between this analogue and a conserved amino acid sequence of HisI ([S/T]RXX-[LI]WXKG[E/A]TSG). Notably, the SR[S/T] section of the motif was predicted to interact with the N9-phosphoribosyl moiety of PRAMP and the KG[E/A]TSG section of the motif was predicted to hydrogen bond with the N1-phosphoribosyl moiety of PRAMP[64].

A catalytic mechanism for HisI was proposed by d'Ordine and collegaues[65], Figure 1.10, in which a Zn^{2+}-activated H_2O molecule attacks the purine ring of PRAMP at C6, forming a tetrahedral intermediate[65]. A subsequent proton transfer between the 6-OH and N1 of the tetrahedral intermediate leads to the C6-N1 bond breaking and collapse of the tetrahedral intermediate[65]. In support of the mechanism, a chemical intermediate,

assumed to be the tetrahedral intermediate was detected upon analysis of the reaction catalysed by *M. vannielii* HisI under pre-steady state conditions[65]. d'Ordine and colleagues also postulated that a conserved active site histidine residue (His110) acts as a catalytic base to deprotonate the Zn^{2+}-activated water[65]. This proposal was supported by the observation that mutagenesis of the conserved histidine (H110A) residue resulted in a severely catalytically impaired enzyme[65]. d'Ordine and colleagues further speculated that p*K*a values (7.3 and 7.5) extracted from pH profiles of HisI k_{cat}/K_M reflect that protonation of the conserved active site histidine would render it unable to extract a proton from the nucleophilic water[63–65], however, it is possible that the p*K*a values extracted from the pH profile of k_{cat}/K_M may be reporting on the activity of a general base that abstracts a proton from the 6-OH of the tetrahedral intermediate. The mechanism proposed by d'Ordine and colleagues has similarities to that of purine and pyrimidine deaminases which also employ Zn^{2+}-activated water as a nucelophile[66–69].

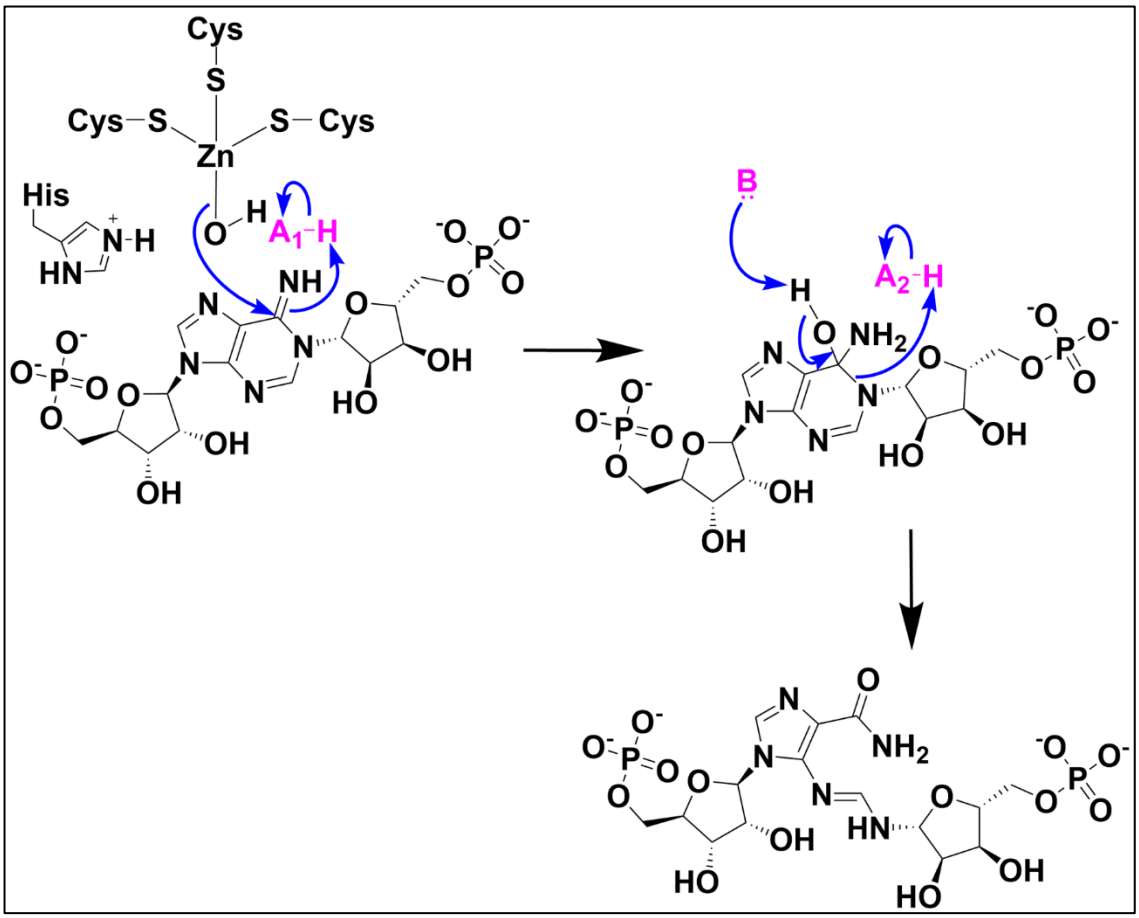

Figure 1.10 Catalytic mechanism of HisI. PRAMP **5**, ProFAR **6**. B denotes a, as yet unidentified, catalytic base. A_1-H and A_2-H represent, as yet unidentified, proton donors. The mechanism presented here is modified from the mechanism proposed by d'Ordine and colleagues[65].

1.3.4 Bifunctional HisIE

The first crystal structures of bifunctional HisIE from *Shigella flexneri* (PDB ID: 6J22 and 6J2L) and HISN2 from *Medicago truncatula* (PDB ID: 7BGM and 7BGN) were reported very recently (2019 and 2021, respectively)[70,71]. HISN2 is the plant equivalent of bifunctional HisIE[47]. In both cases, crystal structures depicted a dimer of polypeptide chains composed of an N-terminal PRAMP cyclohydrolase domain (PRAMP-CH) domain and a c-terminal α-helical PRATP pyrophosphohyrolase domain (PRATP-PH) domain connected by a largely disordered fusion loop, Figure 1.11[70,71]. In solution studies confirmed HisIE from *S. flexneri* and HISN2 from *M. truncatula* form dimers in solution[70,71]. Structural overlays of *S. flexneri* HisIE and *M. truncatula* HISN2 indicate differences in the orientation of the PRATP-PH and PRAMP-CH domains relative to each other, Figure 1.11C. Further differences are evident in the fusion loop, which is longer and adopts a strand-helix-loop motif in the plant enzyme but is completely disordered in the *S. flexneri* HisIE structure, Figure 1.11C. However, the isolated PRATP-PH and PRATP-CH domains from the *S. flexneri* HisIE and *M. truncatula* HISN2 crystal structures are similar to each other and to HisI from *M. thermoautotrophicum* and HisE from *M. tuberculosis*, *B. cereus*, *C. violaceum* and *S. coelicolor*, Figure 1.12.

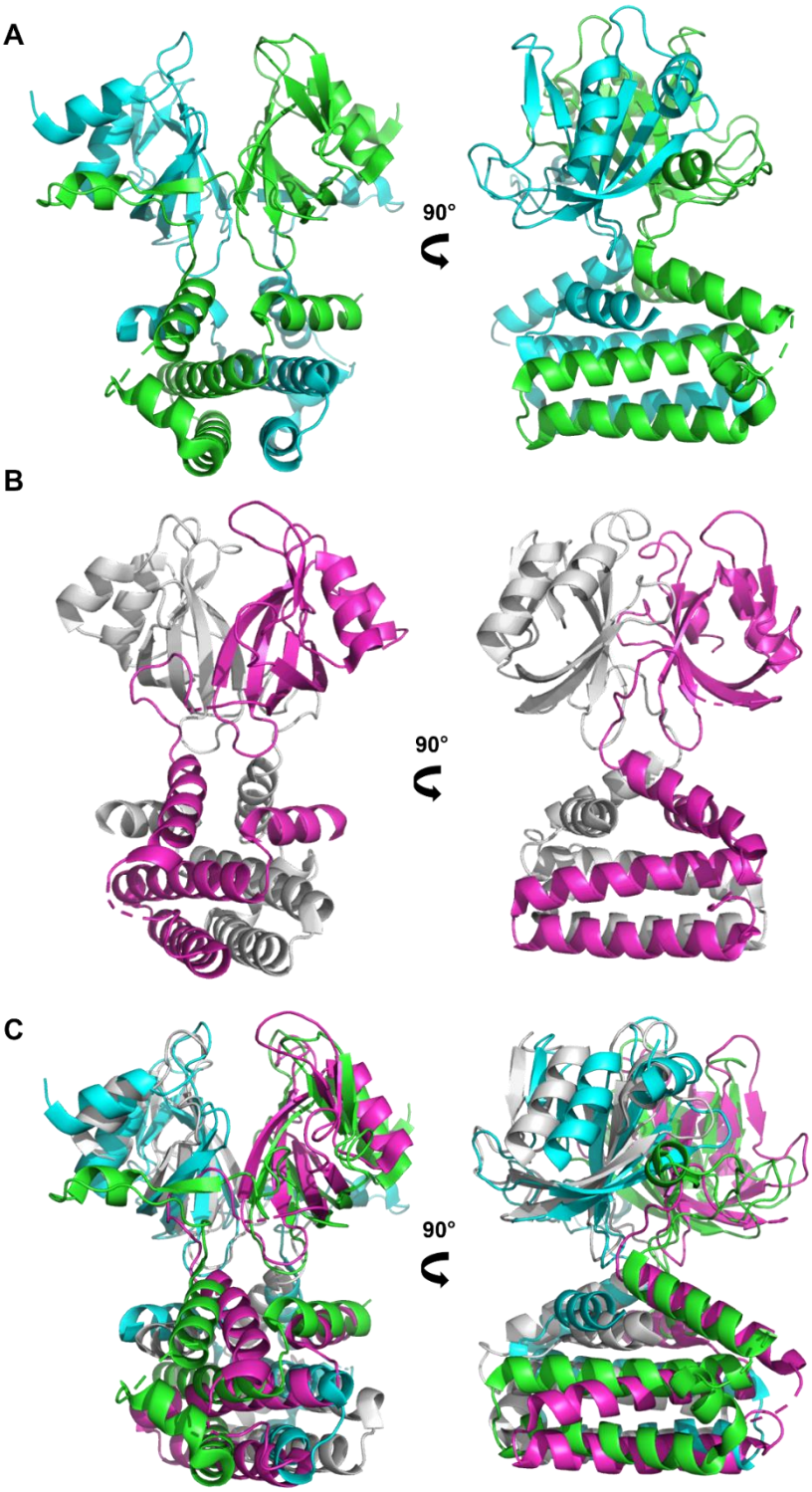

Figure 1.11 Crystal structures of bifunctional HisIE. Crystal structures of HisIE from (A) *S. flexneri* (PDB ID: 6J22) and (B) HISN2 from *M. truncatula* (PDB ID: 7BGM). (C) Overlays of *S. flexneri* HisIE and *M. truncatula* HISN2. Proteins are shown with ribbon diagrams and coloured in either green and cyan (*M. truncatula* HISN2) or grey and magenta (*S. flexneri* HisIE). Images were generated in Pymol.

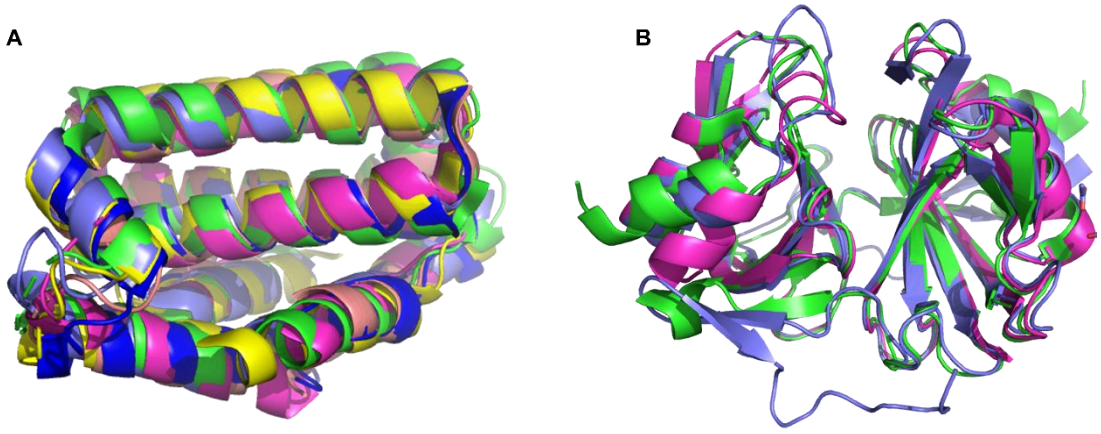

Figure 1.12 Overlays of isolated catalytic domains from *S. flexneri* HisIE and *M. truncatula* HISN2 with HisE from various organisms or *M. thermoautotrophicum* HisI. (A) Overlays of isolated PRATP-PH domains from *S. flexneri* HisI (green) (PDB ID: 6J22) and *M. truncatula* HISN2 (magenta) with HisE from *M. tuberculosis* (PDB ID: 3C90, blue), *B. cereus* (PDD: 1YVW, yellow), *C. violaceum* (PDB ID: 2A7W, purple), and *S. coelicolor* (PDB ID: 1YXB, coral). (B) Overlays of isolated PRAMP-CH domains from *S. flexneri* HisI (green), *M. truncatula* HISN2 (magenta) with *M. thermoautotrophicum* HisI (PDB ID: 1ZPS, purple) (B). Proteins are shown with ribbon diagrams. Images were generated in Pymol.

The Zn^{2+}- and Mg^{2+}-binding sites of the PRATP-PH and PRAMP-CH domains can be readily identified in *S. flexneri* HisIE and *M. truncatula* HISN2 crystal structures, Figures 1.13 and 1.14. In the *M. truncatula* HISN2 structure all metal-binding sites are occupied by Zn^{2+}. Although no metal ions were bound in *S. flexneri* HisIE structure, structural overlays revealed that the architecture of the metal binding-sites is almost identical between the two structures, Figures 1.13 and 1.14.

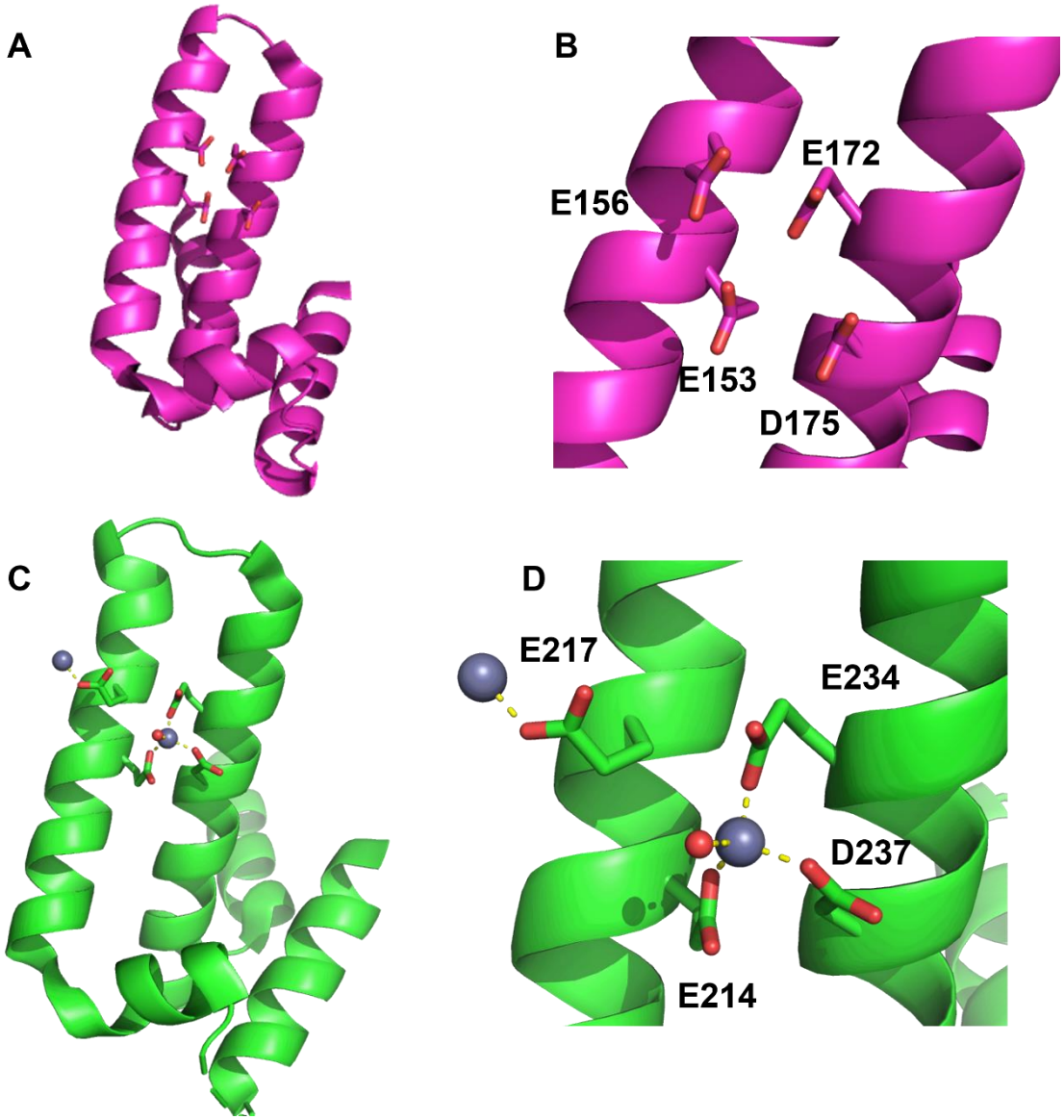

Figure 1.13 Isolated PRATP-PH domain from *S. flexneri* HisIE (PDB ID: 7BGM) and *M. truncatula* HISN2 (PDB ID: 6J22). PRATP-PH domain from (A) *S. flexneri* HisIE and (B) *M. truncatula* HISN2. Close-up views of the Mg^{2+} binding-sites of *S. flexneri* HisIE (C) and *M. truncatula* HISN2 (D). *S. flexneri* HisIE and *M. truncatula* HISN2 subunits are shown with ribbon diagrams and coloured in magenta or green, respectively. Residues of the putative Mg^{2+}-binding site are shown as stick models with nitrogen in blue, oxygen, in red, and carbon in either magenta (*S. flexneri* HisIE) or green (*M. truncatula* HISN2). Zn^{2+} is depicted as grey spheres. Images were generated in Pymol.

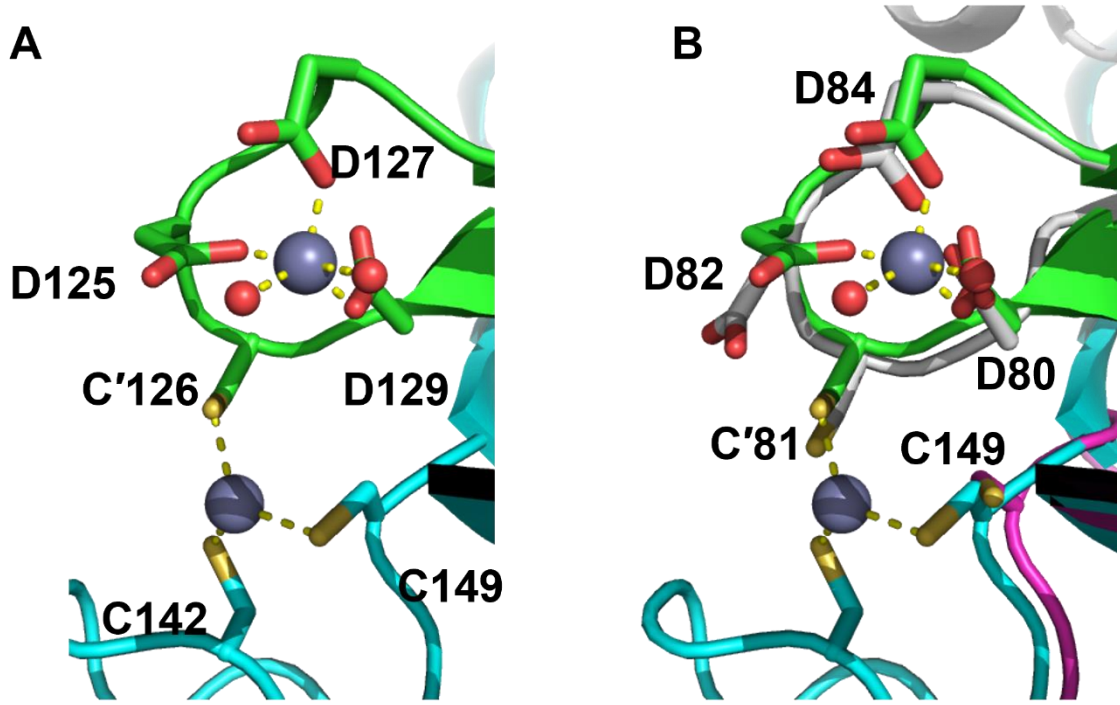

Figure 1.14 Metal binding sites of the PRAMP-CH domain from *M. truncatula* HISN2 (PDB ID: 6J22) and *S. flexneri* HisIE (PDB ID:7BGM). (A) Metal binding sites of the PRAMP-CH domain from *M. truncatula* HISN2 (PDB ID: 6J22). (B) The Zn^{2+}-bound *M. truncatula* HISN2 was overlaid with *S. flexneri* HisIE in to highlight the overall similarity of the metal binding sites. Protein subunits are shown with ribbon diagrams and coloured in either cyan and green (*M. truncatula* HISN2) or magenta and grey (*S. flexneri* HisIE). Residues of the putative Zn^{2+} and Mg^{2+} binding-site are shown as stick models with nitrogen in blue, oxygen in red, sulphur in yellow and carbon in either cyan, green, magenta or pink. Zn^{2+} ions are depicted as grey spheres. Water molecules are represented by red spheres. Metal binding residues are labelled according the *M. truncatula* HISN2 numbering in (A) and *S. flexneri* HisIE numbering in (B). Images were generated in Pymol.

Interestingly, an additional crystal structure of *M. truncatula* HISN2 with AMP bound to both the PRATP-PH and PRATP-CH domains was also recently reported (2021)[71]. The AMP bound to the PRATP-PH domain was considered unlikely to be catalytically relevant as the phosphate of AMP had bound away from the Mg^{2+}-binding site[71]. Contrastingly, at the PRATP-CH domain, AMP bound in an orientation that was considered compatible with catalysis, Figure 1.15A. AMP was rotated 180° relative to the conformation of the same moiety in PRATP in previous docking experiments[64,65,71]. Thus, the SR[S/T] motif from the conserved substrate binding sequence that was proposed to bind the N9-phosphoribosyl moiety may, in fact, bind the N1-phosphoribosyl moiety, whereas the N9-phosphoribosyl moiety may be positioned by the WXKG[E/A]TS motif, Figure 1.15A. Nevertheless, in support of the mechanism proposed by d'Ordine and colleagues, the *M. truncatula* HISN2 crystal structure depicts distances between the Zn^{2+}-bound water and C6 of AMP (3.1 Å) and between His143 and the Zn^{2+}-bound water (3.0 Å) and consistent with the Zn^{2+}-bound water attacking PRAMP at C6 and with histidine serving to activate and orient the Zn^{2+}-bound water, Figure 1.15B. Furthermore, no catalytic activity was detected from a H143E variant of *M. truncatula* HISN2.

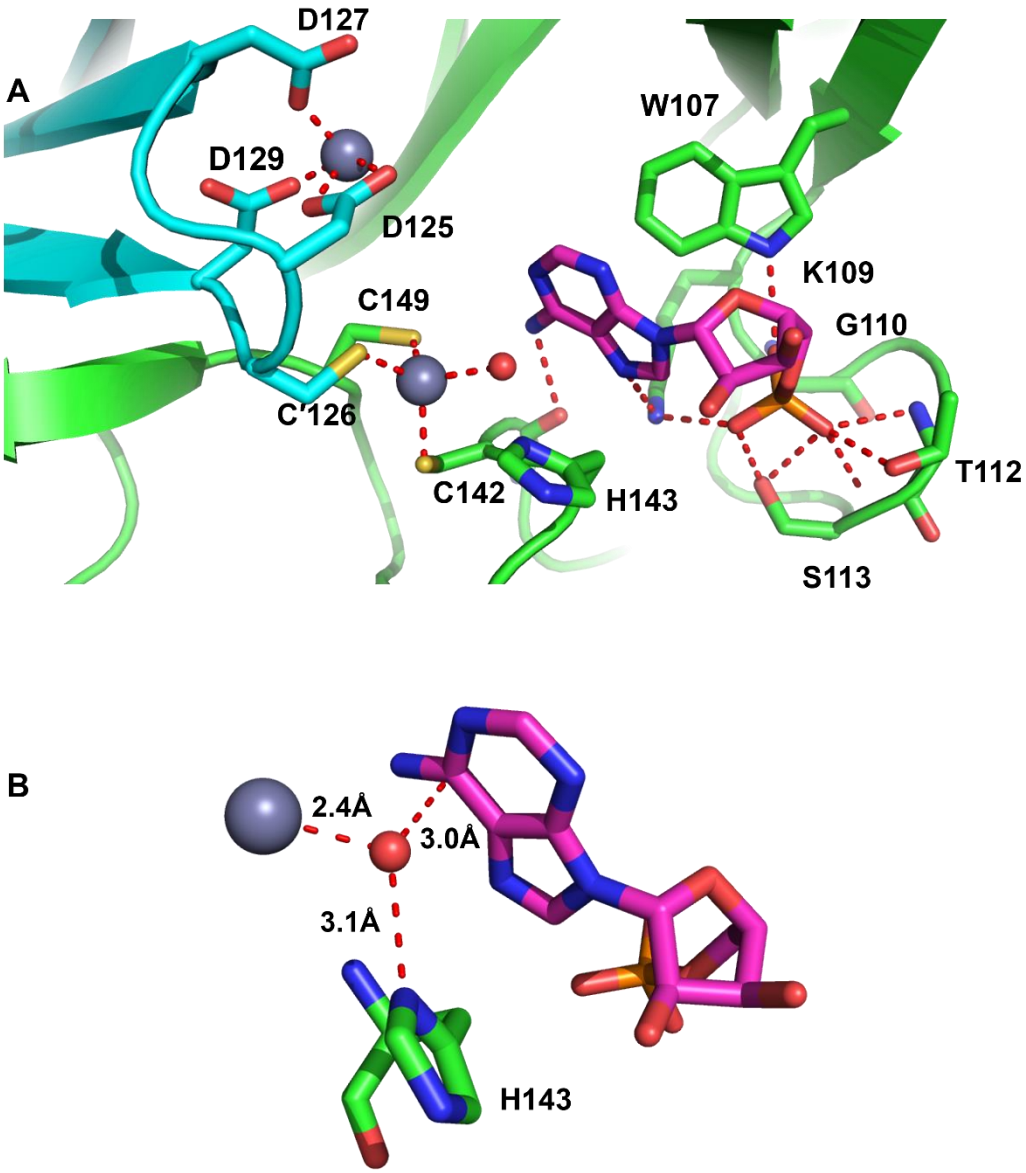

Figure 1.15 Crystal structure of *M. truncatula* HISN2 with AMP bound. (A) Close-up view of AMP-bound to the PRATP-CH domain of *M. truncatula* HISN2 (PDB ID: 7BGN). (B) Distances between Zn^{2+}-H_2O and H143 or C6 of AMP. Protein subunits are shown with ribbon diagrams and coloured in either cyan and green. Residues of the Zn^{2+}- and Mg^{2+}-binding sites and ligands are depicted as stick models with nitrogen in blue, oxygen in red, sulphur in yellow, phosphate in orange and carbon in either cyan, green or magenta. Zn^{2+} ions are represented by a grey sphere. H_2O is shown as a red sphere. Residues that coordinate Zn^{2+} or form polar contacts with AMP are labelled. Red dashed lines depict polar interactions or coordination to a metal ion. Images were generated in Pymol.

Prior to this work, the steady-state kinetic parameters and rate-limiting steps of bifunctional HisIE were not established. Furthermore, no steady-state kinetic parameters had been reported for reactions catalysed by HisE and the only reported steady-state kinetic parameters of HisI were from archaeal organisms, *M. vannielii*[63] and *M. thermoautotrophicum*[64]. The histidine biosynthetic pathway is an attractive target for novel antimicrobial agent development in various pathogenic bacteria and HisI, specifically, has been highlighted as a possible target for novel antimicrobial development[72]. Kinetic and biophysical characterisation of bifunctional HisIE *in vitro* is required for inhibitor development/screening.

1.4 Applications of studying the histidine biosynthetic pathway

1.4.1 Overcoming histidine feedback inhibition for industrial histidine biosynthesis

Industrial biosynthesis of amino acids and related compounds is a rapidly growing multi-billion dollar market[3]. L-glutamate and L-lysine were the first amino acids to be produced by fermentation on a commercial scale over six decades ago[73]. Nowadays, approximately 3.2 and 2.6 million tonnes of L-glutamate and L-lysine are produced by fermentation per annum, respectively, and demand for more specialised amino acids is growing[3]. Amino acids may be used to supplement animal feed and as building blocks for the synthesis of pharmaceutical, cosmetic or agricultural products[74]. Histidine, specifically, is used as a buffer in several vaccines including Gardasil® (a human papillomavirus vaccine) and Vaxzevria (a SARS-CoV-2 vaccine [also known as the Oxford/AstraZeneca Covid-19 Vaccine)[4,5]. Histidine is also found in solutions/emulsions for parenteral nutrition[6,7], infant formula[8] and cosmetic products[9].

Traditional routes of histidine production include protein hydrolysis[75], however, this method has notable drawbacks including dependence of the availability of naturally histidine-rich compounds[75–77]. On the other hand, producing histidine via industrial fermentation in which microorganisms convert sugars into a desired end-product has several advantages including the ability to scale-up synthesis to meet demand and mild

conditions that maintain product integrity/stability[75–77]. Overcoming histidine feedback inhibition of ATPPRT is vital for generating histidine accumulating microbes. Efforts to produce an ATPPRT suitable for industrial application have included targeted mutagenic strategies which aim to disrupt histidine binding to $HisG_L$-type ATPPRTs[2,41,78,79]. Unfortunately, truncations of the C-terminal histidine binding domain severely impairs $HisG_L$ activity[38,78] and though point mutations at the histidine binding site and/or signal transmission pathway can facilitate histidine accumulation, *in vitro* data demonstrated these mutant $HisG_L$ proteins may still be partially inhibited by high concentrations of histidine[41,78]. For example, S143F *C. glutamicum* $HisG_L$ retains only 35% activity at 200 mM histidine[78].

Contrastingly, when expressed in the absence of HisZ, $HisG_S$-type ATPPRTs are completely insensitive to histidine[32,35]. Thus, a detailed understanding of the molecular mechanism underpinning allosteric activation of $HisG_S$ by HisZ may facilitate rationale engineering of $HisG_S$ in order to generate a more-active, industrially-viable $HisG_S$ variant that that is truly insensitive to feedback inhibition. Previous work by Buller and colleagues, has demonstrated that it is possible to introduce mutations which mimic the effects of allosteric activation in tryptophan synthase[80]. Such mutations may shift the rate-limiting step and/or influence the protein conformational landscape[80].

1.4.2 Histidine biosynthesis as a target for novel antimicrobial development

Novel antimicrobial agents are urgently required to address the escalating threat to global health posed by antibiotic resistance. Globally, antimicrobial resistance is estimated to be responsible for approximately 700,000 deaths per annum and this is predicted to rise to 10 million deaths per annum by 2050 if no action is taken[81].

Recent work suggests the enzymes of the histidine biosynthetic pathway are an untapped source of novel antimicrobial targets in key resistant bacteria such as *Acinetobacter baumaunnii* and *Mycobacterium tuberculosis*. High-throughput transposon library analysis demonstrated that six enzymes of the histidine biosynthetic pathway are required for *A. baumannii* persistence in the lungs, including ATPPRT, bifunctional HisIE, and HisC[10]. Similarly, histidine biosynthesis has been shown to protect *M. tuberculosis* from host-mediated histidine starvation *in vivo*[13]. Histidine biosynthesis has also been

implicated in *Aspergillus fumigatus*[15] and *Brucella suis*[14,82] virulence *in vivo*. Mammals do not biosynthesise histidine which bodes well for development of selective antimicrobial agents which exhibit minimal off-target effects, providing that the target organism cannot scavenge histidine from the host

The need for novel antibiotics effective against carbapenem-resistant *A. baumannii*, specifically, was classified as critical by the World Health Organisation in 2017[83]. *A. baumannii* is a gram-negative and opportunistic pathogen which enters the body via mucous membranes, broken skin or medical devices, such as intravascular catheters and mechanical ventilators[84,85]. Ventilator-associated pneumonia is a common manifestation of *A. baumannii* associated with high mortality rates[86–89]. *A. baumannii* and carbapenem-resistant *A. baumannii* infections account for approximately 20.9% and 13.6%, respectively, of all hospital-associated infections in intensive care units across Europe, the Eastern Mediterranean Region and Africa[90].

Carbapenems are members of the β-lactam class of antibiotics and are typically reserved for treatment of multi-drug resistant (MDR) infections[91,92]. Widespread deployment of carbapenems to tackle increasing incidences of MDR infections has been associated with a striking rise in carbapenem resistance reported in several organisms including *A. baumanii*[93,94]. Carbapenem-resistant *A. baumannii* is classified as extensively drug resistant (XDR) and poses a serious threat to global public health as treatment options are extremely limited[95]. Alarmingly, studies in Southern Vietnam and across Europe identified ~85% and 97% of *A. baumannii* isolated from patients with pneumonia were carbapenem resistant[96,97]. Additionally, 48% of the isolates from the European study were classified as resistant to the colistin, which is a last-resort treatment[97]. Thus, novel antibiotics are urgently required to treat drug-resistant *A. baumannii* infections.

As previously highlighted, high-throughput transposon analysis identified six enzymes of the histidine biosynthetic enzymes pathway required for *A. baumannii* persistence in the lungs during pneumonia, including ATPPRT, bifunctional HisIE, and HisC[10]. Approximately 2 μM histidine was detected in the extracellular space in lungs of mice infected with *A. baumannii*[98]. *A. baumannii* is considered an extracellular pathogen and the IC_{50} of *A. baumannii* ATPPRT for histidine is approximately 135 uM[45]. Thus, it is very likely that available concentration of histidine during infection does not match the

requirements of *A. baumannii*. The role of the histidine biosynthetic enzymes during *A. baumannii* colonisation of the lungs is likely multi-faceted. Histidine catabolism is posited to play key roles in *A. baumannii* Zn^{2+}-homeostasis[98,99] and biofilm formation[100]. Deficiency in histidine catabolic enzymes leads to avirulent strains towards lung infection and inability to form biofilms[98,100]. Furthermore, Martínez-Guitián and colleagues recently demonstrated HisF is upregulated in *A. baumannii* during lung infection and that the survival rate in murine pneumonia models is significantly greater ($p < 0.001$) when mice are infected with HisF-deficient *A. baumannii* compared with WT *A. baumannii*[11,12]. Crucially, Martínez-Guitián and colleagues observed significantly greater concentrations of the pro-inflammatory cytokine IL-6 and leukocytes in tissue extracted from mice infected with the HisF-deficient *A. baumannii* compared with WT *A. baumannii*[12]. *In vitro* phagocytosis assays suggested that a by-product of the reaction catalysed by HisF, 5-aminoimidazol-4-carboxamide (AICAR), plays a role in suppression of the host innate immune system[12]. Nonetheless, the requirement for HisC, which catalyses a step of histidine biosynthesis after formation of AICAR, for *A. baumannii* persistence in the lungs[10] suggests histidine biosynthetic enzymes are required independently of possible AICAR-mediated host immune-suppression.

In summary, novel antimicrobials are urgently required to treat *A. baumannii* infections. HisIE is one of six histidine biosynthetic enzymes required for *A. baumannii* persistence in the lungs, however, HisIE from *A. baumannii* has not been characterised and no kinetic characterisation has been reported for any bifunctional HisIE. Kinetic characterisation of HisIE from *A. baumannii* is the first step towards inhibitor development/screening with a view towards novel antibiotic development.

1.5 Project Aims

1.5.1 Project Aim 1

The first aim of this work is to define the mechanism underpinning allosteric activation of *P. arcticus* $HisG_S$ by *P. arcticus* HisZ, as henceforth referred to as *Pa*$HisG_S$ and *Pa*HisZ, respectively, with a view toward biocatalytic production of histidine. *Psychrobacter arcticus* is a gram-negative, rod-shaped, psychrophilic bacterium from the

Siberian permafrost[101] which encodes a $HisG_S$-type ATPPRT previously characterised in the da Silva laboratory[32]. More specifically, this work sought to define the kinetic-mechanism of *Pa*$HisG_S$; establish the identity of ADP as either a substrate or inhibitor of *Pa*$HisG_S$; uncover the rate-limiting steps of *Pa*$HisG_S$ alone and in the presence of the allosteric modulator, *Pa*HisZ; identify key catalytic residues of *Pa*$HisG_S$ and propose a model of allosteric activation of *Pa*$HisG_S$ by *Pa*HisZ.

1.5.2 Project Aim 2

The second aim of this work was to establish key kinetic and biophysical parameters of HisIE from *A. baumannii*, henceforth referred to as *Ab*HisIE. More specifically, it was sought to clone, produce and purify recombinant *Ab*HisIE; enzymatically synthesise and isolate the substrate of *Ab*HisIE, PRATP; determine the steady-state kinetic parameters of *Ab*HisIE and probe the rate-limiting steps of this complex bifunctional system. It was envisioned this work would pave the way for future inhibitor development.

Chapter 2 Materials and Methods

2.1 Reagents

All commercially available chemicals were used without further purification. BaseMuncher endonuclease was purchased from AbCam. Ampicillin sodium, dithiothreitol (DTT), isopropyl β-D-1-thiogalactopyranoside (IPTG) and 2-(*N*-morpholino)ethanesulfonic acid-sodium dodecyl sulfate (MES-SDS) gel running buffer were purchased from Formedium. DH5α (high efficiency) *E coli*, Gibson Assembly Cloning Kit and Dpn1 were purchased from New England Biolabs. QIAprep Spin Miniprep, PCR clean-up and Plasmid Midi kits were purchased from Qiagen. Ethylenediaminetetraacetic acid (EDTA)-free cOmplete protease inhibitor cocktail was purchased from Roche. Ammonium bicarbonate, ammonium sulfate, ATP, C43 (DE3) chemically competent *E. coli.*, D_2O, glycerol, histidine, imidazole, lysozyme, PRPP, potassium chloride, tricine, ZnCl were purchased from Sigma-Aldrich. Agarose, dNTPSs, kanamycin sulfate , 4-(2-hydroxyethyl)piperazine-1-ethanesulfonic acid (HEPES EnzCheck^{TM} Pyrophosphate Kit, $MgCl_2$, NaCl, PageRuler Plus Prestained protein ladder, PageRuler^{TM} Plus Prestained protein ladder, Phusion High-Fidelity polymerase and SYPRO orange protein gel stain were purchased from ThermoFisher Scientific. gBlocks and primers were synthesised by Integrated DNA technologies (IDT)

2.2 Materials

Ultrafiltration membranes were manufactured by Millipore. Dialysis bags and Vivaspin centrifugal units were purchased from Sigma-Aldrich. The high-pressure cell disruptor used for cell lysis was manufactured by Constant Systems. All protein purification was carried out using an AKTA Start FPLC system and all columns were purchased from GE Lifesciences.

2.3 Protein Sequences

Mass and extinction coefficients at 280 nm (ε280) for the proteins were calculated by the software ProtParam.

*Pa*HisG$_S$ (25213 Da, ε280 = 8,940 M^{-1} cm^{-1})

GMTEVTNSLPTSGLLNEANDEFLGLTLALSKGRILEETMPLLRAAGVELLEDPE
ASRKLIFPTSNPNVRVLILRASDVPTYVEHGAADFGVAGKDVLLEHGANHVYE
LLDLKIAQCKLMTAGVKDAPLPNRRLRIATKYVNVARAYFASQGQQVDVIKLY
GSMELAPLVGLGDLIVDVVDTGNTLRANGLEARDHICDVSSRLIVNQVSYKRK
FALLEPILDSFKNSINSTS

*Pa*HisZ (Untagged) (43,028 Da, ε280 = 25,900 M^{-1} cm^{-1})

GMLPDGVADVLFEDAHKQEVLRHQLTQQLITHGYQLVSPPMIEFTESLLSGASE
DLKRQTFKIIDQLTGRLMGIRADITPQILRIDAHHGGDGIARYCYAGDVIHTLPS
GLFGSRTPLQLGAEIFGCESIAADIELIDVLFSMINSLDMSAVLHVDLGHVTIFKR
LAELAALSASDTEQLMQLYANKNLPELKQVCQVLPMGSDFYTLARFGHDIANL
LGRLSENAQQDTKIVTAIDELQRLKAHLQVQWQCAVSIDVTELSGYHYHTGIVF
NGYINSETQPLVRGGRFDGMKSNQLATNQPRQATGFSMDVSRLLAHTQLDAPF
IVLIDYDAFNNLDSAQRQLLLQQVASLRQQGYRVTMPLTAEDMPVGLTHRLSL
ADNQWRLHAV

*Pa*HisZ (His-tagged) (44,703 Da, ε280 = 27,390 M^{-1} cm^{-1})

HHHHHHENLYFQGMLPDGVADVLFEDAHKQEVLRHQLTQQLITHGYQLVSPP
MIEFTESLLSGASEDLKRQTFKIIDQLTGRLMGIRADITPQILRIDAHHGGDGIAR
YCYAGDVIHTLPSGLFGSRTPLQLGAEIFGCESIAADIELIDVLFSMINSLDMSAV
LHVDLGHVTIFKRLAELAALSASDTEQLMQLYANKNLPELKQVCQVLPMGSDF
YTLARFGHDIANLLGRLSENAQQDTKIVTAIDELQRLKAHLQVQWQCAVSIDV
TELSGYHYHTGIVFNGYINSETQPLVRGGRFDGMKSNQLATNQPRQATGFSMD
VSRLLAHTQLDAPFIVLIDYDAFNNLDSAQRQLLLQQVASLRQQGYRVTMPLT
AEDMPVGLTHRLSLADNQWRLHAV

*Pa*HisIE (31,035 Da, ε280 = 43,430 M^{-1} cm^{-1})

MTLPAWLTAVNFNADGLIPAIAQDHESGRILMMAWMNAESLQLTADTQTAVY
FSRSRAKLWHKGESSGHTQRVHDIRLDCDADVIVLSVTQAGGIACHTGRESCFY
QRLDLSGQTPEWQTVDKVIKDPAEIYHSNEVANPPPTNDATAHNSVSFDADAN
QAKADKTSILQQLDRVLAERKQADADSSYVASLYDKGLNKILEKVGEESTESII
AAKDFANCDENIDKSQYDEARSELIYEVADVWFHTLVGLAWFGIESDAVLNEL
GRRFGLSGIDEKAAR

*Ab*HisIE (29,196 Da, ε280 = 40,910 M^{-1} cm^{-1})

MNNTQWLDEVKFNEQGLIPAIAQHHQTGRILMVAWMNRESLALTAEKNQAVY
FSRSRQKLWHKGEESGHFQTVYEIRLDCDGDVIVLQVEQHGGIACHTGRESCFY
RKLTPQGWEIVDAQLKDPTAIYGDNAKTESHDHAHTTEQVDVLAHLGQLMQE
RKQAEADTSYVASLYKKGINKILEKVGEEGVETIIAAKDYATQNTESNLNDLIY
ETADLWFHSIVMLGYFDLNPQLIIDELGRRQGLSGLVEKANRNKV

2.4 General Methods

2.4.1 Measurement of *Pa*HisG$_S$ and *Pa*ATPPRT initial velocities.

Initial rates were measured as previously described[32] at 20 ºC in Tricine (100 mM), KCl (100 mM), $MgCl_2$ (15 mM), DTT (4 mM) (pH 8.5) with 10 µM *Mt*PPase. *Mt*PPase irreversibly hydrolyses pyrophosphate into inorganic phosphate thus rendering the overall reaction irreversible[32]. Reactions (500 µl) were monitored for an increase in absorbance at 290 nm corresponding to the formation of PRATP or PRADP (pH 8.5, Ɛ290nm = 3600 M^{-1} cm^{-1})[102] for 60 seconds in 1 cm path-length quartz cuvettes (Hellma) using a Shimadzu UV-2600 spectrophotometer. Cuvettes were incubated for 3 minutes inside the spectrophotometer before reactions were started by addition of PRPP. All measurements were carried out in at least duplicates.

2.4.2 Measurement of *Pa*HisIE and *Ab*HisIE initial velocities.

Initial rates were measured at either 20 ºC (*Pa*HisIE) or 25 ºC (*Ab*HisIE) in HEPES (100 mM) and $MgCl_2$ (either 12 mM [*Pa*HisIE] or 15 mM [*Ab*HisIE]). Additionally, reactions with *Ab*HisIE also contained DTT (4 mM). Reactions (500 µl) were monitored for an increase in absorbance at 300 nm corresponding to the formation of ProFAR (pH 7.5, ΔƐ300nm = 6700 M^{-1} cm^{-1})[102] for 30 – 120 seconds in 1 cm path-length quartz cuvettes (Hellma) using a Shimadzu UV-2600 spectrophotometer. Cuvettes were incubated for 3 minutes inside the spectrophotometer before reactions were started by addition of PRATP. All measurements were carried out in at least duplicates.

2.4.3 Pre-steady state kinetics

Pre-steady state measurements were performed at either 20 °C (*Pa*HisGS and *Pa*ATPPRT) or 25 °C (*Ab*HisIE) in an Applied Photophysics SX-20 stopped-flow

spectrophotometer (0.5-cm path length and 0.9-ms dead-time) and a circulating water bath for temperature control. Absorbance was recorded at either 290 nm (*Pa*HisG$_S$ or *Pa*ATPPRT) or 300 nm (*Ab*HisIE). For reactions with *Pa*HisG$_S$ and *Pa*ATPPRT, one syringe carried enzyme (*Pa*HisG$_S$ with or without *Pa*HisZ)and PRPP while the other carried ATP. For reactions with *Ab*HisIE one syringe carried *Ab*HisIE whilst the other carried PRATP. All pre-steady state measurements were triggered by rapidly mixing 55 µl from each syringe.

2.4.4 Differential scanning fluorometry (DSF)

DSF measurements (λ_{ex} = 490 nm, λ_{em} = 610 nm) were performed in 96-well plates on a Stratagene Mx3005p instrument. Reactions (50 µL) typically contained 7 µM protein and 5X Sypro Orange (Invitrogen) was added to all wells. Thermal denaturation curves were recorded over a temperature range of 25 ºC – 93 ºC with increments of 1 ºC min^{-1}. Control curves lacked enzyme and were subtracted from curves containing enzymes. All measurements were carried out in triplicate unless stated otherwise.

2.4.5 ^{31}P-NMR Spectroscopy of *Pa*HisG$_S$ and *Pa*ATPPRT catalysed reactions

*Pa*HisG$_S$ and/or *Pa*ATPPRT reactions were evaluated by ^{31}P-NMR spectroscopy as previously described[32]. Typically, either *Pa*HisG$_S$ or *Pa*ATPPRT were incubated with PRPP, ATP and *Mt*PPase (20 µM) in 100mM tricine (pH 8.5), 15 mM $MgCl_2$, 100 mM KCl, DTT (4 mM) with *Mt*PPase (20 µM) for 1 hour at 20 °C. Proteins were removed by passage through 10,000 kDA MWCO Vivaspin centrifugal concentrators and 100 µL D_2O was added to each reaction. ^{31}P-NMR spectra were recorded on either a Bruker AV 400 or Bruker AVII 400 spectrophotometer and a total of 128 scans were collected.

2.4.6 Liquid chromatography-mass spectrometry (LC-MS) analysis of reactions catalysed by *Pa*HisIE and *Ab*HisIE.

Reactions (500 µL) typically contained either PRATP or PRADP and either *Pa*HisIE or *Ab*HisIE in HEPES (100 mM) and $MgCl_2$ (15 mM). Reactions were incubated for 1 hour at 20 °C and proteins were removed by passage through a 10,000 kDA MWCO Vivaspin centrifugal concentration. LC-MS analysis of the proteins free mixtures was performed by Dr Alison Dickson, formerly of the Czekster Laboratory. Samples (either 0.5 or 1 µL)

were loaded onto an Atlantis Premier BEH C18 AX column (2.1 × 100 mm, 1.7 μm) on a Waters ACQUITY UPLC system coupled to a Xevo G2-XS QToF mass spectrometer equipped with an ESI source. Reaction components were separated in (A) ammonium acetate pH 6, (B) acetonitrile and (C) ammonium acetate pH 10. The following sequence was employed to separate products : 0 – 0.5 min 90% (A) and 10% (B); 0.5 – 2.5 min linear gradient from 90% (A) and 10% (B) to 50% (A), 10% (B) and 40% (C); hold from 2.5 – 7 min 50% (A), 10% (B) and 40% (C).at a flow rate of 300 μM min^{-1}. Electrospray ionisation data were acquired in negative mode with a capillary voltage of 2500 V. The source and desolvation gas temperatures of the mass spectrometer were 100 °C and 250 °C, respectively. The cone gas flow was 50 L $hour^{-1}$, whilst the gas flow was 600 L $hour^{-1}$. A scan was performed between 50 – 1200 m/z. A lockspray signal was measured and a mass correction was applied by collecting every 10 seconds, averaging 3 scans of 0.5 seconds each, using Leucine Enkephalin as a correction factor for mass accuracy

2.4.7 Data Analysis

All kinetic data were analysed using the non-linear regression function of SigmaPlot 12 (SPSS Inc.). For ATPPRT, data collected at fixed concentrations of *Pa*HisG$_S$ and substrates with varying concentrations of *Pa*HisZ or *Ab*HisZ were fitted to Equation 2.1. The concentration of either *Pa*ATPPRT or *Ab*HisZ-*Pa*HisG$_S$ in future measurements was calculated using Equation 2.2 All substrate saturation data were fitted to Equation 2.3. In Equations 2.1-2.3, v is the initial rate, Vmax is the maximal velocity, G is the concentration of *Pa*HisG$_S$, Z is the concentration of *Pa*HisZ, K_D is the equilibrium dissociation constant, *Pa*ATPPRT is the concentration of the *Pa*HisG$_S$-*Pa*HisZ complex, S is the concentration of the varying substrate, k_{cat} is the steady-state turnover number, K_M is the apparent Michaelis constant, E_T is the total enzyme concentration.

Equation 2.1

$$PaATPPRT = \frac{(G + Z + K_D) - \sqrt{(G + Z + K_D)^2 - 4GZ}}{2}$$

Equation 2.2

$$v = V_{max}\frac{(G + Z + K_D) - \sqrt{(G + Z + K_D)^2 - 4GZ}}{2G}$$

Equation 2.3

$$\frac{v}{E_T} = \frac{k_{cat}S}{K_M + S}$$

Pre-steady state multiple- and single-turnover data were fitted to Equations 2.4 and 2.5, respectively, where P(t) is product concentration at time t, A_B is the amplitude of the burst phase, A_{sto} is the amplitude change for the single-turnover reaction, k_{burst} is the first-order rate constant of the product formation in the burst phase, k_{sto} is the single turnover rate constant, *v* is initial velocity and t is the reaction time,.

Equation 2.4

$$P(t) = A_B\,(1 - e^{-k_{burst}t}) + vt$$

Equation 2.5

$$P(t) = A_{sto}(1 - e^{-k_{sto}t})$$

DSF thermal denaturation data were fitted to Equation 2.6, where F_U is fraction unfolded, T is the temperature in °C, T_M is the melting temperature, c is the slope of the transition region and LL and UL are folded and unfolded baselines, respectively. Equation 2.6 is from reference[103].

Equation 2.6

$$F_U = LL + \frac{UL - LL}{1 + e^{\frac{Tm - T}{c}}}$$

2.5 Methods for Chapter 3

Materials and methods for Chapter 3 have previously been published in "Fisher G., Thomson C. M., Stroek R., Czekster C. M., Hirschi J. M., and da Silva R. G., Allosteric activation shifts the rate-limiting step in a short-form ATP phosphoribosyl transferase. *Biochemistry* **2018,** 57, (29), 4357-4367."

*Pa*HisG$_S$, *Pa*HisZ, *Mt*PPase and TEVP were produced using methods previously established by the da Silva laboratory[29,32,104]. The procedures are briefly outlined in the following paragraphs.

2.5.1 Protein production

Glycerol stocks of expression cells transformed with expression vectors encoding N-terminal His-tagged *Pa*HisG$_s$, *Pa*HisZ, *Mt*PPase and TEVP (codon-optimised), were provided by Dr Rafael da Silva. The specific expression cell type, expression vector, antibiotic required for selection, and induction temperature for each protein are detailed in Table 2.1. Starter cultures were prepared by inoculating lysogeny broth (LB) (5 mL) containing either kanamycin (50 µg mL^{-1}) or ampicillin (100 µg mL^{-1}) with a scraping from the appropriate glycerol stock, and incubated overnight at 37 ºC in a shaker. Starter cultures were then transferred to 1 L of LB containing either kanamycin (50 mg mL^{-1}) or ampicillin (100 mg mL^{-1}) and grown at 37 ºC in a shaker until an optical density at 600 nm (OD_{600}) between 0.6 – 0.8 was reached. Cultures were subsequently cooled to the appropriate induction temperature for overnight incubation, Table 2.1, and protein synthesis was induced by addition of IPTG (0.5 mM). The following day, cells were harvested by centrifugation at 6774 g for 15 minutes and cell pellets were stored at -20 ºC.

Table 2-1 Expression cell type, expression vector, antibiotic required for selection and induction temperature for *Pa*HisG$_S$, *Pa*HisZ, *Mt*PPase and TEVP expression.

Protein	Expression cell type	Expression vector	Antibiotic required for selection	Induction temperature (°C)
***Pa*HisG$_S$**	C43 (DE3)	pJexpress431	kanamycin	16
***Pa*HisZ**	BL21 (DE3)	pJexpress414	ampicillin	16
***Mt*PPase**	Bl21 (DE3)	pJexpress411	kanamycin	20
TEVP	Rosetta (DE3)	pRK793	ampicillin	20

2.5.2 *Pa*HisG$_S$ and *Pa*HisZ purification

All purification procedures were performed at 4 ºC. Cell pellets were resuspended in Buffer A (HEPES [50 mM], NaCl [either 300 mM {*Mt*PPase} or 500 mM {*Pa*HisG$_S$, *Pa*HisZ, *Mt*PPase}], imidazole [10 mM] [pH 8.0]) with lysozyme (0.2 mg mL^{-1}), BaseMuncher Endonuclease (750 U) (Abcam) and half a tablet of EDTA-free cOmplete protease inhibitor cocktail (Roche). *Mt*PPase resuspension buffer also contained $MgCl_2$ (5 mM) and $CaCl_2$ (1 mM). Cells were lysed in a high-pressure cell disruptor and fractionated by centrifugation at 48,000 g for 30 min. Supernatants was filtered through a 0.45 µM membrane and loaded onto a 5 mL HisTrap FF Column.

Columns were washed with 10 column volumes (CV) of buffer A after which proteins were eluted across a 20 CV linear gradient of either 0 – 40% (*Pa*HisG$_s$) or 0 – 60% (*Pa*HisZ, *Mt*PPase, TEVP) buffer B (HEPES [50 mM], NaCl [either 300 mM {*Mt*PPase} or 500 mM {*Pa*HisG$_S$, *Pa*HisZ, *Mt*PPase}], imidazole [500 mM] [pH 8.0]).

For His-tagged *Pa*HisZ, *Mt*PPase and TEVP, fractions were analysed by sodium dodecyl sulfate−polyacrylamide gel electrophoresis (SDS−PAGE) and fractions found to contain only the protein of interest were pooled and dialysed twice against 2 L of either buffer C

(His-tagged *Pa*HisZ and *Mt*PPase, HEPES [20 mM] [pH 8.0]) or buffer D (TEVP, phosphate buffered saline, NaCl [10 g L^{-1}], glycerol [10%] [*v*/*v*]). After dialysis, protein solutions were concentrated using 10,000 molecular weight cutoff (MWCO) ultrafiltration membranes (Millipore) and protein concentrations were determined spectrophotometrically using the theoretical extinction co-efficient (ε280) 27,930 M^{-1} cm^{-1} for His-tagged *Pa*HisZ, 19,949 M^{-1} cm^{-1} for *Mt*PPase and the theoretical ε280 for 1 % (*w*/*v*) = 11.26 for TEVP. The intact mass of His-tagged *Pa*HisZ was determined by electrospray ionisation mass-spectrometry(ESI-MS). Mass-spectrometry was performed by the BSRC mass-spectrometry facility at the University of St Andrews.

For *Pa*HisG$_S$ and non-His tagged *Pa*HisZ, TEVP was added to fractions containing the protein of interest at a ratio of either 1 mg TEVP : 10 mg *Pa*HisG$_S$ or 1 mg TEVP: 15 mg *Pa*HisZ and samples were dialysed twice against 2 L of buffer E (HEPES [20 mM], NaCl [150 mM], DTT[2 mM], and glycerol [10%] [pH 7.5]) and then twice against 2 L of buffer A. Protein mixtures were reloaded onto a HisTrap FF 5 mL column and the flow-through was collected and analysed via SDS-PAGE and fractions found to contain only *Pa*HisG$_s$ or *Pa*HisZ were pooled and dialysed twice against 2 L of buffer C. *Pa*HisG$_S$ and *Pa*HisZ were concentrated using either 10,000 (*Pa*HisG$_S$) or 30,000 (*Pa*HisZ) MWCO ultrafiltration membranes, aliquoted, and stored at −80 °C. The concentrations of *Pa*HisG$_s$ and *Pa*HisZ were determined spectrophotometrically using the theoretical extinction coefficients (Ɛ280) = 8,940 M^{-1} cm^{-1} for *Pa*HisG$_s$ and 25,900 M^{-1} cm^{-1} for *Pa*HisZ). The intact mass of *Pa*HisG$_S$ and *Pa*HisZ was determined by ESI/TOF-MS performed by the BSRC mass-spectrometry facility at the University of St Andrews. In this work, *Pa*HisZ denotes non-His tagged *Pa*HisZ and His-tagged *Pa*HisZ denotes *Pa*HisZ with the His-tag still in place.

2.5.3 DSF of *Pa*HisG$_S$ with and without substrates

Thermal denaturation curves of *Pa*HisG$_S$ (7.5 µM) were recorded in the presence and absence of substrates (ATP [6 mM]; PRPP [2 mM]; PRATP [208 µM] or PPi [3.6 mM]) with and without glycerol (22% [*v*/*v*]) in either assay buffer (tricine [100 mM], KCl [100mM] and $MgCl_2$ [15 mM] [pH8.5] with DTT [4 mM]) or phosphate buffer KH_2PO_4 (10mM) and KF (10 mM) [pH 8.0]).

2.5.4 Isothermal titration calorimetry (ITC)

ITC measurements were carried out at 20 °C in a MicroCal PEAQ-ITC calorimeter (Malvern Instruments). *Pa*HisG and ligands were solubilised and/or diluted in 100 mM tricine (pH 8.5), 100 mM KCl, 15 mM $MgCl_2$, 4mM DTT. After a small injection of 0.4 µL, 18 successive injections of 2 µL of ligand (0.8 mM PRPP or 10 mM ATP) were made into 300 µL of 50 µM *Pa*HisG$_S$ with 150 s spacing between injections and a reference power of 10 µcal s^{-1}. Titrations of ligand were performed in duplicate. Heat of dilution was measured by titrating ligand into assay buffer and subtracted from the appropriate binding curve. Data for PRPP binding were fitted to a single-site binding model using PEAQ-ITC analysis software (Malvern Instruments).

2.5.5 Determination of *Pa*ATPPRT equilibrium dissociation constant (K_D) in 0%, 18% and 27% glycerol.

Initial velocities were measured at saturating concentrations of both substrates, 5.6 mM ATP and 2 mM PRPP, with 0.38 µM *Pa*HisG$_S$ and varying concentrations of *Pa*HisZ. in 0% (0.9 – 8.5 µM *Pa*HisZ), 18% (0.5 – 16.3 µM *Pa*HisZ) and 27% (0.5 – 16.3 µM *Pa*HisZ) glycerol (*v/v*).

2.5.6 Initial velocity patterns

*Pa*HisG$_S$ (2.2 µM) initial rates were measured at 20 ºC at varying concentrations of both substrates ATP (0.2 - 2.8 mM ATP) and PRPP (0.1 - 2.0 mM). Measurements were performed in quadruplicate. Data were fitted to Equation 2.7, where *v* is the initial rate, E_T is the total concentration of enzyme, k_{cat} is the steady-state turnover number, K_I is the inhibitor dissociation constant, A and B are the first and second substrates to bind to the enzyme, respectively, and K_A and K_B are their respective Michaelis constants.

Equation 2.7

$$\frac{v}{E_T} = \frac{k_{cat}AB}{K_{IA}K_{IB} + K_AB + K_bA + AB}$$

2.5.7 *Pa*ATPPRT and *Pa*HisG$_S$ saturation kinetics with ATP and PRPP.

*Pa*ATPPRT (0.37 µM) initial rates were measured at saturating concentrations of one substrate and varying concentrations of the other, either ATP (0.4 – 5.6 mM) or PRPP (0.1 – 2.0 mM). *Pa*HisG$_S$ (2.2 or 2.5 µM) initial rates were measured at saturating concentrations of one substrate and varying concentrations of the other, either ATP (either 0.4 – 2.8 mM or 0.4 – 5.6 mM) or PRPP (0.1 – 2.0 mM).

2.5.8 *Pa*HisG$_S$ saturation kinetics with ADP and PRPP.

*Pa*HisG$_S$ (2.2 µM) initial rates were measured at saturating concentrations of one substrate and varying concentrations of the other, either ADP (0.4 mM – 5.6 mM) or PRPP (0.1 – 2.0 mM).

2.5.9 *Pa*ATPPRT and *Pa*HisG$_S$ saturation kinetics in glycerol

*Pa*ATPPRT (0.37 µM) and *Pa*HisG$_s$ (2.2 µM) initial rates were measured at saturating concentrations of one substrate and varying concentrations of the other, either ATP (0.4 – 5.6 mM) or PRPP (0.1 – 2.0 mM), in 0%, 18% and 27% glycerol (*v/v*). Data for *Pa*HisG$_S$ was collected by Dr Rafael G. da Silva. Kinetic solvent viscosity data were fitted to Equation 2.8 where k_0 and k_n are the rate constants in the absence and presence of glycerol, respectively, η_{rel} is the relative viscosity of the solution and m is the slope.

Equation 2.8

$$\frac{(k_o)}{(k_n)} = m(n_{rel} - 1) + 1$$

2.5.10 *Pa*ATPPRT and *Pa*HisG$_S$ saturation kinetics with Mn^{2+}.

15 mM $MgCl_2$ was replaced by $MnCl_2$. *Pa*ATPPRT (0.37 µM) initial rates were measured at saturating concentrations of one substrate and varying concentrations of the other either ATP (0.1 – 1.4 mM) or PRPP (0.1 – 2.0 mM). *Pa*HisG$_S$ (1.1 µM) initial rates were measured at saturating concentrations of one substrate and varying concentrations of the other either ATP (0.1 – 1.4 mM) or PRPP (0.05 – 2.0 mM).

2.5.11 Pre-steady state kinetics

Approach to steady state in *Pa*HisG and *Pa*ATPPRT reactions was investigated under multiple turnover conditions, each syringe contained tricine (100 mM), KCl (100 mM) and $MgCl_2$ (15 mM) (pH 8.5) with DTT (4 mM) and 20 µM *Mt*PPase. In addition, one syringe carried *Pa*HisG$_S$ (40 µM) (with or without *Pa*HisZ [100 µM]) and PRPP (4 mM), while the other carried ATP (11.2 mM). Reaction was triggered by rapidly mixing 55 µl from each syringe. The reaction catalysed by *Pa*HisG$_S$ was monitored across a linear-time base, 5000 data points were collected over 5 seconds. *Pa*ATPPRT absorbance data was collected over a split time-base for 2 seconds, with 4000 data points collected in the first 0.2 seconds and 4000 in the following 1.8 seconds. 8 traces were acquired for each enzyme.

*Pa*HisG$_S$ single-turnover reactions were prepared as described above except the PRPP syringe carried only 5 µM PRPP and the enzyme syringe carried *Pa*HisG$_S$ at 0 µM, 20 µM, 40 µM, and 80 µM. Absorbance at 290 nm was monitored across a linear-time base, 5000 data points were collected over either 250 seconds (20 µM *Pa*HisG$_S$) or 120 seconds (0 µM, 40 µM, 80, µM *Pa*HisG$_S$).

2.5.12 Comparison of *Pa*HisG$_S$ reactions by ^{31}P-NMR Spectroscopy

Reaction mixtures (500 µl) were prepared in duplicate and contained tricine (100 mM), KCl (100 mM) and $MgCl_2$ (15 mM) (pH 8.5) with DTT (4 mM), *Mt*PPase (20 µM), PRPP (3 mM), either ATP (3 mM) or ADP (3mM) and *Pa*HisG (10 µM). Control reactions were prepared without *Pa*HisG$_S$. Samples were incubated for 1 hour at 20 °C after which 100 µl of D_2O was added to each sample and proteins were removed by passage through 10,000 MWCO Vivaspin centrifugal concentrators.^{31}P-NMR spectra were acquired as described in the General Methods Section.

2.5.13 Analysis of the reaction catalysed by *Pa*HisG$_S$ in the presence of $MnCl_2$ by LC-MS

LC-MS was performed under the supervision of Dr Clarissa M. Czekster. Reaction mixtures (500 µL) prepared in duplicate contained tricine (100 mM), KCl (100 mM) and $MnCl_2$ (15 mM) (pH 8.5) with DTT (4 mM), *Mt*PPase (20 µM), ATP (1.4 mM), PRPP

(2.0 mM) and *Pa*HisG$_S$ (10.3 μM). Control reactions did not contain *Pa*HisG$_S$. Reactions were incubated for 1 hour at 20 °C then frozen at -80 ºC. After thawing, proteins were removed by passage through 10,000 MWCO Vivaspin centrifugal concentrators. LC-MS analysis of the protein free mixtures was performed on an EC250/4.6 Nucleodur 100-10 C18 ec HPLC column (10 μm x 4.6 mm x 250 mm) on a 1260 infinity HPLC system coupled to a G6130B Single Quadrupole mass spectrophotometer (Agilent Technologies). Reaction components were separated in TEAA (50mM, pH 7.4) (A) and methanol (B). The following programme was used to PRATP and ATP: 0 - 3 min 100% A, 3 - 3.1 min 90% A 10% B, 3.1 min – 13 min 80% A 20% B, at a flow rate of 1 mL min^{-1}. Column eluent was scanned for absorbance at 260 nm and 290 nm. Electrospray ionisation-mass spectrometry data were acquired in negative mode with a capillary voltage of 4,500 V.

2.6 Methods for Chapter 4

Some of the methods for Chapter 4 have previously been published in "Alphey M. S., Fisher G., Ge Y., Gould E. R., Machado T. F. G., Liu H., Florence G. J., Naismith J. H., and da Silva R. G., Catalytic and anticatalytic snapshots of a short-form ATP phosphoribosyltransferase. *ACS Catalysis* **2018**, 8, 5601-5610.

The majority of the methods for Chapter 4 are have been deposited on ChemRxiv and submitted for publication: Fisher G., Corbella M., Alphey M. S., Nicholson H., Read B. J., Kamerlin S. C. L., and da Silva R. G. Allosteric rescue of catalytically impaired ATP phosphoribosyltransferase variants links protein dynamics to active site electrostatic preorganisation. **2022.** (DOI: 10.26434).

2.6.1 Site-directed mutagenesis of *Pa*HisGs

Site-directed mutagenesis was carried out according with overlapping primers according to the method of Liu and Naismith[105]. Each PCR typically contained: template DNA (40 ng μL^{-1}), primers (1 μM each), dNTPs (200μM) and either Phusion-high fidelity polymerase (4 units) (ThermoFisher) or Q5 high-fidelity polymerase (4 units) (NEB), buffer (1X), and sterile H_2O. Primer sequences are listed in Table 2.2 and Table 2.3 alongside the specific annealing temperatures used in each PCR. Briefly, an initial

denaturation step for 7 minutes (94 °C) was followed by 2 RAM stages. The first RAM step included 12 cycles of denaturation (94 °C, 1 minute), annealing (T_M RAM1, Tables 2.2 and 2.3, 1 minute) and extension (72 °C, 5 minutes) steps. The second RAM step included 3 cycles of denaturation (95 °C, 1 minute), annealing step (T_M RAM2, Tables 2.2 and 2.3, 1 minute) extension (72 °C, 5 minutes) steps. A final extension step (72°C, 10, minutes) was added to the reactions.

PCR products were incubated with DPN1 (5 units) (NEB) overnight at 37 ºC. Plasmids encoding C115S and R32A *Pa*HisG$_S$ were cloned by Dr Rafael G. da Silva. Plasmids were transformed into DH5α (high-efficiency) *E coli* (NEB). A single colony of transformed cells was used to inoculate LB (10 mL) with kanamycin (50 µg mL^{-1}) and incubated overnight at 37 °C. Plasmids were then extracted using either QIAprep Spin Miniprep or Plasmid Midiprep kits (Qiagen) according to manufacturer instructions. Correct insertion of each mutation was confirmed by DNA sequencing performed by either Eurofins Genomics or DNA Sequencing & Services (MRC I PPU, School of Life Sciences, University of Dundee). Plasmids confirmed to be carrying the correct mutation were transformed into C43 (DE3) *E. coli* cells.

***Pa*HisGs Mutation**	**Forward Primer**	**Reverse Primer**	**Annealing Temperatures**
C115A	5′ - TTGCGCAGGCTAAAC TGATGACCGCCGGTG TCAAAGACG - 3´	5′ - ATCAGTTTAGCCTGC GCAATCTTCAGATCC AACAGTTCATAAAC GTGGTTC - 3´	57 ºC (Ram 1) 49 ºC (Ram2)
C115S	5′ - TTGCGCAGTCTAAAC TGATGACCGCCGGTG TCAAGACG - 3´	5′ - ATCAGTTTAGACTGC GCAATCTTCAGATCC AACAGTTCATAAAC GTGGTTCG - 3´	57 ºC (Ram 1) 49 ºC (Ram2)
D179A	5′ - TCGTGGCCACCGGTA ATACGCTGCGTG - 3′	5′ - ACCGGTGGCCACGA CGTCAACAATCAGGT CACCCAGGC -3′	57 ºC (Ram 1) 49 ºC (Ram2)
D179N	5′ - GTCGTGAACACCGGT AATACGCTGCGTGCG AACGG - 3′	5′ - CCGGTGTTCACGACG TCAACAATCAGGTCA CCCAGGC -3′	57 ºC (Ram 1) 49 ºC (Ram2)
R32A	5′ - AAGGGTGCCATCCTG GAAGAGACTATGCC GCTGTTGCG-3′	5′ - CAGGATGGCACCCTT GCTCAGTGCCAGGGT CAGACC-3′	57 ºC (Ram 1) 49 ºC (Ram2)
R56A	5′- GCGCTAAGCTGATCT TCCCGACCAGCAACC CTAATGTG-3′	5′- GGAAGATCAGCTTA GCGCTCGCTTCCGGA TCTTCCAGC-3′.	57 ºC (Ram 1) 51 ºC (Ram2)
R56AK57A	5’- GCGCTGCGCTGATCT TCCCGACCAGCAACC CTAATGTG-3’	5’- GAAGATCAGCGCAG CGCTCGCTTCCGGAT CTTCCAGC-3’	59 ºC (Ram 1) 51 ºC (Ram2)

Table 2-2 Primer sequences and annealing temperatures for *Pa*HisG$_S$ site-directed mutagenesis.

Table 2-3 Primer sequences and annealing temperature for *Pa*HisG$_S$ site-saturation mutagenesis at position 56.

***Pa*HisGs Mutation**	**Forward Primer**	**Reverse Primer**	**Annealing Temperatures**
R56A	5′-GCGCTAAGCTGATCTTCCCGACCAGCAACCCTAATGTG-3′	5′-GGAAGATCAGCTTAGCGCTCGCTTCCGGATCTTCCAGC-3′.	57 ºC (Ram 1) 51 ºC (Ram2)
R56C	GCTGTAAGCTGATCTTCCCGACCAGCAACCCTAATGTG	GGAAGATCAGCTTACAGCTCGCTTCCGGATCTTCCAGC	57 ºC (Ram 1) 49 ºC (Ram2)
R56D	GCGATAAGCTGATCTTCCCGACCAGCAACCCTAATGTG	GGAAGATCAGCTTATCGCTCGCTTCCGGATCTTCCAGC	57 ºC (Ram 1) 49 ºC (Ram2)
R56E	GCGAAAAGCTGATCTTCCCGACCAGCAACCCTAATGTG	GGAAGATCAGCTTTTCGCTCGCTTCCGGATCTTCCAGC	57 ºC (Ram 1) 49 ºC (Ram2)
R56F	GCTTTAAGCTGATCTTCCCGACCAGAACCCTAATGTG	GGAAGATCAGCTTAAAGCTCGCTTCCGGATCTTCCAG	55 ºC (Ram 1) 47 ºC (Ram2)
R56G	GCGGTAAGCTGATCTTCCCGACCAGCAACCCTAATGTGC	GGAAGATCAGCTTACCGCTCGCTTCCGGATCTTCCAGCA	61 ºC (Ram 1) 51 ºC (Ram2)
R56H	GCCATAAGCTGATCTTCCCGACCAGCAACCCTAATGTG	GGAAGATCAGCTTATGGCTCGCTTCCGGATCTTCCAGC	57 ºC (Ram 1) 49 ºC (Ram2)
R56I	GCATTAAGCTGATCTTCCCGACCAGCAACCCTAATGTG	GGAAGATCAGCTTAATGCTCGCTTCCGGATCTTCCAGC	55 ºC (Ram 1) 47 ºC (Ram2)
R56L	GCCTTAAGCTGATCTTCCCGACCAGCAACCCTAATGTG	GGAAGATCAGCTTAAGGCTCGCTTCCGGATCTTCCAGC	57 ºC (Ram 1) 49 ºC (Ram2)

R56M	GCATGAAGCTGATCTTCC CGACCAGCAACCCTAATG TG	GGAAGATCAGCTTCATG CTCGCTTCCGGATCTTCC AGC	57 ºC (Ram 1) 49 ºC (Ram2)
R56N	GCAATAAGCTGATCTTCC CGACCAGCAACCCTAATG TG	GGAAGATCAGCTTATTG CTCGCTTCCGGATCTTC	55 ºC (Ram 1) 47 ºC (Ram2)
R56P	GCCCTAAGCTGATCTTCC CGACCAGCAACCCTAATG TGC	GGAAGATCAGCTTAGGG CTCGCTTCCGGATCTTCC A CA	61 ºC (Ram 1) 51 ºC (Ram2)
R56Q	GCCAAAAGCTGATCTTCC CGACCAGCAACCCTAATG TG	GGAAGATCAGCTTTTGG CTCGCTTCCGGATCTTCC AGC	57 ºC (Ram 1) 49 ºC (Ram2)
R56S	GCTCTAAGCTGATCTTCC CGACCAGCAACCCTAATG TG	GGAAGATCAGCTTAGAG CTCGCTTCCGGATCTTCC AGC	57 ºC (Ram 1) 49 ºC (Ram2)
R56T	GCACTAAGCTGATCTTCC CGACCAGCAACCCTAATG TG	GGAAGATCAGCTTAGTG CTCGCTTCCGGATCTTCC AGC	57 ºC (Ram 1) 49 ºC (Ram2)
R56V	GCGTTAAGCTGATCTTCC CGACCAGCAACCCTAAT GTG	GGAAGATCAGCTTAACG CTCGCTTCCGGATCTTCC AGC	57 ºC (Ram 1) 49 ºC (Ram2)
R56Y	GCTATAAGCTGATCTTCC CGACCAGCAACCCTAAT GTG	GGAAGATCAGCTTATAG CTCGCTTCCGGATCTTCC AG	55 ºC (Ram 1) 47 ºC (Ram2)
R56W	GCTGGAAGCTGATCTTCC CGACCAGCAACCCTAAT GTGC	GGAAGATCAGCTTCCAG CTCGCTTCCGGATCTTCC AGCA	61 ºC (Ram 1) 51 ºC (Ram2)

2.6.3 Production of WT, C115A, C115S, D179A, D179N, R32A, R56A, R56A/K57A *Pa*HisGS.

WT, C115A, C115S, D179A, D179A, R32A, R56A, R56A/K57A and R32A/R56A/K57A *Pa*HisG were produced as described for WT *Pa*HisG$_S$ in Methods for Chapter 3. The intact mass of C115A, C115S, D179A, D179A, R32A, R56A, R56A/K57A and R32A/R56A/K57A *Pa*HisG was determined by ESI-MS performed by the BSRC mass-spectrometry facility at the University of St Andrews. Trypsin digest followed by MS/MS analysis of tryptic peptides confirmed the D179N variant of *Pa*HisG$_S$ was carrying the correct mutation. R32A/R56A/K57A *Pa*HisG$_S$ was purified by John Nicholson, formerly Lab Manager and technician of the da Silva Laboratory.

2.6.4 Production of *Pa*HisZ

Non-tagged and His-tagged *Pa*HisZ were produced as described in Methods for Chapter 3.

2.6.5 DSF of WT, C115A, C115S, D179N, R32A, R56A, R56A/K57A and R32A/R56A/K57A *Pa*HisGS

Thermal denaturation curves of C115A, C115S, D179A, R32A, R56A, R56A/K57A and R32A/R56A/K57A *Pa*HisG$_S$ (~ 7 µM) in assay buffer (tricine [100 mM], KCl [100mM] and $MgCl_2$ [15 mM] [pH8.5] with DTT [4 mM]) were recorded in the presence and absence of PRPP (2mM). Control curves lacked enzyme and were subtracted from curves containing enzymes. Measurements were carried out in triplicate except for D179N apo measurements which were quintuplicates.

2.6.6 Oligomeric state determination of WT, C115S, R32A, R56A and R56A/K57A *Pa*HisGS

Analytical size-exclusion chromatography was performed on a Superdex 200 10/300 GL column (GE Healthcare) attached to a Bio-Rad NGC FPLC at 4 °C. WT, C115S, R32A, R56A and R56K57A *Pa*HisG$_S$ (1 mg/ mL, pre-incubated with DTT [2 mM]) were loaded onto the column which was washed with 1 CV of HEPES (20 mM, pH 8.0) at 0.225 mL min^{-1}. Absorbance at 280 nm was recorded.

2.6.7 WT, C115A, C115S, D179N, R32A, R56A, and R56A/K57A *Pa*HisGS activity

C115A, C115S, D179A, D179A, R32A, R56A and R56A/K57A *Pa*HisG (5 and 10 µM) were assayed for catalytic activity at under initial rate-conditions at 20 ºC for either 60 or 870 seconds in the presence of ATP (5.6 mM) and PRPP (2 mM). WT *Pa*HisGS (5 µM) was included in the analysis as a positive control. The measurement with D179A at (5 µM) was only performed as a single measurement.

2.6.8 Determination of WT C115S, R32A, R56A and R56A/K57A *Pa*ATPPRT equilibrium dissociation constant (K_D).

Initial velocities were measured at saturating concentrations of both substrates, ATP (5.6 mM) and PRPP (2 mM) with WT (0.42 µM), C115A (0.59 µM), R32A (1.1 µM), R56A (1.1 µM) and R56A/K57A (1.7 µM) *Pa*HisGS and varying concentrations of *Pa*HisZ (either 0.2 – 5.1 µM [WT] or 1 – 15 µM [C115S] or 0.4 – 8 µM [R32A] or 2 – 15 µM [R56A] or 0.7 – 11 µM [R56AK57A]).

2.6.9 Determination of WT and R56A *Pa*HisGS-*Ab*HisZ equilibrium dissociation constant (K_D)

Initial velocities were measured at saturating concentrations of both substrates, ATP (5.6 mM) and PRPP (2 mM), with either WT (0.19 µM) or R56A (2.5 µM) *Pa*HisGS and varying concentrations of *Ab*HisZ (either 0.8 – 19.7 µM [WT] or 1.7 – 26.9 µM [R56A]). Measurements with R56A *Pa*HisGS were performed in at least triplicate. Data for R56A *Pa*HisGS were fitted to Equation 2.9 where *v* is the initial rate, *V*max is the maximal velocity and n is the Hill number.

Equation 2.9

$$v = \frac{V_{max}[S]^n}{{K_{50}}^n + S^n}$$

2.6.10 Determination of WT, R32A and R56A *Pa*ATPPRT equilibrium dissociation constant (K_D) with His-tagged *Pa*HisZ.

Initial velocities were measured at saturating concentrations of both substrates, ATP (5.6 mM) and PRPP (2 mM), with either 0.23 µM (WT), 0.49 µM (R32A), 0.79 µM (R56A) *Pa*HisG$_S$ and varying concentrations of *Pa*HisZ (0.02 – 1.6 µM [WT], 0.1 – 1.6 µM [R32A and R56A]).

2.6.11 WT, C115A, D179A and D179N *Pa*HisG$_S$ saturation kinetics with ATP and PRPP.

WT (3.4 µM), C115A (10.1 µM), D179A (9.2 µM) and D179N (10.0 µM) *Pa*HisG$_S$ initial rates were measured at saturating concentrations of one substrate and varying concentrations of the other, either ATP (either 0.4 – 5.6 mM [WT, D179A, D179N] or 0.7 mM – 5.6 mM [C115A]) or PRPP (0.1 – 2.0 mM [WT, D179A, D179N] or 0.2 mM – 2 mM [C115A]).

2.6.12 C115S, R32A, R56A and R56A/K57A *Pa*ATPPRT saturation kinetics with ATP and PRPP.

WT (0.4 µM), C115S (0.5 µM), R32A (0.9 µM), R56A (0.9 µM) and R56A/K57A (1.2 µM) *Pa*ATPPRT initial rates were measured at saturating concentrations of one substrate and varying concentrations of the other, either ATP (0.4 – 5.6 mM) or PRPP (0.1 – 2.0 mM). Control reactions were performed in the absence of *Pa*HisZ with bovine serum albumin (BSA) (20 µM) to demonstrate allosteric activation is a specific effect.

2.6.13 WT and R56A *Pa*HisG$_S$-*Ab*HisZ saturation kinetics with ATP and PRPP.

WT (0.36 µM *PaH*isG, 19.7 µM *Ab*HisZ [0.26 µM *Pa*HisG$_S$-*Ab*HisZ]) and R56A (2.5 µM R56A *Pa*HisG$_S$, 19.7 µM *Ab*HisZ) *Pa*HisG$_S$-*Ab*HisZ initial rates were measured at saturating concentrations of one substrate and varying concentrations of the other, either ATP (either 0.2 – 2.8 mM [WT] or 0.4 – 5.6 mM [R56A]) or PRPP (0.1 – 2.0 mM). Control reactions with both substrates at saturating concentrations were performed in the presence and absence of histidine (1 mM). Additional control reactions with WT *Pa*HisG$_S$ in the absence of *Ab*HisZ were performed and subtracted from data where appropriate.

2.6.14 *Pa*ATPPRT saturation kinetics with ATP and PRPP (His-tagged *Pa*HisZ).

WT (0.22 µM) *Pa*ATPPRT initial rates were measured at saturating concentrations of one substrate and varying concentrations of the other, either ATP (0.1 – 2.8 mM) or PRPP (0.1 – 2.0 mM).

2.6.15 Inhibition of reactions catalysed by C115S, R32A, R56A and R56A/K57A *Pa*ATPPRT (His-tagged) by histidine.

C115S (0.43 µM), R32A (0.48 µM), R56A *Pa*HisG$_S$ (0.73 µM) and R56A/K57A *Pa*HisG$_S$ (2.6 µM) *Pa*ATPPRT (His-tagged *Pa*HisZ) initial rates were measured with saturating concentrations of ATP (5.6 mM) and PRPP (2 mM) in the presence and absence of histidine (1 mM).

2.6.16 WT, R32A and R56A *Pa*ATPPRT (His-tagged *Pa*HisZ) initial rates with Mn^{2+}.

WT (0.22 µM), R32A (0.08 µM) and R56A *Pa*ATPPRT (0.18 µM) initial rates were measured with saturating concentrations of ATP (either 1.4 mM [WT] or 5.6 mM [R32A and R56A]) and PRPP (either 1 mM [WT] or 2 mM [R32A and R56A]) in the presence of Mn^{2+} as a substitute for Mg^{2+} (15 mM). Control reactions were performed in the absence of HisZ. Additional controls were performed with with WT (0.22 µM), R32A (0.16 µM) and R56A *Pa*HisG$_S$ (0.34 µM) with saturating concentrations of ATP (5.6 mM), PRPP (2 mM) in the presence of Mg^{2+} (15 mM).

2.6.17 R32A/R56A/K57A *Pa*HisG$_S$ activity

R32A/R56A/K57A *Pa*HisG$_S$ (either 10 µM or 5 µM with 20 µM *Pa*HisZ [His-tagged]) were assayed for catalytic activity at under initial rate-conditions at 20 ºC for either 60 seconds in the presence of ATP (5.6 mM) and PRPP (2 mM). Control reactions were performed in the absence of *Pa*HisG$_S$. Measurements were performed in duplicate.

2.6.18 Chemical rescue of R56A *Pa*HisG$_S$

Rates of PRATP synthesis from reactions catalysed by R56A *Pa*HisG$_S$ (12 µM) were measured in assay buffer (tricine [100 mM], KCl [100mM] and $MgCl_2$ [15 mM] [pH8.5] with DTT [4 mM]) in the presence and absence of either methyl-guanidine or

methylamine or ethylamine or propylamine (50 mM, 100 mM and 200 mM) with saturating concentrations of substrates,ATP (5.6 mM) and PRPP (2 mM), for 30 minutes at 30 °C as previously described.

2.6.19 Comparison of C115S, R32A, R56A and R56K57A *Pa*HisG$_S$ and *Pa*ATPPRT reactions by ^{31}P-NMR Spectroscopy.

Mutant *Pa*HisG$_S$ (either 10 µM [R56A and C115S *Pa*HisG$_S$] or 20 µM [R32A and R56AK57A *Pa*HisG$_{S]}$) was incubated with and without *Pa*HisZ (30 µM) in assay buffer (tricine [100 mM], KCl [100mM] and $MgCl_2$ [15 mM] [pH8.5] with DTT [4 mM]) with *Mt*PPase (20 µM), PRPP (2 mM), ATP (5.6 mM) for 1 hour at 20 °C. Proteins were removed by passage through 10,000 kDA MWCO Vivaspin centrifugal concentrators and 100 µL D_2O was added to each reaction. ^{31}P-NMR spectra were recorded as described in the General Methods section.

2.6.20 Saturation Mutagenesis of *Pa*HisG$_S$ at residue 56

Site-directed mutagenesis of *Pa*HisG$_S$ at residue 56 was carried out as described under site-directed mutagenesis. Constructs confirmed to carry desired R56X mutations were transformed into *E. coli* C43 (DE3) competent cells. Starter cultures of LB (10 mL) with kanamycin (50 µg mL^{-1}) were inoculated with a single colony of the transformed cells and incubated overnight at 37 °C. The following morning, 50 µL of starter culture was transferred to fresh LB (15 mL) with kanamycin (50 µg mL^{-1}) and the cultures were grown at 37 °C until an OD_{600nm} of 0.6 was reached. Cultures were subsequently cooled to 16 °C, protein synthesis was induced with IPTG (0.5 mM) and cultures were incubated at 16 °C overnight. The following morning, two 1 mL samples were taken from each culture and cells were harvested by centrifugation (5 minutes, 11,500 g 4°C).

For each mutation, one pellet was resuspended in 100 µL of BugBuster protein extraction reagent (Merck). The cells resuspended in BugBuster were fractionated via centrifugation (30 minutes, 11,500 g , 4 °C) and the analysed by SDS-PAGE to confirm mutant *Pa*HisG$_S$ production. The other pellet was resuspended in 500 µL of HEPES (20 mM) (pH 8.0). Cells were lysed via sonication at (3 x 10 seconds) at 4 °C and fractionated by centrifugation (30 minutes, 11,500 g , 4 °C). R56X *Pa*HisG$_S$ initial rates were measured

with 100 µL of the cell lysate soluble fraction, ATP (5.6 mM) and PRPP (2 mM) for 60 seconds at 20 °C as previously described.

2.6.21 Crystallisation of R56A *Pa*HisG$_S$

Dr Magnus S. Alphey supervised all crystallography work. Crystals of R56A *Pa*HisG$_S$ were obtained at 4 °C as described for WT *Pa*HisG$_S$[40]. *Pa*HisG$_S$ was buffer exchanged into TRIS (20 mM, pH 8.0), KCl (50 mM), $MgCl_2$ (10 mM), DTT (2 mM) and concentrated to approximately 10 mg mL^{-1}. Protein was mixed in a 1:1 ratio with precipitant (PEG 3350 [32%], MOPS [0.1 M, pH 6.0] and K/Na tartrate [0.1 M]) and hanging drops of protein over mother liquor containing PEG 3350 (32%), MOPS (0.1 M, pH 6.0) and K/Na tartrate (0.1 M) were prepared are previously described[40].Crystals were washed in PEG 3350 (32%), bicine (0.1 M pH 8.5) K/Na tartrate (0.1 M) and $MgCl_2$ (20 mM) then transferred to a solution with PRPP and ATP and incubated for overnight at 4 °C. Crystals were then transferred to a solution with methylpentanediol (MPD) (20%) and flash cooled in liquid nitrogen.

2.6.22 Crystallisation of R56A *Pa*ATPPRT

Crystals of R56A *Pa*ATPPRT were obtained at 4 °C as described for WT *Pa*ATPPRT[32,40]. *Pa*HisG$_S$ and *Pa*HisZ were mixed in a 1:1 molar ratio and buffer exchanged into TRIS (20 mM, pH 7.0), KCl (50 mM), $MgCl_2$ (10 mM), DTT (2mM) and ATP (10 mM) and concentrated to approximately 8 mg mL^{-1}. Protein was mixed in a 1:1 ratio with precipitant (PEG 3350 [12%], Bicine [0.1 M], $SrCl_2$ [0.15 M], KBr [0.15 M]and 1,6-hexaninediol [2%]) and hanging drops of protein over mother liquor containing PEG 3350 (12 %), Bicine (0.1 M), $SrCl_2$ (0.15 M), KBr (0.15 M) and 1,6-hexaninediol (2%) were prepared are previously described[32,40].Crystals were washed in PEG 3350 (10%), Bicine (1 M), $MgCl_2$ (50 mM), KBr (0.1 M) and hexanediol (4%) then transferred to a drop of this solution with PRPP and ATP and incubated for 2.5 hours at 4 °C. Crystals were then transferred to a solution with 20% MPD and flash cooled in liquid nitrogen.

2.6.23 X-ray data collection and processing

Data collection and processing was performed with help and guidance from Dr Magnus S. Alphey. R56A *Pa*HisG$_S$ X-ray diffraction data were collected in house as previously

described[32], processed using iMosfilm[106] and scaled with Aimless[107]. *Pa*ATPPRT X-ray diffraction data were collected at the Diamond Light Source, Oxfordshire, U.K., and processed via the automated pipeline at Diamond with Xia2[108] and integrated with DIALS[109]. R56A *Pa*HisG$_S$ and *Pa*ATPPRT were solved by molecular replacement using MOLREP[110] with 6FCT and 6FU2 as a search models, respectively. Models were refined using cycles of model building in COOT[111] and refinement with Refmac[112]. ATP was modelled at either 70% or 80% occupancy in R56A *Pa*ATPPRT structures. Data collection and refinement statistics are shown in Table 4.7

2.7 Methods for Chapter 5

The purification of PRATP described here has been published in "Read B. J., Fisher G., Wissett O. L. R., Machado T. F. G., Nicholson J., Mitchell J. B. O., and da Silva R. G. Allosteric Inhibition of a *Acinetobacter baumanii* ATP phosphoribosyltransferase by protein:dipeptide interactions and protein:protein interactions. *ACS Infectious diseases* **2022,** *8*(1), 197-209.

2.7.1 *Pa*HisIE production

Untagged *Pa*HisIE in pJexpress411 was provided by Dr Teresa F. G. Machado. Starter cultures were prepared by inoculating LB (5 mL) containing kanamycin (50 µg mL^{-1}) with a scraping from a glycerol stock of BL21 (DE3) *E. coli* cells transformed with pJexpress411 encoding *Pa*HisIE. and incubated overnight at 37 ºC in a shaker. Starter cultures were then transferred to 1 L of LB containing kanamycin (50 mg mL^{-1}) and grown at 37 ºC in a shaker until an OD_{600} between 0.6 – 0.8 was reached. Cultures were subsequently cooled to 16 °C for overnight incubation and protein synthesis was induced by addition of IPTG (0.5 mM). The following day, cells were harvested by centrifugation at 6774 g for 15 minutes and cell pellets were stored at -20 ºC.

2.7.2 *Pa*HisIE purification

All purification procedures were performed at 4 ºC. Cell pellets were resuspended in Buffer A (HEPES [50 mM] pH 7.5) with lysozyme (0.2 mg mL^{-1}), BaseMuncher Endonuclease (750 U) (Abcam) and half a tablet of EDTA-free cOmplete protease

inhibitor cocktail (Roche). Cells were lysed in a high-pressure cell disruptor and fractionated by centrifugation at 48,000 g for 30 min. Buffer A with 3.5 M $(NH_4)_2SO_4$ was added dropwise to the supernatant until a concentration of 1.5 M M $(NH_4)_2SO_4$ was reached. The sample was left to stir for 30 minutes then centrifuged at 48,000 g for 30 minutes to remove the precipitate. The supernatant was dialysed against 3 x 2L of buffer A, filtered through a 0.45 µM membrane and loaded onto a 10 mL HiTrapQ FF column pre-equilibrated with buffer A. The column was washed with 20 CV of 8% buffer B (HEPES [50 mM), NaCl [2 M], pH 7.5) and the adsorbed proteins were eluted across a 30 CV linear gradient of 8-20% buffer B. Fractions were analysed via SDS-PAGE and fractions found to contain *Pa*HisIE were pooled and dialysed against 2 x 2L of buffer C (HEPES [50 mM), NaCl [250 mM], pH 8.0), filtered through a 0.45 µM membrane and loaded onto a 5 mL HisTrap FF column charged with $ZnCl_2$, pre-equilibrated with buffer C. The column was washed with 10 CV of buffer C and the adsorbed proteins were eluted across a 20 CV linear gradient of 0-20% buffer D (HEPES [50 mM], NaCl [250 mM], imidazole [50 mM] pH 8.0). Fractions were analysed via SDS-PAGE and fractions found to contain *Pa*HisIE were pooled, concentrated using 10,000 MWCO ultrafiltration membranes and loaded onto a HiPrep 26/60 S200 HR column equilibrated with buffer A. The column was washed with 1 CV of buffer A. Fractions were analysed via SDS-PAGE and fractions found to contain *Pa*HisIE were pooled and loaded onto a 5 mL HiTrapQ HP equilibrated with buffer E (HEPES [50 mM] pH 8.0). The column was washed with 10 CV of 11% buffer F (HEPES [50 mM], NaCl [2 M], pH 8.0) and the adsorbed proteins were eluted across a 20 CV linear gradient of 11-18% buffer B. Fractions were analysed by SDS-PAGE and fractions found to contain *Pa*HisIE, in the absence of major contaminants were pooled, dialysed against 2 x 2L of buffer G (HEPES [20 mM] pH 8.0), concentrated using 10,000 MWCO ultrafiltration membranes, aliquoted, and stored at −80 °C. The concentration of *Pa*HisiE was determined spectrophotometrically (NanoDrop) using the theoretical extinction coefficient (Ɛ280) of 43430 M^{-1} cm^{-1}. The identity of the protein was confirmed via tryptic digest and MS/MS analysis of the tryptic peptides performed by the BSRC mass-spectrometry facility at the University of St Andrews.

2.7.3 Enzymatic synthesis and purification of PRATP and PRADP

PRATP and PRADP were enzymatically synthesised as previously described[40]. Briefly, reactions (10 mL) with *Pa*HisG$_S$ (30 μM), either ATP or ADP (12 mM) PRPP (10 mM) and PPase (25 μM) in tricine (100 mM) (pH 8.5), KCl (100 mM), $MgCl_2$ (15 mM) and DTT (4 mM) and incubated for 90 minutes at room temperature. Proteins were removed by passage through a 10,000 MWCO Vivaspin centrifugal concentrator and frozen at –80 °C in 0.5 mL aliquots. Purification steps were carried out at 4 º C, on a Biorad NGC Liquid Chromatography System. Briefly, the reaction mixtures were loaded onto a 20 mL HiTrap Q FF column in 0.5 mL aliquots equilibrated with water. For mixtures containing PRATP, the column was washed with 1 CV of water, 2 CV of 16% ammonium bicarbonate (1 M), ATP and PRATP were then eluted across a 20 CV linear gradient from 16 to 30% ammonium bicarbonate (1M). For mixtures containing PRADP, the column was washed with 1 CV of water, 5 CV of 10 % ammonium bicarbonate (1 M), ADP and PRADP were then eluted across a 25 CV linear gradient from 10 to 30% ammonium bicarbonate (1M).UV absorbance was recorded at 220, 260 and 290 nm. Fractions exhibiting absorbance at 290 nm were pooled, lyophilised, then solubilised in HEPES (20 mM) (pH 7.5) and the concentration of PRATP was determined spectrophotometrically at 290 nm based on ethe extinction co-efficient ($\varepsilon_{290\ nm}$) of 2800 M^{-1} cm^{-1} at 290 nm[18]. ^{31}P-NMR spectra were recorded on Bruker 500 AVIII spectrophotometer and a total of 192 scans were collected. Samples containing purified PRATP and PRADP were submitted for LC-MS analysis, carried out by Dr Alison Dickson, formerly of the Czekster laboratory as detailed in the General Methods section.

2.7.4 Dynamic light scattering.

Dynamic light scattering (DLS) measurements were carried out in a 20 µl quartz cuvette using a Zetasizer Nano S90 instrument (Malvern). DLS measurements were performed in storage buffer (HEPES [20 mM) pH 7.5) with *Pa*HisIE (1 mg/mL) at 4 °C. Measurements were carried out in triplicate.

2.7.5 DSF of *Pa*HisIE

Thermal denaturation curves of *Pa*HisIE (~7 μM)were recorded in HEPES, (100 mM) (pH7.5) with $MgCl_2$ (15 mM). Control curves were measured in the absence of *Pa*HisIE and were subtracted from curves containing enzymes. Measurements were performed in triplicate.

2.7.6 *Pa*HisIE activity

Method 1 (coupled assay with *Pa*ATPPRT to produce PRATP)

*Pa*HisIE initial rates were measured in HEPES (100 mM), KCl (100 mM) , $MgCl_2$ (15 mM) and DTT (4 mM) with *Pa*ATPPRT (9.8 μM) and either ATP (5.6 mM) or ADP (5.6 mM) and PRPP (2 mM). Initial rates were measured with various concentrations of *Pa*HisIE ([with ATP: 80 nM, 160 nM and 320 nM] [with ADP: 320 nM, 640 nM and 1280 nM]) for 60 seconds. Control reactions performed in the absence of *Ab*HisIE were subtracted from data.

Method 2 (with enzymatically synthesised and purified PRATP)

*Pa*HisIE initial rates were measured in HEPES (100 mM) and $MgCl_2$ (12 mM) (pH 7.5) with PRATP (38 μM). Initial rates were measured with various concentrations of *Pa*HisIE (100 nM, 200 nM and 500 nM) for 60 seconds. Control reactions were performed in the absence of *Pa*HisIE. Reactions with 200 nM *Pa*HisIE were incubated until all PRATP was consumed.

2.7.7 *Pa*HisIE saturation kinetics with PRATP

*Pa*HisIE (0.3 μM) initial rates were measured in HEPES (100 mM) and $MgCl_2$ (12 mM) (pH 7.5) with varying concentrations of PRATP (4.7−188 μM) for 60 seconds.

2.7.8 *Pa*HisIE saturation kinetics with PRADP

*Pa*HisIE (1.7 μM) initial rates were measured in HEPES (100 mM) and $MgCl_2$ (12 mM) (pH 7.5) with varying concentrations of PRADP (32−432 μM) for 300 seconds.

2.7.9 LC-MS analysis of products from reactions catalysed by *Pa*HisIE

Reaction mixtures (500 µl) were prepared in HEPES (100 mM) and $MgCl_2$ (15 mM) (pH 7.5) with *Pa*HisIE (13.6 µM) and either PRATP (135 µM) or PRADP (372 µM). Samples were incubated for 1 hour at 20 °C after which proteins were removed by passage through 10,000 MWCO Vivaspin centrifugal concentrators. LC-MS was carried out as described in the General Methods section by Dr Alison Dickson

2.8 Methods for Chapter 6

2.8.1 Cloning of *Ab*HisIE

The DNA encoding *Ab*HisIE (*A. baumannii* strain ATCC17978), codon optimised for expression in *E. coli* was purchased a gBlock (IDT). The sequence of the gBlock can found in Table 2.4. *Ab*HisIE gBlocks were inserted into the pJexpress414 vector via Gibson Assembly[113] using the Gibson Assembly Cloning Kit (New England Biolabs) according to the manufacturer instructions. Overlapping extensions were added to *Ab*HisIE and pJexpress414 were via PCR. The primer sequences and annealing temperatures for the PCRs are detailed in Table 2.4. Reactions contained: reaction buffer (1X), dNTPs (0.2 mM), DNA primers (0.5 µM), Q5 polymerase (0.02 U/mL) (NEB) and either pJexpress414 (1 pg) or *Ab*HisIE gBlock (1 pg). PCRs were heated to 98 °C for 3 minutes for an initial denaturation step followed by 30 cycles of denaturation (98 °C, 30 seconds), annealing (X °C, 30 seconds) and extension (72 °C, 40 seconds) steps, then a final extension step (72 °C, 10 minutes). PCR products were purified with PCR clean-up kits (Qiagen). Fragments were mixed in a 5:1 ratio of vector to insert and incubated with the Gibson Assembly Master Mix (50 °C, 50 minutes). Constructs were transformed into DH5α competent cells (NEB). A single colony of transformed cells was used to inoculate LB (10 mL) with ampicilin (100 µg mL^{-1}) and incubated overnight at 37 °C. Plasmids were extracted using QIAprep Spin Miniprep kits (Qiagen) according to manufacturer instructions. Correct assembly of the construct was confirmed by DNA sequencing performed by DNA Sequencing & Services (MRC I PPU, School of Life Sciences, University of Dundee). Constructs were transformed into BL21 (DE3) *E. coli* cells.

Table 2-4 gBlock and primer sequences for *Ab*HisIE cloning.

Sequences			
***Ab*HisIE gBlock**	5′- GGAATTCCATATGAATAATACCCAGTGGCTTGACGAGGTCAAATTC AACGAGCAGGGTCTTATCCCGGCAATCGCTCAACACCACCAAACAG GCCGCATCTTAATGGTAGCATGGATGAACCGTGAGTCTCTGGCGCT TACTGCGGAAAAGAATCAAGCAGTATACTTCTCCCGTAGCCGCCAG AAGTTGTGGCACAAAGGGGAAGAATCCGGTCACTTTCAAACGGTCT ATGAGATCCGCTTAGATTGCGACGGCGATGTAATCGTCTTGCAAGT AGAGCAGCATGGGGGTATCGCGTGTCACACCGGGCGTGAATCCTGC TTCTACCGCAAATTAACGCCGCAAGGGTGGGAGATCGTTGATGCTC AACTTAAAGACCCGACCGCAATTTATGGAGATAATGCGAAAACGGA ATCGCATGACCATGCCCATACCACGGAGCAAGTCGATGTTTTAGCT CACTTGGGCCAGCTGATGCAAGAGCGCAAACAGGCTGAGGCTGAC ACAAGTTACGTGGCATCCTTATATAAGAAAGGAATCAATAAAATTT TAGAAAAGGTAGGAGAAGAAGGAGTTGAGACGATTATCGCGGCGA AAGATTACGCTACTCAGAATACGGAGTCCAACTTAAATGATTTGAT TTACGAAACAGCAGATCTGTGGTTTCATTCCATCGTGATGCTGGGTT ACTTTGATCTTAACCCCCAGCTTATTATCGACGAGCTTGGTCGTCGC CAAGGGCTTTCAGGCTTGGTTGAAAAAGCAAACCGTAATAAAGTTT GAAAGTTGGGG - 3′		
Primers			
Plasmid	5′- CCCCCTAGCATAAC CCCTTG-3′	5′- AAAAGTTAAACAAA ATTATTTCTAGAGG GGAATTG-3′	64.5
gBlock	5′- GAAATAATTTTGTTT AACTTTTGGAATTC CATATGAATAATAC CC-3′	5′- CAAGGGGTTATGCT AGGGGGCCCCAACT TTCAAACTTTATTAC -3′	58.7

2.8.2 *Ab*HisIE production

Starter cultures were prepared by inoculating LB (5 mL) containing ampicillin (100 µg mL^{-1}) with a scraping from a glycerol stock of BL21 (DE3) *E. coli* cells transformed with pJexpress414 encoding *Ab*HisIE. and incubated overnight at 37 ºC in a shaker. Starter cultures were then transferred to 1 L of LB containing ampicillin (100 mg mL^{-1}) and

grown at 37 ºC in a shaker until an OD_{600} between 0.6 – 0.8 was reached. Cultures were subsequently cooled to 20 °C for overnight incubation and protein synthesis was induced by addition of IPTG (0.5 mM). The following day, cells were harvested by centrifugation at 6774 g for 15 minutes and cell pellets were stored at -20 ºC.

2.8.3 *Ab*HisIE purification

All purification procedures were performed at 4 ºC. Cell pellets were resuspended in Buffer A (HEPES [50 mM] pH 7.5) with lysozyme (0.2 mg mL^{-1}), BaseMuncher Endonuclease (750 U) (Abcam) and half a tablet of EDTA-free cOmplete protease inhibitor cocktail (Roche). Cells were lysed in a high-pressure cell disruptor and fractionated by centrifugation at 48,000 g for 30 min. Buffer A with 3.5 M ammonium sulfate was added dropwise to the supernatant until a concentration of 1.5 M $(NH_4)_2SO_4$ was reached. The sample was left to stir for 1 hour then centrifuged at 48,000 g for 30 minutes. The insoluble fraction was collected and resuspended in buffer A, dialysed against 3 x 2L of buffer A, filtered through a 0.45 µM membrane and loaded onto a 10 mL HiTrapQ FF column pre-equilibrated with buffer A. The column was washed with 10 CV of 2.5% buffer B (HEPES [50 mM), NaCl [2 M], pH 7.5) and the adsorbed proteins were eluted across a 30 CV linear gradient of 2.5-15% buffer B. Fractions were analysed via SDS-PAGE and fractions found to contain *Ab*HisIE were pooled and dialysed against 2 x 2L of buffer C (HEPES [50 mM), NaCl [250 mM], pH 8.0), filtered through a 0.45 µM membrane and loaded onto a 5 mL HisTrap FF column charged with $ZnCl_2$, pre-equilibrated with buffer C. The column was washed with 10 CV of buffer C and the adsorbed proteins were eluted across a 20 CV linear gradient of 0-15% buffer D (HEPES [50 mM), NaCl [250 mM], imidazole [50 mM] pH 8.0). Fractions were analysed via SDS-PAGE and fractions found to contain *Ab*HisIE were pooled, concentrated using 10,000 MWCO ultrafiltration membranes and loaded onto a HiPrep 26/60 S200 HR column equilibrated with buffer A. The column was washed with 1 CV of buffer A. Fractions were analysed via SDS-PAGE and fractions found to contain *Ab*HisIE, in the absence of major contaminants were pooled concentrated using 10,000 MWCO ultrafiltration membranes, aliquoted, and stored at −80 °C. The concentration of *Pa*HisiE was determined spectrophotometrically (NanoDrop) using the theoretical extinction coefficient (Ɛ280) of 40910 M^{-1} cm^{-1}. The identity of the protein was confirmed via tryptic

digest and MS/MS analysis of the tryptic peptides performed by the BSRC mass-spectrometry facility at the University of St Andrews

2.8.4 DLS

DLS experiments were carried out in a 20 µl quartz cuvette using a Zetasizer Nano S90 instrument (Malvern). DLS measurements were performed in storage buffer (HEPES [20 mM) pH 7.5) with *Ab*HisIE (1 mg/mL) at 4 °C. Measurements were carried out in quintuplicate.

2.8.5 DSF of *Ab*HisIE

Thermal denaturation curves of *Ab*HisIE (8.3 µM)were recorded in HEPES, (100 mM) (pH7.5) with $MgCl_2$ (15 mM). Control curves were measured in the absence of *Pa*HisIE and were subtracted from curves containing enzymes. Measurements were performed in triplicate.

2.8.6 Determination of $\Delta\varepsilon_{300\ nm\ m}$ for ProFAR formation at pH 7.0, pH 7.5 and pH 8.0

The extinction coefficients at 300 nm (ε_{300nm}) of PRATP at pH 7.0, pH 7.5 and pH 8.0 was determined by measuring the absorbance at 300 nm of known concentrations of PRATP (pH 7.0 [0.45 mM, 0.91 mM and 1.8 mM]; pH 7.5 [0.51 mM, 1.0 mM and 2 mM]; pH 8.0 [0.46 mM, 0.92 mM and 1.8 mM]) (NanoDrop). These values were subtracted from the ε300nm of ProFAR (8000 M^{-1} cm^{-1})[63] to generate $\Delta\varepsilon_{300\ nm}$ (6800 M^{-1} cm^{-1} [pH 7.0], 6700 M^{-1} cm^{-1} [pH 7.5], 6200 M^{-1} cm^{-1} [pH 8.0]) for formation of ProFAR from PRATP. Measurements were performed in triplicate.

2.8.7 *Ab*HisIE activity

*Ab*HisIE initial rates were measured in HEPES (100 mM) , $MgCl_2$ (12 mM) and DTT (4 mM) (pH 7.5) with PRATP (37 µM) at various concentrations of *Ab*HisIE (10 nM, 20 nM and 40 nM) for 300 seconds. Additionally, reactions with 20 nM *Ab*HisIE were incubated until all substrate was consumed (1650 seconds). Control reactions were performed in the absence of *Ab*HisIE.

2.8.8 *Ab*HisIE saturation kinetics with PRATP.

*Ab*HisIE (18 nM) initial rates were measured in HEPES (100 mM) and $MgCl_2$ (15 mM) (pH 7.5) with varying concentrations of PRATP (2.6 μM – 42 μM) for 30 – 120 seconds (2.6μM PRATP: 30 seconds; 5.2μM PRATP: 60 seconds; 10 μM PRATP: 90 seconds, 21 μM PRATP: 90 seconds; 42 μM PRATP; 120 seconds).

2.8.9 *Ab*HisIE saturation kinetics in glycerol

*Ab*HisIE (18 nM) initial rates were measured in HEPES (100 mM) and $MgCl_2$ (15 mM) (pH 7.5) at varying concentrations of PRATP (2.6 μM – 42 μM) for 30-120 seconds (2.6μM PRATP: 30 seconds; 5.2μM PRATP: 60 seconds; 10 μM PRATP: 90 seconds, 21 μM PRATP: 120 seconds; 42 μM PRATP; 120 seconds) in 0%, 18% and 27% glycerol (*v*/*v*). Kinetic solvent viscosity data were fitted to Equation 2.8.

2.8.10 *Ab*HisIE saturation kinetics with PRATP in H_2O at pH 7.0, pH 7.5 and pH 8.0

*Ab*HisIE (pH 7.0 [31 nM], pH 7.5 [18 nM] and pH 8.0 [7.5 nM]) initial rates were measured in HEPES (100 mM) and $MgCl_2$ (15 mM) at pH 7.0, pH 7.5 and pH 8.0 with varying concentrations of PRATP (pH 7.0 [2.3 – 37 μM], pH 7.5 [2.6 μM – 42 μM] and pH 8.0 [1.4 μM – 40 μM]) for 30-120 seconds (pH 7.0 [2.3 μM PRATP: 30 seconds; 4.6μM PRATP: 60 seconds; 9.2 μM PRATP: 90 seconds, 18 μM PRATP: 120 seconds; 37 μM PRATP; 120 seconds], pH 7.5 [2.6μM PRATP: 30 seconds; 5.2 μM PRATP: 60 seconds; 10 μM PRATP: 90 seconds, 21 μM PRATP: 90 seconds; 42 μM PRATP; 120 seconds], pH 8.0 [1.4 μM PRATP: 30 seconds; 3.6 μM PRATP: 60 seconds; 14 μM PRATP: 60 seconds, 28 μM PRATP: 60 seconds; 40 μM PRATP; 120 seconds]). Reactions were monitored for an increase in absorbance at 300 nm corresponding to the formation of ProFAR (pH 7.0, $\Delta\varepsilon_{300\,nm} = 6800\ M^{-1}\ cm^{-1}$; pH 7.5, $\Delta\varepsilon_{300\,nm} = 6700\ M^{-1}\ cm^{-1}$; pH 8.0, $\Delta\varepsilon_{300\,nm} = 6200\ M^{-1}\ cm^{-1}$).

2.8.11 *Ab*HisIE saturation kinetics with PRATP in D_2O at pD 7.0, pD 7.5 and pD 8.0.

*Ab*HisIE (pD 7.0 [186 nM], pD 7.5 [74 nM] and pD 8.0 [19 nM]) initial rates were measured in HEPES (100 mM) and $MgCl_2$ (15 mM) at pD 7.0, pD 7.5 and pD 8.0 with varying concentrations of PRATP (pD 7.0 [2.3 – 59 μM], pD 7.5 [2.4 μM – 38 μM] and pD 8.0 [2.6 μM – 48 μM]) for 30-120 seconds (pD 7.0 [2.3 μM PRATP: 60 seconds; 4.7 μM PRATP: 60 seconds; 9.4 μM PRATP: 90 seconds, 19 μM PRATP: 90 seconds; 38 μM PRATP; 120 seconds; 59 μM PRATP; 120 seconds], pD 7.5 [2.4 μM PRATP: 60 seconds; 4.8 μM PRATP: 60 seconds; 9.5 μM PRATP: 60 seconds, 19 μM PRATP: 60 seconds; 28 μM PRATP; 60 seconds], pD 8.0 [2.6 μM PRATP: 30 seconds; 5.2 μM PRATP: 10 seconds; 21 μM PRATP: 90 seconds, 42 μM PRATP: 120 seconds[]). Reactions were monitored for an increase in absorbance at 300 nm corresponding to the formation of ProFAR (pD 7.0, $\Delta\varepsilon_{300\ nm}$ = 6800 M^{-1} cm^{-1}; pD 7.5, $\Delta\varepsilon_{300\ nm}$ = 6700 M^{-1} cm^{-1}; pD 8.0, $\Delta\varepsilon_{300\ nm}$ = 6200 M^{-1} cm^{-1}). Solvent kinetic isotope effect data were fitted to Equation 2.9, where k_{cat} is the steady-state turnover number, S is the concentration of the varying substrate, F_i is the fraction of deuterium label in the substrate, K_M is the apparent Michaelis constant, $E_{kcat/KM}$ and E_{kcat} are the isotope effects −1 on k_{cat} and k_{cat}/K_M, respectively[114].

Equation 2.9

$$v = \frac{k_{cat}[S]}{K_M\left(1 + F_i E_{\left[\frac{k_{cat}}{K_M}\right]}\right) + [S](1 + F_i E_{[k_{cat}]})}$$

2.8.12 EnzCheck™ pyrophosphatase assay.

The activity of the *Ab*HisE domain was independently assessed via the EnzCheck™ pyrophosphate assay kit (Invitrogen). Initial rates were measured in HEPES (100 mM), $MgCl_2$ (15 mM) and DTT (4 mM) (pH 7.5). Reactions (500 μL) were monitored for an increase at 360 nm corresponding to formation of 2-amino-6-mercapto-7-methylpurine ($\Delta\varepsilon_{360\ nm}$ = 11,000 M^{-1} cm^{-1})[115] at 25 °C for 60 seconds in 1 cm pathlength cuvettes (Hellma) using a Shimadzu UV-2600 spectrophotometer. Initial rates were collected with

varying concentrations of *Ab*HisIE (1.6 nM, 3.2 nM and 6.4 nM) and a fixed concentration of PRATP (8.4 μM) to demonstrate that the rate of reaction is dependent on *Ab*HisIE. Substrate saturation data were collected with *Ab*HisIE (3.2 nM) and varying concentrations of PRATP (1 - 16 μM). 2-amino-6-mercapto-7-methylpurine ribonucleoside (MESG) (200 μM), purine nucleoside phosphorylase (PNP) (1 U mL^{-1}) and PPase (0.03 U mL^{-1}) were included in assays at the recommended concentrations. Controls were performed in the absence of *Ab*HisIE and PRATP. Cuvettes were incubated for 3 minutes inside the spectrophotometer before reactions were started by addition of *Ab*HisIE. All measurements were carried out in duplicate.

2.8.13 Pre-steady state kinetics

Pre-steady state measurements were performed at 25 °C in an Applied Photophysics SX-20 stopped-flow spectrophotometer. Approach to steady state in *Ab*HisIE was investigated under multiple turnover conditions, each syringe contained HEPES (100 mM), MgCl (15 (pH 7.5) with DTT (4 mM). In addition, one syringe carried *Pa*HisIE (10 μM) while the other carried ATP (50 μM). Reaction was triggered by rapidly mixing 55 μl from each syringe. Absorbance at 300 nm was collected over a split time-base for 0.475 seconds, with 3000 data points collected in the first 0.225 seconds and 2000 in the following 2.5 s. 6 traces were acquired and 4 traces were averages.

2.8.14 LC-MS analysis of products from reactions catalysed by *Ab*HisIE with PRATP

Reaction mixtures (500 μL) were prepared in HEPES (100 mM) and $MgCl_2$ (15 mM) (pH 7.5) with *Ab*HisIE (16 μM) and PRATP (135 μM). Samples were incubated for 1 hour at 20 °C after which proteins were removed by passage through 10,000 MWCO Vivaspin centrifugal concentrators. LC-MS was carried out as described in the General Methods section by Dr Alison Dickson

Chapter 3 Kinetic mechanism and rate-limiting steps of *Pa*ATPPRT

The majority of the results for Chapter 3 have previously been published in "Fisher G., Thomson C. M., Stroek R., Czekster C. M., Hirschi J. M., and da Silva R. G., Allosteric activation shifts the rate-limiting step in a short-form ATP phosphoribosyl transferase. *Biochemistry,* **2018,** *57*(29), 4357-4367."

3.1 Chapter introduction

ATPPRT catalyses the first committed reaction of this histidine biosynthetic pathway, the condensation of PRPP and ATP to form PRATP and pyrophosphate, Figure 1.1. Protocols for purification of the *Pa*HisG$_S$ (*P. arcticus* HisG$_S$) and *Pa*HisZ (*P. arcticus* HisZ) subunits of *P. arcticus* ATPPRT were established by the da Silva Laboratory prior to this work[32] Furthermore, protocols for assaying the catalytic subunit *Pa*HisG$_S$ in the absence (non-activated *Pa*HisG$_S$) and presence of the allosteric activator *Pa*HisZ (activated *Pa*ATPPRT) were also previously established[32]. Non-activated *Pa*HisG$_S$ and activated *Pa*ATPPRT were primed for mechanistic studies to probe the mechanism underpinning allosteric activation. The aims of this chapter were to elucidate the kinetic mechanism of *Pa*HisG$_S$, to establish if ADP is a substrate of *Pa*HisG$_S$ and to characterise the rate-limiting steps of *Pa*HisG$_S$ in the presence and absence of *Pa*HisZ.

3.1.1 Kinetic mechanism of ATPPRTs

Prior to this work, only the kinetic mechanism of HisG$_L$-type ATPPRTs had been investigated. Early studies of *S.* Typhimurium ATPPRT, a HisG$_L$-type ATPPRT, incorrectly hypothesised ATPPRTs operate via a double displacement mechanism[21,116], Figure 3.1A. The double-displacement mechanism of *S.* Typhimurium ATPPRT was later disproven due to stereochemical abnormalities[117]; a double-displacement mechanism would have resulted in retention of stereochemistry at C1″ of PRATP, however, inversion of stereochemistry was observed[117]. Further kinetic analysis of *S.* Typhimurium ATPPRT demonstrated intersecting lines on initial velocity patterns, consistent with a sequential, Bi Bi kinetic mechanism[42,118]. Product competition assays were used to infer the order of

ligand binding[42,118] and, a sequential ordered kinetic mechanism was proposed for $HisG_L$-type ATPPRTs with ATP as the first substrate to bind and PRATP as the last substrate to leave, Figure 3.1B. Until publication of this work, it was assumed that all ATPPRTs followed this established sequential ordered mechanism with ATP as the first substrate to bind and PRATP as the last substrate to leave.

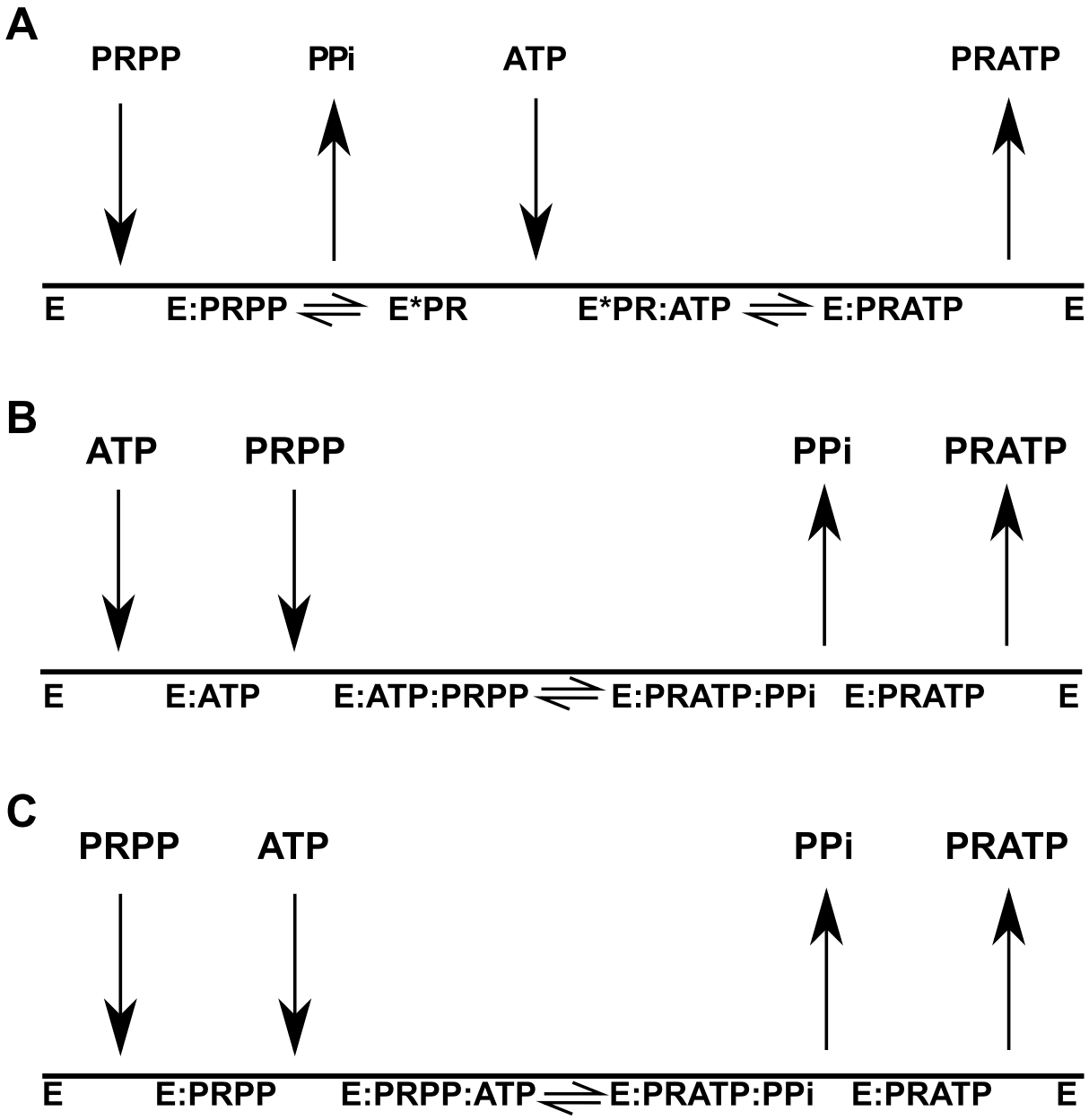

Figure 3.1 Cleland diagram depicting possible kinetic mechanisms for ATPPRT. (A) Double displacement (ping-pong) mechanism; (B) ordered, sequential Bi-Bi mechanism with ATP as the first substrate to bind and PRATP as the last product to leave; (C) ordered, sequential Bi-Bi mechanism with PRPP as the first substrate to bind and PRATP as the last product to leave.

The proposed kinetic mechanism was supported by crystal structures of *C. jejuni*[24] and *M.tuberculosis*[37] ATPPRTs ($HisG_L$-type ATPPRTs) in a binary complex with ATP. Additionally, binding of ATP to free *C. jejuni* ATPPRT was demonstrated by ITC (K_D = 158 μM)[24]. The only reported crystal structure of $HisG_L$-type ATPPRT in a binary complex with PRPP is from a truncated variant of *C. jejuni* ATPPRT[38]. The mode of PRPP binding observed in the truncated *C jejuni* ATPPRT structure is likely incompatible with catalysis as the pyrophosphate moiety of PRPP had drifted into the established ATP binding pocket and formed a hydrogen bond with the guanidinium group of R16. R16 forms part of the ATP binding pocket. The interaction between R16 and the α-phosphate of PRPP would likely impede ATP binding[38], Figure 3.2.

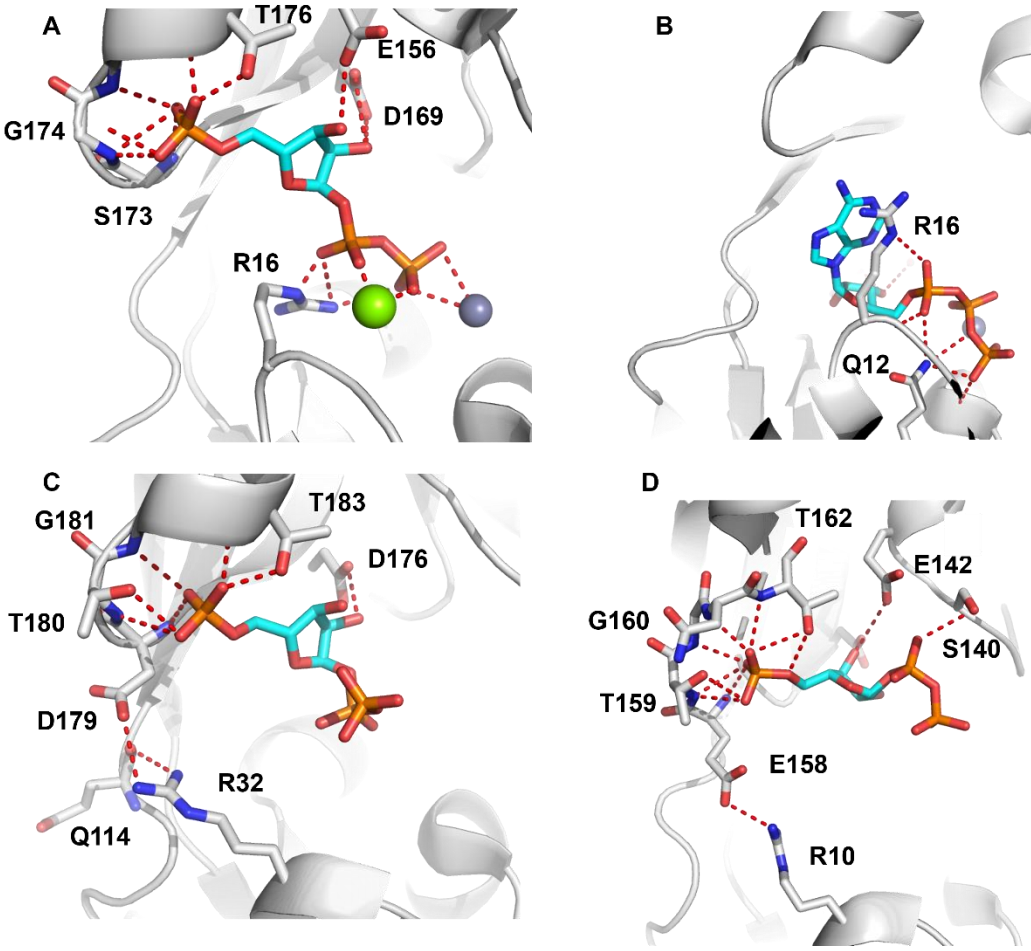

Figure 3.2 *C. jejuni*, *P arcticus* and *L. lactis* ATPPRT in complex with PRPP. Close-up view of the active site from the truncated variant of *C.jejuni* with either (A) PRPP (PDB ID: 5UBI) or (B) ATP (PDB ID: 5UBH). Close-up view of (C) *P. arcticus* (PDB ID: 6FTT) and (D) *L. lactis* ATPPRT (PDB ID:1Z7N) active sites with PRPP bound. Ligands are shown as stick models with carbon in cyan, nitrogen in blue, oxygen in red and phosphorus in orange. Protein backbones are shown with ribbon diagrams, selected residues are depicted as stick models with carbon in grey, nitrogen in blue and oxygen in red. Mg^{2+} and Zn^{2+} are represented by either green or grey spheres, respectively. Polar interactions are represented by dashed lines. The pyrophosphate motif of PRPP had drifted into the ATP binding site of the *truncated C. jejuni* $HisG_L$ creating a $HisG_L$:PRPP dead-end complex, whereas the pose captured in *P. arcticus* and *L. lactis* ATPPRT:PRPP structures is compatible with ATP binding. Images were generated in Pymol

On the other hand, crystal structures of *L. lactis* ATPPRT, *Pa*HisG$_S$ and *Pa*ATPPRT in a binary complex with PRPP[34,40] have been reported, Figure 3.2 . The *Pa*HisG$_S$:PRPP and *Pa*ATPPRT:PRPP complexes were solved by Dr Magnus S. Alphey. Crucially, the mode of PRPP binding in these structures appeared to be compatible with catalysis. In both HisG$_S$:PRPP crystal structures, the conserved arginine that forms the ATP binding pocket (R10 of *L. lactis* HisG$_S$ and R32 of *Pa*HisG$_S$) was engaged in interactions with either E158 (*L. lactis* HisG$_S$) or Q114 and D179 (*Pa*HisG$_S$), thus, prohibited from engaging with the pyrophosphate motif of PRPP and obstructing ATP binding. These structures suggest that HisG$_S$-type ATPPRTs may follow an alternative kinetic mechanism to that of HisG$_L$-type ATPPRTs, which allows for binding of PRPP to free enzyme. In *E. coli* and *C. jejuni* (HisG$_L$-type ATPPRTs) ATPPRT, a serine residue is found in the equivalent position to D179 and E158 from *P. arcticus* and *L. lactis*, respectively.

3.1.2 ADP is an Inhibitor of HisG$_L$-type ATPPRTs

As previously discussed in Chapter 1, AMP is a competitive inhibitor of various HisG$_L$- and HisG$_S$-type ATPPRTs with respect to PRPP and ATP. Kinetic studies of *S.* Typhimurium in 1977, determined ADP is also a competitive inhibitor of *S.* Typhimurium ATPPRT with respect to ATP and PRPP[22]. It was subsequently assumed in the literature that ADP is a universal ATPPRT competitive inhibitor with respect to both substrates[24,31,35,39]. A 2012 study confirmed ADP is a competitive inhibitor of *C. glutamicium* ATPPRT with respect to ATP[41]. A structure of *Pa*HisG$_S$ in complex with ADP, uncovered by Dr Magnus S. Alphey, challenged the assumption of a universal competitive inhibitor with respect to both substrates by revealing that ADP binds comparably with ATP[40], Figure 3.3. Almost all interactions between *Pa*HisG$_S$ and ATP are conserved in the ADP-bound structure with the exception of a hydrogen bond between R′73 of the adjacent *Pa*HisG$_S$ subunit and the γ-phosphate of ATP, Figure 3.3. Crucially, unlike AMP, the phosphates of ADP do not engage with the PRPP binding pocket at all, they are anchored in the ATP binding pocket by interactions with either R32 (α-

phosphate) or K137 (β-phosphate) Figure 3.3. From these data it was hypothesised that ADP may act as a substrate of *Pa*HisG$_S$

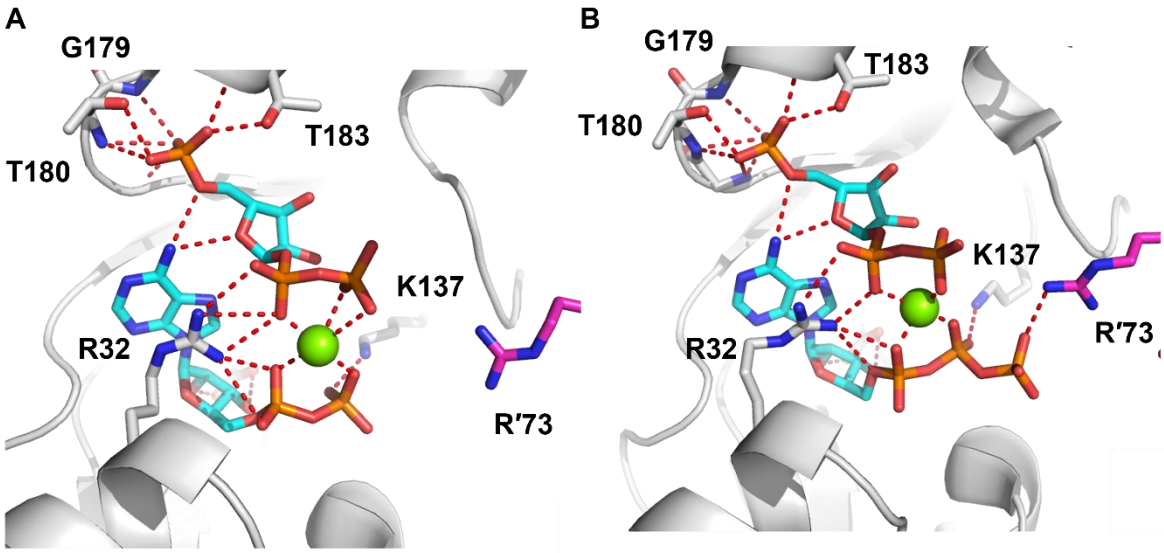

Figure 3.3 The binding mode of ADP to *Pa*HisG$_S$ is comparable to ATP. *Pa*HisG$_S$ in complex with PRPP and either (A) ADP (PDB ID 6FCY) or (B) ATP (PDB ID: 6FCT). Ligands are shown as stick models with carbon in cyan, nitrogen in blue, oxygen in red and phosphorus in orange. Protein backbones are shown with ribbon diagrams, selected residues are depicted as stick models with carbon in either grey (ADP/ATP-bound subunit) or magenta (adjacent subunit), nitrogen in blue and oxygen in red. Mg^{2+} is depicted by green spheres, respectively. Polar interactions are represented by dashed lines. R73′ from the adjacent *Pa*HisG$_S$ monomer interacts with the γ-phosphate of ATP but is approximately 5.5 Å from the terminal phosphate of ADP. Image generated in Pymol.

3.1.3 Rate-limiting steps of ATPPRT

Pre-steady state characterisation of *M. tuberculosis* ATPPRT, a HisG$_L$-type ATPPPRT, indicated that steps after chemistry are at least partially rate-limting[29], this finding is consistent with observations from other phosphoribosyl transferases (PRTs) which have established product release is rate-limiting[119–121]. The rate-limiting steps of HisG$_S$-type ATPPRTs had not been established prior to this work. It was hypothesised that allosteric activation may influence the rate-limiting step of *Pa*HisG$_S$.

3.2 Production of *Pa*HisG$_S$ and *Pa*HisZ

*Pa*HisG$_S$ and *Pa*HisZ were successfully produced using protocols previously established in the da Silva Laboratory, Figure 3.4.

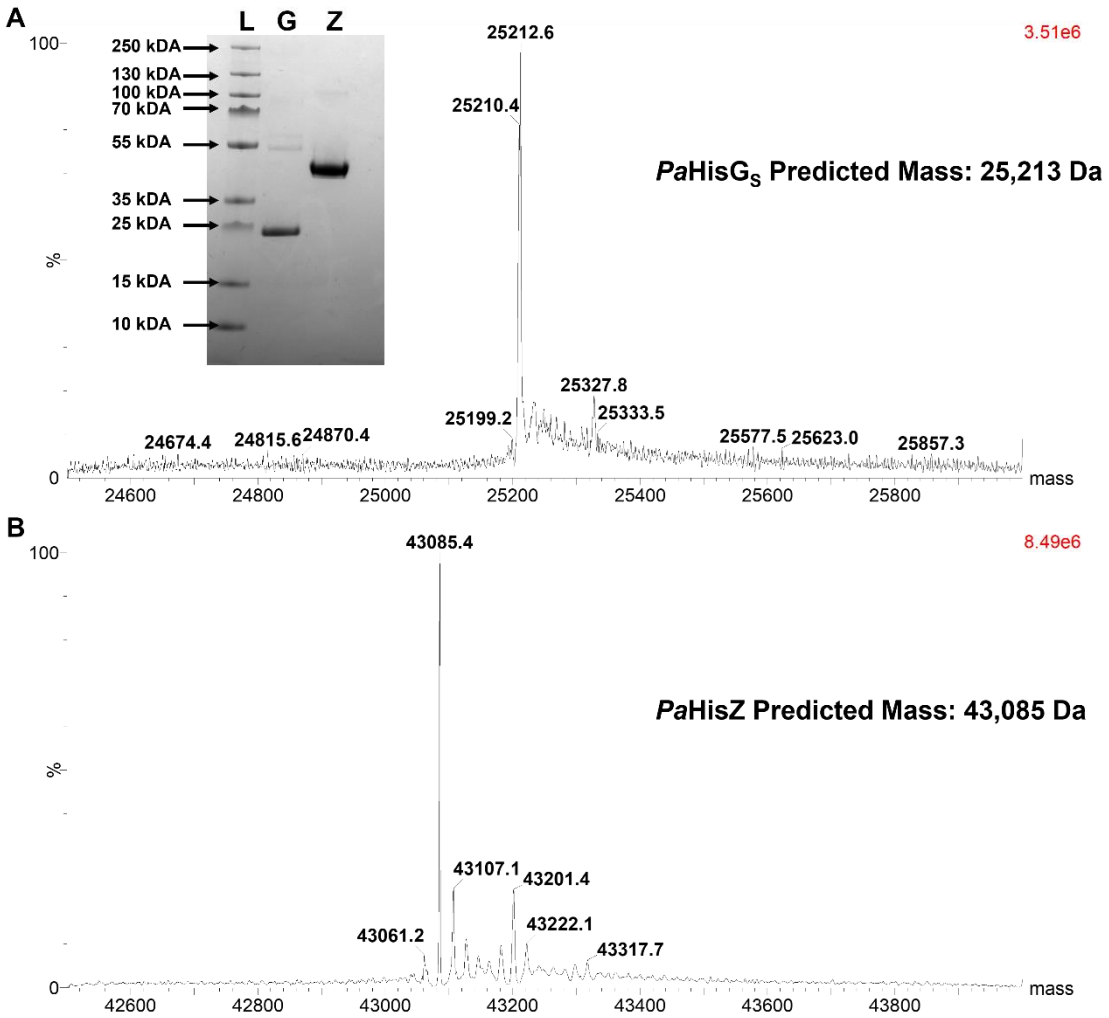

Figure 3.4 Purification of *Pa*HisG$_S$ and *Pa*HisZ. ESI-MS analysis showing the experimentally determined mass of (A) 25,213 Da for *Pa*HisGs and (B) 43,085 Da for *Pa*HisZ. Inset in (A) is SDS-PAGE with protein-ladder (L) (PageRuler Plus Prestained) of *Pa*HisG$_S$ (G) and *Pa*HisZ (Z).

3.3 Kinetic mechanism of *Pa*HisG$_S$ and *Pa*ATPPRT

3.3.1 Inferring order of substrate binding by differential scanning fluorimetry (DSF) and isothermal titration calorimetry (ITC)

Differential scanning fluorimetry (DSF) and ITC were employed to determine which substrates and products can bind to free *Pa*HisG$_S$ in solution. These techniques assess ligand binding via independent signals; DSF correlates ligand binding with an increase in the Gibbs free energy of protein unfolding (ΔG_U), whereas ITC detects heat absorbed or released in solution as a result of a binding event[103,122]

DSF experiments incorporate a dye which fluoresces upon interaction with hydrophobic-rich regions, such as those exposed upon protein unfolding[103] Here, a mixture containing *Pa*HisG$_S$ and the Sypro Orange was gradually heated in the presence and absence of ligands, and the melting temperature (T_M) was determined by fitting fluorescence data to a modified Boltzmann equation[103]. Binding of a ligand to a protein is theorised, in some cases, to increase ΔG_U which may translate to an increase in T_M, though absence of a shift in T_M does not rule-out ligand binding[103]. PRPP and PRATP induce a 6 ºC and 5 ºC increase in T_M compared with apo *Pa*HisG$_S$, suggestive of binding to free *Pa*HisG$_S$, whereas ATP and pyrophosphate did not induce a change in the T_M of *Pa*HisG$_S$ at concentrations tested (2 mM and 3.6 mM, respectively), Figure 3.5 and Table 3.1.

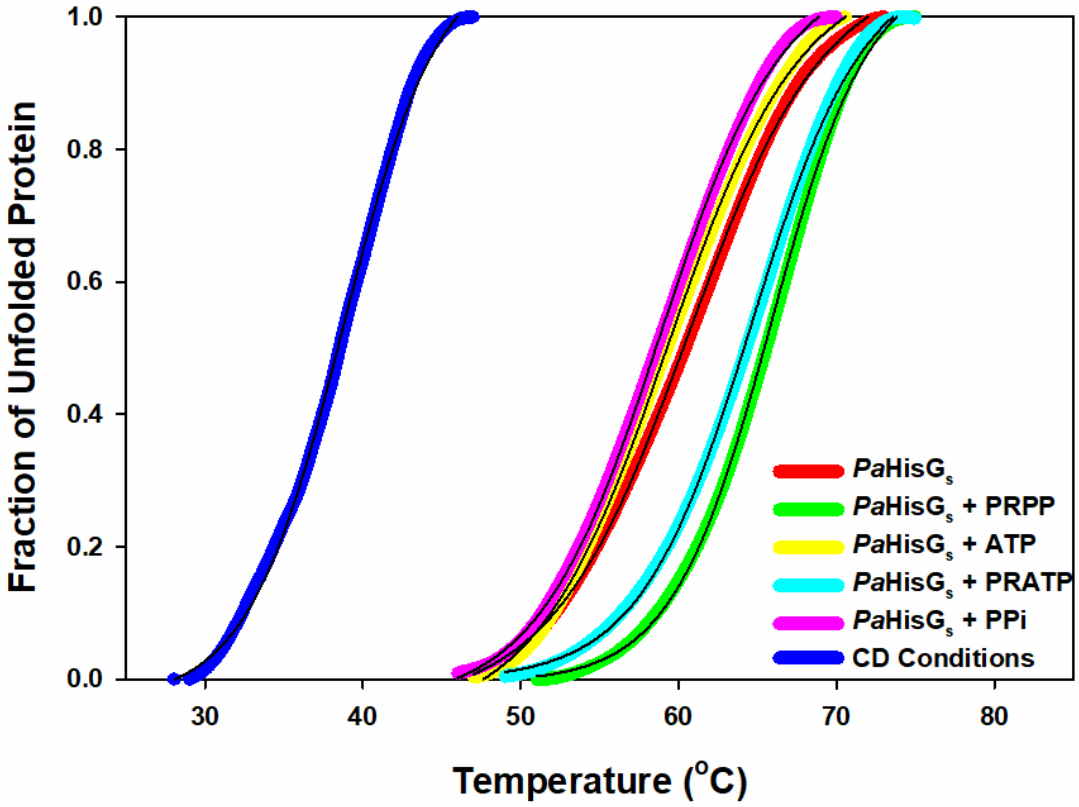

Figure 3.5. DSF-based thermal denaturation curve of *Pa*HisG$_S$ with and without substrates or products. Lines are average of triplicate measurement. Solid black lines are data fitted to Equation 2.6.

Table 3-1 *Pa*HisG$_S$ T_M determined with and without substrates and products.

Condition	**T_M (ºC)**
Apo *Pa*HisG$_S$‡	60.58 ± 0.08
***Pa*HisG$_S$ + PRPP**	65.86 ± 0.08
***Pa*HisG$_S$ + ATP**	59.30 ± 0.08
***Pa*HisG$_S$ + PRATP**	64.67 ± 0.09
***Pa*HisG$_S$ + PPi**	58.85 ± 0.07
***Pa*HisG$_S$ + Glycerol (22%)**	61.19 ± 0.02
***Pa*HisG$_S$ in 10 mM KH_2PO_4, 10 mM KF pH 8.0**	38.7 ± 0.1

Values are ± fitting error of triplicate measurements.

DSF results were validated by additional ITC experiments. Broadly, ITC recognises either an exothermic or endothermic binging event upon titration of a ligand into a sample cell by detecting a change in temperature relative to a reference cell[123]. More specifically, a feedback circuit regulates the power applied to the sample cell to ensure the temperature exactly matches the reference cell; upon ligand titration if either an endothermic or exothermic binding event occur, the power applied to the cell through the feedback circuit is either increased or decreased, respectively[123]. A time-course of power applied to the sample cell is then extracted and replotted as heat evolved per injection against molar ratio. Finally, K_D, ΔH and *n* are extracted by fitting to an appropriate binding model[123]. Hence, in addition to determining K_D, ITC also facilitates an understanding of the forces driving molecular association, either largely hydrophobic or specific polar interactions, by determining ΔH and ΔS[123].

Binding of PRPP to *Pa*HisG$_S$ was confirmed by ITC, Figure 3.6, Table 3.2, (K_D = 12 µM ± 2 µM). Generally, to perform high-quality data fitting of ITC data, it is recommended that C-value from Equation 3.1 is between 20 – 100, and that curve fitting is not performed with data obtained from an experiment with a C-value less than 10. In this case, the calculated C-value is 4.16. Due to the relatively high (>10 µM) K_D obtained in this experiment an unfeasibly high *Pa*HisG$_S$ concentration in the sample cell (~250 µM) would be required to obtain a C-value of 20. Fortunately, the current consensus is that such data can be fit under two conditions: one, that the target can be fully saturated with ligand, and two, that the stoichiometry value is known and fixed during the fitting process[124,125]. Both conditions were met with respect to the PRPP-*Pa*HisG$_S$ binding experiment.

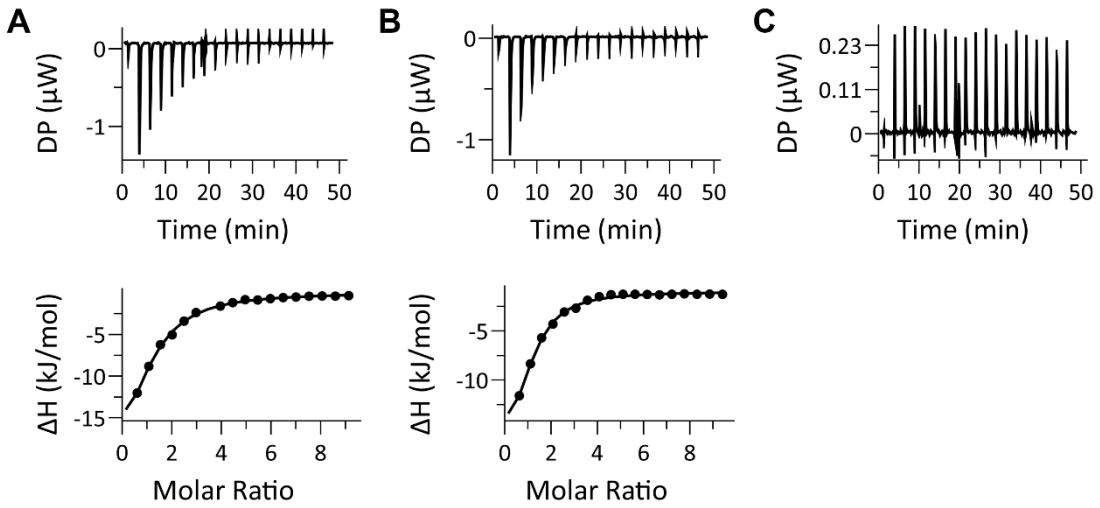

Figure 3.6 ITC binding curves for PRPP-*Pa*HisG$_S$. (A and B) are binding curves. from two independent experiments, raw data (top) and fitted data (bottom) are shown (C) Raw data from control experiment in which PRPP was titrated into buffer. Control data were subtracted from each binding data set. Solid lines are data fit to a single-site binding model.

Table 3-2 *Pa*HisG$_S$-PRPP binding parameters from ITC data-fitting.

Parameter	
K_D **(µM)**	12 ± 2
ΔH (kJ/mol)	-23 ± 3
ΔG (kJ/mol)	-27 ± 0.5
-TΔS (kJ/mol)	-5 ± 3

Values are mean ± standard error of duplicate measurements.

Equation 3.1.

$$C - value = \left(\frac{[Cell]}{K_D}\right) n$$

Upon titration of 500 uM ATP into 25 µM *Pa*HisG$_S$ or 2 mM ATP into 50 µM *Pa*HisG$_S$, no binding could be detected, Figure 3.7. Titration of 10 mM ATP into 50 µM *Pa*HisG$_S$ resulted in a signal that was comparable to a control experiment in which ATP was titrated into assay buffer, likely reflecting heat of dilution, Figure 3.8. Ultimately, ITC corroborated the results of the DSF experiment. Both techniques demonstrated that PRPP can bind to free *Pa*HisG$_S$. On the contrary, no evidence of ATP binding to free *Pa*HisG$_S$ was generated despite a range of concentrations tested in ITC experiments.

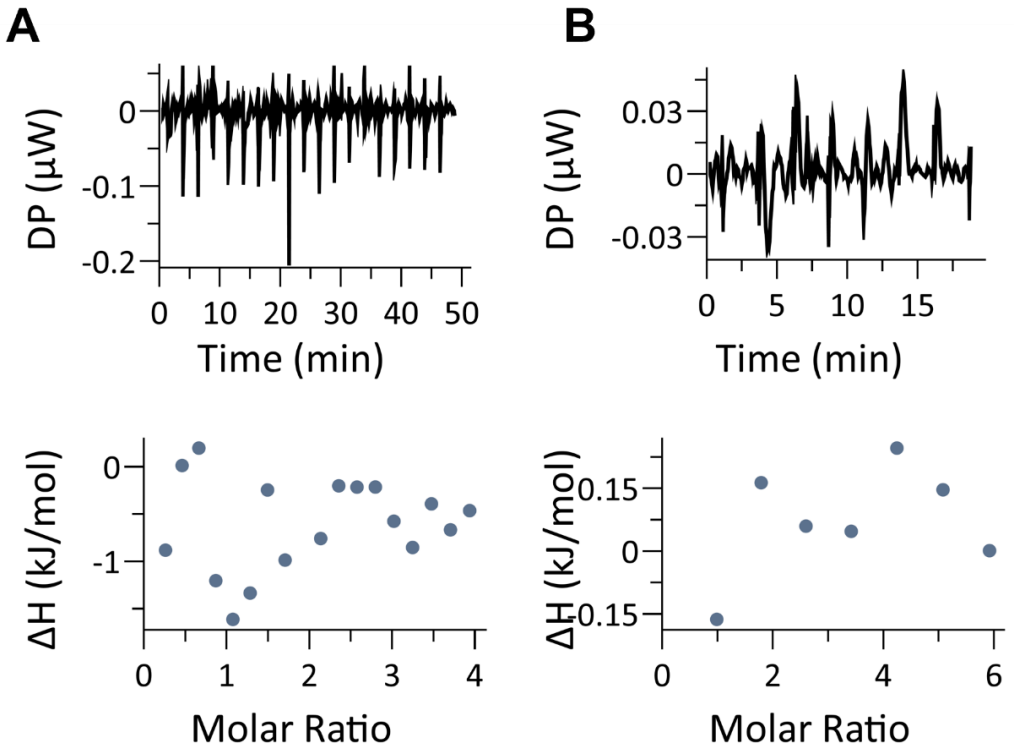

Figure 3.7 Raw data from titration of ATP into *Pa*HisG$_S$. Either 500 µM ATP into 25 µM *Pa*HisG$_S$ (A) or 2 mM ATP into 50 µM *Pa*HisG$_S$. Raw data (top) and replots (bottom) are shown. No data fitting was performed.

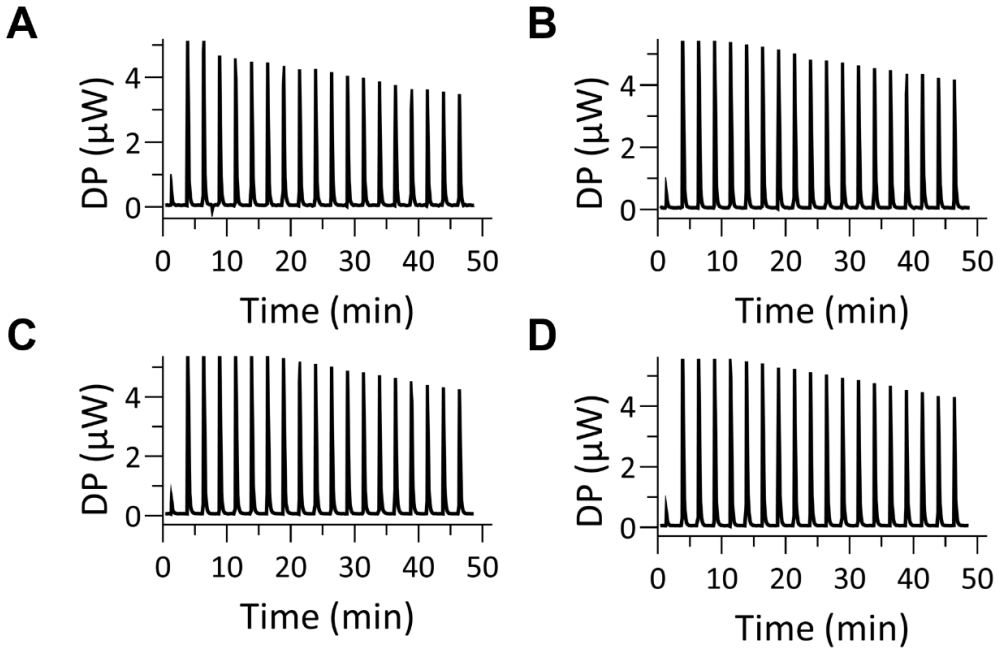

Figure 3.8 Raw data from titration of ATP into *Pa*HisG$_S$. 10 mM ATP was titrated into either (A and B) 50 µM *Pa*HisG$_S$ or (B and C) assay buffer.

3.3.2 Initial Velocity Patterns

Initial velocity patterns were examined to glean further insight into the kinetic mechanism of *Pa*HisG$_S$. Data for initial velocity patterns were collected and analysed on double reciprocal plots, Figure 3.9. Analysis of initial velocity patterns can elucidate if a ternary complex is present, whether substrate binding is ordered or random, and if the mechanism obeys steady-state or rapid equilibrium kinetics[126]. A rapid equilibrium kinetic mechanism is defined by the off rates of the substrates being significantly greater than k_{cat}[126]. For *Pa*HisG$_S$ the intersecting lines observed on double reciprocal plots are consistent with formation of a ternary complex in a sequential mechanism[127], Figure 3.9. An ordered rapid equilibrium mechanism generates diagnostic asymmetrical double reciprocal plots whereby lines intersect on the ordinate when the second reactant is varied[126], hence this mechanism was immediately ruled-out for *Pa*HisG$_s$. Intersecting lines on the ordinate reflect trapping of the Michaelis complex at infinite concentrations of the second reactant leading to maximal rate[126]. Unfortunately, the form of the initial velocity rate equation of a Bi steady-state ordered mechanism is identical to that of a Bi rapid-equilibrium random mechanism, hence, initial velocity patterns and even secondary replots would be identical[126]. When *Pa*HisG$_S$ initial velocity patterns are considered in context with DSF and ITC data, it was considered most likely that *Pa*HisG$_S$ follows a steady-state ordered mechanism where PRPP is the first substrate to bind, Figure 3.9C. Consequently, *Pa*HisG$_S$ data were fit to Equation 2.7[126]. which can represent either a steady-state ordered mechanism with PRPP as the first substrate to bind or a rapid-equilibrium random mechanism, kinetic parameters extracted from the fitting are summarised in Table 3.3

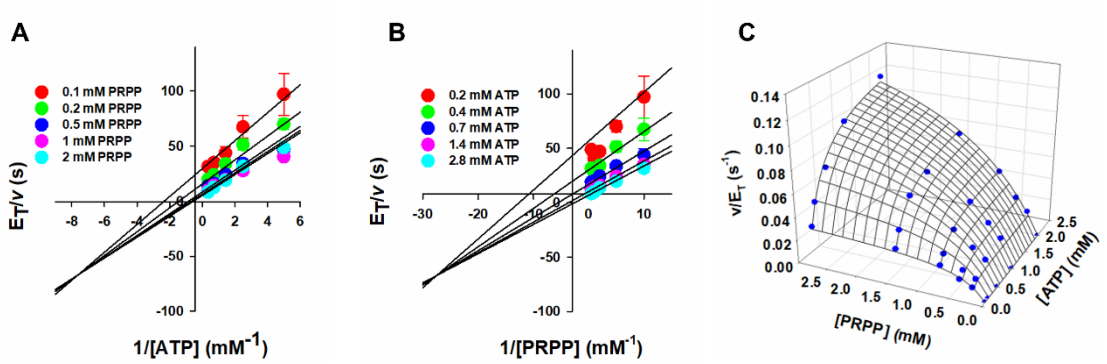

Figure 3.9 Initial velocity patterns for *Pa*HisG$_S$. Double reciprocal plots for *Pa*HisG$_S$ with (A) ATP and (B) PRPP as varying substrates. Each colour represents a different fixed concentration of co-substrate. (C) Initial rate data were fit to a steady-state ordered mechanism, Equation 2.7. Data points are mean ± standard error of quadruplicate measurements.

Table 3-3 *Pa*HisG$_S$ steady-state parameters from initial velocity patterns.

Parameter	***Pa*HisG$_S$**
k_{cat} **(s^{-1})**	0.25 ± 0.02
K_{iPRPP} **(mM)**	0.04 ± 0.03
K_{PRPP} **(mM)**	0.6 ± 0.1
K_{ATP} **(mM)**	2.3 ± 0.3
k_{cat}/K_{PRPP} **(M^{-1} s^{-1})**	416 ± 77
k_{cat}/K_{ATP} **(M^{-1} s^{-1})**	108 ± 16

Values are mean ± fitting error of quadruplicate measurements.

3.3.3 *Pa*HisG$_S$ follows an alternative kinetic mechanism to HisG$_L$-type ATPPRTs

Together, kinetic, ITC, DSF and structural data are consistent with a sequential ordered mechanism of *Pa*HisG$_S$ in which PRPP binds free *Pa*HisG$_S$, followed by ATP, whilst pyrophosphate is the first product to dissociate from the ternary complex followed by

PRATP, Figure 3.1C. *Pa*ATPPRT initial velocity patterns were collected by Rozanne Stroek, an Erasmus exchange student in the da Silva laboratory (data not shown) and also fit well to a steady-state ordered mechanism, when considered in context with available structural data these findings suggest the proposed mechanism is also applicable to *Pa*ATPPRT and perhaps ATPPRT from *L. lactis*. Notably, this work corrected a previous assumption in the literature that $HisG_S$-type ATPPRTs follow the same kinetic mechanism as $HisG_L$-type mechanisms. It is tempting to speculate that a steady-state ordered kinetic mechanism with PRPP as the first substrate to bind may apply to all $HisG_S$-type ATPPRTs, however, very recent kinetic characterisation of *Ab*$HisG_S$ by Benjamin J. Read, a PhD student in the da Silva laboratory, demonstrated that *Ab*$HisG_S$ follows a rapid-equilibrium random kinetic mechanism[45].

3.3.4 *Pa*$HisG_S$ T_M contradicts a previously reported T_M

It was noteworthy that the T_M of *Pa*$HisG_s$ calculated from the DSF experiment, 60.58 ± 0.08 ºC, was greater than the previously reported value of approximately 44 ºC, as determined by CD spectroscopy by the da Silva Laboratory[32]. The CD and DSF experiments were performed under different reaction conditions; the DSF experiment was carried out in 100 mM tricine (pH 8.5), 100 mM KCl, 15 mM $MgCl_2$ and 4 mM DTT to match activity assay conditions, whereas the original CD experiment was performed in 10 mM K_2HPO_4 (pH 8.0), 10 mM KF. DSF was repeated in 10 mM K_2HPO_4 (pH 8.0), 10mM KF and a T_M of 38.7 ± 0.1ºC was calculated, Figure 3.5, Table 3.1. Hence, the difference in *Pa*$HisG_S$ T_M values can be attributed to a different buffer and additives.

Intriguingly, it was previously reported that *Pa*$HisG_S$ and *Pa*ATPPRT deviate from Arrhenius behaviour at approximately 41 ºC and 36 ºC, respectively, and it was hypothesised that this deviation was due to protein denaturation[32]. The T_Ms of *Pa*HisZ under activity assay conditions and 10 mM K_2HPO_4 (pH 8.0), 10 mM KF are similar, ~40 ºC and ~39 ºC, respectively[32,44]. Hence, deviation of *Pa*ATPPRT from Arrhenius behaviour may indeed reflect *Pa*HisZ denaturation and/or dissociation of the hetero-octamer. On the other hand, *Pa*$HisG_S$ deviation from Arrhenius behaviour is unlikely to be explained by protein denaturation, as previously hypothesised. The deviation from Arrhenius behaviour occurs approximately 20 ºC below the now corrected and appropriate T_M value for conditions used in the original temperature study. *Pa*HisGs

deviation from Arrhenius behaviour may therefore be a result of change of rate-limiting step[128], temperature-sensitive flexible loops/regions which contribute to catalysis[129] or a non-zero contribution from activation heat capacity to catalysis[130–132]. Further temperature studies with *Pa*HisG$_S$ may yield interesting insights relevant to ongoing work to establish the mechanisms underpinning enzyme catalysis at low temperature[129,133], but are considered beyond the scope of this work.

It may be tempting to speculate that a T_M of 60 ºC is higher than expected for a psychrophilic enzyme, especially when compared with the T_M of mesophilic *A. baumannii* HisG$_S$ which is approximately 58 ºC[45]. However, a lower T_M of psychrophilic enzymes relative to their mesophilic counterparts may be considered a result of a lack of selective pressure to maintain stability at high temperature rather than a psychrophilic adaptation. Hence, the high T_M of *Pa*HisG$_S$ does not reflect a lack of psychrophilicity[134].

3.4 ADP is a substrate of *Pa*HisG$_S$

3.4.1 ^{31}P-NMR spectroscopy of reactions catalysed by *Pa*HisG$_S$ with ADP as a substrate

The suitability of ADP as a substrate of *Pa*HisG$_S$ was initially investigated via by ^{31}P-NMR spectroscopy using a method developed in the da Silva laboratory [32]. PRATP and PRADP in reaction mixtures is readily detected by ^{31}P-NMR owing to the unique chemical shift of the phosphorus in the N^1-5-phospho-β-$_D$-ribose moiety, at approximately ~3.3 – 3.4 ppm, which is absent from control reactions without *Pa*HisG$_S$[32].

Firstly, ^{31}P-NMR spectra of control reactions in which ATP and PRPP were incubated with and without *Pa*HisG$_S$, respectively, Figures 3.10 and 3.11. A peak with a chemical shift of 3.4 ppm representing the phosphorus of the N^1-5-phospho-β-$_D$-ribose moiety of PRATP was observed only when *Pa*HisG$_S$ was added to the reaction and all other phosphate species are represented by peaks with chemical shifts comparable with previous reports[32]. A peak with a chemical shift of 3.4 ppm was also detected upon incubation of ADP with PRPP in the presence of *Pa*HisG$_S$, Figures 3.10 and 3.12. This peak represents the phosphorus in the N^1-5-phospho-β-$_D$-ribose moiety of PRADP, which exists in a similar chemical environment to that of PRATP. The peak at ~3.4 ppm was

not detected upon incubation of PRPP and ADP in the absence of *Pa*HisG$_S$, Figure 3.10. Other peaks in ^{31}P-NMR spectra from ADP reactions and controls were assigned to either substrate or product, based on previous ^{31}P-NMR standards run in the da Silva laboratory[32], Figure 3.12.

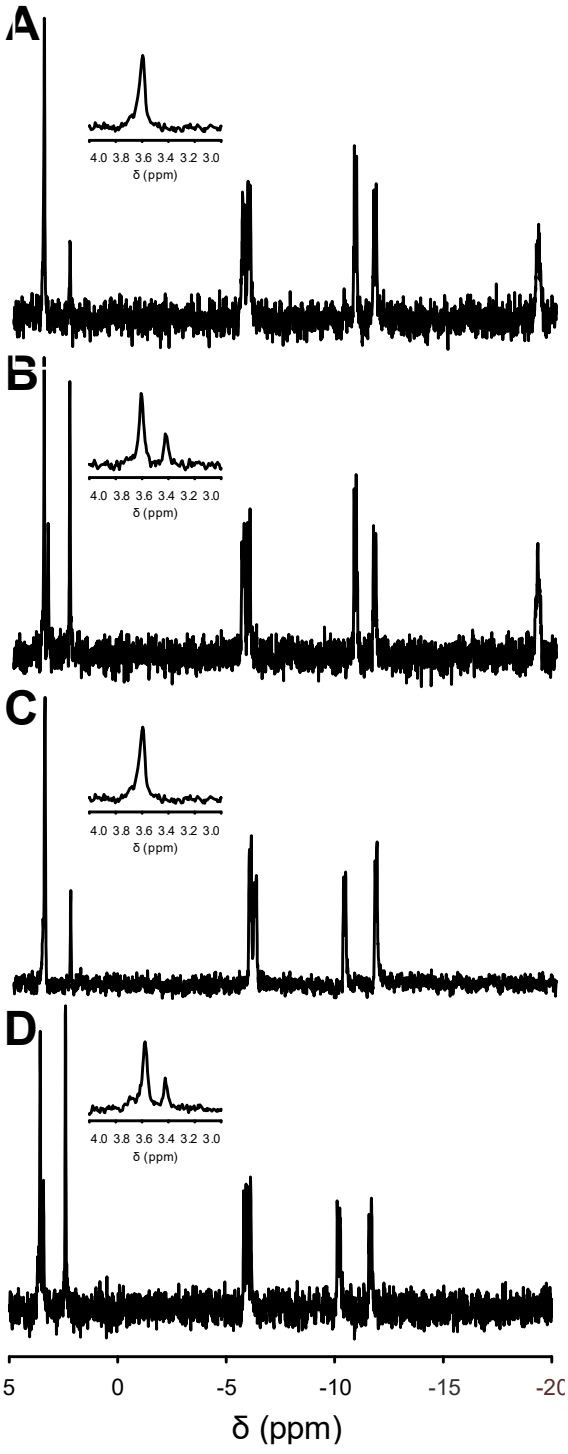

Figure 3.10 ^{31}P-NMR spectra of control reactions and *Pa*HisG$_S$ catalysed reactions with ATP and ADP. Control reaction (without *Pa*HisG$_S$) with (A) ATP or (C) ADP. *Pa*HisG$_S$ catalysed reactions with (B) ATP and (D) ADP. Insets in (A)– (D) are close-ups of the spectra between 4.0 and 3.0 ppm, showing the peak at ca. 3.4 ppm in (B) and (D) corresponding to the phosphorus in the N1-5-phospho-β-$_D$-ribose moiety of PRATP and PRADP, respectively, which is missing in insets in (A) and (C).

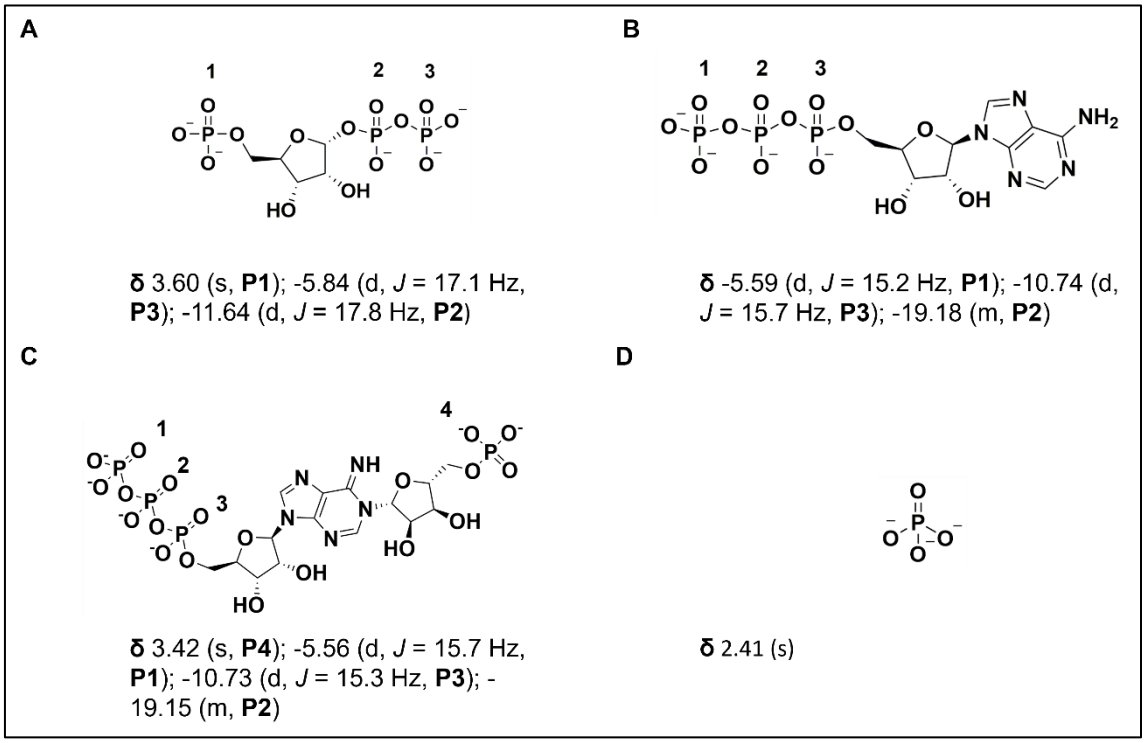

Figure 3.11 Assignments of chemical shifts (δ) in ppm and J values in Hz for peaks in the ^{31}P-NMR spectra to the corresponding phosphates in (A) PRPP , (B), ATP, (C) PRATP and (D) Pi.

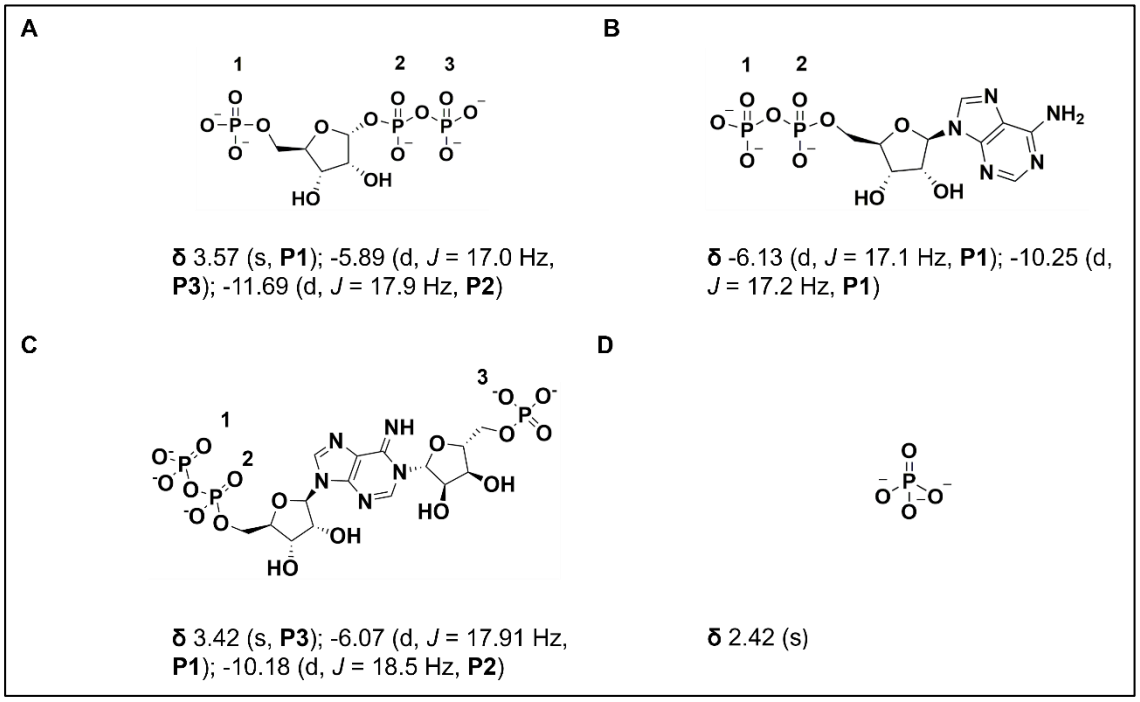

Figure 3.12 Assignments of chemical shifts (δ) in ppm and J values in Hz for peaks in the ^{31}P-NMR spectra to the corresponding phosphates in in (A) PRPP , (B), ADP, (C) PRADP and (D) Pi.

3.4.2 Steady-state kinetic parameters of reactions catalysed by *Pa*HisGs with ADP as a substrate.

The steady-state kinetic parameters of reactions catalysed with ADP and ATP were determined side-by-side for a quantitative analysis of the reaction, Figure 3.13, Table 3.4. The k_{cat} of reactions catalysed with either ADP or ATP are identical within error confirming that ADP is efficiently used as a substrate by *Pa*HisGs. K_M^{ADP} is approximately 3-fold greater than K_M^{ATP}, indicating that the interaction between the γ-phosphate of ATP and R´73 may play a minor role in binding but is not essential for either binding or catalysis. K´50 is the equivalent residue to R´73 in *L. lactis* ATPPRT. Mutagenesis of K´50 to alanine resulted in a 2.5-fold increase in *L. lactis* ATPPRT k_{cat} and a 2-fold increase in K_M^{ATP}, lending support to the conclusion that this interaction is not required for either ATP binding or catalysis[31]

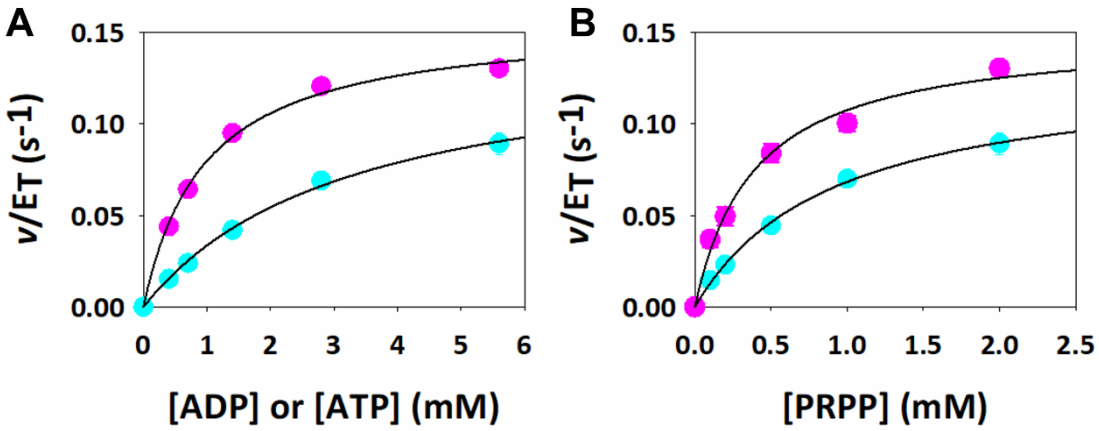

Figure 3.13 *Pa*HisGs substrate saturation curves with either ATP (pink) or ADP (cyan) as a substrate. (A) Varying PRPP concentration with saturating concentration of the nucleotide. (B) Varying the nucleotide concentration with saturating concentration of PRPP. Data points are mean ± standard error. Black lines is data fit to the Michaelis-Menten equation.

Table 3-4 *Pa*HisG$_S$ steady-state parameters with either ATP or ADP as a substrate.

Parameter	**ATP**	**ADP**
k_{cat} **(s^{-1})**	0.15 ± 0.01	0.14 ± 0.01
K_{PRPP} **(mM)**	0.39 ± 0.07	0.91 ± 0.08
$K_{A(X)P}$ **(mM), X = T or D**	0.96 ± 0.09	3.2 ± 0.3
k_{cat}/K_{PRPP} **(M^{-1} s^{-1})**	380 ± 70	153 ± 6
$k_{cat}/K_{A(X)P}$ **(M^{-1} s^{-1})**	160 ± 20	43 ± 5

Values are ± fitting error of duplicate measurements.

3.4.3 ADP is a substrate of *Pa*HisG$_S$

Together, ^{31}P-NMR and steady-state kinetics demonstrated ADP is an adequate substrate for *Pa*HisG$_S$. Whilst this finding has corrected a false assumption in the literature, that ADP is a universal competitive inhibitor of ATPPRT, the *in vivo* relevance of this finding is difficult to ascertain as the intracellular concentration of free adenine nucleotides in *P. arcticus* has not been reported in the literature. However, it is well established that intracellular ATP concentrations exceed intracellular ADP concentrations. It is difficult to define average values of the intracellular ATP/ADP ratio; in *E. coli* ATP/ADP ratios of 3[135], 10[136] and 30[137] have all been reported and factors including growth phase[137] and carbon source (glucose, glycerol or acetate)[136] may alter this ratio. More recent studies in *E coli*. using FRET-based indicators, in contrast to traditional HPLC and/or LC-MS methods, add further complexity by drawing attention to the large variation in nucleotide pools across individual cells within a population[138]. The fate of PRADP in *P. arcticus* is addressed in Chapter 5.

3.5 Determining the rate-limiting steps of reactions catalysed by *Pa*HisG$_S$ and *Pa*ATPPRT

3.5.1 Viscosity studies of *Pa*HisG$_S$ and *Pa*ATPPRT

Viscosity studies rapidly distinguish reactions which are diffusion-controlled, that is to say rate-limited by substrate diffusion, product release or isomerisation steps, from reactions in which the chemical step of catalysis is rate-limiting[139]. A viscosity study typically measures the Michaelis constants k_{cat} and k_{cat}/K_M across a range of viscosigen concentration and reports kinetic solvent viscosity effects (KSVEs) on these constants[139]. The Michaelis constants k_{cat} and k_{cat}/K_M report on different stages of the catalytic cycle, Figure 3.14. Hence, if a KSVE is observed, depending on which constant(s) is/are perturbed it is possible to deduce where in the catalytic cycle a rate-limiting diffusional step lies.

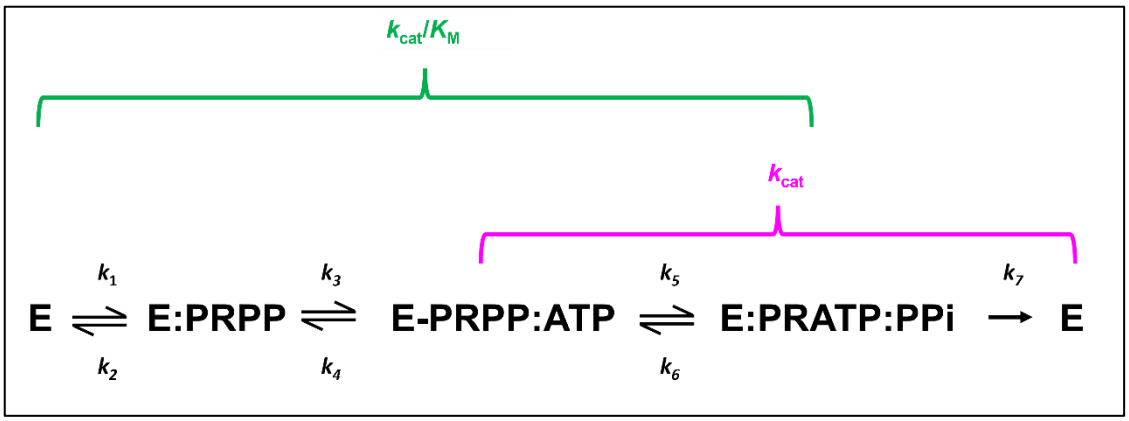

Figure 3.14 The steady-state kinetic constants k_{cat} and k_{cat}/K_M report on different stages of the catalytic cycle. In the current work, enzymatic cleavage of PPi by pyrophosphatase renders product release (k_7) irreversible. Steps that contribute to k_{cat} are denoted by a magenta bracket. Steps that contribute to k_{cat}/K_M are denoted by a green bracket.

A viscosity study of activated *Pa*ATPPRT and non-activated *Pa*HisG$_S$ was initiated. Firstly, the K_D of *Pa*HisG$_S$ and *Pa*HisZ was determined in 0, 18 and 27 % glycerol, Figure 3.15 and Table 3.5. These K_Ds were used to calculate the concentration of the *Pa*ATPPRT holoenzyme in steady-state kinetic experiments. *Pa*ATPPRT and *Pa*HisG$_s$ steady-state kinetic parameters were determined in 0, 18 and 27% glycerol, Figure 3.16, Tables 3.5 and 3.6. Data for *Pa*HisG$_S$ was collected by Dr Rafael. G. da Silva. Replots of the data

were constructed according to reference[139] and KSVEs were extracted following data fitting, Figure 3.17, Table 3.7.

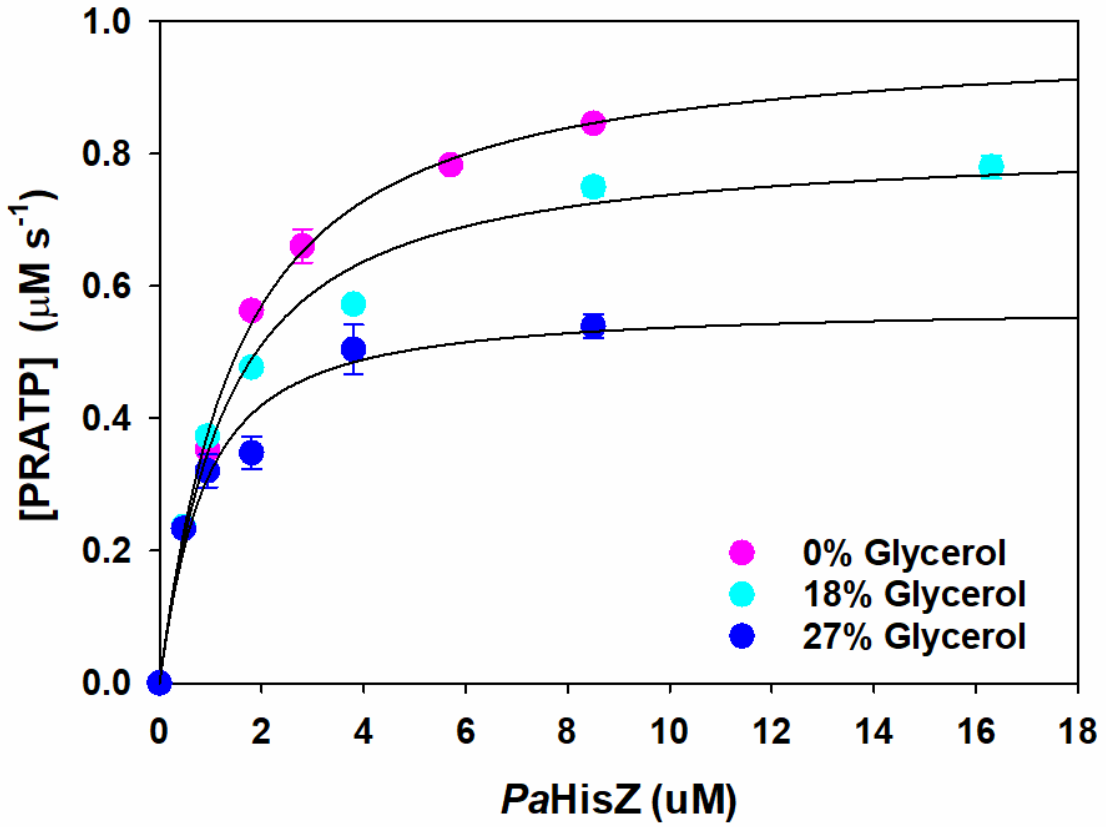

Figure 3.15 Determination of K_D for equilibrium dissociation of *Pa*HisZ from the *Pa*ATPPRT holoenzyme in 0% (magenta), 18% (cyan) and 27% (blue) glycerol. (*v*/*v*). . Data points are mean ± standard error. Solid lines are data fitted to Equation 2.1.

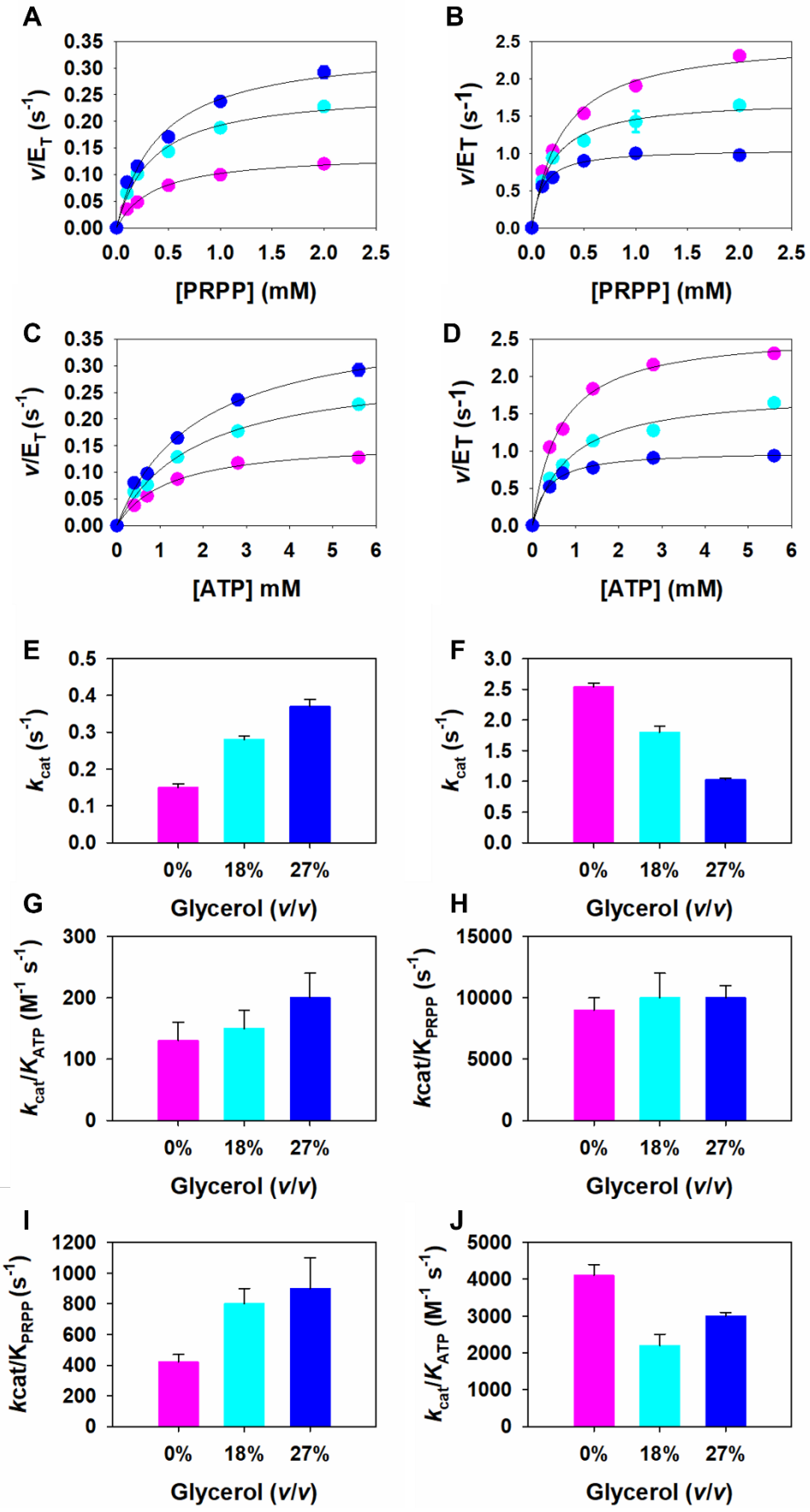
A
v/E_T (s^-1)
[PRPP] (mM)
B
v/ET (s^-1)
[PRPP] (mM)
C
v/E_T (s^-1)
[ATP] mM
D
v/ET (s^-1)
[ATP] (mM)
E
k_cat (s^-1)
Glycerol (v/v)
F
k_cat (s^-1)
Glycerol (v/v)
G
k_cat/K_ATP (M^-1 s^-1)
Glycerol (v/v)
H
kcat/K_PRPP (s^-1)
Glycerol (v/v)
I
kcat/K_PRPP (s^-1)
Glycerol (v/v)
J
k_cat/K_ATP (M^-1 s^-1)
Glycerol (v/v)
0%
18%
27%

Figure 3.16 The effect of solvent viscosity on *Pa*HisG$_S$ and *Pa*ATPPRT steady-state kinetic parameters. (A and C) *Pa*HisG$_S$ and (B and D) *Pa*ATPPRT saturation curves were measured in 0% (pink), 18% (cyan), and 27% (blue) glycerol (*v*/*v*). (E, G and I) *Pa*HisG$_S$ and (F, H and I) *Pa*ATPPRT steady-state kinetic constant dependence on glycerol concentration. Data are either mean ± standard error (scatter plots) or value ± fitting error (bar plots). Solid lines in (A-D) are data fit to the Michaelis-Menten equation. Data for *Pa*HisG$_S$ was collected by Dr R. G. da Silva.

Table 3-5 The effect of solvent viscosity on *Pa*ATPPRT steady-state kinetic parameters.

Parameter	**0% glycerol (*v*/*v*)**	**18% glycerol (*v*/*v*)**	***27% glycerol* (v/v)**
K_D	1.2 ± 0.1	1.1 ± 0.1	0.6 ± 0.2
k_{cat} **(s^{-1})**	2.54 ± 0.06	1.8 ± 0.1	1.03 ± 0.02
K_{PRPP} **(mM)**	0.29 ± 0.04	0.18 ± 0.03	0.10 ± 0.01
K_{ATP} **(mM)**	0.62 ± 0.05	0.8 ± 0.1	0.35 ± 0.03
k_{cat}/K_{PRPP} **(M^{-1} s^{-1})**	9000 ± 1000	10000 ± 2000	10000 ± 1000
k_{cat}/K_{ATP} **(M^{-1} s^{-1})**	4100 ± 300	2200 ± 300	3000 ± 300

Values are ± fitting error of duplicate measurements.

Table 3-6 The effect of solvent viscosity on *Pa*HisG$_S$ steady-state parameters.

Parameter	**0% glycerol (v/v)**	**18% glycerol (v/v)**	***27% glycerol (v/v)***
k_{cat} **(s^{-1})**	0.15 ± 0.01	0.28 ± 0.01	0.37 ± 0.01
K_{PRPP} **(mM)**	0.36 ± 0.04	0.35 ± 0.05	0.41 ± 0.08
K_{ATP} **(mM)**	1.2 ± 0.1	1.9 ± 0.2	1.9 ± 0.2
k_{cat}/K_{PRPP} **(M^{-1} s^{-1})**	420 ± 50	800 ± 100	900 ± 200
k_{cat}/K_{ATP} **(M^{-1} s^{-1})**	130 ± 30	150 ± 30	190 ± 40

Values are ± fitting error of duplicate measurements. Data collected by Dr Rafael.G. da Silva.

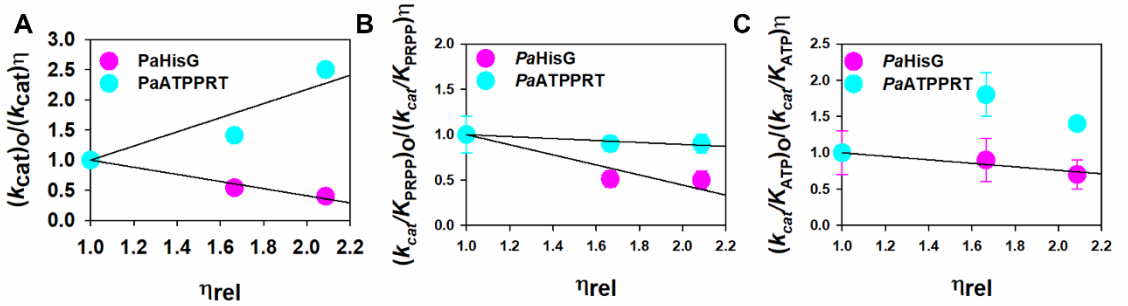

Figure 3.17 Kinetic solvent viscosity effects on *Pa*HisG$_s$ and *Pa*ATPPRT catalysed reactions. Kinetic solvent viscosity effects on (A) k_{cat}, (B) k_{cat}/K_M^{PRPP} and (C) k_{cat}/K_M^{ATP} for *Pa*HisG$_S$ and *Pa*ATPPRT catalysed reactions Data points are mean ± fitting error. Solid lines are data fit to Equation 2.8.

Table 3-7 Kinetic solvent viscosity effects on k_{cat}, k_{cat}/K_M^{PRPP} and k_{cat}/K_M^{ATP} for *Pa*HisG$_S$ and *Pa*ATPPRT catalysed reactions

Kinetic Solvent Viscosity Effect	$(k_{cat})_0/(k_{cat})_\eta$	$(k_{cat}/K_{PRPP})_0/(k_{cat}/K_{PRPP})_\eta$	$(k_{cat}/K_{ATP})_0/(k_{cat}/K_{ATP})_\eta$
***Pa*HisG$_S$**	-0.59 ± 0.04	-0.55 ± 0.08	-0.24 ± 0.04
***Pa*ATPPRT**	1.2 ± 0.2	-0.11 ± 0.02	N.A.

Values are ± fitting-error.

A KSVE of 1.2 ± 0.2 was observed on activated *Pa*ATPPRT k_{cat}, indicative that the release of products from the active site (k_7, Figure 3.14) is fully rate-limiting for the overall turnover of the enzyme[139]. A negligible KSVE was recorded on *Pa*ATPPRT k_{cat}/K_M^{PRPP} which suggests diffusional processes are not rate-limiting for steps encompassing substrate capture to product formation[139]. *Pa*ATPPRT k_{cat}/K_M^{ATP} data could not be reliably fit to either a linear or hyperbolic equation.

Contrastingly, a moderate inverse viscosity effect was observed on non-activated *Pa*HisG$_S$ k_{cat}, k_{cat}/K_M^{PRPP} and k_{cat}/K_M^{ATP}. Inverse viscosity effects suggest that diffusional steps are not rate-limiting. Inverse viscosity effects typically reflect either non-specific viscosigen effects or internal isomerisations[140]. Inverse microviscosigen KSVEs of a similar magnitude to that reported here has previously been attributed to mild rate accelerations owing to non-specific interactions[139,141,142].

An additional experiment(s) modulating a different microviscogen may elucidate if glycerol is modulating enzyme activity via binding to the enzyme in the case of *Pa*HisG$_S$, however, such experiments were considered beyond the scope of this work as the rate-limiting steps of *Pa*HisG$_S$ were uncovered via alternate methods. Critically, this data provided the first insight that *Pa*HisG$_S$ and *Pa*ATPPRT may have different rate-limiting steps.

3.5.2 Analysis of *Pa*HisG$_S$ and *Pa*ATPPRT product formation time-courses under pre-steady state conditions

Further probing of the difference in rate-limiting step between nonactivated *Pa*HisG$_S$ and activated *Pa*ATPPRT was achieved by monitoring product formation time-courses under pre-steady-state conditions. Briefly, multiple-turnover reactions catalysed by non-activated *Pa*HisG$_S$ or activated *Pa*ATPPRT were studied under pseudo-first order conditions in a stopped-flow spectrophotometer facilitating the capture of the first milliseconds of a reaction, Figure 3.18.

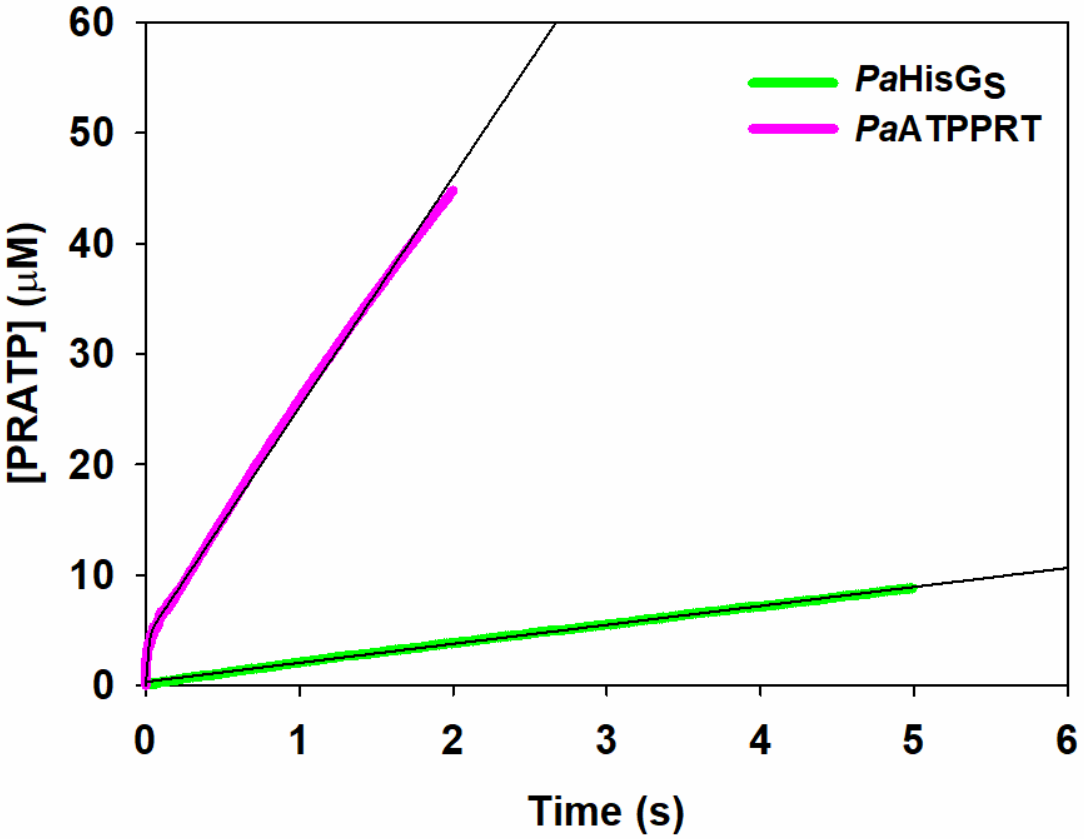

Figure 3.18 Pre-steady-state kinetics with *Pa*ATPPRT and *Pa*HisG$_S$. Time-courses product formation for reactions catalysed by *Pa*ATPPRT (magenta) and *Pa*HisGs (green) with a burst in product formation observed with the former but not the latter. Black solid lines represent either a linear regression of *Pa*HisG$_S$ data or *Pa*ATPPRT data fitted to Equation 2.4

A burst of product formation followed by a linear relationship between product formation and time was observed for the reaction catalysed by activated *Pa*ATPPRT, Figure 3.18. From data fitting, k_{burst} = 80 ± 1 s^{-1} and A_0 = 4.3 μM. The burst in product formation

represents initial rapid synthesis, but accumulation of product on the enzyme active site[143]. Product formation in subsequent turnovers then becomes dependent on a second rate constant, k = 1.11 ± 0.01 s^{-1}. The burst in PRATP production is diagnostic of a mechanism where chemistry is faster than steps after chemistry ($k_7 << [k_5 + k_6]$)[143].

Generally, the amplitude of the burst (A_0) should approximate the number of active sites[143], however, for *Pa*ATPPRT, A_0 (4.3 μM) represents only ~26% of the theoretical concentration of the *Pa*ATPPRT Michaelis complex (16.5 μM) used in this experiment. Examination of Figure 6.19 and Equations 2.2 and 2.3 highlighted that whilst A_0 and k_{burst} are both functions of the rate constants of the chemical reaction and product release, as the rate constant for the reverse reaction (k_6) increases k_{burst} increases, whereas A_0 decreases. Therefore, an A_0 that is lower than expected may reflect internal reversibility[143]. Indeed, for *Pa*ATPPRT, crystal structures solved by Dr Magnus S. Alphey with both substrates present unreacted in the enzyme active site in the presence of Mg^{2+}, may suggest that the on-enzyme equilibrium lies towards substrates. Examining the reaction in the reverse direction under pre-steady state conditions could theoretically generate a burst with a maximal amplitude, providing ATP and/or PRPP dissociation was sufficiently rate-limiting[143]. However, it was not possible to examine the *Pa*ATPPRT reaction in reverse due to pyrophosphate insolubility at concentrations required to saturate the enzyme.

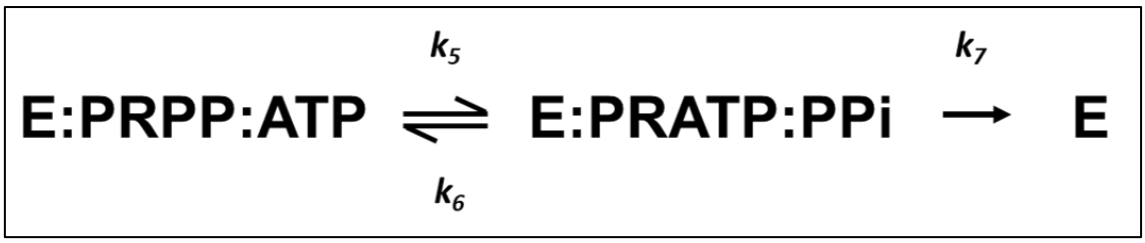

Figure 3.19. Two step reversible mechanism used to approximate burst kinetics. Scheme modified from Johnson (1992).

Equation 3.2

$$k_{burst} = k_5 + k_6 + k_7$$

Equation 3.3

$$A_0 = \frac{k_5(k_5 + k_6)}{(k_5 + k_6 + k_7)^2}$$

A similar pre-steady state burst experiment was conducted with *M. tuberculosis* ATPPRT and a burst of product formation was also observed, k_{burst} = 0.67 s^{-1} [29]. The *M. tuberculosis* ATPPRT burst amplitude more closely approximated the protein concentration used in the experiment (78%). It may be the case that the internal equilibrium lies more towards substrates than products for *Pa*ATPPRT compared with ATPPRT from *M. tuberculosis*.

No burst of product formation was detected for reactions catalysed by non-activated *Pa*HisG$_S$, Figure 3.18. An apparent rate-constant of 0.091 ± 0.001 s^{-1}, was extracted from a linear regression of data, which is in reasonable agreement with k_{cat} (0.15 s^{-1}). The absence of a burst of PRATP production in the first few milliseconds of the reaction reflects a mechanism whereby steps after chemistry are not rate-limiting ([k_5 + k_6] << k_7)[143]. Fundamentally, pre-steady state data provided further confirmation of different rate-limiting steps for *Pa*HisG$_s$ and activated *Pa*ATPPRT

3.5.3 *Pa*HisG$_S$ single turnover rates cannot be measured

As viscosity and pre-steady state data indicated neither diffusional steps nor steps after chemistry are rate-limiting for *Pa*HisG$_S$, it was sought to investigate if interconversion between ternary complexes, including chemistry, could be rate limiting. Thus, a pre-steady state, single turnover experiment was devised. Single turnover measurements are performed with enzyme in excess of substrate in a stopped flow spectrophotometer. A single round of conversion from substrate to products is observed[143]. When considered in context with viscosity and pre-steady state data, if the rate constant for the single turnover (k_{sto}) catalysed by *Pa*HisG$_S$ were to be equivalent to k_{cat} (the lower limit of k_{sto}), providing PRPP is fully saturated with enzyme, this would support a mechanism where interconversion between *Pa*HisG$_S$:PRPP:ATP to *Pa*HisG$_S$:PRATP:PPi is rate limiting[133].

Unfortunately, attempts to measure k_{sto} of *Pa*HisG$_S$ were unsuccessful as it was not possible to saturate PRPP with *Pa*HisG$_S$. Product formation data were fitted to a single exponential rise to maximum and rate constants extracted were dependent on enzyme concentration, Figure 3.20 and Table 3.8. As the affinity of *Pa*HisG$_S$ for PRPP is known, K_D = 12 μM, it is possible to calculate the theoretical saturation of *Pa*HisG$_S$ in the experiment. The maximum theoretical saturation of PRPP achieved in this experiment was 74%, however, the value of apparent rate constant extracted from these data reflected only 14% of $k_{cat.}$ The experiment was abandoned and it was hypothesised that internal reversibility and/or aggregation of HisG$_s$ at concentrations used in this experiment may account for the low rate of reaction observed.

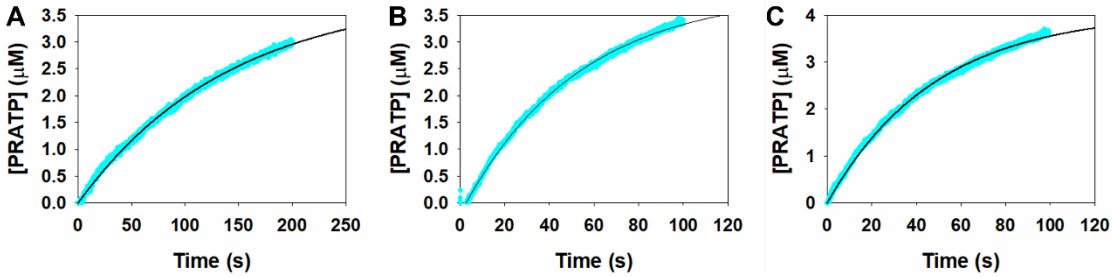

Figure 3.20 Product formation time-courses from reactions catalysed by *Pa*HisG$_S$ under single-turnover conditions. 5 μM PRPP was incubated with either 10 (A), 20 (B) or 40 μM *Pa*HisG$_S$. Solid black lines are data fitted to Equation 2.5.

Table 3-8.Apparent rate-constants extracted from fitting *Pa*HisG$_S$ single-turnover data,

***Pa*HisG (μM)**	***k* (s^{-1})***	**% Saturation of 5 μM PRPP**
10	0.0071 ± 0.00001	40
20	0.0154 ± 0.00003	58
40	0.0209 ± 0.00005	74

*Data are ± fitting error of multiple independent measurements.

3.5.4 Effect of substitution of magnesium by manganese on *Pa*HisG$_S$ and *Pa*ATPPRT catalysed reactions.

Mg^{2+} is considered essential for ATPPRT activity; the activity of ATPPRT from *S.* Typhimurium and *M. tuberculosis* is abolished by addition of EDTA, and studies have indicated ATPPRTs from different organisms exhibit varying tolerances for divalent metal substitutions. For example, *S.* Typhimurium ATPPRT can tolerate Mn^{2+} as a substitute for Mg^{2+} but not Cu^{2+}, Ni^{2+} and Zn^{2+} [17], whereas *C. glutamicum* ATPPRT was able to accept Co^{2+}, Ni^{2+} and Mn^{2+} at varying efficacies[41].

Transition state modelling of reactions catalysed by *Pa*HisG$_S$ carried out by the da Silva Laboratory in collaboration with Dr Jennifer S. Hirschi (Binghamptom University) carried out in parallel with this work predicted an S_N2-like transition state structure with two equivalents of Mg^{2+} required at the transition state[43] (discussed in Chapter 1). The first Mg^{2+} ion acts as a Lewis acid to stabilise negative charges upon ATP binding[43]. The second Mg^{2+} ion was posited to stabilise the pyrophosphate leaving-group at the transition state[43].

The previous experiments in this chapter have demonstrated the k_{cat}s of activated *Pa*ATPPRT and non-activated *Pa*HisG$_S$ are reporting on different steps. It was hypothesised that substituting Mn^{2+} for Mg^{2+} may effect *Pa*ATPPRT and *Pa*HisG$_S$ steady-state kinetic parameters differently and provide further elucidation of the rate-

limiting step(s) of *Pa*HisG$_S$. Specifically, it was hypothesised that if chemistry was at least partially rate-limiting for *Pa*HisG$_S$, exchanging Mg^{2+} for Mn^{2+} may perturb k_{cat}.

PRATP production in reactions catalysed by *Pa*HisG$_S$ with Mn^{2+} was confirmed by LC-MS, Figure 3.21, using a separation method previously defined by the da Silva laboratory[40]. LC-MS was performed under the supervision of Dr Clarissa M. Czekster. PRPP and ATP were incubated in the presence of Mn^{2+} with and without *Pa*HisG$_S$. A sole peak corresponding to ATP was observed in the LC-MS analysis of control reactions (no *Pa*HisG$_S$). Two peaks were observed in LC-MS analysis of reactions with *Pa*HisG$_S$ corresponding to ATP and PRATP. It was concluded that *Pa*HisG$_S$ catalyses the conversion of ATP and PRPP to PRATP and pyrophosphate with Mn^{2+} as a substitute for Mg^{2+}.

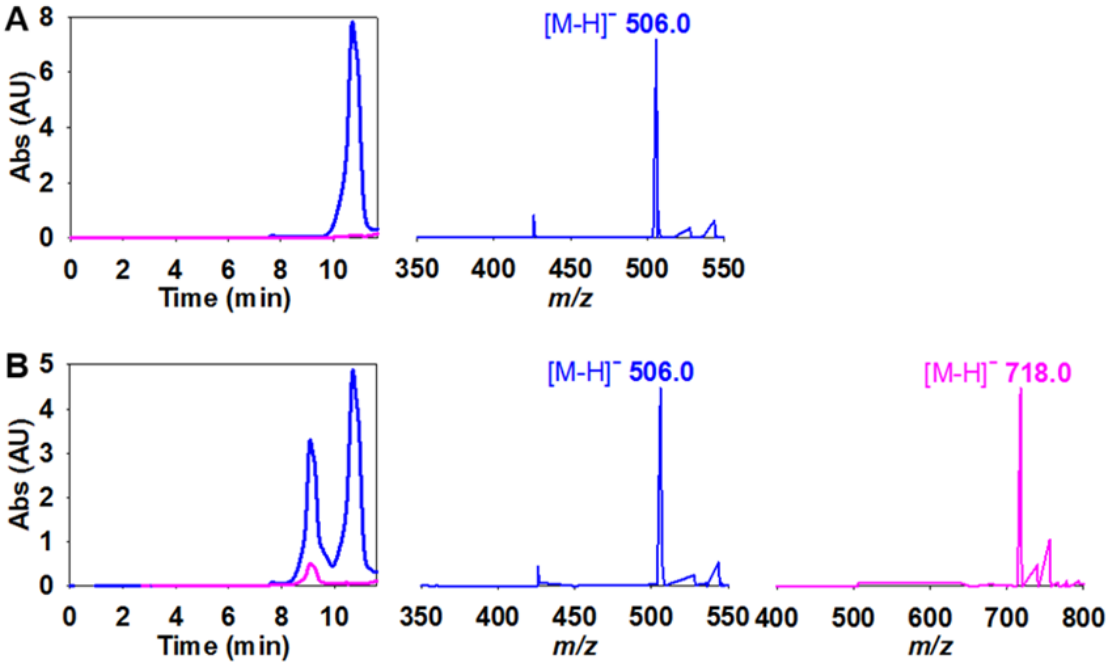

Figure 3.21 LC-MS analysis of the reaction catalysed by *Pa*HisG with Mn^{2+}.(A) Chromatogram from a control reaction, without *Pa*HisG$_S$, showing a peak with absorbance at 260 nm (blue), and mass spectra of the peak showing the expected m/z for ATP (blue). (B) Chromatogram from reaction with *Pa*HisG$_S$, showing two peaks: one with absorbance at 260 nm (blue) and a second peak exhibiting absorbance at both 260 nm (blue) and 290 nm (pink). Mass spectra of the peak absorbing only at 260 nm (blue) confirms the expected m/z for ATP (blue). Mass spectra of the peak absorbing at both 260 nm and 290 nm confirms s the expected m/z for PRATP (pink).

The steady-state kinetic parameters of reactions catalysed by *Pa*HisG$_S$ and *Pa*ATPPRT were determined side-by-side for a quantitative assessment of metal ion substitution, Figure 3.22 and Table 3.9. Exchanging, Mg^{2+} for Mn^{2+} results in a ~2.6-fold increase *Pa*HisG$_S$ k_{cat} and an ~11.8-fold increase in k_{cat}/K_M^{ATP}, whereas only a negligible effect on k_{cat}/K_M^{PRPP} was observed. Contrastingly, there is a negligible effect of exchanging Mg^{2+} for Mn^{2+} on *Pa*ATPPRT k_{cat} and k_{cat}/K_M^{PRPP} and a ~3-fold increase in k_{cat}/K_M^{ATP} was observed, wholly driven by a decrease in K_M^{ATP}.

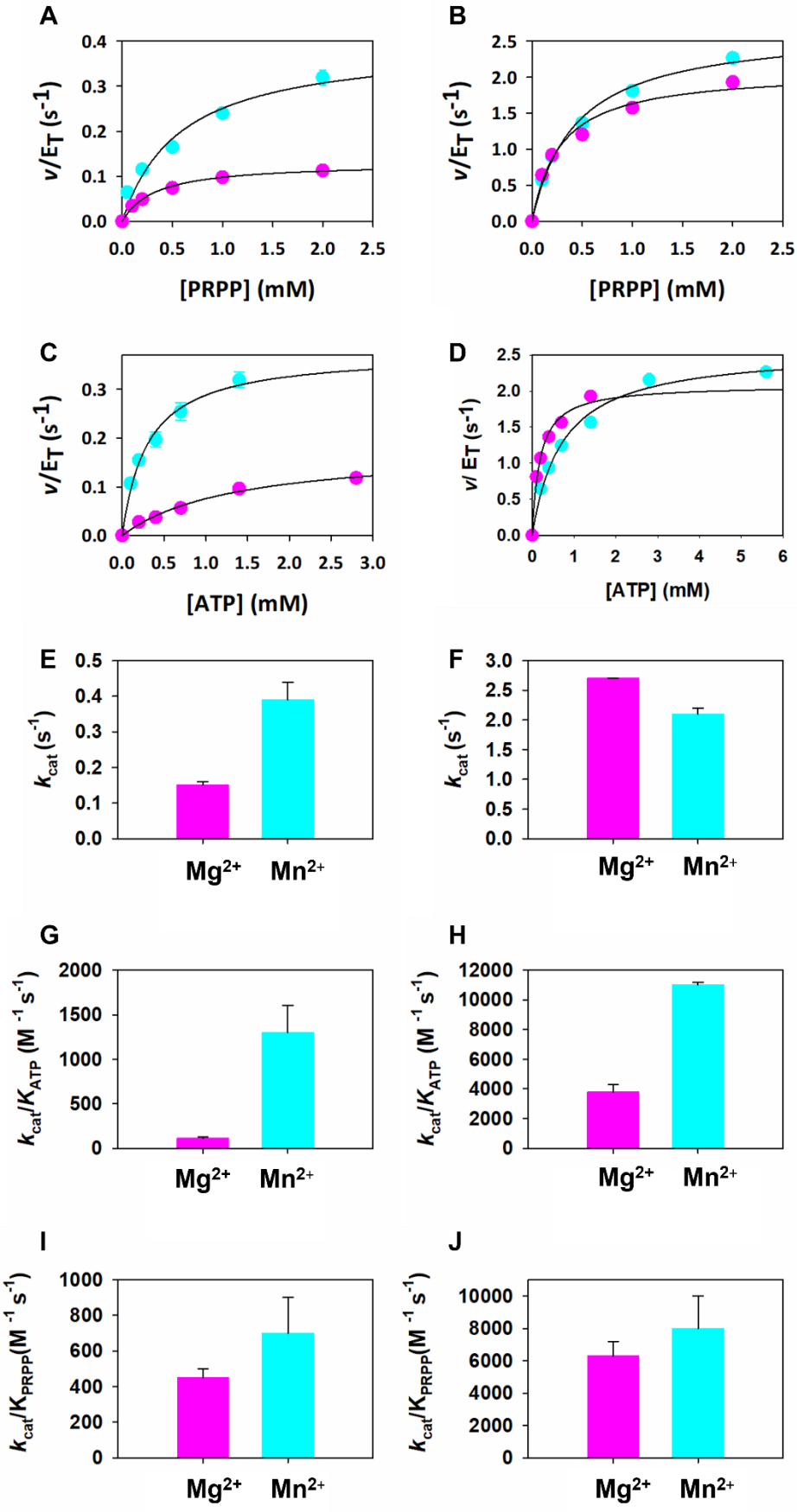
A
v/ET (s-1)
[PRPP] (mM)
B
v/ET (s-1)
[PRPP] (mM)
C
v/ET (s-1)
[ATP] (mM)
D
v/ ET (s-1)
[ATP] (mM)
E
kcat (s-1)
Mg2+
Mn2+
F
kcat (s-1)
Mg2+
Mn2+
G
kcat/KATP (M -1 s-1)
Mg2+
Mn2+
H
kcat/KATP (M -1 s-1)
Mg2+
Mn2+
I
kcat/KPRPP(M -1 s-1)
Mg2+
Mn2+
J
kcat/KPRPP(M -1 s-1)
Mg2+
Mn2+

Figure 3.22 The effect of substituting Mn^{2+} for Mg^{2+} on *Pa*HisG$_S$ steady-state parameters. .(A and C) *Pa*HisG$_S$ and (B and D) *Pa*ATPPRT substrate saturation curves with Mg^{2+} (pink) and Mn^{2+} (cyan). The effect of Mn^{2+} substitutions on (E, G and I) *Pa*HisG$_S$ and (F, H and I) *Pa*ATPPRT steady-state kinetic constants. Data are mean ± standard error (scatter plots) or value ± fitting error (bar plots). Solid lines in (A)-(D) are data fitted to the Michaelis Menten equation.

Table 3-9 The effect of Mn^{2+} on *Pa*HisG$_S$ and *Pa*ATPPRT steady-state parameters.

Parameter	***Pa*HisG$_S$ (Mg^{2+})**	***Pa*HisG$_S$ (Mn^{2+})**	***Pa*ATPPRT (Mg^{2+})**	***Pa*ATPPRT (Mn^{2+})**
k_{cat} (s^{-1})	0.15 ± 0.01	0.39 ± 0.05	2.65 ± 0.07	2.1 ± 0.1
K_{PRPP} (mM)	0.33 ± 0.03	0.6 ± 0.2	0.43 ± 0.05	0.28 ± 0.06
K_{ATP} (mM)	1.4 ± 0.2	0.30 ± 0.05	0.72 ± 0.09	0.19 ± 0.03
k_{cat}/K_{PRPP} (M^{-1} s^{-1})	450 ± 50	700 ± 200	6200 ± 700	8000 ± 2000
k_{cat}/K_{ATP} (M^{-1} s^{-1})	110 ± 20	1300 ± 300	3700 ± 500	11000 ± 2000

Values are ± fitting error of duplicate measurements.

Viscosity and pre-steady-state data indicate that the k_{cat} of *Pa*HisG$_S$ catalysed reactions is not reporting on product release, hence, it is unlikely that Mn^{2+} is exerting an effect via product off rates. The increase in *Pa*HisG$_S$ k_{cat} was speculatively attributed to an increased rate of chemistry owing to an increased ability of Mn^{2+} to attenuate negative charge on the pyrophosphate leaving group compared with Mg^{2+}. This hypothesis was later supported by transition state modelling of *Pa*HisG$_S$ catalysed reactions with PRPP and ADP as substrates in the presence of both Mg^{2+} and Mn^{2+} carried out by Dr Jenifer Hirschi[43]. Briefly, analysis of the transition state models demonstrated Mn^{2+} is better able to attenuate the negative charge of the pyrophosphate leaving group at the transition state through d-orbital bonding to coordinating oxygens[43]. Dr Jennifer Hirschi's work was published alongside data from this chapter.

3.5.5 *Pa*HisG$_S$ and *Pa*ATPPRT have different rate-limiting steps

In this work, a viscosity effect of ~1 was reported on activated *Pa*ATPPRT k_{cat} indicative that product release is fully rate-limiting for the overall turnover of the enzyme[139]. A pre-steady burst experiment confirmed the rate of chemistry is greater than steps after chemistry. Exchanging Mg^{2+} for Mn^{2+}, a substitution that was posited to affect the rate of the chemical step, had no effect on *Pa*ATPPRT k_{cat}. These observations necessitate chemistry occurs faster than products can be released from the active site, Figure 3.23, and that *Pa*ATPPRT k_{cat} is reporting solely on product release.

On the other hand, small inverse viscosity effects reported on non-activated *Pa*HisG$_S$ may reflect either an isomerisation of the Michaelis complex or non-specific glycerol effects. Examination of reactions catalysed by *Pa*HisG$_S$ under pre steady state conditions revealed that steps after chemistry, including product release, are not rate-limiting. It was considered likely that interconversion between ternary complexes was rate-limiting. Unfortunately, *Pa*HisG$_S$ single turnover rates could not be measured, which may have yielded further insights. Exchanging Mg^{2+} for Mn^{2+} resulted in an approximately 2-fold increase in *Pa*HisG$_S$ k_{cat}, predicted to be a result of better attenuation of negative charge at the transition state by Mn^{2+}compared with Mg^{2+}. These observations suggest *Pa*HisG$_S$ k_{cat} is reporting on interconversion between ternary complexes (which could include an isomerisation of the Michaelis complex) and at least partially on chemistry, Figure 3.23.

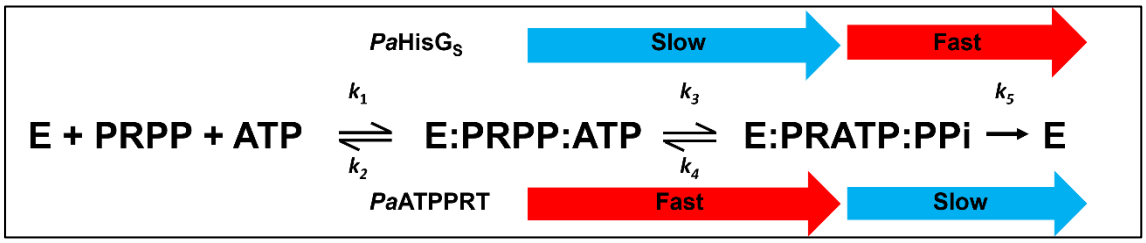

Figure 3.23 Non-activated *Pa*HisG$_S$ and activated *Pa*ATPPRT reaction scheme with rate-limiting steps highlighted

3.7 Chapter summary

This chapter sought to characterise key mechanistic features of *Pa*ATPPRT, namely, the kinetic mechanism and rate-limiting steps of *Pa*HisG$_S$.in the presence and absence of *Pa*HisZ. Kinetic and binding data suggested a steady-state ordered mechanism with PRPP as the first substrate to bind applies to *Pa*HisG$_S$ and *Pa*ATPPRT, this mechanism may apply to other HisG$_S$-type ATPPRTs. The proposed mechanism is different to that of HisG$_L$-type ATPPRTs which operate via an ordered mechanism with ATP as the first substrate to bind. This work also demonstrated ADP is a substrate of *Pa*HisG$_S$, despite previous work showing ADP is a competitive inhibitor of *S.* Typhmurium HisG$_L$ with respect to both substrates. ADP is not likely to be a substrate of *Pa*ATPPRT *in vivo* due to low ADP intracellular concentration relative to ADP, the fate of PRADP is explored in Chapter 5. Finally, it was determined that product release is rate-limiting for the reaction catalysed by activated ATPPRT. The activated hetero-octamer is likely the predominant form of ATPPRT *in vivo*. Contrastingly, the rate-limiting step for reactions catalysed by the non-activated catalytic subunit of ATPPRT, HisG$_s$, in the absence of HisZ, is interconversion between ternary complexes. This shift in rate-limiting step demonstrates that *Pa*HisZ allosterically accelerates the rate of interconversion between ternary complexes such that the rate exceeds that of product release. Other allosteric effectors capable of inducing a shift in rate-limiting step have previously been reported in literature. For example, kinetic isotope effect studies demonstrated that the rate-limiting step of the catalytically active β-subunit of tryptophan synthase from *Pyrococcus furiosusis* is Cα-H deprotonation, however, introduction of the α-subunit shifts the rate-limiting step to an unidentified step in stage II of catalysis[80]. Additionally, the ATPase, ArsAB, exhibits burst kinetics attributed to a rate-limiting isomerisation of an enzyme-product species, however, on addition of the allosteric activator, antimonite, a burst is no longer observed, suggesting the isomerisation is no longer rate-limiting[144]. Importantly, this work provided the first insight into the mechanism of allosteric activation of a HisG$_S$-type ATPPRT by HisZ and paved the way for further studies to elucidate the molecular mechanism underpinning the increased rate of interconversion between ternary complexes induced by HisZ.

Chapter 4 Biophysical, kinetic and structural analysis of *Pa*HisG$_S$ active site variants

Some of the results included in this chapter have previously been published in Alphey M.S., Fisher G. Ge Y., Gould E.R., Machado T. F. G., Liu H., Florence G. J., Naismith J. H., and da Silva R. G. Catalytic and Anticatalytic Snapshots of a Short-Form ATP Phosphoribosyltransferase. *ACS Catalysis* **2018** *8*, 5601-5610.

The majority of the results presented in this chapter are have been deposited on ChemRxiv and submitted for publication: Fisher G., Corbella M., Alphey M. S., Nicholson H., Read B. J., Kamerlin S. C. L., and da Silva R. G. Allosteric rescue of catalytically impaired ATP phosphoribosyltransferase variants links protein dynamics to active-site electrostatic preorganisation. **2022.** (DOI: 10.26434).

4.1 Chapter introduction

The work described in Chapter 3 demonstrated that allosteric activation of *Pa*HisG$_S$ by *Pa*HisZ leads to an increase in the rate of interconversion between ternary complexes. To explore the mechanism underpinning this increase in rate of interconversion between ternary complexes, it was sought to identify *Pa*HisG$_S$ and *Pa*ATPPRT amino acid residues required for catalysis. Prior to this work, despite a plethora of ATPPRT crystal structures no amino acid residues had been identified, which are essential for catalysis by either HisG$_S$ or HisG$_L$. Mutagenesis of two lysine residues which were considered possible candidates for leaving group stabilisation in ATPPRT from *L. lactis* induced only a moderate effect on k_{cat}, which indicated that these residues did not play a major role in catalysis[31].

Several WT *Pa*HisG$_S$ and activated *Pa*ATPPRT crystal structures with and without substrates were solved by Dr Magnus S. Alphey prior to the undertaking of this work, these structures are now published[40]. These crystal structures were carefully examined in order to identity conserved *Pa*HisG$_S$ residues which may contribute to catalysis and/or allosteric activation, and C115, D179, R32, and R56 were selected, Figure 4.1. Over the course of the ATPPRT catalysed reaction, the 6-NH_2 group of ATP must be deprotonated

to yield the 6-NH group of PRATP, Figure 4.2. C115 and D179 were identified as candidates for a putative catalytic base, which could abstract the 6-NH_2 proton. D179 is also part of the loop which binds the 5-phosphate of PRPP. R32 forms a salt bridge with the α-phosphate of the pyrophosphate leaving group, but may play multiple roles, including orientating ATP for catalysis, Figure 4.1. Intriguingly, crystal structures also depicted a salt bridge between R′56 of the adjacent *Pa*HisG$_S$ monomer and the β-phosphate of the pyrophosphate leaving group, however, this interaction was captured only when *Pa*HisZ and both substrates are present and requires reorganisation of a flexible loop encompassing residues A44-V67[40], Figure 4.3. The cross-dimer interaction between R′56 and the pyrophosphate leaving-group is possible as *Pa*HisG$_S$ subunits of the activated structure are observed to move closer to one another upon binding of both substrates[40], Figure 4.3. The loop on which R56 resides is equivalent to the loop identified in the *L. lactis* crystal structure which was postulated to exclude solvent from the active-site and R34 is the equivalent residue in *L. lactis* to R56 in *Pa*HisG$_S$[34].

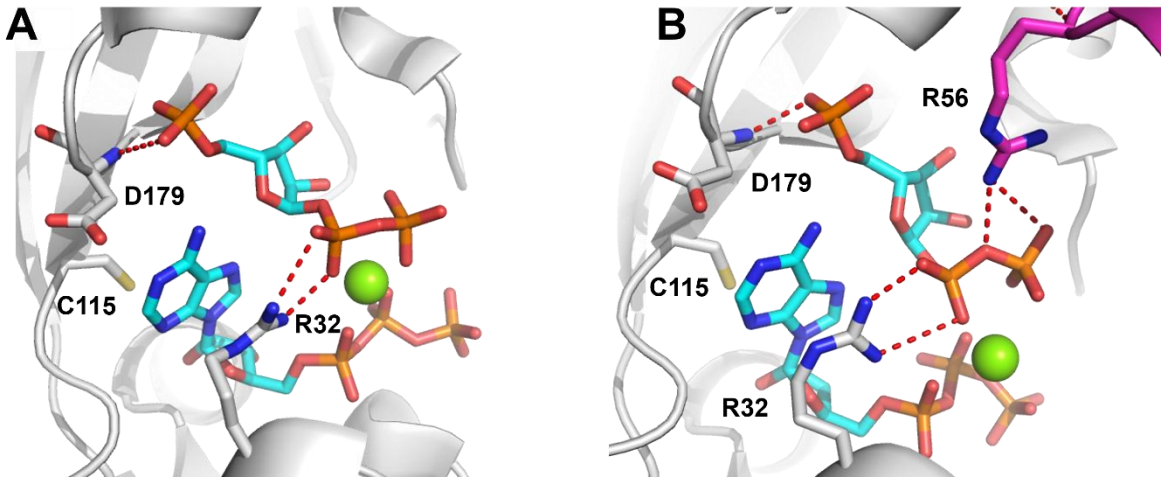

Figure 4.1 Active site views of non-activated *Pa*HisG$_S$ and *Pa*ATPRPT. (A) *Pa*HisG$_S$:PRPP:ATP (PDB ID: 6FCT) and (B) *Pa*ATPPRT:ATP:PRPP (PDB ID: 6FU2). *Pa*HisG$_S$ subunits are shown with ribbon diagrams in either grey (bound subunit) or magenta (adjacent subunit). Residues that were mutated in this chapter are labelled and shown as stick models with nitrogen in blue, oxygen, in red, and carbon in either grey or cyan. Substrates are represented as stick models with nitrogen in blue, oxygen, in red, phosphorus in orange, and carbon in cyan. Mg^{2+} ions are depicted by green spheres. Polar interactions are represented by red dashed lines. *Pa*HisZ subunits are omitted for clarity. Structures are published in Alphey et al[40]. Images were generated in Pymol

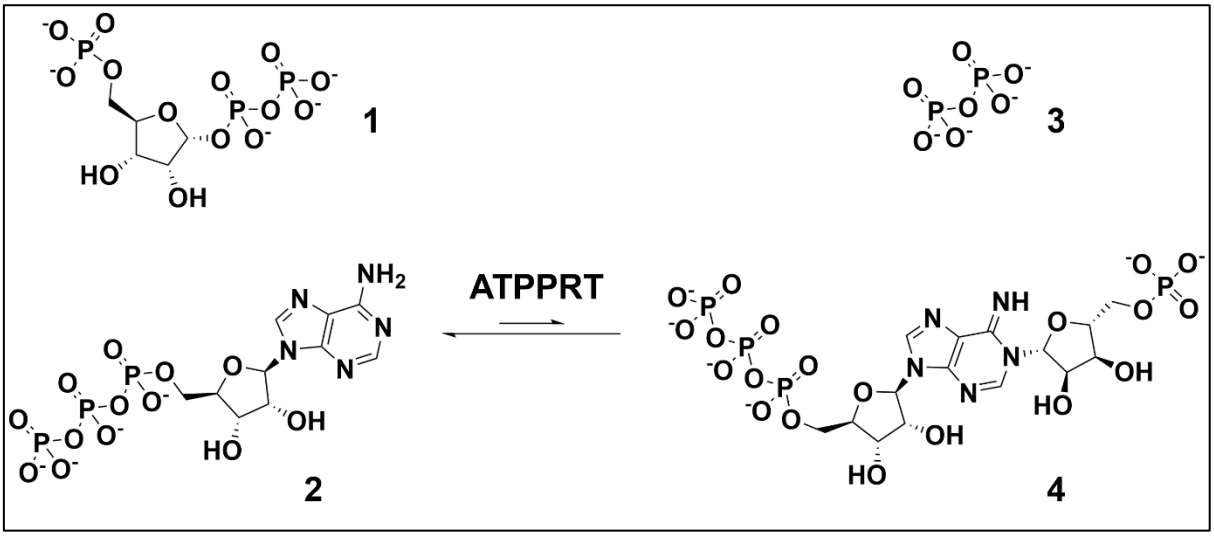

Figure 4.2 Reaction catalysed by ATPPRT. PRPP **1**, ATP **2**, PPi **3** and PRATP **4**.

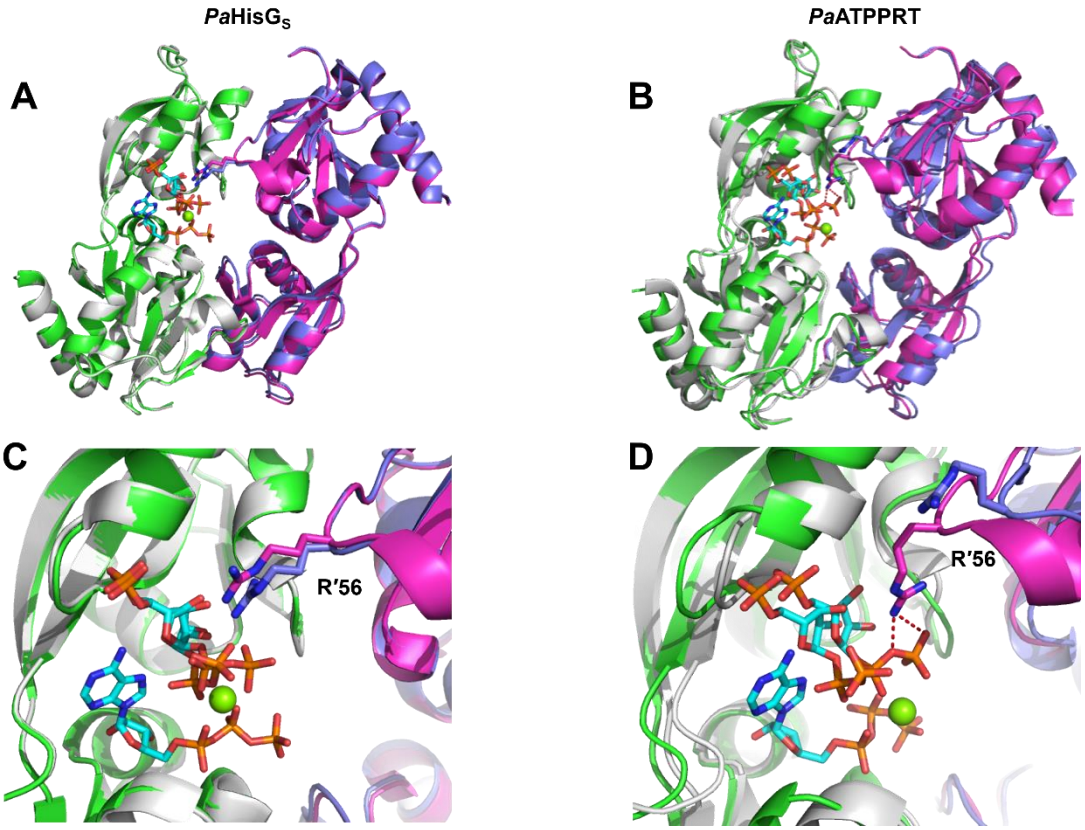

Figure 4.3 *Pa*HisG$_S$ and *Pa*ATPPRT crystal structures with either PRPP or PRPP and ATP bound. (A) Overlay of *Pa*HisG$_S$:PRPP (PDB ID: 6FCA) and *Pa*HisG$_S$:PRPP:ATP (PDB ID: 6FCT) crystal structures. (B) Overlay of *Pa*ATPPRT:PRPP (PDB ID: 6FTT) and *Pa*ATPPRT:ATP:PRPP (PDB ID: 6FU2) crystal structures. ATP and PRPP bound subunits are shown in grey and magenta, whereas PRPP bound subunits are shown in green and purple. (C) Active site view of *Pa*HisG$_S$:PRPP and *Pa*HisG$_S$:PRPP:ATP overlays. (D) Active site view of *Pa*ATPPRT:PRPP and *Pa*HisG$_S$:ATPPRT overlays. *Pa*HisGS subunits are shown with ribbon diagrams. Labelled residues are depicted as stick models with nitrogen in blue, oxygen, in red, and carbon in either magenta (ATP and PRPP bound subunits) or purple (PRPP bound subunits). Substrates are represented by stick models with nitrogen in blue, oxygen, in red, phosphorus in orange, and carbon in cyan. Mg^{2+} ions are depicted by green spheres. Polar interactions are depicted by red dashed lines. *Pa*HisZ subunits are omitted for clarity. Structures are published in Alphey et al[40]. Images were generated in Pymol.

Crystal structures represent static snapshots of dynamic molecules. It was hypothesised that R56 may be an essential residue for stabilisation of the pyrophosphate leaving group at the transition state, but that activated *Pa*ATPPRT may sample conformations with R56 primed to accept the pyrophosphate leaving group at a higher frequency compared with *Pa*HisG$_S$, facilitating the capture of the interaction by crystallography. This hypothesis would account for allosteric activation of *Pa*HisG$_S$ by *Pa*HisZ and is consistent with contemporary interpretations of allostery, which state that binding of an allosteric effector induces a population redistribution within the protein conformation ensemble such that conformers with altered catalytic properties are favoured[145–150].

The aim of this chapter was to identify *Pa*HisG$_S$ residues essential for catalysis and to propose a model for allosteric activation of *Pa*HisG$_S$ by *Pa*HisZ. Thus, C115A, C115S, D179A, D179N, R32A, R56A, R56A/K57A and R32A/R56A/K57A *Pa*HisG$_S$ were produced. The biophysical and kinetic parameters of the *Pa*HisG$_S$ mutants alongside WT *Pa*HisG$_S$ were examined. K57 is adjacent to R56 and resides on the same loop that extends into the active site of the adjacent monomer, though normally points in the opposite direction of R56, away from the active site. R56A/K57A *Pa*HisG$_S$ was constructed to assess if K57 was able to compensate for the loss of R56. R32A/R56A/K57A *Pa*HisG$_S$ was produced and characterised after studies of the other *Pa*HisG$_S$ mutant activities were completed and the rationale behind this is discussed in section 4.14.

4.2 Production and purification of C115A, C115S, D179A, D179N, R32A, R56A, R56A/K57A and R32A/R56A/K57A *Pa*HisG$_S$

C115A, C115S, D179A, D179N, R32A, R56A, R56A/K57A and R32A/R56A/K57A *Pa*HisG$_S$ were produced analogously to WT *Pa*HisG$_S$, Figure 4.4. The expected mass for each of the *Pa*HisG$_S$ variants was observed via ESI/TOF-MS analysis (performed by the BSRC Mass Spectrometry and Proteomics Facility), Figure 4.5, except for D179N, where tryptic digestion and MS/MS analysis of tryptic fragments confirmed successful insertion of the mutation (sequence coverage = 73%), Appendix 1.

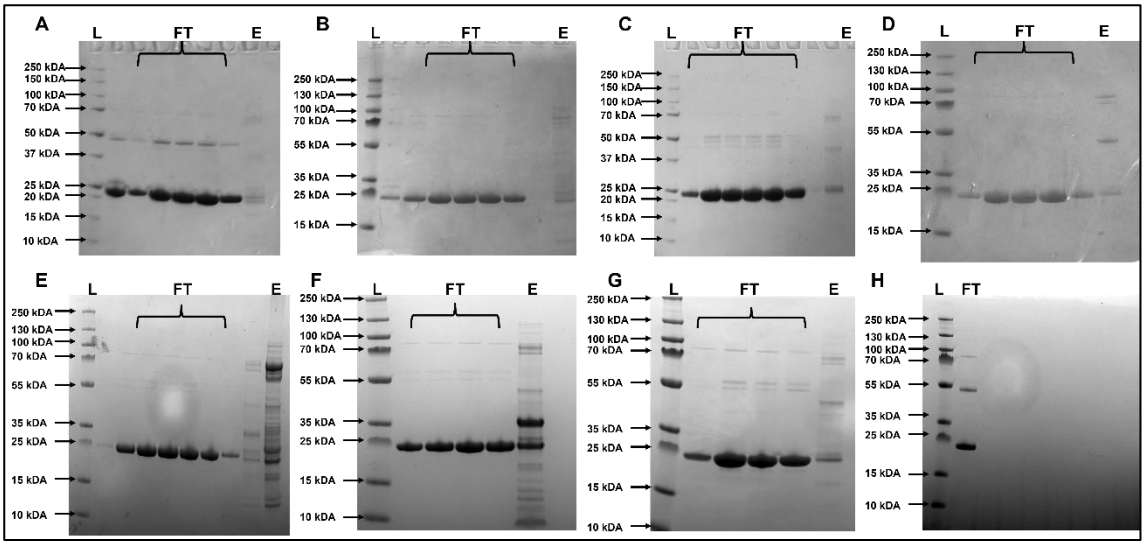

Figure 4.4 SDS-PAGE gels from *Pa*HisG$_S$ variant purifications after the second HisTrap FF column.(A) C115A, (B) C115S, (C) D179A, (D) D179N, (E) R32A, (F) R56A, (G) R56A/57A and (H) R32A/R56A/K57A *Pa*HisG$_S$. L denotes protein Ladder, FT is column flow-through and E corresponds to fractions eluted with imidazole. Protein ladder is either PageRuler Plus Prestained (B, D, E, F, G & H) or Precision Plus All Blue Protein Prestained (A & C). R32A/R56A/K57A *Pa*HisG$_S$ was purified by John Nicholson.

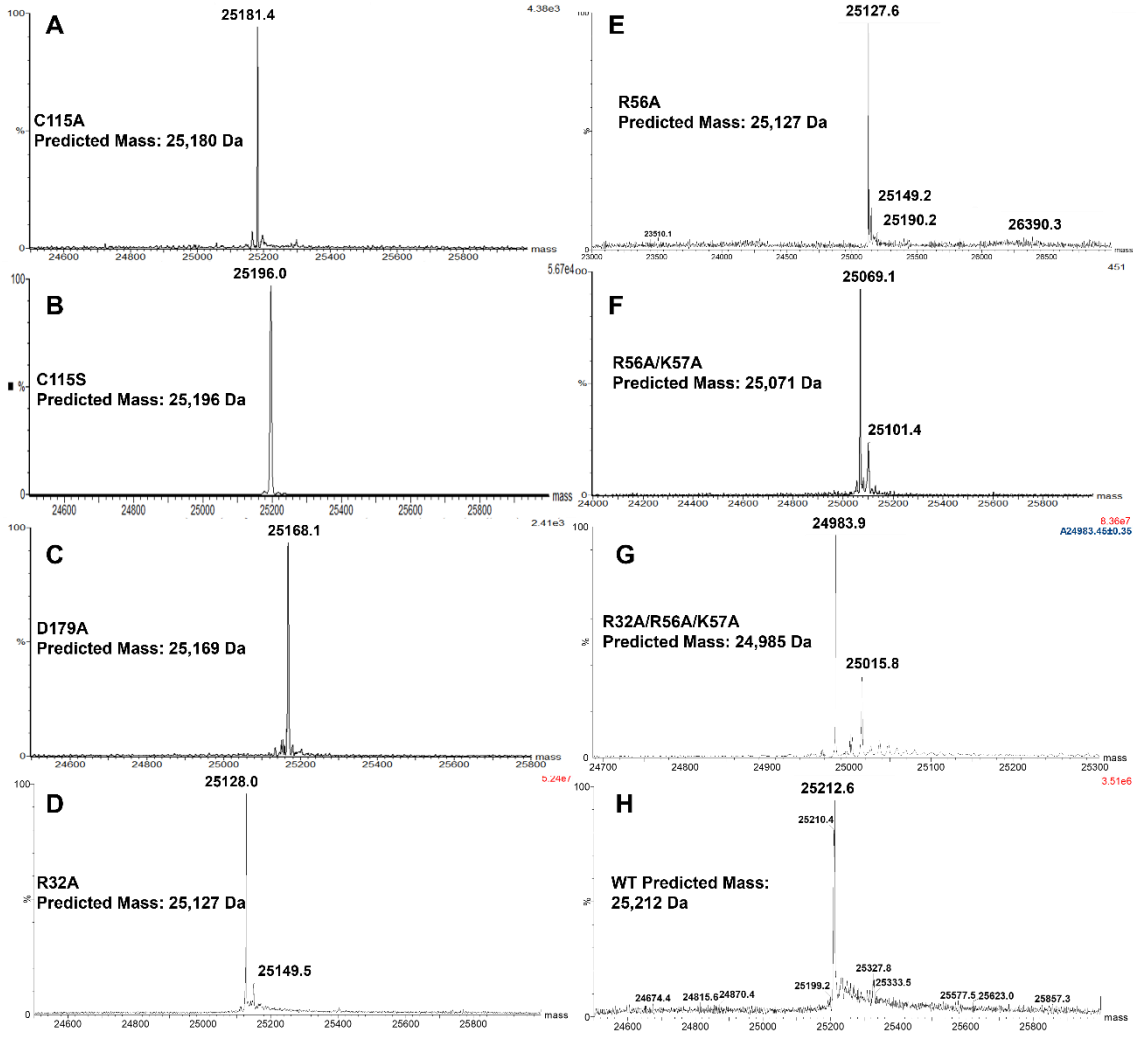

Figure 4.5 ESI-MS analyses showing the experimentally determined mass in Da for *Pa*HisG$_S$ variants. .(A) C115A, (B), C115S, (C) D179A, (D) R32A, (E) R56A, (F) R56A/K57A (G) R32A/R56A/K57A and (H) WT *Pa*HisG$_S$. Mass spectrometry was carried out by the BSRC Mass Spectrometry facility at the University of St Andrews.

4.3 *Pa*HisG$_S$ variants are thermally stable.

DSF was performed to assess the thermal stability of the *Pa*HisG$_S$ variants. The *Pa*HisG$_S$ variants exhibit similar thermal unfolding profiles to WT *Pa*HisG$_S$, Figure 4.6A and Table 4.1. Furthermore, the PRPP-induced shift in T_M is observed again in WT *Pa*HisG$_S$, and in all mutant *Pa*HisG$_S$ proteins, Figure 4.6B and Table 2.1. No change in fluorescence signal was observed for D179A *Pa*HisG$_S$ from 25 – 95 °C, hence, a T_M could not be obtained. Repetition of the experiment did not improve this result. It is possible that D179A *Pa*HisG$_S$ unfolds completely between 20 – 25 °C, however, after activity assays

it was concluded that D179 is not an essential residue and this result was not investigated further.

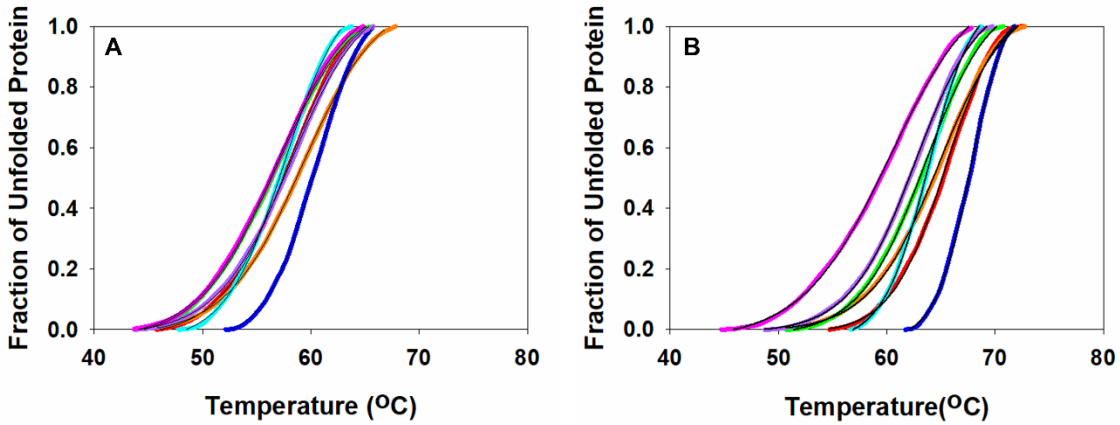

Figure 4.6 DSF-based thermal denaturation of WT and *Pa*HisG$_S$ variants. Thermal denaturation curves of WT (red) and variant (C115A [orange], C115S [light-green], D179N [cyan], R32A [blue], R56A [purple] and R56A/K57A [magenta]) *Pa*HisG$_S$ proteins in the (A) absence and (B) presence of PRPP. Lines are an average of triplicate measurement except for D179N PaHisG$_S$ (apo) data, which are an average of 5 replicates. Solid black lines are data fitted to Equation 2.6.

Table 4-1 WT and mutant *Pa*HisG$_S$ T$_M$s determined with and without PRPP.

***Pa*HisG$_S$ Mutant**	**Apo T$_M$ (^{o}C)**	**+PRPP T$_M$ (^{o}C)**	**PRPP-induced shift (^{o}C)**
WT *Pa*HisG$_S$*	57.83 ± 0.07*	65.4 ± 0.09*	7.75 ± 0.16
C115A *Pa*HisG$_S$*	59.21 ± 0.04*	64.83 ± 0.08*	5.62 ± 0.12
C115S *Pa*HisG$_S$*	56.75 ± 0.09*	63.53 ± 0.09*	8.78 ± 0.18
D179N *Pa*HisG$_S$‡	57.55 ± 0.09‡	67.73 ± 0.06‡	10.18 ± 0.15
R32A *Pa*HisG$_S$*	60.39 ± 0.06‡	63.81 ± 0.06*	3.42 ± 0.12
R56A *Pa*HisG$_S$*	58.11 ± 0.07*	62.59 ± 0.07*	4.49 ± 0.17
R56A/K57A *Pa*HisG$_S$*	56.77 ± 0.07*	60.3 ± 0.1*	3.53 ± 0.17

Values are ± fitting error of either triplicate* or quintuplicate‡ measurements.

4.4 Activity of *Pa*HisG$_S$ variants

Initially, mutant *Pa*HisG$_S$ activity was qualitatively assessed by measuring activity with 5 µM and 10 µM protein and substrate concentrations that would saturate WT *Pa*HisG$_S$, Figure 4.7 and Table 4.2. C115A, D179A and D179N *Pa*HisG$_S$ all displayed good levels of activity when assayed as non-activated *Pa*HisG$_S$ and the steady-state kinetic parameters of these variants were determined for a quantitative assessment of activity, Figure 4.8 and Table 4.3. A 4.0-, 2.6-, and 4.2-fold reduction in k_{cat} was observed for C115A, D179A and D179N *Pa*HisG$_S$ respectively, relative to WT. *Pa*HisG$_S$. Ultimately, C115 and D179 are not essential residues for *Pa*HisG$_S$ catalysis, as k_{cat} is decreased by

less than one order of magnitude, thus C115 and D179 are unlikely to act as a catalytic base.

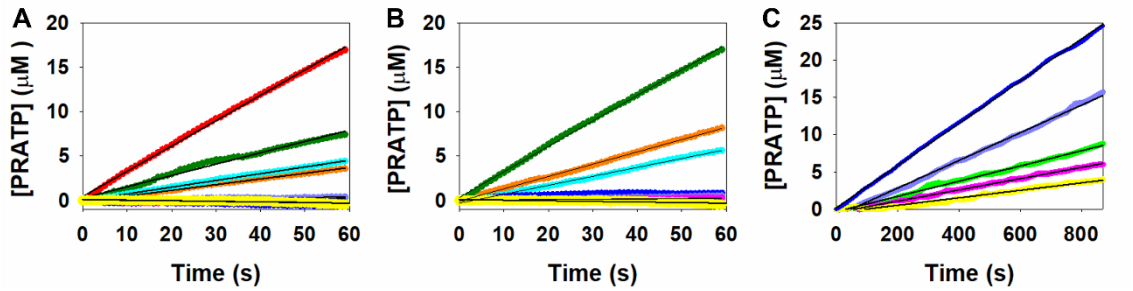

Figure 4.7 *Pa*HisG$_S$ variant activity in the absence of *Pa*HisZ. Product formation time courses from WT (red) and mutant (C115A [orange], C115S [light-green], D179A [dark-green], D179N [cyan], R32A [blue], R56A [purple] and R56A/K57A [magenta]) *Pa*HisG$_S$ catalysed reactions. A control was performed in the absence of enzyme (yellow). Reactions contained either (A) 5 or (B and C) 10 μM *Pa*HisG$_S$ and concentrations of substrate that would saturate WT *Pa*HisG$_S$ (2 mM PRPP and 5.6 mM ATP). Product formation was measured for either (A and B) 60 seconds or (C) 870 seconds. Data are average of duplicate measurements except for D179A at 5μM which is only a single measurement. Solid black lines are linear regressions of data.

Table 4-2 Rates of PRATP synthesis in reactions catalysed by *Pa*HisG$_S$ active site variants.

***Pa*HisG$_S$**	***v* (μM s^{-1}) 5 μM *Pa*HisG$_S$ (60 seconds)**	***v* (μM s^{-1}) 10 μM *Pa*HisG (60 seconds)**	***v* (μM s^{-1}) 10 μM *Pa*HisG (875 seconds)***
WT *Pa*HisG$_S$	0.29 ± 0.01	N.A.	N.A.
C115A *Pa*HisG$_S$	0.06 ± 0.01	0.14 ± 0.01	N.A.
C115S *Pa*HisG$_S$	0.006 ± 0.002	0.0027 ± 0.0003	0.0053 ± 0.003
D179A *Pa*HisG$_S$	0.128 ± 0.008	0.29 ± 0.001	N.A
D179N *Pa*HisG$_S$	0.08 ± 0.01	0.1007 ± 0.002	N.A
R32A *Pa*HisG$_S$	No Data	0.0111 ± 0.0007	0.023 ± 0.0001
R56A *Pa*HisG$_S$	0.0073 ± 0.0001	0.005 ± 0.009	0.0136 ± 0.0001
R56A/K57A *Pa*HisG$_S$	No Data	No Data	0.0022 ± 0.0003

Values are mean ± standard-error of duplicate measurements. No data indicates activity was not detectable. Traces from reactions catalysed by 10 μM WT *Pa*HisG$_S$ were not linear. *No enzyme control was subtracted from data.

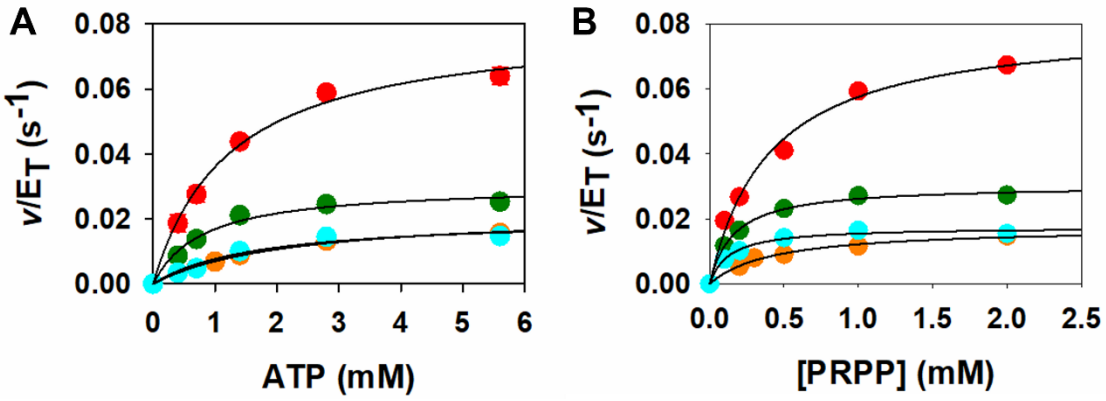

Figure 4.8 WT and variant *Pa*HisG$_S$ substrate saturation curves. WT (red) C115A (orange), D179A (dark-green), D179N (cyan) *Pa*HisG$_S$ Data points are mean ± standard error of duplicate measurements. Solid lines are data fit to the Michaelis-Menten equation.

Table 4-3 WT, C115A, D179A, D179N *Pa*HisG$_S$ steady-state kinetic parameters

Parameter	**WT *Pa*HisG$_S$**	**C115A *Pa*HisG$_S$**	**D179A *Pa*HisG$_S$**	**D179N *Pa*HisG$_S$**
k_{cat} (s^{-1})	0.081 ± 0.003	0.020 ± 0.001	0.030 ± 0.001	0.020 ± 0.002
K_{PRPP} (mM)	0.4 ± 0.06	0.42 ± 0.07	0.16 ± 0.01	0.13 ± 0.02
K_{ATP} (mM)	1.2 ± 0.2	2.2 ± 0.3	0.8 ± 0.2	1.7 ± 0.5
k_{cat}/K_{PRPP} (M^{-1} s^{-1})	200 ± 30	47 ± 9	200 ± 10	150 ± 30
k_{cat}/K_{ATP} (M^{-1} s^{-1})	70 ± 11	9 ± 1	40 ± 10	11 ± 4

Values are mean ± fitting error of duplicate measurements.

Linear regressions performed on one minute product formation time-courses from reactions catalysed by C115S, R32A, R56A, and R56A/K57A *Pa*HisG$_S$ are poor quality and have low R_2 values, likely reflecting an extremely low rate of PRATP synthesis such that the total amount of PRATP present is below the detectable limit of the assay, Figures 4.7A and 4.7B and Table 4.2. C155A, R32A, R56A and R56A/K57A *Pa*HisG$_S$ were

subsequently incubated with assay buffer and concentrations of substrates that would saturate WT *Pa*HisG$_S$ for 870 seconds to facilitate PRATP accumulation which allowed for better data fitting (R_2 > 98%), Figure 4.7C. The rate of PRATP synthesis in reactions catalysed by C115S, R32A, R56A and R56A/K57A *Pa*HisG$_S$ was approximately 109-, 25-, 43-, and 263-fold below WT *Pa*HisG$_S$, upon correction for protein concentration. The activity of these variants is much too low for determination steady-state kinetic parameters via the assay employed in this work. It was concluded that mutation of either R32 or R56 results in a catalytically impaired variant of *Pa*HisG$_S$. Furthermore, a serine in place of C115 is detrimental for ATPPRT catalysis, although C115 does not appear to be required for activity. It was hypothesised that serine at position 115 is forming an hydrogen bond that is not conducive for catalysis. Structural studies may elucidate why the cysteine to serine mutation is detrimental for catalysis but the cysteine to alanine mutation is not. However, as C115 is not an essential residue this unusual result was not investigated further.

4.5 *Pa*HisG$_S$ variant activity in the presence of *Pa*HisZ.

Unexpectedly, when *Pa*HisZ was added to assays with C155A, R32A, R56A and R56A/K57A *Pa*HisG$_S$ activity was recovered, Figures 4.9 and 4.10 and Table 4.4. Steady-state kinetic parameters of C115S, R32A, R56A and R56A/K57A *Pa*ATPPRT were characterised alongside WT *Pa*ATPPRT. A 1.8-, 3.8-, 5.3- and 15-fold reduction in C115A, R32A, R56A and R56A/K57A *Pa*ATPPRT k_{cat} relative to WT *Pa*ATPPRT was observed, whereas no significant changes in K_M^{ATP} or K_M^{PRPP} were detected. Critically, the values of k_{cat} for C115S, R32A and R56A *Pa*ATPPRT were within one order of magnitude of the WT *Pa*ATPPRT, indicative that these residues are not required for catalysis by *Pa*ATPPRT despite the observation that catalysis by *Pa*HisG$_S$ is impaired by mutagenesis at these positions. Unexpectedly, this data indicated that *Pa*HisZ can allosterically rescue catalytically impaired mutants of *Pa*HisG$_S$. It was hypothesised that the recovery of R56A *Pa*HisG$_S$ in the presence of *Pa*HisZ may be explained by compensation by K57. Specifically, it was hypothesised that binding of *Pa*HisZ to R56A *Pa*HisG$_S$ modulated protein conformational sampling in order that conformations in which K57 could stabilise the pyrophosphate leaving-group were adopted. Interestingly, R56A/K57A *Pa*ATPPRT was the only mutant to exhibit a k_{cat} more than a single order of

magnitude (15-fold) lower than that of the WT *Pa*ATPPRT, however, as the activity R56A/K57A *Pa*HisG$_S$ was increased by 520-fold in the presence of *Pa*HisZ this would suggest that the activated complex can still compensate for simultaneous mutagenesis at these positions and that *Pa*HisZ is able to rescue R56A *Pa*HisG$_S$ activity independently of K57.

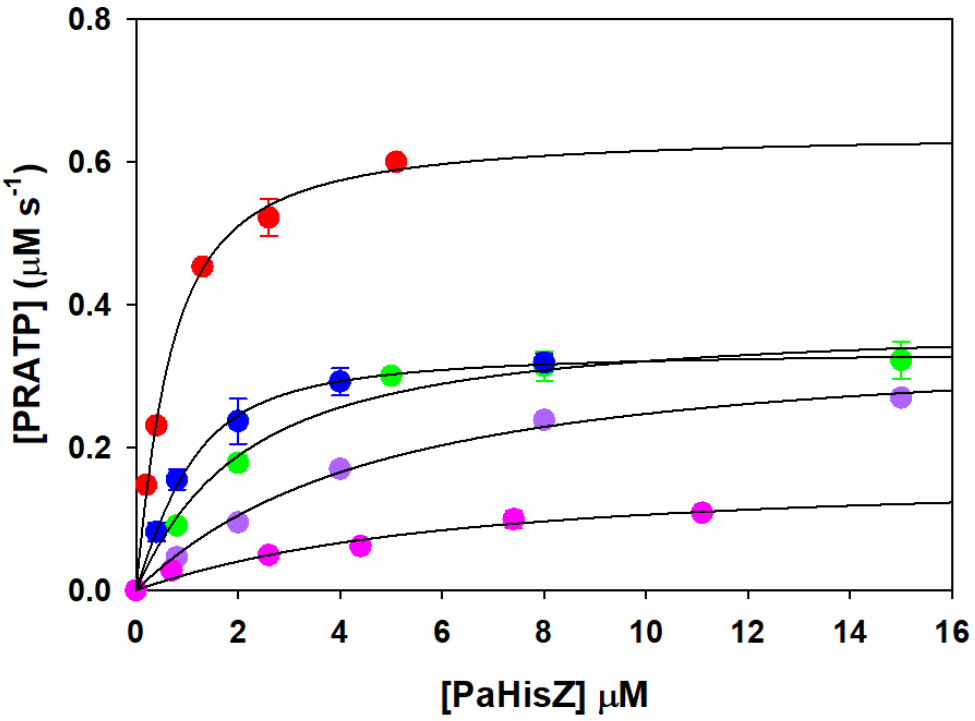

Figure 4.9 Determination of K_D for equilibrium dissociation of *Pa*HisZ from WT and mutant *Pa*ATPPRT holoenzyme. WT (red), C115S (green), R32A (dark blue), R56A (purple) and R56A/K57A (magenta) *Pa*HisG$_S$. Data points are mean ± standard error of duplicate measurements. Solid lines are data fitted to Equation 2.1

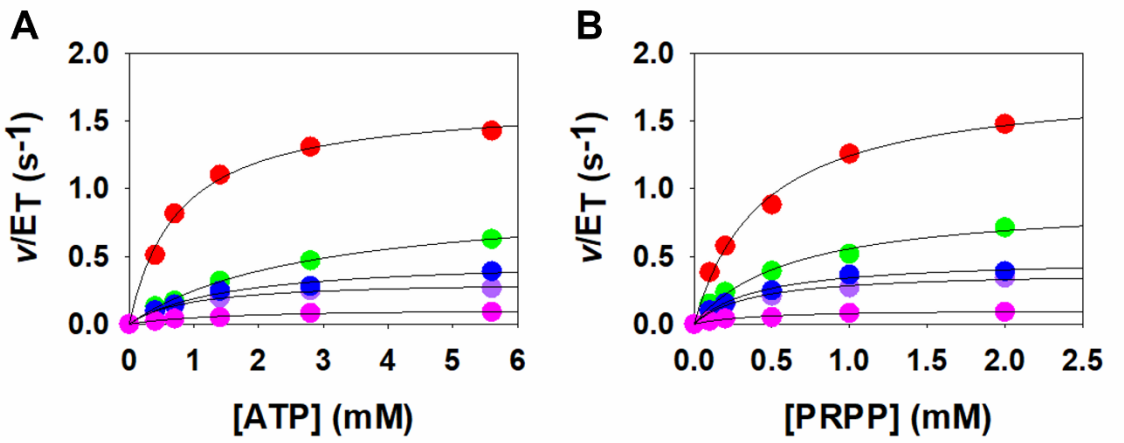

Figure 4.10 WT and variant *Pa*ATPPRT substrate saturation curves. WT (red), C115S (green), R32A (blue), R56A (magenta) and R56A/K57A *Pa*HisG$_S$. Data are mean ± standard error of duplicate measurements.

Table 4-4 WT, C115S, R32A, R56A and R56A/K57A *Pa*ATPPRT steady-state kinetic parameters.

Parameter	**WT *Pa*HisG$_S$**	**C115S *Pa*HisG$_S$**	**R32A *Pa*HisG$_S$**	**R56A *Pa*HisG$_S$**	**R56A/K57A *Pa*HisG$_S$**
K_D	0.44 ± 0.05	1.7 ± 0.4	0.49 ± 0.06	4.0 ± 0.6	5.0 ± 2.0
k_{cat} (s^{-1})	1.72 ± 0.07	0.93 ± 0.08	0.48 ± 0.03	0.35 ± 0.05	0.115 ± 0.007
K_{PRPP} (mM)	0.44 ± 0.05	0.6 ± 0.1	0.41 ± 0.06	0.37 ± 0.04	0.4 ± 0.1
K_{ATP} (mM)	0.76 ± 0.07	2.8 ± 0.2	1.5 ± 0.3	0.9 ± 0.1	1.5 ± 0.3
k_{cat}/K_{PRPP} (M^{-1} s^{-1})	3900 ± 500	1500 ± 300	1200 ± 200	1000 ± 200	290 ± 70
k_{cat}/K_{ATP} (M^{-1} s^{-1})	2300 ± 200	330 ± 40	320 ± 70	360 ± 60	80 ± 20
Activation by *Pa*HisZ	30-fold	1800-fold	190-fold	230-fold	520-fold

Values are mean ± standard error of duplicate measurements.

To demonstrate that the rescue of *Pa*HisG$_S$ mutants by *Pa*HisZ was a true allosteric effect, a series of control experiments were performed. Firstly, control reactions were performed with 15 μM *Pa*HisZ, in the absence of any *Pa*HisG$_S$ to ensure *Pa*HisZ was not contaminated with either WT *Pa*HisG$_s$ or ATPPRT from *E. coli* expression cells. The rate of PRATP synthesis from these reactions (0.0081 ± 0.0005 μM s^{-1}) was found to be negligible. Secondly, C115S, R32A, R56A and R56AK56A *Pa*HisG$_S$ were incubated in the presence of 20 μM BSA to address the effect of nonspecific protein-binding, Figure 4.11A and Table 4.5. Only negligible activity was detected upon incubation of C115S,

R32A, R56A and R56A/K56A *Pa*HisG$_S$ with BSA which confirms that *Pa*HisZ is inducing a specific effect. Thirdly, it was demonstrated that C115S, R32A, R56A and R56A/K56A *Pa*ATPPRT can be inhibited by histidine, Figure 4.11B and Table 4.5.

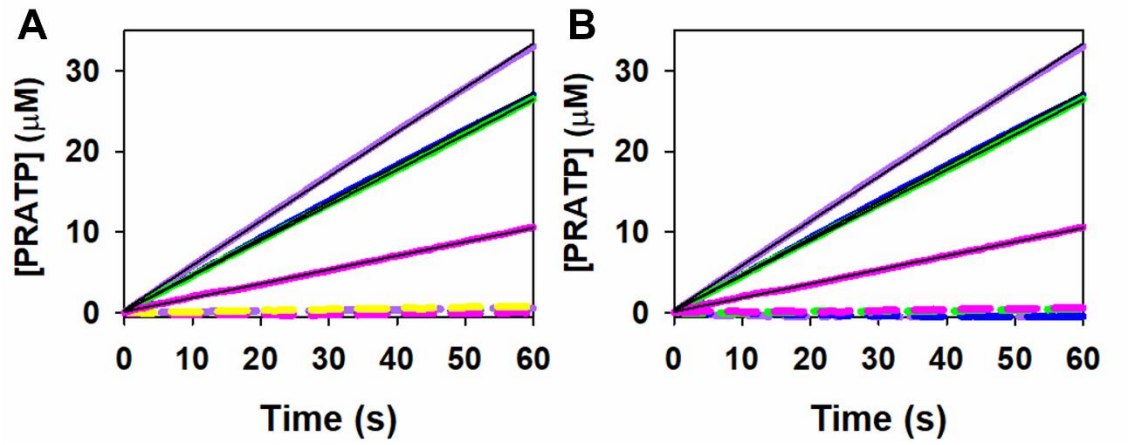

Figure 4.11 Control reactions for allosteric activation of variant *Pa*HisG$_S$ by *Pa*HisZ.(A) Product formation time courses upon incubation of C115S (light-green) R32A (blue), R56A (purple), R56A/K57A (magenta) *Pa*HisG$_S$ with saturating concentrations of substrates and BSA (20 μM) (dashed-line). A negative control reaction was performed in the absence of *Pa*HisG$_S$ (yellow dashed-line) Positive control reactions were performed with *Pa*HisZ in place of BSA (solid-lines). (B) Product formation time-courses upon incubation of C115S (light-green) R32A (blue), R56A (purple), R56A/K57A (magenta) activated *Pa*ATPPRT with saturating concentrations of substrates in the presence (dashed-lines) and absence (solid-lines) of histidine (1 mM). Solid black lines are linear regressions of data. Control data with *Pa*HisZ were collected with His-tagged *Pa*HisZ (Section 4.13)

Table 4-5 Rates of PRATP synthesis from reactions catalysed by C115S, R32A, R56A and R56A/K57A *Pa*HisG$_S$ in the presence of either BSA (20 μM), *Pa*HisZ (His-tagged) or *Pa*HisZ (His-tagged) with histidine (1 mM),

***Pa*HisG$_S$**	**v/E$_T$ (s^{-1}) + BSA**	**v/E$_T$ (s^{-1}) + *Pa*HisZ**	**v/E$_T$ (s^{-1}) +*Pa*HisZ + histidine**
C115S *Pa*HisG$_S$	0.007 ± 0.002	0.74 ± 0.0003	0.00 ± 0.01
R32A *Pa*HisG$_S$	0.004 ± 0.003	0.94 ± 0.02	No data
R56A *Pa*HisG$_S$	0.0062 ± 0.0007	1.03 ± 0.07	0.020 ± 0.004
R56A/K57A *Pa*HisG$_S$	0.004 ± 0.001	0.069 ± 0.004	0.003 ± 0.001

Values are mean ± standard error of duplicate measurements. No data indicates that activity was not detected.

4.6 Analysis of reactions catalysed by C115S, R32A, R56A or R56A/K57A *Pa*HisG$_S$ and *Pa*ATPPRT by ^{31}P-NMR Spectroscopy

Next, it was sought to employ ^{31}P-NMR spectroscopy to confirm that allosterically rescued *Pa*HisG$_S$ variants catalyse formation of the expected product, PRATP. Briefly, 10 μM of C115S, R32A, R56A, and R56A/K57A *Pa*HisG$_S$ was incubated with saturating concentrations of substrates with and without 30 μM *Pa*HisZ and the products of reactions were analysed by ^{31}P-NMR. The characteristic peak at approximately 3.3 ppm, representative of the 5′′-PO_4^{2-} group of PRATP (reviewed in Chapter 3), was only detectable in reactions containing *Pa*HisZ, Figure 4.12. Contrastingly, upon incubation of 10 μM WT *Pa*HisG$_S$ with saturating concentration of substrates in the absence of *Pa*HisZ, the peak at approximately 3.3 ppm representing PRATP formation was readily detected (Figure 3.10). ^{31}P-NMR spectroscopy confirms that allosterically rescued

*Pa*HisG$_S$ mutants catalyse formation of PRATP, as expected and that PRATP synthesis in the absence of *Pa*HisZ is too low for detection by ^{31}P-NMR.

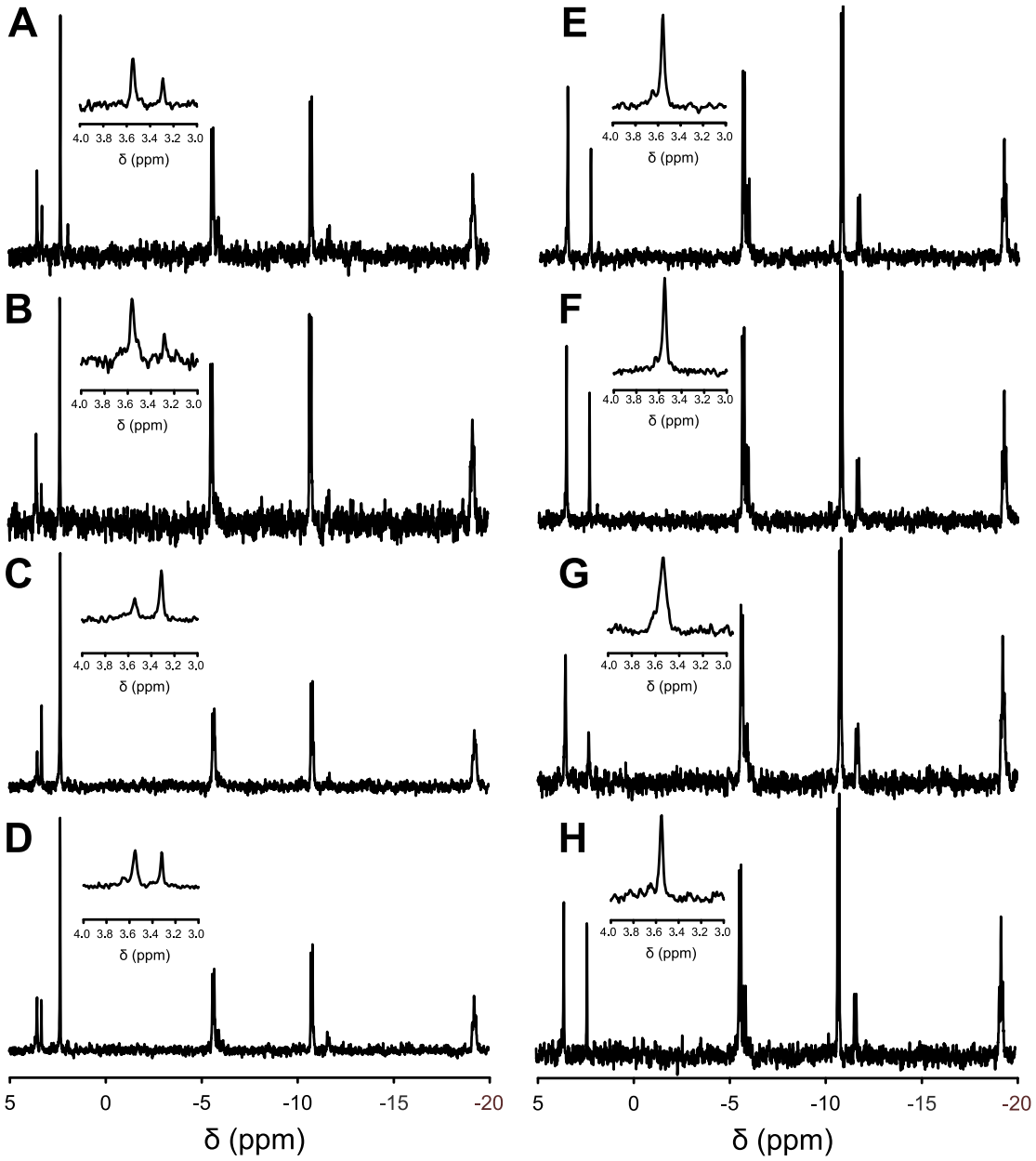

Figure 4.12 ^{31}P-NMR spectra of reactions catalysed by *Pa*HisG$_S$ and *Pa*ATPPRT variants. C115S, R32A, R56A, and R56A/K57A *Pa*HisG$_S$ with (A [R56A], B [R56A/K57A], C [C115S], D [R32A]) and without (E [R56A], F [R56A/K57A], G [C115S], H [R32A]) 30 µM *Pa*HisZ. Insets are close-ups of the spectra between 4.0 and 3.0 ppm, showing the peak at ca. 3.3 ppm in (A – D) corresponding to the phosphorus in the N1-5-phospho-β-$_D$-ribose moiety of PRATP which is missing in insets in (E – H).

4.8 Oligomeric state of C115S, R32A, R56A and R56A/K57A *Pa*HisG$_S$

The oligomeric state of C115S, R32A, R56A and R56A/K57A *Pa*HisG$_S$ was investigated via analytical size-exclusion chromatography. Previous SEC-MALS and structural characterisations concluded *Pa*HisG$_S$ forms dimers in solution and that the dimer is the catalytically active species[40]. A possible explanation for the extremely large activation of C115S, R32A, R56A and R56A/K57A *Pa*HisG$_S$ by *Pa*HisZ is that the mutations impaired the ability of *Pa*HisG$_S$ to dimerise independently. If this were true, *Pa*HisG$_S$ dimers could be stabilised by *Pa*HisZ upon formation of the hetero-octamer leading to a large enhancement in catalytic activity. It was decided to investigate the oligomeric state of C115S, R32A, R56A and R56A/K57A *Pa*HisG$_S$ by analytical size-exclusion chromatography. Analytical size-exclusion chromatography recently performed by Benjamin J. Read, independently of this work, confirmed that *Pa*HisG$_S$ forms dimers in solution[45].

A peak in the UV absorbance at 280 nm at approximately 14 mL was observed in the WT *Pa*HisG$_S$ analytical gel filtration chromatogram and the same elution volume was also observed for C115S, R32A, R56A and R56A/K57A, Figure 4.13. A secondary peak in the void volume of WT, C115S, R32A and R56A/K57A *Pa*HisG$_S$ chromatograms was also observed, likely reflecting some aggregation of the proteins. In summary, C115S R32A, R56A and R56A/K57A *Pa*HisG$_S$ chromatograms overlay well with the WT *Pa*HisG$_S$ chromatogram, the mutations do not affect the oligomeric state of *Pa*HisG$_S$. It was noted that C115S, R32A, R56A/K57A and WT *Pa*HisG$_S$ proteins have some tendency to aggregate, however, the proportion of aggregated protein is not different between C115S R32A, R56A, R56A/K57A and WT *Pa*HisG$_S$, Figure 4.13.

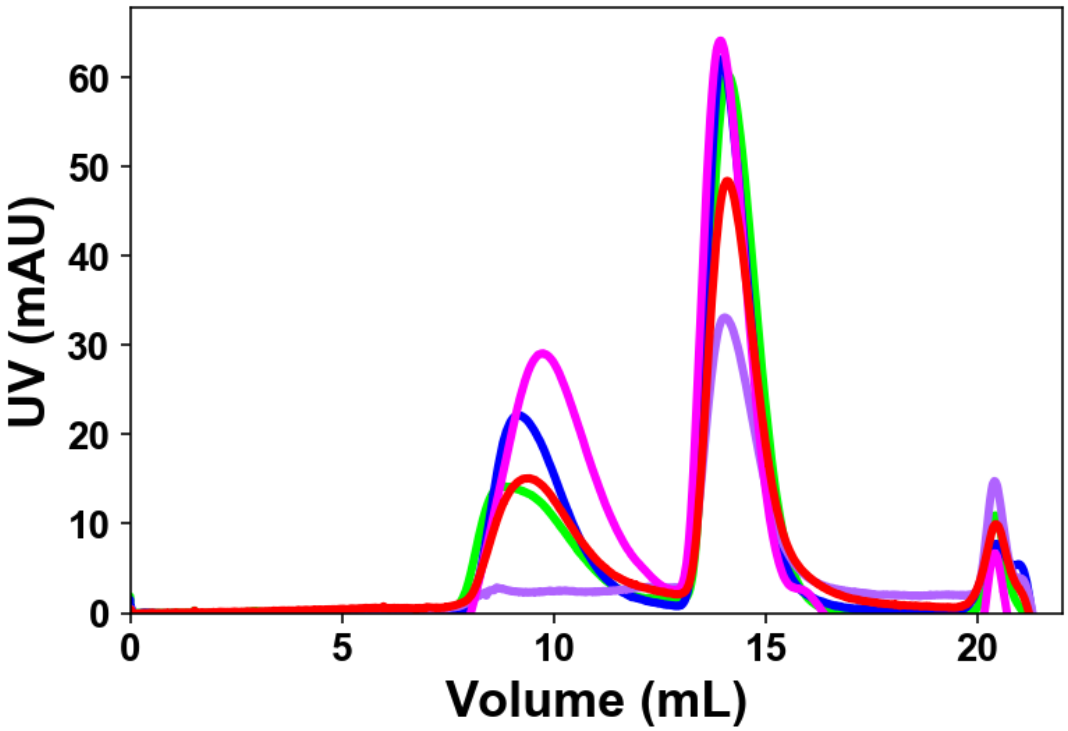

Figure 4.13 Analytical size-exclusion profile of WT and variant *Pa*HisG$_S$. WT (red), C115S (green), R32A (blue), R56A (purple) and R56A/K57A (magenta) PaHisG$_S$.

4.9 Allosteric activation of WT and R56A *Pa*HisG$_S$ by HisZ from *A. baumannii*

The work outlined so far in this chapter indicated that the activity of several catalytically impaired variants of *Pa*HisG$_S$ can be restored by the allosteric activator, *Pa*HisZ. The following experiments were devised in order to probe this allosteric recovery of activity. R56A *Pa*HisG$_S$ was selected specifically for further investigations, due to the posited role of R56 in allosteric activation. Firstly, it was sought to determine if R56A *Pa*HisG$_S$ could also be rescued by an orthologous HisZ. ATPPRT from *A. baumannii*, a HisG$_S$-type ATPPRT, is studied in the da Silva laboratory by Benjamin J. Read. HisZ from *A. baumannii*, henceforth referred to as *Ab*HisZ, shares 69% sequence identity with *Pa*HisZ[45] and preliminary tests indicated that *Ab*HisZ activates both WT and R56A *Pa*HisG$_S$. The steady-state kinetic parameters of reactions catalysed by WT *Pa*HisG$_S$-*Ab*HisZ and R56A *Pa*HisG$_S$-*Ab*HisZ were determined, Figure 4.14 and Table 4.6.

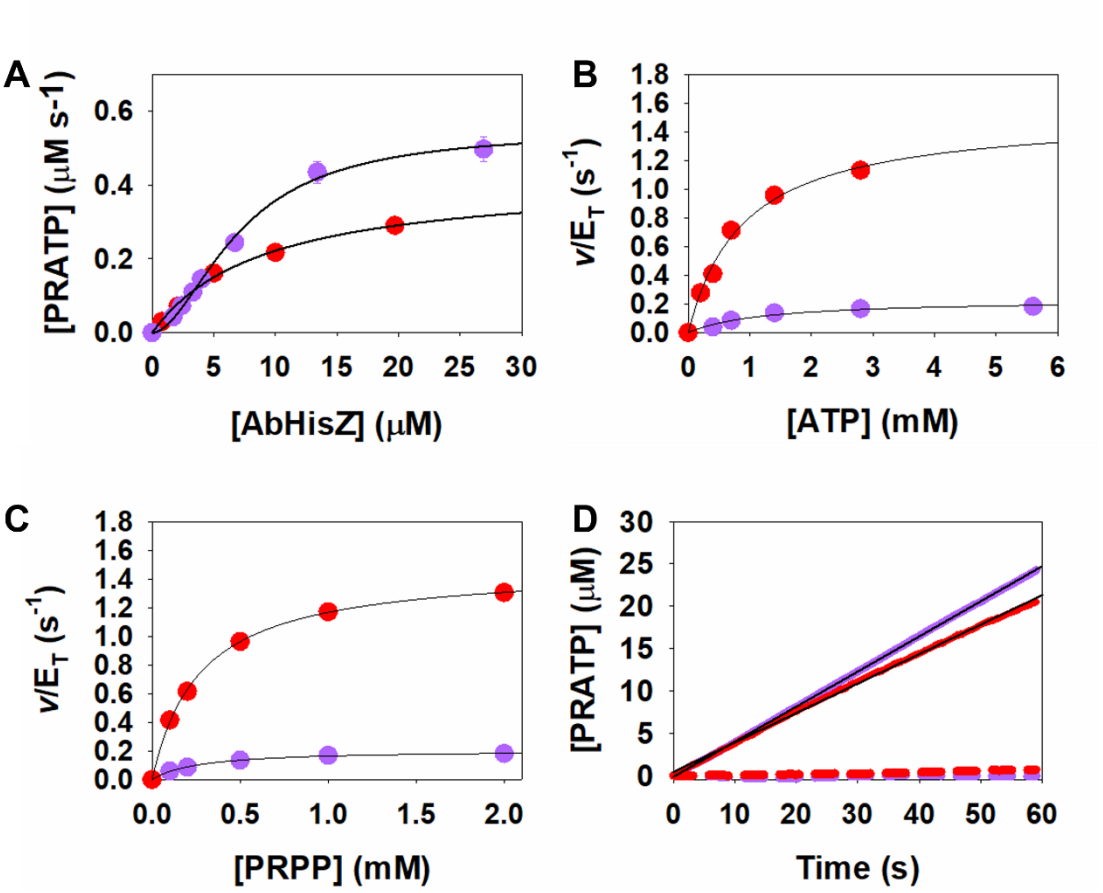

Figure 4.14 Steady-state kinetics of WT *Pa*HisG$_S$-*Ab*HisZ and R56A *Pa*HisG$_S$-*Ab*HisZ. (A) Dependence of rate of reaction catalysed by WT (red) and R56A (purple) *Pa*HisG$_S$ on *Ab*HisZ. (B-C) Substrate saturation curves with either (B) ATP or (C) PRPP as the varying substrate. (D) Product formation time-courses in the presence (dashed line) and absence (solid line) of histidine (1 mM). Data points are mean ± standard-error of at least duplicate measurements. Solid black lines in (A) are data fit to either Equation 2.1(WT) or the Hill equation (R56A). Solid black lines in (B) and (C) are data fit to the Michaelis-Menten equation. Solid black lines in (D) are linear regressions of data.

Table 4-6 WT *Pa*HisG$_S$-*Ab*HisZ and R56A *Pa*HisG$_S$-*Ab*HisZ steady-state kinetic parameters.

Parameter	**WT *Pa*HisG$_S$**	**R56A *Pa*HisG$_S$**
K_D	9 ± 1	N.A.
k_{cat} (s^{-1})	1.49 ± 0.05	0.22 ± 0.02
K_{PRPP} (mM)	0.270 ± 0.008	0.27 ± 0.01
K_{ATP} (mM)	0.9 ± 0.1	1.2 ± 0.3
k_{cat}/K_{PRPP} (M^{-1} s^{-1})	5500 ± 200	810 ± 80
k_{cat}/K_{ATP} (M^{-1} s^{-1})	1700 ± 200	180 ± 50

Values are mean ± fitting error of duplicate measurements.

The K_D for the WT *Pa*HisG$_S$-*Ab*HisZ complex was approximately 20-fold greater compared with the K_D of the WT *Pa*HisG$_S$-*Pa*HisZ complex, Tables 4.4 and 4.6. Upon saturation of WT *Pa*HisG$_S$ by *Ab*HisZ, the steady-state kinetic parameters were remarkably similar to those determined from reactions catalysed by WT *Pa*HisG$_S$-*Pa*HisZ, Tables 4.4 and 4.6.

Unexpectedly, the rate of reactions catalysed by R56A *Pa*HisG$_S$-*Ab*HisZ appeared to exhibit sigmoidal dependence on [*Ab*HisZ], Figure 4.14A. It was not possible to model data with Equation 2.1. Instead, R56A *Pa*HisG$_S$-*Ab*HisZ data were fitted to the Hill equation to highlight the sigmoidal nature of the data, Figure 4.14A. Unfortunately, values obtained from the fit are not meaningful as concentrations of *Ab*HisZ employed in the experiment were not sufficiently greater than the concentration of R56A-*Pa*HisG$_S$ to satisfy pseudo-first order conditions. Subsequent data for substrate saturation curves were collected with concentrations of *Ab*HisZ that saturated R56A-*Pa*HisG$_S$ and it was assumed that 100% of R56A-*Pa*HisG$_S$ was bound by *Ab*HisZ. The steady-state kinetic parameters of R56A *Pa*HisG$_S$-*Ab*HisZ are also in good agreement with those reported for

R56A *Pa*ATPRPT, Tables 4.4 and 4.6. It was also demonstrated that the enzymatic activities of both WT *Pa*HisG$_S$-*Ab*HisZ and R56A *Pa*HisG$_S$-*Ab*HisZ are sensitive to histidine inhibition, Figure 4.14D, indicating that the allosteric network required for transmission of the histidine feedback inhibition signal is intact in these hybrid ATPPRTs. Critically, these experiments demonstrate that activity R56A *Pa*HisG$_S$ can also be allosterically rescued by *Ab*HisZ, an orthologous HisZ with 69% sequence identity to *Pa*HisZ. An analysis of the *Pa*HisG$_S$-*Pa*HisZ interface, carried out by Benjamin J. Read, determined that 25 and 34 out of 46 *Pa*HisZ residues found at the interface are strictly and functionally conserved in *Ab*HisZ, respectively (manuscript submitted Fisher G., Corbella M., Alphey M. S., Nicholson H., Read B. J., Kamerlin S. C. L., and da Silva R. G. [2022])

4.10 Crystal structures of substrate bound R56A *Pa*HisG$_S$ and *Pa*ATPPRT

The crystal structures of non-activated R56A *Pa*HisG$_S$ and activated R56A *Pa*ATPPRT were determined. It was envisioned that a side-by-side comparison of R56A *Pa*HisG$_S$ and R56A *Pa*ATPPRT active sites may illuminate the mechanism underpinning allosteric recovery of activity. The crystal structures of R56A *Pa*HisG$_S$:PRPP:ATP and *Pa*ATPPRT:PRPP:ATP were solved at 2.00 Å and 2.55 Å resolution, respectively. All crystallography was performed under the supervision of Dr Magnus S. Alphey. Data collection and refinement was performed with help and guidance from Dr Magnus S. Alphey. Refinement statistics are summarised in Table 4.7. R56A *Pa*HisG$_S$ and *Pa*ATPPRT crystallised in identical space groups to WT *Pa*HisG$_S$ and *Pa*ATPPRT, I2 and C2, respectively. One monomer of R56A *Pa*HisG$_S$ was found in the asymmetric unit of R56A *Pa*HisG$_S$ crystal structures, whereas a tetramer, composed of two R56A *Pa*HisG$_S$ subunits and two *Pa*HisZ subunits, was found in the asymmetric unit of R56A *Pa*ATPPRT crystal structures. The R56A *Pa*HisG$_S$ dimer and *Pa*ATPPRT hetero-octamer were generated from crystallographic symmetry, Figure 4.15. Experimental density maps for ATP, PRPP and Mg^{2+} are shown in Figure 4.16. Data did not allow for modelling of the active site Mg^{2+} ion in the R56A *Pa*ATPPRT structure. Root-mean-square deviation (rmsd) values calculated from structural alignments of R56A and WT

*Pa*HisG$_S$ (0.235 Å) and R56A and WT *Pa*ATPPRT (1.044 Å), indicated that the crystal structures of the R56A variant are similar to the crystal structures of WT *Pa*HisG$_S$ and WT *Pa*ATPPRT, Figure 4.17.

Table 4-7. Data processing and refinement statistics for R56A *Pa*HisG$_S$:ATP:PRPP and R56A *Pa*ATPPRT:ATP:PRPP

Parameter	**R56A *Pa*HisG$_S$**	**R56A *Pa*ATPPRT**
PDB ID	7Z8U	7Z6R
Data collection		
Resolution (Å)*	22.01 – 2.00 (2.05 – 2.00)	56.97 – 2.55 (2.61 – 2.55)
Space group	I2	C2
Unit cell parameters a, b, c	70.09, 33.90, 89.27	102.16, 145.53, 93.81
Unit cell parameters α, β, γ	90.00, 103.52, 90.00	90.00, 102.48, 90.00
R_{merge}*	0.11 (0.36)	0.17 (3.17)
MeanI/σI*	7.2 (2.5)	10.9 (0.8)
Completeness (%)*	93.8 (88.2)	99.9 (99.3)
Redundancy*	3.0 (2.6)	6.5 (7.2)
$CC_{1/2}$*‡	0.99 (0.84)	0.99 (0.28)
Refinement		
Number of reflections	12411	41555

R_{work}/R_{free} (%)	22.1/26.8	23.4/27.6
Number of atoms		
Protein	1573	8431
Ligand/ion	54	106
Water	42	16
B-factors		
Protein	21.04	79.9
Ligand/ion	40.01	104.8
Water	20.24	58.3
R.M.S deviations[†]		
Bond lengths (Å)	0.008	0.005
Bond angles (°)	1.623	1.374
Ramachandran		
Ramachandran favoured (%)	97	96
Ramachandran allowed (%)	3	4
Ramachandran outliers (%)	0	0

[*]*Values in brackets are for the high resolution shell.* [‡]*$CC_{1/2}$, correlation coefficient. RMSD, root mean square deviation.* [†]*RMS, root mean square*

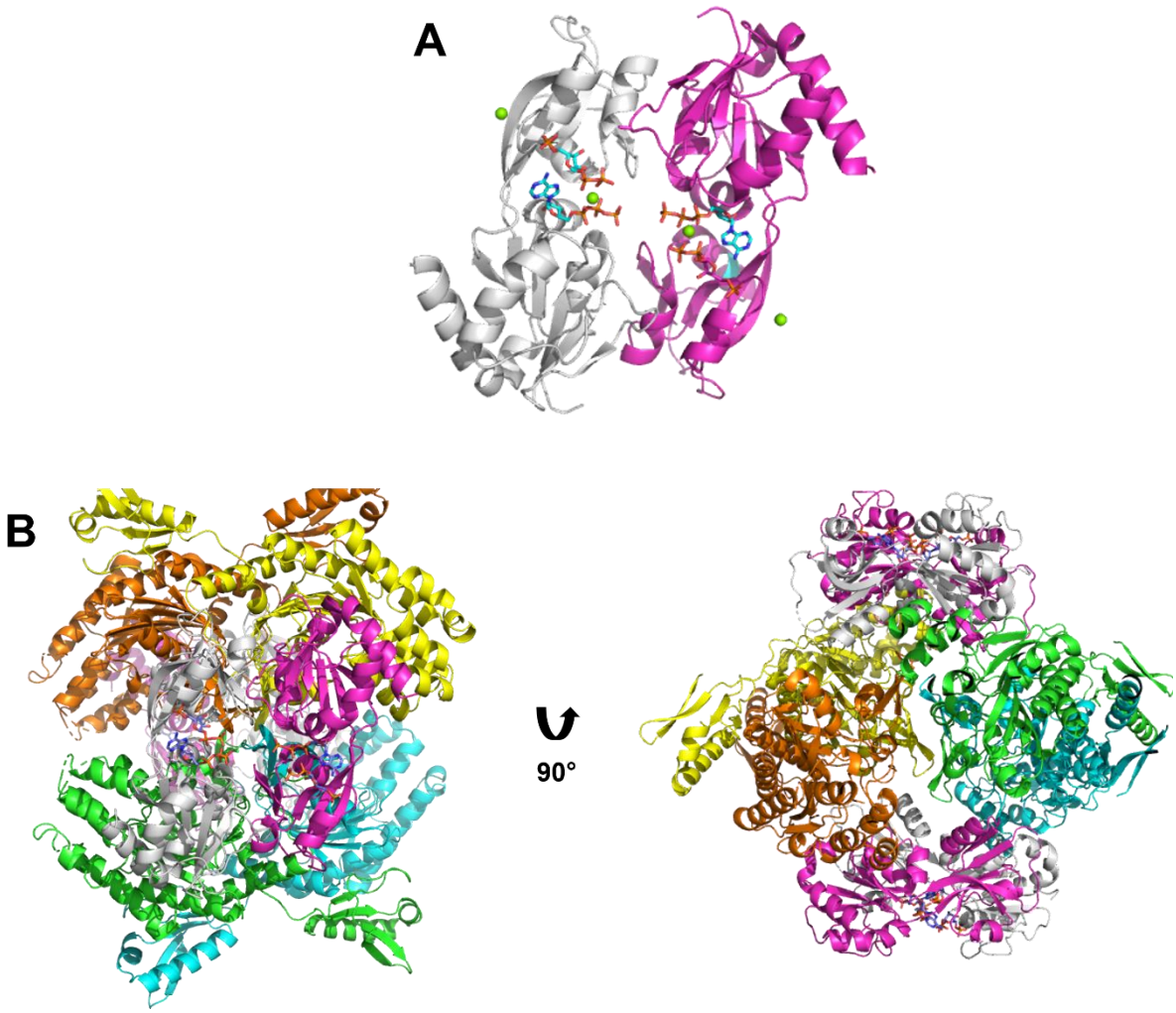

Figure 4.15 Crystal structures of R56A *Pa*HisG$_S$ and R56A *Pa*ATPPRT with ATP and PRPP bound. (A) R56A *Pa*HisG$_S$. (B) R56A *Pa*ATPPRT. *Pa*HisG$_S$ subunits are shown in grey and magenta. *Pa*HisZ subunits are shown in cyan, green, yellow and brown. Substrates are depicted with stick models with nitrogen in blue, oxygen, in red, phosphorus in orange, and carbon in either cyan (*Pa*HisG$_S$) or purple (*Pa*ATPPRT). Mg^{2+} ions are depicted as green spheres. Images were generated in Pymol

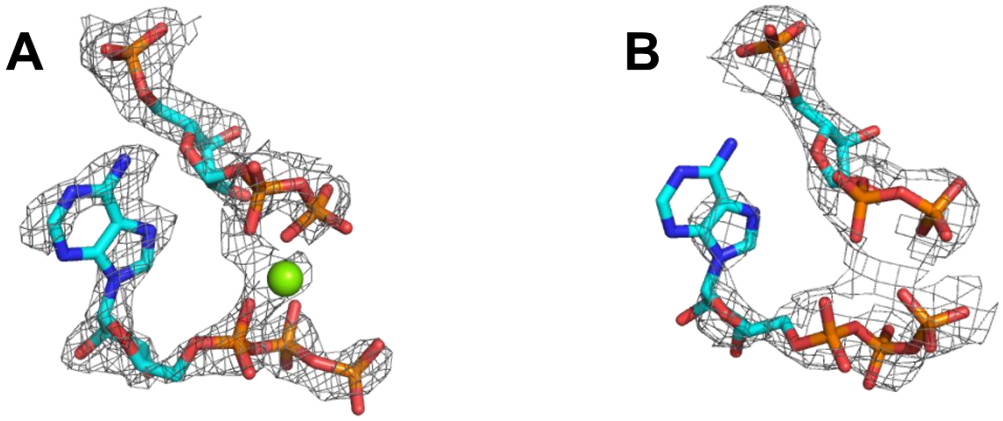

Figure 4.17 Omit maps at 1σ for ligands in the (A) R56A *Pa*HisG$_S$ and (B) R56A *Pa*ATPPRT crystal structures. Ligands are depicted by stick models with nitrogen in blue, oxygen, in red, phosphorus in orange, and carbon in cyan. The Mg^{2+} ion in the *Pa*HisG$_S$ structure is depicted by a green sphere. Image generated in Pymol..

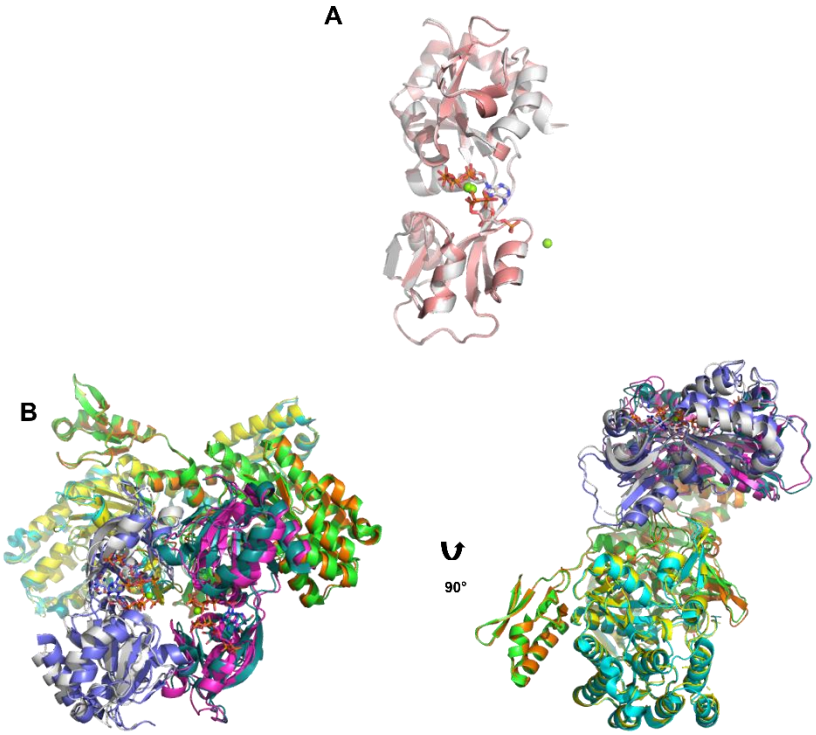

Figure 4.16 Overlays of ATP and PRPP bound R56A and WT *Pa*HisG$_S$ and *Pa*ATPPRT. (A).Overlay of WT and R56A *Pa*HisG$_S$ structures. (B) Overlay of WT and R56A *Pa*ATPPRT structures. Proteins are shown with ribbon diagrams. R56A *Pa*HisG$_S$ subunits are shown in either grey (*Pa*HisG$_S$) or grey and magenta (*Pa*ATPPRT). WT *Pa*HisG$_S$ subunits are shown in coral (*Pa*HisG$_S$) or purple and teal (*Pa*ATPPRT). PaHisZ subunits are shown in yellow and orange (R56A *Pa*ATPPRT) or cyan and green (WT *Pa*ATPPRT). Substrates are depicted as stick models with nitrogen in blue, oxygen in red, phosphorus in orange, and carbon in the colour of the protein backbone. Mg^{2+} is depicted by green spheres. WT *Pa*HisG$_S$:PRPP;ATP (PDB ID: 6FCT) and *Pa*ATPPRT:PRPP:ATP (PDB ID: 6FU2) structures are from Alphey et al[40]. Image generated in Pymol

4.10.1 Analysis of R56A *Pa*HisG$_S$ crystal structure

The crystal structure of R56A *Pa*HisG$_S$ is almost identical to the WT *Pa*HisG$_S$ structure. An additional Mg^{2+} ion was modelled into the R56A *Pa*HisG$_S$ structure, at the edge of the protein, however, this was considered to be a crystallisation artefact, Figure 4.17. The additional Mg^{2+} ion bound away from the active site and was not considered mechanistically relevant. A56 of R56A *Pa*HisG$_S$ is approximately 10 Å away from the pyrophosphate leaving group, Figure 4.18A. All hydrogen bonds from PRPP (T183, G181, T180, D179, R32) and ATP (R32, D94, R73, K137) to WT *Pa*HisG$_S$ are observed in the R56A *Pa*HisG$_S$ structure and no additional interactions were identified, Figure 4.18A. Notably, the interaction between R32 to the pyrophosphate leaving group is preserved in the absence of R56. The structural work presented here provides further evidence that the R56A mutation does not alter *Pa*HisG$_S$ folding, oligomeric state or ability to bind substrate, and is consistent with the hypothesis that the loss of activity in R56A *Pa*HisG$_S$ is due to loss of the electrostatic stabilisation of the pyrophosphate leaving group at the transition state

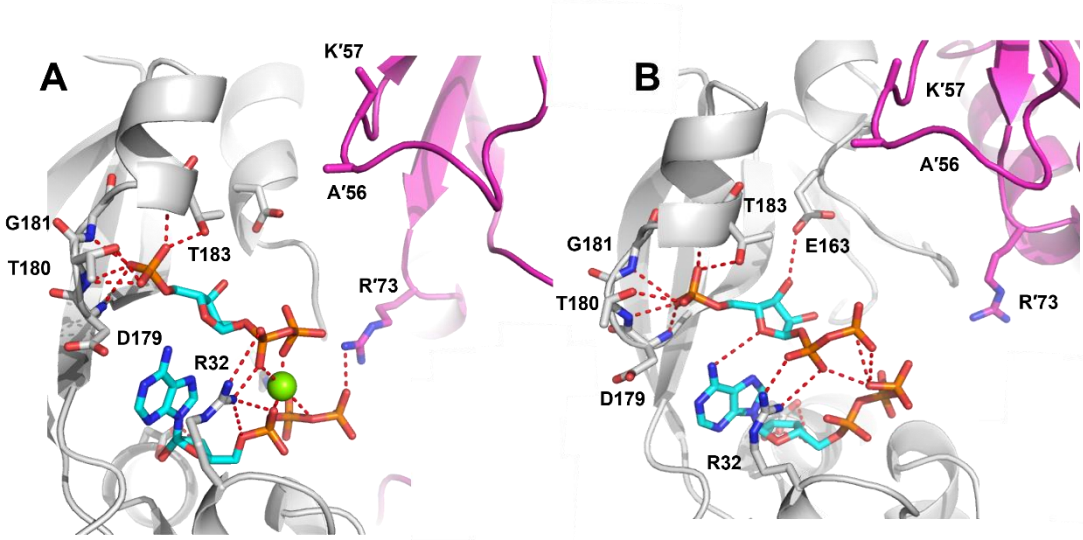

Figure 4.18 Comparison of substrate-bound R56A *Pa*HisG$_S$ and R56A PaATPPRT active sites. (A) R56A *Pa*HisGs. (B) R56A *Pa*ATPPRT. *Pa*HisGs subunits are shown as ribbon diagrams in either grey (ligand-bound subunit) or magenta (adjacent subunit) selected residues are depicted as stick models with carbon in either grey or magenta, nitrogen in blue, oxygen in red and phosphorus in orange. Ligands are presented as stick models with carbon in cyan, nitrogen in blue, oxygen in red and phosphorus in orange. Mg^{2+} is depicted by green spheres. Polar interactions are represented by dashed lines. Images were generated in Pymol

4.10.2 Analysis of R56A *Pa*ATPPRT crystal structure

Previous structural studies of *Pa*ATPPRT:PRPP, *Pa*ATPPRT:PRPP:ATP and *Pa*ATPPRT:PRPP:histidine complexes carried out by Dr Magnus S. Alphey and Dr Catherine M. Thomson indicated that Apo *Pa*ATPPRT, *Pa*ATPPRT:PRPP and *Pa*ATPPRT:PRPP:histidine complexes reflect similar non-activated conformations of the protein, whereas the crystal structure of *Pa*ATPPRT:PRPP:ATP reflects an activated form of the protein[32,40,44]. The proposed the structural hallmarks of protein activation include subunits of the *Pa*HisG$_S$ dimer moving closer to one another and repositioning of the *Pa*HisG$_S$ A44-V67 upon formation of the ternary complex[40,44]. The repositioning of the A44-V67 loop in the WT *Pa*ATPPRT:PRPP:ATP structure facilitates formation of a salt-bridge between R56 and the pyrophosphate leaving group of the adjacent dimer[40]and this interaction was hypothesised to play a key role in allosteric activation of *Pa*HisG$_S$ by *Pa*HisZ at the beginning of this chapter.

Structural alignments were performed with the *Pa*HisG$_S$ dimer from the R56A *Pa*ATPPRT:PRPP:ATP structure to the *Pa*HisG$_S$ dimers from activated WT *Pa*ATPPRT:PRPP:ATP and non-activated WT *Pa*ATPPRT:PRPP, Figure 4.19A. RMSDs obtained from the *Pa*HisG$_S$ structural alignments suggest that the *Pa*HisG$_S$ dimer from the R56A *Pa*ATPPRT:PRPP:ATP structure is more similar to the non-activated WT *Pa*ATPPRT:PRPP structure (RMSD: 0.423 Å) than the activated WT *Pa*ATPPRT:PRPP:ATP structure (RMSD: 1.950 Å). Indeed, upon examination of Figure 4.19A, it was concluded that the *Pa*HisG$_S$ dimer from the R56A *Pa*ATPPRT:PRPP:ATP structure is held more loosely than the *Pa*HisG$_S$ dimer from the activated WT *Pa*ATPPRT:PRPP:ATP structure. Unfortunately, only the protein backbone and partial side chains of the *Pa*HisG$_S$ loop encompassing A44-V67, on which A56 resides, could be modelled in the R56A *Pa*ATPPRT:ATP:PRPP structure, possibly due to increased flexibility of this loop in the absence of R56. Nonetheless, the position of A44-V67 loop in the R56A *Pa*ATPPRT:PRPP:ATP structure overlays well with the position occupied in the non-activated WT *Pa*ATPPRT:PRPP structure, Figure 4.19B. A56 is approximately 11 Å from the pyrophosphate leaving group. Critically, the position of the *Pa*HisG$_S$ A44-V67 loop in the R56A *Pa*ATPPRT:PRPP:ATP crystal structure would not facilitate interaction between K57 and the pyrophosphate leaving group, Figure 4.19B.

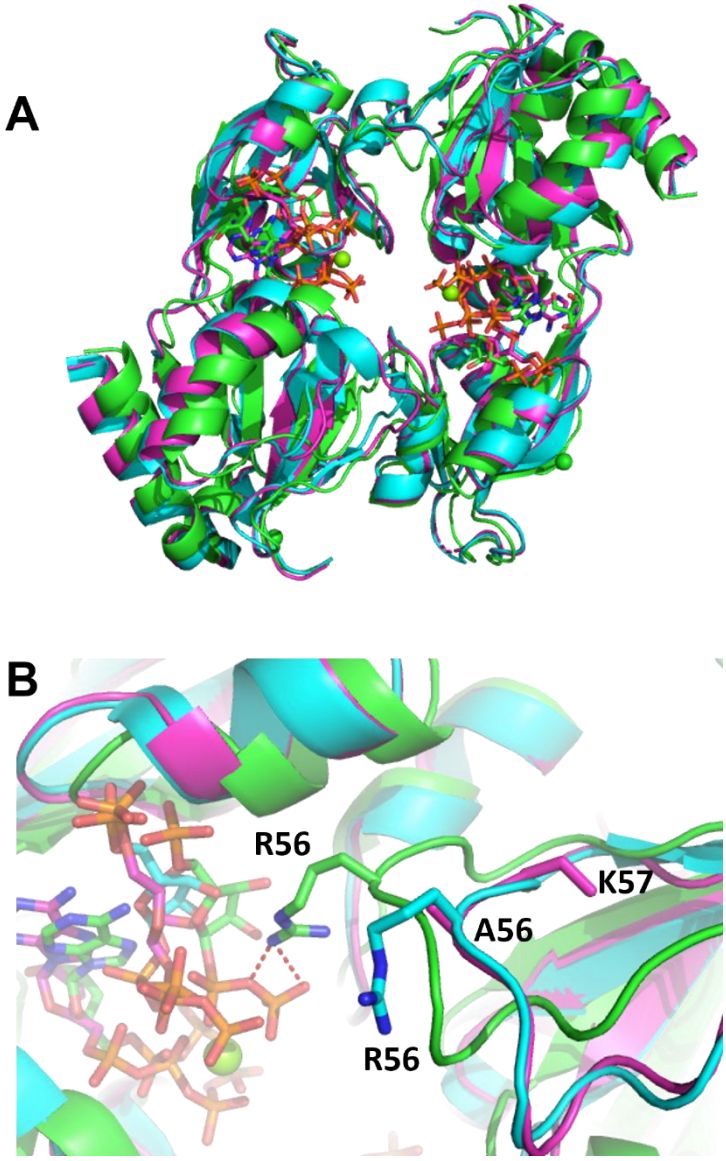

Figure 4.19 The *Pa*HisG$_S$ dimer from the R56A *Pa*ATPPRT:PRPP:ATP structure is more similar to that of the WT *Pa*ATPPRT:PRPP structure than the WT *Pa*ATPPRT:PRPP:ATP structure. (A) Overlay of *Pa*HisG$_S$ dimers from R56A *Pa*ATPPRT:PRPP:ATP (magenta), WT *Pa*ATPPRT:PRPP:ATP (green) (PDB ID :6FU2), and WT *Pa*ATPPRT:PRPP (cyan) (PDB ID: 6TFF) structures. (B) Overlay of the PaHisG$_S$ A44-V67 loop from R56A *Pa*ATPPRT:PRPP:ATP (magenta), WT *Pa*ATPPRT:PRPP:ATP (green), and WT *Pa*ATPPRT:PRPP (cyan) structures. Proteins are shown with ribbon diagrams. Ligands are shown in stick representation with oxygen coloured in red, nitrogen in blue and carbon in either magenta (R56A ATPPRT:PRPP:ATP), green (WT PaATPPRT:PRPP:ATP), or cyan (WT PaATPPRT:PRPP). Mg^{2+} is depicted by green spheres. Dashed lines represent polar interactions. *Pa*HisZ subunits have been omitted for clarity. *Pa*ATPPRT:PRPP:ATP (PDB ID: 6FU2) and *Pa*ATPPRT:PRPP:ATP (PDB ID: 6FTT) structures are from Alphey et al.[40]. Only part of the K57 side chain in the R56A *Pa*ATPPRT:PRPP:ATP structure could be modelled from density. Images generated in Pymol.

The active sites of R56A *Pa*HisG$_S$ and R56A *Pa*ATPPRT were examined side-by-side in order to identify possible structural explanations for allosteric recovery of activity, Figure 4.17. The active site of R56A *Pa*ATPPRT was structurally similar to that of R56A *Pa*HisG$_S$, an interaction between E216 and the 3-OH of PRPP was the only additional interaction captured in the R56A *Pa*ATPPRT that was not present in the R56A *Pa*HisG$_S$. Despite a thorough study of both active sites, no alternative interactions to the pyrophosphate leaving-group that could compensate for loss of R56 were identified, nor was any alternative hypothesis generated that could account for the allosteric rescue of R56A *Pa*HisG$_S$ by *Pa*HisZ. It was noted that the adenine ring of ATP must rotate 180° from the position observed in the active site of the R56A *Pa*ATPPRT:PRPP:ATP structure for catalysis to occur. An anticatalytic ATP rotamer was also observed in the "activated" WT *Pa*ATPPRT:PRPP:ATP crystal structure[40]. Thus, the view of active site captured by X-ray crystallography, does not reflect the catalytically competent conformation. Crystallisation with ATP in an anticatalytic conformation explains why both substrates can be observed in the active site without reaction. It was concluded that the mechanism underpinning allosteric rescue of catalytically impaired R56A *Pa*HisG$_S$ may not have been captured in these snapshots. It was envisioned that dynamic studies of WT *Pa*HisG$_S$ and *Pa*ATPPRT alongside R56A *Pa*HisG$_S$ and R56A *Pa*ATPPRT may provide further insight into the allosteric rescue of catalytically impaired R56A *Pa*HisG$_S$. Indeed, the crystal structures of R56A *Pa*ATPPRT:PRPP:ATP and R56A *Pa*HisG$_S$:PRPP:ATP described here, later served as starting points for molecular dynamics simulations performed by Dr Marina Corbella of the Kamerlin laboratory at Uppsala University. These simulations yielded interesting insights into the proposed mechanism of allosteric activation of *Pa*HisG$_S$ by *Pa*HisZ and allosteric rescue of catalytically impaired R56A *Pa*HisG$_s$ and are discussed in Sections 4.14 and 4.15.

4.11 Site-saturation mutagenesis (SSM) at position 56 of *Pa*HisG$_S$

Whilst molecular dynamics simulations were carried out by Dr Marina Corbella to address the role of protein dynamics in allosteric rescue of R56A *Pa*HisG$_S$ by *Pa*HisZ, subsequent experiments reported here were devised to further explore the function of R56

in catalysis. Site-saturation mutagenesis (SSM) is a powerful technique, commonly applied in biotechnology, in which a particular amino acid residue is mutated to each of the 19 remaining proteinogenic amino acids. SSM has been used to evolve enzymes with: increased activity, altered substrate specificity/enantioselectivity[151,152], increased thermal stability[153,154] and changes in co-factor preference[155]. SSM was carried out at position 56 of *Pa*HisG$_S$. SSM was envisioned to provide a wider examination of the function of R56. Results from SSM studies have previously challenged catalytic mechanisms established from studies in which an amino acid(s) is mutated solely to alanine[156–158]. On the other hand, SSM can support a proposed amino acid function by confirming a catalytic requirement for an ionizable group[159], a hydrophobic interaction[160], or charged amino acid[161,162].

Saturation mutagenesis PCRs were performed with specific primers rather than degenerate primers, which is considered more suitable approach when randomising two or more positions simultaneously[163]. A "medium-throughput" approach, developed by Dr Teresa F. G. Machado, was employed to evaluate variant *Pa*HisG$_S$ production and activity. WT and R56A *Pa*HisG$_S$ were included in the analyses as positive and negative controls, respectively. All 20 mutant *Pa*HisG$_S$ proteins were successfully produced, Figure 4.20, and protein production levels are generally comparable with WT *Pa*HisG$_S$, with the exception of R56F *Pa*HisG$_S$, which was produced at a low level.

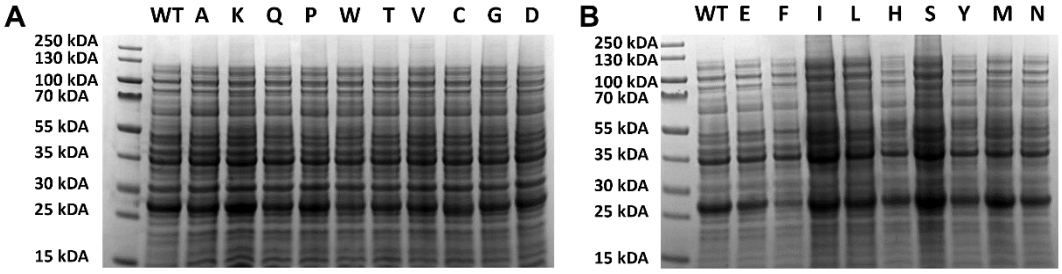

Figure 4.20 Production of R56X *Pa*HisG$_S$. SDS-PAGE gel with protein ladder (PageRuler Plus Prestained) and samples of the soluble fraction from C43 (DE3) cells expressing R56X variants. *Pa*HisG$_S$ band is between 25 and 35 kDA bands on ladder. X represents the amino acid to which R56 was mutated.

Following confirmation of *Pa*HisG$_S$ variant production, the soluble fraction of cell lysate from cells expressing each of the mutant *Pa*HisG$_S$ proteins was evaluated for *Pa*HisG$_S$ activity, Figure 4.21. R56X *Pa*HisG$_S$ mutants displayed only minimal catalytic activity.

At this point, it is expected that total protein concentration would be determined for each cell lysate and activities converted to specific activity for a quantitative comparison of the mutant activities. However, R56X *Pa*HisG$_S$ mutants did not exhibit catalytic activity sufficiently greater than the negative R56A control to warrant further investigation and it was concluded that only arginine is tolerated at position 56 of *Pa*HisG$_S$ and no further data was collected. It had been hypothesised that an R56K mutation may be tolerated by *Pa*HisG$_S$ as lysine has similar chemical properties to arginine and has previously been shown to be a tolerable replacement for arginine[161]. Nevertheless, as no other amino acid could reasonably compensate for loss of R56, SSM provided further, independent, evidence that R56 is essential for *Pa*HisG$_S$. A future research study examining the impact of simultaneous saturation mutagenesis of R32, R56 and K57 which examines *Pa*HisG$_S$ activities with and without *Pa*HisZ could yield further insights into the minimum requirements for stabilisation of the pyrophosphate leaving group.

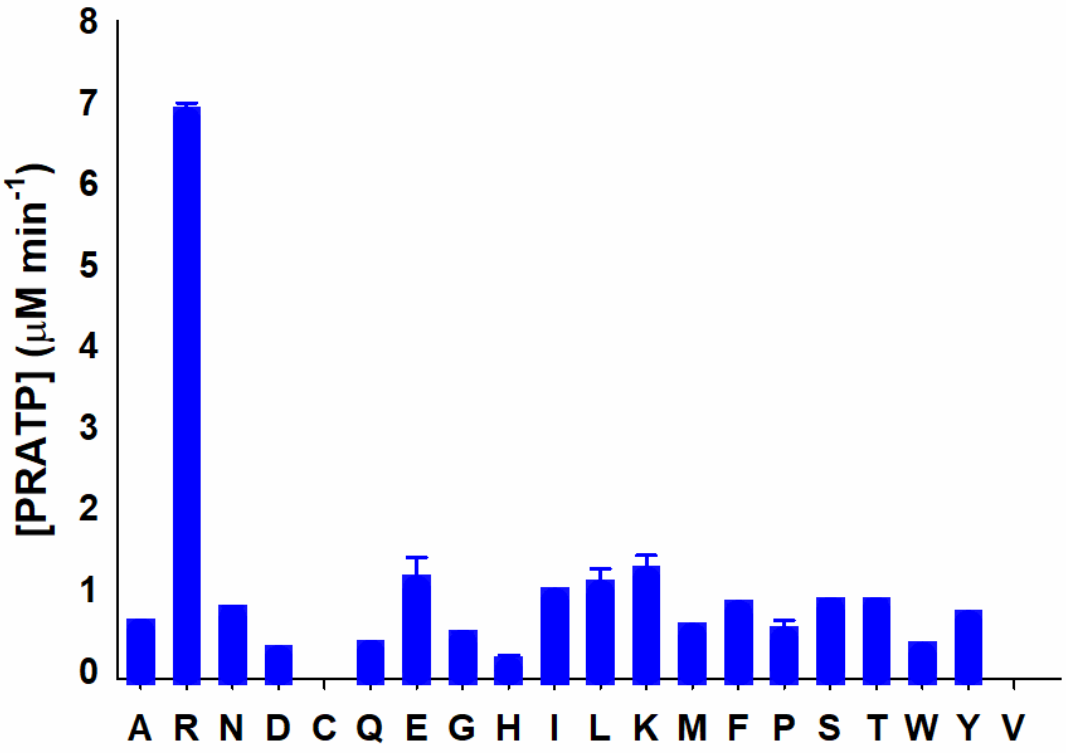

Figure 4.21 Activity of R56X *Pa*HisG$_S$ variants.. PRATP formation was measured in the presence of substrate concentrations that would saturate WT *Pa*HisG$_S$. Data are mean ± standard error of duplicate measurements. R56 and R56A *Pa*HisG$_S$ are positive and negative controls, respectively.

4.12 Attempted chemical rescue of R56A *Pa*HisG$_S$

Loss of enzymatic activity due to a mutation can also often be restored orthosterically by supplementing the reaction mixture with small molecules that have similar chemical properties to the mutated residue. Mechanistic insights can subsequently be gleamed from Brønsted analyses which evaluate the relationship between p*K*a of these small molecules and reaction rate[164]. Brønsted analyses have previously been used to dissect the role of: R57 of ornithine transcarbamoylase[165] and R301 of phosphite dehydrogenase[166]. It was sought to determine if catalytic activity of R56A *Pa*HisG$_S$ activity could be restored by inclusion of various guanidine and amine analogues in activity assays.

Unfortunately, most guanidine analogues tested (guanidine, ethyl-guanidine, propyl-guanidine) precipitated when added to the reaction mixture, only methyl-guanidine was soluble. Upon addition of 200 mM methyl-guanidine to R56A *Pa*HisG$_S$ catalysed reactions, there appeared to be a very small enhancement of catalytic rate relative to control reactions, Figure 4.22. Unfortunately, the rate of reaction was very low and precipitation was observed upon attempts to increase the concentration of methyl-guanidine to 400 mM. R56A *Pa*HisG$_S$ activity was unaffected when methyl-, ethyl-, and propyl-amine were added to reactions at concentrations upto 200 mM, Figure 4.22. Ultimately, chemical rescue studies yielded little information on the function of R56

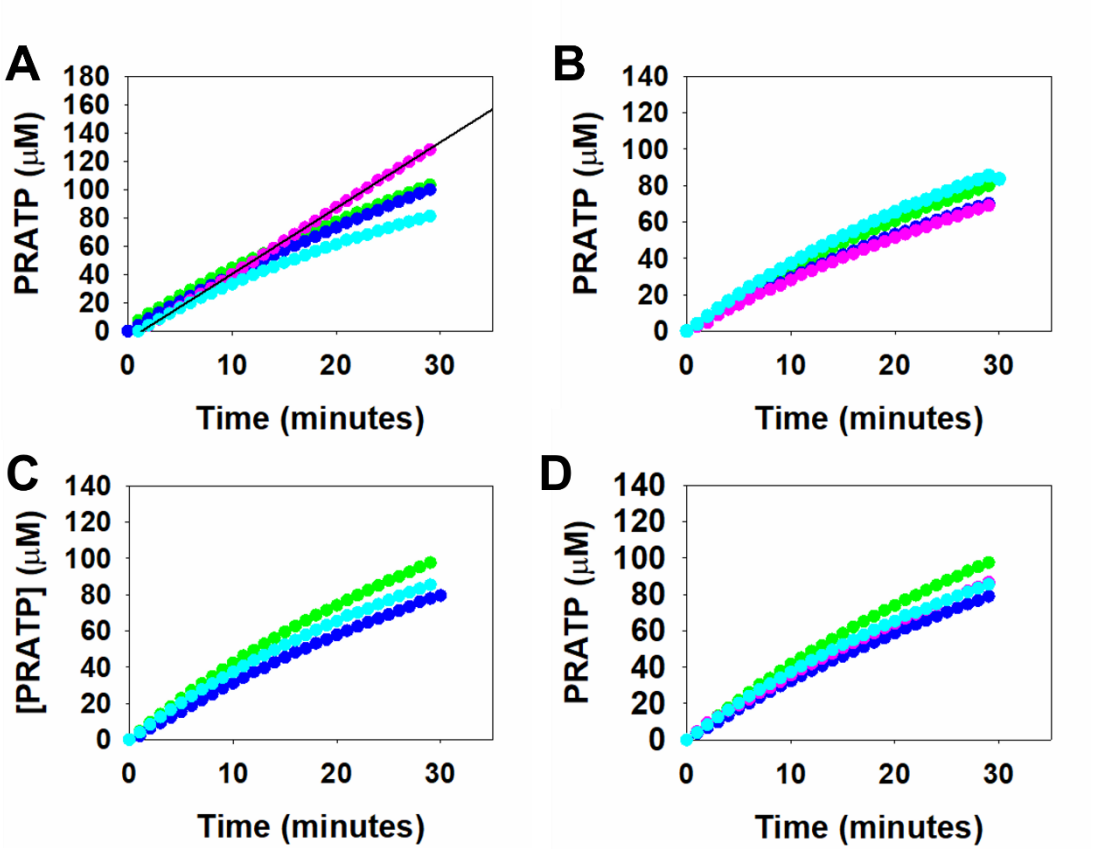

Figure 4.22 Product formation time-courses of reactions catalysed by R56A *Pa*HisG$_S$ in the presence of guanidiniums or amines. (A) methyl-guanidine, (B) methylamine, (C) ethylamine, and (D) propylamine (0 mM [cyan], 50 mM [green], 100 mM [blue] and 200 mM[(magenta])Black line is 200 mM methyl-guanidine data fitted to a linear equation

4.13 R32A and R56A mutations disrupt the chemical step of catalysis

R32 and R56 of *Pa*HisG$_S$ were posited to be required for stabilisation of the pyrophosphate leaving group at the transition state. R32 may play additional roles in orientating ATP for catalysis. In Chapter 3, it was demonstrated that allosteric activation of *Pa*HisG$_S$ by *Pa*HisZ shifts the rate-limiting step from interconversion between ternary complexes, including chemistry, to product release. It was speculated that if R32 and R56 were required for stabilisation of the pyrophosphate leaving-group at the transition state, the rate-limiting step of reactions catalysed by activated R32A and R56A *Pa*ATPPRT may include contributions from the chemical step, which would be disrupted in the absence of these residues.

In Chapter 3, it was also demonstrated that replacement of Mg^{2+} by Mn^{2+} increases the k_{cat} of *Pa*HisG$_S$ catalysed reactions but that the k_{cat} of *Pa*ATPPRT reactions is unaffected by substitution of Mg^{2+} by Mn^{2+}. Subsequent transition state modelling performed by Dr Jennifer S. Hirschi concluded that Mn^{2+} is better able to attenuate negative charge at the transition state due to d-orbital overlap with the two p-orbitals of the oxygens of the pyrophosphate leaving-group[43]. If, as was hypothesised, R32A and R56A mutations disrupted the rate of the chemical step, it would be expected that the rate-limiting step of R32A and R56A *Pa*ATPPRT-catalysed reactions would include contributions from chemistry. Hence, it would also be expected that the rate of reaction would be increased upon measurement with Mn^{2+} instead of Mg^{2+}, as was reported for WT *Pa*HisG$_S$. On the other hand, if the rate-limiting step of R32A and R56A *Pa*ATPPRT is not different from WT *Pa*ATPPRT and is reporting on product release, it would be expected that the rate of reaction would not be influenced by substitution of Mg^{2+} by Mn^{2+}, as was reported for WT *Pa*ATPPRT. Accordingly, the rates of reactions catalysed by WT, R32A and R56A, *Pa*ATPPRT in Mg^{2+} and Mn^{2+} were measured.

At this point in the experimental work, it was discovered that *Pa*HisZ purified with the His-tag still attached also activated *Pa*HisG$_S$. Furthermore, removing the TEVP cleavage step from the *Pa*HisZ purification allowed for quicker production of higher quantities of *Pa*HisZ. His-tagged *Pa*HisZ was purified using nickel affinity chromatography and the expected mass was observed via ESI -MS (carried out by the BSRC mass-spectrometry facility), Figure 4.23. The presence of a His-tag may influence enzymatic activity[167,168], thus, the steady-state kinetic parameters of WT *Pa*HisG$_S$ were redetermined with His-tagged *Pa*HisZ to assess the effect of the His-tag on activated *Pa*ATPPRT activity, Figure 4.24 and Table 4.8.

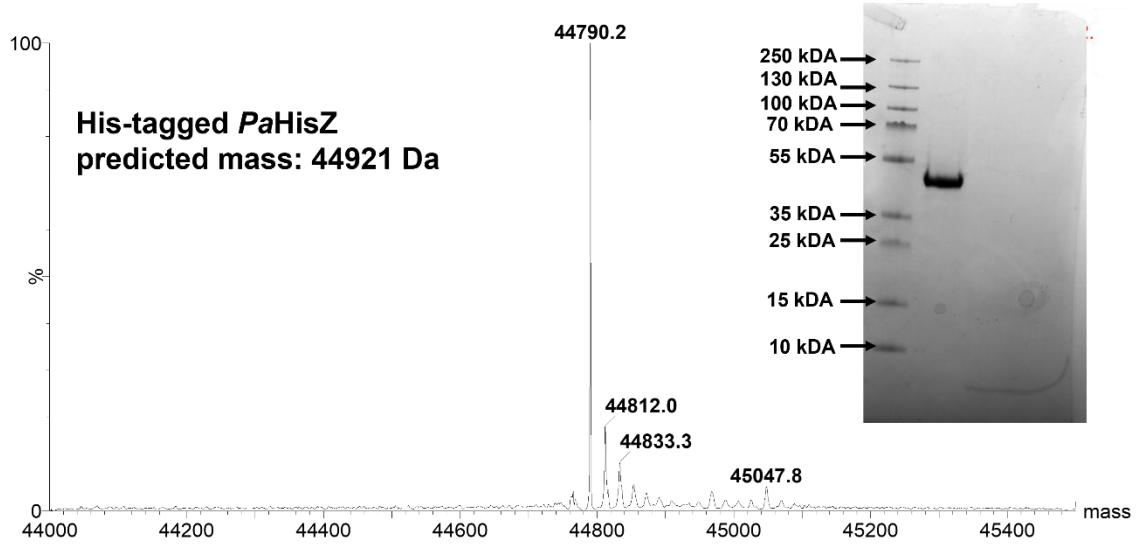

Figure 4.23 Purification of His-tagged *Pa*HisZ. ESI mass-spectrometry analysis showing the experimentally determined mass of 44,790 Da for His-tagged PaHisZ, in agreement with the loss of the N-terminal methionine. Inset is SDS-PAGE with protein ladder (PageRuler Plus Prestained).

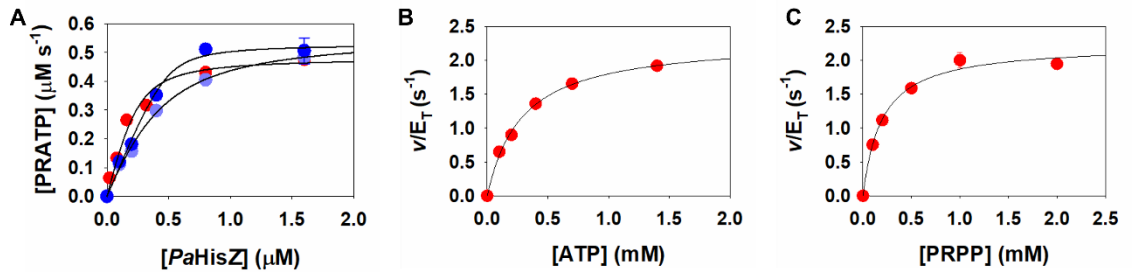

Figure 4.24 WT, R32A and R56A *Pa*HisG$_S$ steady-state kinetics with His-tagged *Pa*HisZ. (A) Determination of K_D for equilibrium dissociation of His-tagged PaHisZ from the *Pa*ATPPRT holoenzyme with WT (red), R56A (purple) and R32A (blue). (B and C) WT *Pa*ATPPRT substrate saturation curves. Solid lines in (A) are data fitted to Equation 2.1. Solid lines in (B) and (C) are data fitted to the Michaelis-Menten equation. Data points are mean ± standard error of at least duplicate measurements.

Table 4-8. WT *Pa*ATPPRT steady-state kinetic parameters with His-tagged *Pa*HisZ.

Parameter	**WT *Pa*HisG$_S$**
K_D	0.06 ± 0.03
k_{cat} **(s^{-1})**	2.33 ± 0.05
K_{PRPP} **(mM)**	0.19 ± 0.03
K_{ATP} **(mM)**	0.26 ± 0.02
k_{cat}/K_{PRPP} **(M^{-1} s^{-1})**	12000 ± 2000
k_{cat}/K_{ATP} **(M^{-1} s^{-1})**	9000 ± 700

Values are mean ± fitting error of duplicate measurements.

The affinity of WT *Pa*HisG$_S$ for His-tagged *Pa*HisZ is approximately 10-fold greater than for non-tagged *Pa*HisZ, Figures 4.7 and 4.24, Tables 4.4 and 4.8. The k_{cat} of WT *Pa*ATPPRT with His-tagged *Pa*HisZ (2.33 ± 0.05 s^{-1}) is similar to the k_{cat} of WT *Pa*ATPPRT with non-tagged *Pa*HisZ (1.72 ± 0.07 s^{-1}). K_M^{ATP} and K_M^{PRPP} are 2.9- and 2.3-fold lower, respectively for WT *Pa*ATPPRT with His-tagged compared with WT *Pa*ATPPRT with non-tagged *Pa*HisZ. Thus, a redetermination of the steady-state kinetic parameters of WT *Pa*ATPPRT completed with His-tagged *Pa*HisZ confirms that His-tagged *Pa*HisZ is a suitable substitute for non-tagged *Pa*HisZ. His-tagged *Pa*HisZ was employed in all further experiments.

The rates of reactions catalysed by WT, R32A and R56A, *Pa*ATPPRT were subsequently determined in Mg^{2+} and Mn^{2+}, control reactions were performed with Mn^{2+} in the absence of His-tagged *Pa*HisZ, Figure 4.25 and Table 4.9. The data in Figure 4.25 and Table 4.9 confirmed the findings reported in Chapter 3, the value of v/E_T for reactions catalysed by

WT *Pa*ATPPRT is similar between measurements performed in Mg^{2+} and Mn^{2+}. On the contrary, rates of reactions catalysed by R32A and R56A *Pa*ATPPRT is increased by approximately 4.5- and 2.7-fold when measurements are performed with Mn^{2+} in place of Mg^{2+}. Controls reaction performed with R32A and R56A *Pa*HisG$_S$ in Mn^{2+}, demonstrated that whilst the background activity of these *Pa*HisG$_S$ variants appears enhanced by Mn^{2+}, it cannot account for the rate enhancement observed when Mn^{2+} replaces Mg^{2+} in reactions catalysed by activated *Pa*ATPPRT. These findings indicate that the k_{cat}s reported in Table 4.4 for R32A and R56A *Pa*ATPPRT are at least partially-reporting on chemistry. Importantly, these findings establish a link between R32 and R56 and the rate of the chemical step for catalysis which is consistent with the proposed role of these residues in stabilising the pyrophosphate leaving-group at the transition state.

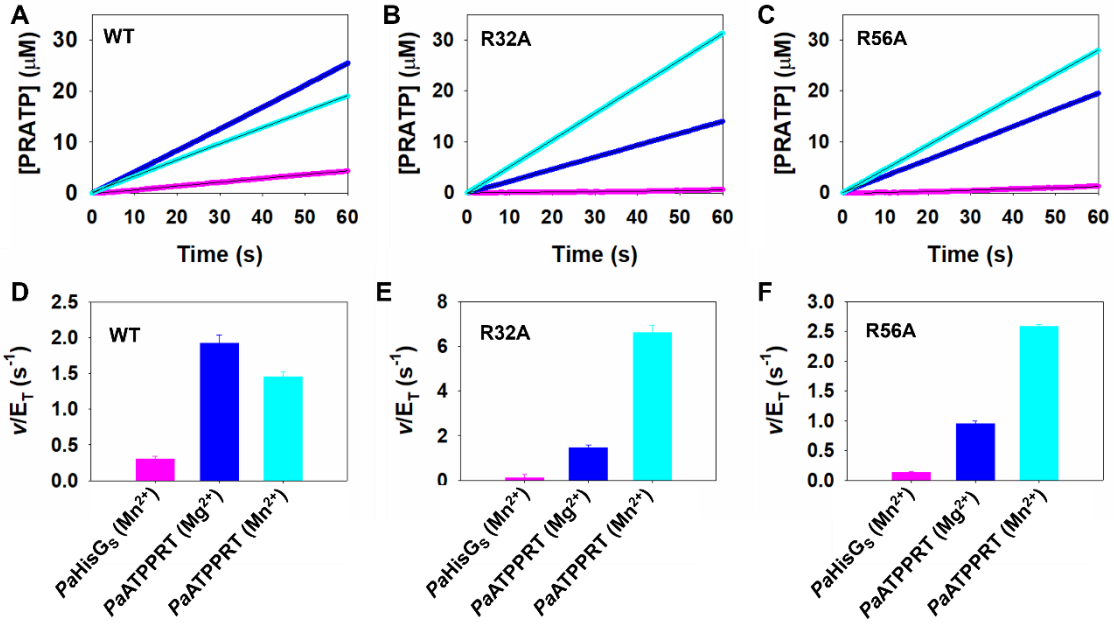

Figure 4.25 The effect of Mn^{2+} on rates of reactions catalysed by R32A, R56A and WT *Pa*ATPPRT. (A, B and C) Product formation time-courses from reactions catalysed by (A) WT, (B) R32A and (C) R56A *Pa*HisG$_S$ or *Pa*ATPPRT at fixed, saturating concentrations of PRPP and ATP. Rates of reaction catalysed by either *Pa*HisG$_S$ with Mn^{2+} (magenta) or *Pa*ATPPRT with Mg^{2+} (blue) or *Pa*ATPPRT with Mn^{2+} (cyan) were measured. WT *Pa*ATPPRT and *Pa*HisG$_S$ measurements were performed with 0.22 μM *Pa*HisG$_S$/*Pa*ATPPRT. R56A measurements were performed with either 0.16 μM *Pa*ATPPRT (Mg^{2+}) or 0.08 μM *Pa*HisG$_S$/*Pa*ATPPRT (Mn^{2+}). R32A measurements were performed with either 0.34 μM *Pa*ATPPRT (Mg^{2+}) or 0.18 μM *Pa*HisG$_S$/*Pa*ATPPRT (Mn^{2+}). (D, E and F) Apparent first-order rate constants for *Pa*HisG$_S$ and *Pa*ATPPRT variants. Two independent measurements were carried out for *Pa*HisG$_S$ variants and four for *Pa*ATPPRT variants except for R56A *Pa*ATPPRT in the presence of Mg^{2+} which is a triplicate measurement. Data are average of independent measurements. Solid black lines are linear regressions of data. Bars are ± standard error of independent measurements..

.

***Pa*HisG$_S$ Variant**	***Pa*HisG$_S$ + *Mn*$^{2+}$ *v*/E$_T$ (s^{-1})***	***Pa*ATPPRT + Mg^{2+} *v*/E$_T$ (s^{-1})‡**	***Pa*ATPPRT + *Mn*$^{2+}$ *v*/E$_T$ (s^{-1})‡**
WT	0.30 ± 0.04	1.9 ± 0.1	1.45 ± 0.06
R32A	0.12 ± 0.1	1.48 ± 0.09	6.6 ± 0.3
R56A	0.13 ± 0.01	0.95 ± 0.04	2.58 ± 0.03

Table 4-9 The effect of Mn^{2+} on rates of reactions catalysed by R32A, R56A and WT *Pa*ATPPRT. Values are mean ± standard error of duplicate* or quadruplicate‡ measurements.

4.14 R32A/R56A/K57A *Pa*HisG$_S$ cannot be rescued by *Pa*HisZ.

As the crystal structures of R56A *Pa*HisGS and R56A *Pa*ATPPRT did not shed light on allosteric activation of R56A *Pa*HisG$_S$ by *Pa*HisZ, it was sought to investigate *Pa*HisG$_S$ conformational sampling in the presence and absence of *Pa*HisZ. Attempts to label *Pa*HisG$_S$ for single molecule fluorescence resonance energy transfer (smFRET) studies were unsuccessful which was unfortunate as smFRET can demonstrate stabilisation of catalytically active enzyme conformations and changes in the rate of interconversion between conformations upon ligand binding[169,170]. The smFRET was carried out as part of a collaboration with Dr Tiange Li of the Penedo Laboratory at the University of St Andrews. Fortunately, an extensive analysis of WT and R56A *Pa*HisG$_S$ and *Pa*ATPPRT conformational sampling via molecular dynamics simulations was performed by Dr Marina Corbella of the Kamerlin laboratory at Uppsala University in collaboration with the da Silva Laboratory. Dr Corbella 's work confirmed that R56 is more likely to occupy a space which facilitates interactions with the pyrophosphate leaving-group when *Pa*HisZ is present. Dr Corbella 's work also revealed that in the absence of R56, R32 is more restricted and spends more time interacting with the pyrophosphate leaving-group (manuscript submitted: Fisher G., Corbella M., Alphey M. S., Nicholson H., Read B. J., Kamerlin S. C. L., and da Silva R. G. [2022]).

The findings from the molecular dynamic simulations illuminated a rationale for allosteric rescue of catalytically impaired R32A, R56A, and R56A/K57A *Pa*HisG. It was hypothesised that in the presence of HisZ, the dynamics of R32 and R56 are altered in order that one arginine can somewhat compensate for loss of the other. To test this prediction, R32A/R56A/K57 *Pa*HisG$_S$ was produced and kinetically characterised. The K57A mutation was included in order that any small compensatory effect of K57 for loss of R56 did not influence the results. SDS-PAGE and ESI/TOF-MS confirmed that R32A/R56A/K57 *Pa*HisG$_S$ was of satisfactory purity and of the expected molecular weight, Figures 4.4 and 4.5.

DSF of R32A/R56A/K57A *Pa*HisG$_s$ was performed to evaluate the thermal stability of the variant and it was concluded that R32A/R56A/K57A *Pa*HisG$_s$ exhibits a similar thermal unfolding profile to WT *Pa*HisG$_S$, Figure 4.26A. The T_M of R32A/R56A/K57A *Pa*HisG$_s$ was calculated in the absence (60.2 ± 0.2 °C) and presence of PRPP (63.53 ± 0.06 °C), The reported T_Ms and magnitude of the PRPP-induced shift were in reasonable agreement with those reported in Table 4.1. R32A/R56A/K57A *Pa*HisG$_S$ is thermally stable and retains the ability to bind PRPP.

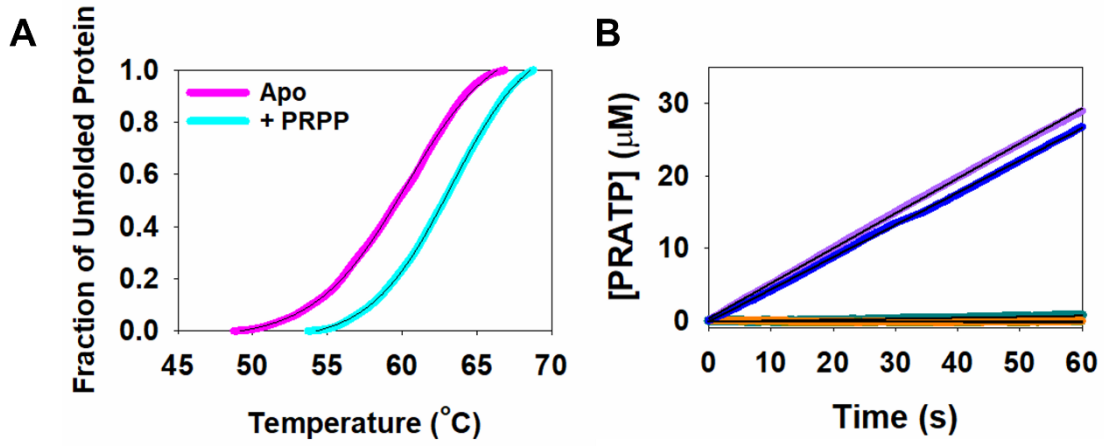

Figure 4.26 DSF and kinetic characterisation of R32A/R56A/K57A PaHisG$_S$. (A) DSF-based thermal denaturation of R32A/R56A/K57A PaHisG$_S$. Traces are averages of three independent measurements. (B) Product formation time-courses from reactions catalysed by R32A/R56A/K57A *Pa*HisG$_S$ (10 μM) (orange), R32A/R56A/K57A PaHisG$_S$ (5 μM) with PaHisZ (20 μM) (teal), R32A *Pa*ATPPRT (0.49 μM) (blue) and R56A *Pa*ATPPRT (0.79 μM). Traces are averages of at least two independent measurements. Solid black lines in (A) are data fitted to Equation 2.6. Solid black lines in (B) are linear regressions of data.

The ability of R32A/R56A/K57A *Pa*HisG$_S$ to catalyse formation of PRATP in the presence and absence of *Pa*HisZ was subsequently evaluated, Figure 4.26B and Table 4.10. PRATP formation was not detectable for reactions catalysed by R32A/R56A/K57A *Pa*HisG$_S$ in the absence of *Pa*HisZ. Upon addition of excess *Pa*HisZ, a low level of PRATP formation was detected. This rate of product formation is approximately 670-, 337- and 226-fold below that of WT, R32A, and R56A *Pa*ATPPRT, respectively. Ultimately, this data demonstrated that the activity of R32A/R56A/K57A *Pa*HisG$_S$ cannot be allosterically recovered by *Pa*HisZ. This finding is consistent with the hypothesis that at least one of R32 or R56 is required for catalysis by *Pa*ATPPRT.

Table 4-10. Rates of PRATP synthesis from reactions catalysed by R32A/R56A/K57A *Pa*HisG$_S$ in the presence and absence of *Pa*HisZ.

***Pa*HisG$_S$ Variant**	***v*/E$_T$ (s^{-1})**
R32A/R56A/K57A *Pa*HisG$_S$	No Data
R32A/R56A/K57A *PaHisG$_S$* + *Pa*HisZ	0.0027 ± 0.0008
R32A *Pa*ATPPRT	0.91 ± 0.08
R56A *Pa*ATPPRT	0.61 ± 0.00

Values are mean ± standard error of at duplicate measurements

4.15 Chapter summary

Ultimately, the work described in this chapter highlighted that stabilisation of the pyrophosphate leaving-group by R32 and R56 is a key feature of catalysis by *Pa*HisG$_S$ and *Pa*ATPPRT. R32A and R56A *Pa*HisG$_S$ were catalytically impaired whilst the rate of the chemical step was diminished in reactions catalysed by R32A and R56A variants of *Pa*ATPPRT compared with WT *Pa*ATPPRT. Upon consideration of these findings in context with the conclusions from the molecular dynamic simulations performed by Dr Marina Corbella , it was proposed that the increase in the rate of interconversion between ternary complexes observed upon allosteric activation of *Pa*HisG$_S$ by *Pa*HisZ can be at

least partially ascribed to *Pa*HisZ inducing a change in the protein conformational ensemble, in order that conformations with R32 and R56 are primed to accept the pyrophosphate leaving-group are sampled more frequently. Electrostatic pre-organisation of the enzyme active site is an established pillar of enzyme catalysis and the stance adopted here is consistent with modern conceptualisations of catalysis which view proteins as dynamic molecules[171,172]. A similar mode of activation to that proposed here was recently reported by Bunzel and colleagues (2021) and Otten and colleagues (20 21) who demonstrated catalytic enhancement of computationally designed KEMP eliminases, achieved via directed evolution, can be linked to narrowing of the conformational landscape such that a conformation with a pre-organised active site is favoured[173,174]. Furthermore, the ability of allosteric modulators to influence the protein conformational landscape is established[41–44].

An unexpected observation in this work was that catalytically impaired R32A and R56A *Pa*HisG$_S$ can be allosterically rescued by *Pa*HisZ. The *Pa*HisG$_S$-*Pa*HisZ interface is found over 20 Å away from the active site[40]. Whilst, chemical rescue of catalytically impaired mutant enzymes by small molecules is commonly observed[164–166], the rescue of catalytically compromised *Pa*HisG$_S$ by *Pa*HisZ and/or *Ab*HisZ appears to be unique as the recovery of activity is mediated via an allosteric effector. A literature search for similar phenomena identified that activity of a catalytically impaired S99T variant of human propyl isomerase, CypA, can be partially rescued via mutations that lie outside the active site[177]. The catalytic impairment of S99T CypA was attributed to a decrease in the rate of interconversion between conformational states whilst allosteric recovery of activity was attributed to restoration of the fast rate of interconversion between these conformations[177]. The literature search also identified a report of recovery of a catalytically compromised E109A variant of the β-subunit of tryptophan synthase mediated via CsCl which was also linked to stabilisation of an activated enzyme conformation[178]. Finally, molecular dynamics simulations indicated that catalytic impairment of an R308K variant of glucokinase could be attributed to inability of the enzyme to efficient sample the catalytically competent closed conformation[179,180]; interestingly, molecular dynamics simulations further suggested that the presence of the allosteric activator, YNKGKA4, R308K glucokinase can sample the closed conformation with similar efficiency as WT glucokinase[180]. Although, it appears that this hypothesis

has not yet been experimentally tested. Upon consideration of the above examples, it was concluded that whilst allosteric rescue of catalytically impaired R32A and R56A *Pa*HisG$_S$ by *Pa*HisZ and/or *Ab*HisZ appears to be the first confirmed example of rescue of catalytically impaired mutants modulated via an allosteric effector, the proposal that *Pa*HisZ and *Ab*HisZ mediate this recovery by moderating the conformational sampling of the remaining active site arginine aligns well with previous observations of recovery of catalytically comprised enzymatic variants via methods that manipulate the protein conformational landscape.

In conclusion, this work identified that R32 and R56 of *Pa*HisG$_S$/*Pa*ATPPRT are important for the chemical step of catalysis and it was proposed that allosteric activation of *Pa*HisG$_S$ by *Pa*HisZ includes biasing the protein conformational landscape in order that conformations with these residues in place to stabilise the pyrophosphate leaving-group are sampled more frequently. Furthermore, in the presence of *Pa*HisZ, R32 and R56 can somewhat compensate for loss of the other.

Chapter 5 PRADP is a substrate of *Pa*HisI but not *Pa*HisE

5.1 Chapter introduction

After PRATP is produced from PRPP and ATP by ATPPRT, the subsequent pyrophosphohydrolysis and cyclohydrolysis reactions of the histidine biosynthetic pathway are catalysed by HisE and HisI, respectively[18], Figure 5.1A. In *P. arcticus*, and in many other organisms, HisE and HisI activities are encoded by a single polypeptide chain termed HisIE. This bifunctional enzyme is composed of a C-terminal pyrophosphohydrolase domain (HisE) and an N-terminal cyclohydrolase domain (HisI) (reviewed in Chapter 1).

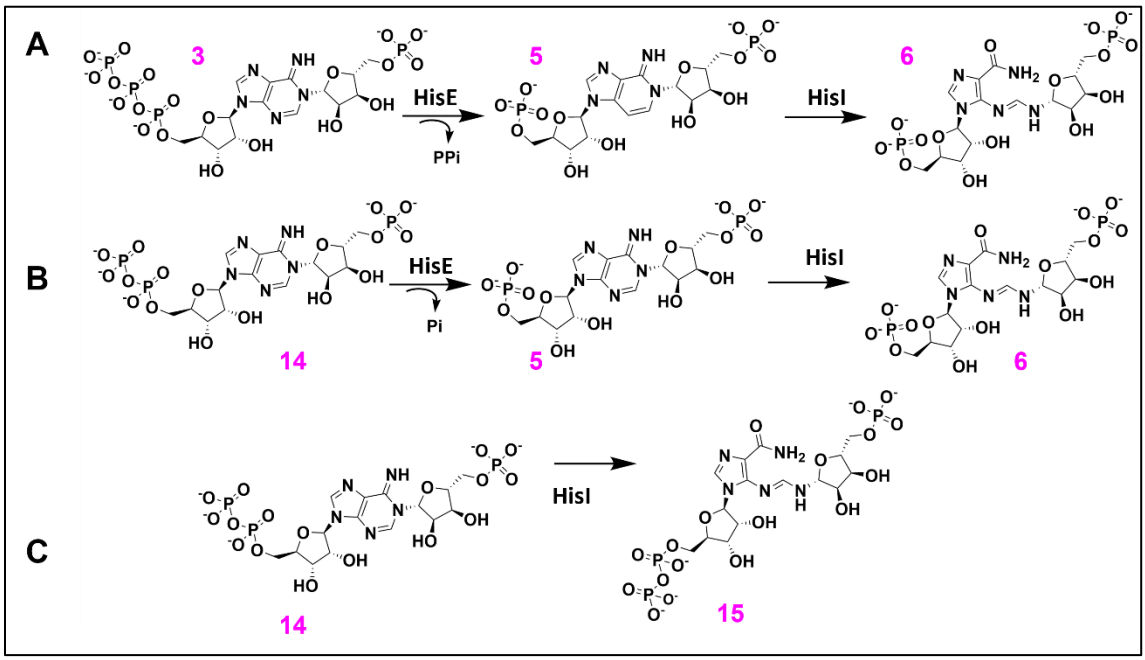

Figure 5.1 Possible products from reactions catalysed with *Pa*HisIE with PRATP and PRADP as substrates. (A) Reaction catalysed by HisIE with PRATP as a substrate. (B and C) Possible products from reactions catalysed by HisIE with PRADP as a substrate. PRATP **3**, PRAMP **5**, ProFAR **6**, PRADP, **14**, Pro-phosphoribosylforminio-5-aminoimidazole-4-carboxamide ribonucleoside disphosphate **15**. Compound numbering is according to Figure 1.1.

In Chapter 3, it was demonstrated that ADP is a substrate of *Pa*HisG$_S$ which catalyses formation of PRADP in place of the native product, PRATP. Dr Catherine. M. Thomson, a former PhD student in the da Silva laboratory, subsequently confirmed that ADP is also a substrate of *Pa*ATPPRT (K_M^{ADP} = 0.68 ± 0.09 mM, k_{cat} = 2.6 ± 0.4 s^{-1})[181]. It was

hypothesised that PRADP, the product of reactions catalysed by either *Pa*HisG$_S$ or *Pa*ATPPRT with ADP, may be a substrate of the pyrophosphohydrolase domain of *P. arcticus* HisIE, henceforth referred to as *Pa*HisE. It has previously been shown that the dimeric α-dUTPases, which belong to the same protein superfamily as HisE and catalyse pyrophosphohydrolysis of dUTP generating dUMP and pyrophosphate as products, can accept dUDP as a substrate[54]. If PRADP is accepted by *Pa*HisE as a substrate, the most likely products of the reaction would be phosphate and PRAMP, the substrate of the next enzyme in the histidine biosynthetic pathway, HisI, Figure 5.1B. Thus, if PRADP is a substrate of *Pa*HisE, histidine biosynthesis within *P. arcticus* could, in theory, be initiated from either ADP or ATP. As previously eluded to, the low intracellular concentration of ADP relative to ATP indicates that ATP is the primary substrate of *Pa*HisG$_S$ and *Pa*ATPPRT *in vivo*, hence, even if PRADP is a substrate of *Pa*HisE *in vitro*, this would not suggest that histidine biosynthesis is commonly initiated from ADP *in vivo*. Alternatively, PRADP could act as a substrate solely for the cyclohydrolase domain of *P. arcticus* HisIE, henceforth referred to as *Pa*HisI, Figure 5.1C, or may not react at all in the presence of *Pa*HisIE.

Bifunctional HisIE is a possible target for development of novel antimicrobial agents against key resistant bacteria (reviewed in Chapter 1) and a model system to study the advantages of gene fusion for catalysis, however, no kinetic characterisation of bifunctional HisIE had been reported in the literature prior to this work. It was envisioned that elucidating the minimal substrate requirements of HisE and HisI from *P. arcticus* could aid future mechanistic characterisation(s) and inhibitor development towards other bifunctional HisIE enzymes. The aim of this chapter was to establish if PRADP is a substrate of *Pa*HisIE.

5.2 Purification of *Pa*HisIE

Previous attempts to purify *Pa*HisIE by Dr Teresa F. G. Machado indicated that *Pa*HisIE could not be purified via Ni^{2+}-affinity chromatography as *Pa*HisIE with the His-tag cleaved still tightly binds Ni^{2+}-resin, and cannot be easily separated from residual His-tagged *Pa*HisIE, TEVP, and other proteins that bind to the column. Wang and colleagues also reported that *S. flexerni* HisIE without a His-tag sticks to Ni^{2+} resin[70]. It was decided

to purify *Pa*HisIE without an affinity tag. Untagged *Pa*HisIE in pJexpress411 was provided by Dr Teresa F. G. Machado.

A strategy for *Pa*HisIE purification was subsequently devised. The first step of purification was an ammonium sulphate precipitation. Ammonium sulphate precipitation is a long-established technique, which capitalises on the differing solubilities of a protein of interest relative to contaminants[182]. In this case, *Pa*HisIE was determined to be soluble in 1.5 M ammonium sulphate, whereas some contaminating proteins were "salted-out", Figure 5.2A. Subsequent purification employed a series of column chromatography steps including: medium and high resolution anion exchange (Figures 5.2B, 5.2C and 5.2F), Zn^{2+}- affinity (figure 5.2D) and size-exclusion chromatography (figure 5.2E) columns. After each purification step, SDS-PAGE was performed to identify appropriate fractions for further purification. After the final high-resolution anion exchange step, *Pa*HisIE was present without major contaminants, Figure 5.2F.

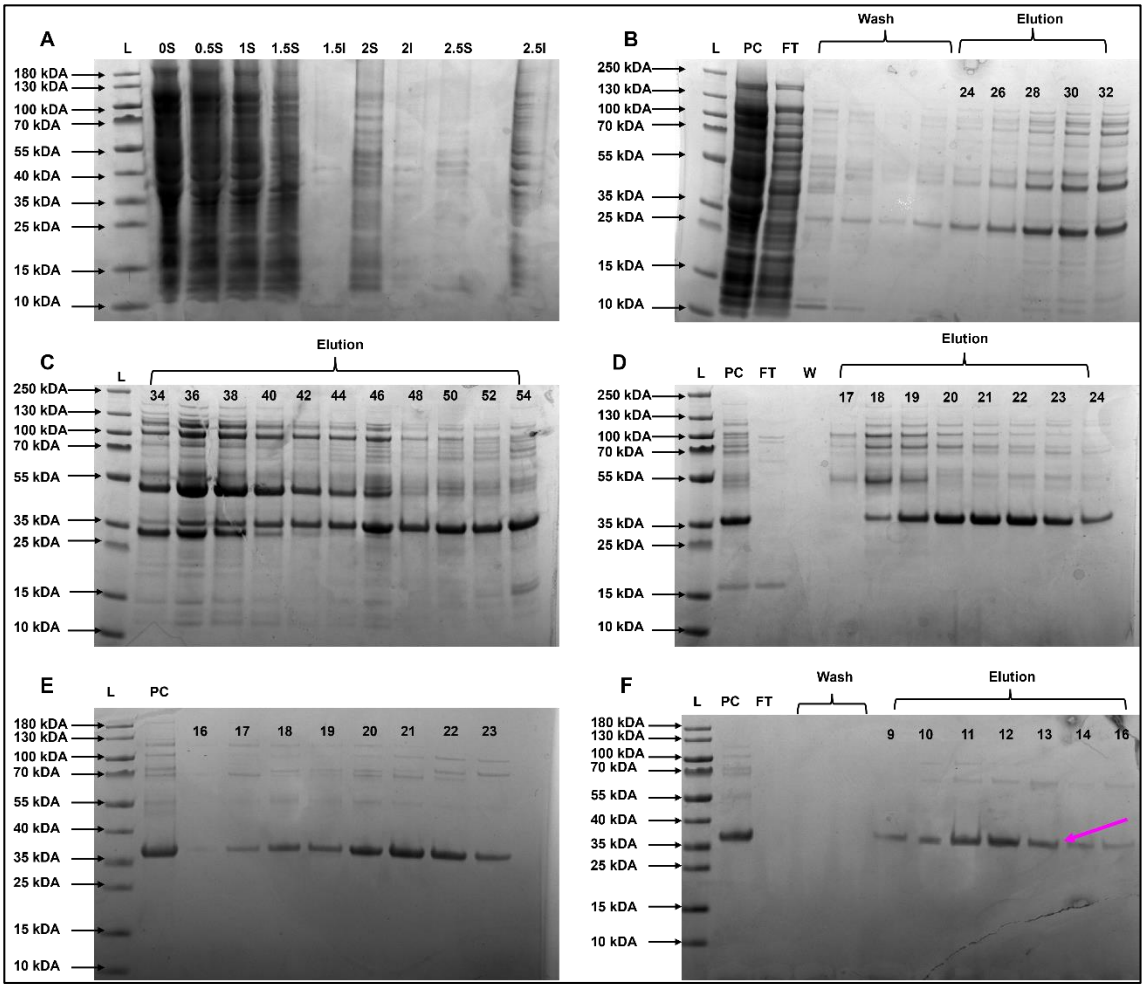

Figure 5.2. SDS-PAGE gels from *Pa*HisIE purification. SDS-PAGE gels with protein ladder (either PageRuler Plus Prestained [B, C & D] or PageRuler Prestained [A, E & F]) carried out after each purification step. (A) SDS-PAGE of cell lysate containing *Pa*HisIE with different concentrations of ammonium sulfate. *Pa*HisIE is soluble in 1.5 M ammonium sulfate whilst some contaminants are "salted-out". SDS-PAGE of fractions from column chromatography using (B and C) HiTrapQ FF (2 x 5 mL columns), (D) Zn^{2+}-affinity (HisTrap FF charged with ZnCl), (E) Sephracyl S200 HR and (F) HiTrapQ HP columns are shown. Fractions 9-13 were pooled after the HiTrapQ HP column. Numbers in (A) indicate molar concentration of ammonium sulfate and "S" and "I" denote soluble and insoluble fractions, respectively. L corresponds to protein ladder, PC refers to pre-column and FT is column flow-through. Numbers shown under elution refer to fraction number. The estimated molecular weight of *Pa*HisIE is 31,304 Da. Pink arrow denotes *Pa*HisIE.

A sample of purified protein was submitted to the BSRC protein mass-spectrometry facility for protein identification. Briefly, the sample was digested with trypsin and MS/MS analysis of the tryptic peptides confirmed that purified protein was *Pa*HisIE (sequence coverage = 65%), Appendix 1.

5.3 Biophysical characterisation of *Pa*HisIE

A brief biophysical characterisation of *Pa*HisIE was carried out in order to determine the oligomeric state and thermal stability of *Pa*HisIE. The oligomeric state of *Pa*HisIE was investigated via dynamic light scattering (DLS), Table 5.1. DLS correlates the intensity of light scattered to particle size[183]. Brownian motion of molecules in solution causes the intensity of the light they scatter to fluctuate and by analysing these fluctuations, it is possible to determine the velocity of molecules in solution[183]. The size (hydrodynamic diameter) of a molecule can be extracted by inputting the velocity to the Stokes-Einstein equation[183]. The molecular weight of *Pa*HisIE was estimated as 52 ± 20 kDa via DLS though a small proportion of the sample (1.9%) was predicted to exist in a higher oligomeric state, likely reflecting some aggregation of the protein. A very large standard deviation was observed on the estimated molecular weight extracted from the DLS experiment which prevents unambiguous assignment of a single oligomeric species from DLS data alone. The theoretical monomeric mass of *Pa*HisIE is 31,304 Da, thus, the DLS data indicate that *Pa*HisIE forms either mostly monomers or mostly dimers or a mixture of monomers and dimers in solution. Previous work has demonstrated that HisI from *M. vannielii* and *M. thermoautotrophicum* purify with Zn^{2+} tightly bound in the active site. Structural analyses have confirmed that the Zn^{2+}-binding site of HisI and bifunctional HisIE is composed of cysteines from two distinct HisI or HisIE polypeptide chains (reviewed in introduction)[63,64,70,71]. After activity studies it was hypothesised that *Pa*HisIE also purifies with Zn^{2+} bound, hence, it was considered likely that *Pa*HisIE exists exclusively as dimers in solution and that the large standard deviation observed is a technical artefact perhaps due to aggregation or debris within the sample or imperfections in the quartz cuvette used for measurement.

Table 5-1 DLS studies of *Pa*HisIE. The estimated molecular weight is listed alongside the sizes of the particles present in the sample and the mass (%) per volume of each of these species.

	Estimated MW (kDA)	**Mass (%)**	**Z-Average (nm)**
***Pa*HisIE**	52 ± 20	98.1%	6.4 ± 0.9
	500 ± 70	1.9%	17 ± 2

Values are mode ± standard deviation of triplicate measurements.

DSF was performed to evaluate the thermal stability of *Pa*HisIE, Figure 5.3. DSF data are biphasic and most likely reflect unfolding of at least two distinct domains with distinct T_M values[184]. The first T_M value lies between 40 – 50 °C which is similar to reported T_Ms for enzymes from other psychrophilic organisms including α-amylase from *Pseudoalteromonas haloplanktis* (44 °C)[185], adenylate kinase from *Bacillus subtilis* (48 °C) [186] and DNA ligase from *Psychromonas sp*[187]. An additional T_M value lies between 60 – 70 °C which is similar to the T_M reported for *Pa*HisG$_S$ in Chapters 3 and 4.

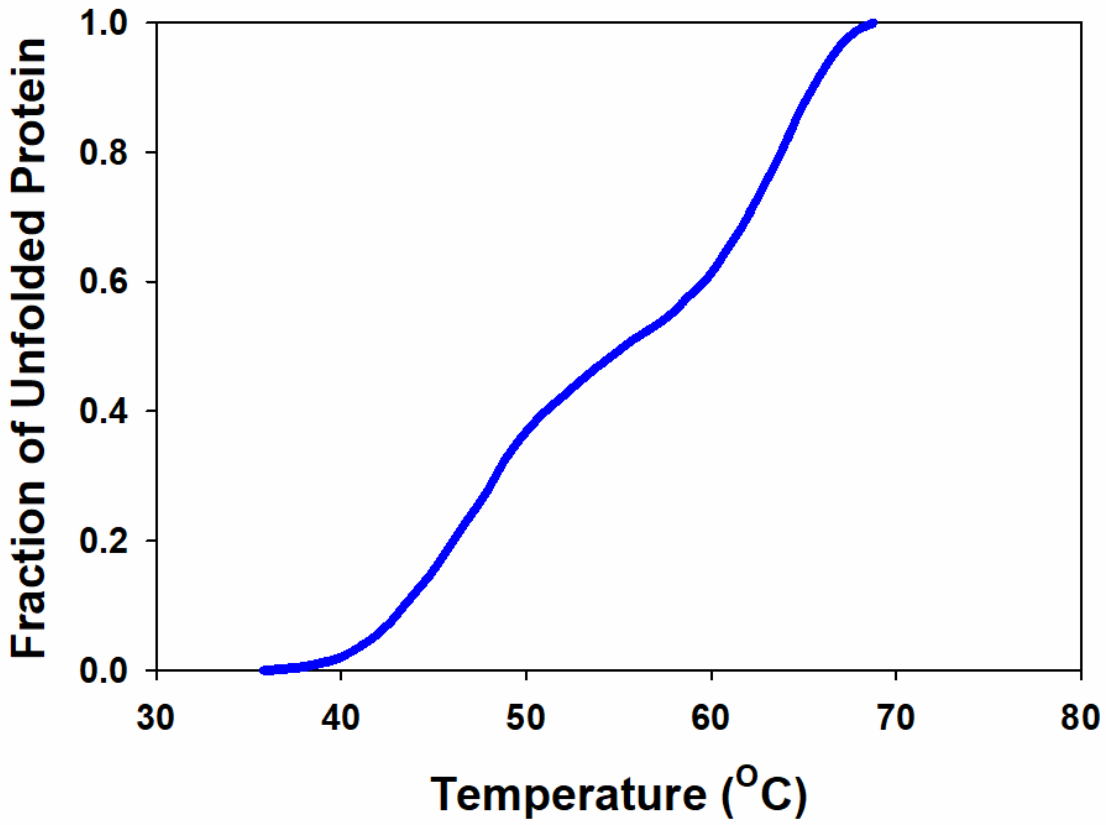

Figure 5.3 Biphasic DSF thermal denaturation curve of *Pa*HisIE. Data are average of triplicate measurements.

5.4 Preliminary studies of *Pa*HisIE activity in a coupled system with *Pa*ATPPRT

*Pa*HisIE activity was initially assayed as part of a coupled system with *Pa*ATPPRT, Figure 5.4 and Table 5.2. Briefly, either ATP or ADP and PRPP were incubated with an excess of *Pa*ATPPRT in the presence and absence of *Pa*HisIE and absorbance at 300 nm, corresponding to ProFAR formation, was recorded. d'Ordine and colleagues previously defined the extinction co-efficient for the product of cyclohydrolase reaction catalysed by HisI, ProFAR, ($\Delta\varepsilon$ = 6700 M^{-1} cm^{-1} [pH 7.5]) at 300 nm[63]. Control reactions with no *Pa*HisIE were subtracted from data. A *Pa*HisIE-dependent rate of reaction was extracted from data, Figures 5.4B and 5.4D. These preliminary data suggest that PRADP is a substrate of *Pa*HisIE. The data from spectrophotometric assay presented here cannot distinguish if PRADP is a substrate of the *Pa*HisE and the *Pa*HisI domain or just the

*Pa*HisI domain. When corrected for total protein concentration the rate of product formation is approximately 13-fold greater in reactions catalysed with ATP as a substrate compared with those with ADP as a substrate.

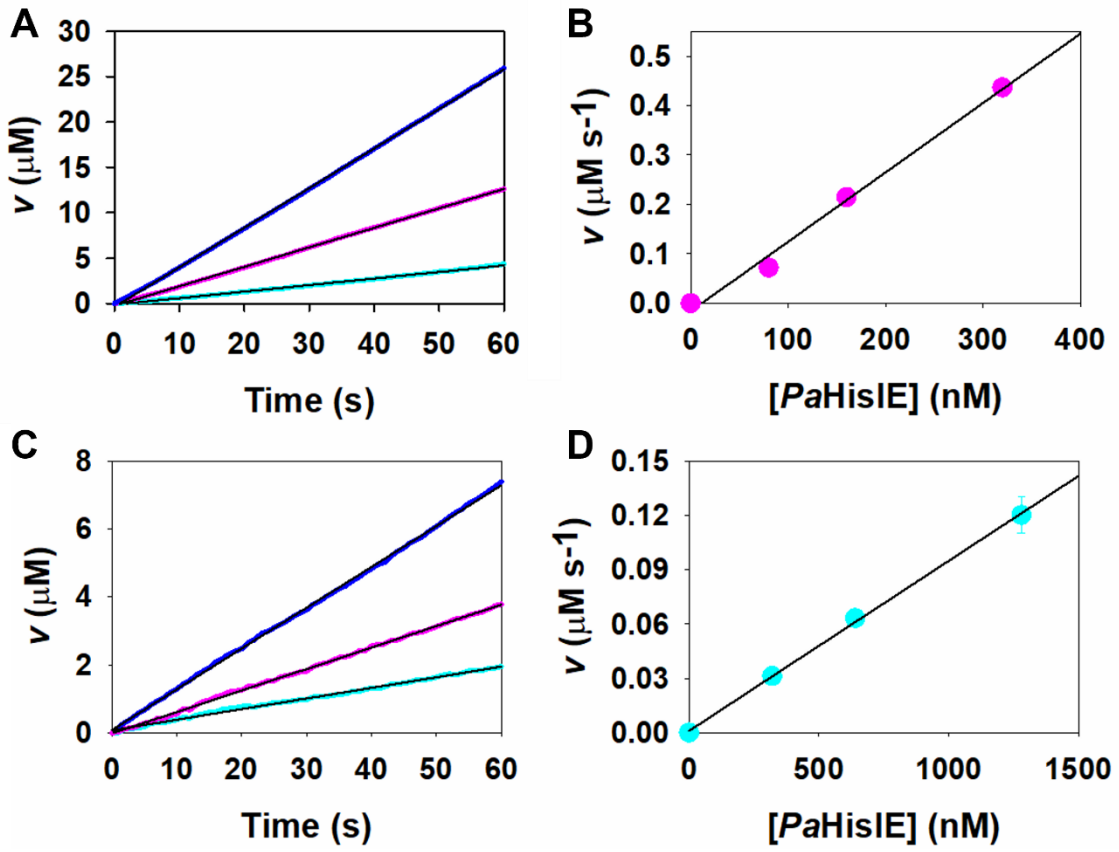

Figure 5.4 *Pa*HisIE activity assay with *Pa*ATPPRT. (A and C) Time-courses of product formation upon incubation of either (A) ATP (5.6 mM) or (C) ADP (5.6mM) with PRPP (2 mM) and *Pa*ATPPRT (8.9 μM) with $MgCl_2$ (15 mM) at pH 7.5 in the presence of varying concentrations of *Pa*HisIE. Product formation was recorded with either (A) 80 (cyan), 160 (magenta) and 320 (blue) nM of *Pa*HisIE or (C) 320 (cyan), 640 (magenta) or 1280 (blue) nM of *Pa*HisIE. (B and D) Rates extracted from time-courses recorded with ATP (B) and ADP (D) as substrates were plotted against enzyme concentration. Solid black lines are linear regressions of data. Data are average of two replicates. Data points are mean ± standard error

Table 5-2. Rates of product formation time-courses upon incubation of either ATP or ADP with PRPP in the presence of *Pa*HisIE and *Pa*ATPPRT

ATP		**ADP**	
***Pa*HisIE (nM)**	***v* (µM s^{1})**	***Pa*HisIE (nM)**	***v* (µM s^{-1})**
80	0.072 ± 0.002	**320**	0.031 ± 0.003
160	0.214 ± 0.002	**640**	0.0632 ± 0.0001
320	0.4365 ± 0.003	**1280**	0.12 ± 0.01

Values are mean ± standard error of duplicate measurements.

5.5 Enzymatic synthesis and purification of PRATP and PRADP

For a more thorough biochemical investigation of the reaction catalysed by *Pa*HisIE with the native substrate PRATP and the alternative substrate PRADP both substrates were enzymatically synthesised and purified. PRATP and PRADP were produced from PRPP and either ATP or ADP, respectively, by *Pa*$HisG_S$ using a method previously defined in the da Silva Laboratory[40]. A novel purification for extracting PRATP and PRADP from reaction mixtures was developed in this work. PRATP and PRADP must be separated from starting materials to accurately determine concentration of these compounds spectrophotometrically.

Briefly, reaction mixtures containing PRATP were loaded onto a 20 mL HiTrap Q HP column equilibrated with water, the column was washed with 1 CV of water and 2 CV of 16% ammonium bicarbonate (1 M), ATP and PRATP were eluted across a 20 CV linear gradient from 16 to 30% ammonium bicarbonate (1M), Figure 5.5A. Absorbance at 220, 260 and 290 nm was monitored. Two peaks were observed in the elution, Figure 5.5A. The first peak which eluted at approximately 22% ammonium bicarbonate (1 M)

exhibited a low ratio of absorbance at 290 nm: 260 nm, assumed to be ATP, whereas the 2nd peak which eluted at approximately 24% ammonium bicarbonate (1 M) exhibited a greater ratio of absorbance at 290 nm: 260 nm, assumed to be PRATP. Fractions from each peak were pooled and lyophilised. ^{31}P-NMR was spectra were collected on a sample suspected to contain PRATP, Figure 5.6. The distinctive chemical shift at approximately 3.3 ppm, which represents the phosphoribosyl moiety of PRATP, (discussed in Chapter 3) was observed, confirming that the sample contained PRATP. Chemical shifts corresponding to the triphosphate moiety of PRATP were also readily assigned, Figure 5.6. The sample was further analysed by high-resolution LC-MS which demonstrated that the sample contained a species with m/z 717.9947, in good agreement with the theoretical m/z of PRATP, 717.9971, Figure 5.7. LC-MS was performed by Dr Alison Dickson formerly of the Czekster laboratory.

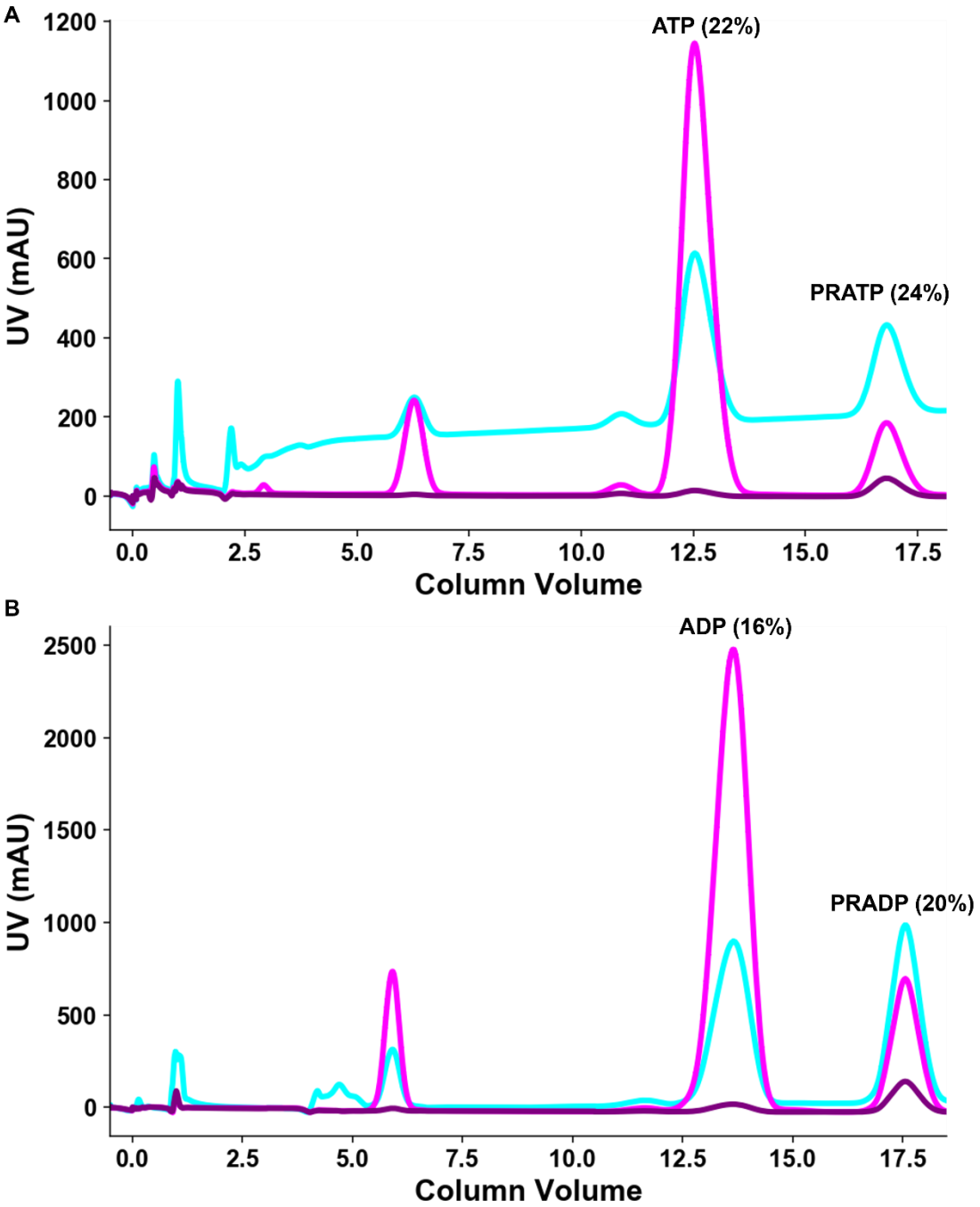

Figure 5.5 Chromatogram depicting separation of either (A) PRATP or (B) PRADP from starting materials on a HiTrapQ HP column. Absorbance at 220 (cyan), 260 (magenta) and 290 (purple) nm was recorded. Peaks proposed to represent ATP, ADP, PRATP and PRADP are labelled.

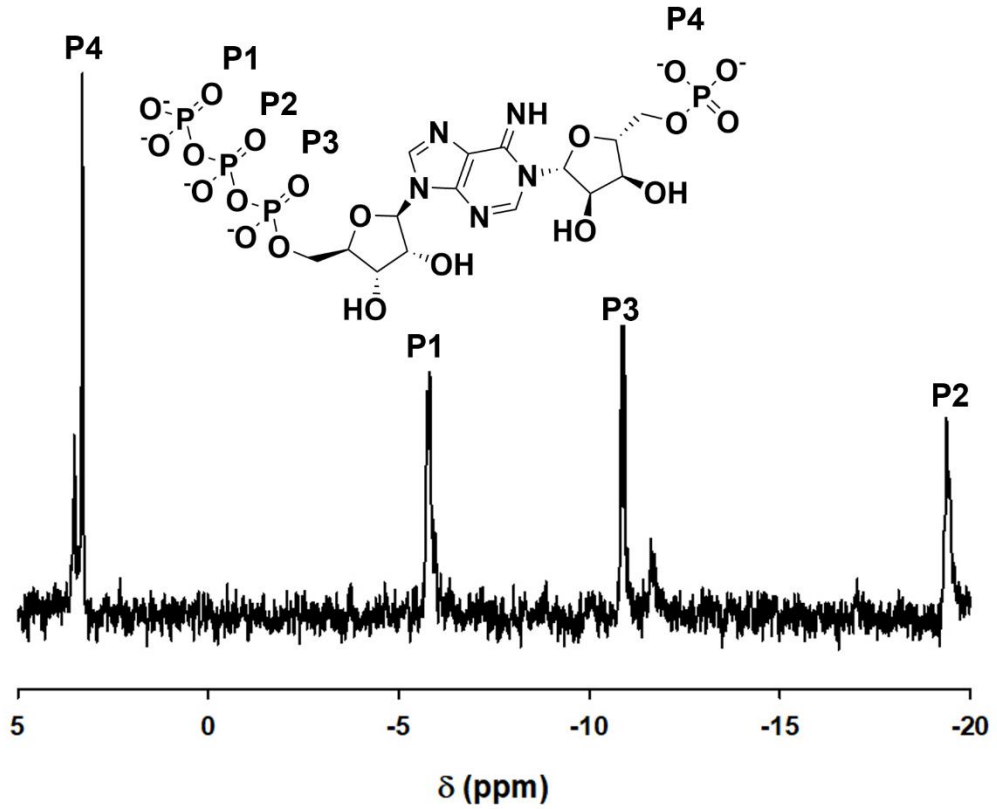

Figure 5.6 ^{31}P-NMR spectrum of pooled fractions containing PRATP. Assignments of chemical shifts (δ) in ppm and J values in Hz: **δ** 3.31 (s, **P4**); -5.78 (d, *J* = 13.3 Hz, **P1**); -10.88 (d, *J* = 15.6 Hz, **P3**); -19.12 - -19.68 (m, **P2**)

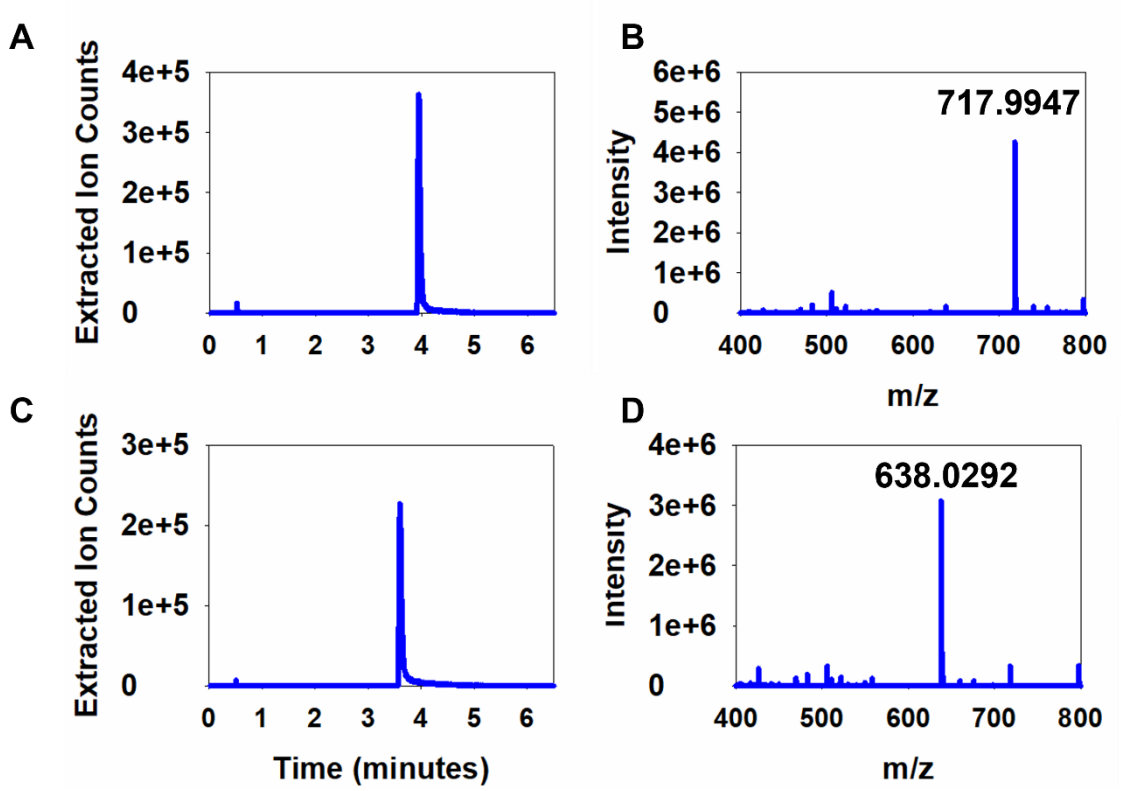

Figure 5.7 High-resolution LC-MS analysis of enzymatically synthesised PRATP and PRADP purified via FPLC.Analysis was performed on an Atlantis Premier BEH C18 AX column on a Waters ACQUITY UPLC system coupled to a Xevo G2-XS QToF mass spectrometer equipped with an ESI source. HPLC was performed in ammonium acetate pH 6, acetonitrile and ammonium acetate pH 10. Extracted ion chromatograms for either (A) PRATP (expected m/z 717.9971) or (C) PRADP (expected m/z 638.0307) are shown alongside m/z spectra of samples containing either (B) PRATP or (D) PRADP. Spectra were acquired in negative mode. LC-MS was performed by Dr Alison Dickson.

Similarly, reaction mixtures containing PRADP were loaded onto a 20 mL HiTrap Q HP column equilibrated with water, the column was washed with 1 CV of water and 5 CV of 10% ammonium bicarbonate (1 M), ATP and PRATP were eluted across a 20 CV linear gradient from 10 to 30% ammonium bicarbonate (1M), Figure 5.5B. Again two peaks were observed in the elution, Figure 5.5B. The first peak was eluted with 16% ammonium bicarbonate (1M) and exhibited a low ratio of absorbance at 290 nm: 260 nm, assumed to be ADP, whereas the second peak was eluted with 20% ammonium bicarbonate (1M) and exhibited a high ratio of absorbance at 290 nm: 260 nm, assumed to be PRADP. Fractions suspected to contain PRADP were pooled and lyophilised. A sample was analysed by LC-MS, performed by Dr Alison Dickson, Figure 5.7. LC-MS confirmed that the sample contained a species with m/z 638.0292, in good agreement with the theoretical m/z of

contained a species with m/z 638.0292, in good agreement with the theoretical m/z of PRADP, 638.0307 Da.

5.6 Steady-state kinetics of reactions catalysed by *Pa*HisIE

An increase in absorbance at 300 nm, corresponding to ProFAR formation, was detected upon incubation of enzymatically synthesised and purified PRATP with *Pa*HisIE in the presence of Mg^{2+}. Control reactions were performed in the absence of *Pa*HisIE and only negligible background activity was detected. Addition of exogenous Zn^{2+} resulted in precipitation and it was hypothesised that *Pa*HisIE purifies with Zn^{2+} bound, as has been reported for other HisI[63,64] and HisIE[70,71] enzymes. The activity was dependent on enzyme concentration, Figures 5.8, Table 5.3. Furthermore, when activity is monitored until a plateau in A_{300} is reached, the calculated molar concentration of ProFAR produced equates to approximately 71% of the molar concentration of PRATP added to the reaction, Figure 5.8C. It was expected that both reactions catalysed by *Pa*HisIE are irreversible, however, incomplete consumption could be attributed to product inhibition. Overall, these preliminary studies indicate that the enzymatically synthesised and purified PRATP is a suitable substrate for determining the steady-state kinetics of reactions catalysed by *Pa*HisIE.

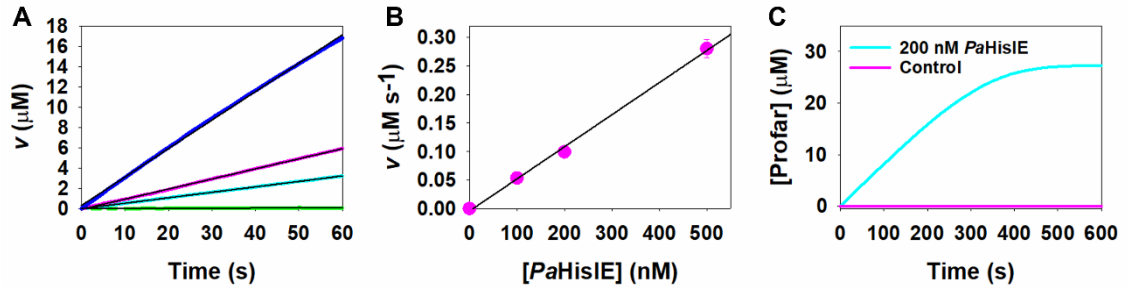

Figure 5.8 *Pa*HisIE activity with purified PRATP. (A) Time-courses of product formation upon incubation of PRATP (38 μM) with 15 mM $MgCl_2$ in the presence of varying concentrations *Pa*HisIE at pH 7.5. Product formation was recorded with 0 (green), 100 (cyan), 200 (magenta) and 400 (blue) nM of *Pa*HisIE. (B) Rates extracted from time-courses were plotted against enzyme concentration. (C) Reactions with 200 nM *Pa*HisIE were also monitored until product formation plateaued. Solid black lines represent linear regressions of data. Data are average of two replicates. Data points are mean ± standard error. The difference in absorbance between control and reaction in (C) equates to 27 μM ProFAR

Table 5-3. Rates of product formation from reactions catalysed by *Pa*HisIE with PRATP as a substrate.

[*Pa*HisIE] (nM)	***v* (μM s^{-1})**
100	0.0537 ± 0.0002
200	0.994 ± 0.003
500	0.28 ± 0.02

Values are mean ± standard error of duplicate measurements.

The steady-state kinetic parameters of reactions catalysed by *Pa*HisIE with PRATP were determined at 20 °C, Figure 5.9 and Table 5.4. Reactions k_{cat} of 1.04 ± 0.01 s^{-1} and a K_M of 50 ± 1 μM. The k_{cat} reported here is lower than the k_{cat} reported for activated *Pa*ATPPRT, which catalyses the flux-controlling step of histidine biosynthesis (Chapters 1: 2.1 – 2.5 s^{-1} and Chapter 2: 1.7 s^{-1}). In contrast to *Pa*ATPPRT, which likely operates under conditions which most closely resemble k_{cat} *in vivo*, k_{cat}/K_M, is likely the relevant steady-state kinetic parameter *in vivo*, due to the limiting intracellular concentrations of pathway intermediates PRATP and PRAMP. The k_{cat} obtained here is similar to the v/E_T reported from the coupled assay (Table 5.2).

PRADP is a substrate of PaHisI but not PaHisE

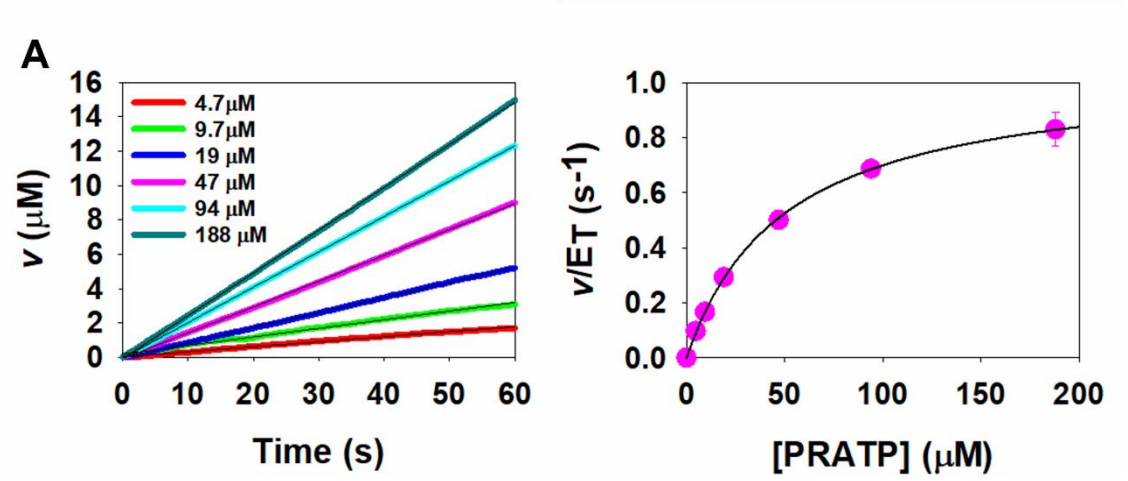

Figure 5.9 Steady-state kinetics of *Pa*HisIE catalysed reactions with PRATP as a substrate. (A)Time-courses of product formation upon incubation of *Pa*HisIE (300 nM) with various concentrations of PRATP in the presence of 12 mM Mg^{2+} at pH 7.5. PRATP concentration is indicated in legend. (B) *Pa*HisIE saturation curve. Data are average of two replicates. Data points are mean ± standard error. Solid black lines in (A) are linear regressions of data and solid black line in (B) is data fitted to the Michaelis-Menten equation.

Table 5-4 *Pa*HisIE steady-state kinetic parameters with PRATP and PRADP as substrates.

Parameter	**PRATP**	**PRADP**
k_{cat} **(s^{-1})**	1.04 ± 0.01	0.043 ± 0.003
K_{PRAXP} **(μM)**	50 ± 1	100 ± 20
k_{cat}/K_{PRAXP} **(M^{-1} s^{-1})**	20800 ± 500	430 ± 90

Values are mean ±fitting error of duplicate measurements.

Upon incubation of PRADP with *Pa*HisIE in the presence of Mg^{2+}, time-courses of product formation exhibited a lag phase prior a linear phase, Figure 5.10. The duration of the lag phase was inversely proportional to substrate concentration. High concentrations of *Pa*HisIE (1.7 μM) were required to generate data of satisfactory quality for PRADP reactions. Upon inspection of the time-courses in Figure 5.10, one must conclude that the lag-phase occurs prior to the first turnover of substrate. If PRADP is accepted by *Pa*HisE as a substrate, such an observation may indicate that the reaction catalysed by the

pyrophosphohydrolase domain is rate-limiting, however, if PRADP were to be exclusively turned over by *Pa*HisI such an observation implies turnover of PRATP is slow enough that pre-steady state/approach to steady-state data can be captured without the requirement for stopped-flow apparatus. Substrate-dependent lag phases on approach to steady-state have previously been reported for uridine phosphorylase from *Trypanosoma cruzi*, although those data were captured with a stopped-flow spectrophotometer[188]. Steady-state kinetic parameters for reactions catalysed by *Pa*HisIE with PRADP as a substrate were determined, Figure 5.10 and Table 5.4. The k_{cat} and k_{cat}/K_M values of reactions with PRADP as a substrate are approximately 24- and 48-fold lower than those from reactions with PRATP as a substrate.

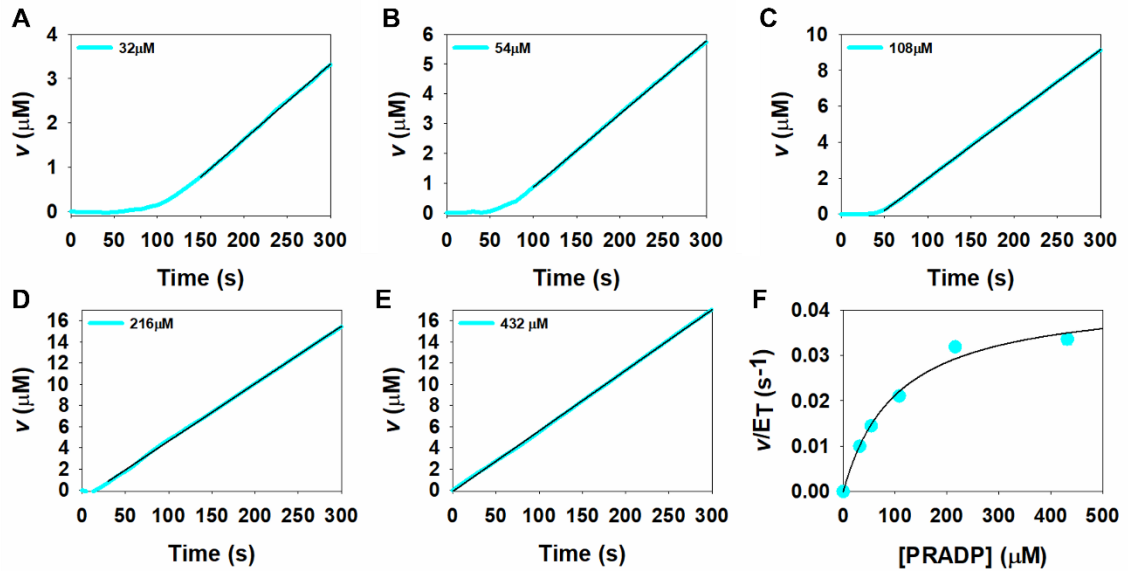

Figure 5.10 Steady-state kinetics of *Pa*HisIE catalysed reactions with PRADP as a substrate. (A - F) Time-courses of product formation upon incubation of *Pa*HisIE (1.7 μM) with various concentrations of PRATP in the presence of 12 mM Mg^{2+}. at pH 7.5. PRADP concentration is indicated in legend. Initial rates were extracted from linear phase only. (F) *Pa*HisIE saturation curve. Data are averages of two replicates. Data points are mean ± standard error. Solid black lines in (A – E) are linear regressions of data. Solid line in (F) is data fit to the Michaelis-Menten equation.

5.7 LC-MS analysis of reactions catalysed by *Pa*HisIE with PRADP and PRATP as substrates.

The products of reactions catalysed by *Pa*HisIE with PRADP and PRATP as substrates were analysed by LC-MS, performed by Dr Alison Dickson, Figure 5.11. A species with m/z 576.0724 was observed in reactions with PRATP as a substrate, in good agreement with the theoretical m/z of the expected product, ProFAR, 575.0750. Contrastingly, a species with m/z 656.0400 was the main product identified in reactions with PRADP as a substrate. This value is in good agreement with the theoretical m/z of pro-phosphoribosylformino-5-aminoimidazole-4-carboxamide ribonucleoside diphosphate, 656.0412, Figure 5.1C. These data indicate that PRADP is a substrate of *Pa*HisI, but not *Pa*HisE.

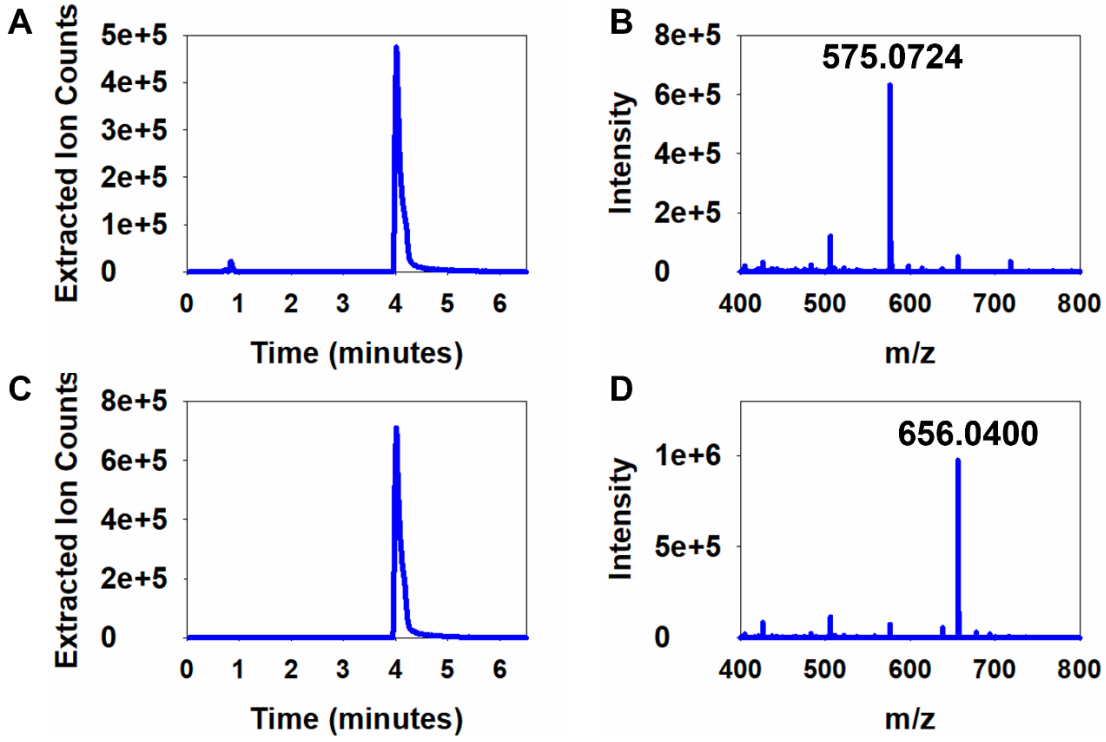

Figure 5.11 High-resolution LC-MS analysis of products from reactions catalysed by *Pa*HisIE with either PRATP or PRADP. Analysis was performed on an Atlantis Premier BEH C18 AX column on a Waters ACQUITY UPLC system coupled to a Xevo G2-XS QToF mass spectrometer equipped with an ESI source. Reaction components were separated in ammonium acetate pH 6, acetonitrile and ammonium acetate pH 10. Extracted ion chromatograms for either (A) ProFAR (expected m/z 575.0750) or (B) phosphoribosylformino-5-aminoimidazole-4-carboxamide ribonucleoside diphosphate (expected m/z 656.0412) are shown alongside m/z spectra from reactions catalysed by *Pa*HisIE with either (B) PRATP or (D) PRADP. Spectra were acquired in negative mode. LC-MS was performed by Dr Alison Dickson.

5.8 Chapter summary

In summary, this work represents the first characterisation of HisIE from *P. arcticus*. Activity was detected upon incubation of either ATP or ADP with PRPP in the presence of *Pa*ATPPRT and *Pa*HisIE. PRATP and PRADP were enzymatically synthesised and purified via anion exchange chromatography. The steady-state kinetic parameters of *Pa*HisIE catalysed reactions with PRATP and PRADP as substrates were determined. LC-MS performed by Dr Alison Dickson confirmed that the product of reactions catalysed by *Pa*HisIE with PRATP is ProFAR, however, reactions with PRADP produce a novel product, phosphoribosylformino-5-aminoimidazole-4-carboxamide ribonucleoside diphosphate. Unexpectedly, PRADP is a substrate of *Pa*HisI but not *Pa*HisE. The dimeric α-dUTPases, which belong to the same superfamily as HisE, can accept dUDP as a substrate[54]. Contrastingly, DR2231, another member of the α-helical pyrophosphohydrolase superfamily was shown to accept dUTP, but not dUDP as a substrate[58]. It is possible that HisE recognises and binds substrate more similarly to DR2231 compared with the dimeric α-dUTPases, however, in the absence of further data from HisE from a range of organisms, it is not possible to draw a generalised conclusion.

The findings from the LC-MS analysis necessitates that the steady-state kinetic parameters of *Pa*HisIE with PRADP as a substrate are reporting solely on the activity of the HisI domain. The k_{cat} and k_{cat}/K_M values suggest PRADP is a poor substrate of *Pa*HisI. The k_{cat} and k_{cat}/K_M from reactions catalysed by *Pa*HisIE with PRADP as a substrate were 24- and 48-fold lower than the k_{cat} and k_{cat}/K_M from reactions catalysed by *Pa*HisIE with PRATP as a substrate which encompass both the pyrophosphohydrolase and cyclohydrolase reactions.

Prior to this work, no steady-state kinetic parameters have been reported for HisE or bifunctional HisIE. Steady-state kinetic parameters have been reported from HisI from *Methanococcus vannielii* (k_{cat} = 4.1 s^{-1}, k_{cat}/K_M = 4.1 x 10^5 M^{-1} s^{-1}) and *Methanobacterium thermoautotrophicum* (k_{cat} = 8 s^{-1} , k_{cat}/K_M = 6 x 10^5 M^{-1} s^{-1}). Interestingly, whilst the k_{cat} reported here for reactions catalysed by *Pa*HisIE with PRATP as substrate is of a similar (~4-8 fold lower) magnitude to the values reported for *M. vannielii* and *M.*

thermoautotrophicum, the value of k_{cat}/K_M is ~19.7- and 28.8-fold lower than the values reported for *M. vannielii* and *M. thermoautotrophicum,* respectively[63,64].

Here, the steady-state kinetic parameters, k_{cat}, and k_{cat}/K_M, encompass reactions catalysed by both domains of *Pa*HisIE. From this data, it is not possible to speculate as to whether the pyrophosphohydrolase or cyclohydrolase is rate-limiting. It was anticipated that future characterisation of HisI and HisE domains split from a bifunctional enzyme alongside the full-length enzyme may lead to interesting insights to the catalytic mechanism of HisIE and evolutionary incentive for gene fusion.

Chapter 6 Biochemical characterisation of *Ab*HisIE

6.1 Chapter introduction

In the previous chapter, protocols to produce PRATP and to determine the activity of bifunctional HisIE were established. The subsequent work in the previous chapter demonstrated that PRADP is a substrate of *Pa*HisI but not *Pa*HisE, thus, provided the first reported insight into the substrate scope of bifunctional HisIE. This work sparked interest in kinetically characterising this complex bifunctional system, which has so far only been investigated structurally.

Bifunctional HisIE is a potential target for novel antimicrobial development in *A. baumannii* (reviewed in Chapter 1). Here, it was sought to carry out the first biochemical characterisation of bifunctional HisIE from *A. baumannii*, henceforth referred to as *Ab*HisIE, with a view to paving the way for future inhibitor development. More specifically, the aims of this chapter were to determine the kinetic parameters of bifunctional *Ab*HisIE and to probe the rate-limiting steps of this complex bifunctional system.

Previous to this work, no kinetic characterisation of a bifunctional HisIE or standalone HisE had been reported. A catalytic mechanism for monofunctional HisI had been proposed by d'Ordine and colleagues[65] which informed the work carried out in this chapter. The proposed mechanism entails nucleophilic attack at the C6 position of PRATP by a Zn^{2+}-activated water molecule followed by a series of proton transfers which leads to collapse of the tetrahedral intermediate and breakage of the C6-N1 bond[65] (reviewed in Chapter 1), Figure 6.1.

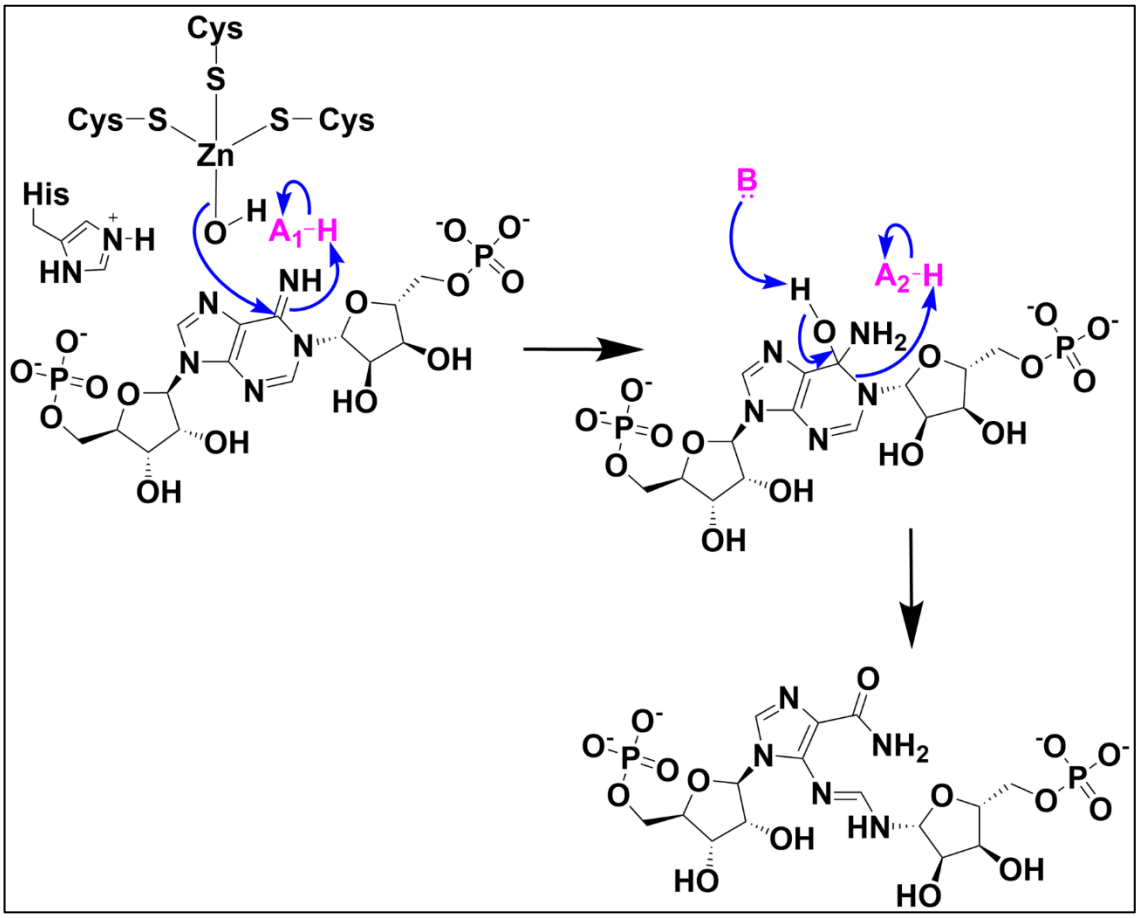

Figure 6.1 Catalytic mechanism of HisI. PRAMP **5**, ProFAR **6**. B denotes a, as yet unidentified, catalytic base. A_1-H and A_2-H represent, as yet unidentified, proton donors. The mechanism presented here is modified from the mechanism proposed by d'Ordine and colleagues[65]. Compounds are numbered according to Figure 1.1..

6.2 Production of *Ab*HisIE

The *Ab*HisIE-encoding sequence was successful cloned into a pJexpress414 vector via the Gibson Assembly method[113] and expressed in BL21 (DE3) cells. *Ab*HisIE was purified from cell lysate via a similar procedure to that previously described for *Pa*HisIE. In contrast to *Pa*HisIE, tests revealed *Ab*HisIE is insoluble in 1-2 M ammonium sulphate, Figure 6.2A. Fortunately, many contaminating proteins remained soluble in 1.5 M ammonium sulphate. In all further purifications ammonium sulphate was titrated into cell lysate until a concentration of 1.5 M was reached, after which the insoluble fraction was collected via centrifugation and *Ab*HisIE was returned to solution upon removal of ammonium sulphate by dialysis. Further purification employed a series of column

chromatography steps including: anion exchange (Figure 6.2B and 6.2C), Zn^{2+}-affinity (Figure 6.2D and 6.2E) and size-exclusion chromatography (Figure 6.2F) columns. After each purification step, SDS-PAGE was performed to identify appropriate fractions for further purification. After size-exclusion chromatography, bands representing both the monomeric (~30 kDA) and dimeric (~60 kDA) forms of *Ab*HisIE were present without major contaminants, Figure 6.2F. Trypsin digestion of both bands followed by MS/MS analysis of the tryptic peptides confirmed both bands contained *Ab*HisIE (~30 kDA band = 68% sequence coverage; ~60kDA band = 79% sequence coverage), Appendix 1.

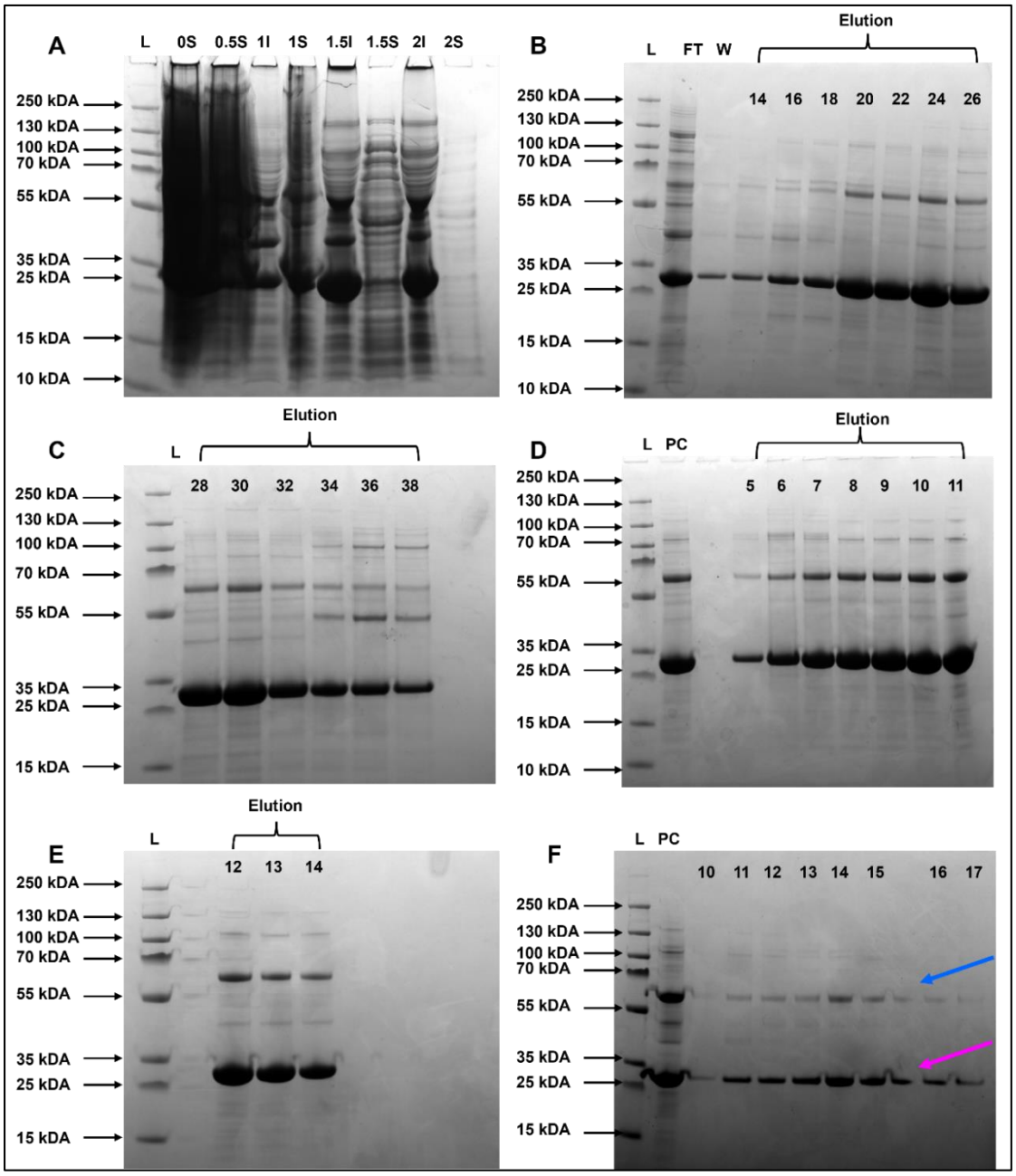

Figure 6.2 SDS-PAGE gels from *Ab*HisIE Purification. SDS-PAGE gels with protein ladder (PageRuler Plus Prestained [ThermoFisher]) carried out after each purification step. (A) SDS-PAGE of cell lysate treated with various concentrations of ammonium sulfate. *Ab*HisIE is insoluble at 1 - 2 M ammonium sulfate. SDS-PAGE of fractions from column chromatography using: (B and C) HiTrapQ FF coulmns (2 x 5 mL columns); (D and E) a Zn^{2+}-affinity column (HisTrap FF charged with ZnCl); and (F) a Sephracyl S200 HR column. Fractions 12-17 were pooled after size-exclusion chromatography. The band between 55 and 70 kDA in (F) was confirmed as an *Ab*HisIE dimer by mass-spectrometry. Numbers in (A) indicate molar concentration of ammonium sulfate. "S" and "I" denote soluble and insoluble fractions, respectively. L corresponds to protein ladder, PC refers to pre-column and FT is column flow-through. Numbers shown under elution refer to fraction number. The expected molecular weight of *Ab*HisIE is 29,195 Da. Pink and blue arrows in (F) indicate monomeric and dimeric *Ab*HIsIE, respectively.

6.3 Biophysical characterisation of *Ab*HisIE

A brief biophysical characterisation was carried out to determine the oligomeric state and thermostability of *Ab*HisIE. The oligomeric state of *Ab*HisIE was investigated via DLS as previously described, Table 6.1. The estimated molecular weight of *Ab*HisIE in solution was approximately 150 kDA ± 40 kDA. The particle size was not influenced by addition of DTT (4 mM). The molecular weight of monomeric *Ab*HisIE is approximately 30 kDA. Thus, although the large standard deviation prevents unambiguous assignment of the oligomeric state, DLS data are consistent with formation of either a tetramer, pentamer or hexamer in solution. As previously highlighted HisI from *M. vannielii* and *M. thermoautotrophicum* purify with Zn^{2+} tightly bound in the active site and structural analyses have confirmed that the Zn^{2+}-binding site of HisI and bifunctional HisIE is composed of cysteines from two distinct HisI or HisIE polypeptide chains[63,64,70,71]. If *Ab*HisIE also purifies with Zn^{2+} bound, it is unlikely that *Ab*HisIE exists as a pentamer in solution, however, it is possible that *Ab*HisIE adopts either a dimer of dimers or a trimer of dimers arrangement in solution. HisIE from *S. flexneri*, HISN2 from *M. truncatula* and *Pa*HisIE are all posited to form dimers in solution[70,71]. Determining the crystal structure of *Ab*HisIE may shed light on interactions that could facilitate formation of a higher-order oligomeric state in solution relative the other characterised HisIE proteins.

Table 6-1. DLS studies of *Ab*HisIE. The estimated molecular weights is listed alongside the sizes of particles present in the sample and the mass (%) per volume of each of these species

	Estimated MW (kDA)	**Mass (%)**	**Z-Average (nm)**
Replicate 1	140 ± 50	100%	10 ± 3
Replicate 2	170 ± 60	100%	11 ± 3
Replicate 3	150 ± 50	100%	10 ± 3
Replicate 4	150 ± 40	100%	10 ± 3
+ 4 mM DTT	150 ± 30	91.8%	10 ± 2
	$7 \times 10^5 \pm 3 \times 10^5$	7.1%	400 ± 150
	$4.2 \times 10^8 \pm 4 \times 10^7$	1.1%	5700 ± 700

Values are mode ± standard deviation of triplicate measurements.

DSF was performed to evaluate the thermal stability of *Ab*HisIE, Figure 6.3. It was not possible to define a global T_M for the enzyme as the data most likely reflect unfolding of at least two domains with distinct T_M values. DSF data indicate *Ab*HisIE is more thermostable than *Pa*HisIE.

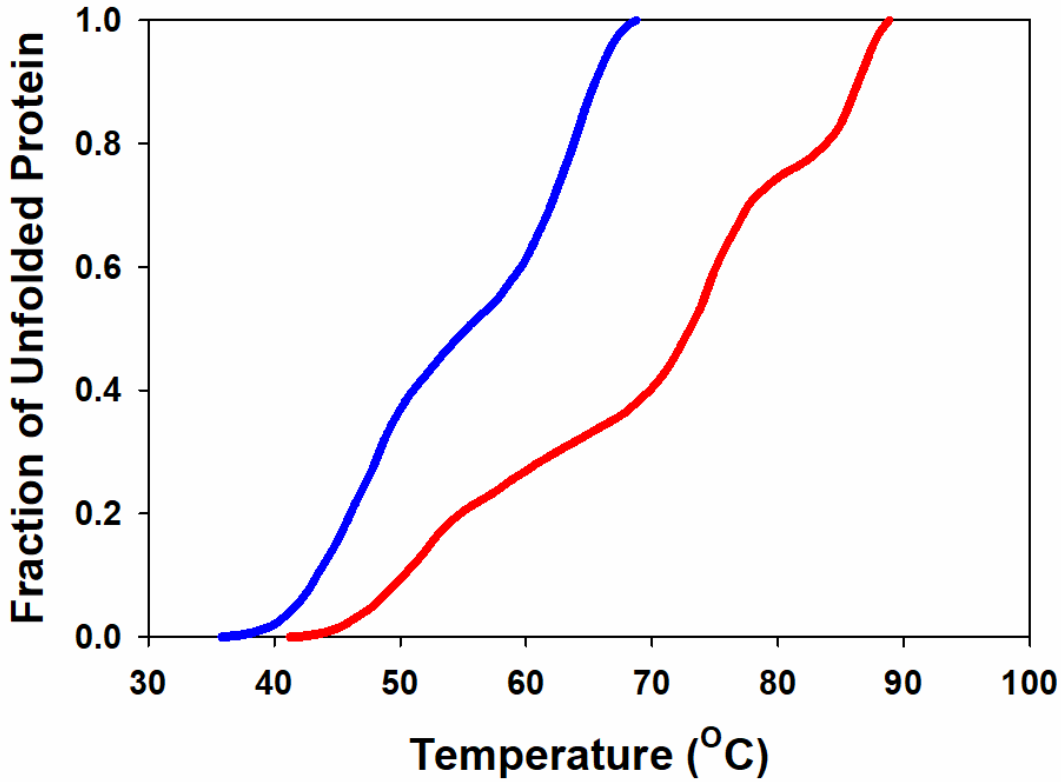

Figure 6.3. DSF-based thermal denaturation curves of *Ab*HisIE. Curves from *Ab*HisIE (red) and *Pa*HisIE (blue) are shown. Data are average of triplicate measurements.

6.4 *Ab*HisIE Activity

The substrate of *Ab*HisIE, PRATP, was prepared as described in Chapter 5. *Ab*HisIE activity was initially assessed by monitoring increase in absorbance at 300 nm corresponding to ProFAR formation ($\Delta\varepsilon$ = 6700 M^{-1} s^{-1} [pH 7.5])[63]. Mg^{2+} was required for activity. Activity was demonstrated to be dependent on enzyme concentration, Figures 6.4A, 6.4B and Table 6.2. Reactions containing 21 nM *Ab*HisIE were incubated until product formation plateaued and 100% of the PRATP initially added (38 μM) to the reaction was consumed, Figure 6.5C. *Ab*HisIE was hypothesised to co-purify with Zn^{2+}, as addition of exogenous Zn^{2+} resulted in either mild inhibition or precipitation. Inhibition of HisI by excess Zn^{2+} has previously been reported by d'Ordine and colleagues[63]. The enzyme activity was not influenced by addition of EDTA but addition of DTT (4 mM) increased the rate of reaction and was included in all future assays.

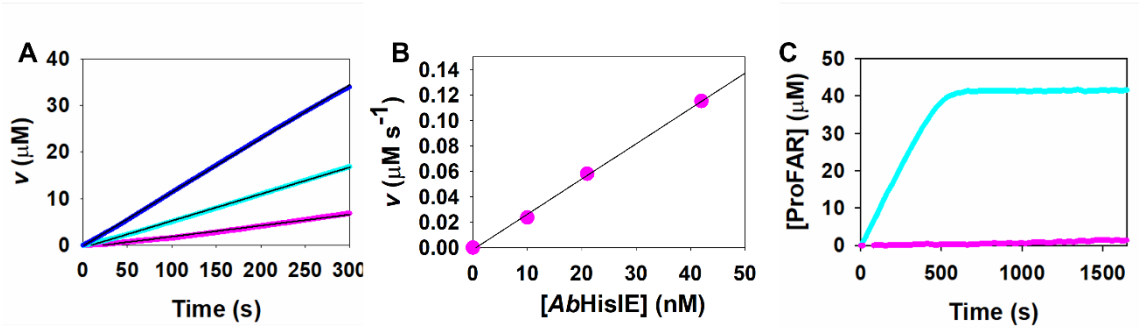

Figure 6.4 AbHisIE activity with PRATP. (A) Time-courses of product formation upon incubation of PRATP (38 μM) with 12 mM $MgCl^{2+}$ at pH 7.5 with varying concentrations of *Ab*HisIE. Product formation was recorded with 10 (cyan), 21 (magenta) and 42 (blue) nM *Ab*HisIE. (B) Rates extracted from time-courses were plotted against enzyme concentration. (C) Reactions with 20 nM AbHisIE (cyan) and controls (magenta) were also monitored until product formation plateaued (C). Solid black lines represent linear regressions of data. Data are average of two replicates except for cyan line in (C) which is a single measurement. Data points are mean ± standard error. The difference in absorbance between control and reaction in (C) equates to 40 μM ProFAR.

Table 6-2 Rates of product formation from reactions catalysed by *Ab*HisIE.

[*Ab*HisIE] (nM)	***v* (μM s^{-1})**
10	0.0236 ± 0.0002
21	0.058 ± 0.003
42	0.1152 ± 0.003

Values are mean ± standard error of duplicate measurements.

6.5 Steady-state kinetics of reactions catalysed by *Ab*HisIE

The steady-state kinetic parameters of reactions catalysed by *Ab*HisIE were subsequently determined, Figure 6.5 and Table 6.3. At high concentrations of PRATP (21 µM and 42 µM), time-courses of product formation depicted an initial lag phase, Figure 6.5 (0 – 40 s). In such cases, rates were extracted from data collected between 40 – 120 seconds. It was hypothesised that this initial lag-phase may reflect that the rate is dependent on production of PRAMP by HisE. The value of k_{cat} at 25 °C for *Ab*HisIE (5.6 ± 0.3 s^{-1}) is less than the k_{cat} reported at 25 °C for *Ab*ATPPRT (11.4 ± 0.4 s^{-1})[7] , which is considered the flux-controlling enzyme of histidine biosynthesis, however, as previously highlighted *Ab*HisIE likely operates under conditions that most closely resemble k_{cat}/K_M *in vivo*, owing to the limiting intracellular concentrations of the pathway intermediates. Furthermore, the k_{cat} of *Ab*ATPPRT was determined at pH 8.5, whereas the k_{cat} of *Ab*HisIE was determined at pH 7.5. The values of k_{cat} and k_{cat}/K_M (k_{cat} = 5.6 ± 0.3 s^{-1} , k_{cat}/K_M 1.40 x 10^6 ± 3 x 10^5 M-1 s^{-1}) reported here are similar to the values reported for HisI from *M. vannielii* (k_{cat} = 4.1, k_{cat}/K_M = 4.1 x 10^5 M^{-1} s^{-1}) and *M. thermoautotrophicum* (k_{cat} = 8 s^{-1} , k_{cat}/K_M = 6 x 10^5 M^{-1} s^{-1})[63,64].

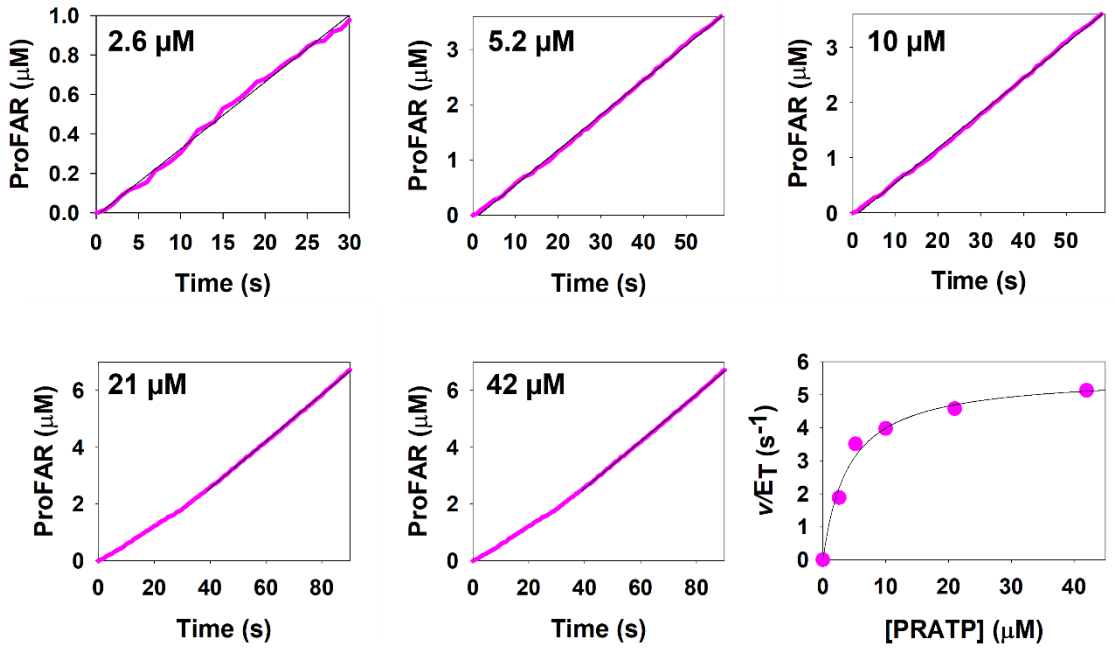

Figure 6.5 *Ab*HisIE steady-state kinetic parameters. (A – E) Time-courses of reactions catalysed by *Ab*HisIE (18 nM) in the presence of varying concentrations of PRATP with 15 mM $MgCl_2$ at pH 7.5. The concentration of PRATP is indicated in the legend. (F) *Ab*HisIE saturation curve .Data are average of at least two replicates. Data points are mean ± standard error Solid black lines in (A – E) represent linear regressions of data. Solid line in (F) is data fitted to the Michaelis-Menten equation. For data collected with 21 µM and 42 µM PRATP linear regressions were performed on data between 40-120 seconds.

Table 6-3 *Ab*HisIE steady-state kinetic parameters

Parameter	**PRATP**
k_{cat} **(s^{-1})**	5.6 ± 0.3
K_{PRATP} **(µM)**	4.0 ± 0.7
k_{cat}/K_{PRATP} **(M^{-1} s^{-1})**	1.4 x 10^6 ± 3 x 10^5

Values represent mean ± fitting-error of duplicate measurements.

6.6 LC-MS analysis of the reaction catalysed by *Ab*HisIE

A product with m/z 575.0724 was identified from LC-MS analysis of the reaction catalysed by *Ab*HisIE, in good agreement with the theoretical m/z of ProFAR, 575.0750, Figure 6.6. LC-MS was performed by Dr Alison Dickson, formerly of the Czekster laboratory.

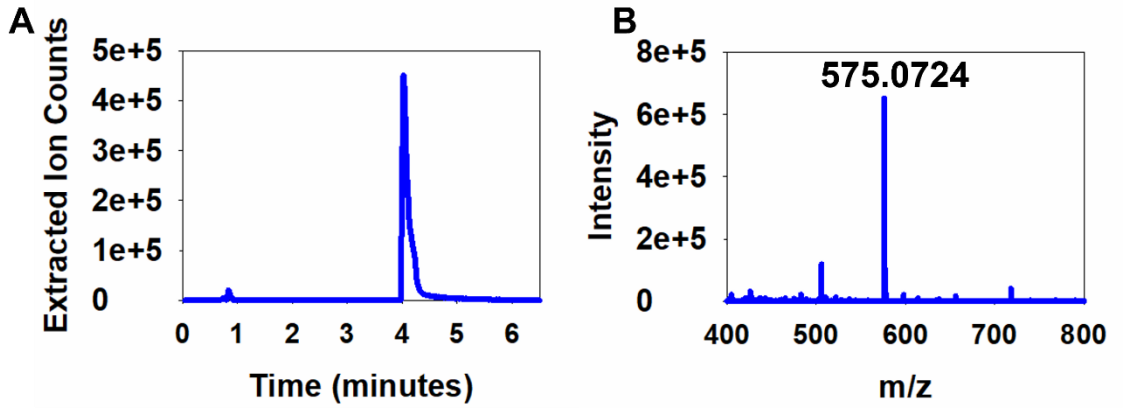

Figure 6.6 LC-MS analysis of the reaction catalysed by *Ab*HisIE with PRATP as a substrate. Analysis was performed on an Atlantis Premier BEH C18 AX column on a Waters ACQUITY UPLC system coupled to a Xevo G2-XS QToF mass spectrometer equipped with an ESI source. Reaction components were separated in ammonium acetate pH 6, acetonitrile and ammonium acetate pH 10. The extracted ion chromatogram for ProFAR (A) (expected m/z 575.0750) and m/z spectrum (B) are shown. Spectra were acquired in negative mode. LC-MS was performed by Dr Alison Dickson.

6.7 Uncovering the rate-limiting steps for reactions catalysed by *Ab*HisIE.

As previously highlighted, prior to this work, no investigations of the rate-limiting step of bifunctional HisIE had been reported. The k_{cat} reported in Table 6.3 encompasses both the pyrophosphohydrolase and the cyclohydrolase reactions catalysed by HisIE. The following experiments were devised in order to ascertain which step is rate-limiting. It should be noted previous computational analysis of *M. truncatula* HISN2 with CAVER did not identify any channels/tunnels that could funnel the product of the pyrophosphohydrolase reaction, PRAMP, to the active site of the cyclohydrolase

domain[71]. It is possible that PRAMP is released to the solvent prior to binding the HisI domain.

6.7.1 Steady-state kinetic parameters of *Ab*HisE

Firstly, the steady-state kinetic parameters of the pyrophosphohydrolase domain of *Ab*HisIE were determined via the EnzCheck™ Pyrophosphate Assay kit[115]. The assay is outlined in Figure 6.7. Briefly, pyrophosphate, produced as a bi-product of the pyrophosphohydrolase reaction, is cleaved by inorganic pyrophosphatase generating two equivalents of free phosphate. PNP catalyses conversion of phosphate and 2-amino-6-mercapto-7-methylpurine ribonucleoside (MESG) to 2-amino-6-mercapto-7-methylpurine ($\Delta\varepsilon_{360\ nm}$ = 11,000 M^{-1} cm^{-1}) and ribose-1-phopshate[115]. Ultimately, the EnzCheck™ assay facilitates measurement of the reaction catalysed by *Ab*HisE independently of the reaction catalysed by *Ab*HisI. If the k_{cat} of the reaction catalysed by *Ab*HisE is greater than the previously determined k_{cat} for the conversion of PRATP to ProFAR catalysed by *Ab*HisIE, this would indicate that the overall turnover of PRATP to ProFAR is limited by the cyclohydrolase reaction. Contrastingly, if the k_{cat} of *Ab*HisE is equal to the previously determined k_{cat} for the conversion of PRATP to ProFAR catalysed by *Ab*HisIE, this would suggest that the pyrophosphohydrolase reaction is at least partially rate-limiting for the overall turnover of PRATP to ProFAR.

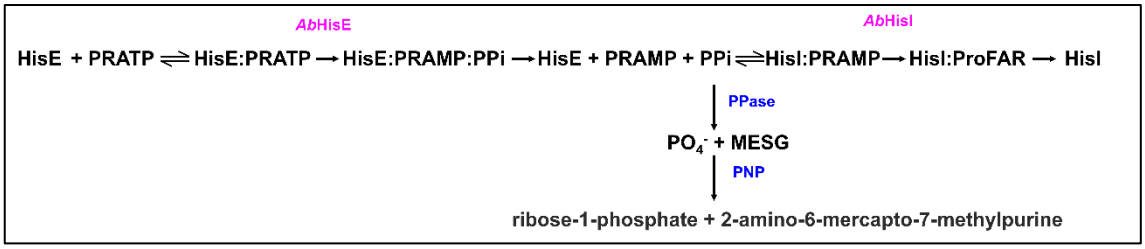

Figure 6.7. Outline of the EnzCheck™ pyrophosphate assay. The catalytic domains of *Ab*HisIE are denoted in pink whilst coupled enzymes are denoted in blue.

Prior to measuring the steady-state kinetic parameters of *Ab*HisE, a series of control experiments were performed to demonstrate that the background activity due to phosphate contamination of the enzyme and/or substrate is negligible and that the assay was reporting on the activity of *Ab*HisE, Figure 6.8. Further control experiments demonstrated that the increase in absorbance at 360 nm requires addition of pyrophosphatase, Figure 6.8. The steady-state kinetic parameters of the reaction catalysed

by *Ab*HisE were subsequently determined, Figure 6.8F and Table 6.4. The k_{cat} of the reaction catalysed by the *Ab*HisE domain is larger (beyond experimental error) than the k_{cat} reported for the overall conversion of PRATP to ProFAR, catalysed by *Ab*HisIE, Figure 6.9. As the k_{cat} for the pyrophosphyrdrolase reaction is greater than the k_{cat} for both the pyrophosphyrdrolase and cyclohydrolase reactions it is likely that the overall turnover of PRATP to ProFAR catalysed by *Ab*HisIE, under steady-state conditions, is limited by the cyclohydrolase reaction.

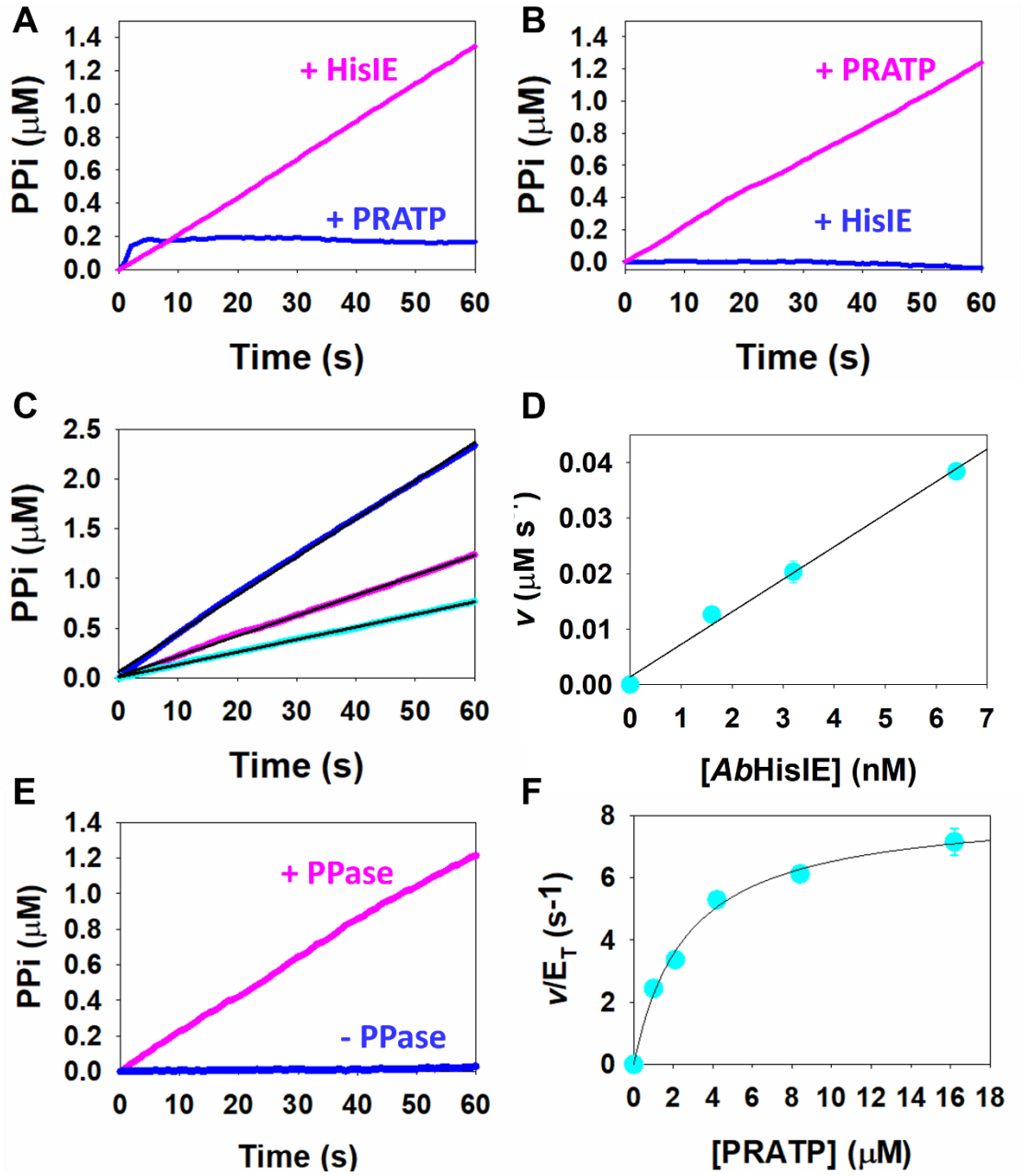

Figure 6.8 Steady-state kinetic parameters of *Ab*HisE catalysed reactions. Reactions were performed with 15 mM $MgCl_2$ at pH 7.5. Product formation time-courses recorded after addition of either (A) PRATP or (B) *Ab*HisIE (blue) to PPase, MESG, and PNP demonstrating negligible background absorption at 360 nm without addition of the final component of the assay, either (A) *Ab*HisIE (B) PRATP (magenta). In all further measurements PRATP was incubated with PPase, MESG, and PNP prior to addition of *Ab*HisIE to start the reaction. (C) Product formation time-courses were recorded at various concentrations of *Ab*HisIE, 1.6 (cyan), 3.2 (magenta) and 6.4 (blue) nM, whilst the concentration of PRATP (10 μM) was held constant. (D) Rates extracted from time-courses were plotted against enzyme concentration. (E) Product formation time-course in the presence and absence of PPase. (F) *Ab*HisIE saturation curve . Solid black lines represent linear regressions of data in (A - E). Solid black line in (F) is data fitted to the Michaelis-Menten equation. Data are average of two replicates and data points are mean ± standard error.

Table 6-4 *Ab*HisE steady-state kinetic parameters

Parameter	**PRATP**
k_{cat} **(s^{-1})**	8.3 ± 0.3
K_{PRATP} **(μM)**	2.7 ± 0.3
k_{cat}/K_{PRATP} **(M^{-1} s^{-1})**	3.1 x 10^6 ± 4 x 10^5

Values represent mean ± fitting error of duplicate measurements.

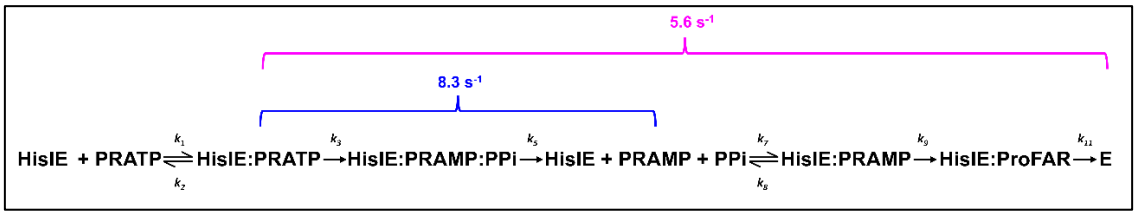

Figure 6.9 Scheme outlining the reaction catalysed by *Ab*HisIE. Steps encompassed by the overall k_{cat} of *Ab*HisIE determined by monitoring absorbance at 300 nm, are denoted by a magenta bracket. Steps encompassed by k_{cat} of *Ab*HisIE, determined via the EnzCheck™ assay, are denoted by a blue bracket.

6.7.2 Solvent isotope effects

Next, a solvent isotope effect study was employed to further probe the rate-limiting step of *Ab*HisIE. Isotope effects are powerful tools to probe the chemical mechanism and rate-limiting steps of an enzyme catalysed reaction. An isotope effect is defined as a change in the rate or equilibrium constant of a reaction upon substitution of a heavy atom for a light atom in a position where bonds are broken or formed or adjacent to that site[126]. Solvent deuterium isotope effects (SIEs) may be observed when rate and/or equilibrium constants are measured in H_2O and D_2O. Upon measurement of an enzyme-catalysed reaction rate in D_2O, solvent exchangeable protons on the enzyme and/or substrate are replaced by deuterium, thus may give rise to an isotope effect.

Bonds formed with a heavy isotope exhibit lower vibrational frequencies and consequently lower zero-point energies than bonds formed with a light isotope[189]. A greater energy input is required in order to break bonds composed of a heavy atom compared with that of a lighter atom, assuming that at the transition state the isotope

substitution will not influence the energy of the activated complex as the reaction coordinate vibrational mode disappears[189]. This phenomenon gives rise to a "normal" kinetic isotope effect, in which the rate constant for the light isotope (^{L}k) is larger than the rate constant for the heavy isotope (^{H}k), ($^{L}k/^{H}k > 1$)[189]. Observation of a kinetic isotope effect greater than 1 on either k_{cat} or k_{cat}/K_M typically indicates that chemistry is at least partially rate-limiting. Kinetic isotope effects may be masked if isotopically insensitive steps dominate k_{cat} and/or k_{cat}/K_M and determining the intrinsic isotope effect (the isotope effect measured if the chemical step were completely rate-limiting) may elucidate valuable information about the structure of the transition state[189–191], although this is beyond the scope of this work. Inverse isotope effects ($^{L}k/^{H}k < 1$) may also be observed which typically reflect either secondary isotope effects or contributions from an equilibrium step prior to the rate-limiting step[189].

Analyses of SIEs are typically more complex than analysis of isotope effects that arise from heavy atom labelling of specific positions within the substrate. All exchangeable positions in the substrate and enzyme are isotopically labelled, thus, pinpointing exactly which and how many proton transfers give rise to an SIE is not straightforward if multiple proton transfers occur within a reaction. Nevertheless, when interpreted alongside other experimental data solvent isotope effects are valuable tools for elucidating the rate-limiting steps and chemical mechanism of an enzyme catalysed reaction. For example, a sizable normal (> 2) solvent kinetic isotope effect (SKIE) observed on k_{cat} or k_{cat}/K_M indicates that at least one solvent-sensitive proton is in flight during the rate-limiting step. Of particular note to this work is that reactions that proceed via rapid-equilibrium exchange of a metal-bound water prior to a slower rate-limiting step may give rise to inverse SKIEs ($^{H2O}k/^{D2O}k < 1$) due to the inverse fractionation factors observed on these species[192]. It must be highlighted that the expression of such inverse SKIEs is dependent on the magnitude of the solvent equilibrium isotope effect relative to any normal SKIE observed on the following rate-determining step[192].

The catalytic mechanism of cyclohydrolase reaction catalysed by HisIE is predicted to employ a Zn^{2+}-bound water as a nucleophile (reviewed in Chapter 1). Whilst, no mechanistic studies of HisE have been reported, the catalytic mechanism for the dUTPases which are evolutionarily related to the HisE are posited to employ a Mg^{2+}-

activated water as a nucleophile[51,62]. Thus, catalysis by either domain of *Ab*HisIE could, theoretically, give rise to an inverse SKIE. Inverse SKIEs reported on AMP deaminase, which catalyses a similar reaction to HisI, have previously been attributed to protonic transfers originating from Zn^{2+}-activated water[66]. An SKIE study of the full reaction catalysed by *Ab*HisIE was initiated in order to determine which, if any, SKIEs would be observed on the steady-state kinetic parameters. The steady-state kinetic parameters were determined by measuring increase absorbance at 300 nm, corresponding to formation of ProFAR, in H_2O and D_2O.

Prior to SKIE measurement, the steady-state parameters of reactions catalysed by *Ab*HisIE were determined in 0%, 9% and 18% glycerol at 25 °C to assess if kinetic solvent viscosity effects (SKVE) are present, Figure 6.10, Table 6.5. The viscosity of D_2O is greater than H_2O[193], to avoid incorrectly assigning a solvent viscosity effect as an SKIE one must account for the effect of increased solvent viscosity on the reaction. At 25 ºC, 9% glycerol produces the same viscosity that 100% D_2O does[194]. No SKVE was detected on reactions catalysed by *Ab*HisIE at 9 and 18% glycerol, indicative that diffusional steps are not rate-limiting for the overall reaction catalysed by *Ab*HisIE and the SKIE experiment was continued.

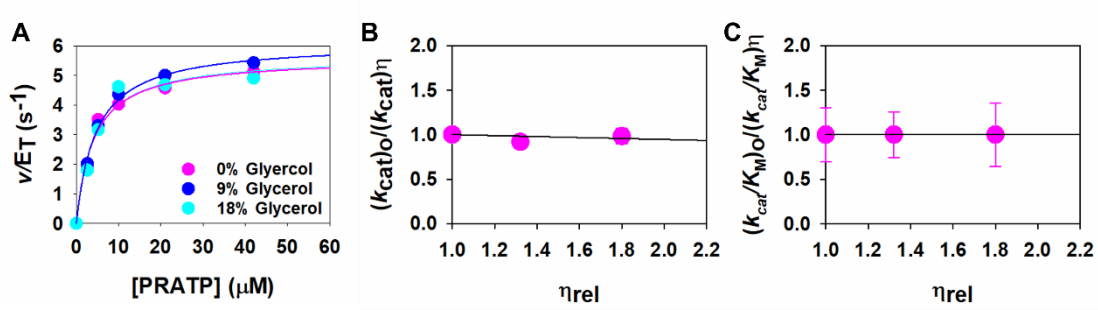

Figure 6.10 The effect of increasing solvent viscosity on *Ab*HisIE steady-state kinetic parameters. (A) Saturation curves were measured in 0% (magenta), 9% (blue) and 18% (blue) glycerol (*v*/*v*). Solvent kinetic viscosity effects on (B) k_{cat} and (C) k_{cat}/K_M^{PRPP}. Data points are mean ± either (A) standard error or (B) fitting error. Magenta, blue and cyan lines in (A) are data fitted to the Michaelis-Menten equation. Solid black lines in (B) and (C) are data fitted to Equation 2.8.

Table 6-5 The effect of increasing solvent viscosity on *Ab*HisIE steady-state kinetic parameters.

Parameter	**0% Glycerol**	**9% Glycerol**	**18% Glycerol**
k_{cat} **(s^{-1})**	5.6 ± 0.3	6.1 ± 0.2	5.7 ± 0.4
K_{PRATP} **(μM)**	4.0 ± 0.7	4.5 ± 0.5	4 ± 1
k_{cat}/K_{PRATP} **(M^{-1} s^{-1})**	1.40 x 10^6 ± 3 x 10^5	1.4 x 10^6 ± 2 x 10^5	1.4 x 10^6 ± 4 x 10^5

Values are ± fitting error of duplicate measurements.

To measure pD using a glass electrode calibrated with buffers prepared in H_2O, the reading must be corrected by adding 0.4 to obtain the correct pD[195]. Furthermore, pK_As may be subject to solvent equilibrium isotope effects. To minimise errors, solvent isotope effects should ideally be measured at a point in the pH profile at which the rate of reaction is independent of pH. To evaluate the effect of pH on the rate of *Ab*HisIE-catalysed reactions, the extinction coefficient at 300 nm for production of ProFAR from PRATP ($\Delta\varepsilon_{300}$ nm) was determined at pH 7.0, 7.5 and 8.0, Table 6.6.

Table 6-6. Extinction coefficients at 300 nm ($\Delta\varepsilon_{300\ nm}$) for production of ProFAR from PRATP at pH 7.0, pH 7.5 and pH 8.0.

pH	**$\varepsilon_{300\ nm}$ (PRATP) (M^{-1} cm^{-1})***	**$\Delta\varepsilon_{300\ nm}$ (ProFAR) (M^{-1} cm^{-1})**
pH 7.0	1200 ± 100	6800
pH 7.5	1310 ± 50	6700
pH 8.0	1810 ± 50	6200

Values are ± fitting error.

The steady-state kinetic parameters of *Ab*HisIE were subsequently determined in H_2O and D_2O at pL 7.0, 7.5 and 8.0, Figure 6.11 and Table 6.7. Product formation was calculated from the extinction coefficients detailed in Table 6.6. Due to time constraints and instability of PRATP at high pH, a full pH rate-profile was not carried out. The k_{cat} and k_{cat}/K_M of *Ab*HisIE were somewhat dependent on pH although data appear to be approaching a plateau in the pH rate-profile. Upon inspection of Figures 6.11C and 6.11D, it was considered likely that there is a solvent equilibrium isotope effect, as in D_2O the rate of reaction is more strongly influenced by pD compared with the effect of pH on reactions catalysed in H_2O. Solvent kinetic isotope effects were determined by fitting v/E_T data to Equation 2.9, Table 6.8. Solvent kinetic isotope effects were observed on k_{cat} and increased from 2.04 to 6.8 as pD decreased from 8.0 to 7.0. Qualitatively, these data suggest at least one protonation step is possibly rate-limiting for the overall turnover of PRATP to ProFAR, however, the absolute values of the SKIEs likely have contributions from the solvent equilibrium isotope effect. It is likely that proton transfer becomes increasingly rate-limiting at lower pH. A similar trend in SKIE was observed on k_{cat}/K_M, although, it should be noted this parameter is more dependent on pD.

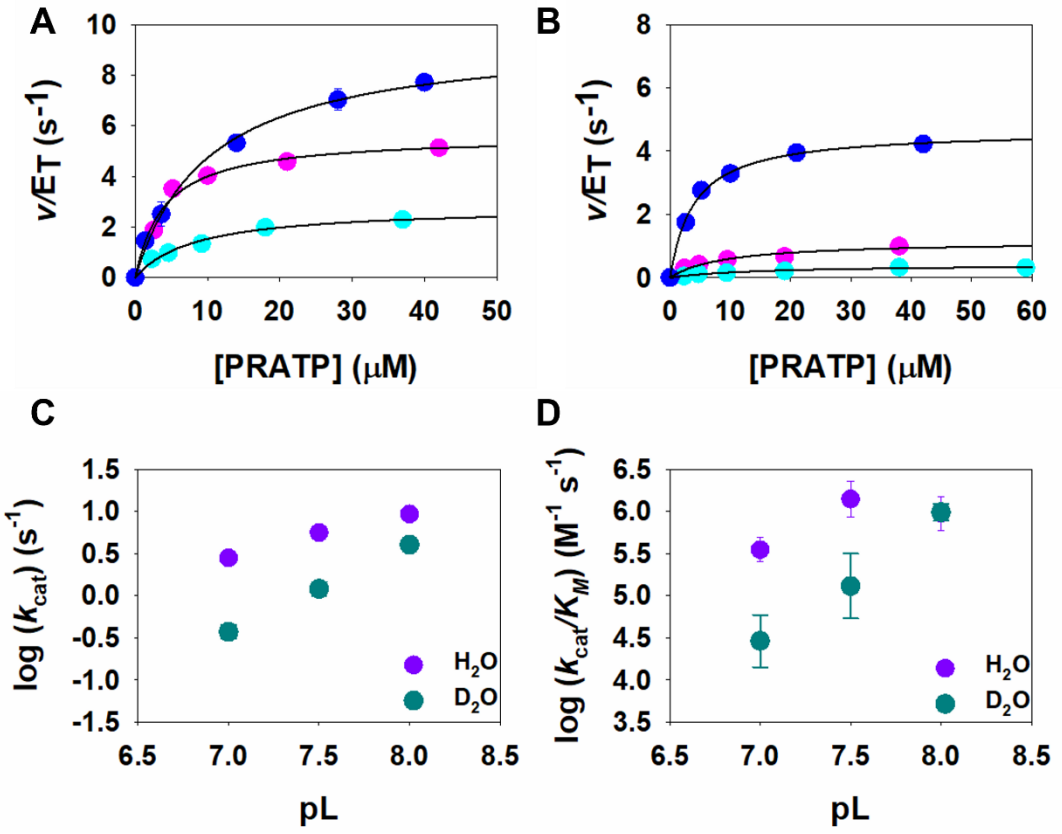

Figure 6.11 SKIE study on *Ab*HisIE steady-state parameters. Substrate saturation curves in (A) H_2O and (B) D_2O at pL 7.0 (cyan), 7.5 (magenta) and 8.0 (blue). pL profiles for (C) k_{cat} and (D) k_{cat}/K_M. Data represent either mean ± standard error (A and B) or mean ± fitting error (C and D). Solid line in (A) is data fitted to the Michaelis-Menten equation. Solid line in (B) is data fitted to Equation 2.8.

Table 6-7 *Ab*HisIE steady state parameters determined at pH 7.0, pH 7.5 and pH 8.0.

Parameter	**pH 7.0**	**pH 7.5**	**pH 8.0**
k_{cat} **(s^{-1})**	2.8 ± 0.2	5.6 ± 0.3	9.5 ± 0.4
K_{PRATP} **(μM)**	8 ± 1	4.0 ± 0.7	10 ± 1
k_{cat}/K_{PRATP} **(M^{-1} s^{-1})**	$3.5 \times 10^5 \pm 5 \times 10^4$	$1.4 \times 10^6 \pm 3 \times 10^5$	$9.5 \times 10^6 \pm 1 \times 10^6$

Values represent ± fitting error of duplicate measurements

.

Table 6-8. Solvent deuterium kinetic isotope effects on reactions catalysed by *Ab*HisIE at pL 7.0, pL 7.5 and pL 8.0.

Parameter	**pL 7**	**pL 7.5**	**pL 8**
$^{D2O}(k_{cat})$	6.8 ± 0.6	4.9 ± 0.6	2.04 ± 0.04
$^{D2O}(k_{cat}/K_M)$	12 ± 2	11 ± 2	0.81 ± 0.05

Values represent ± fitting error of duplicate measurements.

6.7.3 Analysis of *Ab*HisIE product formation time-courses under pre-steady state conditions.

Finally, conversion of PRATP to ProFAR catalysed by *Ab*HisIE was monitored under multiple turnover conditions in a stopped-flow spectrophotometer, facilitating the capture of the first milliseconds of the reaction, Figure 6.12.The experiment was performed at pH 7.5, and absorbance at 300 nm, corresponding to ProFAR formation, was recorded.

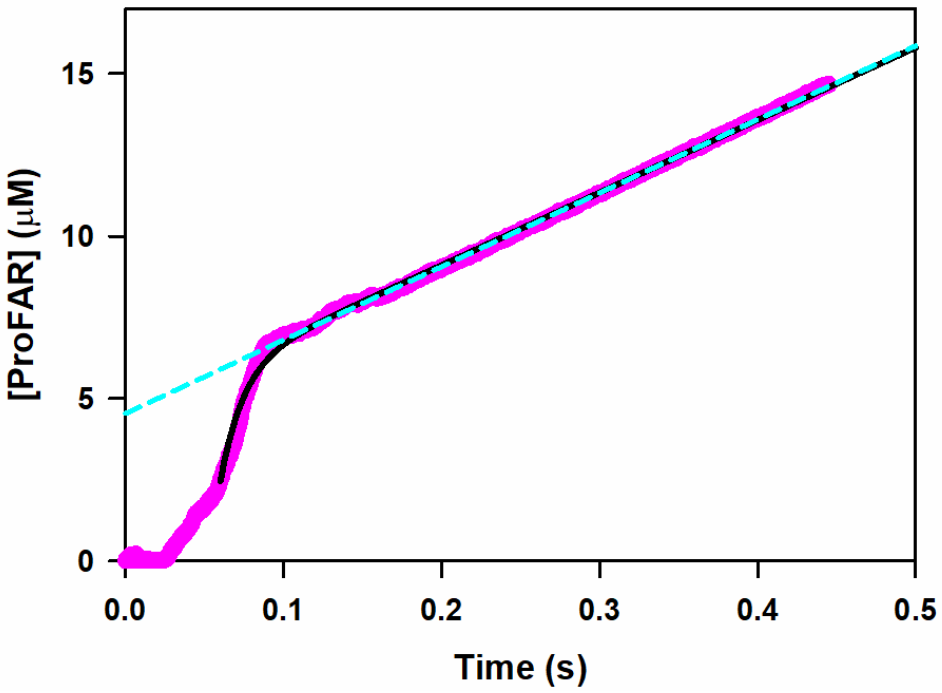

Figure 6.12 Pre-steady state kinetics with *Ab*HisIE. A lag phase followed by a burst in product formation was observed prior to the establishment of the steady-state phase. Solid black line is data fitted to Equation 2.4. Cyan dashed line is linear regression of data between 0.1 – 0.45 s.

A lag-phase (0.030 s, k = 33 s^{-1}) followed by a burst in product formation was observed. Data were fitted to equation 2.4, which is typically employed to model reactions with a burst. It was not possible to fully model the exponential phase of the reaction, possibly due to the influence of the lag-phase. Upon inspection of the fit, it is apparent that the model is underestimating k_{burst} (69.6 ± 0.7 s^{-1}) and the amplitude of the burst, A_0 (3.52 ± 0.01 μM). The values extracted from the fit place a lower limit on the true values for k_{burst} and A_0. A_0 was also extrapolated from a linear regression of data between 0.1 – 0.45 s and the estimated value of A_0 (4.5 μM) was found to be in good agreement with concentration of protein used in this experiment (5 μM). After the burst, the rate of product formation was found to be dependent on a second rate constant, k = 4.527 ± 0.002 s^{-1}, which is in good agreement with k_{cat} (5.6 ± 0.3 s^{-1}).

Observation of a lag-phase under pre-steady state conditions is expected as PRAMP must be first produced by *Ab*HisE before it can be hydrolysed by *Ab*HisI. As discussed in Chapter 3, a burst indicates that steps after chemistry are rate-limiting[143]. For reactions

catalysed by *Ab*HisIE, a burst in product formation necessitates that the rate of conversion of PRAMP to ProFAR must be greater than the rate of steps after ProFAR formation. For the reaction catalysed by HisE, the order of product release for the reaction is not known. It is possible that release of pyrophosphate from the *Ab*HisE active site is slower than PRAMP migration to the active site of *Ab*HisI and conversion to ProFAR, Figure 6.13. Critically, the burst of product formation demonstrates that the chemical step of the reaction catalysed by *Ab*HisI, is faster than the overall steady-state number and is not the rate-limiting step of catalysis. Furthermore, as the apparent rate constant estimated from the lag-phase (k ~33 s^{-1}) is also greater than k_{cat}, this suggests that steps before formation of ProFAR, including migration of PRAMP from the *Ab*HisE domain to the *Ab*HisI domain, are also not rate-limiting under steady-state conditions.

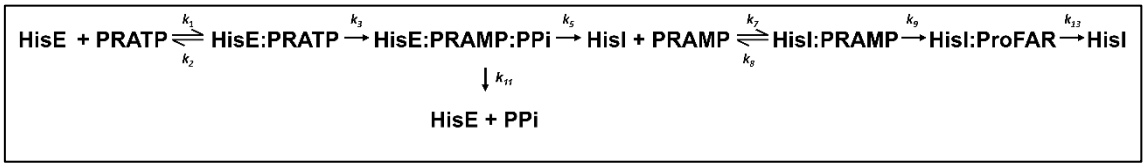

Figure 6.13. Scheme outlining the reaction catalysed by *Ab*HisIE under pre-steady-state conditions.

6.7.4 Analysis of the rate-limiting step of reactions catalysed by *Ab*HisIE

In conclusion, at pH 7.5, steady-state kinetics revealed that under multiple-turnover conditions, the turnover of the pyrophosphohydrolase reaction catalysed by *Ab*HisE is modestly faster than the overall turnover of PRATP to ProFAR catalysed by *Ab*HisIE. Hence, the overall rate-limiting step for the reaction catalysed by *Ab*HisIE likely lies within the cyclohydrolase reaction. A burst in product formation confirmed a step after formation of ProFAR is rate-limiting for the overall turnover of PRAMP to ProFAR. Interestingly, the absence of a SKVE indicated that the rate-limiting step is not a diffusional step. Data from the SKIE study suggested at least one proton transfer is partially rate-limiting at pH 7.5. It is possible that multiple proton transfers from both reactions give rise to the SKIE. Together, these findings indicate that, at pH 7.5, the rate-limiting step of reactions catalysed by *Ab*HisIE is likely a step after the main chemical event catalysed by *Ab*HisI, i.e. collapse of the tetrahedral intermediate and severing of the C6-N1 bond, but prior to the diffusion of products off the enzyme, and said step may involve a proton transfer, Figure 6.14.

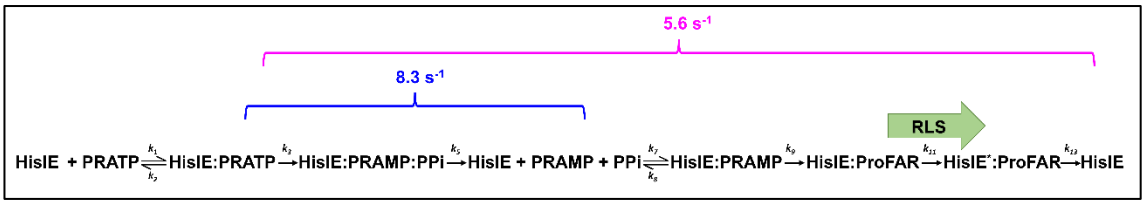

Figure 6.14 Scheme of the reaction catalysed by *Ab*HisIE. The rate-determining step is denoted by a green arrow. Steps encompassed by the overall k_{cat} of *Ab*HisIE, determined by monitoring absorbance at 300 nm, are denoted by a magenta bracket. Steps encompassed by k_{cat} of *Ab*HisE, determined via the EnzCheck™ assay, are denoted by a blue bracket. The proposed rate-limiting step (RLS) of the reaction is indicated with a green arrow.

6.8 Chapter summary

Overall, this chapter represents the first reported biochemical characterisation of *Ab*HisIE, a possible drug target in carbapenem-resistant *A. baumannii*. *Ab*HisIE may adopt a tetrameric or hexameric oligomeric state in solution in contrast to previously characterised HisIE from *S. flexerni*[70], HISN2 from *M. trunantgo*[71] and *Pa*HisIE (Chapter 5 of this work) which form dimers in solution. The steady-state kinetic parameters of *Ab*HisIE were similar to reported parameters from HisI from *M. vannielii*[63] and *M. thermoautotrophicum*[64]. Together, data from steady-state kinetics, solvent kinetic viscosity studies, solvent kinetic isotope studies, and pre-steady state kinetics are consistent with the rate-determining step of the reaction occurring after the main chemical event catalysed by HisI, i.e. collapse of the tetrahedral intermediate and severing of the C6-N1 bond, but before diffusion of substrates off the enzyme, possibly. The rate-determining step may include contributions from a protonation step.

This work will help pave the way for more detailed characterisation of *Ab*HisIE. The individual pyrophosphohydrolase and cyclohydrolase domains were cloned and produced as part of this work. Biochemical characterisation of these isolated domains from *Ab*HisIE will be continued by the da Silva Laboratory as part of ongoing efforts towards development of novel inhibitors of the *A. baumannii* histidine biosynthetic pathway. Indeed, Ennio Pečaver, a BSc student in the da Silva Laboratory purified the *Ab*HisE domain and confirmed that the isolated domain is active in the absence of *Ab*HisI. Future work in the da Silva laboratory will also include isolating the pathway intermediate PRAMP which may facilitate characterisation of the steady-state kinetic parameters of the isolated *Ab*HisI domain. This work suggested that migration of PRAMP between the

active site of *Ab*HisE and *Ab*HisI is not rate-limiting. Characterisation of the steady-state kinetic parameters of the individual *Ab*HisE and *Ab*HisI domains separately and when mixed together may conclusively determine if enhanced speed of PRAMP shuttling between active sites is an advantage of gene fusion. Notably, the SKIE data suggested that a proton transfer becomes increasingly rate-limiting as pH decreases and it was speculated that chemistry becomes increasingly rate-limiting at low pH. This finding raises the possibility of carrying out kinetic isotope effects with isotopically labelled substrates at pH < 7.5, where chemistry is exposed, to probe the architecture of the transition state. Knowledge of the enzyme transition state may facilitate development of tight-binding inhibitors, which may in turn drive development of novel antimicrobial agents[196].

Chapter 7 Conclusions and outlook

The first aim of this work was to propose a mechanism of allosteric activation of *Pa*HisG$_S$ by *Pa*HisZ. Chapters 3 and 4 of this work represent the most detailed kinetic characterisation of a short-form ATPPRT to date. In Chapter 3, it was demonstrated that *Pa*HisG$_S$ operates via a steady-state ordered mechanism with PRPP as the first substrate to bind and PRATP as the last substrate to leave the active site. Further kinetic characterisation demonstrated that allosteric activation of *Pa*HisG$_S$ by *Pa*HisZ shifts the rate-limiting step from interconversion between ternary complexes to product release. Based on these observations, it was hypothesised that *Pa*HisZ may increase the rate of interconversion between ternary complexes by narrowing the conformational landscape of *Pa*HisG$_S$ such that conformations with R56 in position to stabilise the pyrophosphate leaving group are sampled more frequently. In Chapter 4, it was demonstrated that R56A and R32A variants of *Pa*HisG$_s$ are catalytically impaired. Catalytic impairment of R56A-*Pa*HisG$_s$ is consistent with the proposed mechanism of allosteric activation. Unexpectedly, the activity of catalytically impaired R56A and R32A *Pa*HisG$_S$ was mostly restored by addition of the allosteric activator *Pa*HisZ. It was demonstrated that the rate-limiting step of allosterically rescued R32A and R56A *Pa*ATPPRT included contributions from chemistry. This finding linked these arginine residues to the chemical step of catalysis. Molecular dynamics simulations carried out by Dr Marina Corbella indicated in the presence of *Pa*HisZ, R32 can somewhat compensate for the loss of R56. An R32A/R56A/K57A variant of *Pa*HisG$_S$ was constructed to test this hypothesis. R32A/R56A/K57A *Pa*HisG$_S$ was severely catalytically impaired and activity was not restored in the presence of *Pa*HisZ. This finding suggests at least one of R32 and R56 is required for catalysis by *Pa*ATPPRT. Thus, the hypothesis for allosteric activation was refined to *Pa*HisZ increasing the rate of interconversion between ternary complexes by narrowing the protein conformational landscape in order that conformations with R32 and/or R56 in position to stabilise the pyrophosphate leaving group are sampled more frequently.

The mechanism of allosteric activation proposed in this work is consistent with contemporary conceptualisations of catalysis and allostery which emphasise contributions from protein dynamics[145,146,169,172–174]. A deeper understanding of the

contributions of protein dynamics to allostery and catalysis has the potential to accelerate rational evolution of existing enzymes and *de novo* design of enzymes with novel functions not found in nature. Recent studies of Kemp eliminase variants allude to the potential for improved success in *de novo* enzyme design by targeting the conformational dynamics of the transition-state ensemble[173,174]. For ATPPRT specifically, the work reported here suggests that efforts to engineer a constitutively activated short-form HisG$_S$ free from histidine feedback inhibition for industrial histidine biosynthesis should seek to introduce mutations which narrow the conformational sampling of the A45-V67 loop. This work will be continued by the da Silva and the Kamerlin Laboratories.

So far, the molecular mechanism underpinning histidine inhibition of a HisG$_S$-type ATPPRTs has not been determined. It has been demonstrated by pre-steady-state kinetics that histidine traps ATPPRT from *P. arcticus* in an inactive form[44]. It is possible that binding of histidine to *Pa*HisZ disrupts the conformational sampling of R32 and R56. *Pa*ATPPRT is primed for further dynamics studies to investigate the effect of histidine binding to *Pa*HisZ on R32 and R56 conformational sampling. Additional characterisation of the conformational ensemble of *Pa*HisG$_S$ in the presence and absence of *Pa*HisZ by NMR or single molecule FRET (Förester resonance energy transfer) may yield insights into the population of conformations and the rate of interconversion between conformations.

The second aim of this work was to initiate biochemical characterisation of *Ab*HisIE with a view towards inhibitor development. In Chapter 6, *Ab*HisIE was successfully produced and kinetically characterised. A brief analysis of the rate-limiting steps of *Ab*HisIE was performed which indicated that a step after the main chemical event catalysed by *Ab*HisI, *i.e.* collapse of the tetrahedral intermediate and severing of the C6-N1 bond, but before diffusion of product off the enzyme is rate-limiting. This work is the first reported kinetic analysis of bifunctional HisIE and has paved the way for future work in the da Silva Laboratory seeking to further characterise the catalytic mechanisms of *Ab*HisE and *Ab*HisI.

Determining the crystal structure of *Ab*HisIE in the presence of substrate analogues may elucidate key residues for substrate binding and guide inhibitor development. For further biochemical characterisation of HisIE, it is advantageous to reduce the kinetic complexity

of the system by studying isolated *Ab*HisI and *Ab*HisE domains. Both domains have now been successfully produced. Ennio Pečaver, a BSc student in the da Silva Laboratory demonstrated that the isolated *Ab*HisE domain is catalytically active in the absence of *Ab*HisI. The steady-state kinetic parameters of *Ab*HisI will be determined upon isolation of the pathway intermediate PRAMP. Further solvent isotope effect studies of the isolated *Ab*HisI and *Ab*HisE domains may resolve which proton transfers are contributing to the overall solvent kinetic isotope effect observed on *Ab*HisIE. Additional kinetic isotope effect studies with isotopically labelled substrates at pH < 7.5 may probe the architecture of the transition state. Knowledge of the enzyme transition state has the potential to drive development of tight-binding inhibitors[196]

In summary, the work reported in this thesis furthers understanding of the catalytic and regulatory mechanisms of the enzymes underpinning the first three steps of the histidine biosynthetic pathway. This work has the potential to drive the development of improved biocatalysts for efficient production of histidine and has primed *Ab*HisIE for further studies with a view towards novel antimicrobial development.

References

(1) Winkler, M. E.; Ramos-Montañez, S.; Stewart, V. Biosynthesis of Histidine. *EcoSal Plus* **2009**, *3* (2).

(2) Kulis-Horn, R. K.; Persicke, M.; Kalinowski, J. Histidine Biosynthesis, Its Regulation and Biotechnological Application in *Corynebacterium glutamicum*. *Microb. Biotechnol.* **2014**, *7* (1), 5–25.

(3) Wendisch, V. F. Metabolic Engineering Advances and Prospects for Amino Acid Production. *Metab. Eng.* **2020**, *58*, 17–34.

(4) Merck Sharp & Dohme (UK) Limited. Package leaflet: information for the user. Gardasil® suspension for injection in a pre-filled syringe https://www.medicines.org.uk/emc/medicine/19033 (accessed Mar 1, 2022).

(5) AstraZeneca UK Limited. Package Leaflet: Information for the recipient. COVID-19 Vaccine AstraZeneca solution for injection https://www.medicines.org.uk/emc/product/12333/pil (accessed Mar 1, 2022).

(6) Limited, B. H. Numeta G13%E Preterm, emulsion for infusion https://www.medicines.org.uk/emc/product/7400/smpc (accessed Mar 1, 2022).

(7) Baxter Healthcare Limitied. CLINIMIX N14G30E, solution for infusion https://www.medicines.org.uk/emc/product/1807/smpc (accessed Mar 1, 2022).

(8) SMA Nutrition. SMA Pro First Infant Milk. From birth onwards data card. https://www.smahcp.co.uk/sites/default/files/2018-10/sma73250_sma_pro_first_infant_milk_datacard_fa1b_digital.pdf (accessed Mar 1, 2022).

(9) Marsh, J. M.; Davis, M. G.; Flagler, M. J.; Sun, Y.; Chaudhary, T.; Mamak, M.; Mccomb, D. W.; Williams, R. E. A.; Greis, K. D. Advanced Hair Damage Model from Ultra-Violet Radiation in the Presence of Copper. *Int. J. Cosmet. Sci.* **2015**, *37*, 532–541.

(10) Wang, N.; Ozer, E. A.; Mandel, M. J.; Hauser, R. Genome-Wide Identification of *Acinetobacter baumannii* Genes Necessary for Persistence in the Lung. *MBio* **2014**, *5* (3), e01163-14.

(11) Martínez-guitián, M.; Vázquez-ucha, J. C.; Álvarez-fraga, L.; Conde-pérez, K.; Vallejo, J. A.; Perina, A.; Bou, G.; Poza, M.; Beceiro, A. Global Transcriptomic Analysis During Murine Pneumonia Infection Reveals New Virulence Factors in *Acinetobacter baumannii*. *J. Infect. Dis.* **2021**, *223*, 1356–1366.

(12) Martínez-guitián, M.; Vázquez-ucha, J. C.; Álvarez-fraga, L.; Poza, M.; Beceiro, A. Involvement of HisF in the Persistence of *Acinetobacter baumannii* During a Pneumonia Infection. *Front. Cell. Infect. Microbiol.* **2019**, *9* (August).

(13) Dwivedy, A.; Ashraf, A.; Jha, B.; Kumar, D.; Agarwal, N.; Biswal, B. K. De Novo Histidine Biosynthesis Protects *Mycobacterium Tuberculosis* from Host IFN-γ Mediated Histidine Starvation. *Commun. Biol.* **2021**, *4* (1), 410.

(14) Köhler, S.; Foulongne, V.; Ouahrani-bettache, S.; Teyssier, J.; Ramuz, M. The Analysis of the Intramacrophagic Virulome of *Brucella suis* Deciphers the Environment Encountered by the Pathogen inside the Macrophage Host Cell. *Proc. Natl. Acad. Sci.* **2002**, *99* (24), 15711–15716.

(15) Dietl, A.; Amich, J.; Leal, S.; Beckmann, N.; Binder, U.; Beilhack, A.; Pearlman, E.; Haas, H.; Amich, J.; Leal, S.; et al. Histidine Biosynthesis Plays a Crucial Role in Metal Homeostasis and Virulence of *Aspergillus fumigatus*. *Virulence* **2016**, *7* (4), 465–476.

(16) Ames, B. N.; Martin, R. G.; Garry, B. J. The First Step of Histidine Biosynthesis. *J. Biol. Chem.* **1961**, *236* (7), 2019–2026.

(17) Bell, R. M.; Koshland, D. E. Allosteric Properties of the First Enzyme of the Histidine Operon. *Bioorg. Chem.* **1971**, *1*, 409–423.

(18) Ames, B. N.; Smith, D. W. E. Phosphoribosyladenosine Monophosphate, an Intermediate in Histidine Biosynthesis. *J. Biol. Chem.* **1965**, *240* (7), 3056–3063.

(19) Fani, R.; Brilli, M.; Fondi, M.; Lió, P. The Role of Gene Fusions in the Evolution of Metabolic Pathways: The Histidine Biosynthesis Case. *BMC Evol. Biol.* **2007**, *7* (2), S4.

(20) Brenner, M.; Ames, B. N. *The Histidine Operon and Its Regulation. Metabolic Regulation*, 5th ed.; Voge, H. J., Ed.; Academic Press: New York, 1971.

(21) Martin, R. G. The First Enzyme in Histidine Biosynthesis; the Nature of Feedback Inhibition by Histidine. *J. Biol. Chem.* **1963**, *238* (1), 257–268.

(22) Morton, D. P.; Parsons, S. M. Inhibition of ATP Phosphoribosyltransferase by AMP and ADP in the Absence and Presence of Histidine. *Arch. Biochem. Biophys.* **1977**, *181* (2), 643–648.

(23) Dall-Larson, T.; Klumgsøyr, L. The Binding of Specific Ligands to Adenosine-Triphosphate Phosphoribosyltransferase. *Eur. J. Biochem.* **1976**, *69* (1), 195–201.

(24) Mittelstädt, G.; Moggré, G. J.; Panjikar, S.; Nazmi, A. R.; Parker, E. J. *Campylobacter jejuni* Adenosine Triphosphate Phosphoribosyltransferase Is an Active Hexamer That Is Allosterically Controlled by the Twisting of a Regulatory Tail. *Protein Sci.* **2016**, *25*, 1492–1506.

(25) Sissler, M.; Delorme, C.; Bond, J.; Ehrlich, S. D.; Renault, P.; Francklyn, C. An Aminoacyl-tRNA Synthetase Paralog with a Catalytic Role in Histidine Biosynthesis. *Proc. Natl. Acad. Sci.* **1999**, *96* (16), 8985–8990.

(26) Bond, J. P. Proteobacterial Histidine-Biosynthetic Pathways Are Paraphyletic. *J. Mol. Evol.* **2000**, *50* (4), 339–347.

(27) Aklujkar, M. Two ATP Phosphoribosyltransferase Isozymes of *Geobacter sulfurreducens* Contribute to Growth in the Presence or Absence of Histidine and under Nitrogen Fixation Conditions. *Can. J. Microbiol.* **2011**, *57* (7), 547–548.

(28) Lohkamp, B.; McDermott, G.; Campbell, S. A.; Coggins, J. R.; Lapthorn, A. J. The Structure of *Escherichia coli* ATP-Phosphoribosyltransferase: Identification of Substrate Binding Sites and Mode of AMP Inhibition. *J. Mol. Biol.* **2004**, *336* (1),

131–144.

(29) Pedreño, S.; Pisco, J. P.; Larrouy-Maumus, G.; Kelly, G.; de Carvalho, L. P. S. Mechanism of Feedback Allosteric Inhibition of ATP Phosphoribosyltransferase. *Biochemistry* **2012**, *51* (40), 8027–8038.

(30) Cho, Y.; Sharma, V.; Sacchettini, J. C. Crystal Structure of ATP Phosphoribosyltransferase from *Mycobacterium tuberculosis*. *J. Biol. Chem.* **2003**, *278* (10), 8333–8339.

(31) Champagne, K. S.; Piscitelli, E.; Francklyn, C. S. Substrate Recognition by the Hetero-Octameric ATP Phosphoribosyltransferase from *Lactococcus lactis.* *Biochemistry* **2006**, *45* (50), 14933–14942.

(32) Stroek, R.; Ge, Y.; Talbot, P. D.; Glok, M. K.; Bernaś, K. E.; Thomson, C. M.; Gould, E. R.; Alphey, M. S.; Liu, H.; Florence, G. J.; et al. Kinetics and Structure of a Cold-Adapted Hetero-Octameric ATP Phosphoribosyltransferase. *Biochemistry* **2017**, *56* (5), 793–803.

(33) Bovee, M. L.; Champagne, K. S.; Demeler, B.; Francklyn, C. S. The Quaternary Structure of the HisZ-HisG N-1-(5'-Phosphoribosyl)-ATP Transferase from *Lactococcus lactis*. *Biochemistry* **2002**, *41* (39), 11838–11846.

(34) Champagne, K. S.; Sissler, M.; Larrabee, Y.; Doublié, S.; Francklyn, C. S. Activation of the Hetero-Octameric ATP Phosphoribosyl Transferase through Subunit Interface Rearrangement by a tRNA Synthetase Paralog. *J. Biol. Chem.* **2005**, *280* (40), 34096–34104.

(35) Livingstone, E. K.; Mittelstädt, G.; Given, F. M.; Parker, E. J. Independent Catalysis of the Short Form HisG from *Lactococcus lactis*. *FEBS Lett.* **2016**, *590*, 2603–2610.

(36) Pisco, J. P.; De Chiara, C.; Pacholarz, K. J.; Garza-Garcia, A.; Ogrodowicz, R. W.; Walker, P. A.; Barran, P. E.; Smerdon, S. J.; D; de Carvalho, L. P. S. Uncoupling Conformational States from Activity in an Allosteric Enzyme. *Nat. Commun.* **2017**, *8* (1), 203.

(37) Moggré, G.-J.; Poulin, M. B.; Tyler, P. C.; Schramm, V. L.; Parker, E. J. Transition State Analysis of Adenosine Triphosphate Phosphoribosyltransferase. *ACS Chem. Biol.* **2017**, *12* (10), 2662–2670.

(38) Mittelstädt, G.; Jiao, W.; Livingstone, E. K.; Moggré, G.-J.; Nazmi, A. R.; Parker, E. J. A Dimeric Catalytic Core Relates the Short and Long Forms of ATP-Phosphoribosyltransferase. *Biochem. J.* **2018**, *475* (1), 247–260.

(39) Vega, M. C.; Zou, P.; Fernandez, F. J.; Murphy, G. E.; Sterner, R.; Popov, A.; Wilmanns, M. Regulation of the Hetero-Octameric ATP Phosphoribosyl Transferase Complex from *Thermotoga maritima* by a tRNA Synthase-like Subunit. *Mol. Microbiol.* **2005**, *55* (3), 675–686.

(40) Alphey, M. S.; Fisher, G.; Ge, Y.; Gould, E. R.; Machado, T. F. G.; Liu, H.; Florence, G. J.; Naismith, J. H.; Silva, R. G. Catalytic and Anticatalytic Snapshots of a Short-Form ATP Phosphoribosyltransferase. *ACS Catal.* **2018**, *8*, 5601–5610.

(41) Zhang, Y.; Shang, X.; Deng, A.; Chai, X.; Lai, S.; Zhang, G.; Wen, T. Genetic and Biochemical Characterization of *Corynebacterium glutamicum* ATP Phosphoribosyltransferase and Its Three Mutants Resistant to Feedback Inhibition by Histidine. *Biochimie* **2012**, *94* (3), 829–838.

(42) Morton, P.; Parsons, M. Biosynthetic Direction Substrate Kinetics and Product Inhibition Studies on the First Enzyme of Histidine Biosynthesis , Adenosine Triphosphate Phosphoribosyltransferase. *Arch. Biochem. Biophys.* **1976**, *175* (2), 677–686.

(43) Fisher, G.; Thomson, C. M.; Stroek, R.; Czekster, C. M.; Hirschi, J. S.; da Silva, R. G. Allosteric Activation Shifts the Rate-Limiting Step in a Short-Form ATP Phosphoribosyltransferase. *Biochemistry* **2018**, *57* (29), 4357–4367.

(44) Thomson, C. M.; Alphey, M. S.; Fisher, G.; da Silva, R. G. Mapping the Structural Path for Allosteric Inhibition of a Short-Form ATP Phosphoribosyltransferase by Histidine. *Biochemistry* **2019**, *3086* (58), 3078–3086.

(45) Read, B. J.; Fisher, G.; Wissett, O. L. R.; Machado, T. F. G.; Nicholson, J.;

Mitchell, J. B. O.; da Silva, R. G. Allosteric Inhibition of *Acinetobacter baumannii* ATP Phosphoribosyltransferase by Protein:Dipeptide and Protein:Protein Interactions. *ACS Infect. Dis.* **2022**, *8* (1), 197–209.

(46) Pacholarz, K. J.; Burnley, R. J.; Jowitt, T. A.; Ordsmith, V.; Pisco, J. P.; Porrini, M.; Larrouy-Maumus, G.; Garlish, R. A.; Taylor, R. J.; de Carvalho, L. P. S.; et al. Hybrid Mass Spectrometry Approaches to Determine How L-Histidine Feedback Regulates the Enzyzme *Mt*ATP-Phosphoribosyltransferase. *Structure* **2017**, *25* (5), 730–738.

(47) Stepansky, A.; Leustek, T. Histidine Biosynthesis in Plants. *Amino Acids* **2006**, *30*, 127–142.

(48) Moroz, O. V; Murzin, A. G.; Makarova, K. S.; Koonin, E. V; Wilson, K. S.; Galperin, M. Y. Dimeric dUTPases, HisE, and MazG Belong to a New Superfamily of All-α NTP Pyrophosphohydrolases with Potential "House-Cleaning" Functions. *J. Mol. Biol.* **2005**, *347* (2), 243–255.

(49) Kim, M. I.; Hong, M. Crystal Structure of the Bacillus-Conserved MazG Protein, a Nucleotide Pyrophosphohydrolase. *Biochem. Biophys. Res. Commun.* **2016**, *472* (1), 237–242.

(50) Lee, S.; Kim, M. H.; Kang, B. S.; Kim, J.; Kim, G.; Kim, Y.; Kim, K. J. Crystal Structure of *Escherichia coli* MazG, the Regulator of Nutritional Stress Response. *J. Biol. Chem.* **2008**, *283* (22), 15232–15240.

(51) Harkiolaki, M.; Dodson, E. J.; Bernier-villamor, V.; Turkenburg, J. P.; Dolores, G.-P.; Wilson, K. S. The Crystal Structure of *Trypanosoma cruzi* dUTPase Reveals a Novel dUTP/dUDP Binding Fold. *Structure* **2004**, *12* (1), 41–53.

(52) Moroz, O. V; Harkiolaki, M.; Galperin, M. Y.; Vagin, A. A.; González-Pacanowska, D.; Wilson, K. S. The Crystal Structure of a Complex of *Campylobacter jejuni* dUTPase with Substrate Analogue Sheds Light on the Mechanism and Suggests the "Basic Module" for Dimeric d(C/U)TPases. *J. Mol. Biol.* **2004**, *342* (5), 1583–1597.

(53) Hemsworth, G. R.; Moroz, O. V; Fogg, M. J.; Scott, B.; Bosch-Navarrete, C.; González-Pacanowska, D.; Wilson, K. S. The Crystal Structure of the *Leishmania major* Deoxyuridine Triphosphate Nucleotidohydrolase in Complex with Nucleotide Analogues , dUMP , and Deoxyuridine. *J. Biol. Chem.* **2011**, *286* (18), 16470–16481.

(54) Hidalgo-Zarco, F.; Camacho, A. G.; Bernier-Villamor, V.; Nord, J.; Ruiz-Pérez, L. M.; González-Pacanowska, D. Kinetic Properties and Inhibition of the Dimeric dUTPase-dUDPase from *Leishmania major*. *Protein Sci.* **2001**, *10*, 1426–1433.

(55) Larsson, G.; Nyman, P. O.; Kvassman, J. Kinetic Characterization of dUTPase from *Escherichia coli*. *J. Biol. Chem.* **1996**, *271* (39), 24010–24016.

(56) Persson, R.; Cedergren-Zeppezauer, E. S.; Wilson, K. S. Homotrimeric dUTPases; Structural Solutions for Specific Recognition and Hydrolysis of dUTP. *Curr. Protein Pept. Sci.* **2001**, *2* (4), 287–300.

(57) Gonçalves, A. M. D.; de Sanctis, D.; McSweeney, S. M. Structural and Functional Insights into DR2231 Protein, the MazG-like Nucleoside Triphosphate Pyrophosphohydrolase from *Deinococcus radiodurans*. *J. Biol. Chem.* **2011**, *286* (35), 30691–30705.

(58) Mota, C. S.; Gonçalves, A. M. D.; de Sanctis, D. *Deinococcus radiodurans* DR2231 Is a Two-Metal-Ion Mechanism Hydrolase with Exclusive Activity on dUTP. *FEBS J.* **2016**, *283* (23), 4274–4290.

(59) Wu, B.; Liu, Y.; Zhao, Q.; Liao, S.; Zhang, J.; Bartlam, M.; Chen, W.; Rao, Z. Crystal Structure of RS21-C6, Involved in Nucleoside Triphosphate Pyrophosphohydrolysis. *J. Mol. Biol.* **2007**, *367* (5), 1405–1412.

(60) Nonaka, M.; Tsuchimoto, D.; Sakumi, K.; Nakabeppu, Y. Mouse RS21-C6 Is a Mammalian 2′-Deoxycytidine 5′-Triphosphate Pyrophosphohydrolase That Prefers 5-Iodocytosine. *FEBS J.* **2009**, *276* (6), 1654–1666.

(61) Javid-Majd, F.; Yang, D.; Ioerger, T. R.; Sacchettini, J. C. The 1.25 Å Resolution Structure of Phosphoribosyl-ATP Pyrophosphohydrolase from *Mycobacterium*

tuberculosis. *Acta Crystallogr. Sect. D* **2008**, *D64*, 627–635.

(62) Hemsworth, G. R.; González-Pacanowska, D.; Wilson, K. S. On the Catalytic Mechanism of Dimeric dUTPases. *Biochem. J.* **2013**, *456* (1), 81–88.

(63) D'Ordine, R. L. D.; Klem, T. J.; Davisson, V. J. N1-(5′-Phosphoribosyl) Adenosine-5′-Monophosphate Cyclohydrolase: Purification and Characterization of a Unique Metalloenzyme. *Biochemistry* **1999**, *38* (5), 1537–1546.

(64) Sivaraman, J.; Myers, R. S.; Boju, L.; Sulea, T.; Cygler, M.; Davisson, V. J.; Schrag, J. D.; March, R. V. Crystal Structure of *Methanobacterium thermoautotrophicum* Phosphoribosyl-AMP Cyclohydrolase HisI. *Biochemistry* **2005**, *44* (30), 10071–10080.

(65) D'Ordine, R. L. D.; Linger, R. S.; Thai, C. J.; Davisson, V. J. Catalytic Zinc Site and Mechanism of the Metalloenzyme PR-AMP Cyclohydrolase. *Biochemistry* **2012**, *51* (29), 5791–5803.

(66) Merkler, D. J.; Schramm, V. L. Catalytic Mechanism of Yeast Adenosine 5′-Monophosphate Deaminase. Zinc Content, Substrate Specificity, pH Studies, and Solvent Isotope Effects. *Biochemistry* **1993**, *22*, 5792–5799.

(67) Carter Jr, C. W. The Nucleoside Deaminases for Cytidine and Adenosine: Structure, Transition State Stabilization, Mechanism, and Evolution. *Biochemie* **1995**, *77*, 92–98.

(68) Carlow, D. C.; Carter Jr, C. W.; Mejlhede, N.; Neuhard, J.; Wolfenden, R. Cytidine Deaminases from *B. subtilis* and *E. coli*: Compensating Effects of Changing Zinc Coordination and Quaternary Structure. *Biochemistry* **1999**, *38* (38), 12258–12265.

(69) Wilson, D. K.; Rudolph, F. B.; Quiocho, F. A. Atomic Structure of Adenosine Deaminase Complexed with a Transition-State Analog: Understanding Catalysis and Immunodeficiency Mutations. *Science* **1991**, *252* (5010), 1278–1284.

(70) Wang, Y.; Zhang, F.; Nie, Y.; Shang, G.; Zhang, H. Biochemical and Biophysical

Research Communications Structural Analysis of *Shigella flexneri* Bi-Functional Enzyme HisIE in Histidine Biosynthesis. *Biochem. Biophys. Res. Commun.* **2019**, *516* (2), 540–545.

(71) Witek, W.; Sliwiak, J.; Ruszkowski, M. Structural and Mechanistic Insights into the Bifunctional HISN2 Enzyme Catalyzing the Second and Third Steps of Histidine Biosynthesis in Plants. *Sci. Rep.* **2021**, *11* (1), 9647.

(72) Gupta, M.; Prasad, Y.; Sharma, S. K.; Jain, C. K. Identification of Phosphoribosyl-AMP Cyclohydrolase, as Drug Target and Its Inhibitors in *Brucella melitensis* Bv. 1 16M Using Metabolic Pathway Analysis. *J. Biomol. Struct. Dyn.* **2017**, *35* (2), 287–299.

(73) Hashimoto, S. Discovery and History of Amino Acid Fermentation. In *Amino Acid Fermentation*; Yokota, A., Ikeda, M., Eds.; Springer Japan: Tokyo, 2017; pp 15–34.

(74) Leuchtenberger, W.; Huthmacher, K. Biotechnological Production of Amino Acids and Derivatives : Current Status and Prospects. *Appl. Microbiol. Biotechnol.* **2005**, *69*, 1–8.

(75) Ikeda, M. Amino Acid Production Processes. In *Microbial Production of l-Amino Acids*; Faurie, R., Thommel, J., Bathe, B., Debabov, V. G., Huebner, S., Ikeda, M., Kimura, E., Marx, A., Möckel, B., Mueller, U., et al., Eds.; Springer Berlin Heidelberg: Berlin, Heidelberg, 2003; pp 1–35.

(76) D'Este, M. D.; Alvarado-morales, M.; Angelidaki, I. Amino Acids Production Focusing on Fermentation Technologies – A Review. *Biotechnol. Adv.* **2018**, *36* (1), 14–25.

(77) Breuer, M.; Ditrich, K.; Habicher, T.; Hauer, B.; Keßeler, M.; Stürmer, R.; Zelinski, T. Industrial Chemistry Industrial Methods for the Production of Optically Active Intermediates Angewandte. *Angwandte Chemie* **2004**, *43* (7), 788–824.

(78) Kulis-Horn, R. K.; Persicke, M.; Kalinowski, J. *Corynebacterium glutamicum*

ATP-Phosphoribosyl Transferases Suitable for L-Histidine Production - Strategies for the Elimination of Feedback Inhibition. *J. Biotechnol.* **2015**, *206*, 26–37.

(79) Wu, H.; Tian, D.; Fan, X.; Fan, W.; Zhang, Y.; Jiang, S.; Wen, C.; Ma, Q.; Chen, N.; Xie, X. Highly Efficient Production of L-Histidine from Glucose by Metabolically Engineered *Escherichia coli*. *ACS Synth. Biol.* **2020**, *9* (7), 1813–1822.

(80) Buller, A. R.; Van Roye, P.; Cahn, J. K. B.; Scheele, R. A.; Herger, M.; Arnold, F. H. Directed Evolution Mimics Allosteric Activation by Stepwise Tuning of the Conformational Ensemble. *J. Am. Chem. Soc.* **2018**, *140* (23), 7256–7266.

(81) O'neill, J. *Review on Antimicorbial Resistance: Tackling a Crisis for the Health and Wealth of Nations*; London, 2014.

(82) Abdo, M.; Joseph, P.; Mortier, J.; Turtaut, F.; Montero, J.-L.; Masereel, B.; Köhler, S.; Winum, J.-Y. Anti-Virulence Strategy against *Brucella suis*: Synthesis, Biological Evaluation and Molecular Modeling of Selective Histidinol Dehydrogenase Inhibitors. *Org. Biomol. Chem.* **2011**, *9* (10), 3681–3690.

(83) Tacconelli, E.; Carrara, E.; Savoldi, A.; Harbarth, S.; Mendelson, M.; Monnet, D. L.; Pulcini, C.; Kahlmeter, G.; Kluytmans, J.; Carmeli, Y.; et al. Discovery, Research, and Development of New Antibiotics: The WHO Priority List of Antibiotic-Resistant Bacteria and Tuberculosis. *Lancet. Infect. Dis.* **2018**, *18* (3), 318–327.

(84) Howard, A.; Donoghue, M. O.; Feeney, A.; Sleator, R. D. *Acinetobacter baumannii* An Emerging Opportunistic Pathogen. *Virulence* **2012**, *3* (3), 243–250.

(85) Antunes, C. S.; Visca, P.; Towner, K. J. *Acinetobacter baumannii* : Evolution of a Global Pathogen. *Pathog. Dis.* **2014**, *71* (3), 292–301.

(86) Moubareck, C. A.; Halat, D. H. Insights into *Acinetobacter baumannii*: A Review of Microbiological, Virulence, and Resistance Traits in a Threatening Nosocomial Pathogen. *Antibiotics* **2020**, *9* (3), 119.

(87) Chaari, A.; Mnif, B.; Bahloul, M.; Mahjoubi, F.; Chtara, K.; Turki, O.; Gharbi, N.; Chelly, H.; Hammami, A.; Bouaziz, M. *Acinetobacter baumannii* Ventilator-Associated Pneumonia: Epidemiology, Clinical Characteristics, and Prognosis Factors. *Int. J. Infect. Dis.* **2013**, *17* (12), e1225–e1228.

(88) Ebenezer, K.; Ebor, J. G. G.; Michael, J. S.; Kang, G.; Erghese, V. P. Ventialtor-Associated *Acinetobacter baumannii* Pneumonia. *Indian Pediatr.* **2011**, *48* (12), 15–17.

(89) Čiginskienė, A.; Dambrauskienė, A.; Rello, J.; Adukauskienė, D. Ventilator-Associated Pneumonia Due to Drug-Resistant *Acinetobacter baumannii*: Risk Factors and Mortality Relation with Resistance Profiles, and Independent Predictors of In-Hospital Mortality. *Med.* **2019**, *55* (2), 49.

(90) Ayobami, O.; Willrich, N.; Harder, T.; Okeke, I. N.; Eckmanns, T.; Markwart, R. The Incidence and Prevalence of Hospital-Acquired (Carbapenem-Resistant) *Acinetobacter baumannii* in Europe, Eastern Mediterranean and Africa: A Systematic Review and Meta-Analysis. *Emerg. Microbes Infect.* **2019**, *8* (1), 1752–1758.

(91) Nowak, P.; Paluchowska, P. *Acinetobacter baumannii* : Biology and Drug Resistance — Role of Carbapenemases. *Folia Histochem. Cytobiol.* **2016**, *54* (2), 61–74.

(92) Papp-Wallace, K. M.; Endimiani, A.; Taracila, M. A.; Bonomo, R. A. Carbapenems: Past, Present, and Future. *Antimicrob. Agents Chemother.* **2011**, *55* (11), 4943–4960.

(93) Nordmann, P.; Poirel, L. Epidemiology and Diagnostics of Carbapenem Resistance in Gram-Negative Bacteria. *Clin. Infect. Dis.* **2019**, *69*, S521–S528.

(94) Kyriakidis, I.; Vasileiou, E.; Pana, Z. D.; Tragiannidis, A. *Acinetobacter baumannii* Antibiotic Resistance Mechanisms. *Pathogens* **2021**, *10* (3), 373.

(95) Abadi, A. T. B.; Rizvanov, A. A.; Haertlé, T.; Blatt, N. L. World Health Organization Report : Current Crisis of Antibiotic Resistance. *Bionanoscience*

2019, *9*, 778–788.

(96) Hoang Quoc, C.; Nguyen Thi Phuong, T.; Nguyen Duc, H.; Tran Le, T.; Tran Thi Thu, H.; Nguyen Tuan, S.; Phan Trong, L. Carbapenemase Genes and Multidrug Resistance of *Acinetobacter baumannii*: A Cross Sectional Study of Patients with Pneumonia in Southern Vietnam. *Antibiotics* **2019**, *8* (3).

(97) Nowak, J.; Zander, E.; Stefanik, D.; Higgins, P. G.; Roca, I.; Vila, J.; Mcconnell, M. J.; Cisneros, J. M. High Incidence of Pandrug-Resistant A*cinetobacter baumannii* Isolates Collected from Patients with Ventilator-Associated Pneumonia in Greece, Italy and Spain as Part of the MagicBullet Clinical Trial. *J. Antimicrob. Chemother.* **2017**, *72* (12), 3277–3282.

(98) Lonergan, Z. R.; Palmer, L. D.; Skaar, E. P. Histidine Utilization Is a Critical Determinant of Acinetobacter Pathogenesis. *Infect. Immun.* **2020**, *88* (7), e00118-120.

(99) Nairn, B. L.; Lonergan, Z. R.; Wang, J.; Braymer, J. J.; Zhang, Y.; Calcutt, M. W.; Lisher, J. P.; Gilston, B. A.; Chazin, W. J.; de Crécy-Lagard, V.; et al. The Response of *Acinetobacter baumannii* to Zinc Starvation. *Cell Host Microbe* **2016**, *19* (6), 826–836.

(100) Cabral, M. P.; Soares, N. C.; Aranda, J.; Parreira, R.; Rumbo, C.; Poza, M.; Valle, J.; Calamia, V.; Lasa, I.; Bou, G. Proteomic and Functional Analyses Reveal a Unique Lifestyle for *Acinetobacter baumannii* Biofilms and a Key Role for Histidine Metabolism. *J. Proteome Res.* **2011**, *10* (8), 3399–3417.

(101) Ayala-del-Río, H. L.; Chain, P. S.; Grzymski, J. J.; Ponder, M. A.; Ivanova, N.; Bergholz, P. W.; Bartolo, G. Di; Hauser, L.; Land, M.; Bakermans, C.; et al. The Genome Sequence of *Psychrobacter Arcticus* 273-4, a Psychroactive Siberian Permafrost Bacterium, Reveals Mechanisms for Adaptation to Low-Temperature Growth. *Appl. Environ. Microbiol.* **2010**, *76* (7), 2304–2312.

(102) Martin, R. G.; Berberich, M. A.; Ames, B. N.; Davis, W. W.; Goldberger, R. F.; Yourno, J. D. Enzymes and Intermediates of Histidine Biosynthesis in *Salmonella*

Typhimurium. *Methods Enzymol.* **1971**, *17*, 3–44.

(103) Niesen, F. H.; Berglund, H.; Vedadi, M. The Use of Differential Scanning Fluorimetry to Detect Ligand Interactions That Promote Protein Stability. *Nat. Protoc.* **2007**, *2* (9), 2212–2221.

(104) Oke, M.; Carter, L. G.; Johnson, K. A.; Liu, H.; Mcmahon, S. A.; Yan, X.; Kerou, M.; Weikart, N. D.; Kadi, N.; Sheikh, A.; et al. The Scottish Structural Proteomics Facility: Targets, Methods and Outputs. *J. Structual Funct. Genomics* **2010**, *11* (2), 167–180.

(105) Liu, H.; Naismith, J. H. An Efficient One-Step Directed Deletion, Insertion, Single and Multiple-Site Plasmid Mutagenesis Protocol. *BMC Biotechnol.* **2008**, *10* (8), 1–10.

(106) Battye, T. G. G.; Kontogiannis, L.; Johnson, O.; Powell, H. R.; Leslie, A. G. W. Research Papers IMOSFLM : A New Graphical Interface for Diffraction- Image Processing with MOSFLM Research Papers. *Acta Crystallogr. D. Biol. Crystallogr.* **2011**, *D67*, 271–281.

(107) Evans, P. R.; Garib, N. How Good Are My Data and What Is the Resolution ? Research Papers. *Acta Crystallogr. D. Biol. Crystallogr.* **2013**, *D69*, 1204–1214.

(108) Winter, G. Xia2: An Expert System for Macromoleuclar Crystallography Data Reduction. *J. Appl. Crystallogr.* **2010**, *43* (1), 186–190.

(109) Winter, G.; Waterman, D. G.; Parkhurst, J. M.; Aaron, S.; Gildea, R. J.; Gerstel, M.; Fuentes-Montero, L.; Michels-clark, T.; Young, I. D.; Sauter, K.; et al. DIALS : Implementation and Evaluation of a New Integration Package. *Acta Crystallogr. Sect. D, Biol. Crystallogr.* **2018**, *D74*, 85–97.

(110) Vagin, A.; Teplyakov, A. MOLREP: An Automated Program for Molecular Replacement. *J. Appl. Crystallogr.* **1997**, *30* (6), 1022–1025.

(111) Emsley, P.; Cowtan, K. Coot: Model-Building Tools for Molecular Graphics. *Acta Crystallogr. D. Biol. Crystallogr.* **2004**, *D60*, 2126–2132.

(112) Murshudov, G. N.; Vagin, A. A.; Dodson, E. J. Refinement of Macromolecular Structures by the Maximum-Likelihood Method. *Acta Crystallogr. D. Biol. Crystallogr.* **1997**, *53*, 240–2555.

(113) Gibson, D. G. Synthesis of DNA Fragments in Yeast by One-Step Assembly of Overlapping Oligonucleotides. *Nucleic Acids Res.* **2009**, *37* (20), 6984–6990.

(114) da Silva, R. G.; Rosado, L. A.; Santos, D. S.; Basso, L. A. Mycobacterium Tuberculosis β-Ketoacyl-ACP Reductase: α-Secondary Kinetic Isotope Effects and Kinetic and Equilibrium Mechanisms of Substrate Binding. *Arch. Biochem. Biophys.* **2008**, *471* (1), 1–10.

(115) Webb, M. R. A Continuous Spectrophotometric Assay for Inorganic Phosphate and for Measuring Phosphate Release Kinetics in Biological Systems. *Proc. Natl. Acad. Sci. U. S. A.* **1992**, *89* (11), 4884–4887.

(116) Bell, R. M.; Koshland, D. E. A Phosphoribosyl-Enzyme Covalent Intermediate in the First Enzyme of Histidine Biosynthesis. *Biochem. Biophys. Res. Commun.* **1970**, *38* (4), 539–545.

(117) Chelsky, D.; Parsons, S. M. Stereochemical Course of the Adenosine Triphosphate Phosphoribosyltransferase Reaction in Histidine Biosynthesis. *J. Biol. Chem.* **1975**, *250* (14), 5669–5673.

(118) Kleeman, J. E.; Parsons, S. M. Reverse Direction Substrate Kinetics and Inhibition Studies on the First Enzyme of the Histidine Biosynthesis, Adenosine Triphosphate Phosphoribosyl Transferse. *Arch. Biochem. Biophys.* **1976**, *175* (2), 687–693.

(119) Bashor, C.; Denu, J. M.; Brennan, R. G.; Ullman, B. Kinetic Mechanism of Adenine Phosphoribosyltransferase from Leishmania Donovani. *Biochemistry* **2002**, *41* (12), 4020–4031.

(120) Xu, Y.; Eads, J.; Sacchettini, J. C.; Grubmeyer, C. Kinetic Mechanism of Human Hypoxanthine-Guanine Phosphoribosyltransferase: Rapid Phosphoribosyl Transfer Chemistry. *Biochemistry* **1997**, *2960* (96), 3700–3712.

(121) Wang, G. P.; Lundegaard, C.; Jensen, K. F.; Grubmeyer, C. Kinetic Mechanism of OMP Synthase: A Slow Physical Step Following Group Transfer Limits Catalytic Rate. *Biochemistry* **1999**, *38* (1), 275–283.

(122) Rein, C. M.; Desai, U. R.; Church, F. C. Serpin-Glycosaminoglycan Interactions. *Methods Enzymol.* **2011**, *501*, 105–137.

(123) Perozzo, R.; Folkers, G.; Scapozza, L. Thermodynamics of Protein-Ligand Interactions: History, Presence, and Future Aspects. *J. Recept. Signal Transduct.* **2004**, *24*, 1–52.

(124) Turnbull, W. B.; Daranas, A. H. On the Value of c: Can Low Affinity Systems Be Studied by Isothermal Titration Calorimetry? *Biochemistry* **2003**, *48* (12), 14859–14866.

(125) Rühmann, E.; Betz, M.; Fricke, M.; Heine, A.; Schäfer, M.; Klebe, G. Thermodynamic Signatures of Fragment Binding: Validation of Direct versus Displacement ITC Titrations. *Biochim. Biophys. Acta* **2015**, *1850* (4), 647–656.

(126) Cook, P. F.; Cleland, W. W. *Enzyme Kinetics and Mechanism*; Garland Science Publishing: New York, 2007.

(127) Cleland, W. W. The Kinetics of Enzyme-Catalysed Reactions with Two or More Substrates or Products: III. Prediction of Inital Velocity and Inhibition Patters by Inspection. *Biochim. Biophys. Acta* **1963**, *67*, 188–196.

(128) Truhlar, D. G.; Kohen, A. Convex Arrhenius Plots and Their Interpretation. *Proc. Natl. Acad. Sci.* **2000**, *98* (3), 848–851.

(129) Sočan, J.; Purg, M.; Åqvist, J. Computer Similations Explain the Anomalous Temperature Optimum in a Cold-Adapted Enzyme. *Nat. Commun.* **2020**, *11*, 2644.

(130) Arcus, V. L.; Prentice, E. J.; Hobbs, J. K.; Mulholland, A. J.; Kamp, M. W. Van Der; Pudney, C. R.; Parker, E. J.; Schipper, L. A. On the Temperature Dependence of Enzyme-Catalyzed Rates. *Biochemistry* **2016**, *55* (12), 1681–1688.

(131) Hobbs, J. K.; Jiao, W.; Easter, A. D.; Parker, E. J.; Schipper, L. A.; Arcus, V. L. Change in Heat Capacity for Enzyme Catalysis Determines Temperature Dependence of Enzyme Catalyzed Rates. *ACS Chem. Biol.* **2013**, *8* (11), 2388–2393.

(132) Kamp, M. W. Van Der; Prentice, E. J.; Kraakman, K. L.; Connolly, M.; Mulholland, A. J.; Arcus, V. L. Dynamical Origins of Heat Capacity Changes in Enzyme-Catalysed Reactions. *Nat. Commun.* **2018**, *9* (1), 1177.

(133) Machado, T. F. G.; Gloster, T. M.; da Silva, R. G. Linear Eyring Plots Conceal a Change in the Rate-Limiting Step in an Enzyme Reaction. *Biochemistry* **2018**, *57*, 6747–6761.

(134) Wintrode, P. L.; Arnold, F. H. Temperature Adaptation of Enzymes: Lessons from Laboratory Evolution. In *Evolutionary Protein Design*; Advances in Protein Chemistry; Academic Press, 2001; Vol. 55, pp 161–225.

(135) Albe, K. R.; Butler, M. H.; Wright, B. E. Cellular Concentrations of Enzymes and Their Substrates. *J. Theor. Biol.* **1990**, *143* (2), 163–195.

(136) Bennett, B. D.; Kimball, E. H.; Gao, M.; Osterhout, R.; Van Dien, S. J.; Rabinowitz, J. D. Absolute Metabolite Concentrations and Implied Enzyme Active Site Occupancy in *Escherichia coli*. *Nat. Chem. Biol.* **2009**, *5* (8), 593–299.

(137) Buckstein, M. G.; He, J.; Rubin, H. Characterization of Nucleotdie Pools as a Function of Physiological State in *Escherichia coli*. *J. Bacteriol.* **2008**, *190* (2), 718–726.

(138) Yaginuma, H.; Kawai, S.; Tabata, K. V; Tomiyama, K.; Kakizuka, A.; Komatsuzaki, T.; Noji, H.; Imamura, H. Diversity in ATP Concentrations in a Single Bacterial Cell Population Revealed by Quantiative Single-Cell Imaging. *Scienitifc Reports* **2014**, *4*, 6522.

(139) Gadda, G.; Sobrado, P. Kinetic Solvent Viscosity Effects as Probes for Studying the Mechanisms of Enzyme Action. *Biochemistry* **2018**, *57* (25), 3445–3453.

(140) Grace, M. R.; Walsh, C. T.; Cole, P. A. Divalent Ion Effects and Insights into the Catalytic Mechanism of Protein Tyrosine Kinase Csk. *Biochemistry* **1997**, *36* (7), 1875–1881.

(141) Karsten, W. E.; Lai, C.; Cook, P. F. Inverse Solvent Isotope Effects in the NAD-Malic Enzyme Reaction Are the Result of the Viscosity Difference between D_2O and H_2O: Implications for Solvent Isotope Effect Studies. *J. Am. Chem. Soc.* **1995**, *117* (22), 5914–5918.

(142) Rungsrisuriyachai, K.; Gadda, G. On the Role of Histidine 351 in the Reaction of Alcohol Oxidation Catalyzed by Choline Oxidase. *Biochemistry* **2008**, *47* (26), 6762–6769.

(143) Johnson, K. A. *Transient-State Kinetics Analysis of Enzyme Reaction Pathways*; Academic Press Inc, 1992.

(144) Rosen, B. P.; Bhattacharjee, H.; Zhou, T.; Walmsley, A. R. Mechanism of the ArsA ATPase. *Biochim. Biophys. Acta* **1999**, *1461* (2), 207–215.

(145) Goodey, N. M.; Benkovic, S. J. Allosteric Regulation and Catalysis Emerge Via A Common Route. *Nat. Chem. Biol.* **2008**, *4* (8), 474–481.

(146) Swain, J. F.; Gierasch, L. M. The Changing Landscape of Protein Allostery. *Curr. Opin. Struct. Biol.* **2006**, *16* (1), 102–108.

(147) Kar, G.; Keskin, O.; Gursoy, A.; Nussinov, R. Allostery and Population Shift in Drug Discovery. *Curr. Opin. Pharmacol.* **2010**, *10* (6), 715–722.

(148) Peracchi, A.; Mozzarelli, A. Exploring and Exploiting Allostery: Models, Evolution, and Drug Targeting. *Biochim. Biophys. Acta* **2011**, *1814* (8), 922–933.

(149) Gunasekaran, K.; Ma, B.; Nussinov, R. Is Allostery an Intrinsic Property of All Dynamic Proteins? *Proteins.* **2004**, *57* (3), 433–443.

(150) Kumar, S.; Ma, B.; Tsai, C.-J.; Sinha, N.; Nussinov, R. Folding and Binding Cascades: Dynamic Landscapes and Population Shifts. *Protein Sci.* **2000**, *9*, 10–

19.

(151) Yep, A.; Mcleish, M. J. Engineering the Substrate Binding Site of Benzoylformate Decarboxylase. *Biochemistry* **2009**, *48* (35), 8387–8395.

(152) Smith, M. E. B.; Hibbert, E. G.; Jones, A. B.; Dalby, P. A.; Hailes, H. C. Enhancing and Reversing the Stereoselectivity of *Escherichia coli* Transketolase. *Adv. Synth. Catal.* **2008**, *350*, 2631–2638.

(153) Gordeeva, T. L.; Borshchevskaya, L. N.; Kalinina, A. N.; Sineoky, S. P. Increase in the Thermal Stability of Phytase from *Citrobacter freundii* by Site-Directed Saturation Mutagenesis. *Appl. Biochem. Microbiol.* **2019**, *55* (8), 788–796.

(154) Fan, L.; Li, M.; Qiu, Y.; Chen, Q.; Jiang, S.; Shang, Y.; Chao, L.-M. Increasing Thermal Stability of Glutamate Decarboxylase from *Escherichia. coli* by Site-Directed Saturation Mutagenesis and Its Application in GABA Production. *J. Biotechnol.* **2018**, *278*, 1–9.

(155) Holmber, N.; Ryde, U.; Bulow, L. Redesign of the Coenzyme Specificity in L-Lactate Dehydrogenase from *Bacillus stearothermophilus* Using Site-Directed Mutagnesis and Media Engineering. *Protein Eng.* **1999**, *12* (10), 851–856.

(156) Andrews, F. H.; McLeish, M. J. Using Site-Saturation Mutagenesis to Explore Mechanism and Substrate Specificity in Thiamin Diphosphate- Dependent Enzymes. *FEBS J.* **2013**, *280* (24), 6395–6411.

(157) Yep, A.; Kenyon, G. L.; Mcleish, M. J. Saturation Mutagenesis of Putative Catalytic Residues of Benzoylformate Decarboxylase Provides a Challenge to the Accepted Mechanism. *Proc. Natl. Acad. Sci.* **2008**, *105* (15), 5733–5738.

(158) Shim, D. J.; Nemeria, N. S.; Balakrishnan, A.; Patael, H.; Song, J.; Want, J.; Jordan, F.; Farinas, E. T. Assignment of Function to Histidines 260 and 298 by Engineering the E1 Component of the Escherichia Coli 2-Oxoglutarate Dehydrogenase Complex; Subsitution That Lead to Acceptance of Substrates Lacking the 5-Carboxyl Group. *Biochemistry* **2012**, *50* (35), 7705–7709.

(159) Morra, S.; Giraudo, A.; di Nardo, G.; King, P. W.; Gilardi, G.; Valetti, F. Site Saturation Mutagenesis Demonstrates a Central Role for Cysteine 298 as Proton Donor to the Catalytic Site in CaHydA [FeFe] -Hydrogenase. *PLoS One* **2012**, *7* (10), e48400.

(160) Butterworth, A. C.; Medrano, F. J.; Eakin, A. E.; Craig III, S. P. Saturation Mutagenesis , Complement Selection , and Steady-State Kinetic Studies Illuminate the Roles of Invariant Residues in Active Site Loop I of the Hypoxanthine Phosphoribosyltransferase from *Trypanosoma cruzi*. *Biochim. Biophys. Acta* **2004**, *1699*, 87–94.

(161) Ishwar, A.; Tang, Q.; Fenton, A. W. Distinguishing the Interactions in the Fructose 1,6-Bisphosphate Binding Site of Human Liver Pyruvate Kinase That Contribute to Allostery. *Biochemistry* **2015**, *54* (7), 1516–1524.

(162) Veetil, V. P.; Raj, H.; Quax, W. J.; Janssen, D. B.; Poelarends, G. J. Site-Directed Mutagenesis, Kinetic and Inhibition Studies of Aspartate Ammonia Lyase from *Bacillus sp*. YM55-1. *FEBS J.* **2009**, *276* (11), 2994–3007.

(163) Siloto, R. M. P.; Weselake, R. J. Site Saturation Mutagenesis: Methods and Applications in Protein Engineering. *Biocatal. Agric. Biotechnol.* **2012**, *1* (3), 181–189.

(164) Toney, M.; Kirsch, J. F. Direct Brønsted Analysis of the Restoration of Activity to a Mutant Enzyme by Exogenous Amines. *Science* **1989**, *243*, 1485–1488.

(165) Rynkiewicz, M. J.; Seaton, B. A. Chemical Rescue by Guanidine Derivatives of an Arginine-Substituted Site-Directed Mutant of *Escherichia coli* Ornithine Transcarbamylase. *Biochemistry* **1996**, *35* (50), 16174–16179.

(166) Hung, J. E.; Fogle, E. J.; Garg, N.; Chekan, J. R.; Nair, S. K.; Der, W. A. Van. Chemical Rescue and Inhibition Studies to Determine the Role of Arg301 in Phosphite Dehydrogenase. *PLoS One* **2014**, *9* (1), e87134.

(167) Esen, H.; Alpdağtaş, S.; Çakar, M. M.; Binay, B. Tailoring of Recombinant FDH: Effect of Histidine Tag Location on Solubility and Catalytic Properties of

Chaetomium thermophilum Formate Dehydrogenase (CtFDH). *Prep. Biochem. Biotechnol.* **2019**, *49* (5), 529–534.

(168) Meng, L.; Liu, Y.; Yin, X.; Zhou, H.; Wu, J.; Wu, M.; Yang, L. Effects of His-Tag on Catalytic Activity and Enantioselectivity of Recombinant Transaminases. *Appl. Biochem. Biotechnol.* **2020**, *190* (3), 880–895.

(169) Henzler-Wildman, K. A.; Thai, V.; Lei, M.; Ott, M.; Wolf-watz, M.; Fenn, T.; Kern, D.; Pozharski, E.; Wilson, M. A.; Petsko, G. A.; et al. Intrinsic Motions along an Enzymatic Reaction Trajectory. *Nature* **2007**, *450*, 838–844.

(170) Zhu, Y.; He, L.; Liu, Y.; Zhao, Y.; Zhang, X. C. SmFRET Probing Reveals Substrate-Dependent Conformational Dynamics of *E. coli* Multidrug MdfA. *Biophys. J.* **2019**, *116* (12), 2296–2303.

(171) Warshel, A.; Sharma, P. K.; Kato, M.; Xiang, Y.; Liu, H.; Olsson, M. H. M. Electrostatic Basis for Enzyme Catalysis. *Chem. Rev.* **2006**, *106* (8), 3210–3235.

(172) Villali, J.; Kern, D. Choreographing an Enzyme's Dance. *Curr. Opin. Chem. Biol.* **2010**, *14* (5), 636–643.

(173) Otten, R.; Pádua, R. A. P.; Bunzel, H. A.; Nguyen, V.; Pitsawong, W.; Patterson, M.; Sui, S.; Perry, S. L.; Cohen, A. E.; Hilvert, D.; et al. How Directed Evolution Reshapes the Energy Landscape in an Enzyme to Boost Catalysis. *Science* **2020**, *370*, 1442–1446.

(174) Bunzel, H. A.; Anderson, J. L. R.; Hilvert, D.; Arcus, V. L.; Kamp, M. W. Van Der; Mulholland, A. J. Evolution of Dyanamical Networks Enhances Catalysis in a Designer Enzyme. *Nat. Chem.* **2021**, *13*, 1017–1022.

(175) Huang, S. K.; Pandey, A.; Tran, D. P.; Villanueva, N. L.; Kitao, A.; Sunahara, R. K.; Sljoka, A.; Prosser, R. S. Delineating the Conformational Landscape of the Adenosine A2A Receptor during G Protein Coupling. *Cell* **2021**, *184* (7), 1884–1894.

(176) Lechtenberg, B. C.; Freund, S. M. V; Huntington, J. A. An Ensemble View of

Thrombin Allostery. *Biol. Chem.* **2012**, *393* (9), 889–898.

(177) Otten, R.; Liu, L.; Kenner, L. R.; Clarkson, M. W.; Mavor, D.; Tawfik, D. S.; Kern, D.; Fraser, J. S. Rescue of Conformational Dynamics in Enzyme Catalysis by Directed Evolution. *Nat. Commun.* **2018**, *9* (1), 1314.

(178) Ruvinov, S. B.; Ahmed, S. A.; McPhie, P.; Miles, E. W. Monovalent Cations Partially Repair a Conformational Defect in a Mutant Tryptophan SynthaseA2B2 Complex (B-E109A). *J. Biol. Chem.* **1995**, *270* (29), 17333–17338.

(179) Yellapu, N. K.; Valasani, K. R.; Pasupuleti, S. K.; Gopal, S.; Venkata, S. P.; Krishna, G.; Matcha, B. Identification and Analysis of Novel R308K Mutation in Glucokinase of Type 2 Diabetic Patient and Its Kinetic Correlation. *Biotechnol. Appl. Biochem.* **2014**, *61* (5), 572–581.

(180) Yellapu, N. K.; Kandlapalli, K.; Kandimalla, R.; Adi, P. J. Conformational Transition Pathway of R308K Mutant Glucokinase in the Presence of the Glucokinase Activator. *FEBS Open Bio* **2018**, *8* (8), 1202–1208.

(181) Thomson, C. M. Allostery and Inhibition of Psychrobacter Arcticus Adenosine 5'-Triphosphate Phosphoribosyltransferase., University of St Andrews, 2019.

(182) Wingfield, P. Protein Precipitation Using Ammonium Sulfate. *Curr. Protoc. Protein Sci.* **2001**, *Appendix 3*, Appendix 3F.

(183) Lorber, B.; Fischer, F.; Bailly, M.; Roy, H.; Kern, D. Protein Analysis by Dynamic Light Scattering: Methods and Techniques for Students. *Biochem. Mol. Biol. Educ.* **2012**, *40* (6), 372–382.

(184) Gao, K.; Oerlemans, R.; Groves, M. R. Theory and Applications of Differential Scanning Fluorimetry in Early-Stage Drug Discovery. *Biophys. Rev.* **2020**, *12* (1), 85–104.

(185) Cipolla, A.; Delbrassine, F.; da Lage, J.-L.; Feller, G. Temperature Adaptations in Psychrophilic, Mesophilic and Thermophilic Chloride-Dependent Alpha-Amylases. *Biochimie* **2012**, *94* (9), 1943–1950.

(186) Bae, E.; Phillips Jr., G. N. Structures and Analysis of Highly Homologous Psychrophilic, Mesophilic, and Thermophilic Adenylate Kinases. *J. Biol. Chem.* **2004**, *279* (27), 28202–28208.

(187) Georlette, D.; Damien, B.; Blaise, V.; Depiereux, E.; Uversky, V. N.; Gerday, C.; Feller, G. Structural and Functional Adaptations to Extreme Temperatures in Psychrophilic, Mesophilic, and Thermophilic DNA Ligases. *J. Biol. Chem.* **2003**, *278* (39), 37015–37023.

(188) da Silva, R. G.; Schramm, V. L. Uridine Phosphorylase from *Trypanosoma cruzi:* Kinetic and Chemical Mechanisms. *Biochemistry* **2011**, *50* (42), 9158—9166.

(189) Cleland, W. W. The Use of Isotope Effects to Determine Enzyme Mechanisms. *Arch. Biochem. Biophys.* **2005**, *433*, 2–12.

(190) Chem, B.; Northrop, D. B. Steady-State Analysis of Kinetic Isotope Effects in Enzymic Reactions. *Biochemistry* **1975**, *14* (12), 2644–2650.

(191) Hermes, J. D.; Roeske, C. A.; Leary, M. H. O.; Cleland, W. W. Use of Multiple Isotope Effects To Determine Enzyme Mechanisms and Intrinsic Isotope Effects. Malic Enzyme and Glucose-6-Phosphate Dehydrogenase. *Biochemisty* **1982**, *21* (20), 5106–5114.

(192) Fernandez, P. L.; Murkin, A. S. Inverse Solvent Isotope Effects in Enzyme-Catalyzed Reactions. *Molecules* **2020**, *25* (8).

(193) Hardy, B. R. C.; Cottington, R. L. Viscosity of Deuterium Oxide and Water in the Range 5° to 125° C. *J. Res. Natl. Bur. Stand. (1934).* **1949**, *42*, 573–578.

(194) Gannavaram, S.; Gadda, G. Relative Timing of Hydrogen and Proton Transfers in the Reaction of Flavin Oxidation Catalyzed by Choline Oxidase. *Biochemistry* **2013**, *52* (7), 1221–1226.

(195) Glasoe, P. K.; Long, F. A. Use of Glass Electrodes to Measure Acidities in Deuterium Oxide. *J. Phys. Chem.* **1960**, *64*, 188–190.

(196) Schramm, V. L. Enzymatic Transition States, Transition-State Analogs, Dynamics, Thermodynamics, and Lifetimes. *Annu. Rev. Biochem.* **2011**, *80*, 703–732.

Appendix 1 Peptide mapping of proteins digested by trypsin and analysed by MS/MS.

D179N *Pa*HisG$_S$

Protein sequence coverage: 87%

Matched peptides shown in ***bold red***.

```
  1 GMTEVTNSLP TSGLLNEAND EFLGLTLALS KGRILEETMP LLRAAGVELL
 51 EDPEASRKLI FPTSNPNVRV LILRASDVPT YVEHGAADFG VAGKDVLLEH
101 GANHVYELLD LKIAQCKLMT AGVKDAPLPN RRLRCATKYV NVARAYFASQ
151 GQQVDVIKLY GSMELAPLVG LGDLIVDVVN TGNTLRANGL EARDHICDVS
201 SRLIVNQVSY KRKFALLEPI LDSFKNSINS TS
```

*Pa*HisIE

Protein sequence coverage: 65%

Matched peptides shown in ***bold red***.

```
  1 MTLPAWLTAV NFNADGLIPA IAQDHESGRI LMMAWMNAES LQLTADTQTA
 51 VYFSRSRAKL WHKGESSGHT QRVHDIRLDC DADVIVLSVT QAGGIACHTG
101 RESCFYQRLD LSGQTPEWQT VDKVIKDPAE IYHSNEVANP PPTNDATAHN
151 SVSFDADANQ AKADKTSILQ QLDRVLAERK QADADSSYVA SLYDKGLNKI
201 LEKVGEESTE SIIAAKDFAN CDENIDKSQY DEARSELIYE VADVWFHTLV
251 GLAWFGIESD AVLNFIGRRF GLSGIDEKAA R
```

*Ab*HisIE (Monomer Band)

Protein sequence coverage: 68%

Matched peptides shown in ***bold red***.

```
  1 MNNTQWLDEV KFNEQGLIPA IAQHHQTGRI LMVAWMNRES LALTAEKNQA
 51 VYFSRSRQKL WHKGEESGHF QTVYEIRLDC DGDVIVLQVE QHGGIACHTG
101 RESCFYRKLT PQGWEIVDAQ LKDPTAIYGD NAKTESHDHA HTTEQVDVLA
151 HLGQLMQERK QAEADTSYVA SLYKKGINKI LEKVGEEGVE TIIAAKDYAT
201 QNTESNLNDL IYETADLWFH SIVMLGYFDL NPQLIIDELG RRQGLSGLVE
251 KANRNKV
```

*Ab*HisIE (Dimer Band)

Protein sequence coverage: 79%

Matched peptides shown in ***bold red***.

```
  1 MNNTQWLDEV KFNEQGLIPA IAQHHQTGRI LMVAWMNRES LALTAEKNQA
 51 VYFSRSRQKL WHKGEESGHF QTVYEIRLDC DGDVIVLQVE QHGGIACHTG
101 RESCFYRKLT PQGWEIVDAQ LKDPTAIYGD NAKTESHDHA HTTEQVDVLA
151 HLGQLMQERK QAEADTSYVA SLYKKGINKI LEKVGEEGVE TIIAAKDYAT
201 QNTESNLNDL IYETADLWFH SIVMLGYFDL NPQLIIDELG RRQGLSGLVE
251 KANRNKV
```

Appendix 2 Manuscripts

Biochemistry

Article

Cite This: *Biochemistry* 2018, 57, 4357−4367

pubs.acs.org/biochemistry

Allosteric Activation Shifts the Rate-Limiting Step in a Short-Form ATP Phosphoribosyltransferase

Gemma Fisher,[‡] Catherine M. Thomson,[‡] Rozanne Stroek,[‡] Clarissa M. Czekster,[‡] Jennifer S. Hirschi,*[,§] and Rafael G. da Silva*[,‡]

[‡]School of Biology, Biomedical Sciences Research Complex, University of St Andrews, St Andrews, Fife KY16 9ST, United Kingdom

[§]Department of Chemistry, Binghamton University, Binghamton, New York 13902, United States

Supporting Information

ABSTRACT: Short-form ATP phosphoribosyltransferase (ATPPRT) is a hetero-octameric allosteric enzyme comprising four catalytic subunits ($HisG_S$) and four regulatory subunits (HisZ). ATPPRT catalyzes the Mg^{2+}-dependent condensation of ATP and 5-phospho-α-D-ribosyl-1-pyrophosphate (PRPP) to generate N^1-(5-phospho-β-D-ribosyl)-ATP (PRATP) and pyrophosphate, the first reaction of histidine biosynthesis. While $HisG_S$ is catalytically active on its own, its activity is allosterically enhanced by HisZ in the absence of histidine. In the presence of histidine, HisZ mediates allosteric inhibition of ATPPRT. Here, initial velocity patterns, isothermal titration calorimetry, and differential scanning fluorimetry establish a distinct kinetic mechanism for ATPPRT where PRPP is the first substrate to bind. AMP is an inhibitor of $HisG_S$, but steady-state kinetics and ^{31}P NMR spectroscopy demonstrate that ADP is an alternative substrate. Replacement of Mg^{2+} by Mn^{2+} enhances catalysis by $HisG_S$ but not by the holoenzyme, suggesting different rate-limiting steps for nonactivated and activated enzyme forms. Density functional theory calculations posit an S_N2-like transition state stabilized by two equivalents of the metal ion. Natural bond orbital charge analysis points to Mn^{2+} increasing $HisG_S$ reaction rate via more efficient charge stabilization at the transition state. High solvent viscosity increases $HisG_S$'s catalytic rate, but decreases the hetero-octamer's, indicating that chemistry and product release are rate-limiting for $HisG_S$ and ATPPRT, respectively. This is confirmed by pre-steady-state kinetics, with a burst in product formation observed with the hetero-octamer but not with $HisG_S$. These results are consistent with an activation mechanism whereby HisZ binding leads to a more active conformation of $HisG_S$, accelerating chemistry beyond the product release rate.

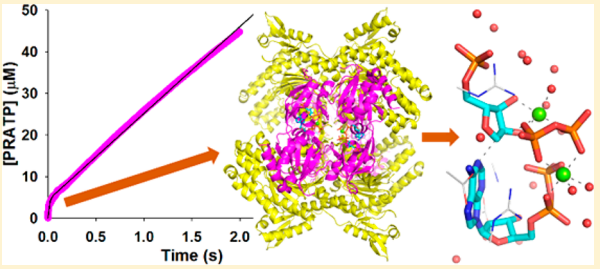

Allosteric control of catalysis is a widespread strategy evolved in biosynthetic pathways.[1−4] The modulation of biochemical pathways for synthetic biology applications often requires overcoming or manipulating allosteric regulation.[5,6] Furthermore, allosteric sites provide a more selective avenue for drug design in comparison with active sites, which tend to be more conserved.[3,7,8] Accordingly, the elucidation of allosteric mechanisms in multiprotein enzymatic complexes paves the way for future therapeutic and biotechnological applications.

The allosteric enzyme adenosine 5′-triphosphate phosphoribosyltransferase (ATPPRT) (EC 2.4.2.17), responsible for the first and flux-controlling step in histidine biosynthesis,[9] is a potential drug target in some pathogenic organisms,[8,10−12] the focus of synthetic biology endeavors to harness the histidine biosynthetic pathway for histidine production in bacteria,[6,13,14] and a model system for the study of allosteric regulation of catalysis.[3,8,15,16]

ATPPRT catalyzes the Mg^{2+}-dependent and reversible nucleophilic substitution of adenosine 5′-triphosphate (ATP) N1 on 5-phospho-α-D-ribosyl-1-pyrophosphate (PRPP) C1 to generate N^1-(5-phospho-β-D-ribosyl)-ATP (PRATP) and inorganic pyrophosphate (PP_i) (Scheme 1),[9] with the chemical equilibrium highly displaced toward reactants.[17] The metabolic status of the cell regulates ATPPRT activity via allosteric inhibition by histidine[9,18] and orthosteric inhibition by

Scheme 1. ATPPRT-Catalyzed Nucleophilic Substitution Reaction

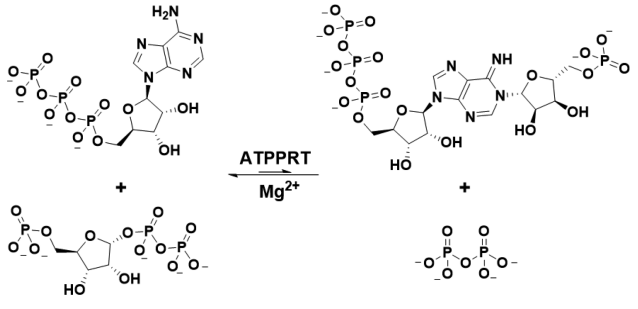

Received: May 17, 2018
Revised: June 15, 2018
Published: June 25, 2018

DOI: 10.1021/acs.biochem.8b00559
Biochemistry 2018, 57, 4357−4367

adenosine 5′-monophosphate (AMP).[19] Intriguingly, orthosteric inhibition by adenosine 5′-diphosphate (ADP) is also reported.[19]

The *his*G gene encodes two forms of ATPPRT. Most histidine-synthesizing organisms possess a long-form of the protein, $HisG_L$,[16,20] a homohexamer with each subunit consisting of two N-terminal catalytic domains and a C-terminal allosteric domain responsible for histidine inhibition.[11] $HisG_L$ ATPPRTs operate by a steady-state ordered kinetic mechanism where ATP is the first substrate to bind to, and PRATP the last product to dissociate from, the enzyme.[21,22]

Archaea and some eubacteria have instead a short-form of the protein, $HisG_S$,[23,24] a homodimer with each subunit comprising two catalytic domains homologous to $HisG_L$'s, but lacking the C-terminal allosteric domain.[20,25] Thus, $HisG_S$ is catalytically active on its own but insensitive to inhibition by histidine.[20,26] $HisG_S$ binds HisZ, the product of the *hisZ* gene, a catalytically inactive paralogue of histidyl-tRNA synthetase,[23] forming the hetero-octameric ATPPRT holoenzyme, where two $HisG_S$ dimers flank a HisZ tetramer.[24,26,27] HisZ has two distinct allosteric functions: in the absence of histidine, it activates catalysis by $HisG_S$, and in the presence of histidine, it binds the final product of the pathway and mediates allosteric inhibition of $HisG_S$.[20,24,26,28] The kinetic mechanism of $HisG_S$ ATPPRTs has not been investigated, but recent crystal structures suggest that the order of substrate binding may be different from $HisG_L$'s.[29] Moreover, little is known about the kinetics of allosteric activation.

We recently reported several crystal structures of the psychrophilic bacterium *Psychrobacter arcticus* dimeric $HisG_S$ (*Pa*$HisG_S$) and hetero-octameric ATPPRT holoenzyme (*Pa*ATPPRT),[26,29] from which an activation mechanism was inferred that involves tightening of the *Pa*$HisG_S$ dimer in the hetero-octamer when both substrates are bound (Figure 1), which facilitates leaving group stabilization at the transition state.[29] Here we employ initial rate studies, isothermal titration calorimetry (ITC), differential scanning fluorimetry (DSF), ^{31}P nuclear magnetic resonance (^{31}P NMR), liquid chromatography−mass spectrometry (LC-MS), density functional theory, solvent viscosity effects, and pre-steady-state kinetics to unveil a distinct kinetic mechanism for *Pa*ATPPRT, the role of ADP as a substrate instead of an inhibitor, the basis for charge-stabilization at the transition state, and a shift in the rate-liming step upon allosteric activation of the enzyme.

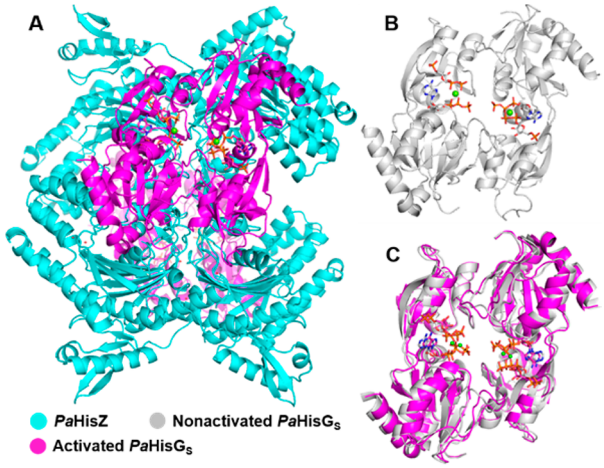

Figure 1. *Pa*$HisG_S$ and *Pa*ATPPRT quaternary structures and allosteric activation. (A) *Pa*ATPPRT hetero-octamer, where catalysis is enhanced. The second *Pa*$HisG_S$ homodimer is behind the *Pa*HisZ tetramer. (B) Nonactivated *Pa*$HisG_S$ homodimer and (C) overlay of activated and nonactivated *Pa*$HisG_S$ dimers. In all structures, *Pa*$HisG_S$ is bound to PRPP, ATP, and Mg^{2+}.[29]

MATERIALS AND METHODS

Materials. ATP, PRPP, PP_i, AMP, ADP, $MgCl_2$, $MnCl_2$, D_2O (99.9 atom % deuterium), tricine, dithiothreitol (DTT), and glycerol were purchased from Sigma-Aldrich. All other chemicals were purchased from readily available commercial sources, and all chemicals were used without further purification. *Pa*$HisG_S$, *Pa*HisZ, *Mycobacterium tuberculosis* pyrophosphatase (*Mt*PPase), and tobacco etch virus protease were obtained as previously published.[26] PRATP was produced as previously described.[29]

***Pa*$HisG_S$ and *Pa*ATPPRT Activity Assay.** All assays were performed under initial rate conditions in the forward direction at 20 °C as previously described[26] by monitoring the increase in absorbance at 290 nm due to formation of PRATP ($\varepsilon_{290\ nm}$ = 3600 M^{-1} cm^{-1})[30] in 1 cm path length quartz cuvettes (Hellma) in a Shimadzu UV-2600 spectrophotometer. Unless stated otherwise, for *Pa*$HisG_S$ activity, *Pa*$HisG_S$ concentration was 2.2 μM, and for *Pa*ATPPRT activity, *Pa*$HisG_S$ and *Pa*HisZ concentrations were 0.38 and 15 μM, respectively. Reactions were started by addition of PRPP. Control reactions lacked either ATP, PRPP, *Pa*$HisG_S$, or *Pa*HisZ. In all kinetic experiments under the various different conditions described below, controls were carried out to ensure that the rate did not depend on *Mt*PPase. Kinetic measurements were performed at least in duplicates unless stated otherwise.

***Pa*ATPPRT Equilibrium Dissociation Constant (K_D) in Glycerol.** Initial velocities were measured in the presence of 5.6 mM ATP, 2 mM PRPP, 0.38 μM *Pa*$HisG_S$, and varying concentrations of *Pa*HisZ (0.9−8.5 μM) in 0%, (0.5−16.3 μM) in 18% and 27% glycerol (v/v). *Pa*HisZ-*Pa*$HisG_S$ K_D values were obtained by fitting initial rate data to a kinetic equation (*vide infra*) as previously reported.[26]

***Pa*ATPPRT and *Pa*$HisG_S$ Saturation Kinetics with ATP and PRPP.** *Pa*ATPPRT initial rates were measured at saturating concentrations of one substrate and varying concentrations of the other, either ATP (0.4−5.6 mM) or PRPP (0.1−2.0 mM). Initial rates for *Pa*$HisG_S$ were determined at saturating concentrations of one substrate and varying concentrations of the other, either ATP (either 0.4−2.8 or 0.4−5.6 mM) or PRPP (0.1−2.0 mM).

***Pa*ATPPRT and *Pa*$HisG_S$ Saturation Kinetics with $MnCl_2$.** *Pa*ATPPRT initial rates were measured at saturating concentrations of one substrate and varying concentrations of the other, either ATP (0.1−1.4 mM) or PRPP (0.1−2.0 mM), while initial rates for *Pa*$HisG_S$ (1.1 μM) were determined at saturating concentrations of one substrate and varying concentrations of the other, either ATP (0.1−1.4 mM) or PRPP (0.05−2.0 mM), in the presence of 15 mM $MnCl_2$ instead of $MgCl_2$.

Analysis of *Pa*$HisG_S$ Reaction with $MnCl_2$ by LC-MS. Reaction mixtures (500 μL) contained 100 mM tricine pH 8.5, 100 mM KCl, 4 mM DTT, 15 mM $MnCl_2$, 19.7 μM *Mt*PPase, 1.4 mM ATP, 2.0 mM PRPP, and 10.3 μM *Pa*$HisG_S$. Reactions were incubated for 1 h at 20 °C, after which proteins were removed by passage through 10000 MWCO Vivaspin centrifugal concentrators. Reactions were run in duplicate,

DOI: 10.1021/acs.biochem.8b00559
Biochemistry 2018, 57, 4357−4367

and control reactions lacked *Pa*HisG$_S$. LC-MS analysis of the protein-free reaction mixtures was performed on an EC250/4.6 Nucleodur 100−10 C18 ec HPLC column (10 μm × 4.6 mm × 250 mm) (Macherey-Nagel) in a 1260 infinity HPLC system coupled to a G6130B Single Quadrupole mass spectrometer (Agilent Technologies). Separation of PRATP and ATP was carried out in (A) 50 mM triethylamine-acetic acid pH 7.4 and (B) methanol as a mobile phase in the following sequence: 0−3 min 100% A, 3−3.1 min 90% A and 10% B, 3.1−12 min 80% A and 20% B at a flow rate of 1 mL min^{-1}, with UV absorbance monitored at 260 and 290 nm. Electrospray ionization-mass spectrometry (ESI-MS) data were acquired in negative mode with a capillary voltage of 4500 V.

_Pa_ATPPRT and _Pa_HisG$_S$ Saturation Kinetics in Glycerol. *Pa*ATPPRT and *Pa*HisG$_S$ initial rates were measured at saturating concentrations of one substrate and varying concentrations of the other, either ATP (0.4−5.6 mM) or PRPP (0.1−2.0 mM), in the presence of 0%, 18%, and 27% glycerol (v/v).

_Pa_HisG$_S$ Inhibition by AMP. The half-maximal inhibitory concentration of AMP was determined by measuring initial rates for *Pa*HisG$_S$ (4.5 μM) in the presence of 5.6 mM ATP, 2 mM PRPP, and varying concentrations of AMP (0−0.8 mM). The inhibition mechanism was investigated by measuring initial rates for *Pa*HisG$_S$ (4.5 μM) at saturating concentrations of one substrate and varying concentrations of the other, either ATP (0.4−5.6 mM) with different concentrations of AMP (0−0.1 mM) or PRPP (0.1−2.0 mM) with different concentrations of AMP (0−0.05 mM). *Pa*HisG$_S$ concentration was more than 4-fold higher than the lowest AMP concentration used, and pseudo-first-order approximation was assumed.

_Pa_HisG$_S$ Saturation Kinetics with ADP and PRPP. Initial rates for *Pa*HisG$_S$ were determined at saturating concentrations of one substrate and varying concentrations of the other, either ADP (0.4−5.6 mM) or PRPP (0.1−2.0 mM).

Comparison of _Pa_HisG$_S$ Reactions with ADP and ATP by ^{31}P NMR Spectroscopy. Analysis of *Pa*HisG$_S$ reactions by ^{31}P NMR spectroscopy was carried out as previously described,[26] except that *Pa*HisG$_S$ concentration was 10.3 μM and ADP replaced ATP in half of the reactions. All reactions were run in duplicate, and control reactions lacked *Pa*HisG$_S$.

_Pa_ATPPRT and _Pa_HisG$_S$ Initial Velocity Patterns. Initial rates for *Pa*ATPPRT were measured in the presence of varying ATP (0.4−5.6 mM) and PRPP (0.1−2.0 mM), with 1 μM *Pa*HisG$_S$ and 20 μM *Pa*HisZ. Initial rates for *Pa*HisG$_S$ were determined in the presence of varying ATP (0.2−2.8 mM) and PRPP (0.1−2.0 mM). Measurements were performed in quadruplicates.

_Pa_HisG$_S$ Binding by ITC. ITC measurements were carried out at 20 °C in a MicroCal PEAQ-ITC calorimeter (Malvern Instruments). Protein and ligand were solubilized in the same ATPPRT assay buffer. After a small injection of 0.4 μL, 18 successive injections of 2 μL of ligand (either 0.8 mM PRPP or 10 mM ATP) were made into 300 μL of 50 μM *Pa*HisG$_S$, with 150-s intervals between successive injections and a reference power of 10 μcal s^{-1}. Heat of dilution for each experiment was measured by titrating ligand into assay buffer, and subtracted from the corresponding binding curve. All measurements were performed in duplicate. Data for PRPP binding were fitted to a single-site binding model as implemented in the PEAQ-ITC analysis software (Malvern Instruments).

_Pa_HisG$_S$ Thermal Denaturation by DSF. DSF measurements (λ_{ex} = 490 nm, λ_{em} 610 nm) were performed in 96-well plates on a Stratagene Mx3005p instrument. Thermal denaturation assays (50 μL) for 7.5 μM *Pa*HisG$_S$ were measured in the presence and absence of ligands (6 mM ATP, 2 mM PRPP, 208 μM PRATP, 3.6 mM PP$_i$), with or without 22% glycerol (v/v) (apoenzyme) in 100 mM tricine, 100 mM KCl, 4 mM DTT and 15 mM $MgCl_2$ pH 8.5. The assay for apoenzyme was also performed in 10 mM KH_2PO_4, 10 mM KF pH 8.0. Sypro Orange (5×) (Invitrogen) was added to all wells. Thermal denaturation curves were recorded over a temperature range from 25−93 °C with 1 °C min^{-1} increments. Control curves lacked enzyme and were subtracted from curves containing enzyme. All measurements were carried out in triplicate.

Density Functional Theory Calculations. Theoretical structures were derived from B3LYP calculations using a 6-31G* basis set with a Lanl2DZ basis set on Mg^{2+} and Mn^{2+} and a Lanl2DZ pseudopotential added to Mg^{2+} and Mn^{2+} as implemented in Gaussian 09.[31] A model system was chosen by including all residues within 5 Å of ADP and PRPP in the crystallographic dimer of the *Pa*HisG$_S$-PRPP-Mg-ADP complex crystal structure[29] and by flipping the adenine ring from its crystal structure orientation to bring N1 in proximity to PRPP. The system was further paired down to include only functional groups, metal ions and water molecules within the 5-Å cutoff that were essential for stabilization of the transition structure. In addition to the divalent metal found in the crystal structure, a second divalent metal had to be included in the system for a transition structure to be located. Initial searches exploring structures with fixed distances along the reaction coordinate were located by performing an optimization of an input structure with the key bond-forming or bond-breaking distances held constant, and frequency calculations resulted in only one imaginary frequency along the reaction coordinate. Final transition structures for the system complexed with either Mg^{2+} or Mn^{2+} were located as stationary points with no geometrical constrains and exhibit only one imaginary frequency along the reaction coordinate. Coordinates for all optimized structures are available in the Supporting Information.

Pre-Steady-State Kinetics. Approach to steady-state in *Pa*HisG$_S$ and *Pa*ATPPRT reactions was investigated under multiple-turnover conditions by monitoring the increase in absorbance at 290 nm upon PRATP formation at 20 °C in an Applied Photophysics SX-20 stopped-flow spectrophotometer outfitted with a 5 μL mixing cell (0.5 cm path length and 0.9 ms dead-time). Each syringe contained 100 mM tricine pH 8.5, 100 mM KCl, 4 mM DTT, 15 mM $MgCl_2$, and 20 μM *Mt*PPase. In addition, one syringe carried 40 μM *Pa*HisG$_S$ (with or without 100 μM *Pa*HisZ) and 4 mM PRPP, while the other carried 11.2 mM ATP. Reaction was triggered by rapidly mixing 55 μL from each syringe. Absorbance increase with *Pa*HisG$_S$ was monitored in a linear-time base for 5 s with 5000 data points collected, and with *Pa*ATPPRT, in a split-time base for 2 s, with 4000 data points collected in the first 0.2 s and 4000 in the following 1.8 s. At least 8 traces were acquired for each enzyme, and controls lacked PRPP.

Data Analysis of Kinetics and Thermal Denaturation. Kinetic and DSF data were analyzed by the nonlinear regression function of SigmaPlot 13 (SPSS Inc.). Data points and error bars in graphs are represented as mean ± standard error, and kinetic and equilibrium constants are presented as

DOI: 10.1021/acs.biochem.8b00559
Biochemistry 2018, 57, 4357−4367

mean ± fitting error. Initial rate data with varying concentrations of *Pa*HisZ were fitted to eq 1. The concentration of *Pa*ATPPRT at any concentration of *Pa*HisG$_S$ and *Pa*HisZ was calculated according to eq 2. Substrate saturation data were fitted to eq 3. Inhibition data at fixed substrate concentrations were fitted to eq 4, and competitive inhibition data were fitted to eq 5. Initial velocity patterns were fitted to eq 6, and pre-steady-state kinetics under multiple-turnover conditions was fitted to eq 7. In eqs 1−7, v is the initial rate, V_{max} is the maximal velocity, G is the concentration of *Pa*HisG$_S$, Z is the concentration of *Pa*HisZ, K_D is the equilibrium dissociation constant, *Pa*ATPPRT is the concentration of *Pa*HisG$_S$-*Pa*HisZ complex, S is the concentration of the varying substrate, k_{cat} is the steady-state turnover number, K_M is the apparent Michaelis constant, E_T is total enzyme concentration, v_i is the initial rate in the presence of inhibitor, IC_{50} is the half-maximal inhibitory concentration, K_i is the inhibitor dissociation constant, A and B are the first and second substrates to bind to the enzyme, respectively, K_a and K_b are their respective Michaelis constants, K_{ia} is the apparent dissociation constant for the complex between enzyme and substrate A when the concentration of B approaches zero, t is time, $P(t)$ is product concentration at time t, A_0 is the amplitude of the burst phase, and k_{burst} is the first-order rate constant of product formation in the burst phase. DSF thermal denaturation data were fitted to eq 8,[32] where F_U is fraction unfolded, T is the temperature in °C, T_m is the melting temperature, c is the slope of the transition region, and LL and UL are folded and unfolded baselines, respectively.

$$v = V_{max}\frac{(G + Z + K_D) - \sqrt{(G + Z + K_D)^2 - 4GZ}}{2G} \quad (1)$$

$$Pa\text{ATPPRT} = \frac{(G + Z + K_D) - \sqrt{(G + Z + K_D)^2 - 4GZ}}{2} \quad (2)$$

$$\frac{v}{E_T} = \frac{k_{cat}S}{K_M + S} \quad (3)$$

$$\frac{v_i}{v} = \frac{1}{1 + \frac{I}{IC_{50}}} \quad (4)$$

$$\frac{v}{E_T} = \frac{k_{cat}S}{(1 + {}^{I}/_{K_i})K_M + S} \quad (5)$$

$$\frac{v}{E_T} = \frac{k_{cat}AB}{K_{ia}K_b + K_aB + K_bA + AB} \quad (6)$$

$$P(t) = A_0(1 - e^{-k_{burst}t}) + vt \quad (7)$$

$$F_U = LL + \frac{UL - LL}{1 + e^{(T_m - T)/c}} \quad (8)$$

RESULTS AND DISCUSSION

***Pa*HisG$_S$ and *Pa*ATPPRT Kinetic Mechanism.** A steady-state ordered kinetic mechanism in which ATP is the first substrate to bind to the enzyme, and PRATP is the last product to dissociate from it, has long been demonstrated for HisG$_L$ ATPPRTs.[21,22] This mechanism has been supported by several structures of *Campylobacter jejuni* and *M. tuberculosis* ATPPRT-ATP binary complexes,[10,16] and by the recent structure of the *C. jejuni* ATPPRT catalytic core in complex with PRPP, where despite being able to bind to the free enzyme, PRPP drifts into the ATP binding site, which would lead to a dead-end complex.[33] The kinetic mechanism of HisG$_S$ ATPPRTs, on the other hand, has not been explored. We recently published the crystal structures of *Pa*HisG$_S$ and *Pa*ATPPRT in binary complexes with PRPP and PRATP, and in ternary complexes with PRPP-ATP, but were unable to obtain structures of enzyme-ATP binary complexes, suggesting a reverse order of substrate binding in comparison with HisG$_L$ ATPPRTs.[29]

To test this hypothesis, the kinetic mechanism of *Pa*HisG$_S$ and *Pa*ATPPRT was investigated. Intersecting patterns of double-reciprocal plots with both ATP and PRPP in initial velocity studies were determined for *Pa*ATPPRT (Figure 2A,B) and *Pa*HisG$_S$ (Figure 2C,D), indicating a ternary

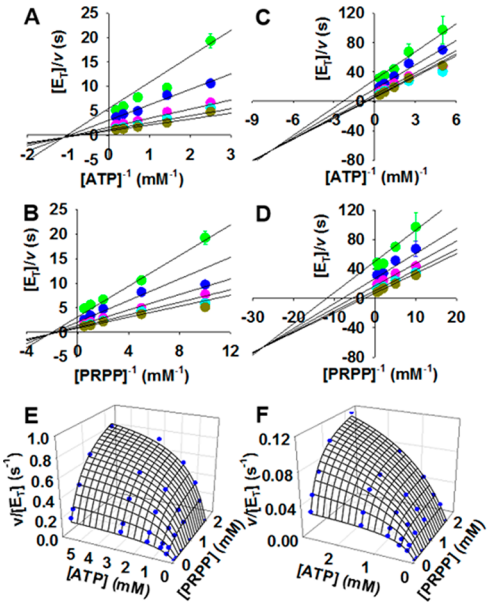

Figure 2. Initial velocity patterns for *Pa*ATPPRT and *Pa*HisG$_S$. Intersecting double-reciprocal plots for *Pa*ATPPRT with (A) ATP and (B) PRPP as varying substrates and for *Pa*HisG$_S$ with (C) ATP and (D) PRPP as varying substrates. Each color represents a different fixed concentration of the cosubstrate. Data points are mean ± SE. Three-dimensional plot of (E) *Pa*ATPPRT and (F) *Pa*HisG$_S$ initial rate data, where lines are data fitting to eq 6.

complex is formed in a sequential mechanism. The double-reciprocal plots intersecting to the left of the y-axes rule out a rapid equilibrium ordered mechanism.[34] Fitting the data to eq 6 (Figure 2E,F) yielded steady-state kinetic parameters summarized in Table S1.

Binding studies were performed with *Pa*HisG$_S$ to elucidate the substrate binding order. Binding of PRPP to *Pa*HisG$_S$ was detected by ITC (Figure S1), and fitting the data from two independent experiments to a single-site binding model (stoichiometry of 1:1 and no cooperativity) resulted in K_D's of 15.4 ± 0.2 and 8.3 ± 0.1 μM (one from each experiment, yielding a mean ± SE of 12 ± 2 μM). ATP binding to *Pa*HisG$_S$, on the other hand, could not be detected, as no signal was observed beyond heat of dilution (Figure S2). This

DOI: 10.1021/acs.biochem.8b00559
Biochemistry 2018, 57, 4357−4367

corroborates the hypothesis that PRPP can bind to the free enzyme, while ATP cannot.

To confirm and expand these results, *Pa*HisG$_S$ thermal denaturation curves in the presence and absence of substrates and products were determined by DSF (Figure 3), and data

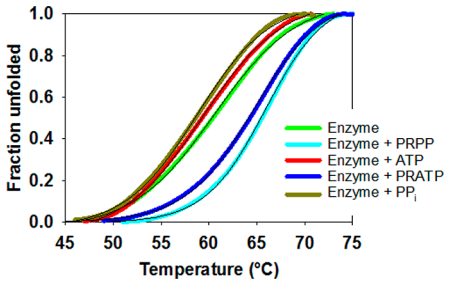

Figure 3. DSF-based thermal denaturation of *Pa*HisG$_S$ apoenzyme and in the presence of substrates and products. Thin black lines are data fitting to eq 8.

fitting to eq 8 produced T_m's shown in Table S2. PRPP and PRATP increased *Pa*HisG$_S$ T_m by 6 and 5 °C, respectively, indicating that these molecules can bind to the free enzyme. Conversely, ATP and PP$_i$ did not alter *Pa*HisG$_S$ T_m. The latter observation alone does not necessarily rule out the possibility that ATP and PP$_i$ can bind to the free enzyme, but the integration of crystallography,[29] initial velocity patterns, ITC, and DSF data supports a steady-state ordered mechanism where PRPP is the first substrate to bind to *Pa*HisG$_S$ and PRATP is the last product to dissociate from it. The strong parallels in corresponding binding modes seen in the *Pa*HisG$_S$ and *Pa*ATPPRT crystal structures[29] suggest that *Pa*ATPPRT follows the same mechanism. Moreover, given the conservation of PRPP position in *Pa*ATPPRT[29] and *Lactococcus lactis* ATPPRT binary complexes,[27] this mechanism may be valid for other HisG$_S$ ATPPRTs.

AMP Is an Inhibitor of *Pa*HisG$_S$. AMP is a competitive inhibitor of HisG$_L$ ATPPRTs against both substrates,[16,19] which is explained structurally by the simultaneous partial occupation of the PRPP and ATP binding sites by AMP's phosphoribosyl and adenine moieties, respectively.[11,16,35] AMP is also a competitive inhibitor against PRPP in *L. lactis* ATPPRT,[28] and the recent crystal structure of the *Pa*HisG$_S$-AMP complex shows a similar binding mode as in HisG$_L$ ATPPRTs.[11,16,29,35] AMP inhibits *Pa*HisG$_S$ with an IC$_{50}$ of 79 ± 6 μM (Figure S3A), and inhibition is competitive against both PRPP and ATP, with K_i's of 25 ± 5 and 52 ± 8 μM, respectively (Figure S3B,C). These values are on average ca. 7- and 10-fold lower than those for HisG$_L$ ATPPRTs,[16,19] and over 27-fold lower than that for *L. lactis* ATPPRT,[28] suggesting *Pa*HisG$_S$ activity is more stringently regulated by this metabolite.

ADP Is a Substrate for *Pa*HisG$_S$. ADP has been shown to be an inhibitor of HisG$_L$ ATPPRTs.[19] However, crystal structures of *Pa*HisG$_S$ and *Pa*ATPPRT in complex with PRPP-ADP reveal that ADP binds in the same manner as ATP.[29] In order to evaluate the ability of *Pa*HisG$_S$ to use ADP as a substrate, we compared the reactions with ADP and ATP by ^{31}P NMR spectroscopy (Figure S4). The spectra of reactions containing ADP (Figure S4A) and ATP (Figure S4C) are similar except for the peak at −19.2 to −19.4 corresponding to the γ-PO_4^{2-} phosphorus of ATP and PRATP, since this group is absent in ADP and N^1-(5-phospho-β-D-ribosyl)-ADP (PRADP). Spectra for both reactions differ from the controls lacking *Pa*HisG$_S$ (Figure S4B,D). The characteristic peak at ca. 3.3 ppm corresponding to the phosphorus in the N^1-5-phospho-β-D-ribose moiety of the product[26] is present in the reaction spectra with ADP (Figure S4A, inset) and ATP (Figure S4C, inset), and absent in the controls (Figure S4B,D, insets), establishing that ADP can replace ATP as a substrate for *Pa*HisG$_S$.

For a quantitative comparison of the reactions with ATP and ADP, steady-state kinetic analysis of the reaction with either substrate was carried out (Figure 4) and kinetic parameters are

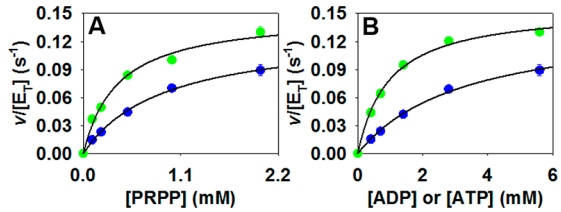

Figure 4. *Pa*HisG$_S$ substrate saturation curves with either ATP (green) or ADP (blue) as a substrate. (A) Varying PRPP concentration with saturating concentration of the nucleotide. (B) Varying the nucleotide concentration with saturating concentration of PRPP. Data points are mean ± SE, and lines are data fitting to eq 3.

summarized in Table S3. Values of k_{cat} are the same within error with either ATP or ADP as a substrate, indicating that once saturated *Pa*HisG$_S$ turns over ATP and ADP just as effectively. The main difference is in the K_M for ADP, which is over 3-fold that for ATP, suggesting some small loss of affinity for the steady-state with ADP.

***Pa*HisG$_S$ and *Pa*ATPPRT Kinetics with Mn^{2+}.** Replacement of Mg^{2+} by Mn^{2+} is a common strategy in enzymology,[36] having been employed to uncover rate-limiting steps in reactions involving stabilization of phosphate groups.[37] HisG$_L$ ATPPRTs have been reported to have their activities either unaltered or decreased by changing the divalent metal in the reaction from the physiological Mg^{2+} to Mn^{2+}, but no mechanistic inference has been drawn.[17,38] To evaluate the effect of Mn^{2+} on a HisG$_S$ enzyme, saturation curves for *Pa*HisG$_S$ and *Pa*ATPPRT with either divalent metal were determined (Figure 5), and kinetic constants are displayed in Table S4. Mn^{2+} led to 2.6- and 11-fold increases in *Pa*HisG$_S$ k_{cat} and k_{cat}/K_M^{ATP}, respectively, as compared with Mg^{2+}. The change in k_{cat}/K_M^{ATP} was driven in large part by a reduction in K_M^{ATP}. LC-MS analysis of the *Pa*HisG$_S$ reaction with Mn^{2+} confirmed the same product, PRATP, was being formed (Figure S5).

In contrast to *Pa*HisG$_S$, steady-state constants for *Pa*ATPPRT were unchanged by Mn^{2+}, except for a 2.9-fold increase in k_{cat}/K_M^{ATP} owing to a reduction in K_M^{ATP}. These results raise the possibility that *Pa*HisG$_S$ and *Pa*ATPPRT reactions have distinct rate-limiting steps. Crystal structures of *Pa*HisG$_S$ and *Pa*ATPPRT with various ligands do not depict any specific interaction between Mg^{2+} and the enzyme,[29] raising the possibility the off-rates of products from the active site might not be affected by the nature of the metal ion. It is possible, nonetheless, that a solution metal stabilizes charges of either PRATP or PP$_i$ concomitantly with product release from the enzyme. The metal ion seen in the structures acts as a Lewis acid to stabilize negative charges in the Michaelis complex upon binding of ATP, with a putative second metal

DOI: 10.1021/acs.biochem.8b00559
Biochemistry 2018, 57, 4357−4367

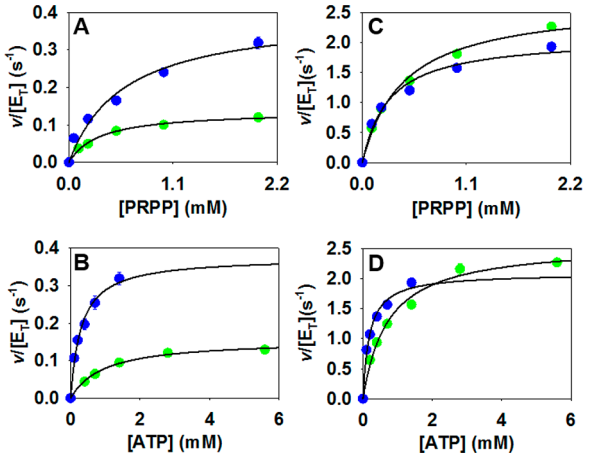

Figure 5. Steady-state kinetics with Mg^{2+} (green) and Mn^{2+} (blue). Saturation curves varying either PRPP or ATP concentration with saturating concentration of the cosubstrate for (A and B) *Pa*HisG$_S$ and (C and D) *Pa*ATPPRT. Data points are mean ± SE, and lines are data fitting to eq 3.

ion likely present at the transition state to facilitate departure of the PP_i leaving group.[29] Thus, one might expect Mn^{2+} to increase the reaction rate if rate-limiting steps are located between ATP binding to the enzyme-PRPP complex and product formation, since a stronger Lewis acid would facilitate catalysis by stabilizing charges more efficiently. The kinetic constants affected would be k_{cat} and k_{cat}/K_M^{ATP}, which is exactly what is observed with *Pa*HisG$_S$. If, on the other hand, ternary complex formation played a minor role in limiting the reaction rate, chemistry was fast, and product release was the slowest step, a modest increase in k_{cat}/K_M^{ATP} only would be expected, which is the case with *Pa*ATPPRT.

A Transition-State Hypothesis for the *Pa*HisG$_S$ Reaction. An S_N1-like, $D_N{*}A_N$[‡39,40] transition-state structure has recently been proposed for *C. jejuni* and *M. tuberculosis* (HisG$_L$) and *L. lactis* (HisG$_S$) ATPPRT-catalyzed reaction based on kinetic isotope effects and computational chemistry, using a simplified model of the reaction for density functional theory calculations.[10] Having established that *Pa*HisG$_S$ utilizes ADP as a substrate with a similar k_{cat} as it does ATP (Table S3), the crystal structure of the *Pa*HisG$_S$-PRPP-Mg-ADP Michaelis complex[29] served as a starting point for density functional theory calculations in order to find a theoretical transition state for the reaction that includes not only the full substrates but also several active-site residue side-chain surrogates and water molecules essential to stabilize the system, with either Mg^{2+} or Mn^{2+} as the metal ion (Figure 6). Transition structures were located as stationary points (i.e., without any constraints on distances or dihedral angles) and possess only one imaginary frequency reflecting vibration along the N1−C1−O1 axis. Inclusion of a second equivalent of the divalent metal ion to stabilize the departing PP_i leaving group was essential to locate transition structures, lending support to a recent proposal based on the crystal structures of *Pa*HisG$_S$ and *Pa*ATPPRT Michaelis complexes[29] and the transition structures of other phosphoribosyltransferases.[41]

The optimized structures indicate an S_N2-like, almost synchronous A_ND_N transition state is possible for the *Pa*HisG$_S$-catalyzed reaction with either Mg^{2+} (Figure 6A) or Mn^{2+} (Figure 6B) as a Lewis acid. The 6-NH_2 group of ADP is protonated in all transition structures and is likely to lose a proton to form the 6-NH group of PRADP only after the nucleophilic substitution is complete, as recently hypothesized.[29] Nucleophilic attack occurs from the charge-neutral resonance structure of adenine in which N1 has transiently a negative charge due to electron donation from N6. This natural resonance structure represents 6.64% of the distribu-

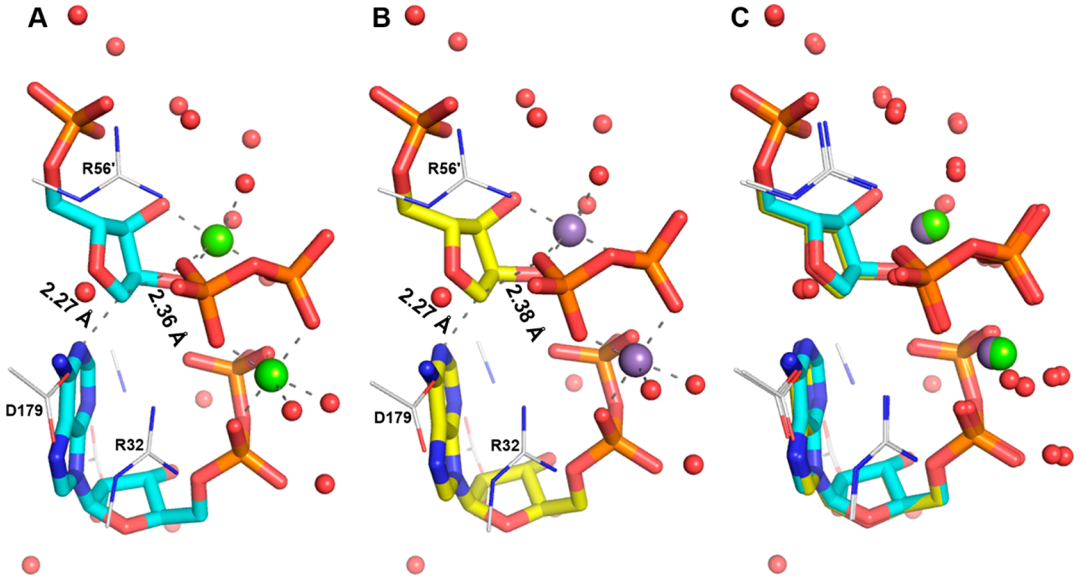

Figure 6. Transition-state model for the *Pa*HisG$_S$-catalyzed reaction. (A) Transition structure with magnesium, (B) transition structure with manganese, and (C) overlay of the transition structures with magnesium and manganese. Substrates are represented as stick models, side-chain mimics as wireframe, and metal ions and water oxygens as spheres. Carbon is in either cyan or yellow for substrates and in gray for side-chain mimics, with oxygen in red, nitrogen in blue, phosphorus in orange, magnesium in green, and manganese in purple. Hydrogens are omitted for simplicity. Partial bonds and metal ion coordination bonds are represented by dashed lines. Distances are shown for the N1−C1 and the C1−O1 bonds. Key residue side-chain mimics are labeled, and the prime denotes a residue of the adjacent subunit in the *Pa*HisG$_S$ dimer.[29]

DOI: 10.1021/acs.biochem.8b00559
Biochemistry 2018, 57, 4357−4367

tion of adenine resonances.[42] The A_ND_N transition state located here contrasts with the $D_N{*}A_N^{\ddagger}$ one proposed for $HisG_L$ and $HisG_S$ ATPPRT reaction.[10] This would mean that different orthologues of ATPPRT catalyze the same reaction via different transition states, which is not uncommon in ribosyl-transfer reactions. For instance, distinct transition-state models based on kinetic isotope effects and density functional theory have been suggested for bovine and human purine nucleoside phosphorylases,[43,44] and for wild-type and mutant human purine nucleoside phosphorylases.[43,45] Kinetic isotope effect measurements for *Pa*$HisG_S$ could test the A_ND_N transition-state hypothesis put forth in this work.

Overlay of the transition structures with Mg^{2+} and Mn^{2+} demonstrates an almost identical arrangement (Figure 6C), indicating transition-state geometry cannot explain the discrimination in *Pa*$HisG_S$ reactivity between the metal ions. Natural bond orbital (NBO) analysis of the transition structures, however, revealed significant differences in charge distribution in the metal ions and the PP_i at the transition state depending on which metal is included (Table S5). Most atoms have very similar charges in the two transition structures, except for the metal ions and PP_i oxygens. The average charge of the two magnesium ions at the transition state is 1.439, over 2-fold higher than the average charge of the manganese ions, 0.649. This is due to more efficient attenuation of the negative charge of the PP_i leaving group by Mn^{2+} through *d*-orbital bonding to coordinating oxygens, as shown by orbital population analysis. As compared with Mg^{2+}, therefore, Mn^{2+} improves catalysis in the *Pa*$HisG_S$ reaction by more effectively stabilizing the negatively charged leaving group at the transition state.

Solvent Viscosity Effects on *Pa*$HisG_S$ and *Pa*ATPPRT Kinetics. In order to probe further the distinct rate-limiting steps governing *Pa*$HisG_S$ and *Pa*ATPPRT catalyses, the effect of solvent viscosity on reaction rates was evaluated (Figure 7), and the data are summarized in Tables S6 and S7. Increasing solvent viscosity by increasing glycerol concentration[46] slows down diffusional steps such as substrate binding and release and product release, and values of kinetic constants will be reduced if such steps are rate-limiting.[47−49] *Pa*$HisG_S$ rate constants did not decrease with increasing glycerol concentration (Table S6), consistent with diffusional steps not contributing to limit the reaction rate. Instead, as shown in Figure 7A and Table S6, glycerol led to an increase in *Pa*$HisG_S$ k_{cat} and k_{cat}/K_M^{PRPP} of up to 2.7- and 2.4-fold, respectively, while k_{cat}/K_M^{ATP} was only marginally affected. Inverse solvent viscosity effects generally suggest that a more active dynamic conformation of the enzyme or the Michaelis complex is favored at high viscosity.[47−49] To rule out the possibility that glycerol might be affecting the overall stability of the enzyme, a thermal denaturation curve was determined by DSF in 22% glycerol (Figure S6), and no difference in T_m was observed in comparison with that determined without glycerol (Table S2). Crystal structures of *Pa*$HisG_S$ apoenzyme and *Pa*$HisG_S$-PRPP-ATP were also obtained with and without soaking crystals in glycerol, and no electron density for glycerol was visualized in any of the structures.[29] This suggests that glycerol is acting as part of bulk solvent, not as a ligand, but with the caveat that crystal lattice might have prevented binding.

To assess the effect of solvent viscosity on *Pa*ATPPRT, first the K_D for the *Pa*$HisG_S$-*Pa*HisZ complex had to be measured in glycerol (Figure S7), and data fitting to eq 1 yielded K_D's of 1.3 ± 0.1, 1.1 ± 0.2, and 0.5 ± 0.1 μM in 0%, 18%, and 27%

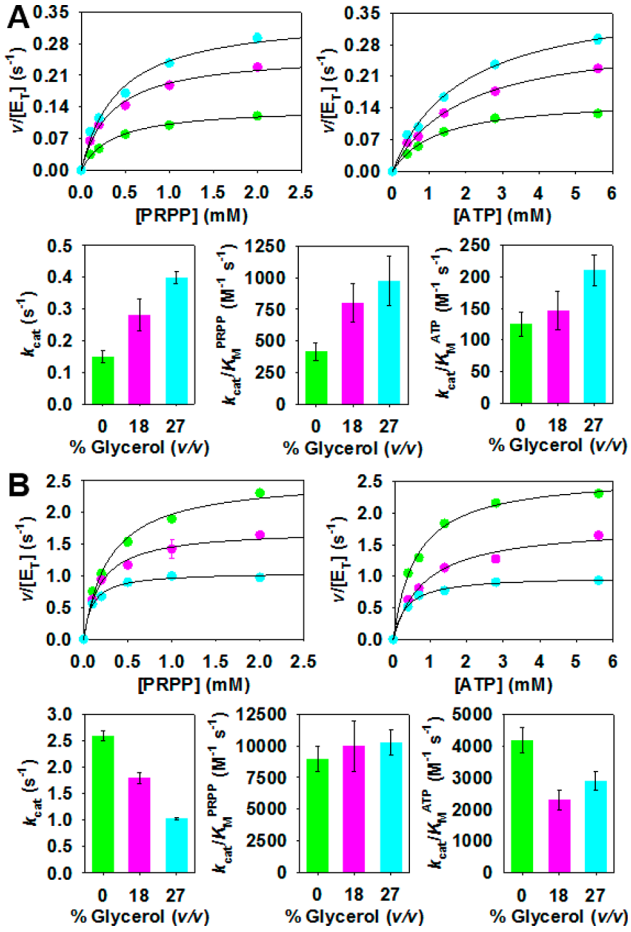

Figure 7. Solvent viscosity effects on steady-state kinetics determined at 0% (green), 18% (pink), and 27% (cyan) glycerol (v/v). (A) *Pa*$HisG_S$ saturation curves (top) and steady-state constants (bottom) dependence on glycerol concentration. (B) *Pa*ATPPRT saturation curves (top) and steady-state constants (bottom) dependence on glycerol concentration. Data represent either mean ± SE (scatter plots) or value ± fitting error (bar plots). Lines are data fitting to eq 3.

glycerol, respectively. Knowledge of the K_D's allowed calculation, using eq 2, of *Pa*ATPPRT concentrations at different glycerol concentrations for measurement of k_{cat}. In contrast to the effect on *Pa*$HisG_S$, increasing solvent viscosity resulted in a decrease of up to 2.5-fold in *Pa*ATPPRT k_{cat}, with negligible effects on k_{cat}/K_M for either substrate, as shown in Figure 7B and Table S7. This points to product dissociation from *Pa*ATPPRT as the rate-limiting step in the reaction, as is the case with $HisG_L$ ATPPRTs.[8,50]

Burst in Product Formation by *Pa*ATPPRT. To glean additional support for distinct rate-limiting steps controlling nonactivated and activated *Pa*$HisG_S$ reactions, product formation time courses were monitored under pre-steady-state conditions for *Pa*$HisG_S$ and *Pa*ATPPRT (Figure 8). PRATP formation with *Pa*$HisG_S$ varies linearly with time with a steady-state rate constant of 0.091 ± 0.001 s^{-1}, in reasonable agreement with k_{cat} (Tables S3, S4, S6). This rules out a slow step after formation of enzyme-bound products[51] and suggests interconversion between ternary complexes ($k_5 + k_6$ in Scheme 2) is rate-limiting.

On the other hand, a burst in PRATP formation precedes the steady-state with *Pa*ATPPRT, and data fitting to eq 7 yielded a k_{burst} of 80 ± 1 s^{-1}, a steady-state rate constant of

DOI: 10.1021/acs.biochem.8b00559
Biochemistry 2018, 57, 4357−4367

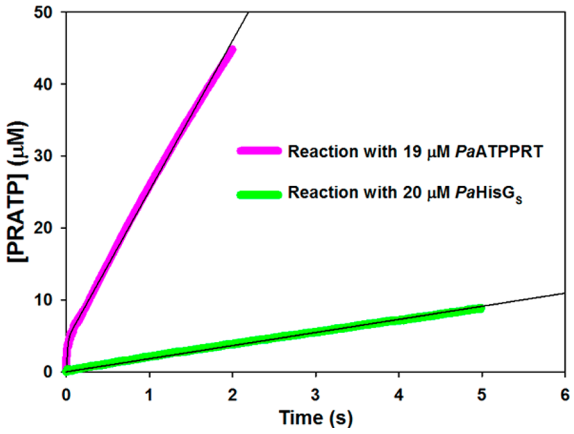

Figure 8. Pre-steady-state kinetics with *Pa*ATPPRT and *Pa*HisG$_S$, with a burst in product formation observed with the former but not the latter. Black lines are data fitting to eq 7 for *Pa*ATPPRT and a linear regression for *Pa*HisG$_S$.

Scheme 2. Interpretation of the Pre-Steady-State of *Pa*HisG$_S$ and *Pa*ATPPRT Reactions

1.11 ± 0.01 s^{-1}, and an A_0 of 4.3 μM. This is consistent with a step after chemistry, likely product release (k'_7 in Scheme 2), limiting the reaction rate,[51,52] in agreement with the conclusion drawn from solvent viscosity effects. *M. tuberculosis* HisG$_L$ ATPPRT also displays a burst in product formation with a k_{burst} of 0.67 s^{-1} at 25 °C.[8] Thus, *Pa*ATPPRT k_{burst} at 20 °C is over 119-fold higher than *M. tuberculosis* HisG$_L$ ATPPRT's at 25 °C, which may be a feature of HisG$_S$ ATPPRTs and/or a consequence of *Pa*ATPPRT being psychrophilic.[26]

The amplitude of the burst phase (A_0) generally reflects the concentration of the Michaelis complex, which at saturating substrate concentrations could be as high as the concentration of enzyme.[53] The A_0 of 4.3 μM is over 4.4-fold lower than the concentration of *Pa*ATPPRT used in the experiment (19 μM). Two main reasons may account, separately or in combination, for this result without invoking the unlikely scenario where ca. 75% of enzyme molecules are inactive. First, the enzyme might not be fully saturated by one or both substrates, which would also explain the steady-state rate constant being slightly smaller than the k_{cat} values extrapolated from substrate saturation curves. This may be the case with the *Pa*HisG$_S$ steady-state rate constant as well. Second, chemical reversibility decreases A_0. Both k_{burst} and A_0 are dependent on all rate constants depicted in Scheme 2, the forward and reverse rate constants for interconversion between enzyme-bound substrates and products, k_5 and k_6, respectively, and the net rate constant for release of products from the enzyme, k'_7, according to eqs 9 and 10.[51]

$$k_{burst} = k_5 + k_6 + k'_7 \tag{9}$$

$$A_0 = \frac{k_5(k_6 + k'_7)}{(k_5 + k_6 + k'_7)^2} \tag{10}$$

Upon inspection of eqs 9 and 10, one must conclude that under the most favorable conditions, full expression of A_0 can only occur when chemistry is irreversible ($k_6 = 0$) and much faster than product release ($k_5 \gg k'_7$). Internal reversibility, described by the magnitude of k_6, will increase k_{burst} while decreasing A_0. Equilibrium in the ATPPRT reaction strongly favors the reactants,[17] making it possible for the crystal structure of the *Pa*ATPPRT-PRPP-ATP ternary-complex to be attained with wild-type enzyme.[29] Hence, k_6 is likely to be much larger than k_5, making k_6 the main contributor to k_{burst} and significantly reducing A_0 from its theoretical upper limit of 19 μM. Relative contributions of k_5 and k_6 to k_{burst} and A_0 notwithstanding, it is clear that activation of *Pa*HisG$_S$ by *Pa*HisZ switches the rate-limiting step of the reaction from interconversion between the ternary complexes to product release.

***Pa*HisZ-Induced Shift in the Rate-Limiting Step.** The results presented here demonstrate that two long-established mechanistic features of HisG$_L$ ATPPRTs, namely, ATP as the first substrate to bind to the enzyme and ADP as an

Scheme 3. Kinetic Mechanism and Rate-Limiting Steps of *Pa*HisG$_S$ (top) and *Pa*ATPPRT (bottom) Reactions and the Corresponding Crystal Structures[26,29] [a]

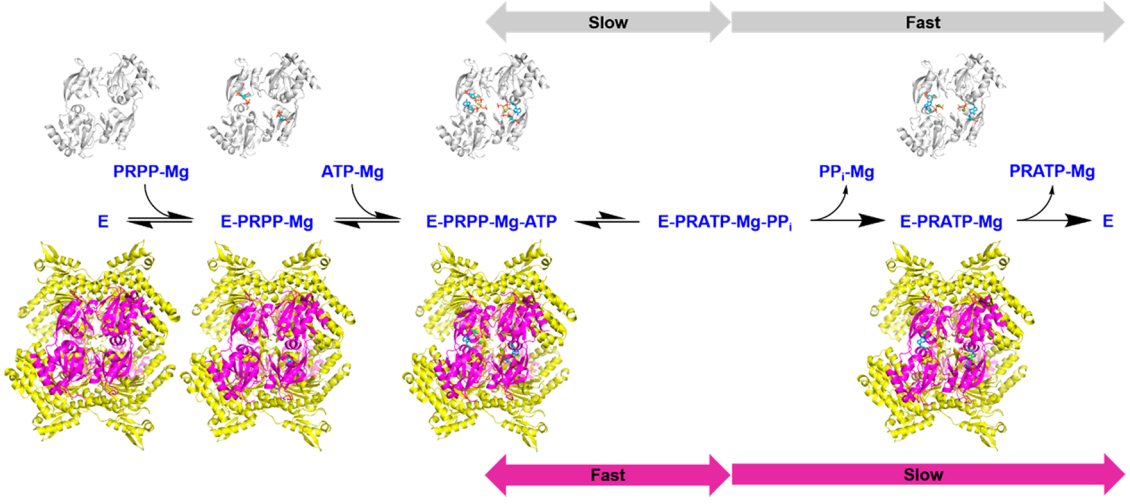

[a]The second *Pa*HisG$_S$ homodimers lie behind the *Pa*HisZ tetramers.

DOI: 10.1021/acs.biochem.8b00559
Biochemistry 2018, 57, 4357−4367

inhibitor,[16,19,21,22,33] do not apply to *Pa*HisG$_S$, and possibly other HisG$_S$ ATPPRTs. Providing functional data to support hypotheses proposed based on extensive crystallography work on *Pa*HisG$_S$ and *Pa*ATPPRT,[29] *Pa*HisG$_S$ is shown to be able to replace ATP for ADP as a substrate and to operate by a steady-state ordered mechanism where PRPP is the first substrate to bind to the enzyme (Scheme 3). *Pa*HisG$_S$ k_{cat} increases when Mn^{2+} replaces Mg^{2+}, which can be accounted for owing to more efficient charge stabilization by Mn^{2+} upon leaving group departure at the transition state. The observation that *Pa*ATPPRT steady-state kinetics is unaltered with Mn^{2+} raises the possibility of k_{cat}'s for the activated and nonactivated enzyme forms reporting on distinct steps. This is confirmed by solvent viscosity effects on steady-state parameters and by pre-steady-state kinetics under multiple-turnover conditions, which indicate that interconversion between *Pa*HisG$_S$–PRPP-ATP and *Pa*HisG$_S$–PRATP-PP$_i$ complexes limits the reaction rate for the nonactivated enzyme, likely with a significant contribution from chemistry given the effect of Mn^{2+}. However, allosteric activation by *Pa*HisZ accelerates this interconversion well beyond the steady-state rate, which now reflects the off-rate of either PP$_i$ from the *Pa*ATPPRT–PRATP-PP$_i$ ternary complex or PRATP from the *Pa*ATPPRT–PRATP binary complex (Scheme 3). This provides fundamental insight into the allosteric regulation of a complex multiprotein enzyme.

■ ASSOCIATED CONTENT

Supporting Information

The Supporting Information is available free of charge on the ACS Publications website at DOI: 10.1021/acs.biochem.8b00559.

ITC curves, *Pa*HisG$_S$ inhibition by AMP, spectra, DSF-based thermal denaturation of *Pa*HisG$_S$, determination of equilibrium dissociation, *Pa*ATPPRT and *Pa*HisG$_S$ steady-state parameters from initial velocity patterns, *Pa*HisG$_S$ T_m's by DSF in the presence and absence of ligands, steady-state kinetic constants, effect of Mn^{2+} on *Pa*ATPPRT and *Pa*HisG$_S$ steady-state kinetic parameters, NBO charge distribution, solvent viscosity effects, and coordinates for all transition structures (PDF)

■ AUTHOR INFORMATION

Corresponding Authors

*E-mail: jhirschi@binghamton.edu.

*E-mail: rgds@st-andrews.ac.uk. Phone: +44 01334 463496.

ORCID

Rafael G. da Silva: 0000-0002-1308-8190

Notes

The authors declare no competing financial interest.

■ ACKNOWLEDGMENTS

This work was supported by a Wellcome Trust Institutional Strategic Support Fund to the University of St Andrews and the Biotechnology and Biological Sciences Research Council (BBSRC) [grant no. BB/M010996/1] via an EASTBIO Doctoral Training Partnership studentship to G.F. The computational work used the Extreme Science and Engineering Discovery Environment (XSEDE) resource comet at the SDSC through allocation CHE150007, supported by the National Science Foundation [grant no. ACI-1548562]. R.S. was the recipient of an Erasmus Undergraduate Fellowship. The authors thank Dr. Eoin R. Gould for his assistance with ^{31}P NMR experiments.

■ ABBREVIATIONS

ATP, adenosine 5′-triphosphate; AMP, adenosine 5′-monophosphate; ADP, adenosine 5′-diphosphate; ATPPRT, ATP phosphoribosyltransferase; PRPP, 5-phospho-α-D-ribosyl-1-pyrophosphate; PRATP, N^1-(5-phospho-β-D-ribosyl)-ATP; PP$_i$, inorganic pyrophosphate; DTT, dithiothreitol; ITC, isothermal titration calorimetry; DSF, differential scanning fluorimetry; LC-MS, liquid chromatography–mass spectrometry; *Pa*ATPPRT, *P. arcticus* ATPPRT; *Pa*HisG$_S$, *P. arcticus* HisG$_S$; *Pa*HisZ, *P. arcticus* HisZ; ^{31}P NMR, ^{31}P nuclear magnetic resonance; *Mt*PPase, *Mycobacterium tuberculosis* inorganic pyrophosphatase; MWCO, molecular weight cut off; ESI-MS, electrospray ionization mass spectrometry; K_D, equilibrium dissociation constant; *Ec*PRPPS, *E. coli* PRPP synthetase; PRADP, N^1-(5-phospho-β-D-ribosyl)-ADP

■ REFERENCES

(1) Barends, T. R., Dunn, M. F., and Schlichting, I. (2008) Tryptophan synthase, an allosteric molecular factory. *Curr. Opin. Chem. Biol. 12*, 593–600.

(2) Fan, Y., Cross, P. J., Jameson, G. B., and Parker, E. J. (2018) Exploring modular allostery via interchangeable regulatory domains. *Proc. Natl. Acad. Sci. U. S. A. 115*, 3006–3011.

(3) Pisco, J. P., de Chiara, C., Pacholarz, K. J., Garza-Garcia, A., Ogrodowicz, R. W., Walker, P. A., Barran, P. E., Smerdon, S. J., and de Carvalho, L. P. S. (2017) Uncoupling conformational states from activity in an allosteric enzyme. *Nat. Commun. 8*, 203.

(4) de Carvalho, L. P., Argyrou, A., and Blanchard, J. S. (2005) Slow-onset feedback inhibition: Inhibition of mycobacterium tuberculosis alpha-isopropylmalate synthase by l-leucine. *J. Am. Chem. Soc. 127*, 10004–10005.

(5) Buller, A. R., Brinkmann-Chen, S., Romney, D. K., Herger, M., Murciano-Calles, J., and Arnold, F. H. (2015) Directed evolution of the tryptophan synthase beta-subunit for stand-alone function recapitulates allosteric activation. *Proc. Natl. Acad. Sci. U. S. A. 112*, 14599–14604.

(6) Schendzielorz, G., Dippong, M., Grunberger, A., Kohlheyer, D., Yoshida, A., Binder, S., Nishiyama, C., Nishiyama, M., Bott, M., and Eggeling, L. (2014) Taking control over control: Use of product sensing in single cells to remove flux control at key enzymes in biosynthesis pathways. *ACS Synth. Biol. 3*, 21–29.

(7) Cramer, J. T., Führing, J. I., Baruch, P., Brütting, C., Knölker, H.-J., Gerardy-Schahn, R., and Fedorov, R. (2018) Decoding allosteric networks in biocatalysts: Rational approach to therapies and biotechnologies. *ACS Catal. 8*, 2683–2692.

(8) Pedreno, S., Pisco, J. P., Larrouy-Maumus, G., Kelly, G., and de Carvalho, L. P. (2012) Mechanism of feedback allosteric inhibition of atp phosphoribosyltransferase. *Biochemistry 51*, 8027–8038.

(9) Ames, B. N., Martin, R. G., and Garry, B. J. (1961) The first step of histidine biosynthesis. *J. Biol. Chem. 236*, 2019–2026.

(10) Moggre, G. J., Poulin, M. B., Tyler, P. C., Schramm, V. L., and Parker, E. J. (2017) Transition state analysis of adenosine triphosphate phosphoribosyltransferase. *ACS Chem. Biol. 12*, 2662–2670.

(11) Cho, Y., Sharma, V., and Sacchettini, J. C. (2003) Crystal structure of atp phosphoribosyltransferase from *mycobacterium tuberculosis*. *J. Biol. Chem. 278*, 8333–8339.

(12) Cho, Y., Ioerger, T. R., and Sacchettini, J. C. (2008) Discovery of novel nitrobenzothiazole inhibitors for *mycobacterium tuberculosis* atp phosphoribosyl transferase (hisg) through virtual screening. *J. Med. Chem. 51*, 5984–5992.

(13) Kulis-Horn, R. K., Persicke, M., and Kalinowski, J. (2015) Corynebacterium glutamicum atp-phosphoribosyl transferases suit-

DOI: 10.1021/acs.biochem.8b00559
Biochemistry 2018, 57, 4357–4367

able for l-histidine production—strategies for the elimination of feedback inhibition. *J. Biotechnol. 206*, 26−37.
(14) Kulis-Horn, R. K., Persicke, M., and Kalinowski, J. (2014) Histidine biosynthesis, its regulation and biotechnological application in corynebacterium glutamicum. *Microb. Biotechnol. 7*, 5−25.
(15) Pacholarz, K. J., Burnley, R. J., Jowitt, T. A., Ordsmith, V., Pisco, J. P., Porrini, M., Larrouy-Maumus, G., Garlish, R. A., Taylor, R. J., de Carvalho, L. P. S., and Barran, P. E. (2017) Hybrid mass spectrometry approaches to determine how l-histidine feedback regulates the enzyme mtatp-phosphoribosyltransferase. *Structure 25*, 730−738.
(16) Mittelstadt, G., Moggre, G. J., Panjikar, S., Nazmi, A. R., and Parker, E. J. (2016) Campylobacter jejuni adenosine triphosphate phosphoribosyltransferase is an active hexamer that is allosterically controlled by the twisting of a regulatory tail. *Protein Sci. 25*, 1492−1506.
(17) Bell, R. M., and Koshland, D. E. (1971) Allosteric properties of the first enzyme of the histidine operon. *Bioorg. Chem. 1*, 409−423.
(18) Martin, R. G. (1963) The first enzyme in histidine biosynthesis: The nature of feedback inhibition by histidine. *J. Biol. Chem. 238*, 257−268.
(19) Morton, D. P., and Parsons, S. M. (1977) Inhibition of atp phosphoribosyltransferase by amp and adp in the absence and presence of histidine. *Arch. Biochem. Biophys. 181*, 643−648.
(20) Livingstone, E. K., Mittelstadt, G., Given, F. M., and Parker, E. J. (2016) Independent catalysis of the short form hisg from *lactococcus lactis*. *FEBS Lett. 590*, 2603−2610.
(21) Morton, D. P., and Parsons, S. M. (1976) Biosynthetic direction substrate kinetics and product inhibition studies on the first enzyme of histidine biosynthesis, adenosine triphosphate phosphoribosyltransferase. *Arch. Biochem. Biophys. 175*, 677−686.
(22) Kleeman, J. E., and Parsons, S. M. (1976) Reverse direction substrate kinetics and inhibition studies on the first enzyme of histidine biosynthesis, adenosine triphosphate phosphoribosyltransferase. *Arch. Biochem. Biophys. 175*, 687−693.
(23) Sissler, M., Delorme, C., Bond, J., Ehrlich, S. D., Renault, P., and Francklyn, C. (1999) An aminoacyl-trna synthetase paralog with a catalytic role in histidine biosynthesis. *Proc. Natl. Acad. Sci. U. S. A. 96*, 8985−8990.
(24) Vega, M. C., Zou, P., Fernandez, F. J., Murphy, G. E., Sterner, R., Popov, A., and Wilmanns, M. (2005) Regulation of the hetero-octameric atp phosphoribosyl transferase complex from *thermotoga maritima* by a trna synthetase-like subunit. *Mol. Microbiol. 55*, 675−686.
(25) Bovee, M. L., Champagne, K. S., Demeler, B., and Francklyn, C. S. (2002) The quaternary structure of the hisz-hisg n-1-(5′-phosphoribosyl)-atp transferase from *lactococcus lactis*. *Biochemistry 41*, 11838−11846.
(26) Stroek, R., Ge, Y., Talbot, P. D., Glok, M. K., Bernas, K. E., Thomson, C. M., Gould, E. R., Alphey, M. S., Liu, H., Florence, G. J., Naismith, J. H., and da Silva, R. G. (2017) Kinetics and structure of a cold-adapted hetero-octameric atp phosphoribosyltransferase. *Biochemistry 56*, 793−803.
(27) Champagne, K. S., Sissler, M., Larrabee, Y., Doublie, S., and Francklyn, C. S. (2005) Activation of the hetero-octameric atp phosphoribosyl transferase through subunit interface rearrangement by a trna synthetase paralog. *J. Biol. Chem. 280*, 34096−34104.
(28) Champagne, K. S., Piscitelli, E., and Francklyn, C. S. (2006) Substrate recognition by the hetero-octameric atp phosphoribosyltransferase from *lactococcus lactis*. *Biochemistry 45*, 14933−14943.
(29) Alphey, M. S., Fisher, G., Ge, Y., Gould, E. R., Machado, T. G., Liu, H., Florence, G. J., Naismith, J. H., and da Silva, R. G. (2018) Catalytic and anticatalytic snapshots of a short-form atp phosphoribosyltransferase. *ACS Catal. 8*, 5601−5610.
(30) Smith, D. W., and Ames, B. N. (1965) Phosphoribosyladenosine monophosphate, an intermediate in histidine biosynthesis. *J. Biol. Chem. 240*, 3056−3063.
(31) Frisch, M. J., Trucks, G. W., Schlegel, H. B., Scuseria, G. E., Robb, M. A., Cheeseman, J. R., Scalmani, G., Barone, V., Mennucci, B., Petersson, G. A., Nakatsuji, H., Caricato, M., Li, X., Hratchian, H. P., Izmaylov, A. F., Bloino, J., Zheng, G., Sonnenberg, J. L., Hada, M., Ehara, M., Toyota, K., Fukuda, R., Hasegawa, J., Ishida, M., Nakajima, T., Honda, Y., Kitao, O., Nakai, H., Vreven, T., Montgomery, J. A., Jr., Peralta, J. E., Ogliaro, F., Bearpark, M. J., Heyd, J. J., Brothers, E. N., Kudin, K. N., Staroverov, V. N., Kobayashi, R., Normand, J., Raghavachari, K., Rendell, A. P., Burant, J. C., Iyengar, S. S., Tomasi, J., Cossi, M., Rega, N., Millam, J. M., Klene, M., Knox, J. E., Cross, J. B., Bakken, V., Adamo, C., Jaramillo, J., Gomperts, R., Stratmann, R. E., Yazyev, O., Austin, A. J., Cammi, R., Pomelli, C., Ochterski, J. W., Martin, R. L., Morokuma, K., Zakrzewski, V. G., Voth, G. A., Salvador, P., Dannenberg, J. J., Dapprich, S., Daniels, A. D., Farkas, O., Foresman, J. B., Ortiz, J. V., Cioslowski, J., and Fox, D. J. (2009), *Gaussian 09*, Gaussian Inc., Wallingford, CT.
(32) Niesen, F. H., Berglund, H., and Vedadi, M. (2007) The use of differential scanning fluorimetry to detect ligand interactions that promote protein stability. *Nat. Protoc. 2*, 2212−2221.
(33) Mittelstadt, G., Jiao, W., Livingstone, E. K., Moggre, G. J., Nazmi, A. R., and Parker, E. J. (2018) A dimeric catalytic core relates the short and long forms of atp-phosphoribosyltransferase. *Biochem. J. 475*, 247−260.
(34) Cleland, W. W. (1967) Enzyme kinetics. *Annu. Rev. Biochem. 36*, 77−112.
(35) Lohkamp, B., McDermott, G., Campbell, S. A., Coggins, J. R., and Lapthorn, A. J. (2004) The structure of *escherichia coli* atp-phosphoribosyltransferase: Identification of substrate binding sites and mode of amp inhibition. *J. Mol. Biol. 336*, 131−144.
(36) Wang, Z., and Cole, P. A. (2014) Catalytic mechanisms and regulation of protein kinases. *Methods Enzymol. 548*, 1−21.
(37) Grace, M. R., Walsh, C. T., and Cole, P. A. (1997) Divalent ion effects and insights into the catalytic mechanism of protein tyrosine kinase csk. *Biochemistry 36*, 1874−1881.
(38) Zhang, Y., Shang, X., Deng, A., Chai, X., Lai, S., Zhang, G., and Wen, T. (2012) Genetic and biochemical characterization of corynebacterium glutamicum atp phosphoribosyltransferase and its three mutants resistant to feedback inhibition by histidine. *Biochimie 94*, 829−838.
(39) Guthrie, R. D., and Jencks, W. P. (1989) Iupac recommendations for the representation of reaction mechanisms. *Acc. Chem. Res. 22*, 343−349.
(40) In IUPAC recommendation for reaction mechanism nomenclature (see ref 39), A_ND_N describes an associative nucleophilic substitution reaction mechanism where the electrophile is partially bonded to both incoming nucleophile and departing leaving group at the transition state. $D_N{*}A_N^{\ddagger}$ describes a dissociative nucleophilic substitution reaction mechanism where the leaving group departs to form an intermediate, and the highest-energy transition state is the one for subsequent nucleophilic attack to the intermediate.
(41) Burgos, E. S., Vetticatt, M. J., and Schramm, V. L. (2013) Recycling nicotinamide. The transition-state structure of human nicotinamide phosphoribosyltransferase. *J. Am. Chem. Soc. 135*, 3485−3493.
(42) Sun, G., and Nicklaus, M. C. (2007) Natural resonance structures and aromaticity of the nucleobases. *Theor. Chem. Acc. 117*, 323−332.
(43) Lewandowicz, A., and Schramm, V. L. (2004) Transition state analysis for human and plasmodium falciparum purine nucleoside phosphorylases. *Biochemistry 43*, 1458−1468.
(44) Kline, P. C., and Schramm, V. L. (1993) Purine nucleoside phosphorylase. Catalytic mechanism and transition-state analysis of the arsenolysis reaction. *Biochemistry 32*, 13212−13219.
(45) Silva, R. G., Hirschi, J. S., Ghanem, M., Murkin, A. S., and Schramm, V. L. (2011) Arsenate and phosphate as nucleophiles at the transition states of human purine nucleoside phosphorylase. *Biochemistry 50*, 2701−2709.
(46) sheely, M. L. (1932) Glycerol viscosity tables. *Ind. Eng. Chem. 24*, 1060−1064.
(47) Karsten, W. E., Lai, C.-J., and Cook, P. F. (1995) Inverse solvent isotope effects in the nad-malic enzyme reaction are the result

DOI: 10.1021/acs.biochem.8b00559
Biochemistry 2018, 57, 4357−4367

of the viscosity difference between d2o and h2o: Implications for solvent isotope effect studies. *J. Am. Chem. Soc. 117*, 5914−5918.
(48) Lin, Y., West, A. H., and Cook, P. F. (2008) Potassium is an activator of homoisocitrate dehydrogenase from saccharomyces cerevisiae. *Biochemistry 47*, 10809−10815.
(49) Lin, Y., Volkman, J., Nicholas, K. M., Yamamoto, T., Eguchi, T., Nimmo, S. L., West, A. H., and Cook, P. F. (2008) Chemical mechanism of homoisocitrate dehydrogenase from saccharomyces cerevisiae. *Biochemistry 47*, 4169−4180.
(50) Goitein, R. K., Chelsky, D., and Parsons, S. M. (1978) Primary 14c and alpha secondary 3h substrate kinetic isotope effects for some phosphoribosyltransferases. *J. Biol. Chem. 253*, 2963−2971.
(51) Johnson, K. A. (1992) 1 transient-state kinetic analysis of enzyme reaction pathways. In *The enzymes* (Sigman, D. S., Ed.), pp 1−61, Academic Press.
(52) Johnson, K. A. (1995) Rapid quench kinetic analysis of polymerases, adenosinetriphosphatases, and enzyme intermediates. *Methods Enzymol. 249*, 38−61.
(53) Hartley, B. S., and Kilby, B. A. (1954) The reaction of p-nitrophenyl esters with chymotrypsin and insulin. *Biochem. J. 56*, 288−297.

DOI: 10.1021/acs.biochem.8b00559
Biochemistry 2018, 57, 4357−4367

SUPPORTING INFORMATION

Allosteric activation shifts the rate-limiting step in a short-form ATP phosphoribosyltransferase

Gemma Fisher,[‡] Catherine M. Thomson,[‡] Rozanne Stroek,[‡] Clarissa M. Czekster,[‡] Jennifer S. Hirschi,[§,*] and Rafael G. da Silva[‡,*]

[‡]School of Biology, Biomedical Sciences Research Complex, University of St Andrews, St Andrews, Fife KY16 9ST UK

[§]Department of Chemistry, Binghamton University, Binghamton, New York 13902 USA

*To whom correspondence may be addressed: rgds@st-andrews.ac.uk, phone: +44 01334 463496, and jhirschi@binghamton.edu.

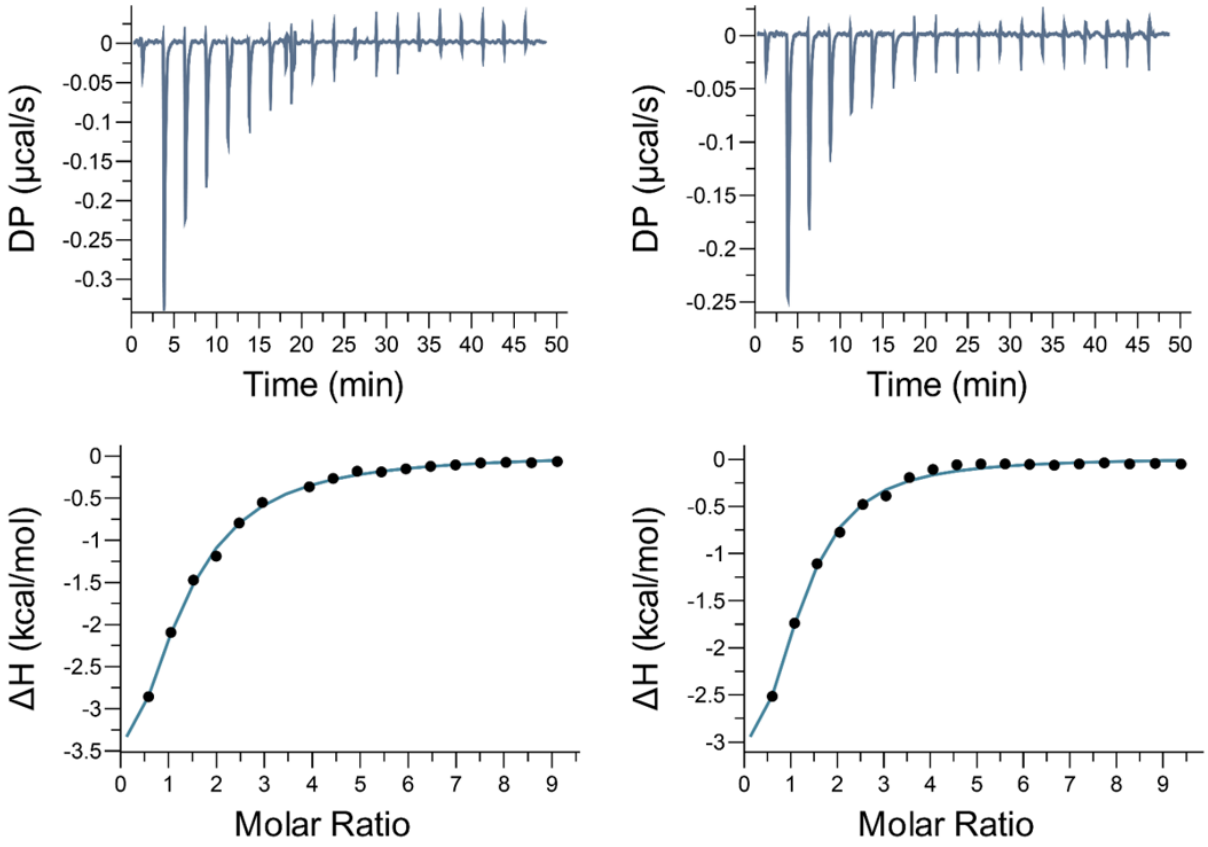

Figure S1. ITC curves for *Pa*HisG$_S$ titration with PRPP in two independent experiments. Controls lacking *Pa*HisG$_S$ have been subtracted from the data, and the solid lines represent data fitting to a single-site binding model.

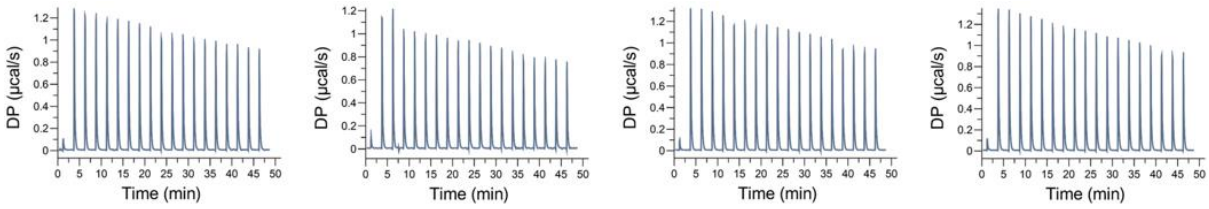

Figure S2. ITC curves for *Pa*HisG$_S$ (two graphs on the left) and buffer (two graphs on the right) titration with ATP in two independent experiments. No signal is detected beyond the heat of dilution when experimental and control sets are compared.

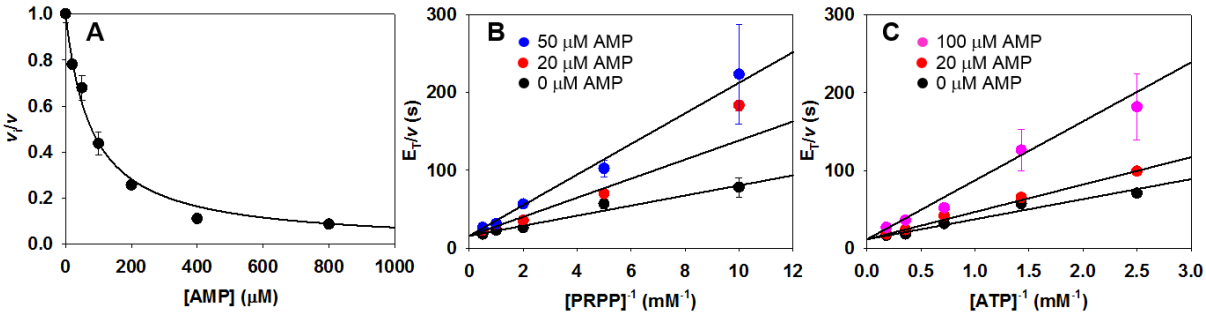

Figure S3. *Pa*HisG$_S$ inhibition by AMP. (A) Dose-response curve for AMP concentration. Line represents data fitting to eq 4. (B) and (C) Double-reciprocals of substrate saturation curves in the presence of AMP. Lines are the reciprocals of data fitting to eq 5.

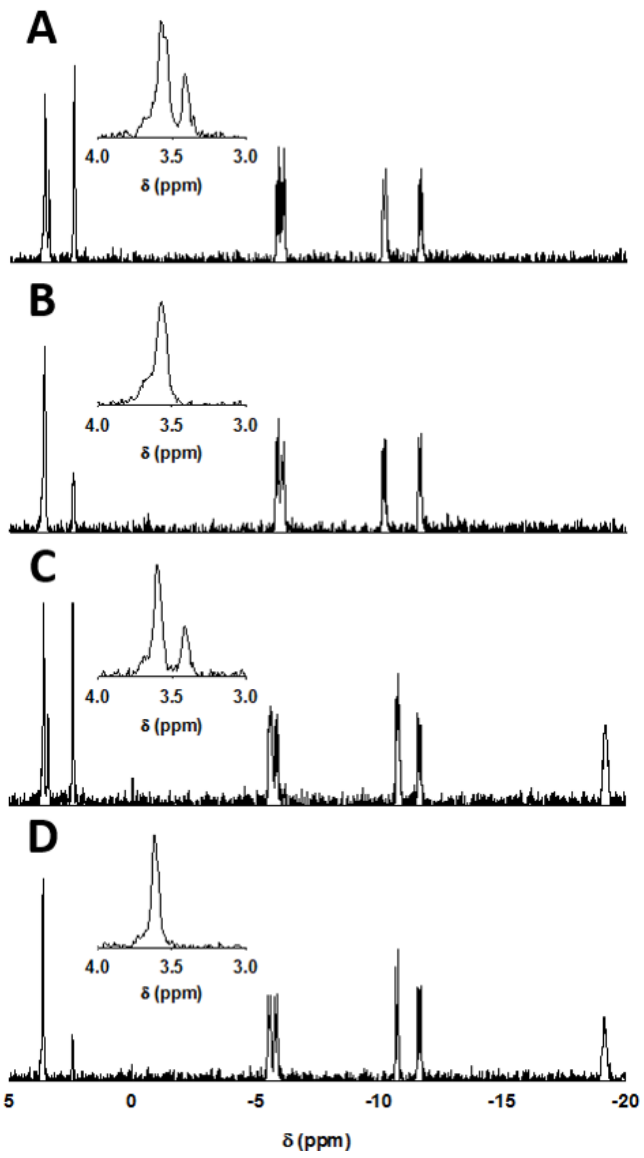

Figure S4. ^{31}P-NMR spectra of *Pa*HisG$_S$ reaction with either (A) ADP or (C) ATP as substrate. (B) and (D) are controls for (A) and (B), respectively, in the absence of *Pa*HisG$_S$. Insets in A – D are close-ups of the spectra between 4.0 and 3.0 ppm, showing the peak at *ca*. 3.3 ppm in A and C corresponding to the phosphorus in the N^1-5-phospho-β-D-ribose moiety of PRATP and PRADP, respectively, which is missing in insets in B and D.

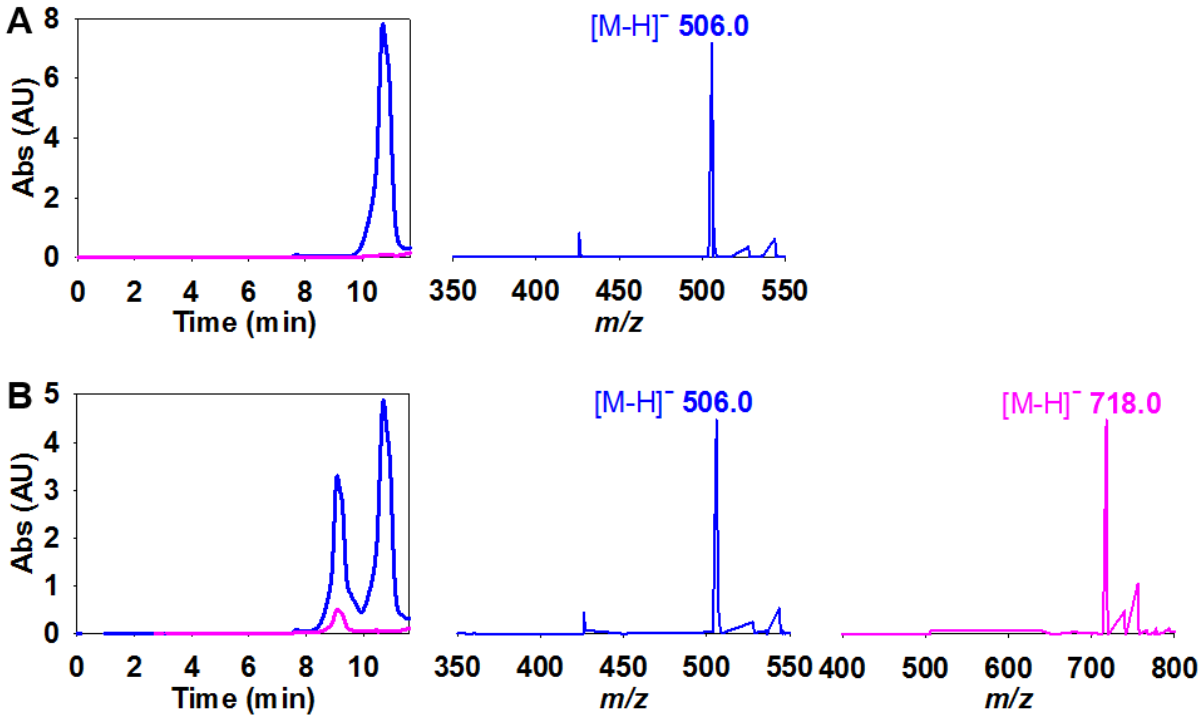

Figure S5. Analysis of *Pa*HisG$_S$-catalysed reaction with Mn^{2+} replacing Mg^{2+}. (A) Chromatogram of the control reaction lacking *Pa*HisG$_S$, showing a peak with absorbance at 260 nm (blue), corresponding to ATP, and mass spectra of the peak showing the expected *m/z* for ATP (blue). (B) Chromatogram of the reaction, showing peaks with absorbance at 260 nm (blue) and at both 260 nm and 290 nm (pink), corresponding to ATP and PRATP, respectively, and mass spectra of the peak absorbing at 260 nm showing the expected *m/z* for ATP (blue), and of the peak absorbing at both 260 nm and 290 nm showing the expected *m/z* for PRATP (pink).

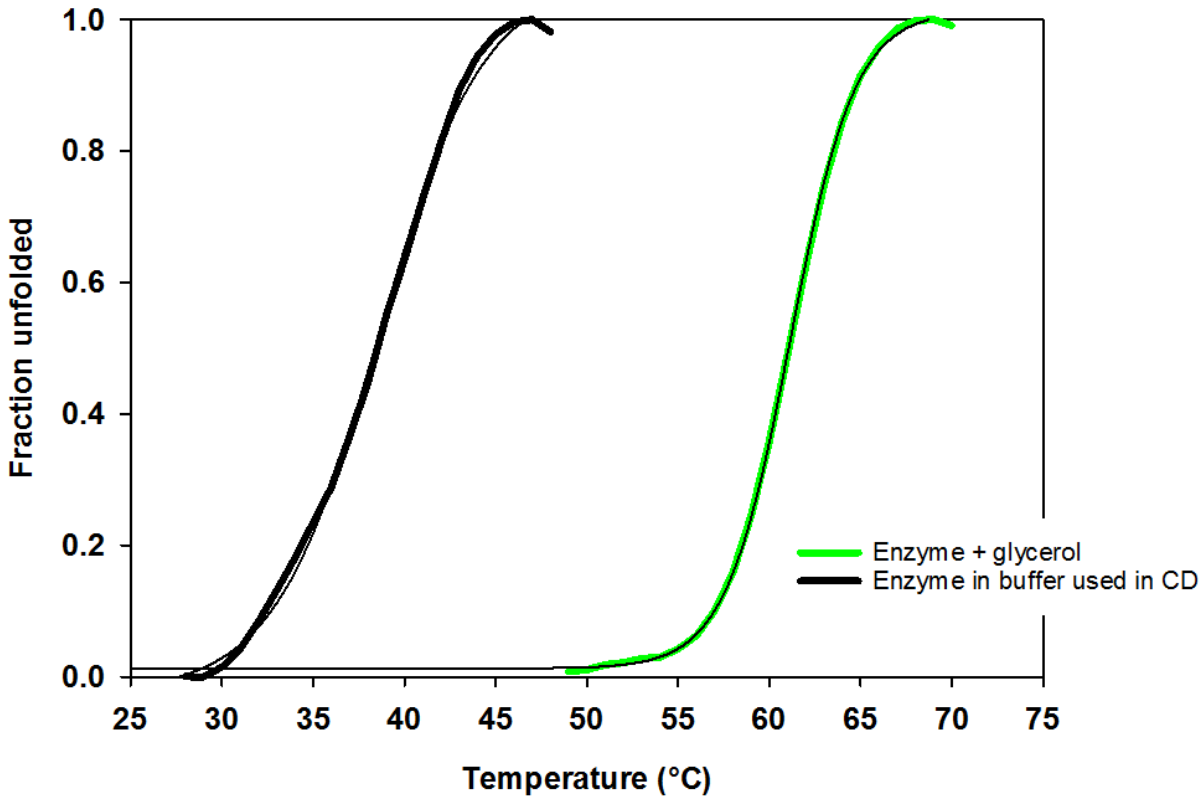

Figure S6. DSF-based thermal denaturation of *Pa*HisG$_S$ in the presence of 22% glycerol (*v/v*), and in 10 mM KH_2PO_4, 10 mM KF pH 8.0, which was the buffer used for circular dichroism (CD) thermal denaturation studies of *Pa*HisG$_S$,[1] indicating that the protein is more thermolabile in that buffer. Data were fitted to eq 8.

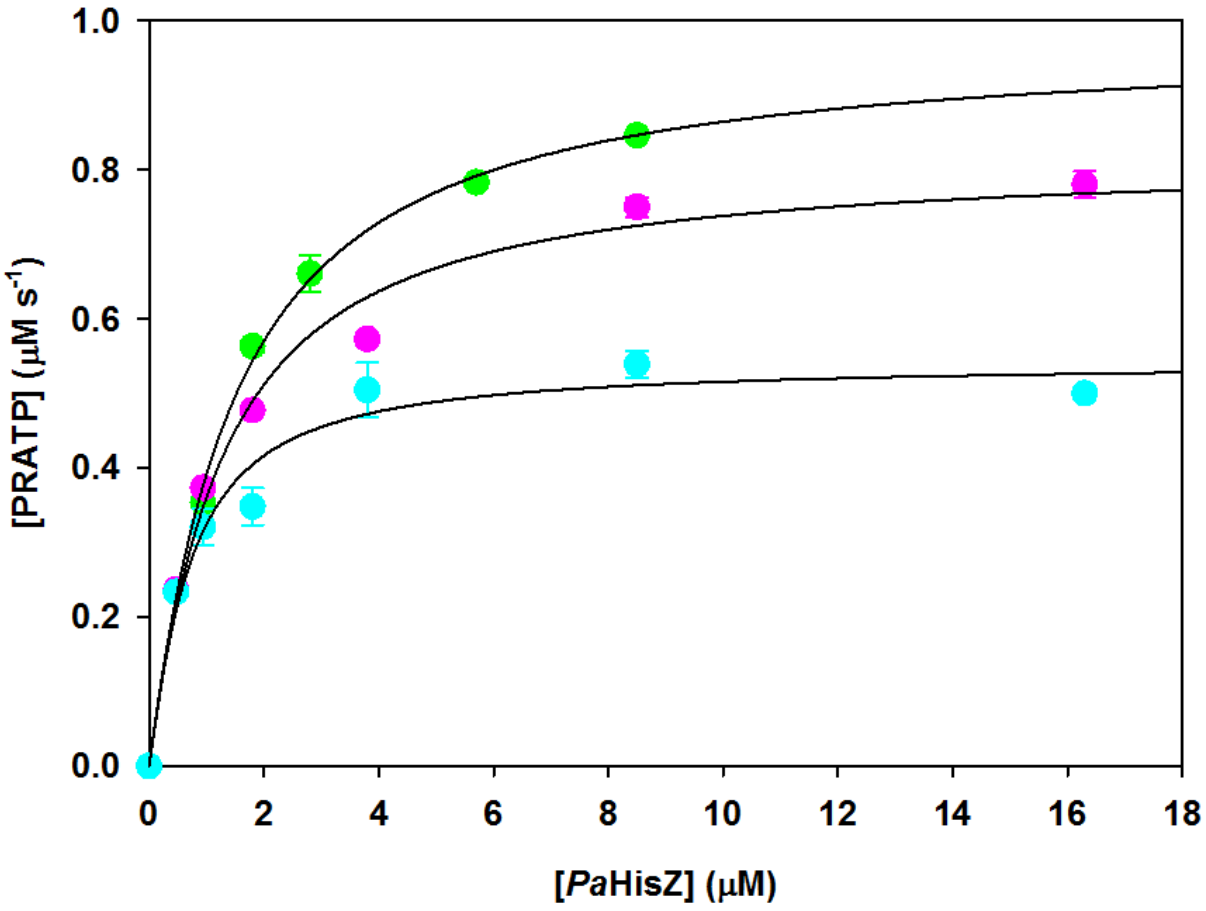

Figure S7. Determination of K_D for equilibrium dissociation of *Pa*HisZ from the *Pa*ATPPRT holoenzyme in 0% glycerol (green), 18% glycerol (pink), and 27% glycerol (cyan) (*v/v*). Lines are data fitting to eq 1.

Table S1. *Pa*ATPPRT and *Pa*HisG$_S$ steady-state parameters from initial velocity patterns.

Parameter	*Pa*ATPPRT[a]	*Pa*HisG$_S$[b]
k_{cat} (s^{-1})	1.5 ± 0.1	0.25 ± 0.02
K_{iPRPP} (mM)	0.4 ± 0.1	0.04 ± 0.03
K_{PRPP} (mM)	0.7 ± 0.1	0.6 ± 0.1
K_{ATP} (mM)	1.4 ± 0.2	2.3 ± 0.3
k_{cat}/K_{PRPP} (M^{-1} s^{-1})	2142 ± 337	416 ± 77
k_{cat}/K_{ATP} (M^{-1} s^{-1})	1071 ± 168	108 ± 16

[a]Values represent mean ± fitting error of duplicate measurements. [b]Values represent mean ± fitting error of quadruplicate measurements.

Table S2. *Pa*HisG$_S$ T_m's by DSF in the presence and absence of ligands.[a]

Ligand	T_m (°C)
Enzyme (no ligand)	60.0 ± 0.1
PRPP	66.0 ± 0.1
ATP	59.0 ± 0.1
PRATP	65.0 ± 0.1
PP_i	59.0 ± 0.1
Enzyme (no ligand) in 22% glycerol (*v*/*v*)	61.0 ± 0.1
Enzyme (no ligand) in 10 mM K_2HPO_4, 10 mM KF, pH 8.0[b]	39.0 ± 0.2

[a]Values represent mean ± fitting error of triplicate measurements. [b]Buffer used in a previous circular dichroism-based thermal denaturation.[1]

Table S3. Steady-state kinetic constants for *Pa*HisG$_S$[a] with either ATP or ADP.

Parameter	ATP	ADP
k_{cat} (s^{-1})	0.15 ± 0.01	0.14 ± 0.01
$K_M^{A(X)P}$ (mM), X = T or D	0.96 ± 0.09	3.2 ± 0.3
K_M^{PRPP} (mM)	0.39 ± 0.07	0.91 ± 0.08
$k_{cat}/K_M^{A(X)P}$ (M^{-1} s^{-1}), X = T or D	156 ± 20	43 ± 5
k_{cat}/K_M^{PRPP} (M^{-1} s^{-1})	384 ± 70	153 ± 6

[a]Values represent mean ± fitting error of duplicate measurements.

Table S4. Effect of Mn^{2+} on *Pa*ATPPRT and *Pa*HisG$_S$ steady-state kinetic parameters.[a]

Parameter	*Pa*HisG$_S$ Mg^{2+}	*Pa*HisG$_S$ Mn^{2+}	*Pa*ATPPRT Mg^{2+}	*Pa*ATPPRT Mn^{2+}
k_{cat} (s^{-1})	0.15 ± 0.01	0.39 ± 0.05	2.7 ± 0.1	2.1 ± 0.1
K_M^{PRPP} (mM)	0.33 ± 0.03	0.6 ± 0.2	0.43 ± 0.06	0.28 ± 0.06
K_M^{ATP} (mM)	1.4 ± 0.2	0.30 ± 0.05	0.72 ± 0.09	0.19 ± 0.03
k_{cat}/K_M^{PRPP} (M^{-1} s^{-1})	450 ± 50	700 ± 200	6000 ± 900	7500 ± 2000
k_{cat}/K_M^{ATP} (M^{-1} s^{-1})	110 ± 20	1300 ± 300	3800 ± 500	11100± 2000

[a]Values represent mean ± fitting error of duplicate measurements.

Table S5. NBO charge distribution of key atoms at the transition state of *Pa*HisG$_S$.

Atom	Transition state with Mg^{2+} NBO charge	Transition state with Mn^{2+} NBO charge
ADP N1	–0.563	–0.562
ADP N6	–0.783	–0.783
ADP C6	0.455	0.453
5-phosphoribosyl C1	0.410	0.399
5-phosphoribosyl O4	–0.459	–0.459
PP_i Os bonded to metal ion 1	–1.208 (average of 2 O atoms)	–1.053 (average of 2 O atoms)
PP_i Os bonded to metal ion 2	–1.162 (average of 2 charges)	–1.026 (average of 2 charges)
Metal ion 1 (bonded to PP_i)	1.437	0.610
Metal ion 2 (bonded to PP_i and ADP)	1.439	0.688

Table S6. Solvent viscosity effects on *Pa*HisG$_S$ steady-state kinetic parameters.[a]

Parameter	0% glycerol (*v/v*)	18% glycerol (*v/v*)	27% glycerol (*v/v*)
k_{cat} (s^{-1})	0.15 ± 0.02	0.28 ± 0.05	0.40 ± 0.02
K_M^{PRPP} (mM)	0.36 ± 0.04	0.35 ± 0.02	0.41 ± 0.08
K_M^{ATP} (mM)	1.2 ± 0.1	1.9 ± 0.2	1.9 ± 0.2
k_{cat}/K_M^{PRPP} (M^{-1} s^{-1})	416 ± 70	800 ± 150	976 ± 197
k_{cat}/K_M^{ATP} (M^{-1} s^{-1})	125 ± 19	147 ± 30	210 ± 24

[a]Values represent mean ± fitting error of duplicate measurements.

Table S7. Solvent viscosity effects on *Pa*ATPPRT steady-state kinetic parameters.[a]

Parameter	0% glycerol (*v/v*)	18% glycerol (*v/v*)	27% glycerol (*v/v*)
k_{cat} (s^{-1})	2.6 ± 0.1	1.8 ± 0.1	1.03 ± 0.03
K_M^{PRPP} (mM)	0.29 ± 0.04	0.18 ± 0.03	0.10 ± 0.01
K_M^{ATP} (mM)	0.62 ± 0.05	0.8 ± 0.1	0.35 ± 0.03
k_{cat}/K_M^{PRPP} (M^{-1} s^{-1})	9000 ± 1000	10000 ± 2000	10300 ± 1000
k_{cat}/K_M^{ATP} (M^{-1} s^{-1})	4200 ± 400	2300 ± 300	2900 ± 300

[a]Values represent mean ± fitting error of duplicate measurements.

Coordinates of DFT-calculated structures

freeTS.log – Transition structure with Mg. No bonds fixed

C-N = 2.27 Å

C-O = 2.36 Å

Free Energy = -6563.285823

Zero-point Energy = -6563.129757

Potential Energy = -6564.43503489

Nimag = 1 (-213.6872 cm-1)

B3LYP/6-31G* Lanl2DZ Mg

Charge = 0 Multiplicity = 1

C 6.00173 2.41014 -3.48936

N 5.38563 2.48673 -2.16756

C 6.04446 2.27531 -1.03983

N 7.34263 1.84189 -1.09453

N 5.49807 2.55615 0.15676

C -3.42882 5.88323 -1.52591

N -2.07112 5.45683 -1.25600

C -1.75014 4.56423 -0.31899

N -0.46749 4.21778 -0.14928

N -2.69914 4.05555 0.49640

C -7.72998 -6.29125 -2.67671

C -6.97081 -5.00119 -2.37462

O -7.68214 -3.99594 -2.04788

O -5.71840 -5.01367 -2.48884

C -2.68316 -4.74773 -1.67193

N -3.73706 -3.79056 -1.25803

C 1.85167 6.39827 -4.04333

C 0.74281 5.91937 -3.11015

O -0.24287 6.65724 -2.90882

O 0.90075 4.75810 -2.57520

O 9.56895 -2.76848 -2.35734

O 6.77660 -0.76212 1.06195

O -8.24201 0.06620 -4.38478

O 5.16032 -3.85934 3.05156

O -8.52193 -3.01436 0.30732

O 8.04709 -4.78102 -1.28557

O 6.39400 -3.55804 0.71943

O 2.68261 2.89820 -2.09953

O -3.38992 3.60041 4.96396

O -1.71523 1.48930 5.26448

O -4.11871 -3.83444 1.45269

O 0.25632 -4.07255 3.62100

O 2.54971 -3.44330 2.43630

O -2.29354 1.86574 2.29591

P -3.60212 1.11901 2.54510

O -4.43716 1.49992 3.73812

O -3.24775 -0.49011 2.66747

P -1.84733 -1.28411 2.42085

O -1.37410 -1.14148 0.98350

O -0.87101 -0.39911 3.42053

O -2.01000 -2.67952 2.97812

O -4.45148 1.21764 1.17564

C -5.87845 0.97356 1.22789

C -6.35182 0.31430 -0.04874

C -5.61835 -0.97722 -0.43762

O -5.97648 -2.10488 0.31892

C -5.90827 -1.03333 -1.95825

O -7.24065 -1.42190 -2.21191

C -5.79294 0.45340 -2.32764

O -6.18081 1.19348 -1.17334

N -4.43696 0.89421 -2.72426

C -3.18745 0.31765 -2.63254

C -2.28328 1.34785 -2.92048

N -2.93822 2.52980 -3.19032
C -4.20328 2.21487 -3.06345
N -2.84020 -0.96188 -2.35426
C -1.52767 -1.12777 -2.33041
N -0.55233 -0.22357 -2.53064
C -0.89766 1.06569 -2.82633
N 0.04052 2.00242 -2.99123
O 7.37272 -2.23004 -3.72734
P 6.44806 -1.86461 -2.48081
O 7.24088 -0.97747 -1.49940
O 5.73189 -3.06321 -1.87461
O 5.33495 -0.90131 -3.21688
C 3.95678 -1.24700 -3.20185
C 3.33739 -1.01370 -1.81439
O 2.24548 -0.01828 -1.91281
C 2.72718 -2.20951 -1.06292
O 3.45328 -2.42304 0.14631
C 1.26299 -1.78359 -0.74202
O 0.94469 -2.04360 0.59364
C 1.25100 -0.32047 -1.14806
O 2.43374 0.26422 0.80300
P 2.11966 1.67642 1.40827
O 2.76431 2.81307 0.63806
O 0.63350 1.86470 1.76016
O 2.93039 1.56518 2.88266
P 2.20367 0.74352 4.08156
O 1.77861 -0.64569 3.52587
O 1.06547 1.54040 4.66380
O 3.40645 0.54861 5.12631
Mg -0.59689 1.79403 3.42999
H 5.39896 3.01198 -4.17304
H 6.03219 1.37866 -3.85506
H 4.36398 2.70486 -2.13400
H 7.78437 1.76839 -0.18658
H 7.47916 0.98231 -1.63850
H 4.49481 2.79835 0.25563
H 5.86041 2.03559 0.94505
H -4.05557 5.05610 -1.88540
H -3.38404 6.63749 -2.31346
H -1.31797 5.87020 -1.85423
H -0.20017 3.50508 0.52569
H 0.18868 4.46957 -0.90135
H -3.66330 4.12638 0.20883
H -2.47905 3.24510 1.08055
H -7.04422 -7.12178 -2.85628
H -8.36042 -6.14151 -3.56064
H -2.55449 -4.70385 -2.75509
H -1.74388 -4.51187 -1.16546
H -3.84509 -3.79286 -0.20452
H -4.65961 -4.10621 -1.70793
H -3.52581 -2.82937 -1.56733
H 2.02028 5.65867 -4.83433
H 2.78933 6.49378 -3.48277
H 9.29456 -2.04387 -1.76777
H 6.89025 -0.80842 0.05029
H -8.99798 0.51097 -3.97245
H -7.99961 -0.61951 -3.72625
H 5.71807 -4.35353 3.67097
H 5.58889 -3.93263 2.14687
H -8.46337 -3.72649 0.96333
H -8.42808 -3.47493 -0.56437
H 7.26063 -4.55191 -1.81855
H 7.75696 -4.50830 -0.39264
H 5.94768 -3.44410 -0.16612
H 6.65654 -2.63318 0.92560
H 2.56979 2.87802 -1.11792
H 2.20009 3.72709 -2.38389
H -3.99493 4.07706 5.55102
H -3.93796 2.94296 4.44235
H -2.42271 2.15537 5.41942

H -2.14300 0.61916 5.28836

H -4.81059 -3.14205 1.40688

H -3.41751 -3.49505 2.05230

H -0.58235 -3.65776 3.28646

H 0.27173 -3.83162 4.55992

H 3.31718 -3.82704 2.91161

H 1.68912 -3.74159 2.86754

H -6.12769 0.31839 2.06743

H -6.38210 1.93382 1.37641

H -7.42228 0.09213 0.07222

H -4.54454 -0.83056 -0.28375

H -6.94886 -2.31771 0.24974

H -5.20119 -1.65552 -2.51236

H -7.30309 -2.42663 -2.19202

H -6.46522 0.70458 -3.15219

H -5.03332 2.89515 -3.20059

H -1.18839 -2.13708 -2.11355

H -0.21171 2.98820 -3.04520

H 3.47030 -0.58318 -3.92097

H 3.81628 -2.28327 -3.52265

H 4.06675 -0.52398 -1.16877

H 2.76744 -3.11908 -1.66432

H 3.21541 -3.30374 0.50207

H 0.58541 -2.31901 -1.41295

H -0.02599 -1.71102 0.77204

H 0.62901 0.45593 -0.73723

H 7.01693 2.81473 -3.45489

H -3.90017 6.33468 -0.64270

H -8.40064 -6.53522 -1.84549

H -3.00570 -5.75179 -1.39397

Mg 2.59711 -1.42550 1.87403

O 4.55375 -1.21690 2.73801

H 4.87573 -2.10587 3.03161

H 5.25742 -0.88558 2.13225

H 1.03202 1.84794 -2.80948

H 4.09073 0.00093 4.69294

O -0.80895 3.81986 3.92837

H -0.21698 4.03435 4.66765

H -1.72870 3.98926 4.24244

H 0.07363 -0.72255 3.49416

H 7.66897 -0.63622 1.42080

H 9.18954 -3.57939 -1.92622

H 8.29984 -2.46213 -3.40320

H 1.59715 7.36192 -4.48860

freeTSMn.log - Transition structure with Mn. No bonds fixed

C-N = 2.27 Å

C-O = 2.38 Å

B3LYP/6-31G* Lanl2DZ Mn

Free Energy = -6769.088921

Zero-point Energy = -6768.934608

Potential Energy = -6770.24007644

Nimag = 1 (-198.4577 cm-1)

Charge = 0 Multiplicity = 1

C 5.99020 2.37355 -3.66551

N 5.36582 2.45176 -2.34818

C 6.01600 2.23946 -1.21699

N 7.32247 1.82812 -1.26093

N 5.45508 2.49620 -0.02053

C -3.33160 6.05514 -1.58227

N -1.98219 5.60355 -1.31096

C -1.67710 4.71176 -0.36792

N -0.40986 4.30569 -0.22633

N -2.62432 4.26361 0.48713

C -7.75572 -6.37769 -2.58434

C -6.98426 -5.08731 -2.31799

O -7.68187 -4.07399 -1.98758
O -5.73475 -5.10744 -2.46167
C -2.69174 -4.79291 -1.68841
N -3.75179 -3.83520 -1.29194
C 1.88377 6.26538 -4.25521
C 0.79075 5.87052 -3.26561
O -0.14903 6.66237 -3.05124
O 0.91320 4.71911 -2.70066
O 9.48104 -2.81673 -2.35636
O 6.61463 -0.62691 0.99142
O -8.29575 -0.06384 -4.41399
O 5.09580 -3.71763 3.07516
O -8.52565 -3.05818 0.34885
O 7.94087 -4.77773 -1.22198
O 6.29482 -3.45859 0.72152
O 2.65699 2.81318 -2.28784
O -3.16684 3.81626 4.60178
O -1.68419 1.60445 5.00826
O -4.11639 -3.84922 1.42009
O 0.36117 -3.56220 3.91294
O 2.49837 -3.46939 2.35714
O -2.26198 1.91438 2.07909
P -3.58279 1.20543 2.40386
O -4.37292 1.68303 3.59377
O -3.25479 -0.39684 2.62212
P -1.89194 -1.24804 2.33937
O -1.45817 -1.14446 0.88793
O -0.84574 -0.37646 3.29079
O -2.06558 -2.61560 2.95188
O -4.46519 1.24311 1.05535
C -5.88975 0.98722 1.16794
C -6.40354 0.28226 -0.06844
C -5.65351 -1.00347 -0.45289
O -5.99073 -2.12506 0.32190
C -5.95626 -1.08353 -1.96976
O -7.28414 -1.49604 -2.20701
C -5.87112 0.39978 -2.35367
O -6.31803 1.13620 -1.22242
N -4.50880 0.87341 -2.70029
C -3.26173 0.28529 -2.69652
C -2.36100 1.33246 -2.93173
N -3.01567 2.53538 -3.08092
C -4.27807 2.21597 -2.93748
N -2.91250 -1.01327 -2.52712
C -1.60055 -1.18464 -2.55657
N -0.62649 -0.26956 -2.71249
C -0.97605 1.03782 -2.90932
N -0.03683 1.97778 -3.04288
O 7.30089 -2.28122 -3.75215
P 6.36935 -1.89449 -2.51690
O 7.15803 -0.99536 -1.54435
O 5.64605 -3.08246 -1.89734
O 5.26041 -0.93953 -3.27109
C 3.88794 -1.30968 -3.28667
C 3.23480 -1.08344 -1.91362
O 2.15005 -0.08590 -2.03059
C 2.60286 -2.27937 -1.17950
O 3.32681 -2.50416 0.03290
C 1.14833 -1.83784 -0.84925
O 0.86712 -2.05681 0.50979
C 1.13759 -0.38565 -1.28640
O 2.34937 0.19197 0.68141
P 2.05618 1.61994 1.27467
O 2.69328 2.72867 0.46443
O 0.56323 1.83652 1.60877
O 2.85518 1.54086 2.73683
P 2.15265 0.69243 3.93319
O 1.67989 -0.67854 3.36186
O 1.03356 1.49754 4.55180
O 3.37842 0.45850 4.93440

Mn -0.60599 1.67512 3.24436
H 5.39687 2.97942 -4.35386
H 6.01553 1.34133 -4.03015
H 4.33884 2.64540 -2.32126
H 7.75613 1.77130 -0.34768
H 7.46790 0.95873 -1.78563
H 4.45478 2.73952 0.06740
H 5.79797 1.93956 0.75271
H -3.98173 5.23200 -1.90836
H -3.27601 6.78155 -2.39493
H -1.22707 5.96776 -1.93786
H -0.16250 3.59942 0.46239
H 0.23593 4.50242 -1.00314
H -3.58990 4.39252 0.22482
H -2.43303 3.41586 1.02811
H -8.40598 -6.23721 -3.45535
H -8.40770 -6.60731 -1.73440
H -2.58122 -4.78714 -2.77448
H -1.74779 -4.52716 -1.20582
H -3.84998 -3.81304 -0.23750
H -4.67640 -4.17386 -1.72539
H -3.55309 -2.88176 -1.62948
H 1.97617 5.50071 -5.03498
H 2.84882 6.31935 -3.73720
H 9.21423 -2.07650 -1.78296
H 6.75672 -0.73160 -0.01144
H -9.04883 0.39344 -4.01015
H -8.05148 -0.73197 -3.73845
H 5.66890 -4.17256 3.71016
H 5.51518 -3.81519 2.16952
H -8.45816 -3.75650 1.01872
H -8.43372 -3.53546 -0.51408
H 7.15637 -4.56076 -1.76341
H 7.65756 -4.45678 -0.34292
H 5.84924 -3.38410 -0.16815
H 6.53312 -2.52314 0.90143
H 2.53034 2.77449 -1.30988
H 2.18001 3.65186 -2.55677
H -3.68515 4.30438 5.25880
H -3.79248 3.18616 4.14070
H -2.36247 2.32070 5.06633
H -2.14758 0.75570 5.10039
H -4.81937 -3.16781 1.37362
H -3.42294 -3.49742 2.02153
H -0.54250 -3.38454 3.54752
H 0.53327 -2.80362 4.49361
H 3.27384 -3.74123 2.89452
H 1.65934 -3.60159 2.90293
H -6.09854 0.35507 2.03578
H -6.39661 1.94688 1.30599
H -7.46052 0.03687 0.10901
H -4.57961 -0.84339 -0.31125
H -6.96134 -2.35046 0.26470
H -5.24282 -1.69903 -2.52249
H -7.32951 -2.50064 -2.17087
H -6.52358 0.62785 -3.20029
H -5.10720 2.90883 -2.98539
H -1.25758 -2.20965 -2.43735
H -0.27898 2.96684 -3.06220
H 3.40595 -0.65666 -4.01856
H 3.77254 -2.34927 -3.60675
H 3.95061 -0.60198 -1.24721
H 2.63612 -3.18663 -1.78504
H 3.10372 -3.39228 0.38189
H 0.43849 -2.39171 -1.46906
H -0.08996 -1.70356 0.70339
H 0.51829 0.39676 -0.88065
H 7.00796 2.77029 -3.62256
H -3.78291 6.54903 -0.71126
H -7.07786 -7.21368 -2.76833

H -2.99640 -5.79013 -1.36878

Mn 2.50790 -1.49507 1.67823

O 4.38417 -1.11935 2.71543

H 4.72597 -2.00794 2.99279

H 5.05939 -0.78146 2.08310

H 0.96204 1.80148 -2.93983

H 4.02973 -0.08566 4.43750

O -0.56395 3.71850 3.50270

H 0.08762 3.88559 4.20560

H -1.44480 3.99934 3.84428

H 0.12181 -0.69305 3.29779

H 7.50135 -0.51061 1.36793

H 9.09300 -3.61323 -1.90576

H 8.22226 -2.52032 -3.41609

H 1.66443 7.23194 -4.71264

pocketrafcutcut14.log

fixed bonds at

C-N = 2.9

C-O = 1.4

B3LYP/6-31G* Lanl2DZ Mg

Zero-point correction= 1.305334 (Hartree/Particle)

Thermal correction to Energy= 1.417149

Thermal correction to Enthalpy= 1.418094

Thermal correction to Gibbs Free Energy= 1.149400

Sum of electronic and zero-point Energies= -6563.173805

Sum of electronic and thermal Energies= -6563.061989

Sum of electronic and thermal Enthalpies= -6563.061045

Sum of electronic and thermal Free Energies= -6563.329739

	E (Thermal)	CV	S
	KCal/Mol	Cal/Mol-Kelvin	Cal/Mol-Kelvin
Total	889.275	406.194	565.513

C,0,-6.0980201217,5.1078923051,-1.6956588565

N,0,-5.4904213768,3.8149741672,-1.9568600753

C,0,-6.0434830118,2.6555622119,-1.6054424761

N,0,-7.2627432202,2.6080797228,-1.012364787

N,0,-5.4157768765,1.5053703652,-1.8787131615

C,0,3.9262370916,4.2366170308,-3.7770063974

N,0,2.5418712012,3.9203098956,-3.4898191004

C,0,2.0909508088,2.6794302063,-3.3128875372

N,0,0.7936694952,2.480906713,-3.0502903007

N,0,2.9194017828,1.6213931674,-3.4556069857

C,0,7.5772068091,-1.0565153302,6.8900674852

C,0,6.8632403843,-0.6136002522,5.6136576744

O,0,7.6140782556,-0.3600174184,4.6148385684

O,0,5.6113786555,-0.5132606515,5.6424133604

C,0,2.5648360782,-1.0253843118,5.0166423266

N,0,3.6047127313,-0.923670143,3.9637904029

C,0,-1.3805134623,6.9529756033,-3.0668490735

C,0,-0.330977395,5.8518289908,-2.9340983323

O,0,0.814021306,6.0493347745,-3.3816820434

O,0,-0.7241619663,4.7625272219,-2.3565843274

O,0,-7.3498676839,1.3730777929,5.6479954578

O,0,-6.4308071901,-1.1969001815,-0.9982514579

O,0,8.2080144211,3.7027768621,2.2923021782

O,0,-5.5623135195,-4.6635791122,1.6579732987

O,0,8.4237630506,-1.9142082015,2.5794129476

O,0,-6.1975356483,-1.0720239921,5.511705245

O,0,-7.1248419845,-2.9309833653,3.0490567547
O,0,-3.1143159796,3.8874154673,-3.2681735391
O,0,3.446044046,-3.2557886177,-5.4538893422
O,0,5.614484081,-1.5694040971,-5.1242587338
O,0,3.9510256477,-3.2854912282,2.5853046517
O,0,-0.3853847145,-5.4878531083,1.7266319236
O,0,-2.7452052778,-4.3344619789,1.5793418407
O,0,2.3291276504,-1.1536394449,-2.7101056211
P,0,3.5801203079,-1.7668885419,-2.0760044139
O,0,4.429763735,-2.7134248171,-2.8819020548
O,0,3.1132170887,-2.545988767,-0.7025927713
P,0,1.6360359835,-2.773437769,-0.0634542827
O,0,1.0445273244,-1.480330481,0.453004996
O,0,0.8091054542,-3.1983484626,-1.4595852136
O,0,1.7159049451,-3.9647638736,0.8581883072
O,0,4.4345755425,-0.5159718519,-1.5371071037
C,0,5.8597031768,-0.6436840733,-1.3201601083
C,0,6.2726037349,0.1539856117,-0.1045536611
C,0,5.5364890396,-0.2000116964,1.1935911504
O,0,5.885435382,-1.4380793045,1.7596060487
C,0,5.8147704126,1.0723073314,2.0314283365
O,0,7.1490951586,1.1026558701,2.4918806654
C,0,5.6740827667,2.1630965486,0.9549106079
O,0,6.0040605463,1.5499405902,-0.2978565852
N,0,4.338992357,2.7678251784,0.8540634236
C,0,3.0814904073,2.3322788668,1.232169261
C,0,2.1836178712,3.2221850454,0.6208263623
N,0,2.853999796,4.1856847218,-0.1089668641
C,0,4.1143365604,3.8783115538,0.0563621332
N,0,2.7331920216,1.3127237196,2.0448834875
C,0,1.4102134652,1.2176501094,2.1817061936
N,0,0.4447607096,1.9633907102,1.6384367933
C,0,0.8022626519,2.9971642671,0.8343061113
N,0,-0.1819898898,3.7415657964,0.2926746172
O,0,-8.0662454466,1.1036129072,3.1278158951
P,0,-6.8814849079,0.6884440445,2.1627186469
O,0,-7.4653405641,0.3825817042,0.7919186925
O,0,-6.0437748485,-0.4612185476,2.7841289699
O,0,-5.9570797849,2.0234385919,2.0565404533
C,0,-4.5261763453,2.1111870166,2.163518174
C,0,-3.7880274688,1.0661902762,1.3182296531
O,0,-2.6731225813,1.6676983171,0.6264364657
C,0,-3.1885445774,-0.1429809948,2.082057248
O,0,-3.8594435276,-1.3535071464,1.7123688597
C,0,-1.7327619603,-0.2090542757,1.5924987309
O,0,-1.3343439633,-1.5542337475,1.4089690009
C,0,-1.7879970364,0.6168669156,0.295230448
O,0,-2.3363703861,-0.2305619728,-0.674899324
P,0,-2.075596858,-0.0994387403,-2.3014659604
O,0,-2.7534920758,1.1014126612,-2.8728653317
O,0,-0.5976452827,-0.341624107,-2.5968434484
O,0,-2.925534097,-1.4516415599,-2.6968970536
P,0,-2.2761296307,-2.9584862707,-2.5992841877
O,0,-1.8613562887,-3.190630231,-1.1322750753
O,0,-1.1320690516,-3.0803208759,-3.5733293991
O,0,-3.5295350877,-3.8738330371,-2.960474078
Mg,0,0.5500105362,-1.9082989677,-3.1559438116
H,0,-5.4319244143,5.8720989037,-2.0995775759
H,0,-6.2218443189,5.2983715276,-0.620646525
H,0,-4.560249139,3.811556915,-2.4456109441
H,0,-7.4557000776,1.7997756796,-0.4066617822
H,0,-7.6315694922,3.4795265038,-0.659433776
H,0,-4.4747647641,1.4849699553,-2.2836290162
H,0,-5.8385206889,0.6074838438,-1.6511495659
H,0,4.5960113773,3.9487356215,-2.9546434337
H,0,3.9974204442,5.3177896295,-3.9069696009
H,0,1.8696535046,4.7137152952,-3.3816090228
H,0,0.4358031243,1.5441120577,-2.8981570405
H,0,0.1882496581,3.2964832103,-2.8496284181
H,0,3.9137231012,1.7796079791,-3.3892598943

H,0,2.6206109377,0.6965836228,-3.1456383079
H,0,6.8627939265,-1.3003726801,7.6790357891
H,0,8.2422313057,-0.2553729899,7.2316833693
H,0,2.4491913391,-0.0573657466,5.5070023071
H,0,1.6164415689,-1.3414897654,4.5765763829
H,0,3.6938666742,-1.833637122,3.4370825525
H,0,4.5338668387,-0.7084629937,4.4440624401
H,0,3.3943266488,-0.1712632587,3.2835766395
H,0,-1.7558905282,7.2297300124,-2.0744560073
H,0,-2.2316157404,6.5756050352,-3.6459612181
H,0,-8.1246566201,1.4474423428,6.2254856432
H,0,-6.86980754,-0.6935355469,-0.2430400631
H,0,8.9424345064,3.5274620682,1.6847241513
H,0,7.9230388272,2.8024331817,2.5591032021
H,0,-6.0515503186,-5.4922452789,1.5402631787
H,0,-6.1395298361,-4.078953305,2.2264962201
H,0,8.3303791203,-2.8338578269,2.8734427878
H,0,8.3305195222,-1.3823726577,3.4104140532
H,0,-5.8946858945,-0.8225851527,4.6120623253
H,0,-6.7716180548,-1.8368833604,5.3416566674
H,0,-6.7283980334,-2.0252431814,2.9519942484
H,0,-8.0184540975,-2.8444787036,2.6826244018
H,0,-2.8599571476,2.9622063005,-3.4433165675
H,0,-2.3103450006,4.2686876005,-2.8198374967
H,0,4.121866338,-2.5747703652,-5.68342255
H,0,3.6881272903,-3.4302422485,-4.5186221471
H,0,6.4220932333,-2.0422856307,-5.3786635862
H,0,5.3951932423,-1.9098521615,-4.2272926351
H,0,4.6477371127,-2.8938794457,2.0187884473
H,0,3.2452522209,-3.6147778827,1.9894443201
H,0,0.3723314735,-4.874897727,1.5321258012
H,0,-0.2710296005,-6.2034241365,1.0828289218
H,0,-3.5311823054,-4.7809736372,1.9387804815
H,0,-1.8880366817,-4.8468071109,1.7197218588
H,0,6.134505727,-1.6901102234,-1.1597457203
H,0,6.3671618647,-0.2810008265,-2.2202350267
H,0,7.3526457476,0.000130303,0.0414542214
H,0,4.4656632505,-0.2509358575,0.9781754025
H,0,6.853113836,-1.4924315167,1.9928962368
H,0,5.1097009871,1.2153346482,2.8537451656
H,0,7.2216183104,0.5667924087,3.341600915
H,0,6.3775297628,2.9786030466,1.1425231253
H,0,4.9502135424,4.4222026428,-0.364001218
H,0,1.0648672641,0.4039459365,2.8169092241
H,0,-0.041051236,4.3027618809,-0.5492567
H,0,-4.2733321686,3.1070488638,1.7925521878
H,0,-4.2386762669,2.0524949788,3.2190107418
H,0,-4.4838186387,0.6873008635,0.5624924556
H,0,-3.2528971974,-0.0280923503,3.1671621268
H,0,-4.8012588502,-1.2050741257,2.0087369883
H,0,-1.0802184792,0.3147130118,2.2886109634
H,0,-0.3685092969,-1.560717581,1.0642128624
H,0,-0.8413471224,1.0421010626,-0.0203912815
H,0,-7.072163369,5.2106165818,-2.1910654732
H,0,4.2705540418,3.7541655048,-4.7010957385
H,0,8.209613962,-1.9269235281,6.6815630052
H,0,2.8936799874,-1.7599203947,5.7526288002
Mg,0,-2.8349384747,-2.6506623147,0.506072891
O,0,-4.6831017771,-3.1764832997,-0.4388181413
H,0,-5.1269321101,-3.789473452,0.207414137
H,0,-5.3269150455,-2.435981259,-0.6329003176
H,0,-1.1282570899,3.4178088012,0.4557949894
H,0,-4.1304730546,-3.8715768738,-2.1768904158
O,0,1.0624888235,-2.3289919199,-5.0545166764
H,0,0.4362837473,-2.9210538199,-5.4989720975
H,0,2.0082399852,-2.633316326,-5.2909542393
H,0,-0.124573806,-3.4515274151,-1.230922372
H,0,-7.145993498,-1.4782036755,-1.5903531652
H,0,-6.9810569822,0.4620018795,5.7951420347
H,0,-7.7935870998,1.2928724835,4.0837161254

H,0,-0.9616687006,7.8331811846,-3.5581400043

pocketrafcutcut17.log

fixed bonds at

C-N = 2.65

C-O = 1.70

B3LYP/6-31G* Lanl2DZ Mg

Zero-point correction= 1.306527 (Hartree/Particle)

Thermal correction to Energy=1.418292

Thermal correction to Enthalpy=1.419236

Thermal correction to Gibbs Free Energy= 1.152773

Sum of electronic and zero-point Energies= -6563.141265

Sum of electronic and thermal Energies= -6563.029500

Sum of electronic and thermal Enthalpies=-6563.028556

Sum of electronic and thermal Free Energies= -6563.295019

	E (Thermal)	CV	S
	KCal/Mol	Cal/Mol-Kelvin	Cal/Mol-Kelvin
Total	889.992	407.893	560.820

C,0,-6.0534120239,4.3388881671,-1.4237117835

N,0,-5.2651018425,3.4460750444,-2.267387414

C,0,-5.6100189184,2.2104479585,-2.6127000589

N,0,-6.654587393,1.5880657084,-2.0304986226

N,0,-4.9527263742,1.5995360687,-3.6325167849

C,0,3.056080565,3.0695001063,-4.9204207208

N,0,1.8050328777,2.5924279322,-4.3592329119

C,0,1.6139740455,1.3852937801,-3.8463462141

N,0,0.3714487258,1.0132459512,-3.4898050434

N,0,2.6272920074,0.5025405859,-3.7155688463

C,0,8.420420419,0.7476702584,6.0938427344

C,0,7.583464168,0.8016335018,4.817166829

O,0,8.2256393803,0.6834101898,3.7227305279

O,0,6.344128513,0.9794139025,4.9315814214

C,0,3.2388301307,0.3903622094,4.8354506604

N,0,4.1621104147,0.1258018302,3.7053223564

C,0,-1.2365375193,6.3515654785,-4.1788404966

C,0,-0.1586691154,5.2805885635,-4.3415462882

O,0,0.7838147073,5.4442580162,-5.116584616

O,0,-0.3192104574,4.2075228365,-3.6044838928

O,0,-9.733370943,1.9928908353,3.0792943959

O,0,-6.7210865836,-1.3594109708,0.7537397582

O,0,8.5707614972,3.8364672504,0.2348052159

O,0,-5.1740601583,-3.5822300745,3.5252959278

O,0,8.8055460128,-1.4353484652,2.1768116833

O,0,-8.2237247636,0.6574701315,4.8676807307

O,0,-6.6112176951,-1.3457952961,3.5074626726

O,0,-2.6483982345,3.1105204249,-3.117971978

O,0,2.9086191749,-4.3134508623,-4.6778919341

O,0,1.2850350522,-5.0197950505,-2.6389916447

O,0,4.3824840006,-2.5458987554,3.105936698

O,0,-0.1841899363,-4.4924302884,3.3692000624

O,0,-2.4779780161,-3.1586383273,3.2040789491

O,0,2.085010092,-2.061300738,-2.3961660718

P,0,3.4099424632,-2.5119898562,-1.7796821893

O,0,4.1449701766,-3.6529378645,-2.4311713761

O,0,3.1337170254,-2.9107797106,-0.2026509129

P,0,1.782000727,-2.8381847365,0.7063343456

O,0,1.3071180418,-1.4125504883,0.9048381967

O,0,0.7442043829,-3.6198342634,-0.3285360718

O,0,2.0136548455,-3.6937979078,1.9299309477

O,0,4.3134549558,-1.1830418003,-1.6831740873

C,0,5.7553313619,-1.2839743041,-1.6286468659
C,0,6.3161210422,-0.1723424349,-0.7719410402
C,0,5.773690308,-0.1046378062,0.6606324155
O,0,6.2004461081,-1.1363825033,1.5126960258
C,0,6.1656765724,1.3438526107,1.0429887837
O,0,7.5475678445,1.4466204241,1.3127624018
C,0,5.8954638766,2.0842332221,-0.2812526992
O,0,5.989586961,1.1091789045,-1.3304364503
N,0,4.5891077491,2.7469798049,-0.3723653778
C,0,3.3649271021,2.4569680704,0.2019452576
C,0,2.4249738046,3.1975320032,-0.5284791111
N,0,3.0383456101,3.9410059296,-1.5183966942
C,0,4.3061940536,3.6443565498,-1.3906711898
N,0,3.080000498,1.6772181626,1.265766392
C,0,1.7733735028,1.6415755454,1.5180441442
N,0,0.7599258758,2.2411814366,0.8789135189
C,0,1.0616796591,3.0528216296,-0.171164902
N,0,0.0569927898,3.6680581292,-0.8201972061
O,0,-7.5543663047,3.2073380037,2.2038004213
P,0,-6.4532982081,2.0846043724,1.9659876043
O,0,-6.8194301933,1.2147214751,0.7472017653
O,0,-6.0572930337,1.3142037834,3.2191318091
O,0,-5.2014738956,3.055449299,1.5182717663
C,0,-3.915596834,2.8103709174,2.0763518733
C,0,-3.3081003948,1.497100744,1.5645718607
O,0,-2.2843934597,1.7654233381,0.551361042
C,0,-2.6185789354,0.5911730591,2.6049525793
O,0,-3.3665269033,-0.6345210219,2.7135637005
C,0,-1.2196024743,0.3056570926,2.0054612963
O,0,-0.8765716719,-1.050502132,2.1704184723
C,0,-1.4073867151,0.7459845559,0.5590372887
O,0,-2.2237785355,-0.6165305888,-0.046814852
P,0,-2.1179680207,-0.8785620136,-1.6658447061
O,0,-2.7337931624,0.2480118297,-2.4323871663
O,0,-0.7095207205,-1.3431569699,-2.0290700906
O,0,-3.0964010769,-2.213131736,-1.6969094692
P,0,-2.4577396428,-3.6762743568,-1.2879744063
O,0,-1.8616999051,-3.5135722493,0.1343377121
O,0,-1.4717977548,-4.131086124,-2.3288810586
O,0,-3.77244076,-4.5772044364,-1.2174282618
Mg,0,0.3459649932,-3.0983404747,-2.4381713608
H,0,-5.8778945153,5.3663478441,-1.7531436965
H,0,-5.784776257,4.2427930965,-0.3683007072
H,0,-4.2994125272,3.6936608854,-2.5251524621
H,0,-6.8994008241,0.6902648631,-2.42595013
H,0,-6.7954384228,1.6725450203,-1.0100792432
H,0,-4.1447159463,2.1350597445,-3.9614247769
H,0,-4.665895471,0.6435988068,-3.4337617273
H,0,3.8323966328,3.1894025361,-4.15502571
H,0,2.838288573,4.047937303,-5.350785768
H,0,1.046224466,3.2867969311,-4.2024393631
H,0,0.176238771,0.1269534723,-3.0279190202
H,0,-0.4114739717,1.5954361147,-3.7508948485
H,0,3.5527458548,0.8729122139,-3.5429927286
H,0,2.4315357259,-0.3861939622,-3.2503690075
H,0,7.7877653718,0.7734499862,6.9835266371
H,0,9.1096342721,1.5996418689,6.1115925368
H,0,3.162658236,1.4670484159,4.997627249
H,0,2.2538376151,-0.0304629098,4.6203123917
H,0,4.2002966053,-0.9072273328,3.48406235
H,0,5.136489882,0.454469047,3.9970920349
H,0,3.8770606776,0.6323462378,2.8485875195
H,0,-1.264881813,6.6986949734,-3.1391584094
H,0,-2.2241424142,5.9330221917,-4.4077294325
H,0,-10.0354079776,1.3482892622,2.4218148741
H,0,-6.7106738001,-0.3353346344,0.7396396951
H,0,9.2562521667,3.4876142876,-0.3548036226
H,0,8.3344552276,3.0600649052,0.7866323858
H,0,-5.7626339744,-4.2869133619,3.8365640779
H,0,-5.6642259696,-2.7160575056,3.6861145906

H,0,8.7436271593,-2.2275716534,2.7330237806

H,0,8.8055666106,-0.6835410931,2.8216631084

H,0,-7.4228091593,1.1394008169,4.5654148424

H,0,-8.016788263,-0.2485586703,4.5678304913

H,0,-6.1832080033,-0.4480094399,3.4711871449

H,0,-6.8922852649,-1.4582811337,2.5695634289

H,0,-2.4332454843,2.2754932833,-2.6604280546

H,0,-1.7836072126,3.5938253471,-3.3124805865

H,0,3.4582188769,-4.7828052924,-5.3228078769

H,0,3.519227078,-3.9845125015,-3.9519932746

H,0,1.9578864075,-5.0540909989,-3.3583041857

H,0,1.7416478466,-5.2624915002,-1.8177159617

H,0,5.0153791888,-2.3714094434,2.3782038583

H,0,3.6212741269,-3.0308084781,2.7199301574

H,0,0.6334254021,-4.1074783576,2.9547807872

H,0,-0.223543459,-5.3903001216,3.0067360568

H,0,-3.267861911,-3.6299592316,3.5385891614

H,0,-1.6354694453,-3.6899196911,3.3537723362

H,0,6.0610236843,-2.2436465239,-1.2025154074

H,0,6.1377384019,-1.2183143348,-2.6522899802

H,0,7.4091252793,-0.2987545264,-0.7379589056

H,0,4.6832908027,-0.1730529795,0.6135840271

H,0,7.1891805621,-1.14679671,1.6437005146

H,0,5.5735842806,1.751306185,1.8668179381

H,0,7.7157695339,1.1925076744,2.2733227983

H,0,6.6499507893,2.8592844445,-0.4421844898

H,0,5.1067253942,4.0476669361,-1.9978667

H,0,1.4911612923,1.0122547648,2.3586361703

H,0,0.1709574651,4.0528223399,-1.7647960651

H,0,-3.2810263175,3.6478683152,1.774751689

H,0,-3.9870143005,2.789952955,3.1675497743

H,0,-4.0874428497,0.9129913878,1.0714837511

H,0,-2.5639120812,1.0541311255,3.5921385027

H,0,-3.0858249493,-1.0977464516,3.5269864973

H,0,-0.48702332,0.9718123055,2.4581493607

H,0,0.0368494851,-1.2127958223,1.7176965893

H,0,-0.5721178179,0.854834924,-0.1114178069

H,0,-7.1148015533,4.1082581321,-1.5441073258

H,0,3.4168892792,2.3889679683,-5.7000238161

H,0,9.035592414,-0.1589457246,6.1013608698

H,0,3.6513412314,-0.075633913,5.7310923155

Mg,0,-2.5579863807,-2.1457537383,1.4063370025

O,0,-4.5279105805,-2.8977282839,0.9890955206

H,0,-4.8482929184,-3.3154264151,1.8329565572

H,0,-5.2579888856,-2.2618886114,0.7466095102

H,0,-0.8870982365,3.448992613,-0.5298483005

H,0,-4.3023194824,-4.2375103844,-0.4583741359

O,0,0.3984570706,-3.1187010531,-4.5361024287

H,0,-0.2261543217,-3.7694741408,-4.8950362996

H,0,1.2999229896,-3.4121831824,-4.8137866145

H,0,-0.1818369604,-3.6890276992,0.0398155421

H,0,-7.444665771,-1.6311562642,0.1688896818

H,0,-9.3172793985,1.452526814,3.8095628536

H,0,-8.4394096409,2.815104294,2.4922802448

H,0,-1.0393873758,7.1986481165,-4.8387041889

twofixCO19.log

fixed bonds at

C-N = 2.48

C-O = 1.90

B3LYP/6-31G* Lanl2DZ Mg

Free Energy = -6563.284078

Zero-point Energy = -6563.127692

Potential Energy = -6564.43315859

Nimag = 1 (-314.5498 cm-1)

Charge = 0 Multiplicity = 1

C 6.16481 2.89172 -3.22129
N 5.49938 2.77765 -1.92809
C 6.10020 2.32089 -0.84159
N 7.39449 1.87714 -0.92324
N 5.50542 2.35943 0.36296
C -3.44630 5.91450 -1.08506
N -2.08166 5.49236 -0.84456
C -1.74582 4.54431 0.03042
N -0.45556 4.21739 0.18597
N -2.68745 3.95771 0.80027
C -7.74214 -5.99506 -3.19131
C -6.97425 -4.73641 -2.79356
O -7.67965 -3.75059 -2.40155
O -5.72079 -4.75290 -2.89524
C -2.69427 -4.57796 -1.97844
N -3.76019 -3.65636 -1.51643
C 1.81290 6.69264 -3.57601
C 0.72830 6.13265 -2.65981
O -0.27512 6.83152 -2.40980
O 0.92244 4.94850 -2.19174
O 9.46596 -2.77915 -2.78724
O 6.77718 -0.78170 1.05183
O -8.18316 0.49438 -4.40955
O 5.16861 -4.13024 2.71799
O -8.56064 -2.94853 0.00494
O 7.81168 -4.74380 -1.82742
O 6.35911 -3.57819 0.40417
O 2.78351 3.12024 -1.90313
O -3.39168 3.10907 5.28560
O -1.69958 1.00173 5.39239
O -4.20294 -3.91341 1.17455
O 0.23142 -4.38829 3.26959
O 2.54652 -3.70245 2.13557
O -2.29272 1.65813 2.46335
P -3.60337 0.89183 2.62805
O -4.44243 1.14969 3.85100
O -3.25671 -0.72148 2.57882
P -1.85723 -1.50768 2.29870
O -1.36022 -1.27115 0.88290
O -0.88921 -0.70392 3.37285
O -2.03977 -2.93681 2.75516
O -4.44285 1.14128 1.27163
C -5.87459 0.92480 1.28175
C -6.33578 0.38072 -0.05243
C -5.62038 -0.89011 -0.53046
O -6.00637 -2.06741 0.13063
C -5.88781 -0.82254 -2.05521
O -7.22000 -1.17485 -2.35780
C -5.74749 0.68710 -2.30813
O -6.11509 1.34368 -1.09680
N -4.38829 1.13185 -2.68257
C -3.14533 0.54527 -2.57421
C -2.22676 1.57621 -2.80580
N -2.86759 2.77014 -3.05996
C -4.13759 2.46042 -2.97648
N -2.81606 -0.74426 -2.32651
C -1.50743 -0.92156 -2.26385
N -0.51823 -0.01908 -2.40955
C -0.84548 1.28188 -2.68188
N 0.10142 2.21738 -2.79438
O 7.27291 -1.80509 -3.89576
P 6.44944 -1.58544 -2.54728
O 7.36224 -0.94867 -1.48448
O 5.66075 -2.81780 -2.11676
O 5.40239 -0.40953 -3.01629
C 4.00706 -0.65330 -3.15740
C 3.31452 -0.66582 -1.78760
O 2.15791 0.24418 -1.81748
C 2.77049 -1.99770 -1.23840
O 3.49389 -2.35703 -0.05785

C 1.27966 -1.71051 -0.89132
O 0.94724 -2.19869 0.37823
C 1.18864 -0.20135 -1.06576
O 2.29214 0.10460 0.80065
P 2.07518 1.48965 1.51843
O 2.76375 2.64002 0.81408
O 0.60907 1.71767 1.91831
O 2.91684 1.22251 2.94915
P 2.20029 0.32621 4.10416
O 1.74716 -1.01147 3.45322
O 1.08376 1.09380 4.76154
O 3.42471 0.04055 5.09913
Mg -0.60094 1.48014 3.58624
H 5.58671 3.58535 -3.83513
H 6.21390 1.92252 -3.72975
H 4.47562 2.98514 -1.90087
H 7.77027 1.58631 -0.02915
H 7.54801 1.13760 -1.61283
H 4.51149 2.62468 0.48023
H 5.83329 1.68639 1.04469
H -4.06251 5.10147 -1.49167
H -3.41495 6.71488 -1.82642
H -1.33463 5.95939 -1.41076
H -0.18186 3.45348 0.79949
H 0.19691 4.53093 -0.54636
H -3.65131 4.02225 0.50991
H -2.45353 3.11862 1.33662
H -7.06208 -6.80484 -3.46345
H -8.39967 -5.76785 -4.03790
H -2.52617 -4.43579 -3.04769
H -1.77361 -4.39463 -1.41892
H -3.89967 -3.74900 -0.47087
H -4.66992 -3.92597 -2.01897
H -3.53724 -2.67279 -1.73256
H 1.98402 6.00767 -4.41430
H 2.75721 6.77321 -3.02447
H 9.33582 -2.12736 -2.07583
H 6.94913 -0.80635 0.04440
H -8.94624 0.90302 -3.97365
H -7.95221 -0.24595 -3.80839
H 5.74268 -4.66908 3.28285
H 5.58386 -4.11315 1.80584
H -8.51477 -3.70945 0.60477
H -8.45474 -3.34114 -0.89799
H 7.01632 -4.35176 -2.24246
H 7.64734 -4.55295 -0.88440
H 5.92076 -3.35471 -0.46519
H 6.65067 -2.69274 0.70789
H 2.62730 2.96694 -0.94149
H 2.26433 3.95045 -2.10559
H -4.00400 3.53285 5.90475
H -3.93438 2.50317 4.69841
H -2.41406 1.64135 5.61391
H -2.11341 0.12608 5.34014
H -4.87063 -3.19657 1.17605
H -3.49250 -3.64223 1.79738
H -0.60761 -3.94982 2.96931
H 0.25051 -4.21373 4.22297
H 3.31061 -4.12099 2.58362
H 1.68548 -4.03231 2.53782
H -6.15336 0.21307 2.06383
H -6.36045 1.88199 1.49596
H -7.41360 0.17574 0.02755
H -4.54735 -0.77293 -0.35116
H -6.97884 -2.26360 0.02485
H -5.17942 -1.40875 -2.64602
H -7.29129 -2.17759 -2.41738
H -6.41903 1.01183 -3.10737
H -4.95904 3.15014 -3.11847
H -1.18401 -1.93612 -2.05303

H -0.14556 3.20558 -2.81765
H 3.61156 0.18653 -3.73358
H 3.82612 -1.58025 -3.71019
H 3.98273 -0.22772 -1.04615
H 2.87721 -2.80071 -1.96839
H 3.37356 -3.31239 0.09711
H 0.65551 -2.17394 -1.65926
H -0.01259 -1.88360 0.59983
H 0.53107 0.47334 -0.54938
H 7.17698 3.28503 -3.09219
H -3.92145 6.30481 -0.17512
H -8.38671 -6.31517 -2.36500
H -3.02944 -5.60130 -1.80539
Mg 2.55877 -1.66385 1.74486
O 4.52552 -1.48208 2.64596
H 4.85387 -2.39274 2.85639
H 5.22974 -1.08945 2.07902
H 1.08955 2.04419 -2.61608
H 4.09039 -0.47552 4.59950
O -0.81549 3.44693 4.27630
H -0.22553 3.60397 5.03125
H -1.73720 3.57762 4.60391
H 0.05128 -1.04404 3.42444
H 7.65401 -0.74396 1.46596
H 9.03147 -3.59943 -2.43362
H 8.18054 -2.18757 -3.67491
H 1.53127 7.67612 -3.95689

218COCNfixed.log

Fixed bonds at
C-N = 2.18
C-O = 2.18

B3LYP/6-31G* Lanl2DZ Mg

Free Energy = -6563.284078
Zero-point Energy = -6563.127692
Potential Energy = -6564.43315859
Nimag = 1 (-314.5498 cm-1)

Charge = 0 Multiplicity = 1
C 6.16481 2.89172 -3.22129
N 5.49938 2.77765 -1.92809
C 6.10020 2.32089 -0.84159
N 7.39449 1.87714 -0.92324
N 5.50542 2.35943 0.36296
C -3.44630 5.91450 -1.08506
N -2.08166 5.49236 -0.84456
C -1.74582 4.54431 0.03042
N -0.45556 4.21739 0.18597
N -2.68745 3.95771 0.80027
C -7.74214 -5.99506 -3.19131
C -6.97425 -4.73641 -2.79356
O -7.67965 -3.75059 -2.40155
O -5.72079 -4.75290 -2.89524
C -2.69427 -4.57796 -1.97844
N -3.76019 -3.65636 -1.51643
C 1.81290 6.69264 -3.57601
C 0.72830 6.13265 -2.65981
O -0.27512 6.83152 -2.40980
O 0.92244 4.94850 -2.19174
O 9.46596 -2.77915 -2.78724
O 6.77718 -0.78170 1.05183
O -8.18316 0.49438 -4.40955
O 5.16861 -4.13024 2.71799
O -8.56064 -2.94853 0.00494
O 7.81168 -4.74380 -1.82742
O 6.35911 -3.57819 0.40417
O 2.78351 3.12024 -1.90313

O -3.39168 3.10907 5.28560
O -1.69958 1.00173 5.39239
O -4.20294 -3.91341 1.17455
O 0.23142 -4.38829 3.26959
O 2.54652 -3.70245 2.13557
O -2.29272 1.65813 2.46335
P -3.60337 0.89183 2.62805
O -4.44243 1.14969 3.85100
O -3.25671 -0.72148 2.57882
P -1.85723 -1.50768 2.29870
O -1.36022 -1.27115 0.88290
O -0.88921 -0.70392 3.37285
O -2.03977 -2.93681 2.75516
O -4.44285 1.14128 1.27163
C -5.87459 0.92480 1.28175
C -6.33578 0.38072 -0.05243
C -5.62038 -0.89011 -0.53046
O -6.00637 -2.06741 0.13063
C -5.88781 -0.82254 -2.05521
O -7.22000 -1.17485 -2.35780
C -5.74749 0.68710 -2.30813
O -6.11509 1.34368 -1.09680
N -4.38829 1.13185 -2.68257
C -3.14533 0.54527 -2.57421
C -2.22676 1.57621 -2.80580
N -2.86759 2.77014 -3.05996
C -4.13759 2.46042 -2.97648
N -2.81606 -0.74426 -2.32651
C -1.50743 -0.92156 -2.26385
N -0.51823 -0.01908 -2.40955
C -0.84548 1.28188 -2.68188
N 0.10142 2.21738 -2.79438
O 7.27291 -1.80509 -3.89576
P 6.44944 -1.58544 -2.54728
O 7.36224 -0.94867 -1.48448
O 5.66075 -2.81780 -2.11676
O 5.40239 -0.40953 -3.01629
C 4.00706 -0.65330 -3.15740
C 3.31452 -0.66582 -1.78760
O 2.15791 0.24418 -1.81748
C 2.77049 -1.99770 -1.23840
O 3.49389 -2.35703 -0.05785
C 1.27966 -1.71051 -0.89132
O 0.94724 -2.19869 0.37823
C 1.18864 -0.20135 -1.06576
O 2.29214 0.10460 0.80065
P 2.07518 1.48965 1.51843
O 2.76375 2.64002 0.81408
O 0.60907 1.71767 1.91831
O 2.91684 1.22251 2.94915
P 2.20029 0.32621 4.10416
O 1.74716 -1.01147 3.45322
O 1.08376 1.09380 4.76154
O 3.42471 0.04055 5.09913
Mg -0.60094 1.48014 3.58624
H 5.58671 3.58535 -3.83513
H 6.21390 1.92252 -3.72975
H 4.47562 2.98514 -1.90087
H 7.77027 1.58631 -0.02915
H 7.54801 1.13760 -1.61283
H 4.51149 2.62468 0.48023
H 5.83329 1.68639 1.04469
H -4.06251 5.10147 -1.49167
H -3.41495 6.71488 -1.82642
H -1.33463 5.95939 -1.41076
H -0.18186 3.45348 0.79949
H 0.19691 4.53093 -0.54636
H -3.65131 4.02225 0.50991
H -2.45353 3.11862 1.33662
H -7.06208 -6.80484 -3.46345

H -8.39967 -5.76785 -4.03790
H -2.52617 -4.43579 -3.04769
H -1.77361 -4.39463 -1.41892
H -3.89967 -3.74900 -0.47087
H -4.66992 -3.92597 -2.01897
H -3.53724 -2.67279 -1.73256
H 1.98402 6.00767 -4.41430
H 2.75721 6.77321 -3.02447
H 9.33582 -2.12736 -2.07583
H 6.94913 -0.80635 0.04440
H -8.94624 0.90302 -3.97365
H -7.95221 -0.24595 -3.80839
H 5.74268 -4.66908 3.28285
H 5.58386 -4.11315 1.80584
H -8.51477 -3.70945 0.60477
H -8.45474 -3.34114 -0.89799
H 7.01632 -4.35176 -2.24246
H 7.64734 -4.55295 -0.88440
H 5.92076 -3.35471 -0.46519
H 6.65067 -2.69274 0.70789
H 2.62730 2.96694 -0.94149
H 2.26433 3.95045 -2.10559
H -4.00400 3.53285 5.90475
H -3.93438 2.50317 4.69841
H -2.41406 1.64135 5.61391
H -2.11341 0.12608 5.34014
H -4.87063 -3.19657 1.17605
H -3.49250 -3.64223 1.79738
H -0.60761 -3.94982 2.96931
H 0.25051 -4.21373 4.22297
H 3.31061 -4.12099 2.58362
H 1.68548 -4.03231 2.53782
H -6.15336 0.21307 2.06383
H -6.36045 1.88199 1.49596
H -7.41360 0.17574 0.02755
H -4.54735 -0.77293 -0.35116
H -6.97884 -2.26360 0.02485
H -5.17942 -1.40875 -2.64602
H -7.29129 -2.17759 -2.41738
H -6.41903 1.01183 -3.10737
H -4.95904 3.15014 -3.11847
H -1.18401 -1.93612 -2.05303
H -0.14556 3.20558 -2.81765
H 3.61156 0.18653 -3.73358
H 3.82612 -1.58025 -3.71019
H 3.98273 -0.22772 -1.04615
H 2.87721 -2.80071 -1.96839
H 3.37356 -3.31239 0.09711
H 0.65551 -2.17394 -1.65926
H -0.01259 -1.88360 0.59983
H 0.53107 0.47334 -0.54938
H 7.17698 3.28503 -3.09219
H -3.92145 6.30481 -0.17512
H -8.38671 -6.31517 -2.36500
H -3.02944 -5.60130 -1.80539
Mg 2.55877 -1.66385 1.74486
O 4.52552 -1.48208 2.64596
H 4.85387 -2.39274 2.85639
H 5.22974 -1.08945 2.07902
H 1.08955 2.04419 -2.61608
H 4.09039 -0.47552 4.59950
O -0.81549 3.44693 4.27630
H -0.22553 3.60397 5.03125
H -1.73720 3.57762 4.60391
H 0.05128 -1.04404 3.42444
H 7.65401 -0.74396 1.46596
H 9.03147 -3.59943 -2.43362
H 8.18054 -2.18757 -3.67491
H 1.53127 7.67612 -3.95689

twofixCO24.log

fixed bonds at

C-N = 2.00

C-O = 2.40

B3LYP/6-31G* Lanl2DZ Mg

Zero-point correction= 1.305798 (Hartree/Particle)

Thermal correction to Energy= 1.418694

Thermal correction to Enthalpy= 1.419638

Thermal correction to Gibbs Free Energy=1.150443

Sum of electronic and zero-point Energies=-6563.133223

Sum of electronic and thermal Energies= -6563.020328

Sum of electronic and thermal Enthalpies= -6563.019383

Sum of electronic and thermal Free Energies= -6563.288578

	E (Thermal)	CV	S
	KCal/Mol	Cal/Mol-Kelvin	Cal/Mol-Kelvin
Total	890.244	410.368	566.569

C,0,6.1442185595,2.9043828187,-3.1743615118

N,0,5.4954688199,2.7886345749,-1.8729297386

C,0,6.1113921351,2.3344467173,-0.7925908652

N,0,7.4036361167,1.8887395254,-0.8934973178

N,0,5.5344414251,2.3802895754,0.419283942

C,0,-3.4683565739,5.8480008608,-1.0477911975

N,0,-2.0979554097,5.429580428,-0.8342057808

C,0,-1.7396129897,4.5062491298,0.0591880495

N,0,-0.4466871358,4.1835627235,0.1944918962

N,0,-2.6640539611,3.9380925468,0.8623537807

C,0,-7.8580367574,-5.9386967007,-3.0973283452

C,0,-7.0688743041,-4.6883848509,-2.7159380688

O,0,-7.758178602,-3.6820934859,-2.3474312781

O,0,-5.8151380182,-4.7307642433,-2.8074055707

C,0,-2.7834573325,-4.6260874354,-1.9179023552

N,0,-3.8235825471,-3.6812983372,-1.4436449267

C,0,1.7667698589,6.6580986692,-3.5936986983

C,0,0.6804933255,6.0857289798,-2.6873428441

O,0,-0.3344805402,6.7699783805,-2.4476216773

O,0,0.8878275907,4.9048475189,-2.213736835

O,0,9.4842225935,-2.7145327589,-2.8263760752

O,0,6.8350157289,-0.7877841045,1.0453372581

O,0,-8.1113008343,0.5315870523,-4.4370903811

O,0,5.2225501368,-4.1298179192,2.6838279422

O,0,-8.5980511152,-2.8217485758,0.0553588379

O,0,7.8599988413,-4.7093565939,-1.8699323636

O,0,6.4003644558,-3.5725929162,0.3650268528

O,0,2.7701176711,3.1118970652,-1.8022251267

O,0,-3.354719044,3.074780717,5.3287595844

O,0,-1.6614035581,0.96494705,5.4119279251

O,0,-4.2353710468,-3.8868352187,1.2510084707

O,0,0.3006193954,-4.3543918217,3.2695522098

O,0,2.6071522794,-3.6710703705,2.1019509661

O,0,-2.2473218632,1.6412562112,2.5013479066

P,0,-3.5605200269,0.8774817493,2.6549969553

O,0,-4.4155507976,1.1394009944,3.8654901596

O,0,-3.2153405322,-0.735149284,2.6114133921

P,0,-1.8179598245,-1.5238560712,2.3181277934

O,0,-1.332720876,-1.2811894718,0.8987936666

O,0,-0.8392538315,-0.7311374769,3.3859115159

O,0,-2.0096987655,-2.9550948904,2.7646718898

O,0,-4.3857076098,1.1289129056,1.2875926631

C,0,-5.8223713919,0.9566282206,1.289532262

C,0,-6.2918537953,0.4247926525,-0.0466828379

C,0,-5.6088370979,-0.8646939626,-0.5199470347

O,0,-6.014213914,-2.0310748194,0.1482090178
C,0,-5.8793449107,-0.79850772,-2.0448009079
O,0,-7.2180891792,-1.1243506645,-2.345064911
C,0,-5.7106431252,0.7079089931,-2.3067994848
O,0,-6.0345799841,1.3790445865,-1.0921522818
N,0,-4.3494591641,1.1217364206,-2.7150266592
C,0,-3.1149331375,0.5345582764,-2.5555906043
C,0,-2.1837505329,1.5459098948,-2.8161102151
N,0,-2.8082805853,2.7292442101,-3.1407748557
C,0,-4.0827052827,2.4338980067,-3.0668465576
N,0,-2.8060309065,-0.7450514332,-2.2302411232
C,0,-1.5106319177,-0.9344453665,-2.1050896362
N,0,-0.5157182159,-0.036534644,-2.2865171655
C,0,-0.8069438277,1.2628713433,-2.6235370079
N,0,0.1444919328,2.1855967809,-2.7295077356
O,0,7.274349218,-1.7521138893,-3.9204335284
P,0,6.4606113648,-1.5572251162,-2.5605431672
O,0,7.3813222098,-0.9295697547,-1.4986300086
O,0,5.6874357512,-2.8037567838,-2.1453844415
O,0,5.4047080467,-0.378583333,-2.9976626586
C,0,4.0130426896,-0.6254354585,-3.1709962506
C,0,3.2879992525,-0.6400840142,-1.8180524356
O,0,2.099436964,0.2118529516,-1.9002716571
C,0,2.7868400377,-1.9877745488,-1.2672957065
O,0,3.5228282946,-2.3284172289,-0.0911801489
C,0,1.283497334,-1.7525059659,-0.9229936565
O,0,0.990325639,-2.1806850483,0.3798485126
C,0,1.1087674557,-0.2550466472,-1.1564261348
O,0,2.401444468,0.1625400962,0.822110562
P,0,2.1427093201,1.5104905651,1.5659349154
O,0,2.8116728553,2.7055588082,0.910791457
O,0,0.6643303818,1.7068993268,1.9558215096
O,0,2.9624371009,1.2455431306,3.0198759603
P,0,2.2416035872,0.3118175671,4.134107994
O,0,1.7954110747,-1.0100872878,3.4435039256
O,0,1.1134052175,1.0508571006,4.8068626146
O,0,3.4535936749,-0.0036159849,5.1374977848
Mg,0,-0.5475558134,1.4585477161,3.6148559983
H,0,5.5563641749,3.5962424062,-3.7811486163
H,0,6.1911962236,1.9353099082,-3.6833217527
H,0,4.47127136,2.9851756155,-1.8330628531
H,0,7.7923312476,1.597938572,-0.00495365
H,0,7.5461844315,1.1492370979,-1.5862566711
H,0,4.5407072834,2.6478517194,0.5508464271
H,0,5.8708311957,1.7096731132,1.0990335158
H,0,-4.0982580563,5.0254106956,-1.4132380909
H,0,-3.4565819627,6.6268992669,-1.8121785228
H,0,-1.3659838235,5.8926104843,-1.4224177776
H,0,-0.153802644,3.439485922,0.8243498551
H,0,0.1937304605,4.496315507,-0.5477232083
H,0,-3.6336279615,3.9964277052,0.5901743426
H,0,-2.419025675,3.1067242593,1.4066608967
H,0,-7.1918629531,-6.7652855332,-3.3525111669
H,0,-8.5074041895,-5.7132349975,-3.9506224141
H,0,-2.623887827,-4.4875953335,-2.9888978407
H,0,-1.8525495678,-4.4649937153,-1.3686090598
H,0,-3.9536324,-3.7656161398,-0.3949683893
H,0,-4.7453881678,-3.9293215445,-1.9362516635
H,0,-3.5824154265,-2.7041973927,-1.6621285541
H,0,1.9683074002,5.9660454065,-4.4191888336
H,0,2.6991954409,6.767773026,-3.0270057548
H,0,9.3364041616,-2.0669238701,-2.1143270566
H,0,6.9871704576,-0.7996812149,0.035296345
H,0,-8.894834079,0.9442376929,-4.04326167
H,0,-7.9118406804,-0.2060674146,-3.8213721789
H,0,5.7956710531,-4.6771697321,3.2412723841
H,0,5.6315764735,-4.1105838029,1.7689697852
H,0,-8.5852317226,-3.5748096792,0.6666309411
H,0,-8.5100599152,-3.2310115279,-0.8420210204
H,0,7.0627612776,-4.3320986252,-2.294313262

H,0,7.6835188788,-4.5131908436,-0.9298155951
H,0,5.9555934968,-3.3435780511,-0.5002339161
H,0,6.6928257163,-2.6892510386,0.6745479955
H,0,2.6415652975,2.998811733,-0.8286985554
H,0,2.2544368331,3.9341004503,-2.0346069843
H,0,-3.9619584434,3.4840062224,5.962517931
H,0,-3.9017037831,2.4822546231,4.7332543779
H,0,-2.3861551233,1.592632166,5.6325747915
H,0,-2.0562057072,0.0806200927,5.3619651036
H,0,-4.8843397194,-3.1538823961,1.2528674929
H,0,-3.5052566201,-3.6243996188,1.8557091442
H,0,-0.5528655219,-3.943389556,2.9726691775
H,0,0.3390847422,-4.1389847525,4.2140327088
H,0,3.3682774785,-4.0945760959,2.5504195079
H,0,1.7467838555,-3.9960093888,2.5064868411
H,0,-6.1277354973,0.2546031442,2.0704242406
H,0,-6.2821564159,1.9276769279,1.4996018776
H,0,-7.3757354908,0.2517456602,0.0260431539
H,0,-4.5333253937,-0.7673746736,-0.3450428669
H,0,-6.9938110091,-2.1991627687,0.0604265279
H,0,-5.1833007146,-1.4012999415,-2.6349467085
H,0,-7.3171093001,-2.1265861012,-2.3833779694
H,0,-6.3879887089,1.0421035535,-3.0974494256
H,0,-4.8950865148,3.1225600002,-3.2578467262
H,0,-1.1957023778,-1.9258824469,-1.805715524
H,0,-0.0983609301,3.1752782401,-2.7989455453
H,0,3.6289259364,0.2152726831,-3.7537155909
H,0,3.8470776032,-1.5507974419,-3.731367129
H,0,3.9227604961,-0.1699404838,-1.0663187429
H,0,2.9174626963,-2.7860328641,-1.9990409858
H,0,3.404318453,-3.2813510261,0.0807513469
H,0,0.679885953,-2.2989242022,-1.6546413669
H,0,0.0355814765,-1.8724299613,0.6128627424
H,0,0.6257396429,0.391168789,-0.4418428099
H,0,7.1564158951,3.3016587496,-3.0575784686
H,0,-3.9178274898,6.2647174352,-0.1365328251
H,0,-8.512318298,-6.2331997342,-2.2690738097
H,0,-3.1400823191,-5.6414926095,-1.7416008445
Mg,0,2.6237485971,-1.6178781067,1.7217401642
O,0,4.5842476926,-1.4761938353,2.6334263698
H,0,4.9093965146,-2.3892815459,2.8352611095
H,0,5.2913214062,-1.0794299532,2.0731821799
H,0,1.1263821099,2.0244088679,-2.4966252543
H,0,4.1297655441,-0.4968593993,4.6297340035
O,0,-0.7691197987,3.4185397843,4.3266083204
H,0,-0.175328972,3.5598277386,5.0818229296
H,0,-1.6888214284,3.5430829293,4.6610141283
H,0,0.1098090604,-1.0564660755,3.4163287267
H,0,7.7198200831,-0.7616164274,1.4429429787
H,0,9.0634165361,-3.5434555108,-2.4763494019
H,0,8.1852397719,-2.1318026877,-3.7104288428
H,0,1.4697357353,7.6301221504,-3.9918801095

Pocketrafcutcut2*6*.log

Fixed bonds at

C-N = 1.73

C-O = 2.60

B3LYP/6-31G* Lanl2DZ Mg

Zero-point correction=1.306299 (Hartree/Particle)

Thermal correction to Energy= 1.419023

Thermal correction to Enthalpy= 1.419968

Thermal correction to Gibbs Free Energy=1.150528

Sum of electronic and zero-point Energies=-6563.155811

Sum of electronic and thermal Energies= -6563.043087

Sum of electronic and thermal Enthalpies=-6563.042142

Sum of electronic and thermal Free Energies=-6563.311581

	E (Thermal)	CV	S
	KCal/Mol	Cal/Mol-Kelvin	Cal/Mol-Kelvin
Total	890.451	409.957	567.082

C	6.13	2.93358	-3.15529
N	5.48111	2.8025	-1.85538
C	6.09652	2.33429	-0.78075
N	7.38825	1.88838	-0.88717
N	5.51962	2.36581	0.43161
C	-3.4792	5.86172	-0.99237
N	-2.10928	5.43912	-0.78399
C	-1.75199	4.5044	0.09792
N	-0.45944	4.17859	0.2292
N	-2.67709	3.92743	0.89401
C	-7.88239	-5.89371	-3.18737
C	-7.0918	-4.64911	-2.79057
O	-7.77995	-3.64666	-2.40965
O	-5.83811	-4.69179	-2.88257
C	-2.80631	-4.6016	-1.99188
N	-3.84535	-3.66155	-1.50597
C	1.75686	6.69721	-3.52814
C	0.66993	6.11493	-2.62892
O	-0.34426	6.79733	-2.38074
O	0.8759	4.92805	-2.16994
O	9.46355	-2.69303	-2.87682
O	6.81655	-0.81125	1.01844
O	-8.12823	0.59293	-4.44706
O	5.20025	-4.17142	2.61553
O	-8.61884	-2.81511	0.00361
O	7.83704	-4.69766	-1.94509
O	6.37871	-3.58693	0.30377
O	2.75614	3.12799	-1.78065
O	-3.36875	3.00977	5.34941
O	-1.67785	0.89713	5.40648
O	-4.25738	-3.8999	1.18594
O	0.27807	-4.39757	3.19849
O	2.58538	-3.70252	2.0394
O	-2.26299	1.61003	2.50449
P	-3.57707	0.84592	2.6487
O	-4.4318	1.09384	3.86235
O	-3.23374	-0.76644	2.58518
P	-1.83726	-1.55307	2.28215
O	-1.35174	-1.29343	0.86592
O	-0.85765	-0.77473	3.35964
O	-2.03064	-2.98949	2.71098
O	-4.40196	1.11518	1.28452
C	-5.83882	0.94453	1.28435
C	-6.30891	0.42979	-0.05833
C	-5.62738	-0.85453	-0.54751
O	-6.03409	-2.02861	0.10619
C	-5.89781	-0.76919	-2.07142
O	-7.23692	-1.08976	-2.37567
C	-5.72738	0.74016	-2.31479
O	-6.05054	1.3966	-1.09193
N	-4.36572	1.15743	-2.71788
C	-3.13187	0.56691	-2.56573
C	-2.19952	1.58034	-2.81375
N	-2.8227	2.76831	-3.12375
C	-4.09746	2.47354	-3.05346
N	-2.82443	-0.71697	-2.25623
C	-1.52925	-0.90938	-2.13345
N	-0.53331	-0.01044	-2.30377
C	-0.82304	1.29336	-2.6247
N	0.12945	2.21624	-2.71928
O	7.09314	-1.76358	-4.20681
P	6.27963	-1.58458	-2.84461

O	7.20106	-0.97116	-1.77503	H	-7.21717	-6.71784	-3.45276
O	5.50502	-2.83526	-2.44488	H	-8.5315	-5.65697	-4.03781
O	5.22508	-0.39942	-3.26711	H	-2.64658	-4.45006	-3.06109
C	3.83313	-0.64251	-3.44347	H	-1.87522	-4.44837	-1.44065
C	3.10807	-0.67305	-2.0908	H	-3.9755	-3.75867	-0.45841
O	1.92048	0.1812	-2.16246	H	-4.76744	-3.90241	-2.00159
C	2.60536	-2.02687	-1.55673	H	-3.60307	-2.6821	-1.71236
O	3.34096	-2.38287	-0.38493	H	1.9576	6.01518	-4.36213
C	1.10229	-1.79415	-1.20953	H	2.68941	6.79881	-2.96015
O	0.80863	-2.23806	0.08793	H	9.31648	-2.05411	-2.15682
C	0.92928	-0.29372	-1.42443	H	6.9687	-0.81083	0.00833
O	2.38408	0.14685	0.80704	H	-8.91129	1.00158	-4.04815
P	2.12689	1.4858	1.56747	H	-7.92962	-0.15251	-3.84051
O	2.79722	2.68811	0.92714	H	5.77275	-4.72628	3.16615
O	0.64873	1.67907	1.95977	H	5.6093	-4.14135	1.70097
O	2.94631	1.20196	3.01801	H	-8.60688	-3.57569	0.60552
P	2.2244	0.25536	4.12063	H	-8.53131	-3.21335	-0.89877
O	1.7767	-1.05739	3.41375	H	7.04024	-4.31427	-2.36476
O	1.09705	0.98733	4.80248	H	7.66078	-4.51293	-1.00261
O	3.43603	-0.07384	5.12003	H	5.9342	-3.34673	-0.55859
Mg	-0.56344	1.41162	3.61563	H	6.67218	-2.70782	0.62418
H	5.54294	3.63356	-3.75347	H	2.62745	3.00303	-0.80859
H	6.17586	1.97082	-3.67619	H	2.2414	3.9536	-2.00284
H	4.45714	2.99971	-1.81307	H	-3.97552	3.41183	5.98819
H	7.77661	1.58618	-0.00229	H	-3.91641	2.42528	4.74664
H	7.52995	1.15734	-1.58902	H	-2.40188	1.52287	5.63487
H	4.52619	2.63287	0.56648	H	-2.07367	0.01394	5.34559
H	5.85524	1.68646	1.10302	H	-4.90551	-3.16628	1.19687
H	-4.11004	5.04443	-1.36795	H	-3.52697	-3.6458	1.79383
H	-3.46653	6.64999	-1.74708	H	-0.57495	-3.98195	2.90672
H	-1.37677	5.90854	-1.36645	H	0.31678	-4.1939	4.14556
H	-0.16741	3.42645	0.84981	H	3.34602	-4.13241	2.48259
H	0.18134	4.49975	-0.5091	H	1.72464	-4.03145	2.4399
H	-3.64659	3.99023	0.62259	H	-6.14499	0.23326	2.05651
H	-2.43301	3.08911	1.428	H	-6.29749	1.91344	1.50641

H	-7.39299 0.2571 0.01226	
H	-4.55175 -0.76061 -0.37143	**nofixNCbound.log**
H	-7.01388 -2.19448 0.01635	
H	-5.20246 -1.36544 -2.66898	no fixed bonds
H	-7.33709 -2.09133 -2.42637	C-N = 1.47
H	-6.40434 1.08487 -3.10123	C-O = 3.10
H	-4.90905 3.16544 -3.23593	
H	-1.21546 -1.90481 -1.84635	B3LYP/6-31G* Lanl2DZ Mg
H	-0.11227 3.20698 -2.77647	Free Energy = -6563.344432
H	3.44998 0.20577 -4.01574	Zero-point Energy = -6563.193803
H	3.6661 -1.56069 -4.01523	Potential Energy = -6564.50414103
H	3.74337 -0.21296 -1.33332	Nimag = 1 (16.7727 cm-1)
H	2.73507 -2.81617 -2.29829	
H	3.22135 -3.33772 -0.22478	Charge = 0 Multiplicity = 1
H	0.49805 -2.33079 -1.94787	C 5.92561 2.78147 -3.03668
H	-0.14576 -1.93162 0.32475	N 5.12774 2.89318 -1.81948
H	0.44699 0.34417 -0.70191	C 5.63054 2.76311 -0.59971
H	7.14265 3.32822 -3.03362	N 6.93395 2.37558 -0.45898
H	-3.92819 6.26766 -0.07603	N 4.91620 3.09238 0.48807
H	-8.53701 -6.19767 -2.36281	C -3.88624 5.91118 -1.69768
H	-3.1641 -5.61869 -1.82814	N -2.52712 5.55746 -1.34414
Mg	2.60434 -1.64481 1.68459	C -2.21606 4.69252 -0.37564
O	4.565 -1.51665 2.59793	N -0.93831 4.36033 -0.17026
H	4.8891 -2.43253 2.78846	N -3.17782 4.20810 0.44362
H	5.27252 -1.1138 2.04263	C -3.51186 -4.55552 -4.59369
H	1.11115 2.05106 -2.48842	C -3.35295 -4.59334 -3.07811
H	4.11164 -0.56154 4.6062	O -4.41366 -4.65218 -2.37984
O	-0.78275 3.36292 4.35155	O -2.18063 -4.55063 -2.60010
H	-0.1888 3.49418 5.10845	C -1.07278 -5.03108 0.65595
H	-1.70231 3.48438 4.68749	N -2.14907 -4.20573 0.05356
H	0.09104 -1.1015 3.38602	C 1.36160 6.20487 -4.29579
H	7.70139 -0.79101 1.41633	C 0.28047 5.80261 -3.29588
H	9.0418 -3.52574 -2.53706	O -0.72356 6.53088 -3.16415
H	8.0036 -2.14688 -4.00153	O 0.48488 4.71561 -2.63482
H	1.46094 7.67442 -3.91428	O 9.62376 -2.04393 -1.73232

O 6.69691 -0.44637 1.53432
O -7.54708 -1.83398 -4.67263
O 4.79757 -3.48210 3.10715
O -6.09513 -5.28379 -0.27294
O 9.32731 -3.78272 0.38102
O 6.73429 -3.23778 1.25744
O 2.38435 2.96790 -2.09734
O -4.12163 3.34060 4.82264
O -2.32285 1.32671 5.00140
O -4.30120 -4.27078 1.79057
O 0.17706 -3.16537 4.15465
O 2.13967 -3.05863 2.32062
O -2.86804 1.84245 2.04423
P -4.11822 0.99097 2.24716
O -5.03641 1.31033 3.39673
O -3.63641 -0.58065 2.41619
P -2.20561 -1.34026 2.20093
O -1.81527 -1.38022 0.72699
O -1.23008 -0.31328 3.02178
O -2.28107 -2.65941 2.93698
O -4.93166 0.99944 0.84323
C -6.33235 0.62060 0.83341
C -6.62788 -0.40515 -0.25180
C -5.65502 -1.59847 -0.28698
O -6.11836 -2.68030 0.49025
C -5.45846 -1.88489 -1.79343
O -6.38236 -2.84057 -2.28401
C -5.72000 -0.50022 -2.42240
O -6.58787 0.20145 -1.56625
N -4.46542 0.30881 -2.55217
C -3.16389 -0.08422 -2.69777
C -2.40690 1.08678 -2.67409
N -3.21203 2.19465 -2.55603
C -4.42206 1.68717 -2.47484
N -2.67605 -1.33833 -2.84861
C -1.38731 -1.42153 -2.75434
N -0.53351 -0.34784 -2.54548
C -0.99724 0.96511 -2.63496
N -0.16357 1.98353 -2.63470
O 7.32152 -2.11201 -2.96954
P 6.42900 -1.39834 -1.86459
O 7.26889 -0.41370 -1.03529
O 5.63736 -2.42727 -1.04441
O 5.38917 -0.48960 -2.72318
C 4.16790 -0.98030 -3.30213
C 3.01089 -0.78020 -2.32207
O 1.78927 -0.51436 -3.03829
C 2.64459 -1.97014 -1.39620
O 3.29469 -1.89534 -0.14054
C 1.09874 -1.86525 -1.23475
O 0.73515 -1.82956 0.12977
C 0.81532 -0.55125 -2.00694
O 1.96114 0.66116 0.61177
P 1.57221 2.00082 1.27325
O 2.16272 3.22151 0.57549
O 0.07900 2.13761 1.64131
O 2.37282 1.89339 2.76875
P 1.68409 0.93219 3.87312
O 1.33512 -0.42859 3.19458
O 0.48965 1.60146 4.50779
O 2.88726 0.67940 4.90571
Mg -1.17304 1.84037 3.23332
H 5.36884 3.26373 -3.84294
H 6.10465 1.73573 -3.30516
H 4.10019 3.00808 -1.93580
H 7.25321 2.32851 0.49998
H 7.19848 1.53741 -0.98923
H 3.89375 3.28355 0.43988
H 5.19640 2.67783 1.36688
H -4.46067 5.04362 -2.05269

H -3.83471 6.63541 -2.51271
H -1.77429 5.90247 -1.98253
H -0.67228 3.66264 0.52610
H -0.25773 4.60460 -0.89819
H -4.13346 4.28781 0.13125
H -2.98301 3.36691 0.99342
H -2.54683 -4.64854 -5.09650
H -3.97773 -3.60652 -4.88413
H -0.11148 -4.75252 0.22109
H -1.04559 -4.85567 1.73201
H -3.05646 -4.36589 0.55519
H -2.24670 -4.39157 -1.00257
H -1.95916 -3.19809 0.19661
H 1.53824 5.38893 -5.00596
H 2.30494 6.38425 -3.76623
H 9.29511 -1.21151 -1.34555
H 6.89381 -0.39371 0.54048
H -8.43805 -1.54621 -4.42253
H -7.24391 -2.34908 -3.89611
H 5.14670 -3.87166 3.92302
H 5.50464 -3.59092 2.41032
H -5.59682 -5.44430 0.54701
H -5.41126 -5.26933 -0.97696
H 9.37202 -4.69537 0.05835
H 8.41950 -3.68523 0.75370
H 6.32541 -3.14693 0.35090
H 6.84519 -2.28727 1.50096
H 2.21721 3.01979 -1.11641
H 1.87230 3.75629 -2.44035
H -4.76898 3.72187 5.43375
H -4.61455 2.69929 4.22954
H -3.07375 1.93416 5.19207
H -2.68663 0.42799 4.98864
H -4.94450 -3.58920 1.47707
H -3.73652 -3.80919 2.44808
H -0.74064 -3.09714 3.79334
H 0.33908 -2.29868 4.56177
H 2.95634 -3.47921 2.65460
H 1.41616 -3.19019 2.99724
H -6.62006 0.20772 1.80394
H -6.91652 1.53005 0.65989
H -7.64792 -0.77505 -0.09088
H -4.69065 -1.27518 0.11523
H -6.34758 -3.47133 -0.06808
H -4.45074 -2.23669 -1.99257
H -5.82418 -3.63691 -2.49565
H -6.18216 -0.58072 -3.40998
H -5.33133 2.25306 -2.34017
H -0.94006 -2.40432 -2.83751
H -0.50122 2.95000 -2.64635
H 3.98664 -0.36806 -4.18895
H 4.27404 -2.02420 -3.61500
H 3.24459 0.08410 -1.68869
H 2.90489 -2.92086 -1.87254
H 4.26616 -2.07170 -0.33782
H 0.63977 -2.73229 -1.71743
H -0.22641 -1.58196 0.27119
H 0.98970 0.25443 -1.28511
H 6.88251 3.29535 -2.90798
H -4.41947 6.37866 -0.85939
H -4.18223 -5.35736 -4.91929
H -1.27668 -6.08399 0.45251
Mg 2.26951 -1.14011 1.50224
O 4.14299 -0.87018 2.63111
H 4.40914 -1.76865 2.95603
H 4.95747 -0.51614 2.20648
H 0.86233 1.92631 -2.58268
H 3.56473 0.16487 4.41565
O -1.54915 3.80132 3.86724
H -0.97103 4.00826 4.61963

H -2.47815 3.88885 4.18707
H -0.24129 -0.54005 3.04142
H 7.49175 -0.12635 1.98857
H 9.58580 -2.68927 -0.97983
H 8.27373 -2.21071 -2.63078
H 1.07452 7.10800 -4.83757

NofixOCbound.log

No fixed bonds
C-N = 3.66
C-O = 1.45

B3LYP/6-31G* Lanl2DZ Mg

Free Energy = -6563.350699
Zero-point Energy = -6563.189679
Potential Energy = -6564.49496868
Nimag = 1 (2.0078 cm-1)

Charge = 0 Multiplicity = 1
C 5.22471 3.99882 -4.08345
N 4.79859 3.77394 -2.71351
C 5.40546 2.93221 -1.87784
N 6.53000 2.26825 -2.24350
N 4.93214 2.76422 -0.63858
C -4.25312 5.99444 -1.82849
N -2.92387 5.42127 -1.77225
C -2.48382 4.66573 -0.76292
N -1.26679 4.12147 -0.83706
N -3.22229 4.48669 0.35252
C -4.92332 -7.60684 -2.41873
C -4.05251 -6.46371 -1.91037
O -4.63703 -5.48883 -1.32166
O -2.81079 -6.52913 -2.08885
C -0.24919 -4.76148 -0.61296
N -1.66546 -4.43112 -0.90133
C 0.47335 5.06407 -5.45287
C -0.29432 4.99244 -4.13369
O -1.32116 5.68314 -3.99885
O 0.19672 4.19837 -3.23847
O 7.28564 -5.03476 -2.23316
O 6.02597 0.79661 1.38117
O -6.83791 -2.44040 -4.57923
O 5.10038 -2.79225 3.98215
O -6.66516 -5.04435 0.37613
O 5.66112 -5.33622 -0.10117
O 6.77940 -3.71084 2.07514
O 2.49615 5.02628 -2.01186
O -4.33498 4.07277 4.54508
O -5.70118 4.39131 2.10544
O -2.93934 -4.13188 1.50897
O 0.11935 -3.13570 4.75075
O 2.34690 -2.76267 3.38151
O -2.76160 2.13862 1.99804
P -4.02170 1.28824 2.18393
O -5.11836 1.83940 3.06247
O -3.55358 -0.16777 2.79188
P -2.07509 -0.84661 2.67591
O -1.56336 -0.79852 1.25173
O -1.23934 0.29479 3.57420
O -2.06181 -2.15316 3.42478
O -4.58585 0.94339 0.71599
C -5.91027 0.35973 0.61029
C -5.93673 -0.74980 -0.42167
C -4.86784 -1.84120 -0.23984
O -5.21405 -2.79715 0.73283
C -4.68571 -2.34088 -1.68733
O -5.74626 -3.20096 -2.06740
C -4.82378 -1.03029 -2.46946

O -5.74877 -0.23029 -1.75221
N -3.55269 -0.27333 -2.57909
C -2.28938 -0.69283 -2.95660
C -1.58050 0.48775 -3.22533
N -2.36380 1.60397 -3.01923
C -3.51890 1.10981 -2.65080
N -1.78269 -1.94308 -3.04150
C -0.51341 -1.93551 -3.46655
N 0.28186 -0.89476 -3.75177
C -0.23394 0.35561 -3.63507
N 0.55014 1.41410 -3.91587
O 7.57456 -2.45545 -1.90744
P 6.34586 -1.70168 -1.26478
O 6.72000 -0.26641 -0.92426
O 5.77803 -2.51003 -0.06324
O 5.20351 -1.76038 -2.42865
C 4.20226 -0.75300 -2.63868
C 3.47785 -0.41230 -1.34201
O 2.47282 0.58495 -1.58972
C 2.75853 -1.59050 -0.64853
O 3.35438 -1.85091 0.62624
C 1.32403 -1.06153 -0.41180
O 0.87678 -1.45316 0.87040
C 1.51208 0.46120 -0.58558
O 2.01325 0.93290 0.68404
P 1.68022 2.46609 1.21695
O 2.35842 3.49519 0.37542
O 0.18038 2.57112 1.48089
O 2.46320 2.30481 2.64911
P 1.76076 1.55740 3.93340
O 1.41359 0.11756 3.50300
O 0.56435 2.34763 4.39579
O 2.97308 1.53625 4.97094
Mg -1.06848 2.33275 3.04751
H 4.51950 4.69694 -4.53762
H 5.21784 3.07561 -4.67958
H 3.92053 4.26124 -2.39812
H 6.74020 1.37537 -1.78187
H 6.83371 2.34463 -3.20250
H 4.01469 3.12712 -0.36096
H 5.39565 2.14610 0.02386
H -5.03732 5.23042 -1.73522
H -4.36577 6.47744 -2.80079
H -2.29562 5.52983 -2.59800
H -0.91415 3.56443 -0.06688
H -0.74616 4.13368 -1.73420
H -4.17334 4.82280 0.42379
H -3.01577 3.68174 0.94399
H -4.31435 -8.41130 -2.83561
H -5.60719 -7.23119 -3.18872
H 0.28170 -4.95760 -1.54718
H 0.22491 -3.93930 -0.07138
H -2.17681 -4.23835 0.00606
H -2.16116 -5.26432 -1.38787
H -1.74712 -3.61376 -1.52390
H 0.51890 4.06786 -5.90837
H 1.50526 5.38604 -5.26672
H 8.12802 -5.50434 -2.14000
H 6.34716 0.27304 0.58511
H -7.58939 -1.91826 -4.26013
H -6.51212 -2.87845 -3.76614
H 5.48736 -2.93509 4.85944
H 5.72983 -3.20613 3.32580
H -6.36123 -5.40782 1.22288
H -6.02419 -5.41377 -0.28454
H 5.38315 -4.40526 -0.22780
H 6.13906 -5.28038 0.74649
H 6.54191 -3.15813 1.27543
H 7.72944 -3.57832 2.21721
H 2.28819 4.76545 -1.09456

H 1.71076 4.71095 -2.53075
H -4.73116 4.55633 3.78727
H -4.62503 3.15345 4.34619
H -6.63524 4.64382 2.16542
H -5.67601 3.42909 2.32792
H -3.81710 -3.74051 1.28475
H -2.58777 -3.54565 2.21060
H -0.68448 -2.87955 4.22790
H 0.03726 -2.62869 5.57245
H 3.17651 -3.09392 3.77603
H 1.54866 -2.97081 3.95782
H -6.22577 -0.05836 1.57053
H -6.60302 1.16015 0.33159
H -6.93212 -1.21364 -0.37237
H -3.93286 -1.37987 0.09106
H -5.88134 -3.46162 0.40620
H -3.72362 -2.81942 -1.86234
H -5.41561 -4.12720 -1.92940
H -5.22221 -1.20160 -3.47316
H -4.39716 1.68468 -2.40164
H -0.05280 -2.91576 -3.58798
H 0.27525 2.37746 -3.68725
H 4.66118 0.14964 -3.05573
H 3.50186 -1.16561 -3.36998
H 4.20028 0.00298 -0.63476
H 2.77149 -2.50600 -1.24566
H 4.30993 -2.11677 0.46095
H 0.65229 -1.42253 -1.19154
H -0.11284 -1.20736 1.00120
H 0.62192 1.01683 -0.87929
H 6.22499 4.44831 -4.13437
H -4.40971 6.75423 -1.05048
H -5.54273 -7.99539 -1.60265
H -0.22564 -5.66045 0.00542
Mg 2.38609 -1.09093 2.26121
O 4.23088 -0.37134 3.08668
H 4.69014 -1.16080 3.47611
H 4.87775 0.06605 2.46621
H 1.53645 1.22369 -4.01638
H 3.65318 0.92912 4.59882
O -1.78351 3.83438 4.16305
H -1.28560 4.05912 4.96305
H -2.77801 3.99428 4.32867
H -0.29755 0.00886 3.72135
H 6.81887 1.17690 1.79046
H 6.71973 -5.32351 -1.46544
H 7.45005 -3.45019 -2.08025
H -0.00437 5.75994 -6.14521

REFERENCE

1. Stroek, R., Ge, Y., Talbot, P. D., Glok, M. K., Bernas, K. E., Thomson, C. M., Gould, E. R., Alphey, M. S., Liu, H., Florence, G. J., Naismith, J. H., and da Silva, R. G. (2017) Kinetics and structure of a cold-adapted hetero-octameric atp phosphoribosyltransferase, *Biochemistry 56*, 793-803.

Allosteric rescue of catalytically impaired ATP phosphoribosyltransferase variants links protein dynamics to active-site electrostatic preorganisation

Gemma Fisher[1], Marina Corbella[2], Magnus S. Alphey[1], John Nicholson[1], Benjamin J. Read[1], Shina C. L. Kamerlin[2,3,*], and Rafael G. da Silva[1,*]

[1]School of Biology, Biomedical Sciences Research Complex, University of St Andrews, St Andrews, KY16 9ST, UK.

[2]Science for Life Laboratory, Department of Chemistry – BMC, Uppsala University, S-751 23 Uppsala, Sweden.

[3]School of Chemistry and Biochemistry, Georgia Institute of Technology, 901 Atlantic Drive NW, Atlanta, GA 30332, USA

*To whom correspondence should be addressed: Rafael G. da Silva, email: rgds@st-andrews.ac.uk; Shina C. L. Kamerlin, email: lynn.kamerlin@kemi.uu.se.

Abstract. ATP phosphoribosyltransferase catalyses the first step of histidine biosynthesis and is controlled via a complex allosteric mechanism where the regulatory protein HisZ enhances catalysis by the catalytic protein $HisG_S$ while mediating allosteric inhibition by histidine. Activation by HisZ was proposed to position $HisG_S$ Arg56 to stabilise departure of the pyrophosphate leaving group. Here we report active-site mutants of $HisG_S$ with impaired reaction chemistry which can be allosterically restored by HisZ despite the HisZ:$HisG_S$ interface lying ~20-Å away from the active site. MD simulations indicate HisZ binding constrains the dynamics of $HisG_S$ to favour a preorganised active site where both Arg56 and Arg32 are poised to stabilise leaving-group departure in WT-$HisG_S$. In the Arg56Ala-$HisG_S$ mutant, HisZ modulates Arg32 dynamics so that it can partially compensate for the absence of Arg56. These results illustrate how remote protein:protein interactions translate into catalytic resilience by restoring damaged electrostatic preorganisation at the active site.

Introduction

Robust reaction rate enhancement and allosteric regulation are hallmarks of enzyme catalysis, and both aspects may be at least in part underpinned by protein conformational flexibility.[1-3] The catalytic prowess of enzymes can be significantly ascribed to substrate binding to an electrostatically preorganised active site, which minimises the reorganisation energy required for optimum stabilisation of the charge redistribution as the reaction progresses from the reactant state to the transition state.[4] Yet several lines of evidence also suggest a contribution from protein dynamics,[5-8] from nonstatistical, femtosecond-timescale vibrations coupled directly to transition-state barrier crossing,[6,8] to slower, thermally equilibrated motions reshaping the enzyme conformational ensemble towards populations where active-site preorganisation is optimised.[5] Nonetheless, this topic is still controversial possibly due to the inherent flexibility of proteins which makes it difficult to isolate motions that may have evolved to facilitate reaction.[7,9,10]

Allosteric modulation of enzymes, *i.e.* the alteration of reaction rate and/or substrate affinity upon ligand binding to, mutation of, or post-translational modification at a site remote from the active site, is a fundamental regulatory mechanism of biochemical reactions.[11,12] It finds applications in drug discovery to facilitate drug-target selectivity as allosteric sites tend to be less conserved than active sites across homologous proteins,[13,14] and in enzyme engineering and synthetic biology, where allosteric control may need to be introduced or, more often, eliminated.[15,16] While enzymes subject to allosteric regulation by ligand binding can be broadly classified as *K*-type, those where substrate affinity is altered, and *V*-type, those where the steady-state catalytic rate constant (k_{cat}) is altered, the specific kinetic steps affected can vary depending on the enzyme.[13,17-19] For instance, in *Mycobacterium tuberculosis* α-isopropylmalate synthase, the rate-limiting step changes from product release to chemistry upon allosteric inhibition by leucine.[17] The role of protein

dynamics in allostery has been much less controversial when discussed in terms of conformational changes to promote physical events such as substrate binding and product release, or the interconversion rate among conformations.[11,20] However, in systems where allosteric regulation affects the rate of the chemical step itself,[17-19] the intersection at which local and remote protein motions, active-site electrostatic preorganisation, and ultimately catalysis meet remains challenging to pinpoint, despite recent advances toward this goal with Kemp eliminase.[5,21]

ATP phosphoribosyltransferase (ATPPRT) (EC 2.4.2.17) catalyses the Mg^{2+}-dependent formation of N^1-(5-phospho-β-D-ribosyl)-ATP (PRATP) and inorganic pyrophosphate (PP_i) from ATP and 5-phospho-α-D-ribosyl-1-pyrophosphate (PRPP) (**Fig. 1a**), the first and flux-controlling step of histidine biosynthesis, and is allosterically inhibited by histidine in a negative feedback control loop.[22,23] ATPPRT is the focus of synthetic biology efforts to enable the production of histidine in bacteria[16,24] and a promising drug target against some pathogenic bacteria.[25-27] Short-form ATPPRTs form an intricate allosteric system comprising catalytic ($HisG_S$) and regulatory (HisZ) subunits assembled as a hetero-octamer with a tetrameric core of HisZ sandwiched by two dimers of $HisG_S$.[28-33] $HisG_S$ on its own is catalytically active and insensitive to inhibition by histidine.[28,34] Binding of HisZ, which has no catalytic power of its own, to form the ATPPRT holoenzyme, allosterically activates catalysis by $HisG_S$.[26,28,31,34] However, HisZ also harbours the pocket where histidine binds and allosterically inhibits ATPPRT. Thus, the regulatory protein plays a dual role, as allosteric activator of catalysis in the absence of histidine and mediator of allosteric inhibition in the presence of histidine. [19,31,33]

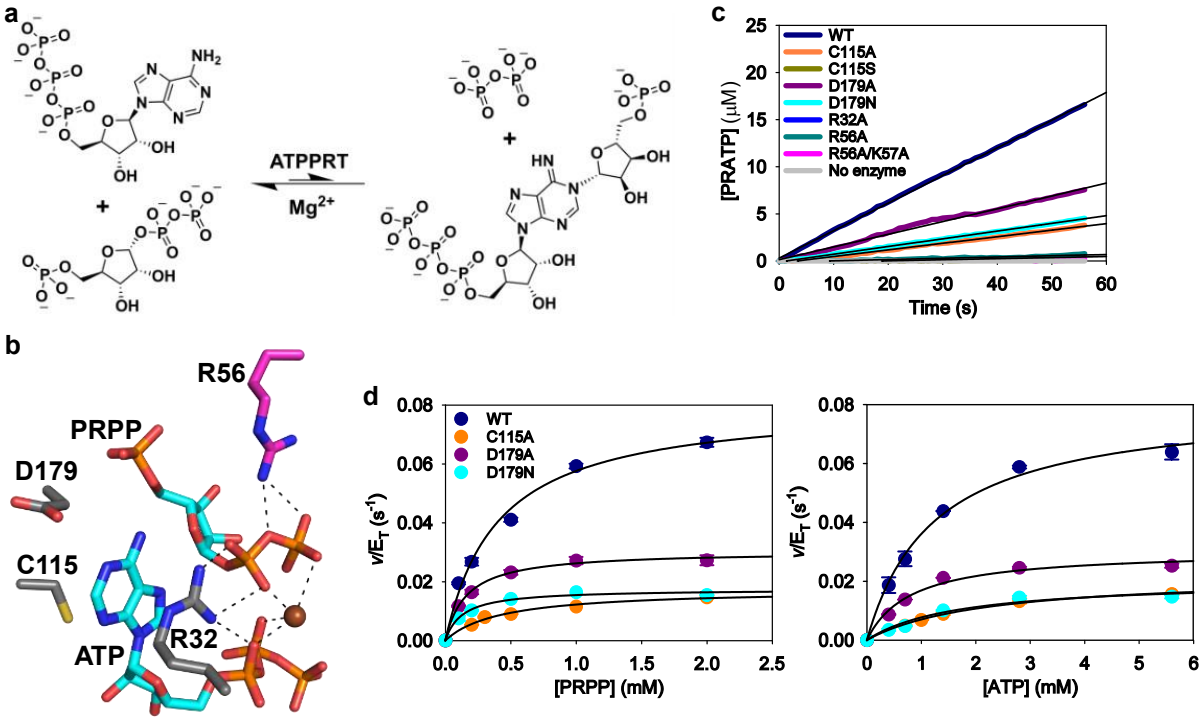

Fig. 1 The effect of active-site mutations on *Pa*HisG$_S$. a The reversible, Mg^{2+}-dependent reaction catalysed by ATPPRT. **b** Stick model of the active site of *Pa*ATPPRT (PDB ID 6FU2).[29] Oxygen is shown in red, nitrogen in blue, phosphorus in orange, sulphur in yellow, and carbon in either cyan (substrates), grey (in one of the *Pa*HisG$_S$ subunits) or magenta (in the other *Pa*HisG$_S$ subunit). Polar interactions are depicted as dashed lines, and the Mg^{2+} as sphere. **c** Representative traces of PRATP formation time course catalysed by 5 μM *Pa*HisG$_S$ variants. Black lines are linear regressions of the data. **d** Substrate saturation curves for WT and mutant *Pa*HisG$_S$. Data are mean ± standard error of two independent measurements. Lines are best fit of the data to equation (1).

In *Psychrobacter arcticus* ATPPRT (*Pa*ATPPRT), structural and functional data indicate allosteric activation of catalysis triggered by HisZ (*Pa*HisZ) binding specifically perturbs the chemical step of the reaction taking place at the HisG$_S$ (*Pa*HisG$_S$) active site located ~23 Å from the nearest *Pa*HisG$_S$:*Pa*HisZ interface.[18,29] First, crystal structures of the Michaelis complexes of the activated, hetero-octameric holoenzyme (henceforth referred to

as *Pa*ATPPRT) and of the nonactivated, dimeric enzyme (henceforth referred to as *Pa*HisG$_S$) showed Arg56 of one of the catalytic subunits reaching across the dimer interface to form a salt-bridge with the pyrophosphate moiety of PRPP in the active site of the other subunit (**Fig. 1b**) in the *Pa*ATPPRT but not in the *Pa*HisG$_S$ structure. Therefore, allosteric activation was proposed to lead to more efficient leaving group departure at the transition state by stabilisation of the negative charge build-up on the pyrophosphate upon nucleophilic attack of ATP N1 on PRPP C1.[29] Second, no burst in product formation was observed for the reaction catalysed by *Pa*HisG$_S$, and the multiple-turnover pre-steady-state rate-constant was in agreement with k_{cat}, suggesting chemistry is rate-limiting in the nonactivated enzyme reaction. In contrast, a burst was observed in the reaction catalysed by *Pa*ATPPRT, producing a rate-constant (k_{burst}) much higher than k_{cat}, supporting a mechanism where allosteric activation speeds up the chemical step, making product release rate-limiting.[18] Finally, replacement of Mg^{2+} by Mn^{2+}, which more efficiently offsets the negative charge at the transition state, led to an ~3-fold enhancement of *Pa*HisG$_S$ k_{cat}, as would be predicted, qualitatively, for a rate-limiting chemical step, but had no effect on *Pa*ATPPRT k_{cat}, where chemistry was already much faster than subsequent steps.[18]

As expected, an R56A-*Pa*HisG$_S$ mutant had a reduced reaction rate in the nonactivated enzyme as measured at a fixed concentration of substrates, since R56 was posited to be important for leaving group departure in *Pa*HisG$_S$ as well, only less efficiently. Intriguingly, upon *Pa*HisZ binding to R56A-*Pa*HisG$_S$, part of the activity was recovered.[29] Here we employed site-directed mutagenesis, differential scanning fluorimetry (DSF), enzyme kinetics, ^{31}P-NMR spectroscopy, protein crystallography, and molecular dynamics (MD) simulations to dissect this phenomenon, reveal that other single- and double-mutations at the *Pa*HisG$_S$ active site display similar behaviour, and demonstrate how modulation of *Pa*HisG$_S$ dynamics by *Pa*HisZ propagates to the active site to affect the chemical step.

Results

C115A-, D179A-, and D179N-*Pa*HisG$_S$ are catalytically active. To assess the importance of active-site residues in catalysis, we introduced single and double mutations into the *Pa*HisG$_S$ amino acid sequence by site-directed mutagenesis of the *Pa*HisG$_S$-coding sequence and expressed and purified the mutant proteins (**Supplementary Fig. 1**). Electrospray ionisation/time-of-flight-mass spectrometry (ESI/TOF-MS) confirmed the molecular mass of WT-, C115A-, C115S-, D179A-, R32A-, R56A-, and R56A/K57A-*Pa*HisG$_S$ variants were in agreement with the predicted value (**Supplementary Fig. 2**). The introduction of the D179N mutation was confirmed by MS/MS analysis of tryptic fragments (**Supplementary Fig. 2**). In an initial activity screen, reactions were monitored for just under 1 min by the continuous and direct UV/VIS absorbance-based assay for ATPPRT activity[18,35] at fixed PRPP and ATP concentrations sufficient to saturate WT-*Pa*HisG$_S$, and PRATP formation was readily detected with C115A-, D179A-, D179N-, and WT-*Pa*HisG$_S$ (**Fig. 1c**), and linear regression of the data yielded apparent rate constants shown in **Supplementary Table 1**.

Substrate saturation curves for WT-, C115A-, D179A-, and D179N-*Pa*HisG$_S$ obeyed Michaelis-Menten kinetics (**Fig. 1d**), and data fit to equation (1) produced the apparent steady-state kinetic parameters in **Supplementary Table 2**. The Michaelis constant for ATP (K_{ATP}) increased less than 2-fold for C115A-*Pa*HisG$_S$, and the Michaelis constant for PRPP (K_{PRPP}) actually decreased between 2- and 3-fold for D179A- and D179N-*Pa*HisG$_S$, suggesting C115 and D179 make negligible contributions to substrate binding. The k_{cat} for the mutants were reduced only ~4-fold in comparison with the WT-*Pa*HisG$_S$, pointing to these residues' modest importance in catalysis. Over the course of the ATPPRT-catalysed reaction, the 6-NH_2 group must donate a proton to yield the 6-NH group of PRATP, and in the case of *Pa*ATPPRT, this proton abstraction happens on the enzyme.[18] Based on their respective

positions in the active site (**Fig. 1b**),[29] both C115 and D179 were candidates to act as general base for this proton abstraction, but the small catalytic effect of their replacements for residues that cannot participate in acid-base catalysis does not support such role, leaving the identity of the general base still elusive.

C115S-, R32A-, R56A-, and R56A/K57A-*Pa*HisG$_S$ are catalytically compromised. No PRATP formation could be detected above the background noise of the assay during the initial activity screen when either C115S-, R32A-, R56A-, or R56A/K57A-*Pa*HisG$_S$ was used as catalyst (**Fig. 1c**), indicating these mutants have impaired catalytic activity. DSF-based thermal denaturation assays showed these mutants display similar thermal unfolding profiles to the WT protein (**Fig. 2a**), and data fit to equation (2) yielded melting temperatures (T_m) shown in **Supplementary Table 3**. Moreover, as described previously[18] and repeated here for WT-*Pa*HisG$_S$, the presence of PRPP increased the T_m of the mutants (**Fig. 2a; Supplementary Table 3**), indicating the catalytically impaired *Pa*HisG$_S$ variants can bind PRPP, in agreement with the ordered kinetic mechanism proposed for this enzyme.[18,29] Analytical size-exclusion chromatography produced similar elution profiles for WT-, C115S-, R32A-, R56A-, and R56A/K57A-*Pa*HisG$_S$ (**Supplementary Fig. 3**). An activity screen with longer reaction times and twice as much enzyme as in the initial screen, to allow more product to accumulate, demonstrated the catalytic ability of C115S-, R32A-, R56A-, and R56A/K57A-*Pa*HisG$_S$ is significantly diminished but not abolished (**Fig. 2b**).

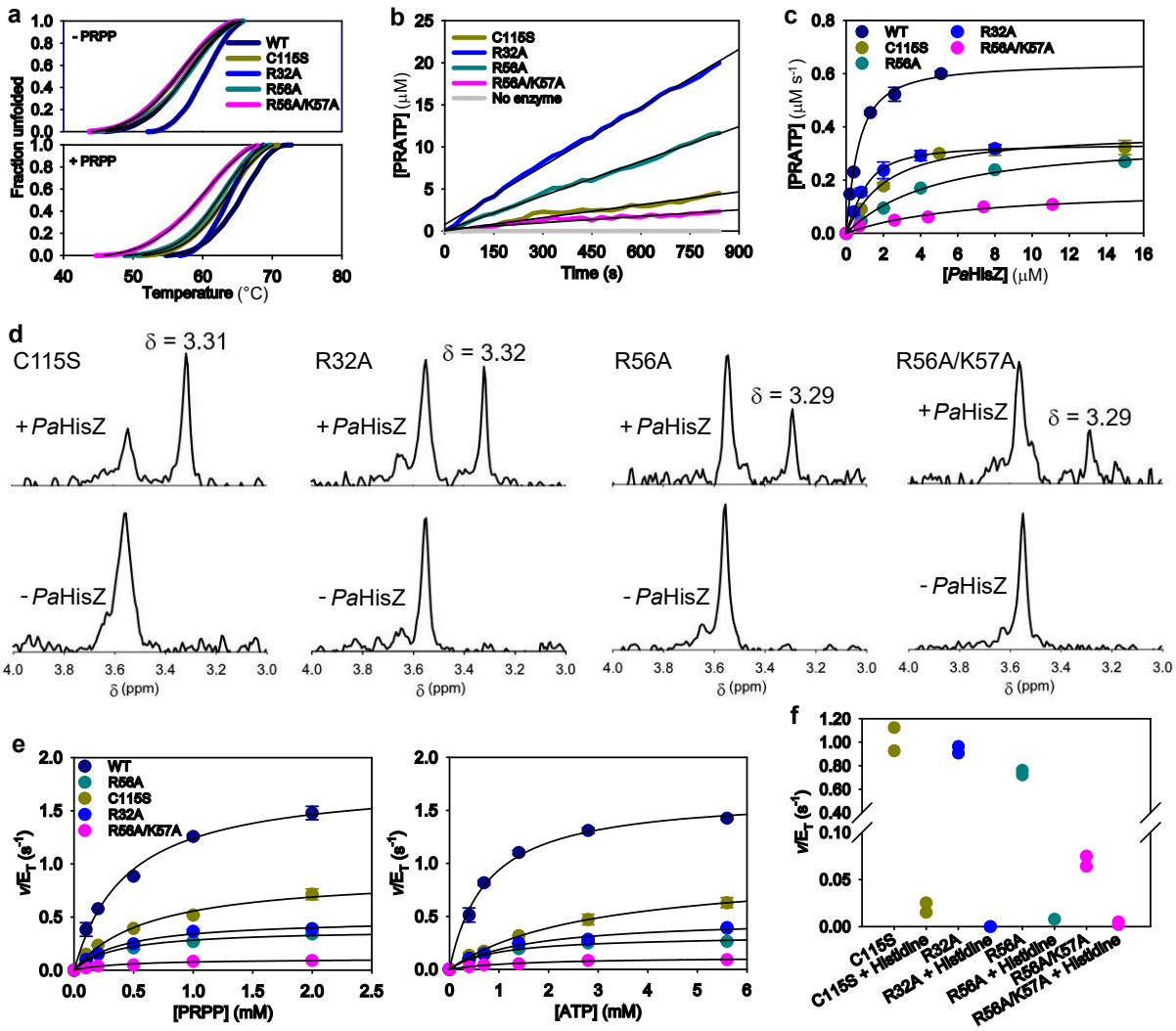

Fig. 2 Allosteric rescue of catalytically impaired *Pa*HisGs mutants by *Pa*HisZ. a DSF-based thermal denaturation of C115S-, R32A-, R56A-, or R56A/K57A-*Pa*HisGS. Traces are averages of three independent measurements. Lines of best fit to equation (2) are in black. **b** PRATP formation time course catalysed by 10 μM *Pa*HisGS variants. Traces are averages of two independent measurements. Black lines are linear regressions of the data. **c** Dependence of rate of reaction catalysed by *Pa*HisGS variants on the concentration of *Pa*HisZ. Data are mean ± standard error of two independent measurements. Lines are best fit of the data to equation (3). **d** Close-up of the 4.0 – 3.0 ppm region of the ^{31}P-NMR spectra of the reaction catalysed by *Pa*HisGS mutants in the presence and absence of *Pa*HisZ. The peak at ~3.30 ppm corresponds to the phosphorus in the N^1-5-phospho-β-D-ribose moiety of PRATP.[28,29] **e**

Substrate saturation curves for WT and mutant *Pa*ATPPRT. Data are mean ± standard error of two independent measurements. Lines are best fit of the data to equation (1). **f** Effect of 1 mM histidine on mutant *Pa*ATPPRT-catalysed reaction. Two independent measurements were carried out, and all data points are shown.

Even though C115 is only modestly important for catalysis, its replacement by serine led to a 117-fold reduction in activity (**Table 1**), perhaps due to the introduction of a detrimental interaction. The activities of R32A- and R56A-*Pa*HisG$_S$ decreased 25- and 42-fold, respectively, in comparison with the WT-*Pa*HisG$_S$ (**Table 1**). This demonstrates the importance of these residues in *Pa*HisG$_S$ catalysis, possibly because R56 and R32 may contribute to leaving group departure at the transition state.[18,29] K57 is adjacent to R56 in the *Pa*HisG$_S$ primary sequence, but in all *Pa*HisG$_S$ and *Pa*ATPPRT crystal structures, it points away from the active site.[19,28,29] We hypothesised that in the absence of the R56 guanidinium group, the K57 ε-NH_3^+ group could move towards the active site and assist in leaving group departure. However, the R56A/K57A-*Pa*HisG$_S$ double mutant displayed a 254-fold decrease in activity (**Table 1**), which is only ~6-fold more catalytically impaired than the R56A-*Pa*HisG$_S$, indicating just a modest catalytic importance for K57. R32, R56, K57, and C115 are highly conserved in HisG$_S$ across species, and D179 is also conserved but sometimes replaced with a glutamate residue.[29] Nevertheless, out of these five residues in *Pa*HisG$_S$, only the arginine residues seem to be significantly important for catalysis.

Table 1 Apparent rate constants (mean ± fitting error) for *Pa*HisG$_S$ mutants from reactions monitored for 840 s.

***Pa*HisG$_S$**	***v*/E$_T$ (s^{-1})**	**Catalytic impairment[a]**
C115S	0.0005 ± 0.0001	117-fold
R32A	0.0023 ± 0.0001	25-fold
R56A	0.0014 ± 0.0001	42-fold
R56A/K57A	0.00023 ± 0.00005	254-fold

[a]Ratio of *v*/E$_T$ reported for WT-*Pa*HisG$_S$ (**Supplementary Table 1**) to *v*/E$_T$ reported here.

***Pa*HisZ allosterically rescues C115S-, R32A-, R56A-, and R56A/K57A-*Pa*HisG$_S$ catalysis.** To assess the extent to which these mutations were also detrimental to *Pa*ATPPRT catalysis, and how much of the R56A-*Pa*HisG$_S$ activity could be recovered in the presence of *Pa*HisZ,[29] the effect of *Pa*HisZ on the reaction catalysed by the impaired *Pa*HisG$_S$ mutants was determined. The regulatory protein surprisingly led to activation of all catalytically impaired *Pa*HisG$_S$ mutants (**Fig. 2c**), and data fit to equation (3) resulted in the apparent equilibrium dissociation constants (K_D) for *Pa*HisZ displayed in **Table 2**. No activity was detected when the *Pa*HisG$_S$ mutant-catalysed reactions were carried out in the presence of bovine serum albumin (BSA) (**Supplementary Fig. 4**), ruling out that allosteric rescue was due to nonspecific protein binding. To gather orthogonal evidence for the allosteric rescue, the reaction catalysed by each *Pa*HisG$_S$ mutant was analysed by ^{31}P-NMR spectroscopy in the presence and absence of *Pa*HisZ (**Supplementary Fig. 5**) under conditions where product can be detected with WT-*Pa*HisG$_S$.[18] The characteristic chemical shift at ~3.30 ppm (**Fig. 2d**) previously assigned to the phosphorus in the N^1-5-phospho-β-D-ribose moiety of PRATP,[28,29] was only detected here when *Pa*HisZ was present in the reaction, confirming the rescue of the catalytically compromised mutants by the regulatory protein.

Table 2. Steady-state kinetic parameters (mean ± fitting error) for *Pa*ATPPRT variants (all mutations are in *Pa*HisG$_S$).

***Pa*ATPPRT**	***Pa*HisZ K_D (μM)**	**k_{cat} (s^{-1})**	**K_{PRPP} (mM)**	**K_{ATP} (mM)**	**Activation by *Pa*HisZ[a]**
WT	0.44 ± 0.05	1.72 ± 0.07	0.44 ± 0.05	0.76 ± 0.07	29-fold
C115S	1.7 ± 0.4	0.93 ± 0.05	0.6 ± 0.1	2.8 ± 0.2	1,860-fold
R32A	0.49 ± 0.06	0.48 ± 0.04	0.41 ± 0.06	1.5 ± 0.3	208-fold
R56A	4.0 ± 0.6	0.35 ± 0.05	0.37 ± 0.04	0.9 ± 0.1	250-fold
R56A/K57A	5 ± 2	0.12 ± 0.01	0.4 ± 0.1	1.5 ± 0.3	521-fold

[a]Ratio of k_{cat} reported here to v/E_T from **Supplementary Table 1** (WT) and **Table 1** (mutants).

Substrate saturation curves for WT-, C115S-, R32A-, R56A-, and R56A/K57A-*Pa*ATPPRT obeyed Michaelis-Menten kinetics (**Fig. 2e**), and data fit to equation (1) produced the apparent steady-state kinetic parameters shown in **Table 2**, with the concentrations of each *Pa*ATPPRT variant calculated from the K_D for *Pa*HisZ using equation (4). *Pa*HisZ allosterically restored most of the catalytic activity of the impaired *Pa*HisG$_S$ mutants. In comparison with the WT-*Pa*ATPPRT, K_{PRPP} was unaltered by the mutations, and K_{ATP} increased by a maximum of 4-fold. The k_{cat} decreased by less than 2-fold for C115S-*Pa*ATPPRT as compared with WT-*Pa*ATPPRT, and by less than 4-fold and 6-fold for R32A- and R56A-*Pa*ATPPRT. Only R56A/K57A-*Pa*ATPPRT k_{cat} was reduced by more than one order of magnitude (~14-fold) in comparison with WT-*Pa*ATPPRT, which is still a small effect in comparison with the 254-fold catalytic impairment of R56A/K57A-*Pa*HisG$_S$.

Due to the long TEVP-cleavage time and low yield of the *Pa*HisZ recovered along with the extensive use of the regulatory protein in this work, a His-tagged *Pa*HisZ was

purified and employed from this point onwards. The steady-state kinetic parameters (**Supplementary Fig. 6**) are very similar whether nor not the His-tagged *Pa*HisZ was used. Histidine binds to *Pa*HisZ and allosterically inhibits *Pa*ATPPRT catalysis, and the suppression of the burst in product formation in the presence of histidine suggests that allosteric inhibition directly affects the chemical step of the reaction.[19] Histidine also inhibits the reaction catalysed by the rescued *Pa*ATPPRT mutants (**Fig. 2f; Supplementary Fig. 7**), indicating the allosteric pathway responsible for inhibition is intact in these mutants.

Allosteric activation of WT- and R56A-*Pa*HisG$_S$ by an orthologous HisZ. *Pa*HisZ and *Pa*HisG$_S$ share 43% and 69% sequence identity with their orthologues from the pathogenic bacterium *Acinetobacter baumannii*, *Ab*HisZ and *Ab*HisG$_S$, respectively, but *Pa*HisZ has been shown to be a potent allosteric inhibitor of *Ab*HisG$_S$.[26] We thus hypothesised that *Ab*HisZ could inhibit WT-*Pa*HisG$_S$. However, addition of *Ab*HisZ activated catalysis by WT-*Pa*HisG$_S$ (**Fig. 3a**), and data fit to equation (3) yielded a K_D for *Ab*HisZ of 9 ± 1 μM. Moreover, *Ab*HisZ also rescued catalysis by R56A-*Pa*HisG$_S$ (**Fig. 3a**), but their interaction involved positive co-operativity as evidenced by the sigmoidal dependence of the reaction rate on the regulatory protein. The R56A-*Pa*HisG$_S$ mutant was chosen due to its significant catalytic impairment and the proposed role in catalysis for R56. The data were fit to equation (5), yielding a concentration of *Ab*HisZ at the inflection point ($K_{0.5}$) and a Hill coefficient (h) of 8.1 ± 0.4 μM and 1.68 ± 0.08, respectively. Nonetheless, this fit is intended only to highlight the sigmoidal behaviour of the data, since the experiment could not be carried out under pseudo-first-order conditions, *i. e.* [R56A-*Pa*HisG$_S$] ~ [*Ab*HisZ] in the experiment, thus equation (5) does not hold.

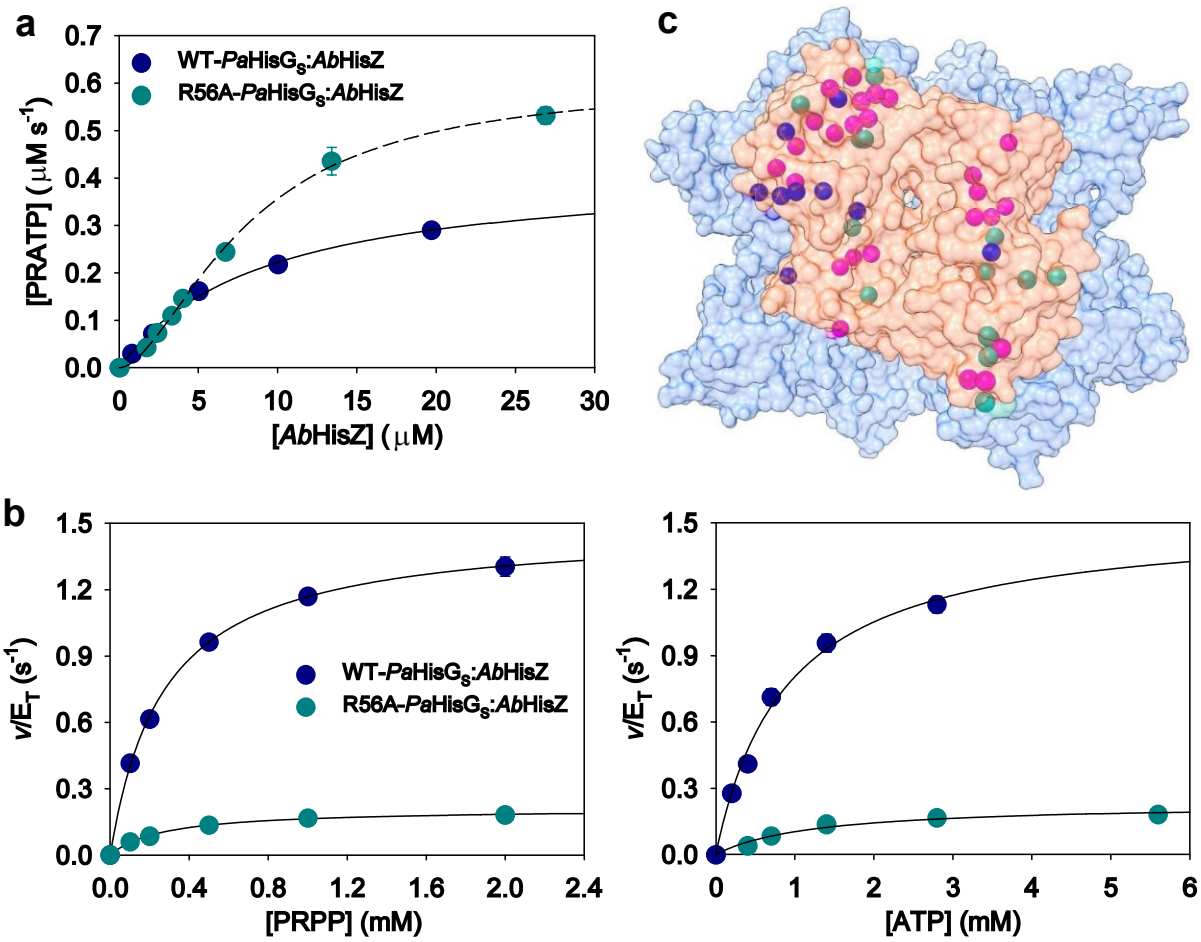

Fig. 3 Allosteric activation of *Pa*HisG$_S$ variants by *Ab*HisZ. a Dependence of rate of reaction catalysed by *Pa*HisG$_S$ variants on the concentration of *Ab*HisZ. Data are mean ± standard error of two independent measurements. Best fit of the data to equation (3) is shown as a solid line. Best fit of the data to equation (5) is shown as a dashed line. **b** Substrate saturation curves for WT-*Pa*HisG$_S$/*Ab*HisZ and R56A-*Pa*HisG$_S$/*Ab*HisZ. Data are mean ± standard error of two independent measurements. Lines are best fit of the data to equation (1). WT-*Pa*HisG$_S$/*Ab*HisZ concentration was calculated from the K_D for *Ab*HisZ with equation (4), while R56A-*Pa*HisG$_S$/*Ab*HisZ concentration was assumed to be the same as R56A-*Pa*HisG$_S$ in the presence of 26 μM *Ab*HisZ. **c** The crystal structure of *Pa*ATPPRT[28] viewed from above the *Pa*HisG$_S$ dimer. *Pa*HisG$_S$ (orange) and *Pa*HisZ (blue) are in surface rendering. The Cα atoms of specific *Pa*HisZ residues at the interface with *Pa*HisG$_S$ are

shown as spheres, with pink depicting identical residues to *Ab*HisZ, blue depicting residues with similar properties to those in *Ab*HisZ, and green, those not conserved in *Ab*HisZ.

Substrate saturation curves for WT-*Pa*HisG$_S$/*Ab*HisZ and R56A-*Pa*HisG$_S$/*Ab*HisZ hybrid complexes obeyed Michaelis-Menten kinetics (**Fig. 3b**), and data fit to equation (1) produced the following apparent k_{cat}, K_{PRPP}, and K_{ATP}: 1.49 ± 0.02 s^{-1}, 0.27 ± 0.01 mM, and 0.9 ± 0.1 mM for WT-*Pa*HisG$_S$/*Ab*HisZ; 0.22 ± 0.02 s^{-1}, 0.27 ± 0.02 mM, and 1.2 ± 0.3 mM for R56A-*Pa*HisG$_S$/*Ab*HisZ. These values are in good agreement with those for WT- and R56A-*Pa*ATPPRT (**Table 2**), indicating *Ab*HisZ recapitulates the catalytic activation of *Pa*HisG$_S$ to a similar extent the native *Pa*HisZ does. Furthermore, *Ab*HisZ is capable of efficiently relaying the histidine inhibition allosteric signal to WT- and R56A-*Pa*HisG$_S$ (**Supplementary Fig. 8**). We mapped the *Pa*HisZ residues at the interface between the *Pa*HisG$_S$ dimer and the *Pa*HisZ tetramer in the *Pa*ATPPRT hetero-octamer[28] (**Fig. 3a**), and found that 25 of those are strictly conserved in *Ab*HisZ. It is possible that these residues have an important role in transmitting the allosteric signal for both activation and inhibition.

Crystal structures of R56A-*Pa*HisG$_S$ and R56A-*Pa*ATPPRT. In an attempt to gain insight into the effect of the R56A mutation at the atomic level, we solved the crystal structures of both R56A-*Pa*HisG$_S$ and R56A-*Pa*ATPPRT bound to PRPP:ATP. Refinement statistics are summarised in **Supplementary Table 4**, and the electron-density maps for PRPP:ATP in both structures are shown in **Supplementary Fig. 9**. Even WT-*Pa*HisG$_S$ and WT-*Pa*ATPPRT are known to form the Michaelis complex *in crystallo*, likely due to a highly unfavourable on-enzyme equilibrium for the forward reaction.[18,29] The active site interactions are very similar between the two structures, except the electron density for Mg^{2+} in R56A-*Pa*ATPPRT was not well defined, so the metal was not modelled in, and the hydrogen bond between E163 and the PRPP 3′-OH is absent in the R56A-*Pa*HisG$_S$ (**Fig. 4**). The structures are also very similar to those of the respective WT enzymes.[29] Therefore, any structural or

conformational differences that may lead to allosteric rescue of R56A-*Pa*HisG$_S$ catalysis are not captured in the static view of the crystal structure.

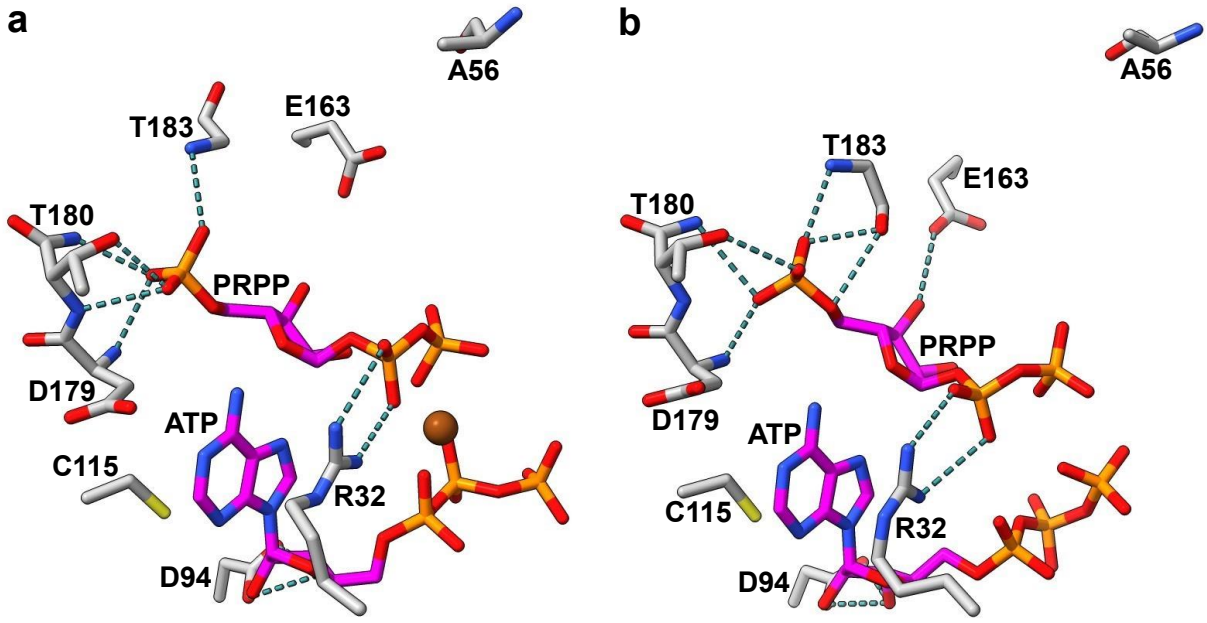

Fig. 4 Crystal structures of R56A-*Pa*HisG$_S$ and R56A-*Pa*ATPPRT bound to PRPP:ATP. **a** Stick model of the active site of R56A-*Pa*HisG$_S$. **b** Stick model of the active site of R56A-*Pa*ATPPRT. In both panels, oxygen is shown in red, nitrogen in blue, phosphorus in orange, sulphur in yellow, and carbon in either magenta (substrates) or grey (protein). The A56 side chain is contributed by the adjacent *Pa*HisG$_S$ subunits. Polar interactions are depicted as dashed lines, and the Mg^{2+} as sphere.

***Pa*HisZ binding alters *Pa*HisG$_S$ dynamics.** MD simulations were performed on the WT-*Pa*HisG$_S$:PRPP:ATP complex both in the presence and absence of the regulatory protein *Pa*HisZ in order to gain insight into the role of *Pa*HisZ in the allosteric modulation of *Pa*HisG$_S$. We then constructed dynamic cross-correlation matrices (DCCM) for the Cα-atoms during simulations of each system (**Supplementary Fig. 10**) to analyze the occurrence of correlated motions in the inactivated and activated dimers. These plots show a clear shift in the *Pa*HisG$_S$ dimer conformational ensemble upon allosteric activation, with losses of both correlated and anti-correlated motions compared to the nonactivated dimer. It is expected that

external structural perturbations (such as ligand binding or, in this case, the binding of *Pa*HisZ to *Pa*HisG$_S$) would alter such conformational fluctuations, as has been observed in other allosteric systems.[36-38] However, it is surprising to observe a loss in correlated motions upon allosteric activation, which suggests that binding of *Pa*HisZ restricts *Pa*HisG$_S$ motions.

The curious conformational behavior of the activated dimer was further explored using the shortest path map (SPM) approach,[39] which enables the identification of pairs of residues in both the active site and distal positions[40] with the highest contributions to the communication pathways in nonactivated and activated *Pa*HisG$_S$. Comparison of the SPM in the nonactivated and activated enzymes (**Fig. 5a,b**) illustrates that *Pa*HisZ binding increases intermonomer communication pathways across the two subunits of the *Pa*HisG$_S$ dimer, which could be expected to in turn facilitate key interactions between R56 and PRPP across the dimer. This is in overall agreement with the allosteric activation mechanism gleaned from the crystal structures of *Pa*HisG$_S$ and *Pa*ATPPRT.[29] Furthermore, when also considering interactions between the dimer and the regulatory protein (**Fig. 5c**,**d**), it can be seen that the SPM spans one of the *Pa*HisZ subunits, bridges both monomers of *Pa*HisG$_S$ and communicates with the regulatory protein mainly through helices α7,8 of *Pa*HisG$_S$ and β4,5,11 of *Pa*HisZ (**Supplementary Fig. 11**). Interestingly, the calculated SPM (**Fig. 6**) contains G268 of the histidine binding loop of *Pa*HisZ (D256 – I269),[19] suggesting a perturbation of the allosteric communication pathway upon histidine binding. We also analyzed the contribution of each residue to the overall protein dynamics by means of the dynamical flexibility indexes (DFI)[41] (**Supplementary Fig. 12**) to reveal *Pa*HisZ binding changes the DFI of *Pa*HisG$_S$ compared with nonactivated *Pa*HisG$_S$, in particular at the helices inferred to be important for communication at the *Pa*HisG$_S$-*Pa*HisZ interface from the SPM analysis (**Fig. 5**), as well as the region containing the R32 and R56.

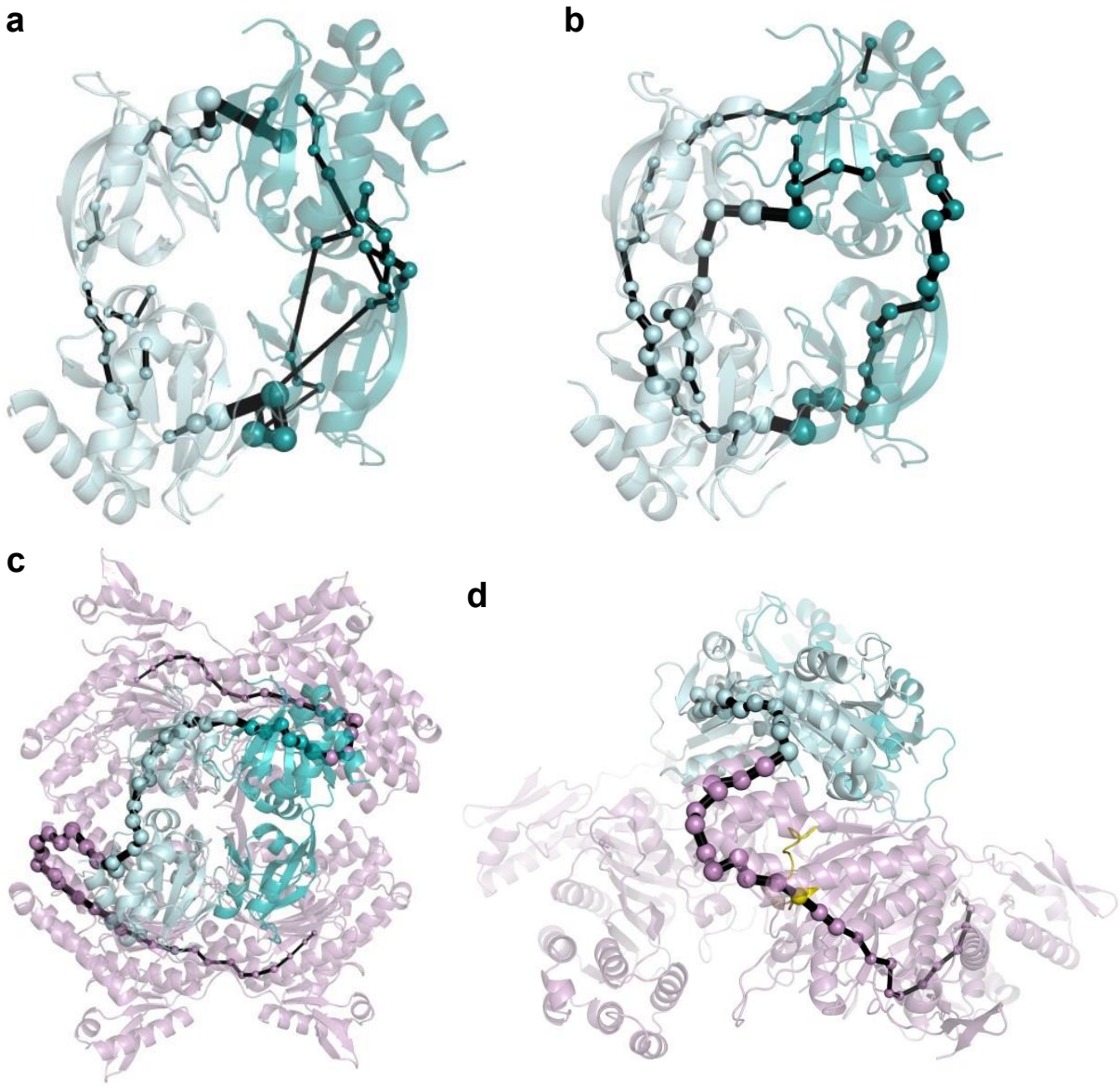

Fig. 5 Effect of *Pa*HisZ binding on *Pa*HisG$_S$ dynamic network. a SPM analysis of nonactivated *Pa*HisG$_S$ dimer. **b** SPM analysis of activated *Pa*HisG$_S$ dimer upon *Pa*HisZ binding (only the catalytic subunits are shown). **c** SPM analysis of *Pa*ATPPRT including *Pa*HisZ residues. **d** Side view (90° rotation) of **c**. *Pa*HisG$_S$ monomers are shown in light and dark teal, while *Pa*HisZ is shown in pink. The histidine binding loop (D256 – I269) is shown in yellow in **d**. The sizes of the edges (black lines) and vertices (spheres) indicate the strength of the network (the larger size the more pathways available, and thus the higher the importance for allosteric communication).

Insights into the dynamics of allosteric rescue of R56A-*Pa*HisGs. Additional MD simulations were performed on both nonactivated and activated R56A-*Pa*HisGS:PRPP:ATP complexes to gather knowledge at the atomic level into the allosteric rescue of this variant. Given the catalytic importance of R32 and R56 and their hypothesized involvement in facilitating leaving group departure, we tracked the distance between the Cζ of each side chain and the Pα of the PP_i moiety of PRPP during our simulations (**Fig. 6a**). It can be gleaned from the data that the R56 side chain displays a bimodal distribution of distances in WT-*Pa*HisGS (**Fig. 6b**). These comprise a peak at ~4.4 Å corresponding to a catalytic conformation in which this side chain forms a salt-bridge with the PRPP PP_i moiety, and another at ~7.8 Å, corresponding to a non-catalytic rotamer of this residue. Binding of *Pa*HisZ shifts the distance distribution towards the catalytically active rotamer (**Fig. 6c**). This furnishes support for *Pa*HisZ binding constraining the conformational dynamics of *Pa*HisGS, fostering a preorganized active site in which the R56 guanidinium group is poised to help stabilize the leaving group at the transition state.

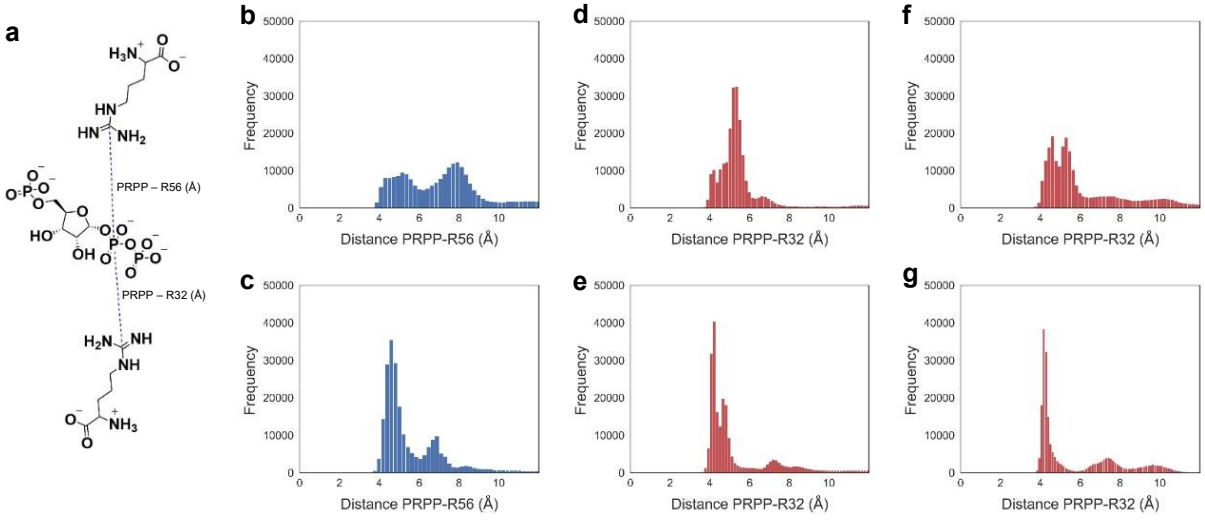

Fig. 6 Effect of *Pa*HisZ binding on *Pa*HisGs R56 and R32 rotamers. a Schematic rendering of the distances (dashed lines) between Cζ of either R56 or R32 and the Pα of the PP_i moiety of PRPP monitored during MD simulations, henceforth referred to as PRPP – R56

distance and PRPP – R32 distance, respectively. **b** Distribution of PRPP – R56 distances in WT-*Pa*HisG$_S$. **c** Distribution of PRPP – R56 distances in WT-*Pa*ATPPRT. **d** Distribution of PRPP – R32 distances in WT-*Pa*HisG$_S$. **e** Distribution of PRPP – R32 distances in WT-*Pa*ATPPRT. **f** Distribution of PRPP – R32 distances in R56A-*Pa*HisG$_S$. **g** Distribution of PRPP – R32 distances in R56A-*Pa*ATPPRT.

Changes in R32 distance distribution upon allosteric activation of WT-*Pa*HisG$_S$ are more subtle, but follow a similar trend as seen for R56, with a peak at ~5.4 Å in WT-*Pa*HisG$_S$ (**Fig. 6d**) shifting to one at ~4.2 Å in WT-*Pa*ATPPRT (**Fig. 6e**) to favor interaction with the PP$_i$ moiety. This effect is exacerbated in the absence of R56, where a broad distribution of R32 distances in R56A-*Pa*HisG$_S$ (**Fig. 6f**) changes to a very narrow peak at ~4.2 Å in WT-*Pa*ATPPRT (**Fig. 6g**). Not only do these simulations reinforce the proposed role of R32 in stabilization of the leaving group at the transition state, but also offer a dynamics-based hypothesis for the allosteric rescue of R56A-*Pa*HisG$_S$: in the absence of R56, *Pa*HisZ binding constrains the conformational ensemble of R56A-*Pa*HisG$_S$ mainly to a population where a very narrow distribution of R32 rotamers is sampled that is optimized for a salt-bridge with the PP$_i$ leaving group at the transition state, partially offsetting the loss of such interaction with R56. It is also tempting to speculate that allosteric rescue of R32A-*Pa*HisG$_S$ by *Pa*HisZ might involve in turn a similar constraint of R56 dynamics to facilitate leaving group departure at the transition state and partially compensate for the loss of R32.

The R32A and R56A substitutions affect the chemical step. The proposal that allosteric rescue of R56A-*Pa*HisG$_S$, and likely R32A-*Pa*HisG$_S$, by *Pa*HisZ is underpinned by constrained *Pa*HisG$_S$ protein dynamics restoring proper active-site electrostatic preorganisation predicts the rescued reaction rates must reflect at least in part the chemical step of the reaction. We have previously demonstrated that replacement of Mg^{2+} by Mn^{2+} increases WT-*Pa*HisG$_S$ k_{cat}, and density-functional theory calculations provided a rationale

for this effect based on more efficient stabilisation of the negative charges by Mn^{2+} via *d*-orbital bonding to the oxygens of the departing PP_i at the transition state.[18] This was corroborating evidence that chemistry was the rate-limiting step in *Pa*HisG$_S$ catalysis, but not in *Pa*ATPPRT where Mn^{2+} had no significant impact on k_{cat}. This observation is reproduced here. At saturating concentrations of both substrates, Mn^{2+} allows product formation to be detected at a WT-*Pa*HisG$_S$ concentration too low to detect reaction with Mg^{2+}, but does not increase the WT-*Pa*ATPPRT reaction rate (**Fig. 7**). In contrast, when R32A-*Pa*ATPPRT and R56A-*Pa*ATPPRT reactions were carried out with Mn^{2+} instead of Mg^{2+}, the rate of product formation increased (**Fig. 7a**), and the apparent first-order rate constants increased by ~5-fold and ~3-fold, respectively, in comparison with those with Mg^{2+} (**Fig. 7b**). This indicates the rates of the rescued mutants reflect the chemical step of the reaction, *i. e.* unlike WT-*Pa*ATPPRT,[18] chemistry is at least partially rate-limiting for R32A-*Pa*ATPPRT and R56A-*Pa*ATPPRT. Surprisingly, the apparent first-order rate constants for R32A-*Pa*HisG$_S$ and R56A-*Pa*HisG$_S$ with Mn^{2+} were measurable, 0.12 ± 0.01 s^{-1} and 0.13 ± 0.01 s^{-1}, respectively, only ~2.5-fold lower than that for WT-*Pa*HisG$_S$ with Mn^{2+}, although still very low in comparison with those for R32A-*Pa*ATPPRT (~54-fold higher) and R56A-*Pa*ATPPRT (~20-fold lower) (**Fig. 7**), suggesting the more efficient charge stabilisation ability of Mn^{2+} can partially rescue the activity of these mutants. This observation highlights the importance of electrostatic catalysis in this enzymatic reaction.

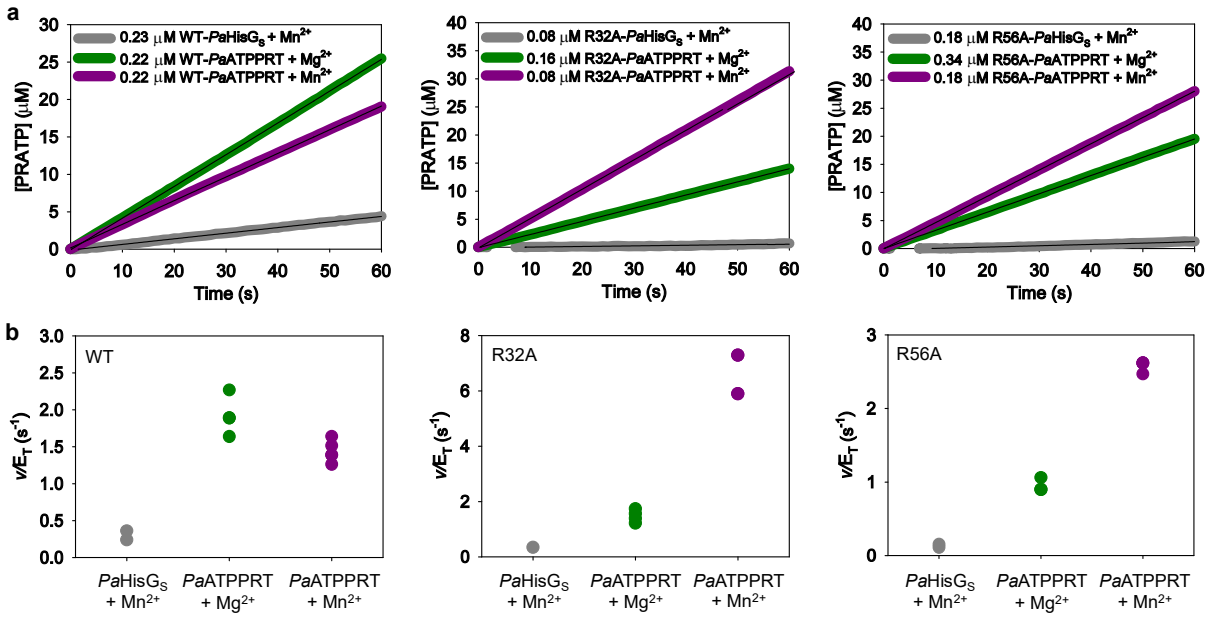

Fig. 7 Effect of Mn^{2+} on R32A-*Pa*ATPPRT and R56A-*Pa*ATPPRT reactions. a PRATP formation time course catalysed by *Pa*HisG$_S$ and *Pa*ATPPRT variants at fixed, saturating concentration of PRPP and ATP. Traces are averages of two to four independent measurements. Black lines are linear regressions of the data. **b** Apparent first-order rate constants for *Pa*HisG$_S$ and *Pa*ATPPRT variants. All data points are shown. Two independent measurements were carried out for *Pa*HisG$_S$ variants, and four for *Pa*ATPPRT. For the latter, where less than four data points are apparent, identical rates for two replicates overlap.

R32A/R56A/K57A-*Pa*HisG$_S$ cannot be rescued by *Pa*HisZ. The hypothesis that R32 and R56 can compensate to a certain extent for the absence of the other in the presence of *Pa*HisZ to restore the electrostatic preorganisation of *Pa*HisG$_S$ active site predicts that removal of both arginine residues would prevent allosteric rescue of catalysis. To test this prediction, the R32A/R56A/K57A-*Pa*HisG$_S$ triple mutant was produced (**Supplementary Fig. 1**) and ESI/TOF-MS analysis resulted in the expected mass (**Supplementary Fig. 2**). DSF indicated that the additional mutation does not alter the T_m of the protein (**Fig. 8a**) as compared with R56A/K57A-*Pa*HisG$_S$ or WT-*Pa*HisG$_S$ T_m. Furthermore, PRPP led to an increase in T_m, showing the triple mutant can bind this substrate. As expected, PRATP

formation could not be detected with R32A/R56A/K57A-*Pa*HisG$_S$ as catalyst (**Fig. 8b**). Upon addition of excess *Pa*HisZ, some PRATP formation could be marginally detected above the assay background noise (**Fig. 8b**), demonstrating R32A/R56A/K57A-*Pa*ATPPRT still retains residual catalytic activity. However, the apparent rate constant is reduced ~777-fold in comparison with that of WT-*Pa*ATPPRT (**Supplementary Fig. 6**), and ~340-fold and ~222-fold in comparison with those of R32A-*Pa*ATPPRT and R56A-*Pa*ATPPRT, respectively (**Supplementary Fig. 13**), in accordance with the proposed necessity for at least one of the two arginine residues to aid in leaving group departure for full catalytic power of *Pa*ATPPRT.

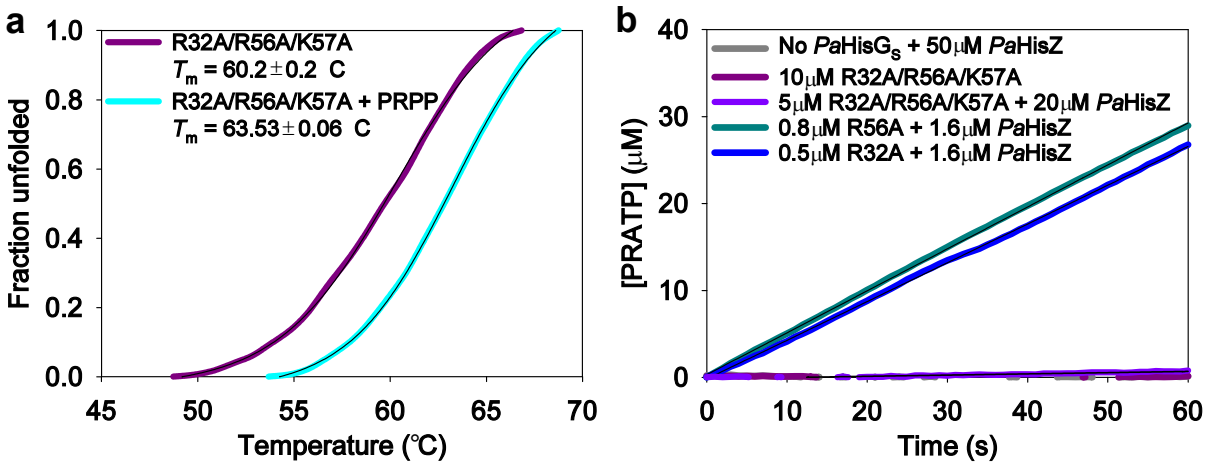

Fig. 8 Biochemical characterisation of R32A/R56A/K57A-*Pa*HisG$_S$. a DSF-based thermal denaturation of R32/R56A/K57A-*Pa*HisG$_S$. Traces are averages of three independent measurements. Lines of best fit to equation (2) are in black. **b** PRATP formation time course catalysed by *Pa*HisG$_S$ variants. Traces are averages of two to four independent measurements. Black lines are linear regressions of the data.

Discussion

Rescue of catalytically impaired enzyme mutants is well established, but not as observed for *Pa*ATPPRT. Chemical rescue by small molecules that mimic missing residue

side chains is a useful tool to probe the function of active-site residues in catalysis,[42] and a hyper-nucleophilic cholesterol analogue in which an –OOH group replaces the sterol –OH group could rescue the base-catalysed endoproteolytic activity of a mutant hedgehog protein where the catalytically essential aspartate general base was mutated to an alanine, which rendered the reaction highly impaired with the natural substrate.[43] A catalytically compromised receptor tyrosine kinase carrying mutations in the activation loop tyrosine residues that would otherwise be autophosphorylated could be allosterically rescued by the juxtamembrane segment via autophosphorylation of this segment's Y687, but in this case the effect of the phospho-Y687 is exerted by direct interaction with arginine residues that normally interact with the phosphorylated tyrosine residues in the activation loop.[44] In hetero-tetrameric tryptophan synthase, where catalysis by the β subunit is allosterically activated by the α subunit, the catalytically inactive E109A mutant of the β subunit could not be rescued by the α subunit, but the activity of the E109A-$\alpha_2\beta_2$ complex could be partially restored by CsCl, possibly by modulation of the conformational ensemble of the complex.[45] In human prolyl isomerase CypA, the second-shell S99T mutation, which is highly detrimental to catalysis, can be partially counteracted by additional mutations outside the active site which rescue the dynamics of interconversion between two essential conformations.[7]

*Pa*ATPPRT is unique because the rescue of catalytically compromised *Pa*HisG$_S$ mutants by *Pa*HisZ, and even by the orthologous *Ab*HisZ, is truly allosteric since the regulatory subunit binds far from the active site where the mutations exert a detrimental effect on transition state stabilisation. The narrowing of the distribution of states sampled by the *Pa*HisG$_S$ upon *Pa*HisZ binding has a direct impact on the positioning and orientation of R32 and R56, which are better poised to facilitate leaving group departure by electrostatic stabilisation of the PP_i negative charges. This implies allosteric activation of catalysis in *Pa*ATPPRT involves modulation of the conformational flexibility of the holoenzyme and

electrostatic preorganisation of the active site. The catalytic recruitment of R32 and R56 in concert with Mg^{2+} to stabilise PP_i is reminiscent of that of arginine residues in adenylate kinase to promote phosphate transfer from ADP to AMP, where thermally equilibrated protein motions were also proposed to help achieve optimal electrostatic preorganisation.[46]

Another important aspect of the allosterically rescued R32A- and R56A-*Pa*ATPPRT is that k_{cat} is at least partially limited by the chemical step, a drastic change from WT-*Pa*ATPPRT in which k_{cat} is determined by product release.[18] Electrostatic preorganisation exerts its effect on catalysis at the chemical step, *i. e.* as the reaction progresses from the preorganised Michaelis complex to the transition state. Thus it is paramount that an experimentally measured rate constant purporting to reflect any coupling of protein motions to the preorganisation of the Michaelis complex be limited by the chemical step.[9,47] This is what is observed with the allosteric rescue of the catalytically compromised mutants of *Pa*HisG$_S$, establishing a direct connection between *Pa*HisZ-modulated rotamers of R32 and R56 and electrostatic preorganisation of the active site, which is required for optimal catalysis.

Methods

Reagents. All commercially available chemicals were used without further purification. BaseMuncher endonuclease was purchased from AbCam. Ampicillin, dithiothreitol (DTT), isopropyl β-D-1-thiogalactopyranoside (IPTG) and 2-(*N*-morpholino)ethanesulfonic acid-sodium dodecyl sulfate (MES-SDS) were purchased from Formedium. DH5α chemically competent *E. coli,* DpnI were purchased from New England Biolabs (NEB). QIAprep Spin Miniprep, PCR clean-up and Plasmid Midi kits were from Qiagen. Ethylenediaminetetraacetic acid (EDTA)-free Cømplete protease inhibitor cocktail was from Roche. ATP, C43(DE3) and BL21(DE3) chemically competent *E. coli*, D_2O,

glycerol, histidine, imidazole, lysozyme, PRPP, potassium chloride, tricine, were purchased from Sigma-Aldrich. Agarose, dNTPSs, kanamycin, 4-(2-hydroxyethyl)piperazine-1-ethanesulfonic acid (HEPES), $MgCl_2$, NaCl, PageRuler Plus Prestained protein ladder, PageRuler^{TM} Plus Prestained protein ladder, and SYPRO orange protein gel stain were from ThermoFisher Scientific. DNA oligonucleotide primers were synthesised by Integrated DNA technologies (IDT).

Site-directed mutagenesis of *Pa*HisGs. Site-directed mutagenesis was carried out with overlapping primers according to the method of Liu and Naismith.[48] Primer sequences are listed in **Supplementary Table 5**. For the triple mutant R32A/R56A/K57A-*Pa*HisG$_S$, the R56A/K57A-*Pa*HisG$_S$ expression vector was used as DNA template. For all other mutants, WT-*Pa*HisG$_S$ expression vector was used. Correct insertion of each mutation was confirmed by DNA sequencing performed by either Eurofins Genomics or DNA Sequencing & Services at University of Dundee.

Protein expression and purification. *Pa*HisG$_S$, *Pa*HisZ, *Mycobacterium tuberculosis* pyrophosphatase (*Mt*PPase), and tobacco etch virus protease (TEVP) were produced as previously described.[28] *Ab*HisZ was produced as previously reported.[26] All *Pa*HisG$_S$ mutants were expressed and purified by the same protocol as *Pa*HisG$_S$.[28] His-tagged *Pa*HisZ was purified by the same protocol as *Pa*HisZ up to and including the first chromatography,[28] after which fractions producing a single band at the expected MW in SDS-PAGE were pooled and dialysed against 2 × 2L of 20 mM HEPES pH 8.0, concentrated using 10,000 molecular weight cutoff (MWCO) ultrafiltration membranes (Millipore), aliquoted and stored at −80 °C. His-tagged *Pa*HisZ, C115A-, C115S-, D179A-, D179A-, R32A-, R56A-, R56A/K57A-, and R32A/R56A/K57A-*Pa*HisG had their intact mass determined by ESI/TOF-MS, and D179N-*Pa*HisG$_S$ tryptic peptides underwent MS/MS analysis to confirm the mutation, all performed by the BSRC Mass-Spectrometry and Proteomics Facility at the

University of St Andrews. The concentration of WT-*Pa*HisG$_S$, WT-*Pa*HisZ, *Mt*PPase and TEVP was determined as published.[28] The concentration of His-tagged *Pa*HisZ and *Pa*HisG$_S$ mutants was determined spectrophotometrically (NanoDrop) at 280 nm based on the theoretical extinction coefficients (ε_{280}) calculated in the ProtParam tool of Expasy: ε_{280} of 27,930 M^{-1} cm^{-1} for His-tagged *Pa*HisZ; 8,940 M^{-1} cm^{-1} for all *Pa*HisG$_S$ mutants.

DSF. DSF measurements (λ_{ex} = 490 nm, λ_{em} = 610 nm) were performed in 96-well plates on a Stratagene Mx3005p instrument. Reactions (50 µL) contained 100 mM tricine, 100 mM KCl, 15 mM $MgCl_2$, 4 mM DTT pH 8.5, 7 µM enzyme, and either 0 mM or 2 mM PRPP, with 5X Sypro Orange (Invitrogen) added to each well. Thermal denaturation curves were recorded over a temperature range of 25 °C – 93 °C with increments of 1 °C min^{-1}. Control curves lacked protein and were subtracted from curves containing protein. All measurements were carried out in triplicate.

Analytical size-exclusion chromatography. Analytical size-exclusion chromatography was performed on a Superdex 200 10/300 GL column (GE Healthcare) attached to a Bio-Rad NGC FPLC at 4 °C. WT-, C115S-, R32A-, R56A- and R56/K57A-*Pa*HisG$_S$ (1 mg mL^{-1}, pre-incubated with DTT [2 mM]) were loaded onto the column (equilibrated with 20 mM HEPES pH 8.0) and eluted with 1 column volume of 20 mM HEPES pH 8.0 at 0.225 mL min^{-1}.

Enzyme activity assay. Unless stated otherwise, all reactions (500 µL) were carried out in 1-cm path-length quartz cuvettes under initial-rate conditions at 20 °C, and the increase in absorbance at 290 nm due to the formation of PRATP (ε_{290} = 3,600 M^{-1} cm^{-1})[35] was monitored for 60 s in a Shimadzu UV-2600 spectrophotometer in 100 mM tricine, 100 mM KCl, 15 mM $MgCl_2$, 4 mM DTT, pH 8.5, 10 µM *Mt*PPase, and various concentrations of

PRPP and ATP. Cuvettes were incubated in the spectrophotometer at 20 °C for 3 min before reaction was initiated by the addition of PRPP. Control reactions lacked enzyme.

Activity of *Pa*HisG$_S$ mutants in the absence of *Pa*HisZ. Activity of C115A-, C115S-, D179A-, D179N-, R32A-, R56A- and R56A/K57A-*Pa*HisG (5 μM) was assayed for 60 s in the presence of 5.6 mM ATP and 2 mM PRPP. WT-*Pa*HisG$_S$ (5 μM) was included in as a positive control. Additionally, the activity of C115S-, R32A-, R56A- and R56A/K57A-*Pa*HisG (10 μM) was assayed for 870 s in the presence of 5.6 mM ATP and 2 mM PRPP.

Determination of apparent K_D for *Pa*HisZ, His-tagged *Pa*HisZ and *Ab*HisZ. Initial velocities were measured in 5.6 mM ATP and 2 mM PRPP. For *Pa*HisZ K_D, 0.42 μM WT-, 0.59 μM C115A-, 1.1 μM R32A-, 1.1 μM R56A- and 1.7 μM R56A/K57A-*Pa*HisG$_S$ were assayed in the presence of varying concentrations of *Pa*HisZ (0 – 5.1 μM for WT-*Pa*HisG$_S$; 0 – 15 μM for C115S-*Pa*HisG$_S$; 0 – 8 μM for R32A-*Pa*HisG$_S$; 0 – 15 μM for R56A-*Pa*HisG$_S$; and 0 – 11 μM for R56A/K57A-*Pa*HisG$_S$). For His-tagged *Pa*HisZ K_D, 0.23 μM WT-, 0.49 μM R32A-, and 0.79 μM R56A-*Pa*HisG$_S$ were assayed in the presence of varying concentrations of His-tagged-*Pa*HisZ (0 – 1.6 μM). For *Ab*HisZ K_D, 0.19 μM WT- and 2.5 μM R56A-*Pa*HisG$_S$ were assayed in the presence of varying concentration of *Ab*HisZ (0 – 19.7 μM for WT-*Pa*HisG$_S$; 0 – 26.9 μM for R56A-*Pa*HisG$_S$). Alternatively, 1 μM C115S-, 1 μM R32A-, 1 μM R56A-, and 1.6 μM R56A/K57A-*Pa*HisG$_S$ were assayed in the presence of 20 μM BSA.

WT-, C115A-, D179A- and D179N-*Pa*HisG$_S$ saturation kinetics. Initial rates for 3.4 μM WT-, 10.1 μM C115A-, 9.2 μM D179A- and 10.0 μM D179N-*Pa*HisG$_S$ were measured at saturating concentrations of one substrate (either 2 mM PRPP or 5.6 mM ATP) and varying concentrations of the other, either ATP (0 – 5.6 mM) or PRPP (0 – 2 mM).

C115S-, R32A-, R56A- and R56A/K57A-*Pa*ATPPRT saturation kinetics. Initial rates for 0.4 μM WT-, 0.5 μM C115S-, 0.9 μM R32A-, 0.9 μM R56A-, and 1.2 μM R56A/K57A-*Pa*ATPPRT were measured at saturating concentrations of one substrate (either 2 mM PRPP or 5.6 mM ATP) and varying concentrations of the other, either ATP (0 – 5.6 mM) or PRPP (0 – 2 mM). Alternatively, initial rates for 0.22 μM WT-*Pa*ATPPRT with His-tagged *Pa*HisZ replacing *Pa*HisZ were measured at saturating concentration of one substrate (wither 2 mM PRPP or 2.8 mM ATP) and varying concentrations of the other, either ATP (0 – 2.8 mM) or PRPP (0 – 2 mM).

WT- and R56A-*Pa*HisG$_S$/*Ab*HisZ saturation kinetics. Initial rates for 0.26 μM WT-, and 2.5 μM R56A-*Pa*HisG$_S$/*Ab*HisZ (the latter was assumed from the concentrations of 2.5 μM R56A-*Pa*HisG$_S$ and 19.7 μM *Ab*HisZ) were measured at saturating concentrations of one substrate (either 2 mM PRPP or 2.8 mM ATP for WT- and 5.6 mM for R56A-*Pa*HisG$_S$/*Ab*HisZ) and varying concentrations of the other, either ATP (0 – 2.8 mM for WT-; 0 – 5.6 mM for R56A-*Pa*HisG$_S$/*Ab*HisZ) or PRPP (0 – 2 mM). For WT-*Pa*HisG$_S$/*Ab*HisZ, background rates of control reactions lacking *Ab*HisZ were subtracted.

Inhibition by histidine. Initial rates for 0.43 μM C115S-, 0.49 μM R32A-, 0.79 μM R56A-, and 2.6 μM R56A/K57A-*Pa*HisG$_S$ with either 3.2 μM His-tagged *Pa*HisZ (for C115S-, R32A-, and R56A-*Pa*HisG$_S$) or 6.4 μM His-tagged *Pa*HisZ (for R56A/K57A-*Pa*HisG$_S$) were measured at saturating concentrations of both substrates (2 mM PRPP and 5.6 mM ATP) in the presence and absence of 1 mM histidine. Initial rates for 0.26 μM WT-, and 2.5 μM R56A-*Pa*HisG$_S$/*Ab*HisZ (the latter was assumed from the concentrations of 2.5 μM R56A-*Pa*HisG$_S$ and 19.7 μM *Ab*HisZ) were measured at saturating concentrations of both substrates (2 mM PRPP and either 2.8 mM ATP for WT- or 5.6 mM for R56A-*Pa*HisG$_S$/*Ab*HisZ) in the presence and absence of 1 mM histidine.

^{31}P-NMR spectra of the *Pa*HisG$_S$ and *Pa*ATPPRT reactions. In 500-μL reactions, either 10 μM R56A-, 10 μM C115S-, 20 μM R32A- or 20 μM R56A/K57A-*Pa*HisG$_S$ was incubated in the presence or absence of 30 μM *Pa*HisZ in 100 mM tricine, 100 mM KCl, 15 mM $MgCl_2$, 4 mM DTT, pH 8.5, 20 μM *Mt*PPase, 2 mM PRPP and 5.6 mM ATP for 1 hour at 20 °C. Proteins were removed by passage through 10,000 MWCO Vivaspin centrifugal concentrators, after which 100 μL of D_2O were added to each sample. ^{31}P-NMR spectra were recorded on either a Bruker AV 400 or Bruker AVII 400 spectrophotometer, and a total of 128 scans were collected for each sample.

Activity of R32A/R56A/K57A-*Pa*HisG$_S$. R32A/R56A/K57A-*Pa*HisG$_S$ (10 μM in the absence of His-tagged *Pa*HisZ and 5 μM in the presence of 20 μM His-tagged *Pa*HisZ) was assayed for catalytic activity under initial-rate conditions in the presence of 5.6 mM ATP and 2 mM PRPP. R32A- and R56A-*Pa*HisG$_S$ (0.5 μM and 0.8μM, respectively) in the presence of 1.6 μM His-tagged *Pa*HisZ were assayed as positive controls for allosteric rescue. Negative controls contained 50 μM His-tagged *Pa*HisZ but lacked *Pa*HisG$_S$.

WT-, R32A- and R56A-*Pa*ATPPRT activities with Mn^{2+}. Initial rates were determined for 0.23 μM WT-*Pa*HisG$_S$, 0.22 μM WT-*Pa*ATPPRT, 0.08 μM R32A-*Pa*HisG$_S$, 0.08 μM R32A-*Pa*ATPPRT, 0.18 μM R56A-*Pa*HisG$_S$, and 0.18 μM R56A-*Pa*ATPPRT in 100 mM tricine, 100 mM KCl, 15 mM $MnCl_2$, 4 mM DTT, pH 8.5 and 10 μM *Mt*PPase at saturating concentrations of ATP (1.4 mM for WT enzymes; 5.6 mM for mutant enzymes) and PRPP (1 mM for WT enzymes; 2 mM for mutant enzymes). Initial rates were also determined for 0.22 μM WT-*Pa*ATPPRT, 0.16 μM R32A-*Pa*ATPPRT, and 0.34 μM R56A-*Pa*ATPPRT in 100 mM tricine, 100 mM KCl, 15 mM $MgCl_2$, 4 mM DTT, pH 8.5 and 10 μM *Mt*PPase at saturating concentrations of ATP (5.6 mM) and PRPP (2 mM).

Crystallisation, X-ray data collection and data processing. Crystals of R56A-*Pa*HisG$_S$ were grown, soaked in PRPP and ATP and stored as described for WT-*Pa*HisG$_S$,[29] whereas crystals of R56A-*Pa*ATPPRT were grown as described for WT-*Pa*ATPPRT[28] and soaked in PRPP and ATP and stored as described for WT-*Pa*ATPPRT.[29] X-ray diffraction data for R56A-*Pa*HisG$_S$ were collected in house as previously reported[28] and processed with iMosflm,[49] while data for R56A-*Pa*ATPPRT were collected at Diamond Light Source (UK) and processed at the automated processing pipeline at Diamond with Xia2[50] integrated with DIALS.[51] R56A-*Pa*HisG$_S$ and R56A-*Pa*ATPPRT structures were solved by molecular replacement in MOLREP using WT-*Pa*HisG$_S$:PRPP:ATP (PDB ID: 6FCT) and WT-*Pa*ATPPRT:PRPP:ATP (PDB ID: 6FU2)[29] structures, respectively, as search models. Structures were refined using cycles of model building with COOT[52] and refinement with Refmac.[53] ATP was modelled at either 70% or 80% occupancy in R56A-*Pa*ATPPRT.

MD simulations. Molecular dynamics simulations were performed on WT-*Pa*HisG$_S$:PRPP:ATP (PDB ID: 6FCT),[29] WT-*Pa*ATPPRT:PRPP:ATP (PDB ID: 65FU2),[29] R56A-*Pa*HisG$_S$:PRPP:ATP (PDB ID: 7Z8U), and R56A-*Pa*ATPPRT:PRPP:ATP (PDB ID: 7Z6R). Any missing regions in the structures were reconstructed using Modeller v. 9.23.[54] In the case of *Pa*HisZ, these were reconstructed using the lowest energy conformation prediction combined with visual inspection; in other systems, *Pa*HisG$_S$ was used as a template (as well as for modeling the position of the binding site magnesium ions). A distal extra Mg^{2+} was deleted from R56A-*Pa*HisG$_S$:PRPP:ATP structure. Finally, the adenine moiety of ATP was flipped into a catalytically productive conformation in all the starting structures. Protonation states of all titratable residues were determined based on a combination of empirical screening using PROPKA v3.1,[55] and visual inspection of the local environment. The E122, E163 and H103 side chains were predicted to be found in their ionized states.

Partial charges for the ligand PRPP, were calculated *in vacuo* at the HF/6-31G* level of theory using Gaussian 16 Rev. A.03,[56] and fitted using the standard restrained electrostatic potential (RESP) protocol as implemented in Antechamber[57] (**Supplementary Table 6**). All other force field terms for PRPP were then described using the Amber force field ff14SB[58] together with revised parameters to describe bioorganic phosphates.[59] The parameters for ATP were taken from the literature.[60] We used an octahedral cationic dummy model to describe Mg^{2+}, following from previous successful results using this model.[61,62]

All MD simulations were performed using the GPU-accelerated version of Amber16,[63] with the protein and water molecules described using the amber force field ff14SB[58] and the TIP3P[64] water model, respectively. All systems were solvated in an octahedral box of water molecules, extended 8 Å from the closest solute molecule in every direction. Each system was neutralized by adding Na^+ or Cl^- counterions to ensure overall charge neutrality. Counterions were placed using the "addions" approach as implemented in Amber16.[63] The dimeric and hetero-octameric forms of the enzyme were simulated for 10 × 600 ns and 5 × 600 ns, respectively, in the NPT ensemble. The solvated systems were first minimized using 5,000 steps of steepest descent minimization with 500 kcal mol^{-1} $Å^{-2}$ positional restraints placed on all solute atoms to minimize all hydrogen atoms and solvent molecules, followed by 5,000 steps of conjugate gradient minimization, with the restraint dropped to 5 kcal mol^{-1} $Å^{-2}$. The minimized system was then heated from 0 to 300 K in an NVT ensemble over 250 ps of simulation time using the Berendsen thermostat[65] with a time constant of 1 ps for the coupling while maintaining the 5 kcal mol^{-1} $Å^{-2}$ restraint. The restraint was then limited to heavy atoms of the substrates for a further 200 ps of NPT equilibration, followed by 200 ps of unrestrained equilibration. After minimization, five distance restraints were applied during the simulations to PRPP and ATP (four to PRPP and one to ATP) to prevent dissociation of the substrates from the active site throughout the MD simulations (see

Supplementary Table 7 for a full list of the restraints applied). Note that no restraints were applied between the substrate and any of the regions of interest to ensure full conformational freedom of such regions.

All production-quality simulations were performed using a 2 fs time step, with the SHAKE algorithm[66] used to constrain all bonds containing hydrogen atoms. Temperature and pressure were controlled by the Langevin thermostat with a collision frequency of 1 ps^{-1},[67] and the Berendsen barostat with a 1 ps coupling constant.[65] A cutoff of 8 Å was applied to all non-bonded interactions, with the long range electrostatics being evaluated using the particle mesh Ewald (PME) approach.[68] The root mean square deviations (RMSD) of all backbone atoms for each system during the production runs is shown in **Supplementary Fig 14.** Unless stated otherwise, all analysis was performed using CPPTRJ.[69] Principal Component Analysis was performed in Cartesian coordinate space on the Cα atoms of the shared dimeric region of all the studied systems, by first root-mean-square fitting all the trajectories to the WT-*Pa*HisG$_S$ crystal structure. DCCMs were generated with Bio3D.[70]

Kinetics and thermal denaturation data analysis. Kinetic and thermal denaturation data were analysed by the nonlinear regression function of SigmaPlot 14.0 (SPSS Inc.). Data points with error bars represent mean ± SEM of two to four independent measurements, and kinetic and equilibrium constants are given as mean ± fitting error. Alternatively, all data points were plotted. Substrate saturation curves at a fixed concentration of the co-substrate were fitted to equation (1). Thermal denaturation data were fitted to equation (2). Initial rate data at varying concentrations of HisZ were fitted to either equation (3) or (5). The concentration of ATPPRT at any concentration of *Pa*HisG$_S$ and either *Pa*HisZ or *Ab*HisZ was calculated according to equation (4). In equations 1 – 5, k_{cat} is the steady-state turnover number, v is the initial rate, E_T is total enzyme concentration, K_M is the apparent Michaelis constant, S is the concentration of the varying substrate, V_{max} is the maximal velocity, F_U is

fraction unfolded, T is the temperature in °C, T_m is the melting temperature, c is the slope of the transition region, and LL and UL are folded and unfolded baselines, respectively, h is the Hill coefficient, $K_{0.5}$ is the concentration of *Ab*HisZ at the inflection point, G is the concentration of *Pa*HisG$_S$, Z is the concentration of either *Pa*HisZ or *Ab*HisZ, K_D^{app} is the apparent equilibrium dissociation constant, and *ATPPRT* is the concentration of either *Pa*ATPPRT of *Pa*HisG$_S$/*Ab*HisZ complex.

$$\frac{v}{E_T} = \frac{k_{cat}S}{K_M+S} \qquad (1)$$

$$F_U = LL + \frac{UL-LL}{1+e^{(T_m-T)/c}} \qquad (2)$$

$$v = V_{max}\frac{(G+Z+K_D^{app})-\sqrt{(G+Z+K_D^{app})^2-4GZ}}{2G} \qquad (3)$$

$$ATPPRT = \frac{(G+Z+K_D^{app})-\sqrt{(G+Z+K_D^{app})^2-4GZ}}{2} \qquad (4)$$

$$v = \frac{V_{max}Z^h}{K_{0.5}+Z^h} \qquad (5)$$

Data availability

The data supporting the findings of this study are available from the corresponding author upon reasonable request. Structure factor amplitudes and coordinates for the crystal structures of R56A-*Pa*HisG$_S$:PRPP:ATP and R56A-*Pa*ATPPRT:PRPP:ATP were deposited to the Protein Data Bank under accession numbers 7Z8U and 7Z6R, respectively. All protein mass spectrometry data were deposited to FigShare and under DOIs 10.6084/m9.figshare.19658367 and 10.6084/m9.figshare.19658229. Parameters used to describe the ligands and the magnesium dummy model, input files, starting structures, topologies and snapshots from our molecular dynamics simulations are available for download from Zenodo (https://zenodo.org) under DOI: 10.5281/zenodo.6565959.

References

1 Goodey, N. M. & Benkovic, S. J. Allosteric regulation and catalysis emerge via a common route. *Nat. Chem. Biol.* **4**, 474-482 (2008).

2 Hammes, G. G., Benkovic, S. J. & Hammes-Schiffer, S. Flexibility, diversity, and cooperativity: pillars of enzyme catalysis. *Biochemistry* **50**, 10422-10430 (2011).

3 Kern, D. & Zuiderweg, E. R. The role of dynamics in allosteric regulation. *Curr. Opin. Struct. Biol.* **13**, 748-757 (2003).

4 Warshel, A. *et al.* Electrostatic Basis for Enzyme Catalysis. *Chem. Rev.* **106**, 3210-3235 (2006).

5 Otten, R. *et al.* How directed evolution reshapes the energy landscape in an enzyme to boost catalysis. *Science* **370**, 1442-1446 (2020).

6 Silva, R. G., Murkin, A. S. & Schramm, V. L. Femtosecond dynamics coupled to chemical barrier crossing in a Born-Oppenheimer enzyme. *Proc. Natl. Acad. Sci. USA* **108**, 18661-18665 (2011).

7 Otten, R. *et al.* Rescue of conformational dynamics in enzyme catalysis by directed evolution. *Nat. Commun.* **9**, 1314 (2018).

8 Pudney, C. R. *et al.* Fast protein motions are coupled to enzyme H-transfer reactions. *J. Am. Chem. Soc.* **135**, 2512-2517 (2013).

9 Warshel, A. & Bora, R. P. Perspective: Defining and quantifying the role of dynamics in enzyme catalysis. *J. Chem. Phys.* **144**, 180901 (2016).

10 Schramm, V. L. & Schwartz, S. D. Promoting vibrations and the function of enzymes. emerging theoretical and experimental convergence. *Biochemistry* **57**, 3299-3308 (2018).

11 Pisco, J. P. *et al.* Uncoupling conformational states from activity in an allosteric enzyme. *Nat. Commun.* **8**, 203 (2017).

12 Fan, Y., Cross, P. J., Jameson, G. B. & Parker, E. J. Exploring modular allostery via interchangeable regulatory domains. *Proc. Natl. Acad. Sci. USA* **115**, 3006-3011 (2018).

13 Pedreno, S., Pisco, J. P., Larrouy-Maumus, G., Kelly, G. & de Carvalho, L. P. Mechanism of feedback allosteric inhibition of ATP phosphoribosyltransferase. *Biochemistry* **51**, 8027-8038 (2012).

14 Pádua, R. A. P. *et al.* Mechanism of activating mutations and allosteric drug inhibition of the phosphatase SHP2. *Nat. Commun.* **9**, 4507 (2018).

15 Buller, A. R. *et al.* Directed evolution of the tryptophan synthase beta-subunit for stand-alone function recapitulates allosteric activation. *Proc. Natl. Acad. Sci. USA* **112**, 14599-14604 (2015).

16 Schendzielorz, G. *et al.* Taking control over control: use of product sensing in single cells to remove flux control at key enzymes in biosynthesis pathways. *ACS Synth. Biol.* **3**, 21-29 (2014).

17 Casey, A. K., Schwalm, E. L., Hays, B. N. & Frantom, P. A. V-type allosteric inhibition is described by a shift in the rate-determining step for α-isopropylmalate synthase from *Mycobacterium tuberculosis*. *Biochemistry* **52**, 6737-6739 (2013).

18 Fisher, G. *et al.* Allosteric activation shifts the rate-limiting step in a short-form ATP phosphoribosyltransferase. *Biochemistry* **57**, 4357-4367 (2018).

19 Thomson, C. M., Alphey, M. S., Fisher, G. & da Silva, R. G. Mapping the structural path for allosteric inhibition of a short-form ATP phosphoribosyltransferase by histidine. *Biochemistry* **58**, 3078-3086 (2019).

20 Pacholarz, K. J. *et al.* Hybrid mass spectrometry approaches to determine how l-histidine feedback regulates the enzyzme MtATP-phosphoribosyltransferase. *Structure* **25**, 730-738 (2017).

21 Bunzel, H. A. *et al.* Evolution of dynamical networks enhances catalysis in a designer enzyme. *Nat. Chem.* **13**, 1017-1022 (2021).

22 Ames, B. N., Martin, R. G. & Garry, B. J. The first step of histidine biosynthesis. *J. Biol. Chem.* **236**, 2019-2026 (1961).

23 Martin, R. G. The First Enzyme in Histidine Biosynthesis: The nature of feedback inhibition by histidine. *J. Biol. Chem.* **238**, 257-268 (1963).

24 Kulis-Horn, R. K., Persicke, M. & Kalinowski, J. *Corynebacterium glutamicum* ATP-phosphoribosyl transferases suitable for L-histidine production-Strategies for the elimination of feedback inhibition. *J. Biotechnol.* **206**, 26-37 (2015).

25 Cho, Y., Ioerger, T. R. & Sacchettini, J. C. Discovery of novel nitrobenzothiazole inhibitors for *Mycobacterium tuberculosis* ATP phosphoribosyl transferase (HisG) through virtual screening. *J. Med. Chem.* **51**, 5984-5992 (2008).

26 Read, B. J. *et al.* Allosteric inhibition of *Acinetobacter baumannii* ATP phosphoribosyltransferase by protein:dipeptide and protein:protein interactions. *ACS infect. Dis.* **8**, 197-209 (2022).

27 Moggre, G. J., Poulin, M. B., Tyler, P. C., Schramm, V. L. & Parker, E. J. Transition state analysis of adenosine triphosphate phosphoribosyltransferase. *ACS Chem. Biol.* **12**, 2662-2670 (2017).

28 Stroek, R. *et al.* Kinetics and structure of a cold-adapted hetero-octameric ATP phosphoribosyltransferase. *Biochemistry* **56**, 793-803 (2017).

29 Alphey, M. S. *et al.* Catalytic and anticatalytic snapshots of a short-form ATP phosphoribosyltransferase. *ACS Catal.* **8**, 5601–5610, doi:10.1021/acscatal.8b00867 (2018).

30 Bovee, M. L., Champagne, K. S., Demeler, B. & Francklyn, C. S. The quaternary structure of the HisZ-HisG N-1-(5'-phosphoribosyl)-ATP transferase from *Lactococcus lactis*. *Biochemistry* **41**, 11838-11846 (2002).

31 Champagne, K. S., Sissler, M., Larrabee, Y., Doublie, S. & Francklyn, C. S. Activation of the hetero-octameric ATP phosphoribosyl transferase through subunit interface rearrangement by a tRNA synthetase paralog. *J. Biol. Chem.* **280**, 34096-34104 (2005).

32 Sissler, M. *et al.* An aminoacyl-tRNA synthetase paralog with a catalytic role in histidine biosynthesis. *Proc. Natl. Acad. Sci. USA* **96**, 8985-8990 (1999).

33 Vega, M. C. *et al.* Regulation of the hetero-octameric ATP phosphoribosyl transferase complex from *Thermotoga maritima* by a tRNA synthetase-like subunit. *Mol. Microbiol.* **55**, 675-686 (2005).

34 Livingstone, E. K., Mittelstadt, G., Given, F. M. & Parker, E. J. Independent catalysis of the short form HisG from *Lactococcus lactis*. *FEBS Lett.* **590**, 2603-2610 (2016).

35 Smith, D. W. & Ames, B. N. Phosphoribosyladenosine monophosphate, an intermediate in histidine biosynthesis. *J. Biol. Chem.* **240**, 3056-3063 (1965).

36 Popovych, N., Sun, S., Ebright, R. H. & Kalodimos, C. G. Dynamically driven protein allostery. *Nat. Struct. Mol. Biol.* **13**, 831-838 (2006).

37 Agoni, C., Ramharack, P. & Soliman, M. E. S. Allosteric inhibition induces an open WPD-loop: a new avenue towards glioblastoma therapy. *RSC Adv.* **8**, 40187-40197 (2018).

38 Townsend, P. D. *et al.* The role of protein-ligand contacts in allosteric regulation of the *Escherichia coli* catabolite activator protein. *J. Biol. Chem.* **290**, 22225-22235 (2015).

39 Romero-Rivera, A., Garcia-Borràs, M. & Osuna, S. Role of conformational dynamics in the evolution of retro-aldolase activity. *ACS Catal.* **7**, 8524-8532 (2017).

40 Maria-Solano, M. A., Kinateder, T., Iglesias-Fernández, J., Sterner, R. & Osuna, S. *In silico* identification and experimental validation of distal activity-enhancing mutations in tryptophan synthase. *ACS Catal.* **11**, 13733-13743 (2021).

41 Nevin Gerek, Z., Kumar, S. & Banu Ozkan, S. Structural dynamics flexibility informs function and evolution at a proteome scale. *Evol. Appl.* **6**, 423-433 (2013).

42 Toney, M. D. & Kirsch, J. F. Direct Brønsted analysis of the restoration of activity to a mutant enzyme by exogenous amines. *Science* **243**, 1485-1488 (1989).

43 Ciulla, D. A., Jorgensen, M. T., Giner, J. L. & Callahan, B. P. Chemical bypass of general base catalysis in Hedgehog protein cholesterolysis using a hyper-nucleophilic substrate. *J. Am. Chem. Soc.* **140**, 916-918 (2018).

44 Plaza-Menacho, I. *et al.* RET functions as a dual-specificity kinase that requires allosteric inputs from juxtamembrane elements. *Cell Rep.* **17**, 3319-3332 (2016).

45 Ruvinov, S. B., Ahmed, S. A., McPhie, P. & Miles, E. W. Monovalent cations partially repair a conformational defect in a mutant tryptophan synthase alpha 2 beta 2 complex (beta-E109A). *J. Biol. Chem.* **270**, 17333-17338 (1995).

46 Kerns, S. J. *et al.* The energy landscape of adenylate kinase during catalysis. *Nat. Struct. Mol. Biol.* **22**, 124-131 (2015).

47 Loveridge, E. J., Behiry, E. M., Guo, J. & Allemann, R. K. Evidence that a 'dynamic knockout' in *Escherichia coli* dihydrofolate reductase does not affect the chemical step of catalysis. *Nat. Chem.* **4**, 292-297 (2012).

48 Liu, H. & Naismith, J. H. An efficient one-step site-directed deletion, insertion, single and multiple-site plasmid mutagenesis protocol. *BMC Biotechnol.* **8**, 91 (2008).

49 Battye, T. G., Kontogiannis, L., Johnson, O., Powell, H. R. & Leslie, A. G. iMOSFLM: a new graphical interface for diffraction-image processing with MOSFLM. *Acta Crystallogr. D Biol. Crystallogr.* **67**, 271-281 (2011).

50 Winter, G. xia2: an expert system for macromolecular crystallography data reduction. *J. Appl. Crystallogr.* **43**, 186-190 (2010).

51 Winter, G. *et al.* DIALS: implementation and evaluation of a new integration package. *Acta Crystallogr. D Biol. Crystallogr.* **74**, 85-97 (2018).

52 Emsley, P. & Cowtan, K. Coot: model-building tools for molecular graphics. *Acta Crystallogr. D Biol. Crystallogr.* **60**, 2126-2132 (2004).

53 Murshudov, G. N., Vagin, A. A. & Dodson, E. J. Refinement of macromolecular structures by the maximum-likelihood method. *Acta Crystallogr. D Biol. Crystallogr.* **53**, 240-255 (1997).

54 Sali, A. & Blundell, T. L. Comparative protein modelling by satisfaction of spatial restraints. *J. Mol. Biol.* **234**, 779-815 (1993).

55 Søndergaard, C. R., Olsson, M. H. M., Rostkowski, M. & Jensen, J. H. Improved treatment of ligands and coupling effects in empirical calculation and rationalization of pKa values. *J. Chem. Theory Comput.* **7**, 2284-2295 (2011).

56 Frisch, M. J. *et al.* Gaussian 16 Rev. A.03. Gaussian, Inc., Wallingford, CT, 2016.

57 Wang, J., Wang, W., Kollman, P. A. & Case, D. A. Automatic atom type and bond type perception in molecular mechanical calculations. *J. Mol. Graph. Model.* **25**, 247-260 (2006).

58 Maier, J. A. *et al.* ff14SB: Improving the accuracy of protein side chain and backbone parameters from ff99sb. *J. Chem. Theory Comput.* **11**, 3696-3713 (2015).

59 Steinbrecher, T., Latzer, J. & Case, D. A. Revised AMBER Parameters for bioorganic phosphates. *J. Chem. Theory Comput.* **8**, 4405-4412 (2012).

60 Meagher, K. L., Redman, L. T. & Carlson, H. A. Development of polyphosphate parameters for use with the AMBER force field. *J. Comput. Chem.* **24**, 1016-1025 (2003).

61 Duarte, F. *et al.* Force field independent metal parameters using a nonbonded dummy model. *J. Phys. Chem. B* **118**, 4351-4362 (2014).

62 Liao, Q., Pabis, A., Strodel, B. & Kamerlin, S. C. L. Extending the nonbonded cationic dummy model to account for ion-induced dipole interactions. *J. Phys. Chem. Lett.* **8**, 5408-5414 (2017).

63 Case, D. A. *et al.* Amber 2016. University of California, San Francisco, CA, 2016.

64 Jorgensen, W. L., Chandrasekhar, J., Madura, J. D., Impey, R. W. & Klein, M. L. Comparison of simple potential functions for simulating liquid water. *J. Chem. Phys.* **79**, 926-935 (1983).

65 Berendsen, H. J. C., Postma, J. P. M., van Gunsteren, W. F., DiNola, A. & Haak, J. R. Molecular dynamics with coupling to an external bath. *J. Chem. Phys.* **81**, 3684-3690 (1984).

66 Ryckaert, J.-P., Ciccotti, G. & Berendsen, H. J. C. Numerical integration of the cartesian equations of motion of a system with constraints: molecular dynamics of n-alkanes. *J. Comput. Phys.* **23**, 327-341 (1977).

67 Schneider, T. & Stoll, E. Molecular-dynamics study of a three-dimensional one-component model for distortive phase transitions. *Phys. Rev. B* **17**, 1302-1322 (1978).

68 Darden, T., York, D. & Pedersen, L. Particle mesh Ewald: An N·log(N) method for Ewald sums in large systems. *J. Chem. Phys.* **98**, 10089-10092 (1993).

69 Roe, D. R. & Cheatham, T. E. PTRAJ and CPPTRAJ: Software for Processing and Analysis of Molecular Dynamics Trajectory Data. *J. Chem. Theory Comput.* **9**, 3084-3095 (2013).

70 Grant, B. J., Rodrigues, A. P. C., ElSawy, K. M., McCammon, J. A. & Caves, L. S. D. Bio3d: an R package for the comparative analysis of protein structures. *Bioinformatics* **22**, 2695-2696 (2006).

Acknowledgements

This work was supported by the Biotechnology and Biological Sciences Research Council (BBSRC) [Grant BB/M010996/1] via EASTBIO Doctoral Training Partnership studentships to B. J. R. and G. F., and by the Knut and Alice Wallenberg Foundation to S.C.L.K. [Grants 2018.0140 and 2019.0431] and by the European Union's Horizon 2020 Research and Innovation Programme *via* a Marie Sklodowska-Curie fellowship [Grant 890562] to M.C. The simulations were enabled by resources provided by the Swedish National Infrastructure for Supercomputing (SNIC, UPPMAX), partially funded by the Swedish Research Council [Grant 2016-07213]. X-ray diffraction data from R56A-*Pa*ATPPRT crystals were collected at Diamond Light Source in the UK.

Author contribution

G.F. carried out all experimental work except where noted, and wrote the manuscript. B.J.R. expressed and purified *Ab*HisZ and carried out the sequence comparison with *Pa*HisZ. J.N. expressed and purified R32/R56A/K57A-*Pa*HisG$_S$. M.S.A. supervised the protein crystallography work. M.C. carried out the computational chemistry work and wrote the manuscript. S.C.L.K. supervised the computational chemistry work and wrote the manuscript. R.G.d.S. Conceived and supervised the research and wrote the manuscript. All authors analysed data.

Competing interests

The authors declare no competing interests.

Additional information

Supplementary information The online version contains supplementary material available

Correspondence and requests for materials should be addressed to R. G. da Silva and S. C. L. Kamerlin.

Supplementary information

Allosteric rescue of catalytically impaired ATP phosphoribosyltransferase variants links protein dynamics to active-site electrostatic preorganisation

Gemma Fisher[1], Marina Corbella[2], Magnus S. Alphey[1], John Nicholson[1], Benjamin J. Read[1], Shina C. L. Kamerlin[2,3,*], and Rafael G. da Silva[1,*]

[1]School of Biology, Biomedical Sciences Research Complex, University of St Andrews, St Andrews, KY16 9ST, UK.

[2]Science for Life Laboratory, Department of Chemistry – BMC, Uppsala University, S-751 23 Uppsala, Sweden.

[3]School of Chemistry and Biochemistry, Georgia Institute of Technology, 901 Atlantic Drive NW, Atlanta, GA 30332, USA

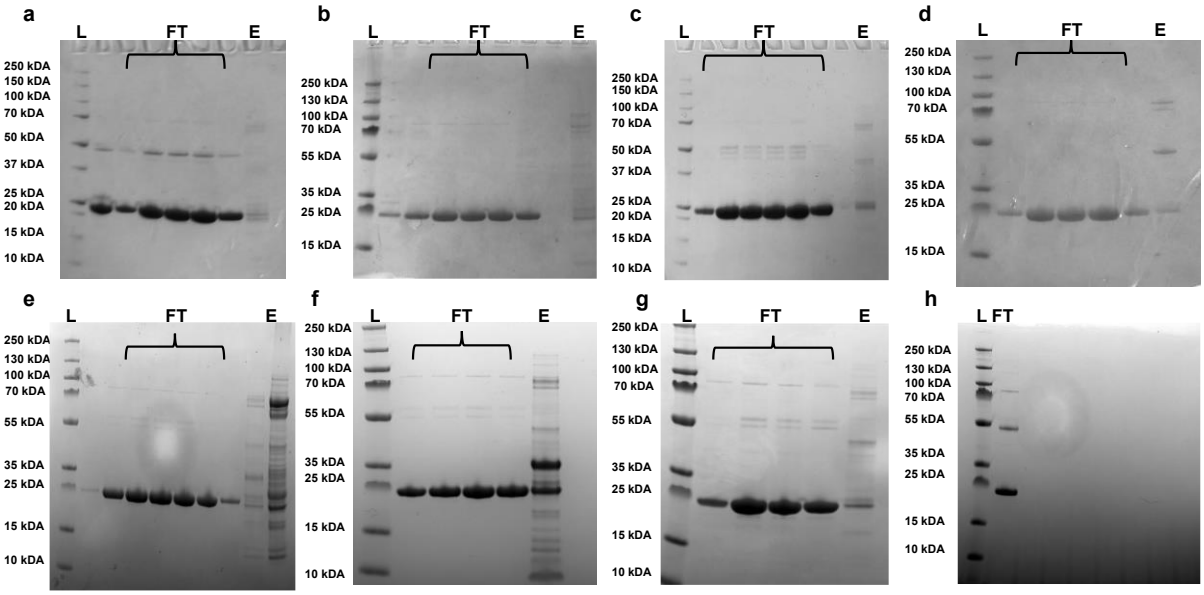

Supplementary Fig. 1 SDS-PAGE analysis of purified *Pa*HisG$_S$ mutants eluted from the HisTrap FF column in the second chromatography. **a** C115A. **b** C115S. **c** D179A. **d** D179N. **e** R32A. **f** R56A. **g** R56A/K57A. **h** R32A/R56A/K57A. Lanes are as follows: L is the MW marker; FT is the flowthrough, which was pooled; E is the elution, which was discarded. The MW marker is either the PageRuler Plus Prestained (**b, d**, **e**, **f**, **g**, **h**) or the Precision Plus All Blue Protein Prestained (**a**, **c**).

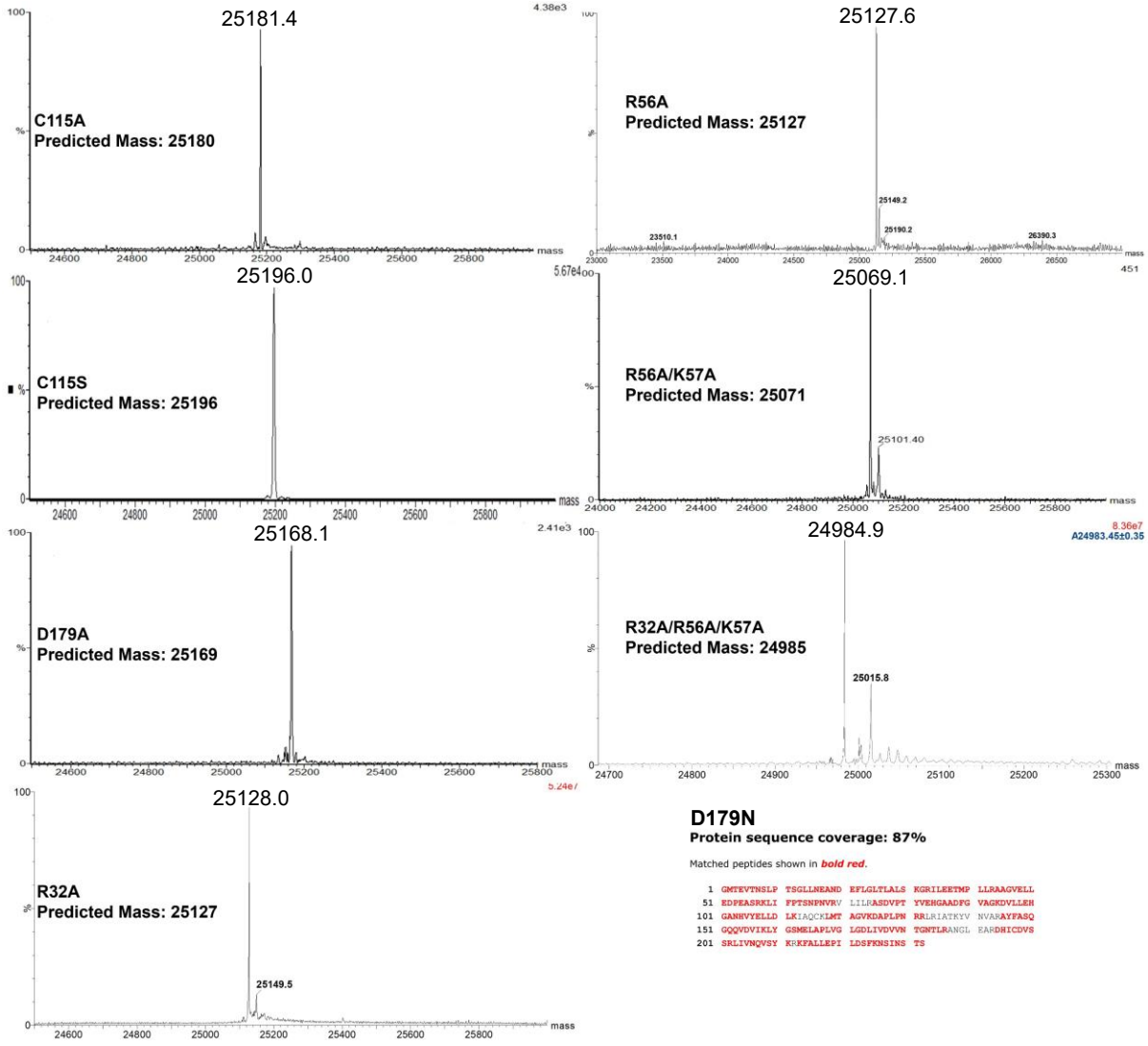

Supplementary Fig. 2 ESI/TFO-MS analysis of *Pa*HisG$_S$ mutants. For the C115A, C115S, D179A, R32A, R56A, R56A/K57A, and R32A/R56A/R32A mutants, the intact molecular mass was determined. For the D179N mutant, peptide mapping of the trypsin-digested protein was carried out.

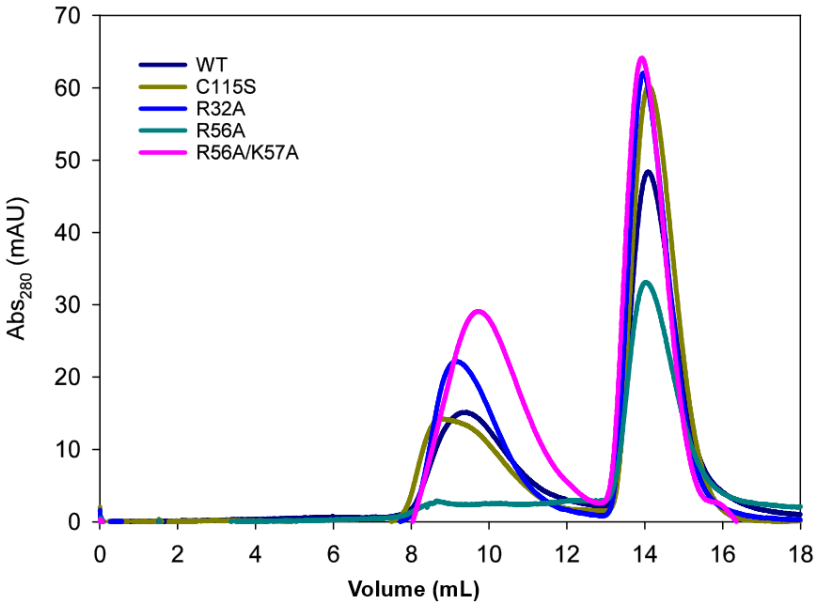

Supplementary Fig. 3 Analytical size-exclusion chromatography elution profile of *Pa*HisG$_S$ mutants. The peaks centred at ~14 mL indicate a dimer, while the peaks at ~9 mL reflect a higher oligomeric state.

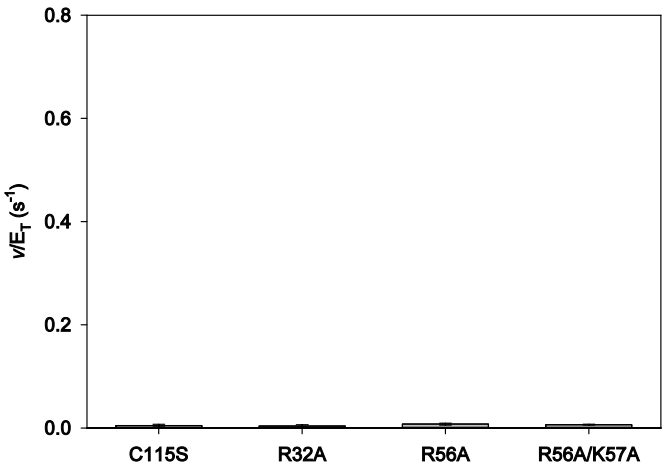

Supplementary Fig. 4 Apparent rate constants for reactions catalysed by *Pa*HisG$_S$ mutants in the presence of 20 μM BSA. Bars indicate mean ± standard error. The scale in the *y*-axis is the same as that of Fig. 2c.

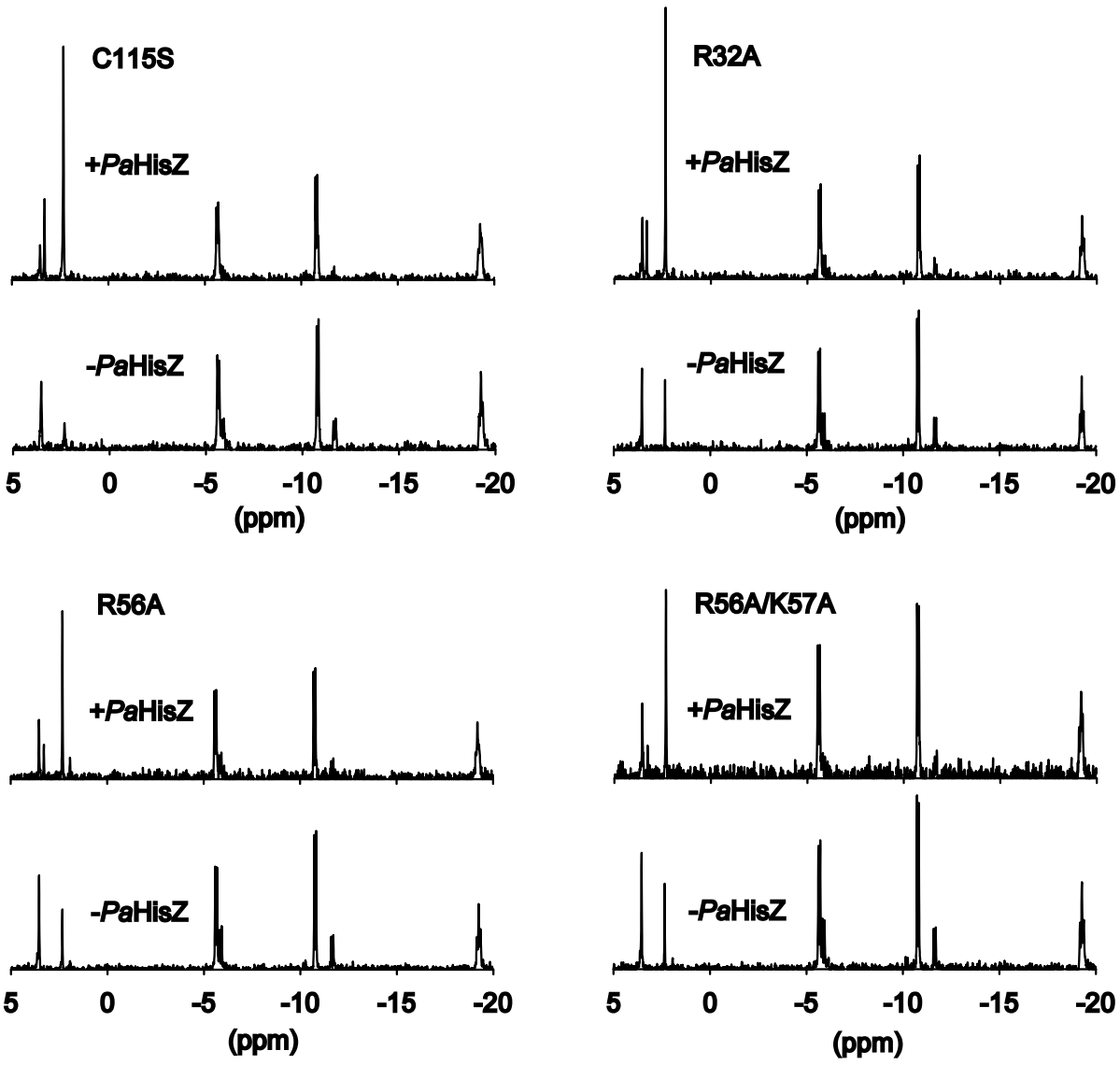

Supplementary Fig. 5 Analysis by ^{31}P-NMR spectroscopy of the reaction catalysed by *Pa*HisG$_S$ mutans in the presence and absence of *Pa*HisZ. The chemical shift at ~2.3 ppm corresponds to inorganic phosphate, which is produced by hydrolysis of the PP_i co-product by a pyrophosphatase used in the assay to drive forward the highly unfavourable ATPPRT reaction equilibrium.

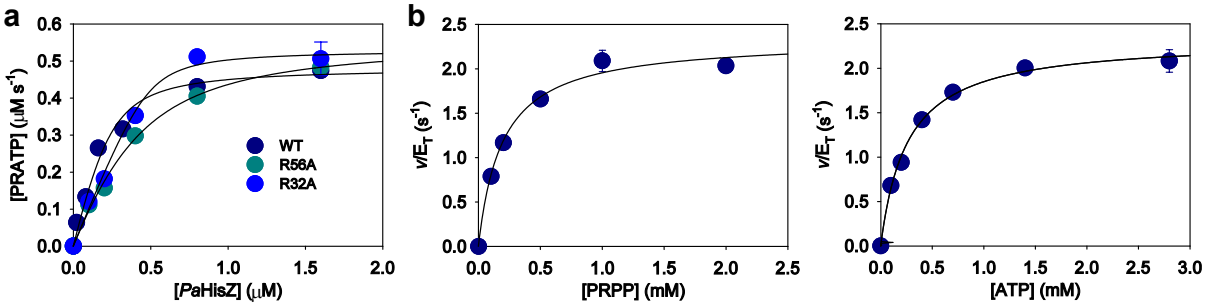

Supplementary Fig. 6 Binding and kinetics of His-tagged *Pa*HisZ **a** Dependence of rate of reaction catalysed by *Pa*HisG$_S$ variants on the concentration of His-tagged *Pa*HisZ. Data are mean ± standard error of two independent measurements. Best fit of the data to equation (3) is shown as solid line. The apparent K_D is 0.06 ± 0.03 μM for WT-*Pa*ATPPRT, 0.03 ± 0.02 μM for R32A-*Pa*ATPPRT, and 0.2 ± 0.1 μM for R56A-*Pa*ATPPRT. **b** Substrate saturation curves for WT-*Pa*ATPPRT with His-tagged *Pa*HisZ. Data are mean ± SEM of two independent measurements. Lines are best fit of the data to equation (1). Steady-state kinetic apparent k_{cat}, K_{PRPP} and K_{ATP} are 2.33 ± 0.05 s^{-1}, 0.19 ± 0.03 mM, and 0.26 ± 0.02 mM, respectively.

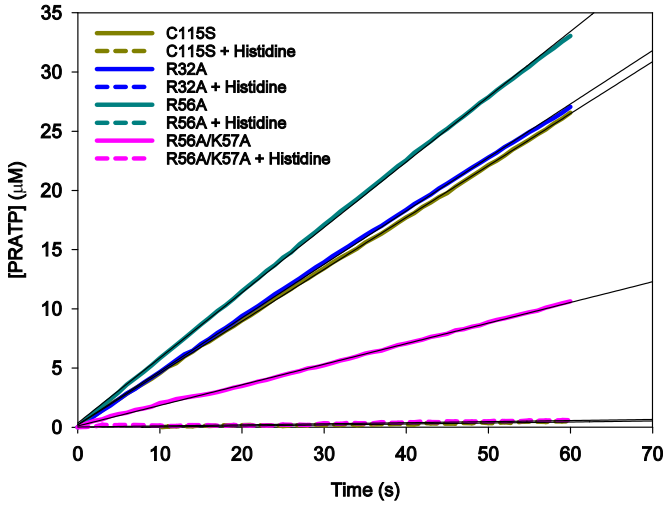

Supplementary Fig. 7 Product formation time course of the reaction catalysed by the rescued *Pa*ATPPR mutants in the presence and absence of 1 mM histidine. Traces are averages of two independent measurements, and black lines are linear regressions of the data.

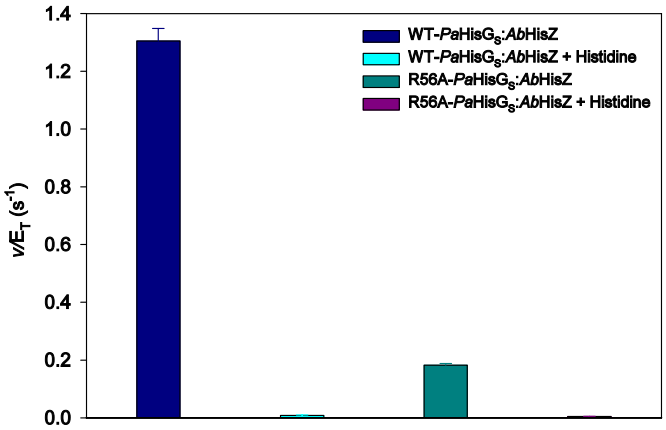

Supplementary Fig. 8 Apparent rate constants for *Pa*HisG$_S$:*Ab*HisZ-catalysed reaction in the presence and absence of 1 mM histidine. Bars indicate mean ± standard error.

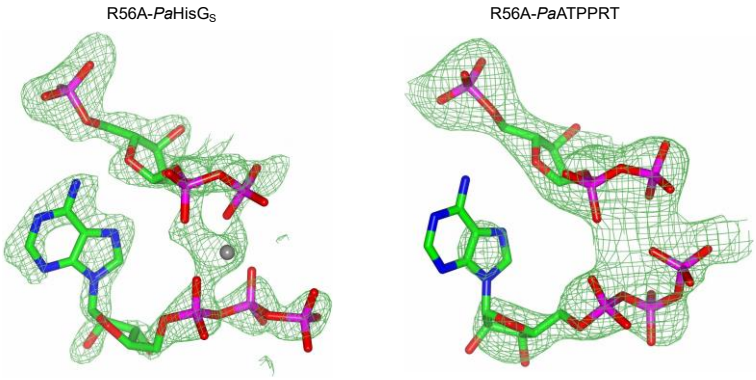

Supplementary Fig. 9 $F_{obs} - F_{calc}$ electron density omit maps at 2.5 σ for the substrates ATP and PRPP in the structures of R56A-*Pa*HisG$_S$ and R56A-*Pa*ATPPRT. Ligands are depicted as sticks with oxygen in red, nitrogen in blue, phosphorus in magenta, and carbon in green. The magnesium atom as a sphere.

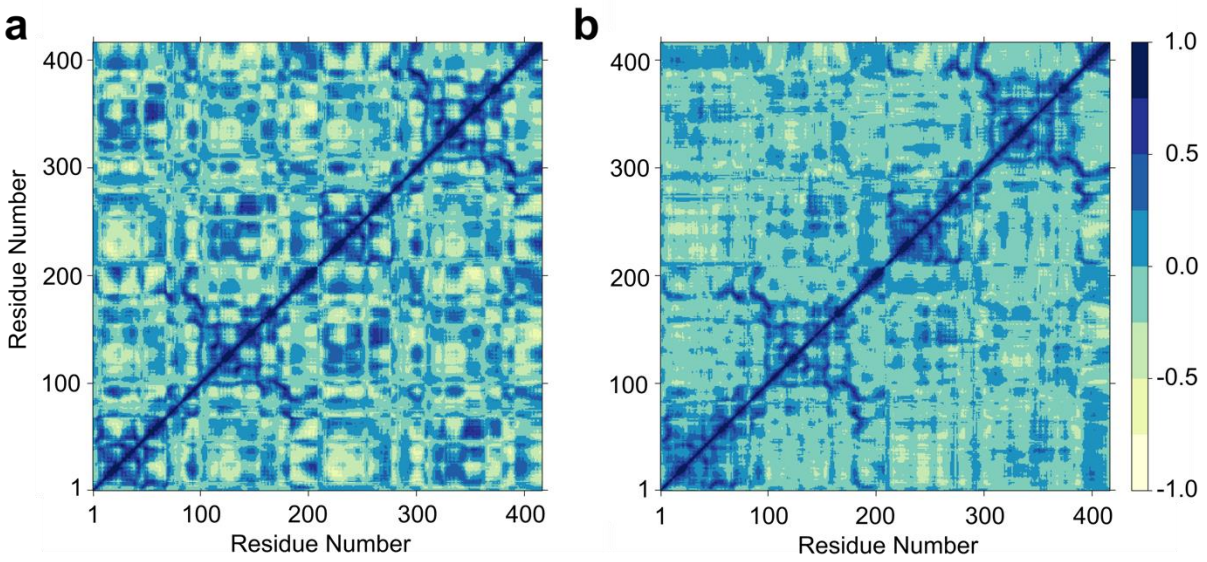

Supplementary Fig. 10 Dynamic cross-correlation matrices of the Cα-atoms. **a** Nonactivated WT-*Pa*HisG$_S$ dimer. **b** Activated WT-*Pa*HisG$_S$ dimer.

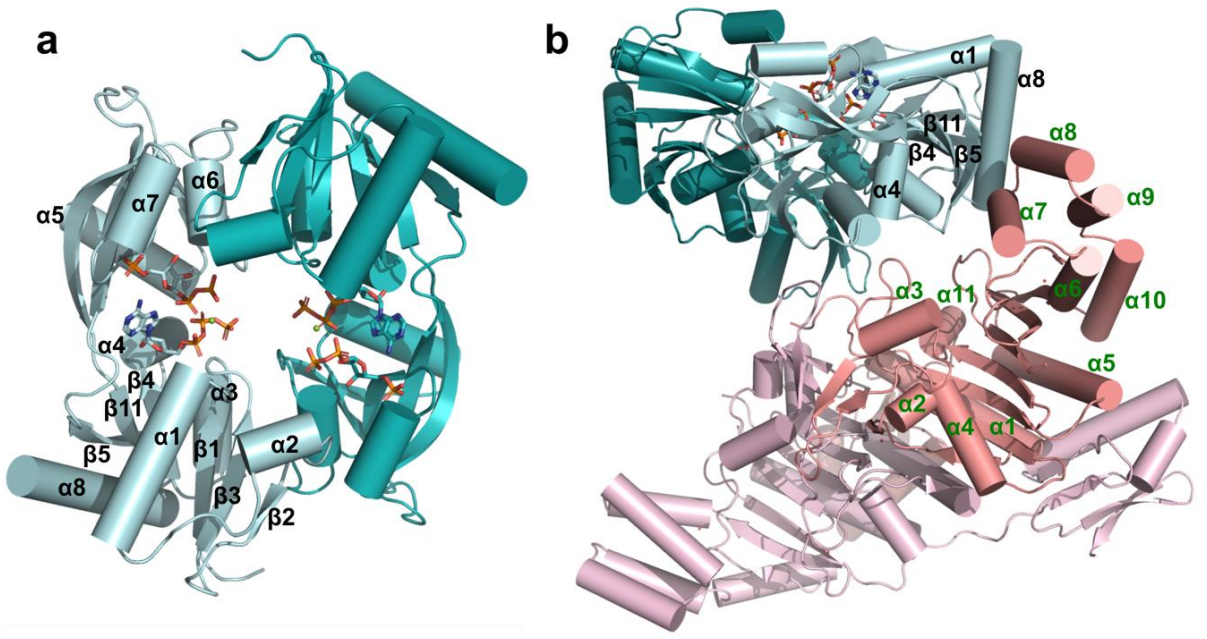

Supplementary Fig. 11 Secondary structure numbering of *Pa*ATPPRT (PDB ID: 6FU2). **a** Cartoon representation of the *Pa*HisG$_S$ dimer. **b** Cartoon representation of the *Pa*HisG$_S$ dimer in complex with one subunit of *Pa*HisZ tetramer. Substrates are depicted as sticks, and Mg^{2+} as spheres.

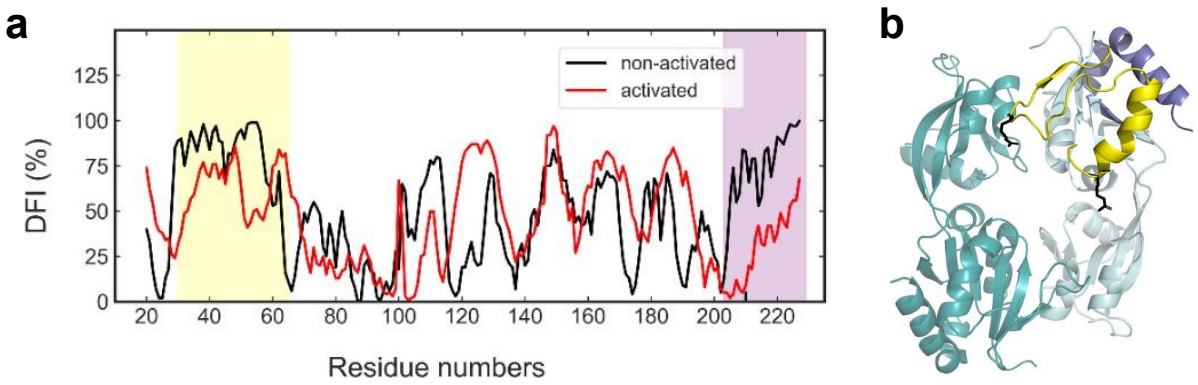

Supplementary Fig. 12 Dynamical flexibility indices. a DFI of monomeric subunits of nonactivated and activated *Pa*HisG$_S$, calculated based on 10 × 500 ns of MD simulations of each system. The higher the DFI score, the more flexible the protein region. **b** Representative structure of *Pa*HisG$_S$ onto which the two regions highlighted in yellow and purple in the DFI plot are mapped. The region highlighted in yellow encompass R32 and R56, whose side chains are depicted in stick models in black. The region highlighted in purple includes the interface with *Pa*HisZ.

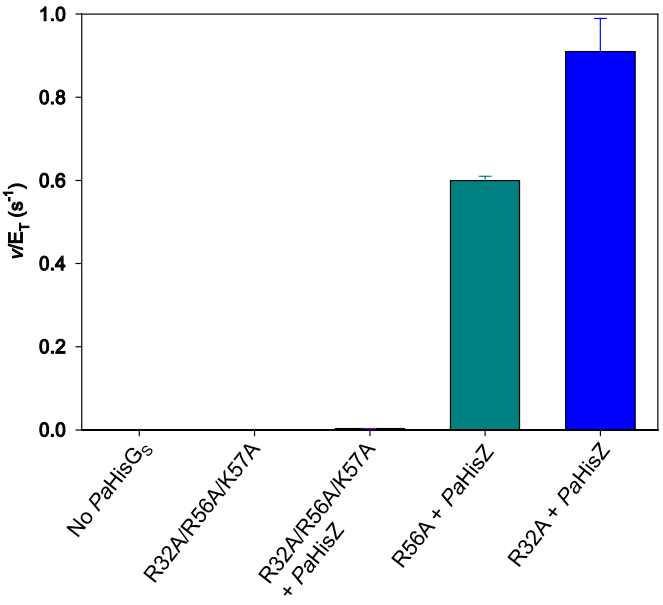

Supplementary Fig. 13 Apparent rate constants for single and triple mutants of *Pa*HisG$_S$.

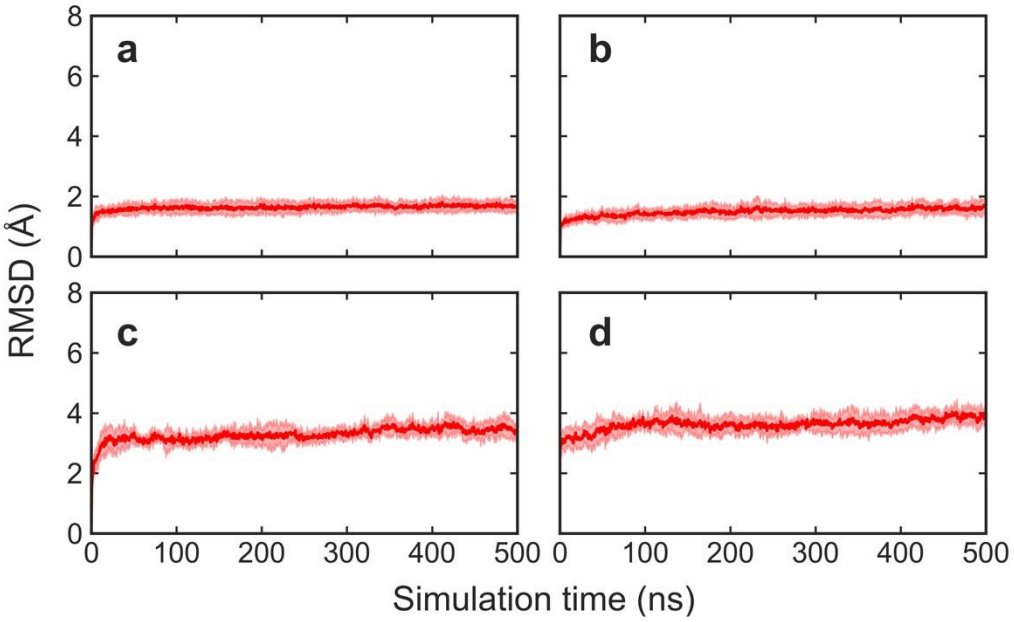

Supplementary Fig. 14 RMSD of all backbone heavy atoms from MD simulations. **a** WT-*Pa*HisG$_S$. **b** R56A-*Pa*HisG$_S$. **c** W|T-*Pa*ATPPRT. **d** R56A-*Pa*ATPPRT. Solid lines show rolling averages of the RMSD over the replicas, and the shaded regions show the corresponding standard deviations in these values.

Supplementary Table 1 Apparent rate constants (mean ± fitting error) for *Pa*HisG$_S$ variants from reactions monitored for 56 s.

***Pa*HisG$_S$**	***v*/E$_T$ (s^{-1})**
WT	0.0586 ± 0.0002
C115A	0.0134 ± 0.0002
C115S	N. d.*
D179A	0.0256 ± 0.0001
D179N	0.0164 ± 0.0002
R32A	N. d.*
R56A	N. d.*
R56A/K57A	N. d.*

*No product formation detected above background noise.

Supplementary Table 2 Steady-state kinetic parameters (mean ± fitting error) for WT-, C115A-, D179A-, and D179N-*Pa*HisG$_S$.

***Pa*HisG$_S$**	**k_{cat} (s^{-1})**	**K_{PRPP} (mM)**	**K_{ATP} (mM)**
WT	0.081 ± 0.003	0.40 ± 0.06	1.2 ± 0.2
C115A	0.020 ± 0.001	0.42 ± 0.07	2.2 ± 0.3
D179A	0.030 ± 0.001	0.16 ± 0.01	0.8 ± 0.2
D179N	0.020 ± 0.002	0.13 ± 0.02	1.7 ± 0.5

Supplementary Table 3 DSF-based T_m (mean ± fitting error) for *Pa*HisG$_S$ mutants in the presence and absence of PRPP.

***Pa*HisG$_S$**	**(–PRPP) T_m (°C)**	**(+PRPP) T_m (°C)**	**ΔT_m (°C)**
WT	57.83 ± 0.07	65.4 ± 0.09	+7.8 ± 0.2
C115S	56.75 ± 0.09	63.53 ± 0.09	+8.8 ± 0.2
R32A	60.39 ± 0.06	63.81 ± 0.06	+3.4 ± 0.1
R56A	58.11 ± 0.07	62.59 ± 0.07	+4.5 ± 0.2
R56A/K57A	56.77 ± 0.07	60.3 ± 0.1	+3.5 ± 0.2

Supplementary Table 4 X-Ray diffraction data collection and refinement statistics.

	R56A-*Pa*HisG$_S$	R56A-*Pa*ATPPRT
Data Collection		
PDB ID	7Z8U	7Z6R
Space group	I2	C2
Cell dimensions		
***a,b,c* (Å)**	70.09, 33.90, 89.27	102.16, 145.53, 93.81
α,β,γ (°)	90.00, 103.52, 90.00	90.00, 102.48, 90.00
Resolution (Å)	22.01 – 2.00 (2.05 – 2.00)	56.97 – 2.55 (2.61 – 2.55)
R_{merge}	0.11 (0.36)	0.17 (3.17)
I/σI	7.2 (2.5)	10.9 (0.8)
Completeness (%)	93.8 (88.2)	99.9 (99.3)
Redundancy	3.0 (2.6)	6.5 (7.1)
CC ½	0.99 (0.84)	0.99 (0.28)
Refinement		
Resolution (Å)	22.01 – 2.00	56.97 - 2.55
No. reflections	12411	41555
R_{work}/R_{free} (%)	22.1/26.8	23.3/27.6
No. atoms		
Protein	1573	8431
Ligand/ion	54	106
Water	42	16
B-factors		
Protein	21.04	79.9
Ligand/ion	40.01	104.8
Water	20.24	58.3
r.m.s. deviations		
Bond lengths (Å)	0.008	0.005
Bond angles (°)	1.623	1.374
Ramachandran		
Favoured (%)	97	96
Allowed (%)	3	4
Outliers (%)	0	0

Numbers in brackets are from the highest resolution shell.

Supplementary Table 5 Primers used for site-directed mutagenesis of *Pa*HisG$_S$.

***Pa*HisGs Mutation**	**Forward Primer**	**Reverse Primer**
C115A	5′ - TTGCGCAGGCTAAACTGATGACCGCCGGTGTCAAAGACG - 3´	5′ - ATCAGTTTAGCCTGCGCAATCTTCAGATCCAACAGTTCATAAACGTGGTTC - 3´
C115S	5′ - TTGCGCAGTCTAAACTGATGACCGCCGGTGTCAAAGACG - 3´	5′ - ATCAGTTTAGACTGCGCAATCTTCAGATCCAACAGTTCATAAACGTGGTTCG - 3´
D179A	5′ - TCGTGGCCACCGGTAATACGCTGCGTG - 3′	5′ - ACCGGTGGCCACGACGTCAACAATCAGGTCACCCAGGC -3′
D179N	5′ - GTCGTGAACACCGGTAATACGCTGCGTGCGAACGG - 3′	5′ - CCGGTGTTCACGACGTCAACAATCAGGTCACCCAGGC -3′
R32A	5′ - AAGGGTGCCATCCTGGAAGAGACTATGCCGCTGTTGCG-3′	5′ - CAGGATGGCACCCTTGCTCAGTGCCAGGGTCAGACC-3′
R56A	5′- GCGCTAAGCTGATCTTCCCGACCAGCAACCCTAATGTG-3′	5′- GGAAGATCAGCTTAGCGCTCGCTTCCGGATCTTCCAGC-3′.
R56A/K57A	5′- GCGCTGCGCTGATCTTCCCGACCAGCAACCCTAATGTG-3’	5′- GAAGATCAGCGCAGCGCTCGCTTCCGGATCTTCCAGC-3’

Supplementary Table 6 Non-standard force field parameters used to describe the substrate PRPP in the conventional MD simulations.

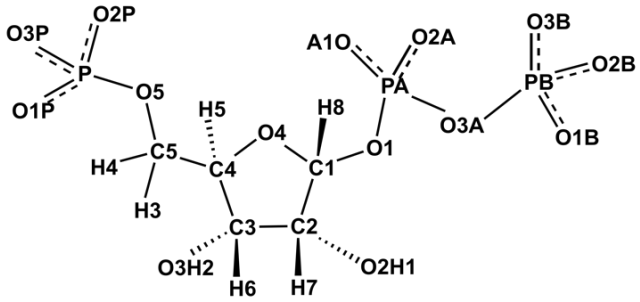

Atom Name	Atom type	Charge	Atom Name	Atom type	Charge
H1	HO	0.434144	O3	OH	-0.723957
H2	HO	0.471932	O4	OS	-0.605498
H3	H1	-0.011850	O5	OS	-0.445750
H4	H1	-0.011850	P	P	1.288976
H5	H1	0.094980	O1P	O3	-0.983784
H6	H1	-0.004183	O2P	O3	-0.983784
H7	H1	-0.028089	O3P	O3	-0.983784
H8	H2	0.010573	PA	P	1.195239
C1	CT	0.496695	O1A	O2	-0.872464
C2	CT	0.074132	O2A	O2	-0.872464
C3	CT	0.095379	O3A	OS	-0.540575
C4	CT	0.399838	PB	P	1.234914
C5	CT	0.111590	O1B	O3	-0.970435
O1	OS	-0.292571	O2B	O3	-0.970435
O2	OH	-0.636483	O3B	O3	-0.970435

Supplementary Table 7 Non-standard force field parameters used to describe the substrates in the conventional MD simulations.

Restraint Index	Atom ID	Distances (Å)			Restraints (kcal mol^{-1} Å^{-2})		
		r^1	r^2	r^3	r^4	rk^2	rk^3
Distance 1	PRP@P Asp179@N	0.0	3.0	4.2	4.5	0.0	10.0
Distance 2	PRP@P Thr180@N	0.0	3.0	4.2	4.5	0.0	10.0
Distance 3	PRP@P Thr183@N	0.0	3.0	4.2	4.5	0.0	10.0
Distance 4	PRP@O3 Asp176@OD2	0.0	2.5	3.0	3.5	0.0	10.0
Distance 5	ATP@O3* Asp94@CG	0.0	3.0	3.7	4.5	0.0	10.0